

Enantioselective Cycloadditions of Vinyl Pyridines and Mechanistic Features of Excited-State  
Photocatalytic Reactions

By

Steven Jeffrey Chapman

A dissertation submitted in partial fulfillment of  
the requirements for the degree of

Doctor of Philosophy

(Chemistry)

at the

UNIVERSITY OF WISCONSIN–MADISON

2021

Date of final oral examination: December 01, 2021

The dissertation is approved by the following members of the Final Oral Committee:

Tehshik P. Yoon, Professor, Chemistry

Jennifer M. Schomaker, Professor, Chemistry

Robert J. McMahon, Professor, Chemistry

Andrew J. Boydston, Yamamoto Family Professor, Chemistry



Enantioselective Cycloadditions of Vinyl Pyridines and Mechanistic Features of Excited-State  
Photocatalytic Reactions

Steven Jeffrey Chapman

Under the supervision of Professor Tehshik P. Yoon

at the University of Wisconsin–Madison

Abstract

The development of stereoselective, photocatalytic transformations has seen immense interest over the past decade. This is due, in part, to the mechanistically distinct reactivity of excited-state intermediates compared to their ground state analogues. The work in this dissertation broadly focuses on new photocatalytic strategies for excited-state transformations. These strategies afforded mechanistic insights toward understanding the activation and stereocontrol of these photochemical reactions. Notably, these insights include the discovery of excited-state matched/mismatched catalyst pairs, the dependence of photocatalyst counteranion identity on a reaction rate, and the full kinetic analysis of an enantioselective excited-state reaction. These insights are currently being implemented in new reactions and applications in our lab.

## Acknowledgments

Above all, I need to thank and express immense gratitude for my principal Ph.D. advisor, Tehshik Yoon. Since my rotation with the lab, Tehshik showed incredible patience with me, not only while I was learning the fundamentals of photochemistry and asymmetric catalysis that would soon become the foundation of my Ph.D. work, but also while I learned what questions to ask and how to ask them. While many lessons Tehshik taught me have been tough to hear and even tougher to implement, each has improved my ability as a scientist, as an independent thinker, and improved me as a person. I am continuously grateful for Tehshik's mentorship and guidance during this particularly impressionable time of my professional career. I hope to carry forward many of his values, his passion for education, and his relentless drive for academic excellence into my future career.

My graduate education wouldn't be complete without Jennifer Schomaker and Bob McMahon serving as invaluable committee members since my 2<sup>nd</sup> year. Jen and Bob challenged me and my scientific thought process with meaningful questions and feedback during each step of my Ph.D. They helped teach me what scientific problems were worth pursuing, and they taught me lessons in efficient scientific communication. Plus, Jen and Bob believed in my progress through the Ph.D. even on the days I couldn't see it for myself.

AJ Boydston joined the department at the end of my 2<sup>nd</sup> year, and he has been instrumental in developing my scientific interests toward a polymers / organic materials direction. From joining his group meetings, brainstorming about research ideas, or chatting about potential postdoc positions, AJ treated me as one of his own students and always kept his door open for me. Through his actions, AJ taught me to be generous with my time and to build collaborations within the department for a richer academic experience for everyone.

The Yoon lab is composed of a variety of uniquely passionate and energetic individuals. Everyone in the Yoon lab, past and present, has impacted my time in graduate school. I want to specifically express my appreciation for my officemates in MiddleEarth over the years: Kaz Skubi, Niecia Flikweert, Jian Zheng, Luca Capaldo, Yukki Li, and Grace Lutovsky. The folks in my office made work a pleasure every day. My officemates were there to support me on the rough days and to celebrate on the exciting ones. I need to thank Wesley Swords for being a key part of nearly all my projects in the lab, listening to my (often extemporaneous) research ideas, and being so generous of his resources to help me become the best scientist I can be. Wes showed me how to excel at being a postdoc, and I hope to take these lessons forward into my postdoc soon. I would be remiss for not thanking Jesse Kidd, Sam Cahoon, and Matt Genzink for their constant encouragement and enthusiastic company during the long days in the lab. Everyone in the group made the daily work a joy, and I'm overly thankful for each day together and each lesson you taught me.

My Ph.D. would not be possible without the help from the instrumentation directors and staff. I need to thank Charlie Fry, Heike Hofstetter, and Cathy Clewett for maintaining the NMR facilities and trainings. Thanks to Martha Vestling and Bob Shanks for maintaining the mass spectrometry facility. Thanks to Ilia Guzei for maintaining the X-ray laboratories. Thanks to Tracy Drier for maintaining the glass shop and teaching his glassblowing class. Additionally, thanks to Jeff Nielsen and Rob McClain for their daily support of the facilities and instrumentation that enable our research.

## Table of Contents

<b>Abstract</b> .....	<b>i</b>
<b>Acknowledgments</b> .....	<b>ii</b>
<b>Table of Contents</b> .....	<b>iv</b>
<b>List of Figures</b> .....	<b>x</b>
<b>List of Schemes</b> .....	<b>xvii</b>
<b>List of Tables</b> .....	<b>xxi</b>
 <b>Chapter 1. Enantioselective Photochemical Reactions Activated by Chiral Phosphoric</b>	
<b>Acids</b> .....	<b>1</b>
1.1. Introduction.....	2
1.1.1. Single Electron Transfer, Atom Transfer, and Energy Transfer Processes .....	2
1.1.2. Primary versus Secondary Photochemical Reactions .....	4
1.1.3. Scope of this Chapter .....	4
1.2. Modes of Photochemical Activation via Brønsted Acid Coordination .....	5
1.3. Direct Photoexcitation in Tandem with a Chiral Phosphoric Acid.....	7
1.4. Chiral Phosphoric Acid Control in Photoredox Catalytic Cycles.....	11
1.5. Chiral Phosphoric Acid Activation in Dexter Energy Transfer Processes .....	24
1.6. Enantioselective Proton Coupled Electron Transfer.....	27
1.7. Conclusions.....	33

1.8. References.....	33
<b>Chapter 2. Cooperative Stereoinduction in Asymmetric Photocatalysis.....</b>	<b>38</b>
2.1. Background.....	39
2.1.1. Matched/Mismatched Effects .....	39
2.1.2. Current Asymmetric Dual Photocatalysis Systems .....	39
2.2. Optimization of the Enantioselective Vinylheteroarene [2+2] Photocycloaddition .....	42
2.3. Original Observation of the Excited-State Matched/Mismatched Effects.....	43
2.4. Scope of the Enantioselective [2+2] Photocycloaddition .....	44
2.5. Mechanistic Investigations.....	46
2.5.1. Energy Transfer to the Protonated Vinyl Pyridine .....	46
2.5.2. Classical Energy-Transfer Mechanism.....	47
2.5.3. Possible Ways for Cooperative Stereoinduction.....	48
2.5.3.1. Ground State Interaction .....	48
2.5.3.2. Excited-State Interaction.....	48
2.5.4. Diastereotopic Reactions with Styrene .....	49
2.6. Proposed Mechanism.....	51
2.7. Computation Investigations .....	51
2.8. Conclusion .....	51
2.9. Contributions .....	52
2.10. Supporting Information.....	53
2.10.1. General Information.....	53

2.10.2. Racemic [Ir(dtbbpy) <sub>2</sub> (dMeObpy)]PF <sub>6</sub> Photocatalyst Synthesis.....	56
2.10.3. Enantioenriched [Ir(dtbbpy) <sub>2</sub> (dMeObpy)]PF <sub>6</sub> Photocatalyst Synthesis .....	57
2.10.4. Starting Material Syntheses .....	61
2.10.5. (R)-4-biphenyl SPINOL Phosphoric Acid Synthesis.....	67
2.10.6. Racemic [2+2] Photocycloadditions .....	71
2.10.7. Enantioselective [2+2] Photocycloadditions .....	73
2.10.8. Unsuccessful Substrates for the Enantioselective [2+2] Photocycloaddition.....	100
2.10.9. Screening of CPAs for the Parent [2+2] Photocycloaddition .....	101
2.10.10. NMR Binding Experiments .....	104
2.10.11. UV-Vis/Emission Experiments.....	109
2.10.12. Stern–Volmer Experiments.....	112
2.10.13. Time-Resolved Emission .....	113
2.10.14. <sup>1</sup> H, <sup>13</sup> C, <sup>19</sup> F, and <sup>31</sup> P NMR Spectra.....	118
2.10.15. SFC Traces.....	179
2.10.16. X-Ray Structure of <b>2.2</b> .....	229
2.10.17. X-Ray Structure of Δ-[Ir].....	242
2.11. References.....	339
 <b>Chapter 3. Discovery and Elucidation of Counteranion Dependence in Photoredox</b>	
<b>Catalysis.....</b>	<b>343</b>
3.1. Previous Publication of this Work .....	344
3.2. Abstract .....	344
3.3. Introduction.....	345



3.4. Results and Discussion .....	347
3.4.1. Counterion Effects in Radical Cation Cycloadditions.....	347
3.4.2. Spectroscopic, Electrochemical, and Quantum Yield Studies.....	352
3.4.3. Hydrogen-Bonding Anion Binders as Cocatalysts.....	356
3.5. Conclusions.....	360
3.6. Contributions .....	361
3.7. Supporting Information.....	362
3.7.1. General Experimental Information for Synthetic Studies.....	362
3.7.2. Synthesis of Polypyridyl Ru(II) Complexes.....	363
3.7.3. Visible Light Photocatalysis of Radical Cation [4+2] Diels–Alder Cycloadditions	371
3.7.4. UV-Vis Spectra, Photoluminescence Spectra, and Chain Length Measurements....	372
3.7.5. Cyclic Voltammetry Experiments.....	376
3.7.6. <sup>1</sup> H NMR Experiments .....	380
3.7.7. <sup>1</sup> H, <sup>13</sup> C, <sup>19</sup> F, <sup>11</sup> B, and <sup>31</sup> P NMR spectra.....	385
3.8. References.....	420
<b>Chapter 4. Visible Light Photosensitized Di-<math>\pi</math>-Methane Rearrangement.....</b>	<b>424</b>
4.1. Background.....	425
4.2. Reaction Optimization .....	426
4.3. Scope of the Rearrangement with Visible Light.....	427
4.4. Trends with the Electronics of the Substrate .....	428
4.5. Effects of a Lewis Acid.....	429

4.6. Proposed Mechanism .....	432
4.7. Conclusion .....	433
4.8. Contributions .....	433
4.9. Supporting Information.....	434
4.9.1. Reagent Preparation .....	434
4.9.2. Product Characterization.....	434
4.9.3. Synthesis of Di- $\pi$ -Methane Substrates .....	435
4.9.4. Di- $\pi$ -Methane Photochemical Rearrangements.....	447
4.9.5. $^1\text{H}$ and $^{13}\text{C}$ NMR Spectra .....	456
4.9.6. IR Spectra.....	508
4.9.7. X-Ray Structure of <b>4.18</b> .....	528
4.10. References.....	541
<b>Chapter 5. Reaction Progress Kinetic Analysis using in situ LED-NMR.....</b>	<b>543</b>
5.1. Background.....	544
5.1.1. Reaction Progress Kinetic Analysis.....	544
5.1.2. “Same Excess” Protocol for RPKA .....	545
5.1.3. Variable Time Normalization Analysis .....	547
5.2. Preliminary Results.....	547
5.2.1. “Same Excess” Experiments.....	548
5.2.2. VTNA Experiments .....	551
5.2.3. Diastereotopic Reaction using a Chiral Maleimide .....	553

5.3. Future Directions .....	555
5.4. Contributions .....	555
5.5. Supporting Information.....	555
5.5.1. General Methods and Materials .....	555
5.5.2. NMR Data Acquisition .....	556
5.5.3. LED Kinetic Data Acquisition.....	556
5.5.4. In Situ Experiments.....	562
5.5.5. Light Intensity Initial Rates; room temperature.....	563
5.5.6. Same Excess Experiments .....	564
5.5.7. VTNA Methods .....	565
5.6. References.....	567
 <b>Appendix A. Tri-Catalytic, Chiral Hydrogen Bonding Catalysis for the Brønsted Acid</b>	
<b>Activation of Enantioselective [2+2] Photocycloadditions .....</b>	<b>569</b>
A.1 Background .....	570
A.2 Preliminary Results .....	573
A.3 Future Directions.....	575
A.4 Supporting Information.....	577
A.4.1 SFC traces .....	577
A.5 References.....	580

## List of Figures

### Chapter 1

Figure 1.1 Mechanisms of Single Electron Transfer and Energy Transfer. .... 3

Figure 1.2 A)  $S_0$ – $S_1$  Lowering of Enones via Brønsted Acid Coordination. B) Representative Iminium Ion Activation of Vinyl Pyridines. .... 6

### Chapter 2

Figure 2.1 (A) Matched/mismatched effects observed in fundamental ground-state asymmetric catalysis. (B) Examples of asymmetric dual-catalytic photochemical reactions where chiral transition metal photocatalysts have been used as racemates. (C) Ooi's report showing no dependence of reaction selectivity on the chirality of the [Ir] photocatalyst. (D) This work highlighting cooperative stereinduction between the [Ir] photocatalyst and the CPA. .... 41

Figure 2.2 (A) Optimization of the enantioselective [2+2] photocycloaddition of vinylpyridine **2.1** using racemic [Ir] as the photocatalyst. (B) Schematic depiction of Brønsted acid activation of **2.1**. (C) Empirical observation of dual-catalytic matched/mismatched effects in the photocycloaddition of **2.1**. (D) Highlighting the marked influence of the chiral [Ir] on the selectivity of the reaction. (E) X-ray crystal structure of **2.2**•HCl. .... 44

Figure 2.3 Scope of the enantioselective [2+2] photocycloaddition. Conditions matched entry 6 in Figure 2.2A, 0.31 mmol. Diastereomer ratios (d.r.) were determined by proton nuclear magnetic resonance ( $^1\text{H}$  NMR) analysis of the unpurified reaction mixture. Enantiomer ratios were determined using chiral supercritical fluid chromatography (SFC) analysis. .... 46

Figure 2.4 (A) Stern–Volmer plot of the quenching of excited-state  $\Delta$ -[Ir] with protonated **2.1** (**2.1H<sup>+</sup>**). Dashed line is a linear regression of the data. (B) Overlaid emission spectra of  $\Delta$ -[Ir] (solid lines) and  $\Lambda$ -[Ir] (dashed lines) in the presence of (**R**)-CPA3 and (**R**)-CPA3 with 10 equiv. **2.1**. With only (**R**)-CPA3 the emission of  $\Delta$ -[Ir] and  $\Lambda$ -[Ir] nearly overlay, while with both (**R**)-CPA3 and **2.1** a larger increase in emission is observed for  $\Delta$ -[Ir]. (C) Quenching of emission of the mixture of  $\Delta/\Lambda$ -[Ir], (**R**)-CPA3, and **2.1** by styrene along with Stern–Volmer plots. (D) Proposed mechanism. .... 50

Figure 2.5 Time Resolved Emission Experimental Setup ..... 55

Figure 2.6 Unsuccessful Substrates for the Enantioselective [2+2] Photocycloaddition ..... 100

Figure 2.7 Diverse Screen of Chiral Brønsted Acids During Reaction Optimization ..... 101

Figure 2.8 Screen of SPINOL CPAs During Reaction Optimization ..... 103

Figure 2.9 NMR Titration with Increasing Quantity of (**R**)-CPA3 from Bottom to Top. Significant ppm Shifts Measured from the Vinyl Pyridine **2.1** ..... 105

Figure 2.10 1:1 Binding Measured Between (**R**)-CPA3 and **2.1** ..... 106

Figure 2.11 <sup>1</sup>H NMR Titration with Increasing (**R**)-CPA3–Pyridine Quantities Indicating No ppm Shift and No Ground State Interaction ..... 107

Figure 2.12 <sup>19</sup>F NMR Titration with Increasing (**R**)-CPA3–Pyridine Quantities Indicating No ppm Shift and No Ground State Interaction ..... 108

Figure 2.13 UV-visible spectra (red line) and emission spectra (dashed green line) of the Ir photocatalyst. The triplet energy ( $E_T$ ) of the photocatalyst was determined from the X-intercept of

a linear regression fit to the blue edge of the emission spectra (solid blue line, X-intercept = 485 nm). $E_T = 2.55$ eV, $58.8$ kcal mol <sup>-1</sup> .....	109
Figure 2.14 UV-visible spectra of the components of the parent reaction. [Ir] = 40 uM, while the other species are close to reaction concentrations. Notably, there is only a subtle difference between the spectra acquired with all three species present and the sum of individual [Ir] and CPA3+2.1 spectra (dashed line). The slight difference can be ascribed to error in the concentrations of the individual components between the acquisition of the spectra. ....	110
Figure 2.15 Experimental and simulated spectra at different concentrations of 5:1 2.1:CPA3 mixture. At every concentration, the spectra have little distinction barring that which can be ascribed to subtle concentration variations. ....	111
Figure 2.16 Photoluminescence quenching of $\Delta$ -[Ir] by vinyl pyridine in the presence of excess trifluoroacetic acid. A) Photoluminescence spectra at the indicated concentration of 2.1 and B) Stern–Volmer plot.....	112
Figure 2.17 Time-resolved emission of Ir photocatalyst in toluene (symbols). Long and short pass filters used to define the range of emission collected. Three ranges were acquired to ensure accuracy of the measured lifetime. Lifetimes were acquired under an argon atmosphere. Excitation at 420 nm. Lifetime of Ir photocatalyst $\tau = 170$ ns. ....	113
Figure 2.18 Time-resolved photoluminescence decays for the <i>matched</i> conditions: $\Delta$ -Ir = 40 $\mu$ M, CPA3 = 1 mM, vinyl pyridine = 10 mM. A) Absolute intensities, B) Normalized intensities, normalized at 200 ns. Wavelength ranges of filter combinations are indicated in the legend. Black lines correspond to the biexponential fitting. Table 2.1 provides the pre-exponential values and lifetimes of the fits. ....	115

Figure 2.19 Time-resolved photoluminescence decays for the <i>mismatched</i> conditions: $\Lambda$ -Ir = 40 $\mu$ M, CPA3 = 1 mM, vinyl pyridine = 10 mM. Wavelength ranges of filter combinations are indicated in the legend. Black lines correspond to the biexponential fitting. Table 2.1 provides the pre-exponential values and lifetimes of the fits. ....	116
Figure 2.20 A molecular drawing of Yoon60 shown with 50% probability ellipsoids. Only selected H atoms are shown. ....	231
Figure 2.21 A molecular drawing of the unit cell content of Yoon77 shown with 50% probability ellipsoids. All H atoms are omitted but all disordered atoms are shown. ....	246
Figure 2.22 A molecular drawing of the Ir1 complex of Yoon77 shown with 30% probability ellipsoids. All H atoms and minor disorder components are omitted. ....	247
Figure 2.23 A molecular drawing of the Ir1 complex of Yoon77 shown with 30% probability ellipsoids. All H atoms are omitted but all disorder components are shown. ....	248
Figure 2.24 A molecular drawing of the Ir2 complex of Yoon77 shown with 30% probability ellipsoids. All H atoms and minor disorder components are omitted. ....	249
Figure 2.25 A molecular drawing of the Ir complex of Yoon77 shown with 30% probability ellipsoids. All H atoms are omitted but all disorder components are shown. ....	250
Figure 2.26 A molecular drawing of the disordered P1 anion of Yoon77 shown with 50% probability ellipsoids. Both disorder components are shown. ....	251
Figure 2.27 A molecular drawing of the disordered P2 anion of Yoon77 shown with 50% probability ellipsoids. Both disorder components are shown. ....	252

Figure 2.28 A molecular drawing of the acetone solvent molecules in structure Yoon77 shown with 50% probability ellipsoids. All H atoms are omitted but all disordered atoms are shown. All molecules except O5 have partial occupancy. The total number of solvent molecules is 3.91.. 253

### Chapter 3

Figure 3.1 Structurally varied Ru(II) photocatalysts. .... 346

Figure 3.2 (A) Stern–Volmer plots for excited-state quenching of catalysts **3.3a–c** in CH<sub>2</sub>Cl<sub>2</sub>. (B, C) Effect of counteranion identity on excited-state properties of [Ru(btfmtb)<sub>3</sub>](X)<sub>2</sub>, where X is indicated in the legend. (B) Absorption (solid line) and photoluminescence (dashed line) spectra in MeCN. (C) Absorption (solid line) and photoluminescence (dashed line) spectra in CH<sub>2</sub>Cl<sub>2</sub>.  
..... 351

Figure 3.3 (A) Effect of anion-binding cocatalyst **3.7** on photoluminescence of **3.3d**. (B) Stern–Volmer plot in the absence and presence of ion binder **3.7**. .... 359

Figure 3.4 Cyclic voltammograms of the [Ru(btfmtb)<sub>3</sub>](X)<sub>2</sub> catalysts in A. CH<sub>2</sub>Cl<sub>2</sub> and B. CH<sub>3</sub>CN at a scan rate of 100 mV/sec and 0.1 M electrolyte solution composed of the *n*-Bu<sub>4</sub>N<sup>+</sup> salt of the indicated counterion. .... 379

Figure 3.5 Aromatic region of the <sup>1</sup>H NMR titration of thiophosphotriamide **3.7** with *n*-Bu<sub>4</sub>N<sup>+</sup> Ar<sup>F</sup>SO<sub>3</sub><sup>-</sup> in CD<sub>2</sub>Cl<sub>2</sub>. The C–H chemical shift of **3.7** is noted in the figure. .... 381

Figure 3.6 Change in chemical shift of the thiophosphotriamide **3.7** C–H resonance, blue circles. Overlaid is the best fit to a 1:1 binding model, solid line. .... 382

Figure 3.7 The <sup>1</sup>H NMR chemical shifts for catalysts **3.3a**, **3.3d**, and **3.3e** in CD<sub>3</sub>OD (A) and CD<sub>2</sub>Cl<sub>2</sub> (B). In CD<sub>2</sub>Cl<sub>2</sub> significant changes in the proton spectra of the btfmtb ligands were



measured between the photocatalysts. These changes tracked the coordinating ability of the counteranion in good agreement with the hypothesis of Meyer and coworkers of specific interactions between the counteranion and specific positions on the ligands..... 384

#### Chapter 4

Figure 4.1 A molecular drawing of Yoon55 shown with 50% probability ellipsoids. .... 531

#### Chapter 5

Figure 5.1 “Same excess” timecourses. Time corrected for initial substrate **5.1** concentration overlay..... 550

Figure 5.2 VTNA analysis. (A) Overlay showing 1<sup>st</sup> order of the substrate. (B) Overlay showing an apparent -1<sup>st</sup> order of the maleimide. (C) Overlay showing 0 order of the [Ir] photocatalyst. (D) Overlay showing 1<sup>st</sup> order of light. .... 552

Figure 5.3 Major diastereomer **5.6** concentration vs time over a range of light intensity. .... 554

Figure 5.4 Graphical representation of the pseudo-2D pulse program used to collect kinetic data in LED-NMR experiments..... 561

Figure 5.5 T1 relaxation times for selected protons on quinolone, maleimide, and product cyclobutane. Both quinolone and cyclobutane protons were monitored for kinetic analysis..... 562

Figure 5.6 Initial rates measured at various light intensities at room temperature. A) Time-courses recorded for initial rate measurements. B) Initial rates at different light intensities. The dotted lines correspond to linear regressions of the data. C) A linear trend between light intensity and initial reaction rate..... 563

## Appendix A

Figure A.1 Select Examples of Common Chiral Phosphoric Acid Backbones.....	570
--	-----

## List of Schemes

### Chapter 1

Scheme 1.1 Formation of tetrahydroquinoline products via enantioselective reduction steps.....	8
Scheme 1.2 A Stoichiometric CPA templated [2+2] Photocycloaddition.....	9
Scheme 1.3 Enantioselective Mannich Reaction in a Ring Contraction Transformation.....	10
Scheme 1.4 Enantioselective [2+2] Photocycloaddition via Chromophore Activation. ....	10
Scheme 1.5 Iminium Activation for the Conjugate Addition into Vinyl Pyridines.....	12
Scheme 1.6 Iminium Activation for a General, Enantioselective Conjugate Addition into Vinyl Pyridines. ....	13
Scheme 1.7 Asymmetric Protonation of a Prochiral Anion after C–C Bond Formation.....	14
Scheme 1.8 Enantioselective Minisci Reaction from the Reduction of a Redox Active Ester. ...	15
Scheme 1.9 Enantioselective Reduction of Azaarene-Based Ketones to Afford Chiral Alcohols. ....	17
Scheme 1.10 Enantioselective Deuteration of Racemic $\alpha$ -chloro-azaarenes. ....	18
Scheme 1.11 Enantioselective Radical Cross Coupling Reaction. ....	19
Scheme 1.12 Scope Expansion to Include 1,2-diketones in an Enantioselective Radical Cross Coupling.....	20
Scheme 1.13 <i>In Situ</i> Formation of an N-aryl imine for an Enantioselective Povarov Reaction...	21
Scheme 1.14 An Enantioselective Povarov Reaction. ....	22

Scheme 1.15 HAT Generated Radical Adds to an Enone Followed by an Enantioselective Protonation.....	22
Scheme 1.16 $\alpha$ -Amination and Subsequent Pyrazole Addition Reaction.....	23
Scheme 1.17 Enantioselective Radical Coupling Affording Tertiary Alcohols.....	24
Scheme 1.18 Oxidation and Subsequent Semipinacol Rearrangement.....	24
Scheme 1.19 Single Catalytic Method for an Enantioselective [2+2] Photocycloaddition with Enones.....	25
Scheme 1.20 Single Catalytic Method for an Enantioselective [2+2] Photocycloaddition with Iminium Ions.....	26
Scheme 1.21 Dual Catalytic Method for the Dicarbofunctionalization of Enamides using a Chiral Phosphate Base.....	27
Scheme 1.22 PCET Promoted Enantioselective Aza-Pinacol Reaction.....	28
Scheme 1.23 Enantioselective Synthesis of Pyrroloindolines via PCET.....	29
Scheme 1.24 Key Photochemical Step in the Enantioselective Total Synthesis of (-)-Verrupyrroloindoline.....	30
Scheme 1.25 Synthesis of Functionalized Pyrroloindoline Scaffolds.....	31
Scheme 1.26 Intramolecular Hydroamination of Alkenes.....	31
Scheme 1.27 Deracemization of Ureas via a Dual Enantioselective PCET and HAT Sequence.....	32

## Chapter 2

Scheme 2.1 Synthesis of Racemic $[\text{Ir}(\text{dtbppy})_2(\text{dMeObpy})]\text{PF}_6$ .....	56
Scheme 2.2 Synthesis of Diastereotopic $[\text{Ir}]$ Complexes.....	57
Scheme 2.3 Synthesis of $\Lambda$ - $[\text{Ir}(\text{dtbppy})_2(\text{dMeObpy})]\text{PF}_6$ .....	60
Scheme 2.4 Synthesis of $\Delta$ - $[\text{Ir}(\text{dtbppy})_2(\text{dMeObpy})]\text{PF}_6$ .....	60
Scheme 2.5 Binding Equilibrium Between ( <i>R</i> )-CPA3 and <b>2.1</b> .....	104
Scheme 2.6 No Ground State Interaction or Equilibrium Found Between ( <i>R</i> )-CPA3–pyridine and $\Delta$ - $[\text{Ir}]$ .....	106

## Chapter 3

Scheme 3.1 Proposed Photocatalytic Radical Cation Diels–Alder Cycloaddition Mechanism .	348
Scheme 3.2 Representation of the Ground State (No Dipole) and Triplet Excited State (Significant Dipole) for $[\text{Ru}(\text{btfmb})_3](\text{X})_2$ .....	355

## Chapter 4

Scheme 4.1 Singlet and Triplet Excited State Reactivity of Di- $\pi$ -Methane Scaffolds.....	426
Scheme 4.2 A) Scope of substituted diarylbarralene scaffolds. B) Examples of oxanorbornadiene rearrangements.....	428
Scheme 4.3 Stern–Volmer Quenching of Substrate <b>4.25</b> .....	431
Scheme 4.4 Rearrangement Timepoints with Lewis Acid.....	432
Scheme 4.5 Proposed Mechanism .....	433

## Chapter 5

Scheme 5.1 Enantioselective [2+2] photocycloaddition via a chiral-at-[Ir] photocatalyst. .... 548

## Appendix A

Scheme A.1 Representative Route to a Common BINOL CPA..... 571

Scheme A.2 Initial Result Showing Proof-of-Concept Enantioselective Cycloaddition..... 574

## List of Tables

### Chapter 2

Table 2.1 Pre-exponential Values and Lifetimes of the Fits for Both Matched and Mismatched Cases .....	117
--	-----

### Chapter 3

Table 3.1 Counteranion Effect on the Rate of Radical Cation Diels–Alder Cycloaddition .....	349
Table 3.2 Spectroscopic Properties and Stern–Volmer Quenching Constants <sup>a</sup> .....	351
Table 3.3 Ground- and Excited-State Redox Potentials for Ru(btmb) <sub>3</sub> <sup>2+</sup> in CH <sub>2</sub> Cl <sub>2</sub> <sup>a</sup> .....	353
Table 3.4 Effect of Ion-Binder Cocatalyst <b>3.7</b> on Radical Cation Diels–Alder Reaction .....	357
Table 3.5 Quantum Yield and Chain Length of Diels–Alder Reaction .....	375
Table 3.6 Electrochemical potentials of [Ru(btmb) <sub>3</sub> ](X) <sub>2</sub> in CH <sub>3</sub> CN. ....	380

### Chapter 4

Table 4.1 Optimization of Reaction Conditions .....	427
Table 4.2 Effect of enone electrophilicity on rearrangement efficiency. ....	429
Table 4.3 Lewis Acid Screen on Piperidyl Amide <b>4.23</b> .....	430
Table 4.4 Lewis Acid Rate Inhibition on the Di- $\pi$ -Methane Rearrangement Rate .....	431

### Chapter 5

Table 5.1 Example set of reactions for the “same excess” experiment. ....	546
---	-----

Table 5.2 “Same excess” experiments for the desired [2+2] cycloaddition using both matched and mismatched products. ....	549
Table 5.3 Experiments for VTNA analysis.....	551
Table 5.4 Experiments to Determine Diastereoselectivity vs Light Intensity. ....	553
Table 5.5 Conditions for preparation of the same excess experiments. Concentration of $\Delta$ - or $\Lambda$ -[Ir] was constant for all conditions (0.3 mM). ....	565
Appendix A	
Table A.1 Desired [2+2] Reactivity with Different Achiral Brønsted Acids .....	573
Table A.2 Preliminary HBD Screen using HCl as the Achiral Brønsted Acid.....	574
Table A.3 Preliminary HBD Screen using TFA as the Achiral Brønsted Acid.....	575



Chapter 1. Enantioselective Photochemical Reactions Activated by Chiral  
Phosphoric Acids

## 1.1. Introduction

### 1.1.1. Single Electron Transfer, Atom Transfer, and Energy Transfer Processes

Modern photocatalytic reactions can be broadly categorized as single electron transfer (SET), hydrogen atom transfer (HAT), or energy transfer processes. Photoinduced SET reactions are commonly termed “photoredox” processes. These require an electronically excited photocatalyst to perform either a single-electron oxidation or reduction of an organic substrate. The resulting radical cation or radical anion intermediate can undergo downstream radical reactions and can be intercepted to afford a variety of successful synthetic transformations. Photoinduced HAT reactions feature a concerted H• transfer from an organic substrate to an excited photocatalyst. Conceptually related to HAT are proton coupled electron transfer (PCET) reactions. A PCET reaction also requires the transfer of a single electron and H<sup>+</sup> in a concerted process, but these species are transferred to different atoms or to different molecules. The distinction between SET and atom transfer reactions is most apparent by their different modes of substrate activation; SET processes are governed by redox potentials while atom transfer processes are governed by bond dissociation energies. Both these SET and atom transfer reactions undergo productive transformations via downstream radical reactivity, which is in contrast to energy transfer reactions. Dexter energy transfer reactions require a concerted, redox-neutral, dual electron transfer process between the excited triplet photocatalyst and an organic substrate; this affords the ground state of the photocatalyst and indirectly accesses the excited triplet state of the substrate. Energy transfer reactions are often used when either the intersystem crossing of a substrate is inefficient or when direct photoexcitation of the substrate is impractical. While short lived, the resulting triplet substrate can further react from its excited state, allowing mechanistically distinct behavior from typical ground state behavior.

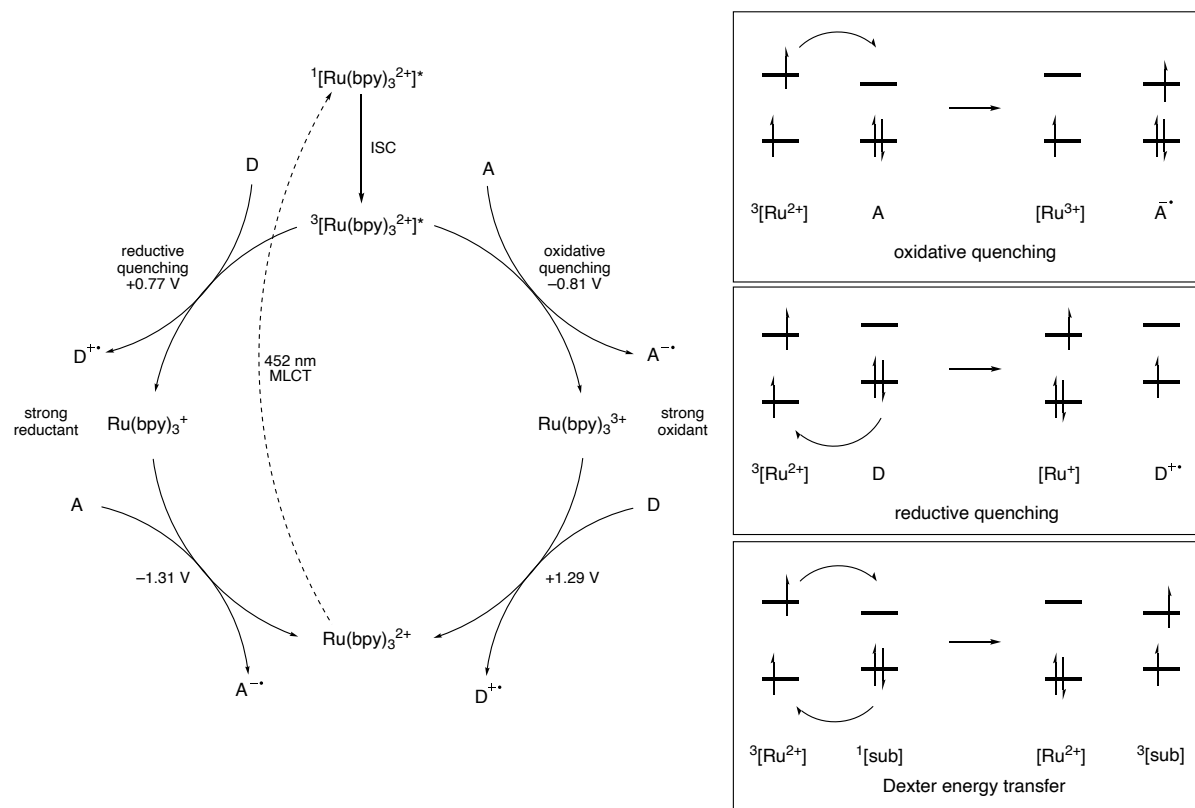


Figure 1.1 Mechanisms of Single Electron Transfer and Energy Transfer.

In recent years, photochemistry has experienced a surge in development, due in part to new photocatalysts with well-defined photochemical properties, long excited state lifetimes, and chemical stability. Different photocatalysts are well-suited for these different activation pathways, including strongly reducing or strongly oxidizing single electron transfer catalysts, hydrogen atom transfer catalysts, and energy transfer catalysts. These photoexcited catalysts can interact with substrates to afford open shell intermediates that undergo a rich array of chemical transformations. With a variety of photoactive catalysts, synthetic photochemistry is providing the means to generate high energy intermediates under mild conditions.

### 1.1.2. Primary versus Secondary Photochemical Reactions

Among the many diverse modes of reactivity accessible in the field, all photochemical transformations can be classified as either secondary or primary photoreactions. Secondary photochemical reactions are those where the photochemical step generates a new intermediate that further reacts from its ground state. These include photoredox processes that afford radical cation or radical anion intermediates, as well as atom transfer processes that afford neutral radical intermediates. These radical intermediates are not in an electronically excited state, and therefore their reactivity is analogous to chemically generated radical intermediates. However, primary photochemical reactions are those where the desired transformation occurs directly from an electronic excited state; these are often energy transfer processes that afford an excited triplet state intermediate. Recent years have marked the development of enantiocontrol over both secondary and primary photochemical reactions. Most methods rely on either Lewis acid catalysis or chromophore activation, which have been subject to recent reviews.<sup>1</sup> While enabling, these methods have only been shown to be applicable to carbonyl-containing substrates. Brønsted–Lowry acid catalysis enables the activation of different classes of substrates, including those containing *N*-heterocycles. Therefore, Brønsted acid catalysis has the potential to expand the breadth and applicability of photochemical systems.

### 1.1.3. Scope of this Chapter

The purpose of this chapter is to discuss the existing methods that use chiral phosphoric acids and bases to control enantioselectivity in photochemical reactions. It compiles the published enantioselective photochemical transformations induced by chiral phosphoric acids, describes the proposed mechanisms, and discusses the origins for their observed enantioselectivity. Systems using other chiral acids or bases will be referenced at the start of each section. Additionally,

hydrogen bonding catalysts will not be covered herein, but some reviews on asymmetric photochemical reactions using hydrogen bonding catalysts are available.<sup>2</sup>

## 1.2. Modes of Photochemical Activation via Brønsted Acid Coordination

Secondary and primary photochemical reactions involve different modes of Brønsted acid activation. In secondary photochemical reactions, the Brønsted acids generally act as LUMO lowering catalysts. Protonation of an *N*-heterocyclic substrate **1.3** forms a pseudo iminium ion **1.4** *in situ*, enabling a more facile nucleophilic attack to the substrate. In many cases, the acid is involved in the dark cycle of the reaction mechanism where it is independent of the photochemical step. Compared to the free substrate, an acid-activated compound generally features a lower LUMO energy, resulting in a rate acceleration for nucleophilic attack. When using a chiral Brønsted acid, the resulting rate acceleration allows for enantioselective catalysis.

When an iminium ion is part of the photochemical cycle, its excited-state reactivity is characterized by a  $\pi, \pi^*$  transition, making their photochemical properties similar to those of analogous olefins.<sup>3</sup> Examples of each of these mechanistically distinct pathways will be discussed below.

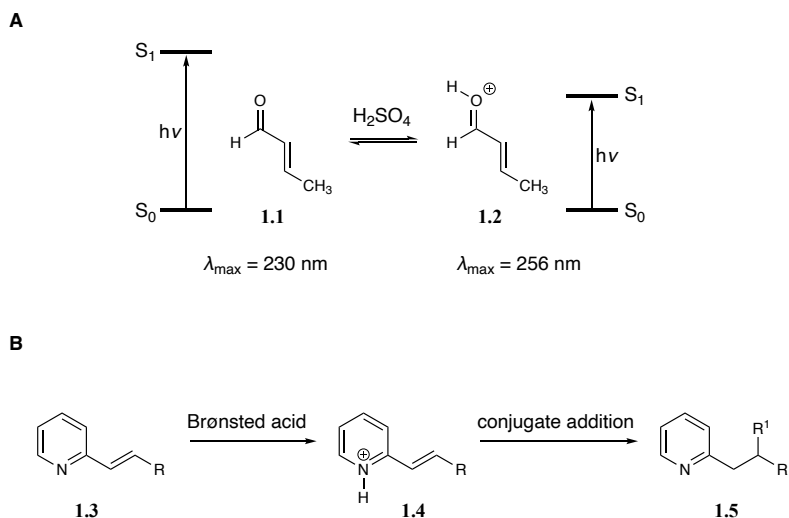


Figure 1.2 A)  $S_0$ – $S_1$  Lowering of Enones via Brønsted Acid Coordination. B) Representative Iminium Ion Activation of Vinyl Pyridines.

In primary photochemical reactions, Brønsted acid catalysis must directly perturb the photochemical steps of the reaction. This occurs either through changing the absorption profile of the substrate (commonly known as chromophore activation) or through lowering the barrier for Dexter energy transfer. These modes of activation are much less explored for enantioselective synthetic photochemistry compared to the activation of secondary photoreactions. For substrates that feature an absorption shift upon chiral catalyst coordination, selective irradiation ensures the bound complex is preferentially photoexcited instead of the free substrate; this allows the chiral Brønsted acid to be involved with product formation. Therefore, the racemic background reactivity that would erode the enantioselectivity is suppressed. For substrates that feature a lower barrier for Dexter energy transfer upon protonation, a judiciously selected photocatalyst can sensitize only the bound complex. Similarly, this allows the chiral acid to be involved in the product formation to afford an enantioselective transformation. These strategies bias reactivity toward the scalemic pathway over the competitive racemic background pathway. At its essence, enantioselective

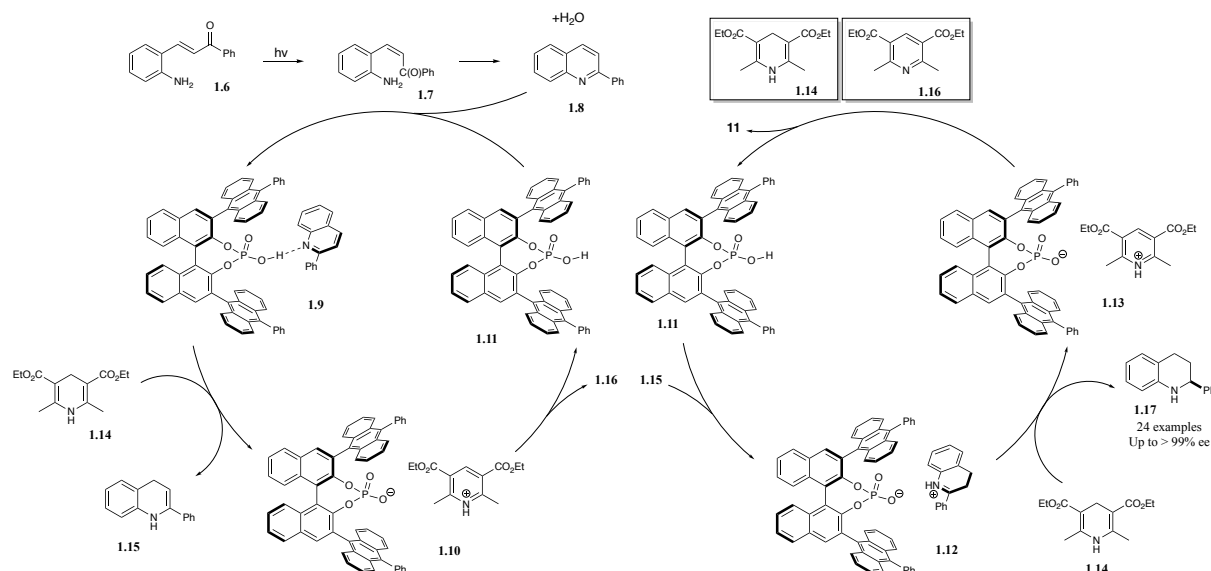
primary photochemistry harnesses the reactivity differences between bound and unbound substrates to favor reactivity in a chiral environment. Each report discussed below relies on one of these methods to activate the scalemic reaction pathway.

### 1.3. Direct Photoexcitation in Tandem with a Chiral Phosphoric Acid

Chiral Brønsted acid coordination to a substrate can shift its UV-vis absorption profile, causing the bound substrate to absorb different wavelengths of light than its unbound counterpart. Selective irradiation of the bound complex can enable enantioselective transformations that outcompete any racemic background reaction. To accomplish this chromophore activation, the Brønsted acid can be a chromophore itself, or it can generate a charge transfer complex with the substrate in solution. Less frequently, the photochemical activation is independent from the stereoinduction step. In these cases, a photochemical reaction occurs followed by a subsequent chiral Brønsted acid activated asymmetric reaction. Current examples of direct photoexcitation in tandem with chiral phosphoric acids are discussed below. An additional example using a chiral amine as a Brønsted base is referenced here,<sup>4</sup> yet is outside the scope of discussion for this chapter.

Yang and coworkers describe a cascade reaction generating enantioenriched tetrahydroquinoline products (Scheme 1.1) with a catalytic chiral phosphoric acid (CPA).<sup>5</sup> Direct irradiation of a highly conjugated enone **1.6** with blue LEDs enables *E/Z* isomerization. As the *Z* diastereomer **1.7**, condensation of the amine to the aryl ketone affords a substituted quinoline **1.8**. Using a Hantzsch ester **1.14** as the terminal reductant, the quinoline is reduced to afford intermediate **1.15**. Again, coordination with the CPA enables a second reduction event. These reduction and protonation events provide a means for an overall Brønsted acid catalyzed

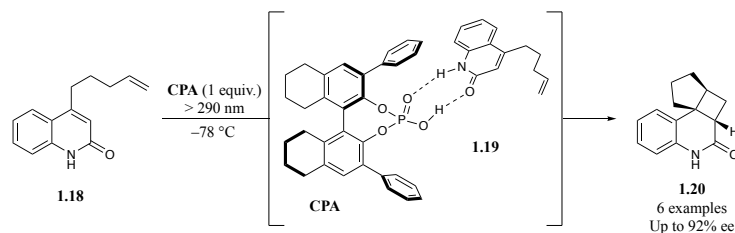
asymmetric hydrogenation to afford tetrahydroquinoline products **1.17**. The same transformation was also reported in flow.<sup>6</sup>



Scheme 1.1 Formation of tetrahydroquinoline products via enantioselective reduction steps.

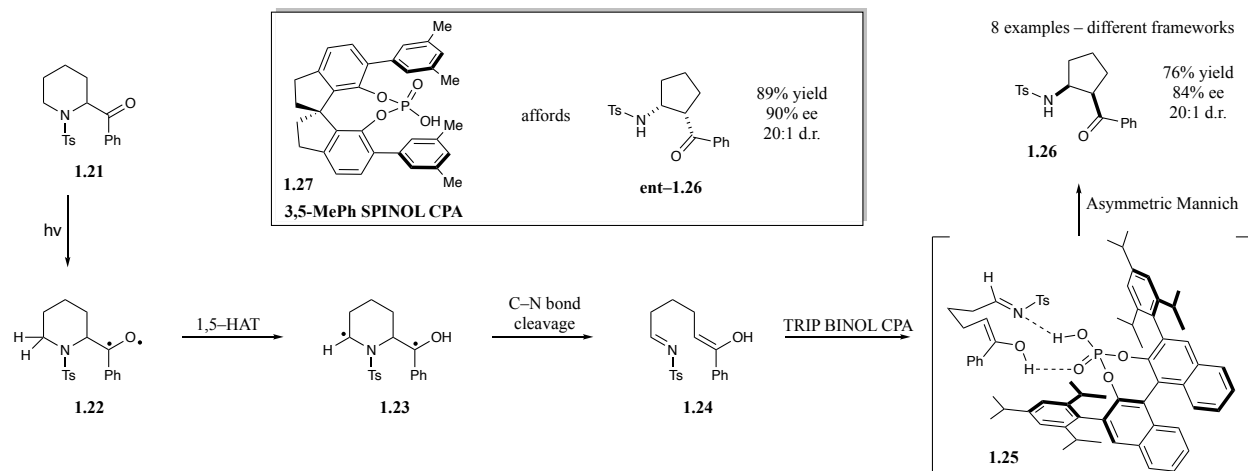
A CPA templated reaction coordinates with a quinolinone substrate **1.18** for an enantioselective [2+2] photocycloaddition to afford **1.20** (Scheme 1.2). Takagi and Tabuchi identified a  $\pi$ - $\pi$  stack between the CPA and the substrate to provide the enantiodetermining geometry **1.19** for the cycloaddition. Notably, 1 equiv. of the CPA was used to achieve 90+% ee, and the authors directly excited the stoichiometric bound complex with high energy (290 nm) light. Since no absorbance or emission data was provided of their substrate or the bound CPA complex, there was no speculation if chromophore activation was possible to render the CPA catalytic.<sup>7</sup>





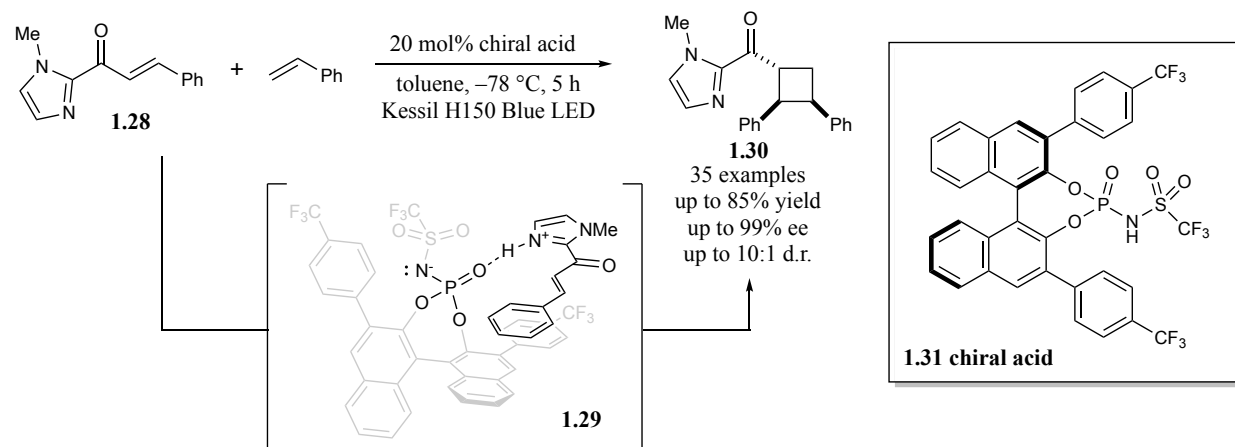
Scheme 1.2 A Stoichiometric CPA templated [2+2] Photocycloaddition.

Sarpong and coworkers developed a unique ring contraction mechanistically hinged on Norrish Type II reactivity (Scheme 1.3).<sup>8</sup> They proposed that  $\alpha$ -acylated piperidine substrates **1.21** could be directly photoexcited and undergo an intersystem crossing to their excited triplet state **1.22**. Subsequent 1,5-hydrogen atom abstraction following a standard Norrish Type II pathway would afford a 1,4-diradical intermediate **1.23**. Homolytic C–N bond cleavage would afford an imine-enol intermediate **1.24**, which is primed for an intramolecular attack of the enol to the imine to generate the ring contracted product **1.26**. This approach is a powerful method to dramatically alter the core framework of a small molecule late into a synthetic route, which was shown in the remodeling of pharmaceuticals and peptides. While most of this work was under racemic conditions, the authors show that coordination to a CPA **1.27** can afford highly enantioselective ring contractions across a variety of useful scaffolds via the intermediate **1.25**.



Scheme 1.3 Enantioselective Mannich Reaction in a Ring Contraction Transformation.

Yoon and coworkers designed a [2+2] photocycloaddition templated by a chiral triflimide BINOL acid **1.31**. This system relies on chromophore activation to shift the absorbance profile of the substrate **1.28** into the visible, allowing selective photoexcitation only of the bound substrate. Their proposed acid-substrate interaction **1.29** is key for high enantioselectivities, as the styrene approaches and reacts at the sterically accessible face of the enone (Scheme 1.4).<sup>9</sup> This reaction affords the cycloadduct **1.30** as the *trans-cis* stereoisomer, which is distinct from previous reports of similar enantioselective [2+2] photocycloadditions.



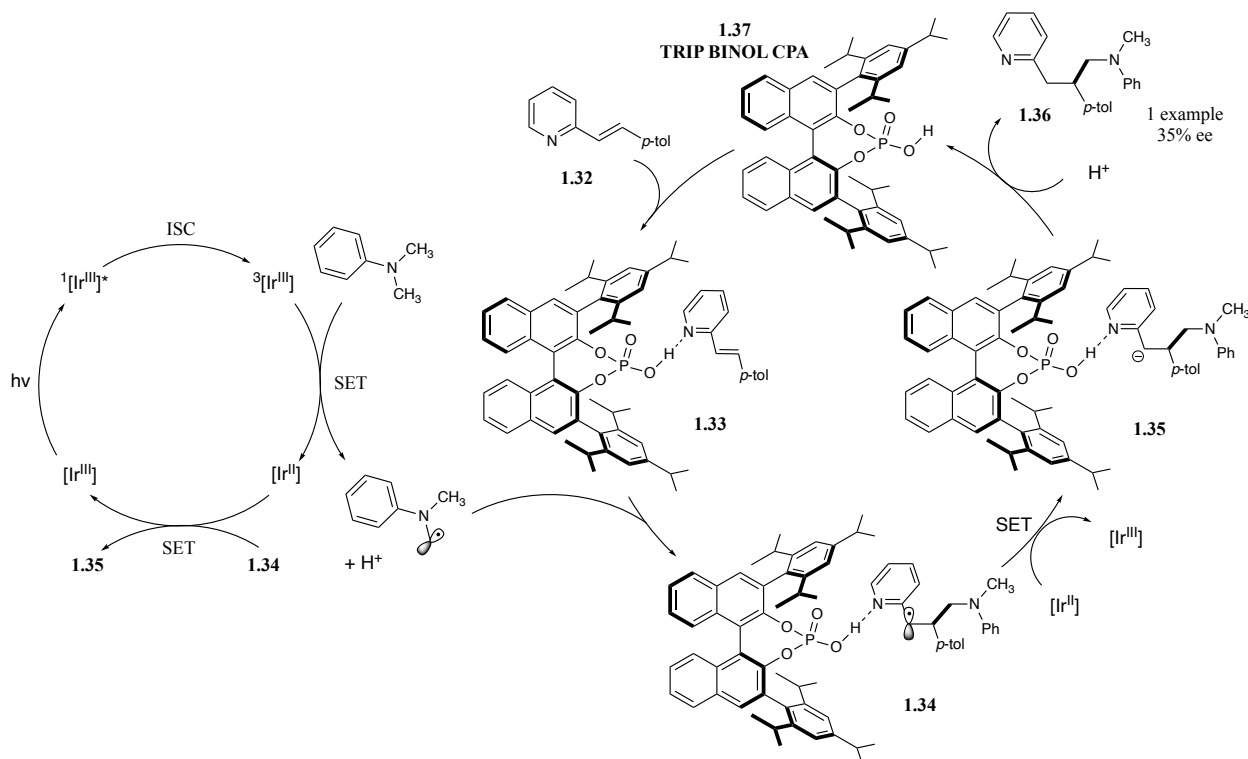
Scheme 1.4 Enantioselective [2+2] Photocycloaddition via Chromophore Activation.

## 1.4. Chiral Phosphoric Acid Control in Photoredox Catalytic Cycles

Single electron transfer photocatalysis is proving to be a powerful synthetic method to generate radical intermediates under mild conditions. The merger of this synthetic strategy with CPA catalysis is enabling the enantiocontrol of new classes of photoredox reactions. The synergistic use of a photocatalyst with a chiral Brønsted acid is synthetically appealing. The photophysical properties of the photocatalyst can be optimized independently from the stereo-defining properties of the chiral Brønsted acid. The exact mode of Brønsted acid activation differs for most photoredox systems, but stereoinduction can occur any time the asymmetric environment is present in the stereo-defining step. All examples of CPA activation in photoredox systems to date are discussed below.

An insightful merger of Brønsted acid and photoredox catalysis arose from the Melchiorre lab highlighting a conjugate addition to a variety of vinyl pyridines (Scheme 1.5).<sup>10</sup> Inspired from the established field of organocatalysis, Melchiorre and coworkers use the embedded C=N imine handle in the pyridine **1.32** to generate a pseudo iminium ion after protonation. As a result, this iminium ion activation has a LUMO lowering effect for the bound substrate, facilitating a facile nucleophilic attack. A nucleophilic  $\alpha$ -amino radical is generated from an alkyl amine via a single electron transfer (SET) process from a photoexcited iridium(III) species and subsequent deprotonation. Rapid addition of this radical occurs to the chiral iminium ion-activated acceptor **1.33**. A second SET process occurs between the resulting intermediate **1.34** and the reduced iridium(II) species to regenerate the photocatalyst and to generate the protonated conjugate addition product **1.35**. The authors highlight an unproductive energy transfer pathway between the photoexcited iridium(III) catalyst and the vinyl pyridines, detected by *E/Z* isomerization of the

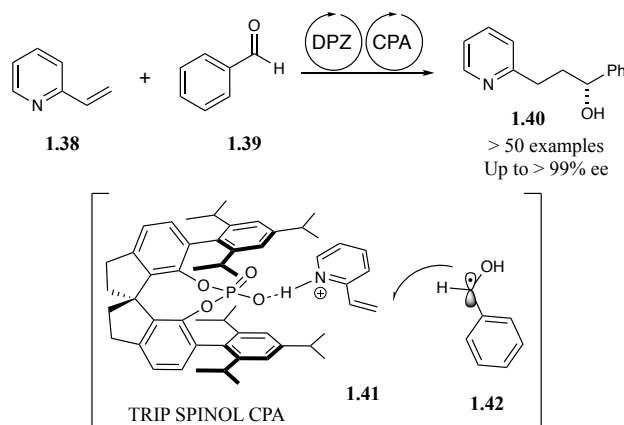
starting materials. The use of a BINOL chiral phosphoric acid enables slight enantioenrichment of the desired conjugate addition products **1.36** up to 35% ee.



Scheme 1.5 Iminium Activation for the Conjugate Addition into Vinyl Pyridines.

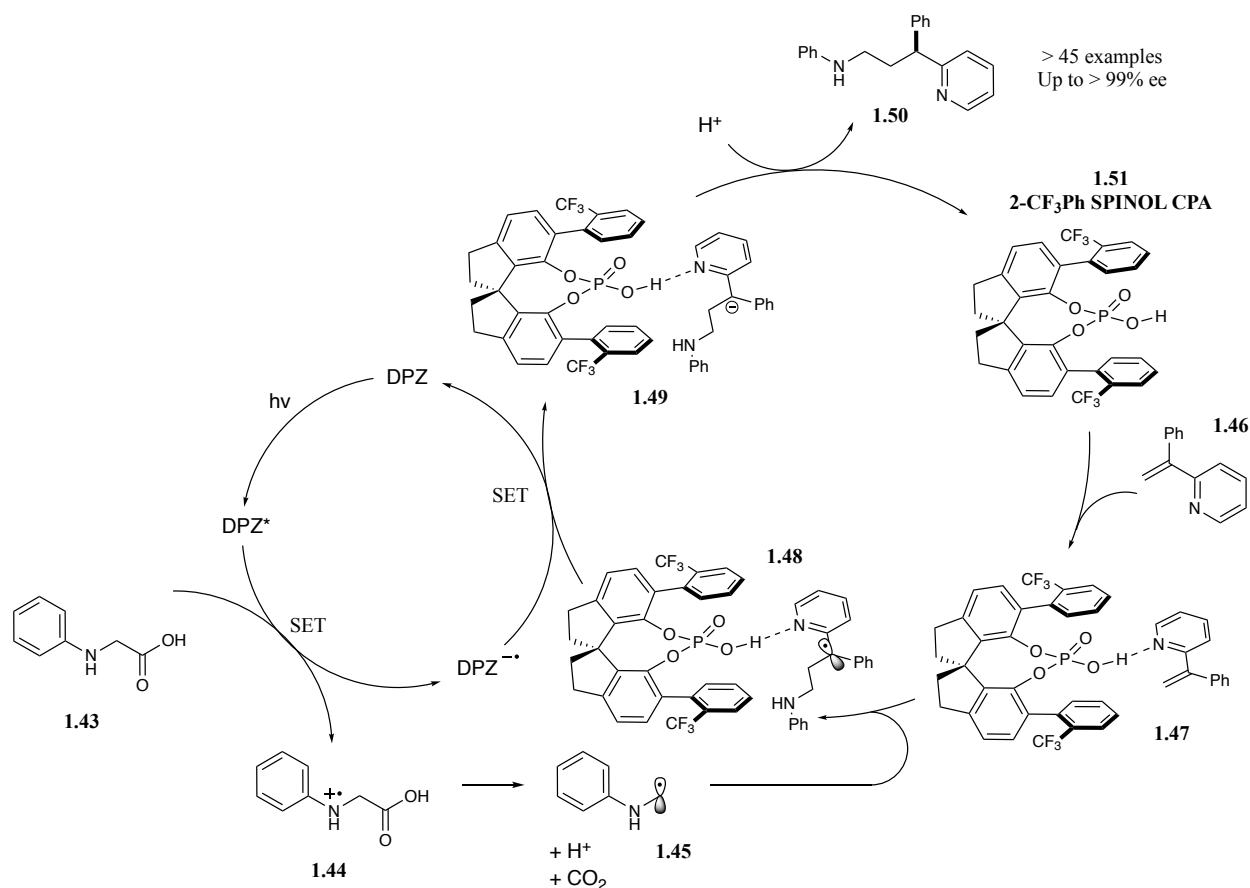
Using the same mode of Brønsted acid activation, Jiang and coworkers optimized the enantioselective conjugate addition into vinyl pyridines to afford chiral adducts in excellent selectivity (Scheme 1.6).<sup>11</sup> The protonated aldehyde (or imine) **1.39** undergoes a single electron reduction to generate a prochiral radical nucleophile **1.42**. Radical addition into the vinyl pyridine **1.38** and subsequent deprotonation affords a variety of chiral  $\gamma$ -hydroxyl (or  $\gamma$ -amino) substituted pyridines **1.40**. This reductive coupling uses a Hantzsch ester as the terminal reductant to close the photocatalytic cycle. At reduced temperatures, control reactions indicate the necessity of both the photocatalyst DPZ and the chiral Brønsted acid for reactivity. Since only the scalemic pathway is

operable under their optimized reaction conditions, excellent enantioselectivities up to >99% ee are reported.



Scheme 1.6 Iminium Activation for a General, Enantioselective Conjugate Addition into Vinyl Pyridines.

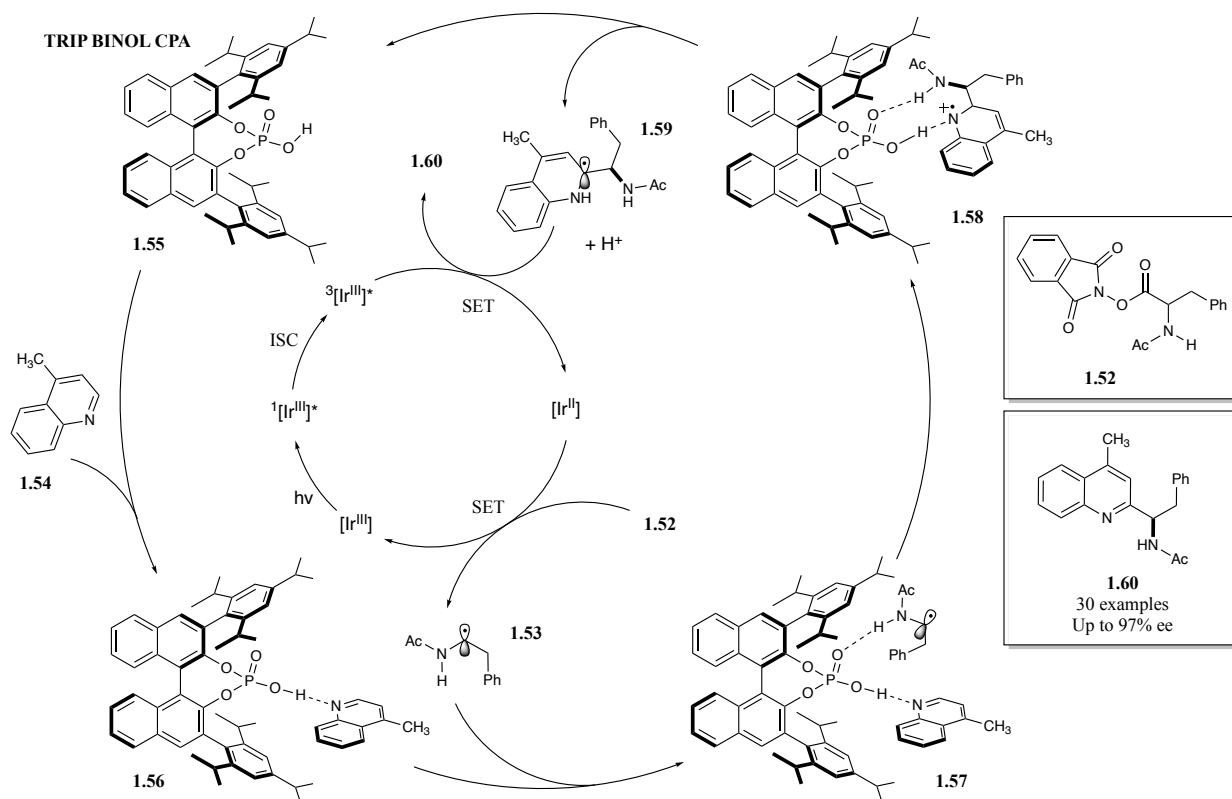
Chiral Brønsted acids are also used for the asymmetric protonation after conjugate addition (Scheme 1.7).<sup>12</sup> Using DPZ as an organic photocatalyst, the amino acid derivative **1.43** is oxidized to **1.44** and undergoes decarboxylation to generate an  $\alpha$ -amino radical **1.45**. This nucleophilic radical undergoes a conjugate addition with a bound vinyl pyridine complex **1.47**. While this radical addition affords a prochiral tertiary radical **1.48**, subsequent SET and asymmetric protonation from the chiral Brønsted acid **1.49** is highly selective to afford enantioenriched conjugate addition adducts **1.50**. This methodology relies on the same LUMO lowering catalysis as the previous conjugate addition reactions where nucleophilic addition occurs as part of the dark cycle. The stereo-defining step is the final protonation of the prochiral anion, rather than the C–C bond formation itself.



Scheme 1.7 Asymmetric Protonation of a Prochiral Anion after C–C Bond Formation.

Enantioselective Minisci-type reactions have been demonstrated using a photoredox generated  $\alpha$ -amino radical (Scheme 1.8).<sup>13</sup> A photoexcited Ir(III) photocatalyst reduces a redox active ester **1.52** to generate the  $\alpha$ -amino radical **1.53**. A ternary complex **1.57** is proposed to form containing a BINOL TRIP CPA, pyridine starting material, and this  $\alpha$ -amino radical. The Minisci radical addition reaction forges a new C–C bond in an asymmetric fashion **1.58**. After deprotonation and single electron oxidation closing the photocatalytic cycle, the Minisci products **1.60** are isolated in high yields and excellent enantioselectivity up to 97% ee. The authors note no reactivity in the absence of a Brønsted acid **1.55**, demonstrating the LUMO lowering activation of the *N*-heterocycle **1.54** upon protonation.<sup>14</sup> A similar Minisci-type reaction was reported by Jiang

and coworkers using the organic photocatalyst DPZ for the synthesis of  $\alpha$ -isoquinoline-substituted secondary amines.<sup>15</sup> The authors propose a similar reduction of a redox active ester and asymmetric radical addition into isoquinoline templated by a SPINOL phosphoric acid.



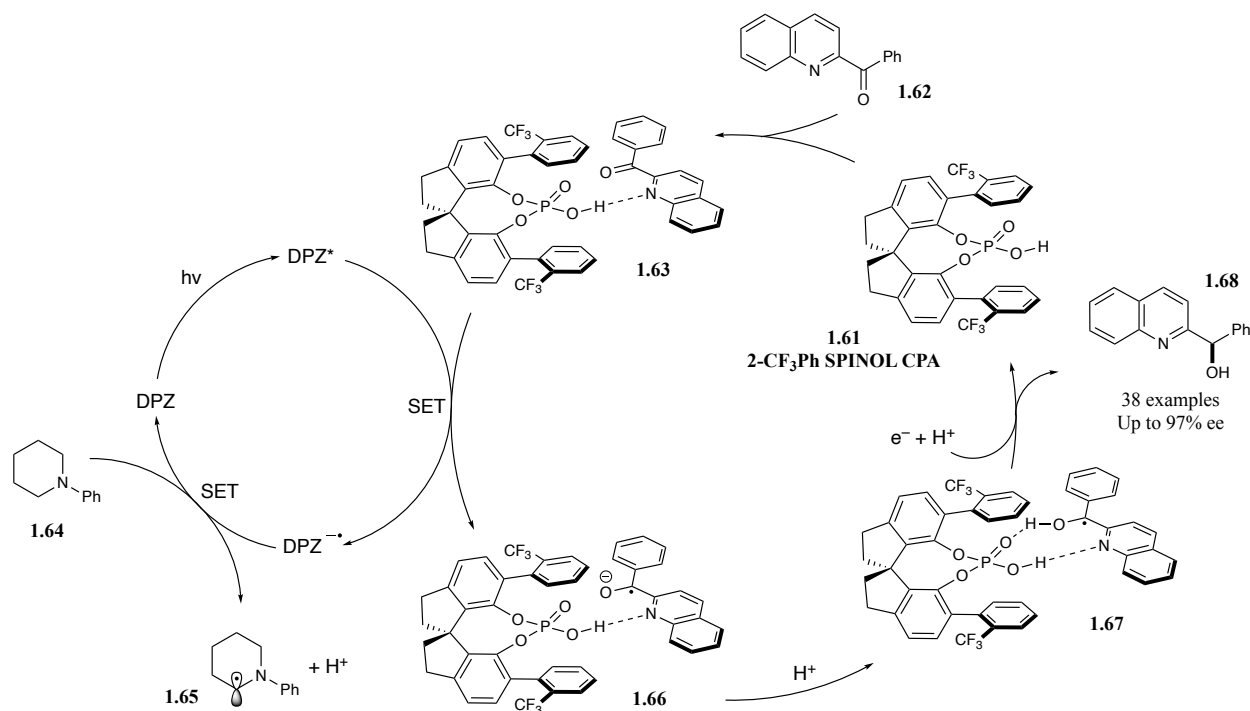
Scheme 1.8 Enantioselective Minisci Reaction from the Reduction of a Redox Active Ester.

Recently, Phipps and coworkers followed up their initial Minisci reaction work by generating the  $\alpha$ -amino radical via a photochemical hydrogen atom transfer (HAT) process. This approach enabled the use of commercial *N*-acetyl amines without the need for prefunctionalization to the redox active ester. They could overcome the challenge of  $\alpha$ -to-amine site selectivity by using diacetyl as the HAT agent. Fortunately, they found direct photoexcitation of diacetyl promoted the reaction without the need for an exogenous photocatalyst. This reaction afforded Minisci products via a CPA catalyzed radical addition in up to 98% ee.<sup>16</sup>

Using the same TRIP BINOL CPA **1.55**, Studer and coworkers optimized a three component Minisci reaction inspired by these previous works for the synthesis of  $\gamma$ -heteroaryl-substituted  $\gamma$ -amino-acid derivatives. This system relies on a single electron reduction of an  $\alpha$ -bromo carbonyl to afford the  $\alpha$ -carbonyl radical. Subsequent radical addition into an enamide affords the amidyl radical that performs the Minisci reaction with quinolines and pyridines. The overall transformation affords these 1,2-diamine products in up to 97% ee.<sup>17</sup>

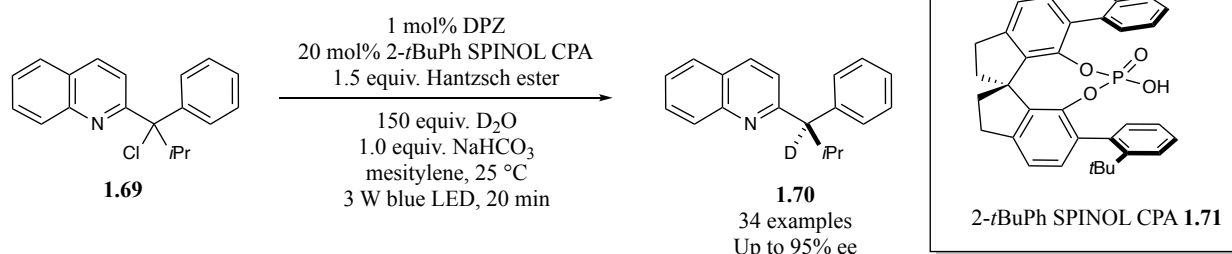
Rather than favoring nucleophilic addition using LUMO lowering catalysis, Jiang and coworkers used Brønsted acid activation to afford a more facile single electron reduction of a bound complex. The authors reported an enantioselective reduction of azaarene-based ketones **1.62** using an organic photoredox catalyst DPZ and a chiral phosphoric acid **1.61** (Scheme 1.9).<sup>18</sup> Two distinct SET processes account for the two-electron reduction of the ketone while the chiral Brønsted acid induces stereocontrol over the resulting chiral alcohol product. The proposed mechanism details the coordination of their chiral Brønsted acid **1.61** to the pyridinyl moiety of their substrate **1.62**, followed by the first single electron reduction to the radical anion **1.66**. The phosphoric acid is proposed to coordinate bidentate with the pyridine heterocycle and the generated radical alcohol intermediate, shown as compound **1.67**. The second single electron reduction and subsequent protonation generates the enantioenriched alcohol **1.68**. The Brønsted acid coordination is expected to make both SET processes more facile, allowing the scalemic pathway to kinetically outcompete the racemic pathway. Enantioselectivity of the resulting alcohols are reported up to 97% ee.





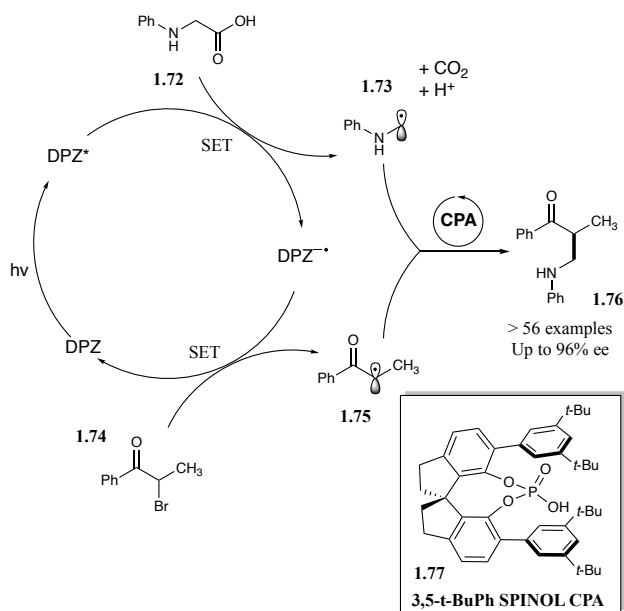
Scheme 1.9 Enantioselective Reduction of Azaarene-Based Ketones to Afford Chiral Alcohols.

Building off this precedent, Jiang and coworkers optimized another enantioselective reduction reaction for the deuteration of racemic  $\alpha$ -chloro-azaarenes **1.69** (Scheme 1.10).<sup>19</sup> This system benefits from using  $D_2O$  as the deuterium source and relies on the H/D exchange with the chiral phosphoric acid **1.71**. This reaction is successful with prochiral azaarene-substituted ketones, furnishing an additional 16 examples of successful enantioselective reductions with high selectivity.



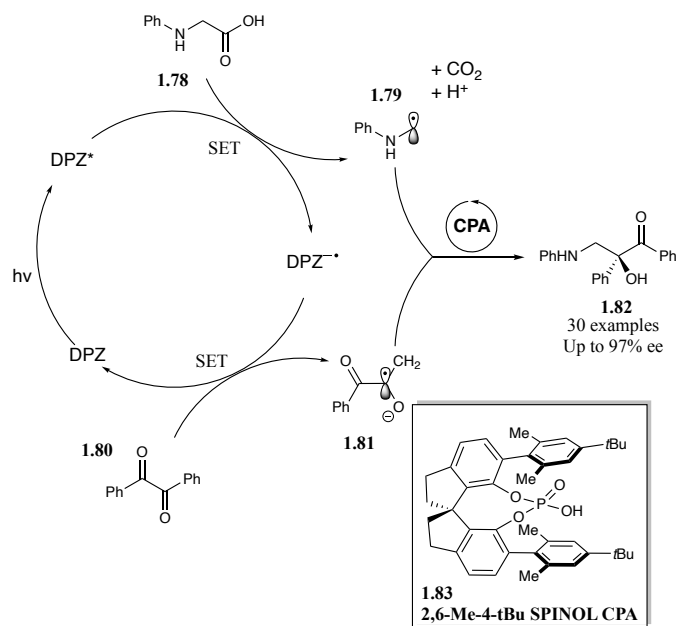
Scheme 1.10 Enantioselective Deuteration of Racemic  $\alpha$ -chloro-azaarenes.

Jiang and coworkers have used a chiral Brønsted acid **1.77** to control a radical cross coupling reaction (Scheme 1.11). The formation of both radicals is coupled to one photocatalyst cycle. An amino acid derivative **1.72** is oxidized and undergoes decarboxylation to generate an  $\alpha$ -amino radical **1.73**. Then the reduced photocatalyst reduces an  $\alpha$ -bromo ketone **1.74** to generate an  $\alpha$ -keto radical **1.75**, in turn closing the DPZ cycle.<sup>20</sup> The authors propose that the CPA acts as a bifunctional hydrogen bonding catalyst after both photochemical SET steps. The CPA can stabilize the electrophilic  $\alpha$ -keto radical while activating the nucleophilic  $\alpha$ -amino radical, templating the radical combination in an enantioselective fashion to afford **1.76**. While no ternary transition state was examined or proposed, the authors reported this radical cross coupling reaction occurring up to 96% ee. The radical combination is favored in the organized environment provided by the CPA because the racemic background radical combination is greatly suppressed under the reaction conditions. A mechanistically similar dual catalytic enantioconvergent radical cross coupling reaction was published by Wang and coworkers. This focused on the synthesis of  $\alpha$ -amino acid derivatives via an  $\alpha$ -keto radical and photochemically generated iminium ion intermediate, achieving up to 99% ee.<sup>21</sup>



Scheme 1.11 Enantioselective Radical Cross Coupling Reaction.

This mechanism proved successful for a variety of radical cross coupling reactions for Jiang and coworkers. An amino acid derivative **1.78** is oxidized and undergoes decarboxylation to generate an  $\alpha$ -amino radical **1.79**. Then the reduced photocatalyst reduces 1,2-diketone **1.80** to generate an  $\alpha$ -keto radical **1.81**, in turn closing the DPZ cycle.<sup>22</sup> The CPA templates the radical cross coupling in an enantioselective fashion, affording highly enantioselective tertiary alcohols **1.82** up to 97% ee (Scheme 1.12).

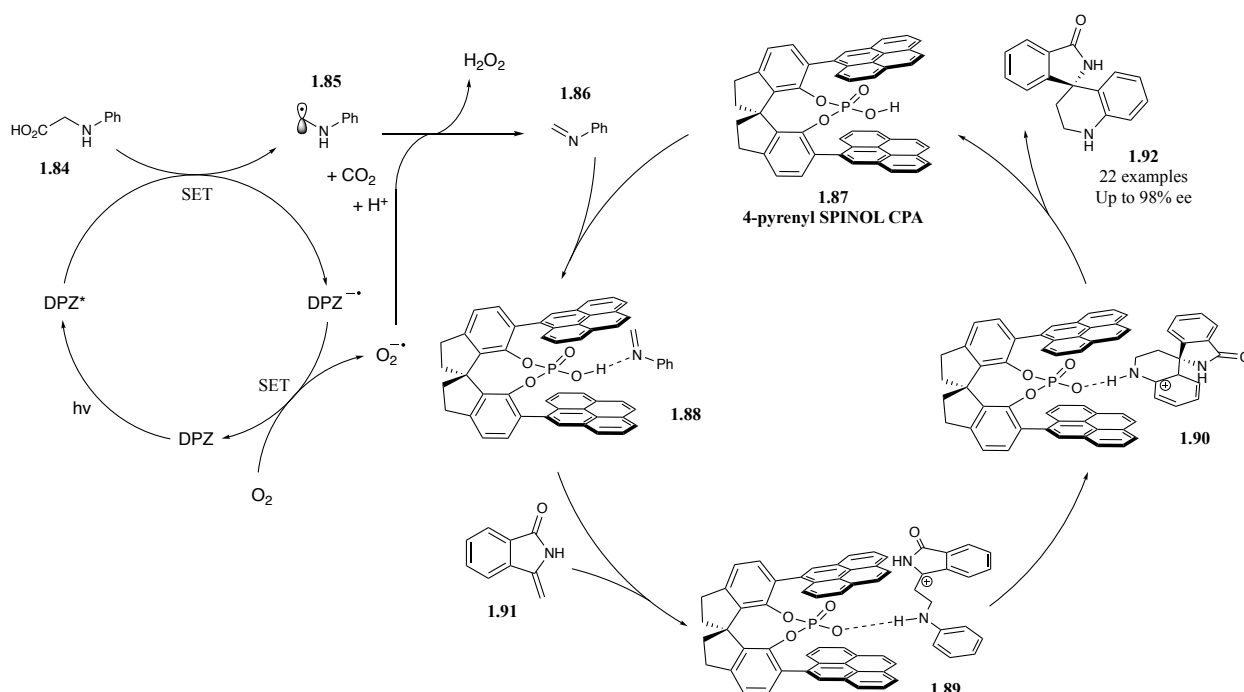


Scheme 1.12 Scope Expansion to Include 1,2-diketones in an Enantioselective Radical Cross Coupling.

Another example following this same mechanism is the enantioconvergent substitution of 3-chlorooxindoles with *N*-aryl glycines. A single electron reduction of the 3-chlorooxindole substrate generates an  $\alpha$ -keto radical while a single electron oxidation of the *N*-aryl glycine affords an  $\alpha$ -amino radical. The enantioselective radical coupling occurs through a proposed tertiary complex with the chiral SPINOL phosphoric acid. This reaction affords chiral 3-aminomethylene-3-substituted oxindole products in up to 98% ee.<sup>23</sup>

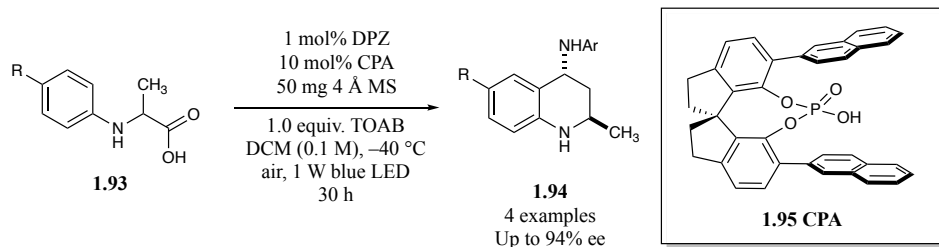
Jiang and coworkers have published an enantioselective decarboxylative Povarov reaction via cooperative dual photoredox and Brønsted acid catalysis (Scheme 1.13).<sup>24</sup> The Povarov reaction is formally a [4+2] cycloaddition between an *N*-aryl imine **1.86** and an alkene **1.91**, and activation of the imine is typically required for reactivity. In this dual catalytic example, *N*-aryl  $\alpha$ -amino acids **1.84** undergo a photochemical single electron oxidation to induce decarboxylation

affording an  $\alpha$ -amino radical intermediate **1.85**. This radical is aerobically oxidized for the *in situ* generation of an *N*-aryl imine **1.86**. The enantioselective Povarov reaction occurs in up to 98% ee with a chiral SPINOL phosphoric acid catalyst **1.87**. A control experiment is consistent with the amide functionality in the starting material **1.91** being important to the stereocontrol.



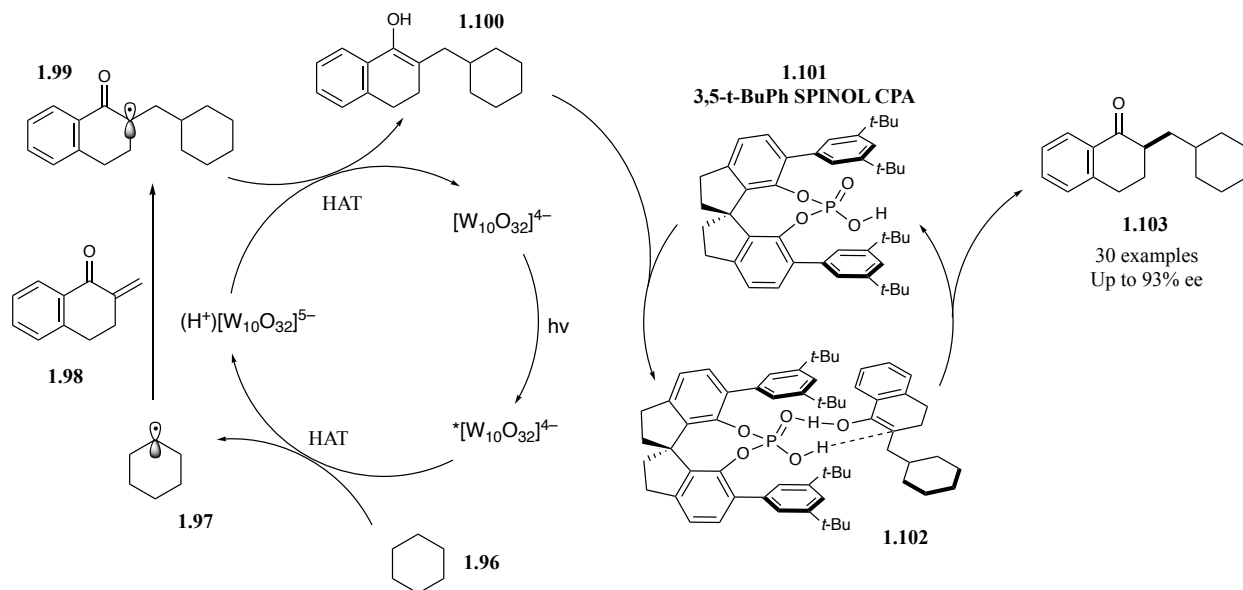
Scheme 1.13 *In Situ* Formation of an *N*-aryl imine for an Enantioselective Povarov Reaction.

Jiang and coworkers have shown a previous example of an enantioselective Povarov reaction for the formation of chiral 4-amino-2-methyl tetrahydroquinolines **1.94**. This requires the single electron oxidation of *N*-aryl alanine **1.93** starting materials by DPZ\* which, following the same mechanism as above, will afford the corresponding imine (Scheme 1.14). The [4+2] annulation with the imine and its enamine tautomer will afford the tetrahydroquinoline product. Using a naphthyl substituted SPINOL chiral phosphoric acid **1.95**, this transformation furnished product in high stereoselectivity.<sup>25</sup>



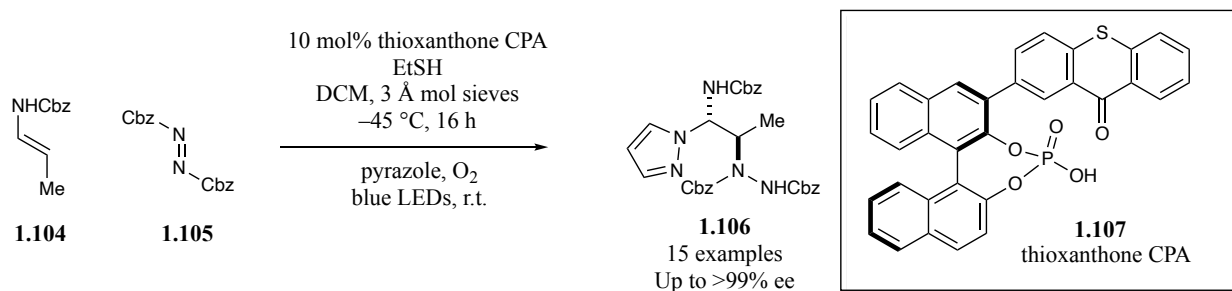
Scheme 1.14 An Enantioselective Povarov Reaction.

Using a hydrogen atom transfer (HAT) approach, Wang and coworkers merged a tetrabutylammonium decatungstate (TBADT) photocatalyst with a chiral SPINOL based phosphoric acid **1.101**.<sup>26</sup> TBADT generates an alkyl radical **1.97** via HAT from a methylene in **1.96**. This alkyl radical adds to an enone **1.98** to afford an  $\alpha$ -keto radical **1.99**. A subsequent hydrogen abstraction produces an enol **1.100**, which coordinates with the chiral phosphoric acid. Enantioselective protonation of this bound enol **1.102** occurs to afford chiral  $\alpha$ -alkyl ketones **1.103** with up to 93% ee while also regenerating the Brønsted acid (Scheme 1.15).



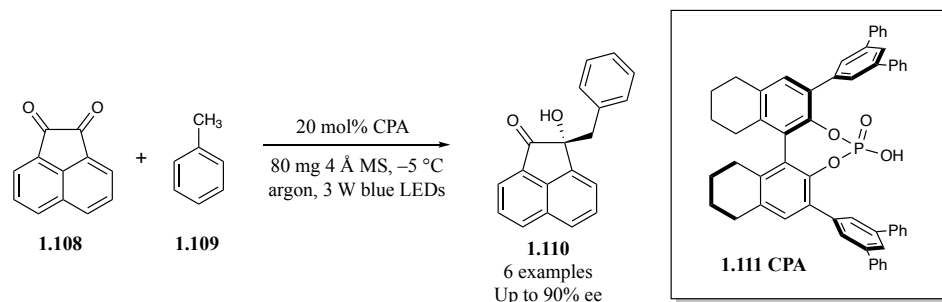
Scheme 1.15 HAT Generated Radical Adds to an Enone Followed by an Enantioselective Protonation.

Masson and coworkers developed thioxanthone substituted CPAs **1.107**, including both a C2 and C1 symmetric version. These catalysts were optimized for an asymmetric  $\alpha$ -amination and subsequent pyrazole addition reaction.<sup>27</sup> Based on their previous studies of an analogous system<sup>28</sup>, they propose formation of a chiral  $\alpha$ -carbamoylsulfide intermediate via an electrophilic three-component thio-amination step. This intermediate can subsequently be oxidized by the excited state thioxanthone catalyst inducing a mesolytic cleavage to afford an imine intermediate. Trapping this imine with pyrazole affords the desired product **1.106** (Scheme 1.16). They note their C1 symmetric catalyst has slightly better catalytic efficiency than the C2 symmetric analog without compromising the enantioselectivity of the transformation.



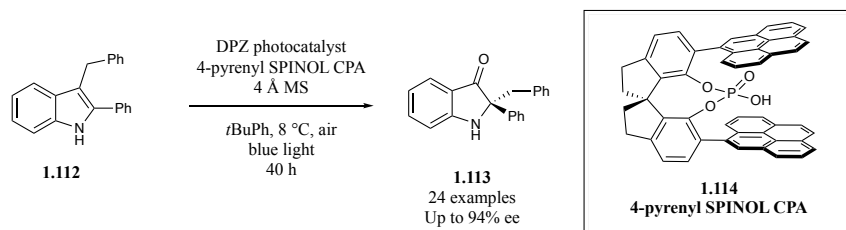
Scheme 1.16  $\alpha$ -Amination and Subsequent Pyrazole Addition Reaction.

Jiang and coworkers optimized a C–H functionalization of toluene derivatives with activated ketones and both Lewis and Brønsted acid catalysis (Scheme 1.17). After photoexcitation of the ketone **1.108**, they postulate either a single electron oxidation or hydrogen atom transfer of the toluene derivative **1.109** to generate the benzylic radical. The resulting ketyl radical can undergo coupling with the benzylic radical with a CPA catalyst. Particularly, this coupling with toluene and acenaphthoquinone is promoted with notable enantioselectivity using a H8-BINOL CPA **1.111**. This reaction affords chiral tertiary alcohols **1.110** in up to 90% ee.<sup>29</sup>



Scheme 1.17 Enantioselective Radical Coupling Affording Tertiary Alcohols.

Jiang and coworkers developed an enantioselective aerobic oxidation and semipinacol rearrangement to afford chiral 2,2-disubstituted indolin-3-ones **1.113** (Scheme 1.18). They propose single electron oxidation of indole **1.112** by the excited state DPZ photocatalyst to initiate the aerobic oxidation. The SPINOL CPA **1.114** is responsible for the enantioselective oxidation, and the chiral intermediate then acts as a chiral promoter for the resulting thermal semipinacol rearrangement. This net reaction provides indolin-3-one products **1.113** in up to 94% ee.<sup>30</sup>



Scheme 1.18 Oxidation and Subsequent Semipinacol Rearrangement.

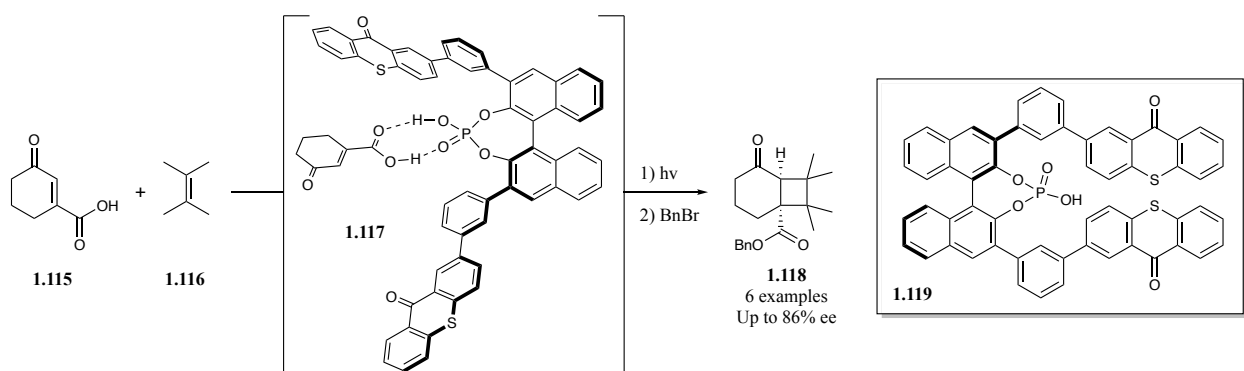
## 1.5. Chiral Phosphoric Acid Activation in Dexter Energy Transfer Processes

Few examples of CPA activation in energy transfer processes have been demonstrated. Spectroscopically, shifts in phosphorescence profiles of organic molecules have been reported upon protonation.<sup>31</sup> Based on these observations, chiral Brønsted acids can theoretically activate organic substrates toward primary photoreactions in an asymmetric environment. This area has



great promise where we expect development during the coming years. Herein, we will discuss the examples of Brønsted acid activation in Dexter energy transfer processes. Recently, Bach published a review on enantioselective photochemistry using Dexter energy transfer<sup>32</sup> which encompasses a wider breadth of catalyst structures than included here.

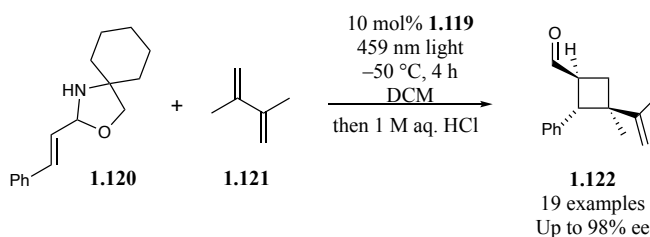
Recently, Bach disclosed a novel chiral motif with an imbedded thioxanthone sensitizer **1.119**. Bach tethered two thioxanthenes moieties toward a chiral phosphoric acid binding site. Conjugated carboxylic acid substrate **1.115** generate a 1:1 complex with the chiral catalyst **1.117**. Upon coordination, the substrate is well positioned for sensitization by the thioxanthone moiety. This preorganization accelerates the rate of sensitization to the bound substrate compared to the free substrate. This pathway in the chiral binding site of the catalyst affords the enantioselective [2+2] cycloaddition reaction to afford highly substituted cyclobutane products **1.118** in up to 86% ee (Scheme 1.19).<sup>33</sup>



Scheme 1.19 Single Catalytic Method for an Enantioselective [2+2] Photocycloaddition with Enones.

Using the same chiral phosphoric acid catalyst **1.119**, Bach and coworkers strategically selected a substrate that would be activated toward energy transfer upon protonation. They relied on the reversible equilibrium from *N,O*-acetals **1.120** to imines which, when protonated to the

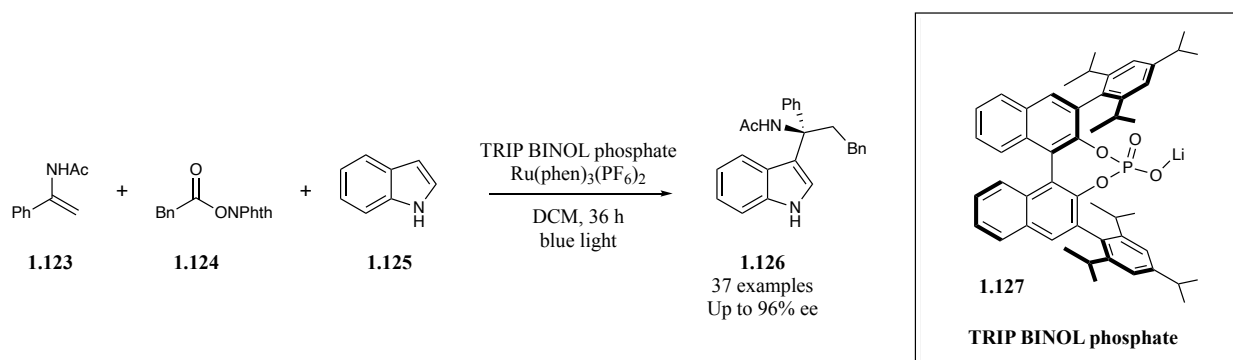
iminium ion, is a suitable substrate for energy transfer reactions. This is the first example of a chiral Brønsted acid catalyzed [2+2] photocycloaddition via energy transfer. Originally, they screened dual catalytic conditions using  $\text{Ru}(\text{bpy})_3(\text{PF}_6)_2$  as the photocatalyst and a separate chiral phosphoric acid catalyst, but the enantioselectivity of product **1.122** did not exceed 34% ee. However, using a single component strategy with a thioxanthone tethered chiral phosphoric acid **1.119**, they achieved enantioselectivity up to 98% ee (Scheme 1.20). They concluded that the phosphoric acid was promoting an exergonic energy transfer to the iminium ion and was providing the enantiodifferentiation for the excellent selectivity observed. Based on notable effects on the d.r., they postulated the chiral phosphoric acid catalyst remains bound to the substrate after the initial bond formation, thereby influencing the subsequent diastereomeric bond formation.<sup>34</sup>



Scheme 1.20 Single Catalytic Method for an Enantioselective [2+2] Photocycloaddition with Iminium Ions.

Wang and coworkers recently published an enantioselective dicarbofunctionalization of enamides using indoles and redox active esters.<sup>35</sup> The chiral environment is templated by a lithium BINOL phosphate catalyst **1.127**, accelerating the aggregation of the reactive species in a well-organized fashion. Mechanistically, the authors propose that the chiral phosphate catalyst can interact with both the enamide **1.123** and redox active ester **1.124** simultaneously to increase the rate of quenching of  $\text{Ru}(\text{II})$ . Plus, in the presence of all three species in solution, they observe a new absorbance feature between 370 – 400 nm suggesting a charge transfer complex in solution.

The reaction proceeds with blue light Ru(II) sensitization or with 390 nm direct absorption in the absence of Ru(II). The photochemical step affords an iminium intermediate, which is subsequently used for an asymmetric Friedel–Crafts reaction with indole **1.125**. This reaction affords a variety of chiral amine derivatives **1.126** containing a quaternary carbon center reaching up to 96% ee (Scheme 1.21).



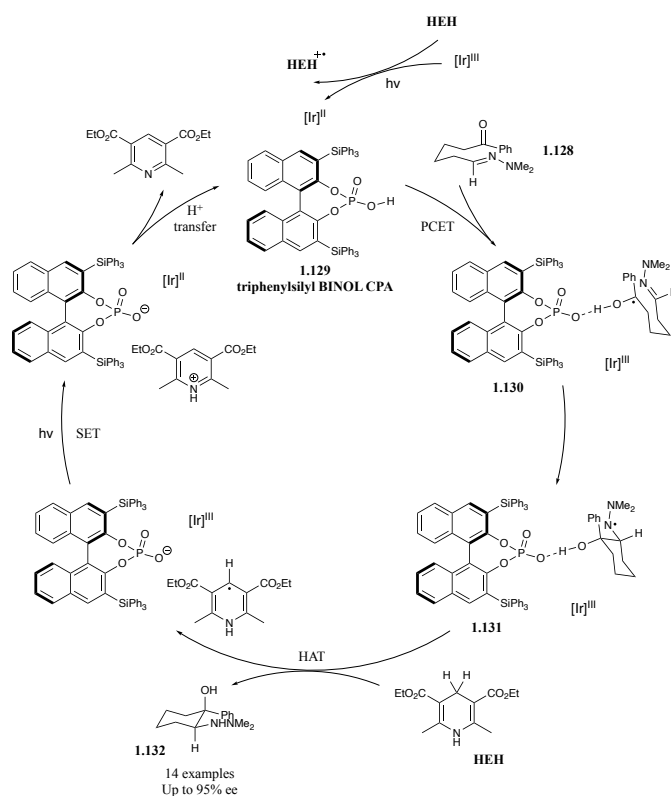
Scheme 1.21 Dual Catalytic Method for the Dicarbofunctionalization of Enamides using a Chiral Phosphate Base.

## 1.6. Enantioselective Proton Coupled Electron Transfer

Knowles and coworkers have pioneered synthetic applications for enantioselective PCET reactions. In 2013, the Knowles group reported a racemic annulation reaction using a Brønsted acid and a photoredox catalyst as the proton and electron source respectively.<sup>36</sup> This report marks the development of a new method for intramolecular ketyl-olefin couplings and paves the way for several enantioselective PCET processes using chiral phosphoric acid scaffolds.

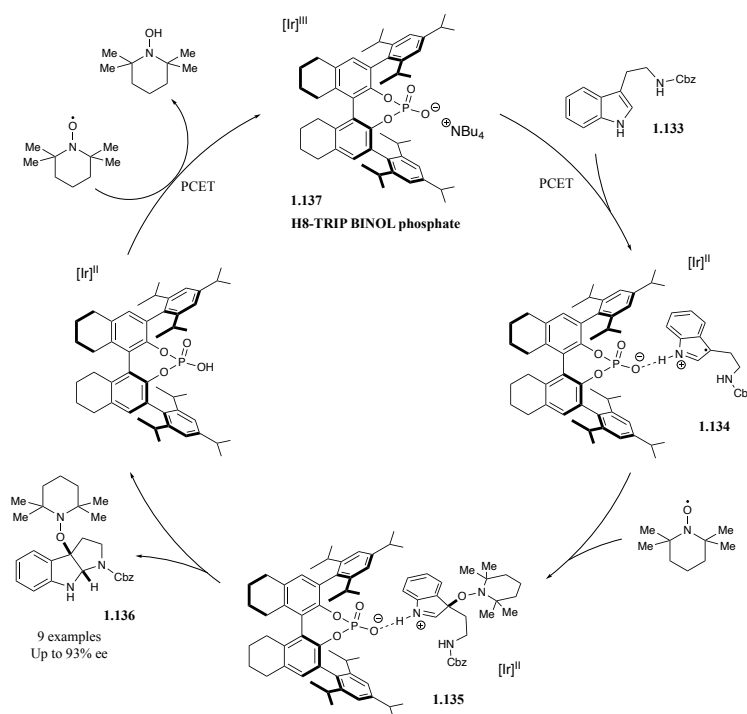
In 2013, the Knowles group reported an enantioselective aza-pinacol cyclization through a PCET pathway using both an iridium photocatalyst and a chiral BINOL phosphoric acid **1.129**.<sup>37</sup> The PCET event is mediated by the chiral Brønsted acid, resulting in a neutral ketyl radical

intermediate hydrogen-bonded to the chiral conjugate base **1.130**. Intramolecular ketyl-imine coupling occurs to forge a new C–C bond. The authors note that deuterium labeling experiments suggest the C–C bond forming step is both turnover-limiting and the enantioselectivity-determining. A subsequent HAT process affords the desired product **1.132** while a separate SET and proton transfer turns over the catalytic cycle (Scheme 1.22). While the exact binding of the chiral conjugate base to the radical intermediate is difficult to verify, the authors do preliminary computational studies to support their proposed H-bonded intermediate. Their calculations suggest that a ketyl-phosphate H-bond interaction is the lowest energy conformation and that the interaction may persist with a notable lifetime after radical generation. This also marks the first report of a catalytic, enantioselective aza-pinacol reaction, highlighting the utility of dual photochemical – Brønsted acid catalyzed systems.



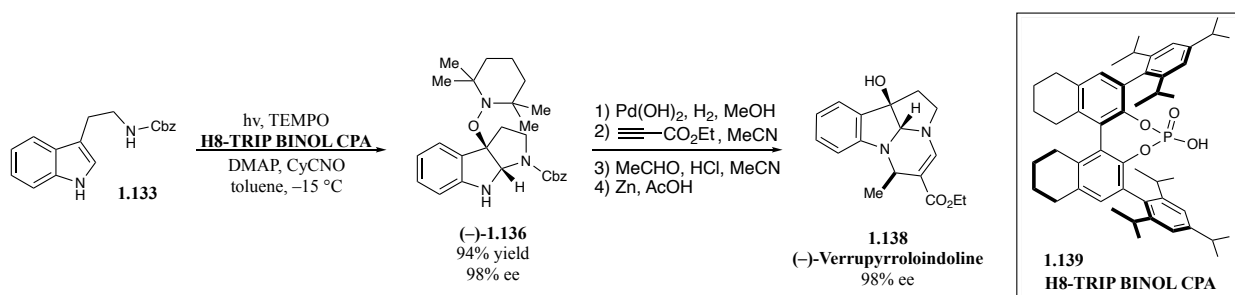
Scheme 1.22 PCET Promoted Enantioselective Aza-Pinacol Reaction.

In this above work, the Brønsted acid activates a ketone toward PCET. In contrast, Brønsted bases coordinate with hydrogen bond donors, making them useful for substrates containing amine-type hydrogen atoms. The Knowles group identified this orthogonal mode of activation, and in 2018 disclosed a PCET approach toward the enantioselective synthesis of pyrroloindoline small molecules.<sup>38</sup> A chiral Brønsted base **1.137** coordinates with a 3-substituted indole **1.133**. PCET generates a tryptamine radical cation and chiral phosphate base hydrogen-bonded complex **1.134**. Asymmetric trapping of this radical with TEMPO followed by annulation to the pyrroloindoline affords products **1.136** in high enantioselectivity (Scheme 1.23). In a separate reaction step, the authors highly the functionalization of the TEMPO substituted pyrroloindolines. Subsequent single electron oxidation and mesolytic cleavage affords loss of TEMPO to the resulting carbocation, enabling intermolecular trapping by a host of nucleophiles.



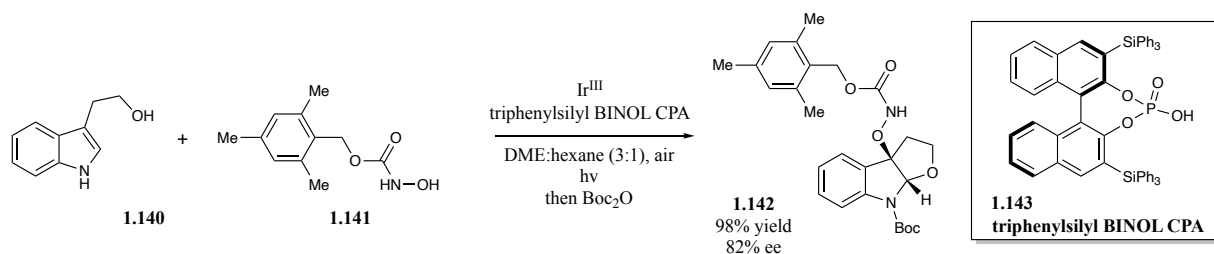
Scheme 1.23 Enantioselective Synthesis of Pyrroloindolines via PCET.

Shortly after, Xia and coworkers disclosed the same transformation without the use of an exogenous photocatalyst.<sup>39</sup> Visible light excitation of TEMPO induced a HAT with tryptamine **1.133** to afford an indole radical. Catalytic chiral H8-BINOL phosphoric acid **1.139** coordinates with this radical. Subsequent annulation and the addition of TEMPO traps the radical to afford pyrroloindoline products **1.136** in excellent selectivity. TEMPOH is generated as a byproduct of the HAT process, but cyclohexyl isocyanate was identified for its *in situ* removal. The authors use this strategy for an enantioselective total synthesis of (–)-Verrupyrroloindoline **1.138** in 5 steps and 98% ee (Scheme 1.24).



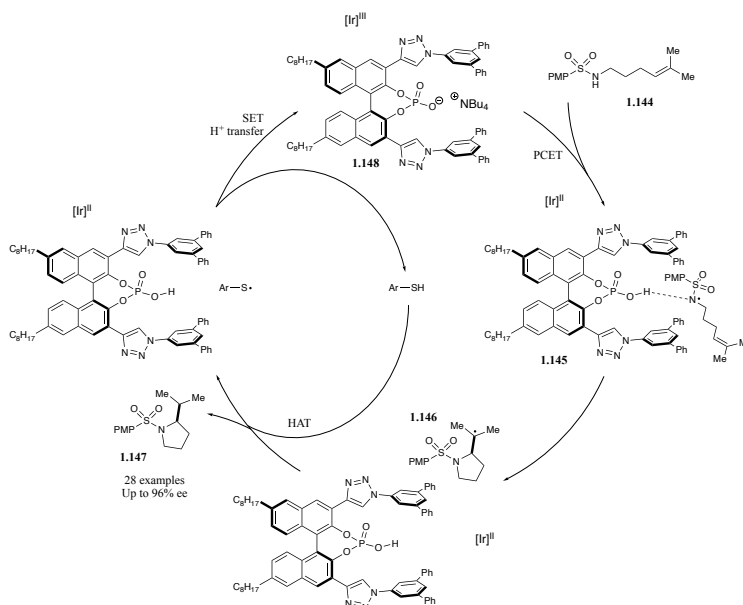
Scheme 1.24 Key Photochemical Step in the Enantioselective Total Synthesis of (–)-Verrupyrroloindoline.

These two previous syntheses of pyrroloindoline products have relied on the trapping with TEMPO and subsequent functionalization. In 2019, You and coworkers disclosed a one-pot route for these functionalized products.<sup>40</sup> Two photoredox SET oxidations access the carbocation intermediate. A chiral BINOL phosphoric acid **1.143** templates the asymmetric nucleophilic attack of various *N*-hydroxycarbamates **1.141** to afford products **1.142** in up to 92% ee (Scheme 1.25).



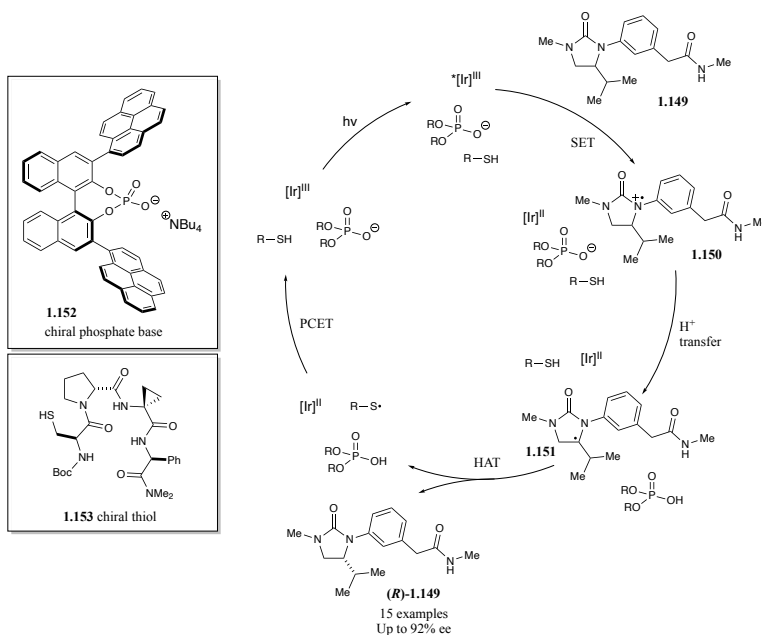
Scheme 1.25 Synthesis of Functionalized Pyrroloindoline Scaffolds.

The Knowles group has published an enantioselective intramolecular hydroamination of alkenes proceeding via a PCET mechanism.<sup>41</sup> The chiral Brønsted base **1.148** deprotonation and concurrent single electron oxidation of the sulfonamide generates a neutral sulfonamidyl radical **1.145**. The hydrogen-bonding interaction creates a chiral environment for the hydroamination to occur in excellent enantioselectivity. An achiral thiol acts as a catalytic HAT reagent to afford their annulated hydroamination products **1.147**. SET and proton transfer completes the catalytic cycle (Scheme 1.26). Consistent with the bound complex **1.145** being a neutral radical, the authors report the insensitivity of the enantioselectivity to solvent polarity.



Scheme 1.26 Intramolecular Hydroamination of Alkenes.

Knowles also disclosed an innovative deracemization of ureas via a dual enantioselective PCET and HAT sequence.<sup>42</sup> An Ir photosensitizer oxidizes a racemic mixture of a urea **1.149** to generate the urea radical cation **1.150**. A chiral Brønsted base **1.152** deprotonates the radical cation enantiomers at different rates, causing the enantioselective proton transfer to generate a prochiral  $\alpha$ -amino radical **1.151** preferentially from one enantiomer of the starting material. A chiral thiol **1.153** induces a subsequent enantioselective HAT process. Similarly, the delivery of the hydrogen atom is more favorable on one side of the prochiral radical. Tuning the selectivity of both the chiral Brønsted base and the chiral thiol enables excellent stereocontrol with this light-driven deracemization (Scheme 1.27). Both chiral catalysts were shown to act synergistically. With each catalyst providing modest selectivity independently, excellent selectivity is observed with the catalysts working in tandem. The authors determine the enantioselectivity of each catalyst, and they show how the synergist action between the two catalysts matches the mathematical product of their independent selectivity.



Scheme 1.27 Deracemization of Ureas via a Dual Enantioselective PCET and HAT Sequence.



## 1.7. Conclusions

Enantioselective photochemical transformations provide a direct route to many complex molecules that may be difficult to access via thermal reactivity. Yet, the methodology to control the stereochemistry of these reactions is still limited, often relying on either Lewis acid or Brønsted acid activation. In this chapter, I have compiled the current publications that control the enantioselectivity of photochemical reactions using chiral Brønsted acids, as this mode of substrate activation is still being developed with the different photocatalytic mechanisms. Compared to the more established field of Lewis acid activation, Brønsted acids can enable new libraries of substrates to be amenable to enantioselective photochemical transformations. Therefore, chiral Brønsted acid catalyzed photochemistry is a promising area for development. Of these synthetic applications discussed above, Brønsted acid catalyzed Dexter energy transfer reactions may uncover more examples of enantiocontrolled primary photochemical reactions. These reactions are notoriously difficult for enantioselective transformations due in part to their short-lived excited state.

Photochemistry is quickly becoming an indispensable tool for synthetic chemists. Techniques to control the stereochemistry in photochemical reactions will be valuable for the rapid assembly of complex small molecules and potential pharmaceutical scaffolds. Development of new chiral binding modes is, and will continue to be, instrumental in the widespread promotion of asymmetric synthetic photochemistry.

## 1.8. References

---

<sup>1</sup> (a) Skubi, K. L.; Blum, T. R.; Yoon, T. P. Dual Catalysis Strategies in Photochemical Synthesis. *Chem. Rev.* **2016**, *116*, 10035–10074. (b) Brenninger, C.; Jolliffe, J. D.; Bach, T. Chromophore

---

Activation of  $\alpha,\beta$ -Unsaturated Carbonyl Compounds and Its Application to Enantioselective Photochemical Reaction. *Angew. Chem. Int. Ed.* **2018**, *57*, 14338–14349. (c) Brimiouille, R.; Lenhart, D.; Maturi, M. M.; Bach, T. Enantioselective Catalysis of Photochemical Reactions. *Angew. Chem. Int. Ed.* **2015**, *54*, 3872–3890. (d) Prentice, C.; Morrisson, J.; Smith, A. D.; Zysman-Colman, E. Recent Developments in Enantioselective Photocatalysis. *Beilstein J. Org. Chem.* **2020**, *16*, 2363–2441.

<sup>2</sup> (a) Lv, X.; Xu, H.; Yin, Y.; Zhao, X.; Jiang, Z. Visible Light-Driven Cooperative DPZ and Chiral Hydrogen-Bonding Catalysis. *Chin. J. Chem.* **2020**, *38*, 1480–1488. (b) Proctor, R. S. J.; Colgan, A. C.; Phipps, R. J. Exploiting Attractive Non-Covalent Interactions for the Enantioselective Catalysis of Reactions Involving Radical Intermediates. *Nat. Chem.* **2020**, *12*, 990–1004.

<sup>3</sup> Mariano, P. S. The Photochemistry of Iminium Salts and Related Heteroaromatic Systems. *Tetrahedron* **1983**, *39* (23), 3845–3879.

<sup>4</sup> Yanagisawa, Y.; Nishiyama, Y.; Tanimoto, H.; Morimoto, T.; Kakiuchi, K. Enantiodifferentiating [2+2] Photocycloaddition of Cyclohexenone Carboxylic Acid with Ethylene using 8-phenylmenthyl amine as a Chiral Template. *Tetrahedron Lett.* **2014**, *55*, 2123–2126.

<sup>5</sup> Xiong, W.; Li, S.; Fu, B.; Wang, J.; Wang, Q.-A.; Yang, W. Visible-Light Induction/Brønsted Acid Catalysis in Relay for the Enantioselective Synthesis of Tetrahydroquinolines. *Org. Lett.* **2019**, *21* (11), 4173–4176.

<sup>6</sup> (a) Liao, H.-H.; Hsiao, C.-C.; Sugiono, E.; Rueping, M. Shedding Light on Brønsted Acid Catalysis – a Photocyclization-reduction reaction for the Asymmetric Synthesis of Tetrahydroquinolines from Aminochalcones in Batch and Flow. *Chem. Commun.*, **2013**, *49*, 7953–7955. (b) Sugiono, E.; Rueping, M. A Combined Continuous Microflow Photochemistry and Asymmetric Organocatalysis Approach for the Enantioselective Synthesis of Tetrahydroquinolines. *Beilstein J. Org. Chem.* **2013**, *9*, 2457–2462.

<sup>7</sup> Takagi, R.; Tabuchi, C. Enantioselective Intramolecular [2+2] Photocycloaddition using Phosphoric Acid as a Chiral Template. *Org. Biomol. Chem.* **2020**, *18*, 9261–9267.

<sup>8</sup> Jurczyk, J.; Lux, M. C.; Adpressa, D.; Kim, S. F.; Lam, Y.; Yeung, C. S.; Sarpong, R. Photomediated Ring Contraction of Saturated Heterocycles. *Science*, **2021**, *373*, 1004–1012.

<sup>9</sup> Sherbrook, E. M.; Genzink, M. J.; Park, B.; Guzei, I. A.; Baik, M.-H.; Yoon, T. P. Chiral Brønsted Acid-Controlled Intermolecular Asymmetric [2+2] Photocycloadditions. *Nat. Commun.*, **2021**, *12*, 5735–5741.

<sup>10</sup> Hepburn, H. B.; Melchiorre, P. Brønsted Acid-Catalysed Conjugate Addition of Photochemically Generated  $\alpha$ -amino Radicals to Alkenylpyridines. *Chem. Commun.* **2016**, *52*, 3520–3523.

<sup>11</sup> Cao, K.; Tan, S. M.; Lee, R.; Yang, S.; Jia, H.; Zhao, X.; Qiao, B.; Jiang, Z. Catalytic Enantioselective Addition of Prochiral Radicals to Vinylpyridines. *J. Am. Chem. Soc.* **2019**, *141*, 5437–5443.

- 
- <sup>12</sup> Yin, Y.; Dai, Y.; Jia, H.; Li, J.; Bu, L.; Qiao, B.; Zhao, X.; Jiang, Z. Conjugate Addition-Enantioselective Protonation of *N*-Aryl Glycines to  $\alpha$ -Branched 2-Vinylazaarenes via Cooperative Photoredox and Asymmetric Catalysis. *J. Am. Chem. Soc.* **2018**, *140*, 6083–6087.
- <sup>13</sup> Proctor, R. S. J.; Davis, H. J.; Phipps, R. J. Catalytic Enantioselective Minisci-Type Addition to Heteroarenes. *Science* **2018**, *360*, 419–422.
- <sup>14</sup> (a) Cheng, W.-M.; Shang, R.; Fu, Y. Photoredox/Brønsted Acid Co-Catalysis Enabling Decarboxylative Coupling of Amino Acid and Peptide Redox-Active Esters with *N*-Heteroarenes. *ACS Catal.* **2017**, *7*, 907–911. (b) Cheng, W.-M.; Shang, R.; Ru, M.-C.; Fu, Y. Photoredox-Catalysed Decarboxylative Alkylation of *N*-Heteroarenes with *N*-(Acyloxy)phthalimides. *Chem. Eur. J.* **2017**, *23*, 2537–2541.
- <sup>15</sup> Liu, X.; Liu, Y.; Chai, G.; Qiao, B.; Zhao, X.; Jiang, Z. Organocatalytic Enantioselective Addition of  $\alpha$ -Aminoalkyl Radicals to Isoquinolines. *Org. Lett.* **2018**, *20*, 6298–6301.
- <sup>16</sup> Proctor, R. S. J.; Chuentragool, P.; Colgan, A. C.; Phipps, R. J. Hydrogen Atom Transfer-Driven Enantioselective Minisci Reaction of Amides. *J. Am. Chem. Soc.* **2021**, *143*, 4928–4934.
- <sup>17</sup> Zheng, D.; Studer, A. Asymmetric Synthesis of Heterocyclic  $\gamma$ -Amino-Acid and Diamine Derivatives by Three-Component Radical Cascade Reactions. *Angew. Chem. Int. Ed.* **2019**, *58*, 15803–15807.
- <sup>18</sup> Qiao, B.; Li, C.; Zhao, X.; Yin, Y.; Jiang, Z. Enantioselective Reduction of Azaarene-based Ketones via Visible Light-Driven Photoredox Asymmetric Catalysis. *Chem. Commun.* **2019**, *55*, 7534–7537.
- <sup>19</sup> Shao, T.; Li, Y.; Ma, N.; Li, C.; Chai, G.; Zhao, X.; Qiao, B.; Jiang, Z. Photoredox-Catalyzed Enantioselective  $\alpha$ -Deuteration of Azaarenes with D<sub>2</sub>O. *iScience* **2019**, *16*, 410–419.
- <sup>20</sup> Li, J.; Kong, M.; Qiao, B.; Lee, R.; Zhao, X.; Jiang, Z. Formal Enantioconvergent Substitution of Alkyl Halides via Catalytic Asymmetric Photoredox Radical Coupling. *Nat. Commun.* **2018**, *9*, 2445–2453.
- <sup>21</sup> Che, C.; Li, Y.-N.; Cheng, X.; Lu, Y.-N.; Wang, C.-J. Visible-Light-Enabled Enantioconvergent Synthesis of  $\alpha$ -Amino Acid Derivatives via Synergistic Brønsted Acid/Photoredox Catalysis. *Angew. Chem. Int. Ed.* **2021**, *60*, 4698–4704.
- <sup>22</sup> Liu, Y.; Liu, X.; Li, J.; Zhao, X.; Qiao, B.; Jiang, Z. Catalytic Enantioselective Radical Coupling of Activated Ketones with *N*-Aryl Glycines. *Chem. Sci.* **2018**, *9*, 8094–8098.
- <sup>23</sup> Zeng, G.; Li, Y.; Qiao, B.; Zhao, X.; Jiang, Z. Photoredox Asymmetric Catalytic Enantioconvergent Substitution of 3-Chlorooxindoles. *Chem. Commun.* **2019**, *55*, 11362–11365.
- <sup>24</sup> Li, J.; Gu, Z.; Zhao, X.; Qiao, B.; Jiang, Z. Asymmetric Aerobic Decarboxylative Povarov Reactions of *N*-aryl  $\alpha$ -Amino Acids with Methylene-phthalimidines via Cooperative Photoredox and Chiral Brønsted Acid Catalysis. *Chem. Commun.* **2019**, *55*, 12916–12919.
- <sup>25</sup> Shao, T.; Yin, Y.; Lee, R.; Zhao, X.; Chai, G.; Jiang, Z. Sequential Photoredox Catalysis for Cascade Aerobic Decarboxylative Povarov and Oxidative Dehydrogenation Reactions of *N*-Aryl  $\alpha$ -Amino Acids. *Adv. Synth. Catal.* **2018**, *360*, 1754–1760.

- <sup>26</sup> Dai, Z.-Y.; Nong, Z.-S.; Wang, P.-S. Light Mediated Asymmetric Aliphatic C–H Alkylation with Hydrogen Atom Transfer Catalyst and Chiral Phosphoric Acid. *ACS Catal.* **2020**, *10*, 4786–4790.
- <sup>27</sup> Lyu, J.; Claraz, A.; Vitale, M. R.; Allain, C.; Masson, G. Preparation of Chiral Photosensitive Organocatalysts and Their Application for the Enantioselective Synthesis of 1,2-Diamines. *J. Org. Chem.* **2020**, *85*, 12843–12855.
- <sup>28</sup> (a) Lebé, C.; Languet, M.; Allain, C.; Masson, G.  $\alpha$ -Carbamoylsulfides as *N*-Carbamoylimine Precursors in the Visible Light Photoredox-Catalyzed Synthesis of  $\alpha,\alpha$ -Disubstituted Amines. *Org. Lett.* **2016**, *18*, 1478–1481. (b) Jarrige, L.; Levitre, G.; Masson, G. Visible-Light Photoredox-Catalyzed Coupling Reaction of Azoles with  $\alpha$ -Carbamoyl Sulfides. *J. Org. Chem.* **2016**, *81*, 7230–7236. (c) Lanzi, M.; Merad, J.; Boyarskaya, D. V.; Maestri, G.; Allain, C.; Masson, G. Visible-light-Triggered C–C and C–N Bond Formation by C–S Bond Cleavage of Benzylic Thioethers. *Org. Lett.* **2018**, *20*, 5247–5250. (d) Le, T.; Courant, T.; Merad, J.; Allain, C.; Audebert, P.; Masson, G. *s*-Tetrazine Dyes: A Facile Generation of Photoredox Organocatalysts for Routine Oxidations. *J. Org. Chem.* **2019**, *84*, 16139–16146.
- <sup>29</sup> Li, F.; Tian, D.; Fan, Y.; Lee, R.; Lu, G.; Yin, Y.; Qiao, B.; Zhao, X.; Xiao, Z.; Jiang, Z. Chiral Acid-Catalysed Enantioselective C–H Functionalization of Toluene and its Derivatives Driven by Visible Light. *Nat. Commun.* **2019**, *10*, 1774–1782.
- <sup>30</sup> Bu, L.; Li, J.; Yin, Y.; Qiao, B.; Chai, G.; Zhao, X.; Jiang, Z. Organocatalytic Asymmetric Cascade Aerobic Oxidation and Semipinacol Rearrangement Reaction: A Visible Light-Induced Approach to Access Chiral 2,2-Disubstituted Indolin-3-ones. *Chem. Asian. J.* **2018**, *13*, 2382–2387.
- <sup>31</sup> (a) Zalewski, R. I.; Dunn, G. E. Protonation of Conjugated Carbonyl Groups in Sulfuric Acid Solution. I. Adaptation of the Amide Acidity Function  $H_A$  for Protonation of the Carbonyl Group in Non-Hammett Bases. *Can. J. Chem.* **1968**, *46*, 2469–2470. (b) Zalewski, R. I.; Dunn, G. E. Protonation of Conjugated Carbonyl Groups in Sulfuric Acid Solutions. II. Protonation and Basicity of  $\alpha,\beta$ -Unsaturated Alicyclic Ketones. *Can. J. Chem.* **1969**, *47*, 2263–2270. (c) Rusakowicz, R.; Byers, G. W.; Leermakers, P. A. Electronically Excited Aromatic Carbonyl Compounds in Hydrogen Bonding and Acidic Media. *J. Am. Chem. Soc.* **1971**, *93*, 3263–3266.
- <sup>32</sup> Großkopf, J.; Kratz, T.; Rigotti, T.; Bach, T. Enantioselective Photochemical Reactions Enabled by Triplet Energy Transfer. *Chem. Rev.* **2021**, Article ASAP. DOI: 10.1021/acs.chemrev.1c00272 (accessed 2021-10-16).
- <sup>33</sup> Pecho, F.; Zou, Y.-Q.; Gramüller, J.; Mori, T.; Huber, S. M.; Bauer, A.; Gschwind, R. M.; Bach, T. A Thioxanthone Sensitizer with a Chiral Phosphoric Acid Binding Site: Properties and Applications in Visible Light-Mediated Cycloadditions. *Chem. Eur. J.* **2020**, *26*, 5190–5194.
- <sup>34</sup> Pecho, F.; Sempere, Y.; Gramüller, J.; Hörmann, F. M.; Gschwind, R. M.; Bach, T. Enantioselective [2+2] Photocycloaddition via Iminium Ions: Catalysis by a Sensitizing Chiral Brønsted Acid. *J. Am. Chem. Soc.* **2021**, *143*, 9350–9354.
- <sup>35</sup> Shen, Y.; Shen, M.-L.; Wang, P.-S. Light-Mediated Chiral Phosphate Catalysis for Asymmetric Dicarbofunctionalization of Enamides. *ACS Catal.* **2020**, *10*, 8247–8253.

- 
- <sup>36</sup> Tarantino, K. T.; Liu, P.; Knowles, R. R. Catalytic Ketyl-Olefin Cyclizations Enabled by Proton-Coupled Electron Transfer. *J. Am. Chem. Soc.* **2013**, *135*, 10022–10025.
- <sup>37</sup> Rono, L. J.; Yayla, H. G.; Wang, D. Y.; Armstrong, M. F.; Knowles, R. R. Enantioselective Photoredox Catalysis Enabled by Proton-Coupled Electron Transfer: Development of an Asymmetric Aza-Pinacol Cyclization. *J. Am. Chem. Soc.* **2013**, *135*, 17735–17738.
- <sup>38</sup> Gentry, E. C.; Rono, L. J.; Hale, M. E.; Matsuura, R.; Knowles, R. R. Enantioselective Synthesis of Pyrroloindolines via Noncovalent Stabilization of Indole Radical Cations and Applications to the Synthesis of Alkaloid Natural Products. *J. Am. Chem. Soc.* **2018**, *140*, 3394–3402.
- <sup>39</sup> Liang, K.; Tong, X.; Li, T.; Shi, B.; Wang, H.; Yan, P.; Xia, C. Enantioselective Radical Cyclization of Tryptamines by Visible Light-Excited Nitroxides. *J. Org. Chem.* **2018**, *83*, 10948–10958.
- <sup>40</sup> Cheng, Y.-Z.; Zhao, Q.-R.; Zhang, X.; You, S.-L. Asymmetric Dearomatization of Indole Derivatives with *N*-Hydroxycarbamates Enabled by Photoredox Catalysis. *Angew. Chem. Int. Ed.* **2019**, *58*, 18069–18074.
- <sup>41</sup> Roos, C. B.; Demaerel, J.; Graff, D. E.; Knowles, R. R. Enantioselective Hydroamination of Alkenes with Sulfonamides Enabled by Proton-Coupled Electron Transfer. *J. Am. Chem. Soc.* **2020**, *142*, 5974–5979.
- <sup>42</sup> Shin, N. Y.; Ryss, J. M.; Xin, Z.; Miller, S. J.; Knowles, R. R. Light-Driven Deracemization Enabled by Excited-State Electron Transfer. *Science* **2019**, *366*, 364–369.

## Chapter 2. Cooperative Stereoinduction in Asymmetric Photocatalysis

## 2.1. Background

### 2.1.1. Matched/Mismatched Effects

The ability to predict and control the stereochemical outcome of a chemical transformation is a defining characteristic of modern organic synthesis. A central concern in stereochemically complex reactions is the combined influence of multiple interacting stereochemical elements. When two chiral components interact in a reaction that forms a product with at least one new stereocenter, they can either reinforce each other's individual preferences in a "matched" case, or their intrinsic preferences can oppose one another in a "mismatched" case.<sup>43</sup> Large differences in the rate and selectivity of matched and mismatched sets of analogous reactions have been documented in classical, ground-state asymmetric synthesis and represent some of the canonical experiments in the field of asymmetric catalysis (Figure 2.1A).<sup>44</sup> Similar effects have rarely been observed in excited-state reactions, in part because general strategies for highly enantioselective photochemical reactions have only recently emerged.<sup>45</sup> Herein, we report the highly enantioselective excited-state [2+2] photocycloaddition reaction of vinyl pyridines using tandem chiral Brønsted acid and Ir(III) photocatalysis. Importantly, we observe a significant stereochemical matching effect between the chirality of the Brønsted acid and Ir(III) co-catalysts. This observation suggests that similar cooperative stereocontrolling effects could be relevant in other tandem asymmetric photocatalytic methods.

### 2.1.2. Current Asymmetric Dual Photocatalysis Systems

Asymmetric dual photocatalysis—the combination of a photocatalyst with a second photoinactive chiral co-catalyst—is arguably among the most flexible methods for controlling stereochemistry in photochemical reactions. Notably, the photocatalysts used in these dual-

catalytic reactions are often pseudo-octahedral Ru- and Ir-polypyridyl complexes that possess helical  $\Delta$ - or  $\Lambda$ -chirality about the metal center.<sup>46</sup> Meggers exploited this metal-centered stereochemistry to design remarkably effective single-component organometallic photocatalysts for a range of useful, highly enantioselective organic photoreactions.<sup>47</sup> However, in dual-catalytic asymmetric photoreactions, the innate chirality of the photocatalysts is largely ignored, and they are used as a racemic mixture that masks any possible matched/mismatched effects between the catalysts. In many reactions, using racemic photocatalyst is sensible. These include, for example, MacMillan's seminal photoredox-organocatalytic alkylation of aldehydes<sup>48</sup> and our group's Lewis acid controlled enantioselective excited-state [2+2] photocycloadditions of chalcones (Figure 2.1B).<sup>49</sup> The collisional photoactivation step in these reactions generates reactive intermediates that can dissociate and react outside the chiral influence of the photocatalyst. As a result, the enantiodetermining environment of the reaction is generally presumed to be determined solely by the stereochemistry of the chiral co-catalyst and not by the chirality of the photocatalyst. To the best of our knowledge, the effect of the photocatalyst chirality in dual catalytic photoreactions has only been investigated by Ooi, who developed a chiral boronate anion that controlled the stereochemistry of an enantioselective photochemical [3+2] cycloaddition. In these studies, the individual enantiomers of the [Ir] photocatalyst cation showed no effect on the rate of reaction or degree of stereinduction (Figure 2.1C).<sup>50</sup>



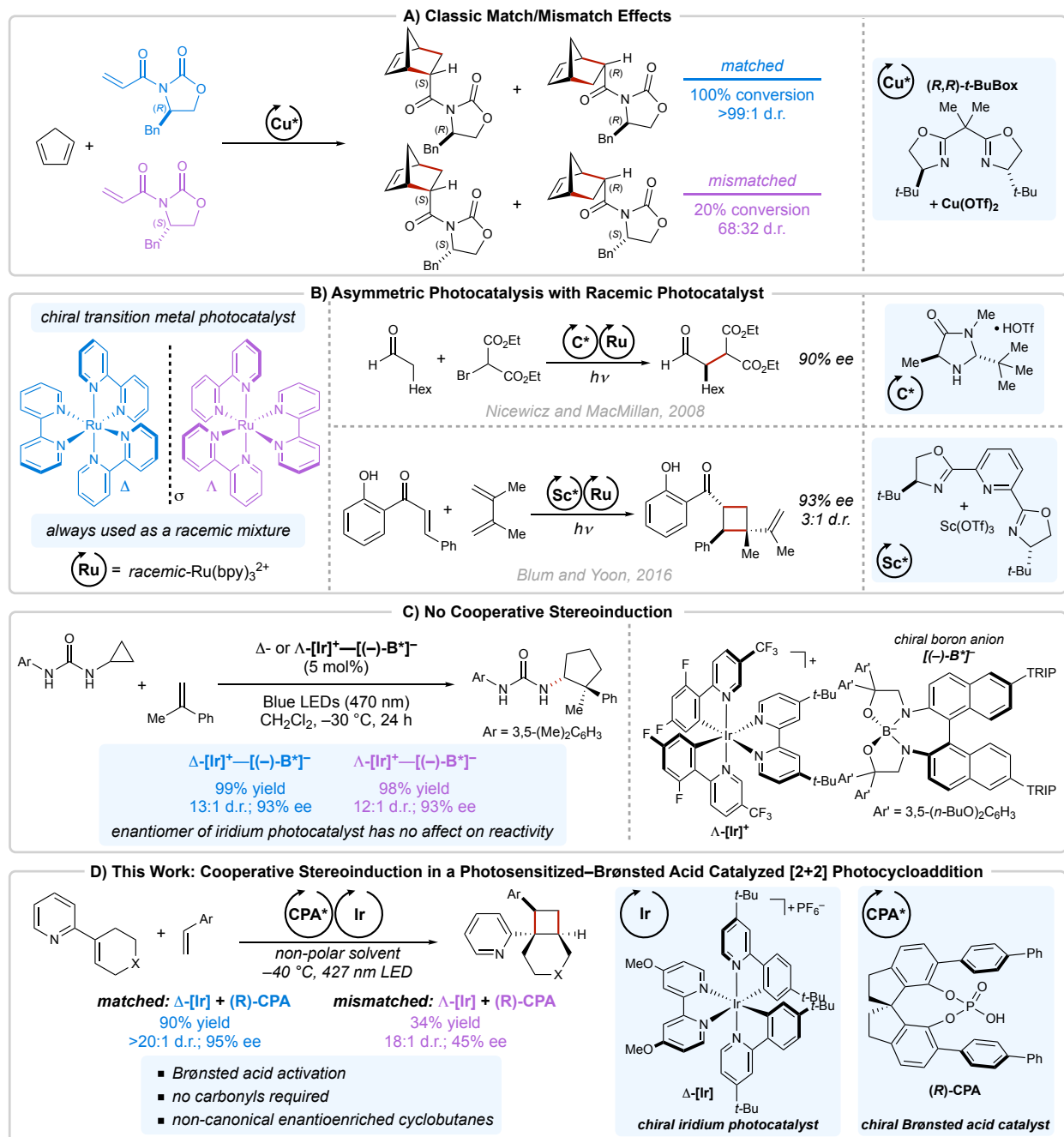


Figure 2.1 (A) Matched/mismatched effects observed in fundamental ground-state asymmetric catalysis. (B) Examples of asymmetric dual-catalytic photochemical reactions where chiral transition metal photocatalysts have been used as racemates. (C) Ooi's report showing no dependence of reaction selectivity on the chirality of the [Ir] photocatalyst. (D) This work highlighting cooperative stereoinduction between the [Ir] photocatalyst and the CPA.

## 2.2. Optimization of the Enantioselective Vinylheteroarene [2+2] Photocycloaddition

We report herein the first example of cooperative stereoinduction involving a chiral [Ir] photocatalyst for a dual-photocatalytic transformation (Figure 2.1D). This observation arose during the development of an asymmetric methodology for the [2+2] photocycloaddition of vinyl pyridines. We were attracted to this problem because nearly all catalytic enantioselective [2+2] photocycloadditions reported to date have involved carbonyl-based substrates,<sup>51</sup> which limits the structural variety of complex cyclobutanes synthetically accessible in enantiopure form.<sup>52</sup> Chiral Brønsted acids are often ideally suited for activating different classes of organic substrates than do Lewis acids,<sup>53</sup> and they have been used effectively in several asymmetric reactions of pyridines. We hypothesized, therefore, that a dual catalytic system comprising a chiral Brønsted acid and a triplet sensitizing photocatalyst<sup>54</sup> might enable the first highly enantioselective [2+2] photocycloaddition of vinyl pyridines. Concurrent with our investigation, Gschwind and Bach published the first chiral Brønsted acid catalyzed enantioselective [2+2] photocycloaddition;<sup>55</sup> however, this reaction involves carbonyl-based substrates similar to previously reported methods. The system we describe herein enables the synthesis of previously inaccessible enantioenriched pyridyl cyclobutanes and reveals excited-state matched-mismatched catalyst pairs that we believe have important implications in the emerging field of asymmetric photocatalysis.

Figure 2.2A summarizes the optimization studies that resulted in this central observation. Irradiation of vinylpyridine **2.1** and styrene in the presence of a BINOL-derived chiral phosphoric acid (CPA1) and *rac*-[Ir(dtbbpy)<sub>2</sub>(dMeObpy)]PF<sub>6</sub> (*rac*-[Ir]) afforded the corresponding cycloadduct in low yield and selectivity (Figure 2.2A, entry 1). The reaction yield increased in less polar solvents (Figure 2.2A, entries 2–3), consistent with enhancement of Brønsted acid/base

interactions in low-dielectric media (Figure 2.2B); the enantiomeric excess (ee), however, remained low. A screen of alternate chiral phosphoric acids revealed that 3,5-CF<sub>3</sub>-SPINOL-derived CPA2 provided the cyclobutane product in a significantly higher 64% ee (Figure 2.2A, entry 4). Lowering the temperature to -40 °C improved cycloadduct d.r. with a modest effect on the ee (Figure 2.2A, entry 5). A 4-biphenyl-SPINOL-derived CPA3 proved optimal, affording the desired cycloadduct in high yields, excellent d.r., and 94% ee (Figure 2.2A, entry 6). Control reactions demonstrated the necessity of the CPA (Figure 2.2A, entry 7), the iridium photosensitizer (Figure 2.2A, entry 8), and light (Figure 2.2A, entry 9).

### 2.3. Original Observation of the Excited-State Matched/Mismatched Effects

Surprisingly, control experiments with an achiral photosensitizer (thioxanthone) resulted in decreased ee (Figure 2.2A, entry 10). Because we observed no background reaction using thioxanthone alone in the absence of CPA3, this result thus seemed to implicate a substrate–photocatalyst interaction in the stereochemistry-determining step of the transformation. As a test for this putative interaction, we first examined the effect of photocatalyst chirality on the enantioselectivity of the [2+2] photoreaction. Enantiopure [Ir] complexes were prepared using the method of Meggers,<sup>56</sup> and upon examining their performance in the model [2+2] photoreaction, we found that  $\Delta$ -[Ir] affords the cycloadduct in significantly higher yield and ee than  $\Lambda$ -[Ir] (Figure 2.2C). We further performed an experiment using enantiopure  $\Lambda$ -[Ir] and racemic CPA3, which provided *ent*-**2.2** in 29% ee despite the lack of any obvious means for interaction between the photocatalyst and substrates (Figure 2.2D). Together, these results implicate an unprecedented cooperative influence of photocatalyst and co-catalyst stereochemistry on the outcome of an asymmetric photochemical transformation.

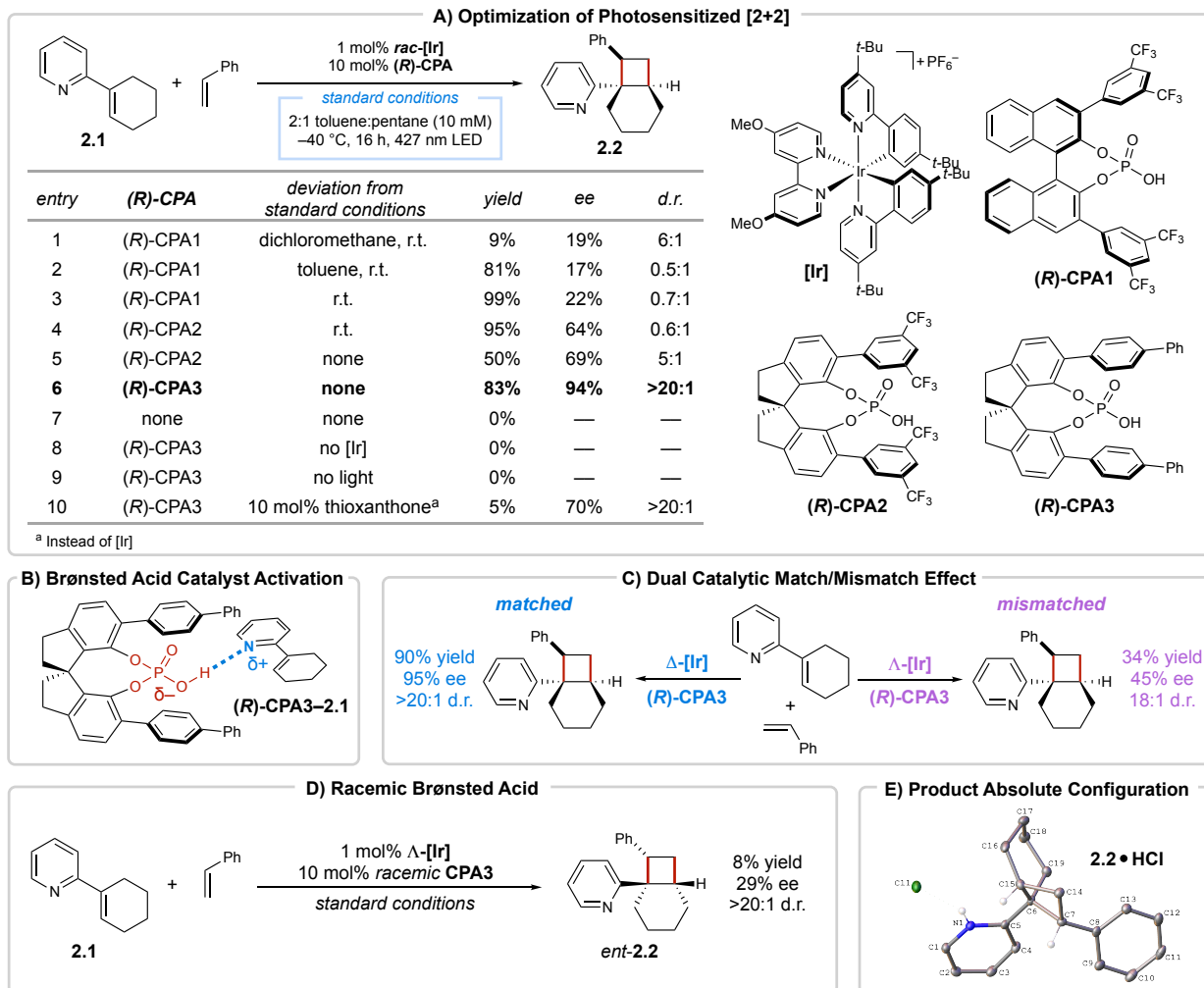


Figure 2.2 (A) Optimization of the enantioselective [2+2] photocycloaddition of vinylpyridine **2.1** using racemic [Ir] as the photocatalyst. (B) Schematic depiction of Brønsted acid activation of **2.1**. (C) Empirical observation of dual-catalytic matched/mismatched effects in the photocycloaddition of **2.1**. (D) Highlighting the marked influence of the chiral [Ir] on the selectivity of the reaction. (E) X-ray crystal structure of **2.2**•HCl.

## 2.4. Scope of the Enantioselective [2+2] Photocycloaddition

There are few methods for the asymmetric synthesis of heteroarene-substituted cyclobutanes and none involving an excited-state vinylheteroarene. Studies investigating the scope

of this novel asymmetric cyclobutane synthesis were therefore conducted and are summarized in Figure 2.3. Notably, cooperative stereocontrol appears to be a general feature of this method, with higher yield, d.r., and ee consistently obtained when  $\Delta$ -[Ir] is used as the photocatalyst compared to either  $\Lambda$ - or rac-[Ir] (see SI). Electron-rich styrenes afford increased rates of cycloaddition in slightly higher ee than electron-poor styrenes. *Meta*-substitution of the styrene maintains excellent selectivity, but we observed a small decrease in ee with *ortho*-substituted styrenes. A reaction with  $\alpha$ -methylstyrene successfully sets two adjacent quaternary stereocenters, and the reaction with  $\beta$ -methylstyrene controls the stereochemistry of all four atoms of the product cyclobutane. In contrast to the generality observed with the styrene coupling partner, we noticed that small structural perturbations to the vinyl pyridine would often cause a significant change in ee, consistent with its putative role in interacting with the chiral acid catalyst. Changes to the alkene moiety allowed for additional diversification; substituted rings, heterocycles, and smaller rings were well tolerated. The absolute configuration of the parent cycloadduct **2.2** was determined from the crystal structure of its HCl salt (Figure 2.2E).

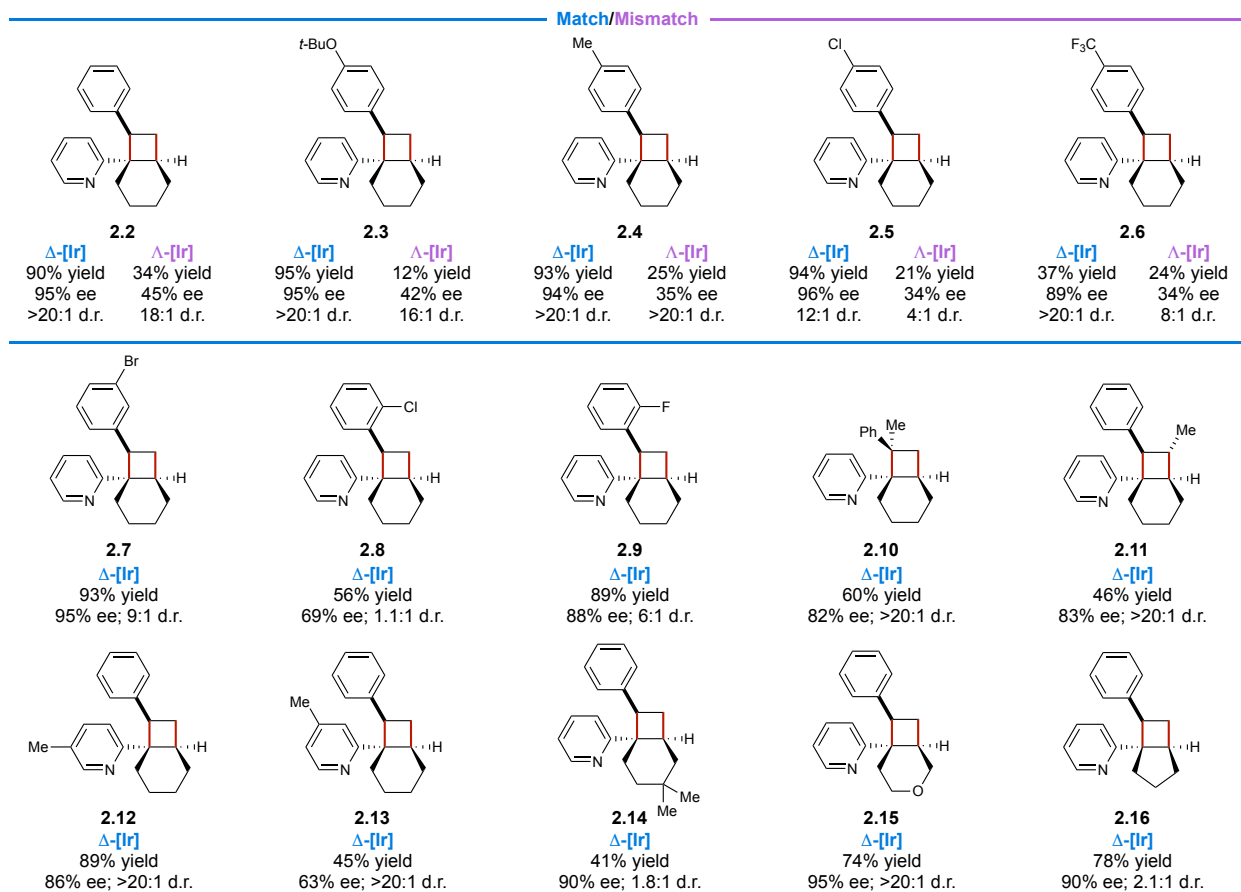


Figure 2.3 Scope of the enantioselective [2+2] photocycloaddition. Conditions matched entry 6 in Figure 2.2A, 0.31 mmol. Diastereomer ratios (d.r.) were determined by proton nuclear magnetic resonance ( $^1\text{H}$  NMR) analysis of the unpurified reaction mixture. Enantiomer ratios were determined using chiral supercritical fluid chromatography (SFC) analysis.

## 2.5. Mechanistic Investigations

### 2.5.1. Energy Transfer to the Protonated Vinyl Pyridine

The unexpected observation of cooperative stereinduction between the chiral photocatalyst and Brønsted acid prompted us to interrogate the mechanism of this asymmetric cycloaddition in greater detail. First, we ruled out electron transfer as an activation mechanism by

cyclic voltammetry; the relative reduction potentials of the photocatalyst and vinyl pyridine in the presence and absence of CPA indicate that excited-state electron transfer is not thermodynamically feasible, and that this reaction most likely occurs through an energy transfer pathway. From the emission spectrum of the photocatalyst, we determined its triplet energy to be  $E_T = 59$  kcal/mol (see SI). Stern–Volmer experiments demonstrated that neither styrene nor free vinylpyridine substantially quench the emission of the [Ir] triplet state. However, in the presence of trifluoroacetic acid (TFA) as a surrogate for the CPA, protonated vinylpyridine substantially quenches the [Ir] emission with a Stern–Volmer constant ( $K_{SV}$ ) of  $10.8 \text{ M}^{-1}$ . These experiments show that energy transfer to the vinylpyridine is accelerated in the presence of Brønsted acids.

### 2.5.2. Classical Energy-Transfer Mechanism

A conventional energy-transfer mechanism would involve a collisional interaction between the CPA3–vinylpyridine salt and excited iridium; in this mechanism, the excited-state vinylpyridine salt would be freely diffusing independent of the photosensitizing [Ir] complex. However, we can readily exclude this standard mechanism given the marked effect of photocatalyst stereochemistry on the enantioselectivity of this reaction. Even if the two enantiomers of [Ir] gave different rates for diffusional energy transfer, no effect on ee would be expected if the enantioselective cycloaddition would occur outside of the stereochemical influence of the photocatalyst. Therefore, we conclude that the [Ir] photocatalyst must be intimately involved in the enantiodetermining step of any proposed mechanism.

### 2.5.3. Possible Ways for Cooperative Stereoinduction

#### 2.5.3.1. Ground State Interaction

We considered two ways in which the chiral co-catalysts ([Ir] and CPA3) might interact to provide cooperative stereoinduction. First, a ground-state interaction would preorganize the chiral photocatalyst and Brønsted acid adduct into the diastereomeric complexes  $\{\Delta\text{-[Ir]---}[(R)\text{-CPA3-2.1}]\}$  and  $\{\Lambda\text{-[Ir]---}[(R)\text{-CPA3-2.1}]\}$ , each of which could operate as a single diastereomerically pure unit. Knowles and Alexanian recently reported a reaction involving an iridium photocatalyst associated with an anionic phosphate co-catalyst via Coulombic and hydrogen-bonding interactions.<sup>57</sup> Unlike this prior report, however, NMR titrations performed with  $\Delta\text{-[Ir]}$  and  $(R)\text{-CPA3}$  provided no evidence for a ground-state interaction with or without pyridine present to act as a surrogate for **2.1**. Similarly, we observed no significant changes in the absorption profile of the photocatalyst upon the addition of either  $(R)\text{-CPA3}$  or  $(R)\text{-CPA3-2.1}$  (see supporting information). Together, these experiments rule out the formation of ground-state diastereomeric complexes as a mechanism for cooperative stereoinduction.

#### 2.5.3.2. Excited-State Interaction

In the absence of any ground-state interaction between the catalysts, we concluded that photoexcited  $\Delta\text{-[Ir]}^3$  and  $\Lambda\text{-[Ir]}^3$  must associate with  $[(R)\text{-CPA3-2.1}]$  into transient diastereomeric excited-state complexes. These diastereomeric complexes would be expected to show distinct photochemical properties and different reactivity towards styrene, consistent with the observed matched/mismatched effect. To interrogate this possibility, we studied the photoluminescence spectra of the iridium photocatalysts. Surprisingly, excitation of [Ir] in the presence of  $(R)\text{-CPA3}$  resulted in an increase in the emission intensity; both  $\Delta\text{-}$  and  $\Lambda\text{-[Ir]}$  gave similar increases. A



substantially larger increase in emission was observed upon the addition of 10 equiv. of vinylpyridine to a solution containing (*R*)-CPA3 and  $\Delta$ -[Ir] (*matched conditions*), along with an apparent hypsochromic shift in the emission signal (Figure 2.4B, data collected by Wesley B. Swords). This feature is not observed upon direct irradiation of CPA-**2.1** in the absence of  $\Delta$ -[Ir] (see supporting information). Under otherwise identical conditions, excitation of  $\Lambda$ -[Ir] resulted in a much smaller increase in emission intensity (*mismatched conditions*). Stern–Volmer analysis of this interaction could not be conducted due to the presence of this new overlapping emission feature and the relatively short lifetime of the free Ir photocatalyst. However, the distinct difference in emission intensity confirms a diastereomeric difference in the interaction of (*R*)-CPA3 with  $\Delta$ - and  $\Lambda$ -[Ir] in the excited state.

#### 2.5.4. Diastereotopic Reactions with Styrene

We were intrigued by the possibility that the matched/mismatched effect might arise from the differential reactivity of the two transient diastereomeric [Ir---CPA3-**2.1**] excited-state complexes. If so, we would expect the diastereomeric complexes to react with styrene at different rates. The addition of styrene to the combination of  $\Delta$ -[Ir] and CPA3-**2.1** quenched the photoluminescence intensity (Figure 2.4C). Notably, the quenching was strongest at shorter wavelengths, the emission from the proposed excited-state complexes. A Stern–Volmer analysis of the quenching between 440–490 nm provided a linear correlation with styrene concentration and a Stern–Volmer constant ( $K_{SV}$ ) of 5.6 M<sup>-1</sup>. The corresponding analysis of the quenching of the diastereomeric  $\Lambda$ -[Ir]/CPA3-**2.1** combination, on the other hand, resulted in 39% less efficient luminescence quenching ( $K_{SV} = 3.4$  M<sup>-1</sup>). Thus, as anticipated, the two diastereomeric catalyst complexes react with styrene with different efficiencies, consistent with the observed matched/mismatched effects.

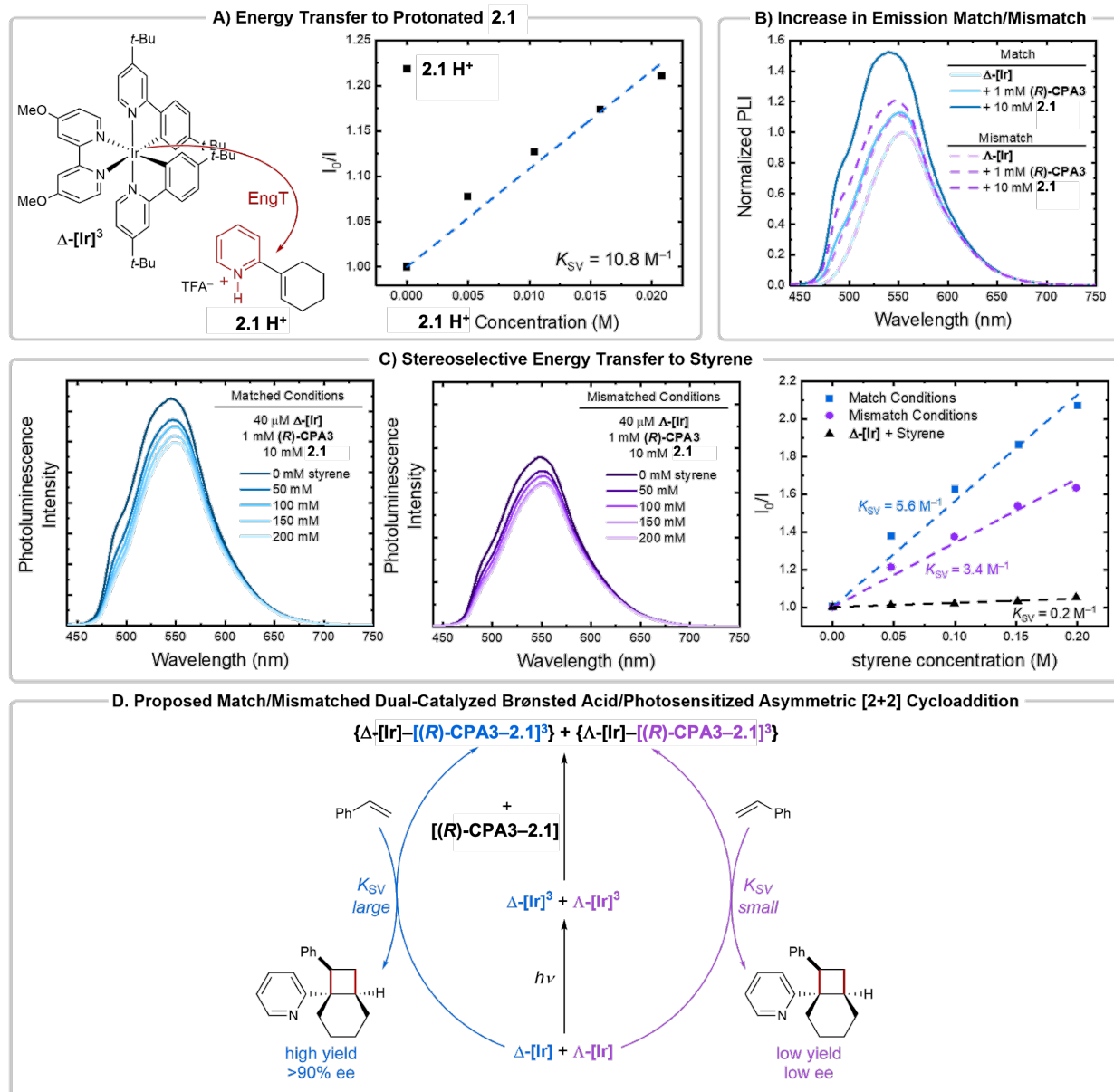


Figure 2.4 (A) Stern–Volmer plot of the quenching of excited-state  $\Delta$ -[Ir] with protonated **2.1** ( $2.1\text{H}^+$ ). Dashed line is a linear regression of the data. (B) Overlaid emission spectra of  $\Delta$ -[Ir] (solid lines) and  $\Lambda$ -[Ir] (dashed lines) in the presence of (*R*)-CPA3 and (*R*)-CPA3 with 10 equiv. **2.1**. With only (*R*)-CPA3 the emission of  $\Delta$ -[Ir] and  $\Lambda$ -[Ir] nearly overlay, while with both (*R*)-CPA3 and **2.1** a larger increase in emission is observed for  $\Delta$ -[Ir]. (C) Quenching of emission of

the mixture of  $\Delta/\Lambda$ -[Ir], (**R**)-CPA3, and **2.1** by styrene along with Stern–Volmer plots. (D) Proposed mechanism.

## 2.6. Proposed Mechanism

Based on these combined observations, we propose the mechanism outlined in Figure 2.4D. The photocatalytic  $\Delta$ -[Ir] chromophore is excited to afford a triplet state ( $\Delta$ -[Ir]<sup>3</sup>) that forms a transient excited-state complex with the preassociated CPA3–**2.1** complex,  $\{\Delta$ -[Ir]—[(*R*)-CPA3–**2.1**]<sup>3</sup>. Intracomplex energy transfer to [(*R*)-CPA3–**2.1**] followed by reaction with styrene results in the formation of highly enantioenriched cycloadduct **2.2**. The mismatched pathway follows a similar mechanism. However, the diastereomeric  $\{\Lambda$ -[Ir]—[(*R*)-CPA3–**2.1**]<sup>3</sup> complex reacts with styrene less efficiently and produces **2.2** with lower ee. When the [Ir] photocatalyst is used as a racemate, both reaction pathways are operative, but the matched case can outcompete the mismatched case as evidenced by the high yield and ee obtained.

## 2.7. Computation Investigations

Computationally identifying the optimized collisional geometries for both the matched and mismatched complexes is not feasible with current computational limitations. However, Mina Son and Yerin Park (Korea Advanced Institute of Science and Technology) are examining the impact of the CPA on the enantioselectivity of the reaction. These investigations are ongoing.

## 2.8. Conclusion

In conclusion, we report the first example of cooperative stereinduction in a photocatalytic reaction, where the most selective conditions necessitate a stereochemical match between a chiral [Ir] photocatalyst and chiral Brønsted acid catalyst. Synthetically, this is the first method capable

of controlling an excited-state vinylheteroarene to afford enantioenriched pyridine-substituted cyclobutane products. The observed matched/mismatched effects originate from the generation of diastereomeric excited-state cocatalyst pairs that have different photophysical dynamics and afford differing rates of reaction with styrene. To our knowledge, this cooperative stereoinduction involving excited-state catalyst pairs is unprecedented in dual catalysis, but it indicates that similar effects may be present across a range of tandem asymmetric photocatalytic methods. Hence, matched/mismatched effects may become a widely consequential variable in the development of future dual-catalytic photochemical transformations.

## 2.9. Contributions

Steven J. Chapman (University of Wisconsin – Madison) performed the reaction optimization, scope, and mechanistic experiments. Wesley B. Swords (University of Wisconsin – Madison) performed the mechanistic data workup and collected the data in Figure 2.4B. Mina Son and Yerin Park (Korea Advanced Institute of Science and Technology) performed the computation investigations. Christine Le (University of California – Berkeley) synthesized the diverse library of CPA backbones in Figure 2.7 used for reaction optimization. Ilia A. Guzei (University of Wisconsin – Madison) collected and analyzed the x-ray crystallographic data. F. Dean Toste (University of California – Berkeley), Mu-Hyun Baik (Korea Advanced Institute of Science and Technology), and Tehshik P. Yoon (University of Wisconsin – Madison) provided their expertise, their resources, and their funding for their respective researchers.

## 2.10. Supporting Information

### 2.10.1. General Information

Styrene starting materials were distilled before use. All other materials were purchased from commercial suppliers and used without further purification or synthesized as described below. Except in the case of aqueous reactions, all reaction glassware was flame- or oven-dried prior to use. Dichloromethane ( $\text{CH}_2\text{Cl}_2$ ), toluene, and diethyl ether ( $\text{Et}_2\text{O}$ ) were dried by passage through columns of activated alumina. Pentane was stored over 4 Å molecular sieves. Flash column chromatography was performed using Purasil 60 Å silica gel. The absolute stereochemistry of the parent cyclobutane product was determined by x-ray diffraction; all other cyclobutane products were assigned by association. Irradiation for photochemical reactions was provided by one Kessil PR160L-427 LED (max 45 W, wavelength maximum 427 nm) placed approximately 10 cm from the reaction vessel. Temperature control for enantioselective photoreactions was provided by a Thermo Scientific EK90 Immersion cooler.

$^1\text{H}$ ,  $^{13}\text{C}\{^1\text{H}\}$ ,  $^{19}\text{F}\{^1\text{H}\}$ , and  $^{31}\text{P}\{^1\text{H}\}$  NMR spectra were obtained using a Bruker Avance-400 or Avance-500 spectrometer with BBFO+ and DCH probes.  $^1\text{H}$  spectra were internally referenced to tetramethyl silane (TMS) at 0.00 ppm. Multiplicities are defined using the following abbreviations: s (singlet), d (doublet), t (triplet), q (quartet), p (pentet), sept (septet), m (multiplet). The diastereomeric ratios for the cycloadducts were determined from the  $^1\text{H}$  NMR of the crude reaction mixture and aligned with the diastereomeric ratios of the purified materials. The NMR spectrometers used in this work are supported by the NSF CHE-1048642 and a generous gift from Paul J. and Margaret M. Bender.

High Resolution Mass spectrometry was performed using a Thermo Q Exactive<sup>TM</sup> Plus supported by the NIH 1S10 OD020022-1.

Enantiomeric excesses were determined for the purified cycloadducts using a chiral SFC (Waters/Thar Investigator) with Daicel CHIRALCEL<sup>®</sup> columns and Chromasolv<sup>®</sup>-grade solvents.

Optical rotations were measured using a Rudolph Research Autopol III polarimeter at room temperature.

Electrochemical measurements were made using a Pine research WaveNow potentiostat/galvanostat.

UV-Visible spectra were recorded on a Varian Cary<sup>®</sup> 50 spectrophotometer at a resolution of 1 nm. Photoluminescence spectra were recorded on a Hitachi F-4500 fluorescence spectrophotometer with a 1 nm resolution.

Time-resolved emission decays were collected on a home-built set-up. Visible light excitation was provided by a colinear optical parametric amplifier (OPA, Light Conversion ORPHEUS-HP) optically coupled to a Yb:KGW amplifier (Light Conversion CARBIDE), which emits 0.4 mJ, 250 femtosecond pulses centered at 1025 nm. During data collection the OPA was tuned to 420 nm. The output laser pulse was 400 femtoseconds, and the native 100 kHz pulse rate was reduced to 1 kHz. This allowed the use of an electronically triggered PC oscilloscope. Under these conditions the power of the laser averaged 0.8  $\mu\text{J}/\text{pulse}$ . From the OPA, the visible laser pulses were directed to the sample with silver mirrors and the laser was *not* refocused onto the sample to reduce localized heating and non-linear effects due to two-photon absorption. At the sample, the unfocused laser had a  $\sim 5$  mm diameter. The samples were prepared in toluene and enclosed within a 1  $\text{cm}^2$  cuvette. The solutions were sparged with argon for 2–3 minutes before

measurement. Emission was collected at  $90^\circ$  to the incident laser pulse. The emission was collimated and refocused onto the photomultiplier tube detector (PMT) with a voltage bias applied (typically 800 mV). A longpass filter (Corning 3-71) was placed between the lenses to filter out any scattered excitation beam. Other shortpass/longpass filters (Corning) were used to modify the wavelength range measured. For simple lifetime measurements, the entire wavelength range of emission ( $\sim 500\text{--}800$  nm) was collected and provided ample signal. The PMT output was passed through a pre-amplifier (Thorlabs) and monitored with a Picoscope 2205A PC oscilloscope (Pico Technology) and provided a 40 ns resolution. The data was digitized using homebuilt LabVIEW code (National Instruments) and analyzed in Origin 2020 (OriginLab).

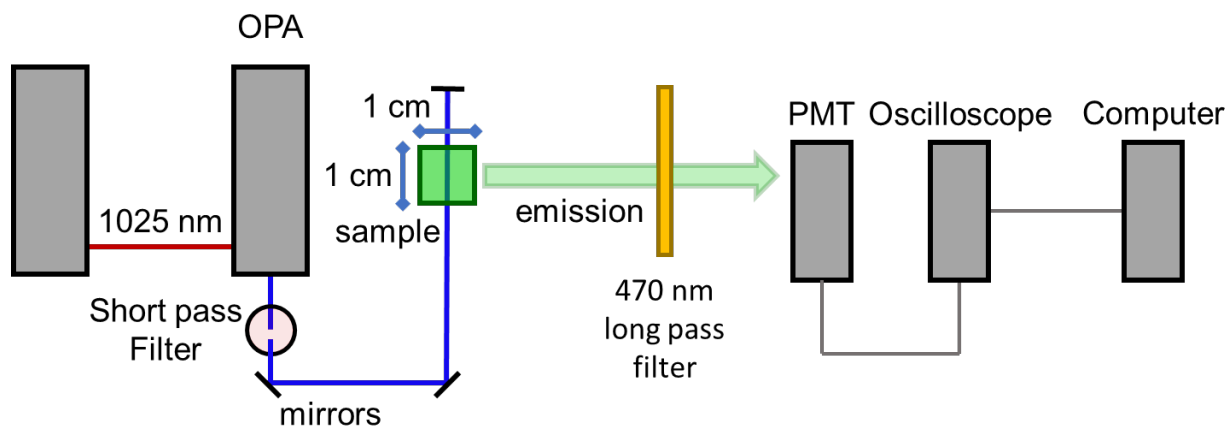
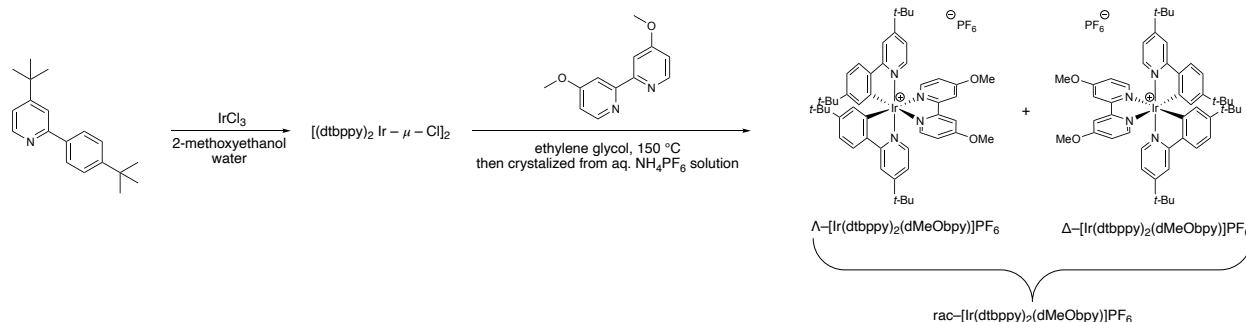


Figure 2.5 Time Resolved Emission Experimental Setup

2.10.2. Racemic  $[\text{Ir}(\text{dtbppy})_2(\text{dMeObpy})]\text{PF}_6$  Photocatalyst SynthesisScheme 2.1 Synthesis of Racemic  $[\text{Ir}(\text{dtbbpy})_2(\text{dMeObpy})]\text{PF}_6$ 

The dtbbpy ligand was synthesized using the method reported by Maiti and coworkers. Spectra match those previously reported.<sup>58</sup>

The  $[(\text{dtbbpy})_2\text{Ir}-\mu-\text{Cl}]_2$  dimer was synthesized using the method reported by Bernhard and coworkers. Spectra match those previously reported.<sup>59</sup>

Racemic  $[\text{Ir}(\text{dtbbpy})_2(\text{dMeObpy})]\text{PF}_6$  was synthesized using a modified procedure reported by Bernhard and coworkers.<sup>59</sup> A vial was charged with the  $[(\text{dtbbpy})_2\text{Ir}-\mu-\text{Cl}]_2$  dimer (367.9 mg, 0.24 mmol, 1.0 equiv.), 4,4'-dimethoxy-2,2'-bipyridine (118.3 mg, 0.55 mmol, 2.2 equiv.) and degassed ethylene glycol (10 mL). The reaction stirred at  $150\text{ }^\circ\text{C}$  for 21 h under  $\text{N}_2$ . The reaction was cooled to room temperature. The crude reaction was diluted with water and washed with hexanes. The aqueous layer was removed and heated to  $85\text{ }^\circ\text{C}$  for 5 minutes to remove residual hexanes. Allowed to cool to room temperature. An aqueous solution of ammonium hexafluorophosphate (4.2 g  $\text{NH}_4\text{PF}_6$  in 42 mL  $\text{H}_2\text{O}$ ) was added to the aqueous reaction layer, resulting in precipitation of an orange solid. This solid was filtered and was collected separately by passing through a frit with acetone. This solution was concentrated *in vacuo*. The product was



crystallized from 1:1 acetone:water. The product was filtered, collected on a frit, and dried under vacuum (295.6 mg, 0.27 mmol, 56% yield).

$^1\text{H NMR}$  (500 MHz,  $\text{CDCl}_3$ )  $\delta$  8.03 (d,  $J = 2.6$  Hz, 1H), 7.78 (d,  $J = 2.1$  Hz, 1H), 7.64 (d,  $J = 6.3$  Hz, 1H), 7.53 (d,  $J = 8.3$  Hz, 1H), 7.47 (d,  $J = 6.2$  Hz, 1H), 7.04 (dd,  $J = 6.3, 2.1$  Hz, 1H), 7.01 (dd,  $J = 8.2, 1.9$  Hz, 1H), 6.85 (dd,  $J = 6.5, 2.5$  Hz, 1H), 6.19 (d,  $J = 1.9$  Hz, 1H), 4.13 (s, 3H), 1.36 (s, 9H), 1.07 (s, 9H).

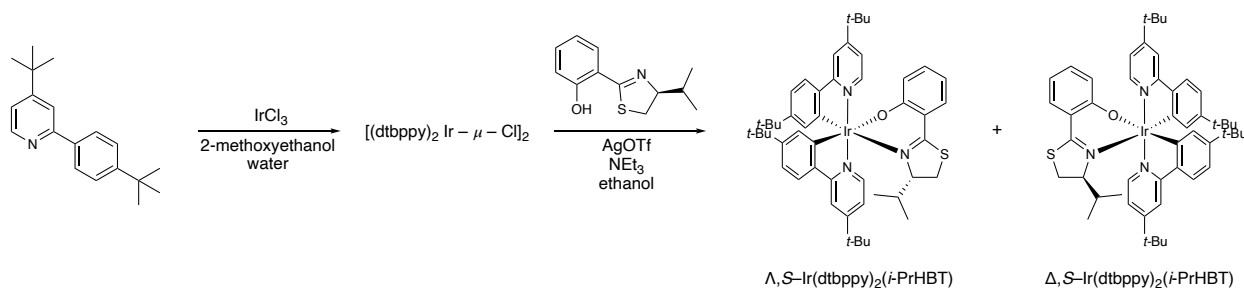
$^{13}\text{C NMR}$  (126 MHz,  $\text{CDCl}_3$ )  $\delta$  167.78, 162.17, 157.96, 153.18, 151.00, 150.44, 147.93, 141.35, 127.80, 123.75, 120.01, 119.21, 115.75, 115.58, 109.34, 57.00, 35.11, 34.48, 31.06, 30.43.

$^{19}\text{F NMR}$  (377 MHz,  $\text{CDCl}_3$ )  $\delta$  -72.89 (d,  $J = 712.7$  Hz).

$^{31}\text{P NMR}$  (162 MHz,  $\text{CDCl}_3$ )  $\delta$  -144.38 (sept,  $J = 712.7$  Hz).

**HRMS** (ESI $^+$ ) calculated for  $[\text{C}_{50}\text{H}_{60}\text{IrN}_4\text{O}_2]^+$  ( $[\text{M}-\text{PF}_6]^+$ ). Requires  $m/z$  941.4344; found  $m/z$  941.4350.

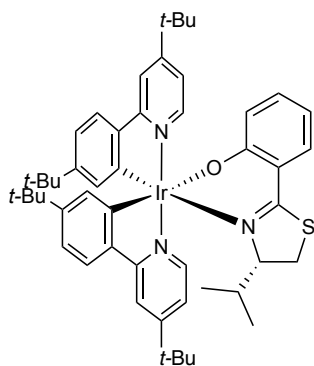
### 2.10.3. Enantioenriched $[\text{Ir}(\text{dtbppy})_2(\text{dMeObpy})]\text{PF}_6$ Photocatalyst Synthesis



Scheme 2.2 Synthesis of Diastereotopic [Ir] Complexes

The (*S*)-2-(4-isopropyl-4,5-dihydrothiazol-2-yl)phenol ligand was synthesized using the method reported by Meggers and coworkers.<sup>60</sup> Spectra match those previously reported.<sup>61</sup>

Resolved iridium diastereomers were prepared using a modification of the procedure reported by Meggers and coworkers.<sup>60,61</sup> A flask was charged with the [(dtbppy)<sub>2</sub>Ir-μ-Cl]<sub>2</sub> dimer (596.6 mg, 0.39 mmol, 1.0 equiv.), silver(I) trifluoromethanesulfonate (228.2 mg, 0.89 mmol, 2.3 equiv.), (*S*)-2-(4-isopropyl-4,5-dihydrothiazol-2-yl)phenol (193.5 mg, 0.87 mmol, 2.2 equiv.), ethanol (39 mL), and triethylamine (0.54 mL). The reaction was heated with stirring to 95 °C under N<sub>2</sub> for 19 h. The reaction was cooled to room temperature, and the solvent was removed *in vacuo*. Purification of the crude material by flash column chromatography (11:1 hexanes:EtOAc) afforded both diastereomers. Λ,*S*-[Ir] eluted ahead of Δ,*S*-[Ir].



**Λ,*S*-Ir(dtbppy)<sub>2</sub>(*i*-PrHBT) (S2.7):**

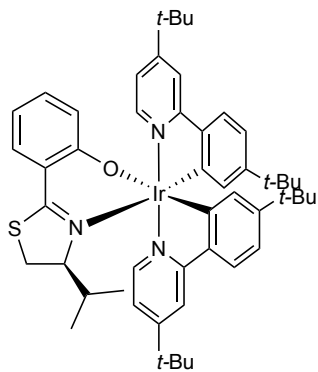
Isolated as a yellow powder. Yield: 31% (226.6 mg)

**<sup>1</sup>H NMR** (500 MHz, CDCl<sub>3</sub>) δ 8.83 (d, *J* = 6.2 Hz, 1H), 8.27 (d, *J* = 6.2 Hz, 1H), 7.77 (d, *J* = 2.2 Hz, 1H), 7.70 (d, *J* = 2.2 Hz, 1H), 7.44 – 7.35 (m, 4H), 7.13 (td, *J* = 6.6, 2.0 Hz, 2H), 7.09 (dd, *J* = 6.2, 2.2 Hz, 1H), 6.80 (dd, *J* = 8.1, 2.0 Hz, 1H), 6.76 (dd, *J* = 8.1, 2.0 Hz, 1H), 6.73 (dd, *J* = 8.7, 1.0 Hz, 1H), 6.30 (ddd, *J* = 8.1, 6.7, 1.3 Hz, 1H), 6.21 (d, *J* = 1.9 Hz, 1H), 5.87 (d, *J* = 2.0 Hz, 1H), 4.59 (d, *J* = 10.0 Hz, 1H), 3.23 (dd, *J* = 11.2, 10.0 Hz, 1H), 2.99 (dd, *J* = 11.4, 1.8 Hz, 1H), 1.43 (s, 9H), 1.37 (s, 9H), 1.06 (s, 9H), 1.01 (s, 9H), 0.30 (d, *J* = 7.0 Hz, 3H), 0.11 (d, *J* = 7.0 Hz, 3H).

**<sup>13</sup>C NMR** (126 MHz, CDCl<sub>3</sub>) δ 168.77, 168.30, 166.53, 166.38, 160.91, 160.44, 151.45, 151.38, 150.86, 149.50, 148.30, 147.16, 142.99, 142.15, 132.89, 132.78, 128.77, 127.85, 125.22, 123.07, 122.75, 118.71, 118.37, 118.14, 118.00, 117.02, 115.46, 114.30, 112.47, 83.73, 60.40, 34.98, 34.85, 34.25, 34.21, 31.13, 31.10, 30.74, 30.59, 18.93, 14.22.

**HRMS** (ESI<sup>+</sup>) calculated for [C<sub>50</sub>H<sub>63</sub>IrN<sub>3</sub>OS]<sup>+</sup> ([M+H]<sup>+</sup>). Requires *m/z* 946.4318; found *m/z* 946.4323.

[α]<sub>D</sub><sup>22</sup>: +235.6° (c0.27, EtOH).



**Δ,S-Ir(dtbbpy)<sub>2</sub>(i-PrHBT) (S2.8):**

Isolated as a yellow powder. Yield: 29% (210.2 mg)

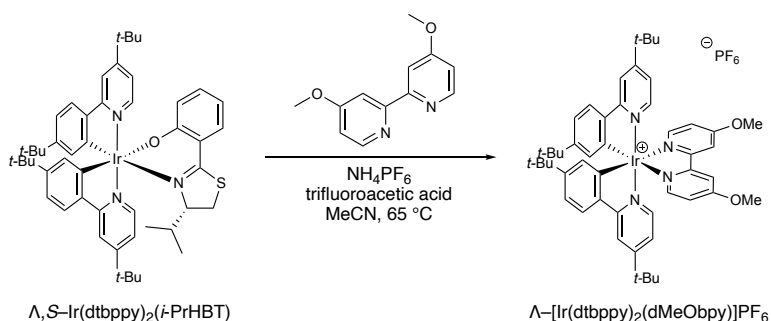
**<sup>1</sup>H NMR** (500 MHz, CDCl<sub>3</sub>) δ 8.84 (d, *J* = 6.1 Hz, 1H), 8.34 (d, *J* = 6.1 Hz, 1H), 7.77 (d, *J* = 1.9 Hz, 1H), 7.71 (d, *J* = 2.1 Hz, 1H), 7.44 (d, *J* = 8.2 Hz, 1H), 7.40 (d, *J* = 8.2 Hz, 1H), 7.30 (dd, *J* = 8.0, 1.8 Hz, 1H),

7.15 (dd, *J* = 6.1, 2.1 Hz, 1H), 7.03 (ddd, *J* = 8.6, 6.9, 1.9 Hz, 1H), 6.86 (dd, *J* = 6.2, 2.2 Hz, 1H), 6.78 (ddd, *J* = 10.0, 8.1, 1.9 Hz, 2H), 6.56 (dd, *J* = 8.6, 1.2 Hz, 1H), 6.32 (ddd, *J* = 8.0, 6.9, 1.2 Hz, 1H), 6.22 (d, *J* = 1.9 Hz, 1H), 5.90 (d, *J* = 1.9 Hz, 1H), 3.63 (d, *J* = 9.6 Hz, 1H), 2.89 – 2.85 (m, 1H), 2.83 – 2.77 (m, 1H), 2.12 – 2.05 (m, 1H), 1.44 (s, 9H), 1.37 (s, 9H), 1.28 – 1.23 (m, 3H), 1.00 (s, 9H), 0.99 (s, 9H), 0.15 (d, *J* = 6.9 Hz, 3H).

**<sup>13</sup>C NMR** (126 MHz, CDCl<sub>3</sub>) δ 168.44, 167.90, 167.02, 166.41, 160.89, 160.37, 150.78, 150.64, 150.51, 149.58, 148.46, 142.32, 141.81, 132.45, 130.98, 130.63, 128.08, 124.71, 123.07, 122.65, 119.28, 118.73, 118.60, 118.06, 117.80, 116.87, 114.90, 114.24, 112.44, 81.81, 35.05, 34.88, 34.19, 34.07, 31.06, 31.03, 30.72, 30.59, 29.90, 20.12, 15.55.

**HRMS** (ESI<sup>+</sup>) calculated for [C<sub>50</sub>H<sub>62</sub>IrN<sub>3</sub>OSNa]<sup>+</sup> ([M+Na]<sup>+</sup>). Requires *m/z* 968.4140; found *m/z* 968.4135.

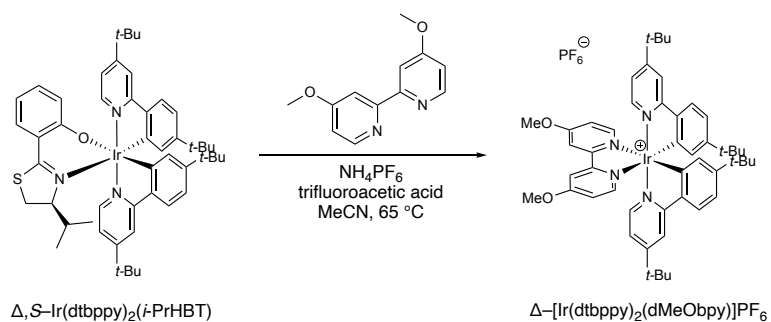
[α]<sub>D</sub><sup>22</sup>: +80.0° (c0.35, EtOH).



Scheme 2.3 Synthesis of  $\Lambda\text{-[Ir}(\text{dtbbpy})_2(\text{dMeObpy})]\text{PF}_6$

A flask was charged with  $\Lambda,S\text{-Ir}(\text{dtbbpy})_2(i\text{-PrHBT})$  (168.6 mg, 0.21 mmol, 1.0 equiv.), ammonium hexafluorophosphate (172.4 mg, 1.06 mmol, 5.0 equiv.), and 4,4'-dimethoxy-2,2'-bipyridine (114.7 mg, 0.53 mmol, 2.5 equiv.). The vial was placed under  $\text{N}_2$ . Acetonitrile (21.1 mL) and trifluoroacetic acid (0.08 mL) were added. Reaction stirred at  $65\text{ }^\circ\text{C}$  for 21 h. The reaction was cooled to room temperature, and the solvent was removed *in vacuo*. The desired product was crystallized from 1:1 acetone:water. Collected the yellow solid on a frit (168.2 mg, 0.15 mmol, 73% yield). Spectra match those of racemic [Ir] reported above.

$[\alpha]_D^{22}$ :  $+293.3^\circ$  ( $c$ 0.27, EtOH).



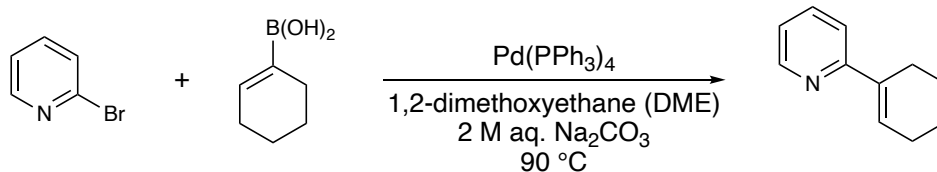
Scheme 2.4 Synthesis of  $\Delta\text{-[Ir}(\text{dtbbpy})_2(\text{dMeObpy})]\text{PF}_6$

A vial was charged with  $\Delta,S$ -Ir(dtbbpy)<sub>2</sub>(*i*-PrHBT) (120.1 mg, 0.13 mmol, 1.0 equiv.), ammonium hexafluorophosphate (104.2 mg, 0.64 mmol, 5.0 equiv.), and 4,4'-dimethoxy-2,2'-bipyridine (71.0 mg, 0.33 mmol, 2.5 equiv.). The vial was placed under N<sub>2</sub>. Acetonitrile (12.5 mL) and trifluoroacetic acid (0.05 mL) were added. Reaction stirred at 65 °C for 24 h. The reaction was cooled to room temperature, and the solvent was removed *in vacuo*. The desired product was crystallized from 1:1 acetone:water. Collected the yellow solid on a frit (82.2 mg, 0.08 mmol, 60% yield). Spectra match those of racemic [Ir] reported above.

$[\alpha]_D^{22}$ : -237.8° (c0.18, EtOH).

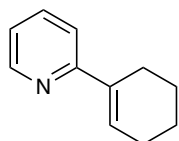
**X-Ray:** see below.

#### 2.10.4. Starting Material Syntheses



A flask was charged with cyclohex-1-en-1-ylboronic acid (1.0079 g, 8.00 mmol, 1.5 equiv.) and tetrakis(triphenylphosphine)palladium(0) (611.5 mg, 0.53 mmol, 0.1 equiv.). The flask was placed under N<sub>2</sub>. Degassed 1,2-dimethoxyethane (50 mL), degassed 2 M aq. Na<sub>2</sub>CO<sub>3</sub> (13 mL), and 2-bromopyridine (0.50 mL, 5.24 mmol, 1.0 equiv.) were added to the flask. The reaction was stirred at 90 °C for 17 h. After the reaction cooled to room temperature, water was added, and the product was extracted into DCM (x3). The organic layer was washed with sat. aqueous NH<sub>4</sub>Cl. The organic layer was then dried with MgSO<sub>4</sub>, filtered, and concentrated *in vacuo*. Purification of

the crude material by flash column chromatography (gradient 20:1 hexanes:EtOAc to 18:1 hexanes:EtOAc) afforded the product **2.1** as a colorless oil (699.6 mg, 4.39 mmol, 83% yield).

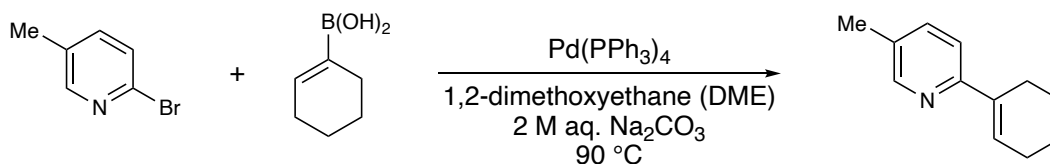


**2-(cyclohex-1-en-1-yl)pyridine (2.1):**

$^1\text{H NMR}$  (500 MHz,  $\text{CDCl}_3$ )  $\delta$  8.55 (dd,  $J = 4.4, 1.5$  Hz, 1H), 7.61 (td,  $J = 7.8, 1.9$  Hz, 1H), 7.36 (d,  $J = 8.0$  Hz, 1H), 7.10 (ddd,  $J = 7.5, 4.8, 1.1$  Hz, 1H), 6.69 (tt,  $J = 3.9, 1.7$  Hz, 1H), 2.51 (tq,  $J = 6.2, 2.4$  Hz, 2H), 2.27 (dt,  $J = 8.9, 6.0, 2.6$  Hz, 2H), 1.85 – 1.74 (m, 2H), 1.74 – 1.63 (m, 2H).

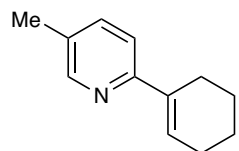
$^{13}\text{C NMR}$  (126 MHz,  $\text{CDCl}_3$ )  $\delta$  159.06, 148.81, 136.52, 136.17, 128.56, 121.32, 118.90, 25.96, 25.92, 22.84, 22.11.

**HRMS** (ESI $^+$ ) calculated for  $[\text{C}_{11}\text{H}_{14}\text{N}]^+$  ( $[\text{M}+\text{H}]^+$ ). Requires  $m/z$  160.1121; found  $m/z$  160.1120.



A flask was charged with cyclohex-1-en-1-ylboronic acid (500.5 mg, 3.97 mmol, 1.5 equiv.), 2-bromo-5-methylpyridine (445.8 mg, 2.59 mmol, 1.0 equiv.), and tetrakis(triphenylphosphine)palladium(0) (307.0 mg, 0.27 mmol, 0.1 equiv.). The flask was placed under  $\text{N}_2$ . Degassed 1,2-dimethoxyethane (26 mL) and degassed 2 M aq.  $\text{Na}_2\text{CO}_3$  (6.6 mL) were added to the flask. The reaction was stirred at 90 °C for 18 h. After the reaction cooled to room temperature, water was added, and the product was extracted into DCM (x3). The organic layer was washed with sat. aqueous  $\text{NH}_4\text{Cl}$ . The organic layer was then dried with  $\text{MgSO}_4$ , filtered, and

concentrated *in vacuo*. Purification of the crude material by flash column chromatography (15:1 hexanes:EtOAc) afforded the product **S2.1** as a colorless oil (285.5 mg, 1.65 mmol, 64% yield).

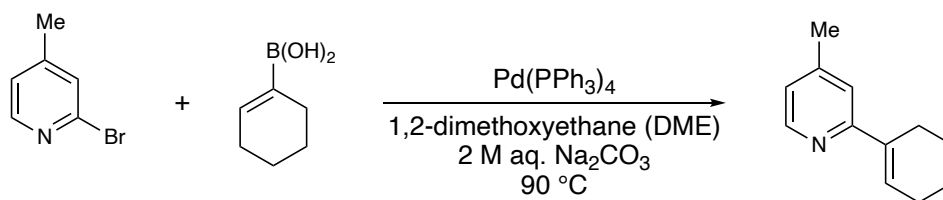


**2-(cyclohex-1-en-1-yl)-5-methylpyridine (S2.1):**

**<sup>1</sup>H NMR** (500 MHz, CDCl<sub>3</sub>) δ 8.37 (s, 1H), 7.42 (dd, *J* = 8.1, 2.3 Hz, 1H), 7.26 (d, *J* = 8.1 Hz, 1H), 6.62 (tt, *J* = 4.0, 1.8 Hz, 1H), 2.49 (tq, *J* = 6.1, 2.3 Hz, 2H), 2.30 (s, 3H), 2.25 (tq, *J* = 6.1, 2.7 Hz, 2H), 1.83 – 1.75 (m, 2H), 1.72 – 1.63 (m, 2H).

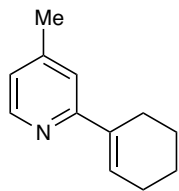
**<sup>13</sup>C NMR** (126 MHz, CDCl<sub>3</sub>) δ 156.52, 149.20, 136.74, 136.40, 130.64, 127.50, 118.40, 26.05, 25.88, 22.89, 22.18, 18.12.

**HRMS** (ESI<sup>+</sup>) calculated for [C<sub>12</sub>H<sub>16</sub>N]<sup>+</sup> ([M+H]<sup>+</sup>). Requires *m/z* 174.1277; found *m/z* 174.1278.



A flask was charged with cyclohex-1-en-1-ylboronic acid (510.8 mg, 4.06 mmol, 1.5 equiv.) and tetrakis(triphenylphosphine)palladium(0) (330.0 mg, 0.29 mmol, 0.1 equiv.). The flask was placed under N<sub>2</sub>. Degassed 1,2-dimethoxyethane (27 mL), degassed 2 M aq. Na<sub>2</sub>CO<sub>3</sub> (6.7 mL), and 2-bromo-4-methylpyridine (0.3 mL, 2.70 mmol, 1.0 equiv.) were added to the flask. The reaction was stirred at 90 °C for 18 h. After the reaction cooled to room temperature, water was added, and the product was extracted into DCM (x3). The organic layer was washed with sat. aqueous NH<sub>4</sub>Cl. The organic layer was then dried with MgSO<sub>4</sub>, filtered, and concentrated *in vacuo*. Purification of the crude material by flash column chromatography (gradient 12:1 hexanes:EtOAc

to 9:1 hexanes:EtOAc) afforded the product **S2.2** as a colorless oil (404.4 mg, 2.33 mmol, 87% yield).



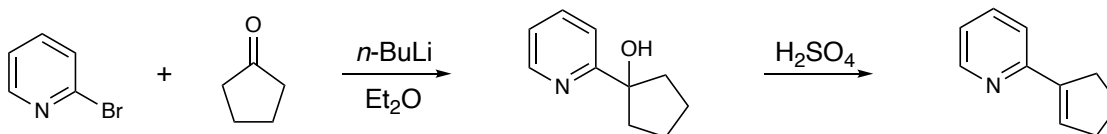
**2-(cyclohex-1-en-1-yl)-4-methylpyridine (S2.2):**

$^1\text{H NMR}$  (500 MHz,  $\text{CDCl}_3$ )  $\delta$  8.40 (d,  $J = 5.0$  Hz, 1H), 7.18 (s, 1H), 6.92 (d,  $J = 5.1$  Hz, 1H), 6.66 (tt,  $J = 3.9, 1.7$  Hz, 1H), 2.50 (ddq,  $J = 6.3, 4.4, 2.2$  Hz, 2H),

2.33 (s, 3H), 2.26 (dtt,  $J = 6.4, 3.8, 2.1$  Hz, 2H), 1.83 – 1.75 (m, 2H), 1.72 – 1.63 (m, 2H).

$^{13}\text{C NMR}$  (126 MHz,  $\text{CDCl}_3$ )  $\delta$  159.00, 148.58, 147.01, 136.55, 128.25, 122.36, 119.84, 26.04, 25.89, 22.86, 22.12, 21.15.

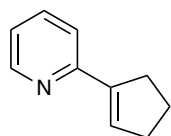
**HRMS** (ESI $^+$ ) calculated for  $[\text{C}_{12}\text{H}_{16}\text{N}]^+$  ( $[\text{M}+\text{H}]^+$ ). Requires  $m/z$  174.1277; found  $m/z$  174.1277.



2-(cyclopent-1-en-1-yl)pyridine was synthesized using a procedure reported by Wang and coworkers.<sup>62</sup> A flask under  $\text{N}_2$  was charged with 2-bromopyridine (0.75 mL, 7.87 mmol, 1.0 equiv.) in dry ether (15.7 mL) and cooled to  $-78$  °C. A 2.5 M solution of *n*-butyllithium (3.5 mL, 8.65 mmol, 1.1 equiv.) was added dropwise and stirred for 30 min at  $-78$  °C. The clear solution turned dark red during the *n*-butyllithium addition. Cyclopentanone (0.77 mL, 8.65 mmol, 1.1 equiv.) was added dropwise at  $-78$  °C, and the reaction gradually warmed to room temperature and stirred for 18 h. The reaction was quenched with 4.25 mL 1 M aq. HCl solution. The product was extracted into EtOAc (x3), dried over  $\text{MgSO}_4$ , filtered, and concentrated *in vacuo*. To the crude product in EtOAc was added concentrated  $\text{H}_2\text{SO}_4$  (4 mL) and stirred for 1 h at room temperature. Water was added and the reaction was neutralized with an aq. sodium hydroxide



solution. The product was extracted into diethyl ether (x3), washed with brine, dried over MgSO<sub>4</sub>, filtered, and concentrated *in vacuo*. Purification of the crude material by flash column chromatography (15:1 hexanes:EtOAc) afforded the product as an oil (462.2 mg, 3.18 mmol, 40% yield).

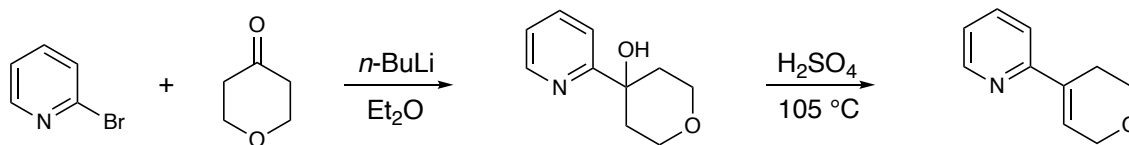


**2-(cyclopent-1-en-1-yl)pyridine (S2.5):**

<sup>1</sup>H NMR (500 MHz, CDCl<sub>3</sub>) δ 8.56 (d, *J* = 4.8 Hz, 1H), 7.61 (td, *J* = 7.7, 1.9 Hz, 1H), 7.37 (dt, *J* = 7.9, 1.1 Hz, 1H), 7.10 (ddd, *J* = 7.5, 4.8, 1.2 Hz, 1H), 6.60 (p, *J* = 2.3 Hz, 1H), 2.80 (ddt, *J* = 10.0, 7.0, 2.3 Hz, 2H), 2.58 (tq, *J* = 7.6, 2.6 Hz, 2H), 2.06 (p, *J* = 7.6 Hz, 2H).

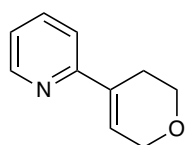
<sup>13</sup>C NMR (126 MHz, CDCl<sub>3</sub>) δ 155.25, 149.24, 143.47, 136.07, 131.11, 121.47, 120.30, 33.52, 32.58, 23.43.

HRMS (ESI<sup>+</sup>) calculated for [C<sub>10</sub>H<sub>12</sub>N]<sup>+</sup> ([M+H]<sup>+</sup>). Requires *m/z* 146.0964; found *m/z* 146.0964.



2-(3,6-dihydro-2H-pyran-4-yl)pyridine was synthesized using a modified procedure reported by Wang and coworkers.<sup>62</sup> A flask under N<sub>2</sub> was charged with 2-bromopyridine (0.75 mL, 7.87 mmol, 1.0 equiv.) in dry ether (15.7 mL) and cooled to −78 °C. A 2.5 M solution of *n*-butyllithium (3.5 mL, 8.65 mmol, 1.1 equiv.) was added dropwise and stirred for 30 min at −78 °C. The clear solution turned dark red during the *n*-butyllithium addition. Tetrahydro-4H-pyran-4-one (0.80 mL, 8.65 mmol, 1.1 equiv.) was added dropwise at −78 °C, and the reaction gradually warmed to room temperature and stirred for 18 h. The reaction was quenched with 4.25 mL 1 M aq. HCl solution. The product was extracted into EtOAc (x3), dried over MgSO<sub>4</sub>, filtered, and

concentrated *in vacuo*. To the crude product in EtOAc was added concentrated H<sub>2</sub>SO<sub>4</sub> (3.4 mL) and stirred for 2 h at 105 °C. After the reaction cooled to room temperature, water was added, and the reaction was neutralized with an aq. sodium hydroxide solution. The product was extracted into dichloromethane (x3), dried over MgSO<sub>4</sub>, filtered, and concentrated *in vacuo*. Purification of the crude material by flash column chromatography (1:1 hexanes:EtOAc) afforded the product as an oil (261.4 mg, 1.62 mmol, 21% yield).

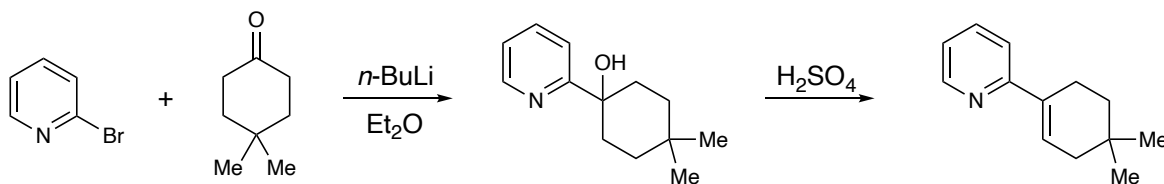


**2-(3,6-dihydro-2H-pyran-4-yl)pyridine (S2.4):**

<sup>1</sup>H NMR (500 MHz, CDCl<sub>3</sub>) δ 8.57 (ddd, *J* = 4.8, 1.9, 0.9 Hz, 1H), 7.66 (td, *J* = 7.8, 1.9 Hz, 1H), 7.38 (dt, *J* = 8.0, 1.0 Hz, 1H), 7.15 (ddd, *J* = 7.5, 4.8, 1.1 Hz, 1H), 6.68 (tt, *J* = 3.1, 1.6 Hz, 1H), 4.38 (q, *J* = 2.8 Hz, 2H), 3.95 (t, *J* = 5.5 Hz, 2H), 2.65 (tt, *J* = 5.5, 2.8, 1.7 Hz, 2H).

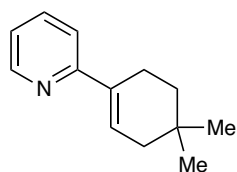
<sup>13</sup>C NMR (126 MHz, CDCl<sub>3</sub>) δ 156.85, 149.06, 136.38, 134.22, 126.03, 121.99, 118.78, 65.84, 64.46, 25.90.

HRMS (ESI<sup>+</sup>) calculated for [C<sub>10</sub>H<sub>12</sub>NO]<sup>+</sup> ([M+H]<sup>+</sup>). Requires *m/z* 162.0913; found *m/z* 162.0914.



2-(4,4-dimethylcyclohex-1-en-1-yl)pyridine was synthesized using a modified procedure reported by Wang and coworkers.<sup>62</sup> A flask under N<sub>2</sub> was charged with 2-bromopyridine (0.30 mL, 3.14 mmol, 1.0 equiv.) in dry ether (5.0 mL) and cooled to -78 °C. A 2.5 M solution of *n*-butyllithium (1.4 mL, 3.46 mmol, 1.1 equiv.) was added dropwise and stirred for 30 min at -78 °C. The clear solution turned dark red during the *n*-butyllithium addition. A solution of 4,4-

dimethylcyclohexanone (433.4 mg, 3.46 mmol, 1.1 equiv.) in dry ether (1.4 mL) was added dropwise at  $-78\text{ }^{\circ}\text{C}$ , and the reaction gradually warmed to room temperature and stirred for 18 h. The reaction was quenched with 3.2 mL 1 M aq. HCl solution. The product was extracted into EtOAc (x3), dried over  $\text{MgSO}_4$ , filtered, and concentrated *in vacuo*. To the crude product in EtOAc was added concentrated  $\text{H}_2\text{SO}_4$  (1.6 mL) and stirred for 1 h at room temperature. Water was added, and the reaction was neutralized with an aq. sodium hydroxide solution. The product was extracted into dichloromethane (x3), washed with brine (x1), dried over  $\text{MgSO}_4$ , filtered, and concentrated *in vacuo*. Purification of the crude material by flash column chromatography (5:1 hexanes:EtOAc) afforded the product as a yellow oil (374.3 mg, 2.00 mmol, 64% yield).



**2-(4,4-dimethylcyclohex-1-en-1-yl)pyridine (S2.3):**

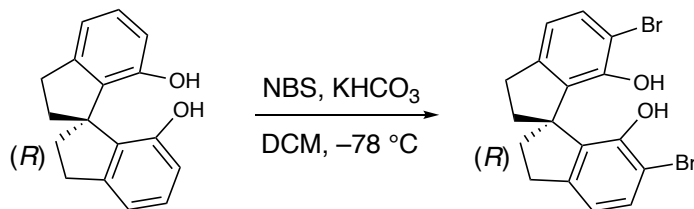
$^1\text{H NMR}$  (500 MHz,  $\text{CDCl}_3$ )  $\delta$  8.55 (ddd,  $J = 4.8, 1.9, 0.9$  Hz, 1H), 7.61 (td,  $J = 7.7, 1.9$  Hz, 1H), 7.38 (d,  $J = 8.0$  Hz, 1H), 7.10 (ddd,  $J = 7.5, 4.8, 1.1$  Hz, 1H), 6.65 (tt,  $J = 3.9, 1.7$  Hz, 1H), 2.54 (tq,  $J = 6.4, 2.1$  Hz, 2H), 2.06 (dt,  $J = 4.7, 2.6$  Hz, 2H), 1.58 – 1.52 (m, 2H), 0.98 (s, 6H).

$^{13}\text{C NMR}$  (126 MHz,  $\text{CDCl}_3$ )  $\delta$  158.73, 148.86, 136.17, 135.11, 127.61, 121.32, 118.93, 39.95, 35.69, 28.55, 28.23, 23.74.

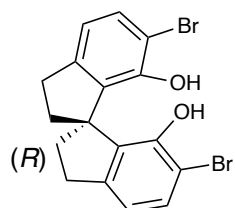
**HRMS** (ESI $^+$ ) calculated for  $[\text{C}_{13}\text{H}_{18}\text{N}]^+$  ( $[\text{M}+\text{H}]^+$ ). Requires  $m/z$  188.1434; found  $m/z$  188.1433.

2.10.5. (*R*)-4-biphenyl SPINOL Phosphoric Acid Synthesis

(*R*)-SPINOL ((*R*)-2,2',3,3'-Tetrahydro-1,1'-spirobi[indene]-7,7'-diol, CAS: 223259-62-9) was purchased from Strem Chemicals and used without further purification.



A flask was charged with (*R*)-SPINOL (996.5 mg, 3.95 mmol, 1.0 equiv.), potassium bicarbonate (798.2 mg, 7.97 mmol, 2.0 equiv.), and dry dichloromethane (50 mL). The reaction was cooled to  $-78\text{ }^{\circ}\text{C}$ . *N*-Bromosuccinimide (1.4153 g, 7.95 mmol, 2.0 equiv.) was added in one portion, and the reaction stirred at  $-78\text{ }^{\circ}\text{C}$  for 7 h. The reaction was warmed to room temperature and quenched with 60 mL 2 M aq. HCl. The product was extracted into DCM (x3), dried over  $\text{MgSO}_4$ , filtered, and concentrated *in vacuo*. Purification of the crude material by flash column chromatography (15:1 hexanes:EtOAc) afforded the product as a white solid (1.2951 g, 3.16 mmol, 80% yield).



**(*R*)-6,6'-dibromo-2,2',3,3'-tetrahydro-1,1'-spirobi[indene]-7,7'-diol**

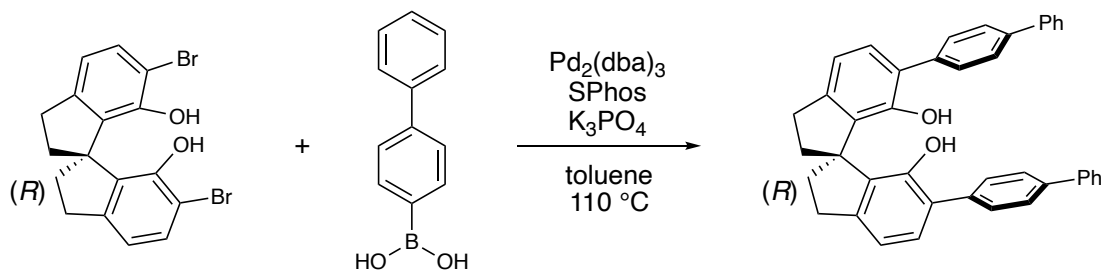
**(S2.6):**

$^1\text{H NMR}$  (500 MHz,  $\text{CDCl}_3$ )  $\delta$  7.31 (d,  $J = 8.0$  Hz, 2H), 6.74 (d,  $J = 8.0$  Hz, 2H), 5.25 (s, 2H), 3.08 – 2.93 (m, 4H), 2.44 – 2.34 (m, 2H), 2.23 (ddd,  $J = 12.8, 7.8, 3.0$  Hz, 2H).

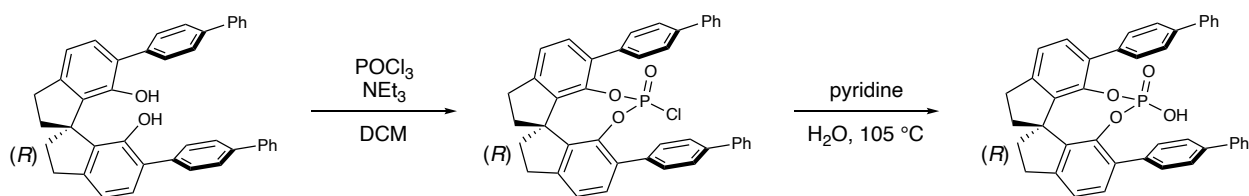
$^{13}\text{C NMR}$  (126 MHz,  $\text{CDCl}_3$ )  $\delta$  148.52, 145.49, 134.20, 131.00, 118.03, 107.97, 59.70, 38.08, 31.18.

**HRMS** (ESI $^-$ ) calculated for  $[\text{C}_{17}\text{H}_{13}\text{Br}_2\text{O}_2]^-$  ( $[\text{M}-\text{H}]^-$ ). Requires  $m/z$  406.9288; found  $m/z$  406.9293.

$[\alpha]_D^{22}$ :  $+148.0^\circ$  ( $c$ 0.20, EtOH).

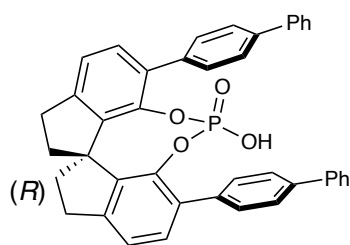


A flask was charged with (*R*)-6,6'-dibromo-2,2',3,3'-tetrahydro-1,1'-spirobi[indene]-7,7'-diol (499.4 mg, 1.22 mmol, 1.0 equiv.), 4-biphenylboronic acid (1.2159 g, 6.14 mmol, 5.0 equiv.), tris(dibenzylideneacetone)dipalladium(0) (22.7 mg, 0.025 mmol, 0.02 equiv.), SPhos (41.6 mg, 0.10 mmol, 0.08 equiv.), and potassium phosphate tribasic (1.8136 g, 8.54 mmol, 7.0 equiv.). The reaction was placed under N<sub>2</sub>, and dry toluene (12.2 mL) was added. The reaction was stirred at 110 °C for 18 h. The reaction was cooled to room temperature, and 25 mL 1 M aq. HCl was added. The product was extracted into dichloromethane (x3), dried over MgSO<sub>4</sub>, filtered, and concentrated *in vacuo*. Purification of the crude material by flash column chromatography (15:1 hexanes:EtOAc) afforded the product as a white solid (495.1 mg, 0.89 mmol, 73% yield).



A flask was charged with (*R*)-6,6'-di([1,1'-biphenyl]-4-yl)-2,2',3,3'-tetrahydro-1,1'-spirobi[indene]-7,7'-diol (495.1 mg, 0.89 mmol, 1.0 equiv.) and put under N<sub>2</sub> at 0 °C. Dry dichloromethane (4.4 mL) and triethylamine (0.5 mL, 3.56 mmol, 4.0 equiv.) were added. Phosphorus oxychloride (0.1 mL, 0.98 mmol, 1.1 equiv.) was added dropwise at 0 °C. The reaction gradually warmed to room temperature and stirred for 18 h. The crude reaction mixture was filtered through a plug of celite with dichloromethane and concentrated *in vacuo*. To the crude material

was added pyridine (28 mL) and water (28 mL). The reaction was stirred at 105 °C for 4 h. The reaction was cooled to room temperature. The product was extracted into dichloromethane (x3), washed with 6 M aq. HCl, dried over MgSO<sub>4</sub>, filtered, and concentrated *in vacuo*. The product was dried under vacuum and collected as a white solid (532.6 mg, 0.86 mmol, 97% yield).



**(R)-4-biphenyl SPINOL Phosphoric Acid (CPA3):**

**1,10-di([1,1'-biphenyl]-4-yl)-12-hydroxy-4,5,6,7-tetrahydroindeno[7,1-*de*:1',7'-*fg*][1,3,2]dioxaphosphocine 12-oxide**

**<sup>1</sup>H NMR** (500 MHz, CD<sub>2</sub>Cl<sub>2</sub>) δ 7.35 – 7.29 (m, 4H), 7.23 – 7.19 (m, 2H), 7.19 – 7.02 (m, 16H), 3.08 (ddd, *J* = 17.1, 11.2, 6.5 Hz, 2H), 2.89 (dd, *J* = 16.2, 7.8 Hz, 2H), 2.29 (dd, *J* = 12.1, 6.4 Hz, 2H), 2.13 (td, *J* = 11.6, 8.3 Hz, 2H).

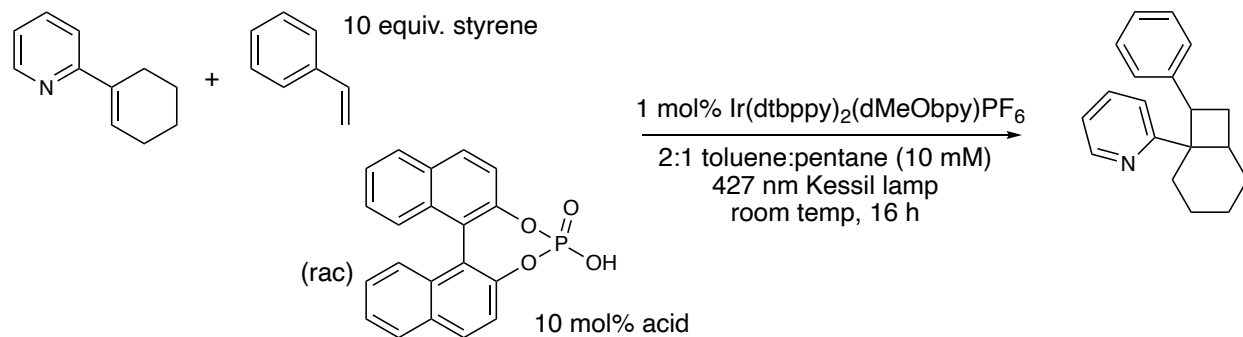
**<sup>13</sup>C NMR** (126 MHz, CD<sub>2</sub>Cl<sub>2</sub>) δ 145.64, 145.62, 140.67, 140.64, 140.36, 139.43, 136.65, 133.69, 133.66, 129.99, 129.60, 128.25, 126.86, 122.62, 59.97, 38.53, 30.13.

**<sup>31</sup>P NMR** (162 MHz, CD<sub>2</sub>Cl<sub>2</sub>) δ -9.34.

**HRMS** (ESI<sup>-</sup>) calculated for [C<sub>41</sub>H<sub>30</sub>O<sub>4</sub>P]<sup>-</sup> ([M-H]<sup>-</sup>). Requires *m/z* 617.1887; found *m/z* 617.1889.

**[α]<sub>D</sub><sup>22</sup>**: +353.8° (*c*0.13, EtOH).

## 2.10.6. Racemic [2+2] Photocycloadditions



General Procedure 2A: A 25 mL Schlenk tube was charged with the racemic photocatalyst [Ir(dtbbpy)<sub>2</sub>(dMeObpy)]PF<sub>6</sub> (0.0009 mmol, 0.01 equiv.), racemic 1,1'-binaphthyl-2,2'-diyl hydrogenphosphate (0.009, 0.10 equiv.), vinyl pyridine (0.09 mmol, 1.0 equiv.), dry toluene (6 mL), pentane (3 mL), and styrene (0.9 mmol, 10.0 equiv.). The reaction was degassed through three sequential freeze–pump–thaw cycles. Irradiation was performed with a 427 nm Kessil lamp with stirring for 16 h. The solvent was removed *in vacuo*. Purification of the crude material by flash column chromatography afforded the racemic cyclobutane product, which was used to develop chiral SFC method. Note: all characterization and spectroscopic data are reported for the enantioenriched species.

Racemic Product **2.2** was synthesized on 0.044 mmol scale using 1,1'-binaphthyl-2,2'-diyl hydrogenphosphate at –40 °C.

Racemic Product **2.3** was synthesized on 0.044 mmol scale using 1,1'-binaphthyl-2,2'-diyl hydrogenphosphate at –40 °C.

Racemic Product **2.4** was synthesized on 0.09 mmol scale using 1,1'-binaphthyl-2,2'-diyl hydrogenphosphate at room temperature.

Racemic Product **2.5** was synthesized on 0.09 mmol scale using 1,1'-binaphthyl-2,2'-diyl hydrogenphosphate at  $-40\text{ }^{\circ}\text{C}$ .

Racemic Product **2.6** was synthesized on 0.09 mmol scale using 1,1'-binaphthyl-2,2'-diyl hydrogenphosphate at room temperature.

Racemic Product **2.7** was synthesized on 0.09 mmol scale using 1,1'-binaphthyl-2,2'-diyl hydrogenphosphate at room temperature.

Racemic Product **2.8** was synthesized on 0.09 mmol scale using 1,1'-binaphthyl-2,2'-diyl hydrogenphosphate at room temperature.

Racemic Product **2.9** was synthesized on 0.09 mmol scale using 1,1'-binaphthyl-2,2'-diyl hydrogenphosphate at room temperature.

Racemic Product **2.10** was synthesized on 0.044 mmol scale using 1,1'-binaphthyl-2,2'-diyl hydrogenphosphate at  $-40\text{ }^{\circ}\text{C}$ .

Racemic Product **2.11** was synthesized on 0.09 mmol scale using 1,1'-binaphthyl-2,2'-diyl hydrogenphosphate at room temperature.

Racemic Product **2.12** was synthesized on a 0.1 mmol scale using 1,1'-binaphthyl-2,2'-diyl hydrogenphosphate at  $-40\text{ }^{\circ}\text{C}$ .

Racemic Product **2.13** was synthesized on 0.044 mmol scale using 1,1'-binaphthyl-2,2'-diyl hydrogenphosphate in 0.01 M toluene at  $-40\text{ }^{\circ}\text{C}$ .

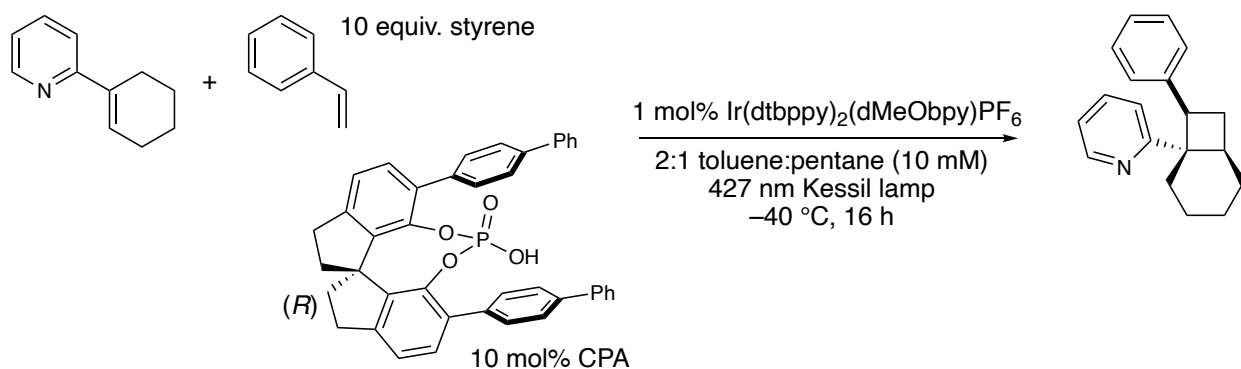
Racemic Product **2.14** was synthesized on 0.044 mmol scale using trifluoroacetic acid at  $-40\text{ }^{\circ}\text{C}$ .



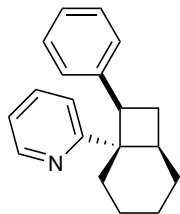
Racemic Product **2.15** was synthesized on 0.09 mmol scale using 1,1'-binaphthyl-2,2'-diyl hydrogenphosphate at room temperature.

Racemic Product **2.16** was synthesized on 0.044 mmol scale using 1,1'-binaphthyl-2,2'-diyl hydrogenphosphate at room temperature.

### 2.10.7. Enantioselective [2+2] Photocycloadditions



General Procedure 2B: A 100 mL Schlenk flask was charged with the photocatalyst  $[\text{Ir}(\text{dtbbpy})_2(\text{dMeObpy})]\text{PF}_6$  (either *rac*-[Ir],  $\Delta$ -[Ir], or  $\Lambda$ -[Ir]. 0.0031 mmol, 0.01 equiv.), (R)-biphenyl SPINOL phosphoric acid (0.031 mmol, 0.10 equiv.), vinyl pyridine (0.31 mmol, 1.0 equiv.), dry toluene (20.9 mL), pentane (10.5 mL), and styrene (3.1 mmol, 10.0 equiv.). The reaction was degassed through three sequential freeze-pump-thaw cycles. The solution was cooled to  $-40\text{ }^\circ\text{C}$  in an isopropanol bath and maintained at this temperature using an immersion cooler. Irradiation was performed with a 427 nm Kessil lamp with stirring for 16 h. The reaction was warmed to room temperature, and the solvent was removed *in vacuo*. Purification of the crude material by flash column chromatography afforded the enantioenriched cyclobutane product.



**2-((1S,6R,8R)-8-phenylbicyclo[4.2.0]octan-1-yl)pyridine (2.2):** Prepared according to General Procedure 2B using racemic  $[\text{Ir}(\text{dtbppy})_2(\text{dMeObpy})]\text{PF}_6$  (3.5 mg, 0.0032 mmol, 0.01 equiv.), (*R*)-biphenyl SPINOL phosphoric acid (19.4 mg, 0.031 mmol, 0.10 equiv.), 2-(cyclohex-1-en-1-yl)pyridine (**2.1**, 51.7 mg, 0.32 mmol, 1 equiv.), dry toluene (20.9 mL), pentane (10.5 mL), and styrene (0.36 mL, 3.1 mmol, 10.0 equiv.). The crude material was purified by flash column chromatography on silica gel with 15:1 hexanes:EtOAc to afford the cyclobutane as a colorless oil (71.1 mg, 0.27 mmol, 83% yield). 94% ee.

**SFC:** Daicel CHIRALCEL<sup>®</sup> OD-H, 5% *i*-PrOH, 3 g/min,  $t_1 = 9.11$  min,  $t_2 = 10.58$  min; Area% = 97.00 : 3.00 (94% ee).

Prepared according to General Procedure 2B using  $\Delta$ - $[\text{Ir}(\text{dtbppy})_2(\text{dMeObpy})]\text{PF}_6$  (1.0 mg, 0.0009 mmol, 0.01 equiv.), (*R*)-biphenyl SPINOL phosphoric acid (5.8 mg, 0.009 mmol, 0.10 equiv.), 2-(cyclohex-1-en-1-yl)pyridine (**2.1**, 13.2 mg, 0.08 mmol, 1 equiv.), dry toluene (6 mL), pentane (3 mL), and styrene (0.10 mL, 0.90 mmol, 10.0 equiv.). The crude material was purified by flash column chromatography on silica gel with 15:1 hexanes:EtOAc to afford the cyclobutane as a colorless oil (19.7 mg, 0.075 mmol, 90% yield). 95% ee.

**SFC:** Daicel CHIRALCEL<sup>®</sup> OD-H, 5% *i*-PrOH, 3 g/min,  $t_1 = 8.99$  min,  $t_2 = 10.52$  min; Area% = 97.59 : 2.41 (95% ee).

Prepared according to General Procedure 2B using  $\Lambda$ - $[\text{Ir}(\text{dtbppy})_2(\text{dMeObpy})]\text{PF}_6$  (1.1 mg, 0.0009 mmol, 0.01 equiv.), (*R*)-biphenyl SPINOL phosphoric acid (6.0 mg, 0.010 mmol, 0.10

equiv.), 2-(cyclohex-1-en-1-yl)pyridine (**2.1**, 13.3 mg, 0.084 mmol, 1 equiv.), dry toluene (6 mL), pentane (3 mL), and styrene (0.10 mL, 0.90 mmol, 10.0 equiv.). The crude material was purified by flash column chromatography on silica gel with 15:1 hexanes:EtOAc to afford the cyclobutane as a colorless oil (7.5 mg, 0.028 mmol, 34% yield). 45% ee. 18:1 d.r.

**SFC:** Daicel CHIRALCEL<sup>®</sup> OD-H, 5% *i*-PrOH, 3 g/min,  $t_1 = 8.84$  min,  $t_2 = 10.34$  min; Area% = 72.61 : 27.39 (45% ee).

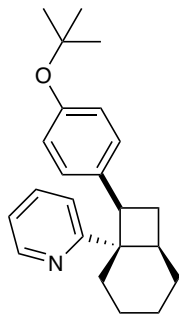
**<sup>1</sup>H NMR** (500 MHz, CDCl<sub>3</sub>)  $\delta$  8.66 (ddd,  $J = 4.8, 1.9, 0.9$  Hz, 1H), 7.64 (td,  $J = 7.7, 1.9$  Hz, 1H), 7.32 (dt,  $J = 8.0, 1.0$  Hz, 1H), 7.27 (m, 4H), 7.20 – 7.15 (m, 1H), 7.12 (ddd,  $J = 7.5, 4.8, 1.1$  Hz, 1H), 3.81 (dd,  $J = 10.6, 7.6$  Hz, 1H), 3.00 – 2.94 (m, 1H), 2.35 (q,  $J = 10.5$  Hz, 1H), 2.17 (dt,  $J = 10.0, 7.9$  Hz, 1H), 1.81 – 1.75 (m, 1H), 1.65 – 1.57 (m, 4H), 1.51 – 1.43 (m, 2H), 1.13 – 1.03 (m, 1H).

**<sup>13</sup>C NMR** (126 MHz, CDCl<sub>3</sub>)  $\delta$  167.22, 149.17, 141.71, 135.83, 128.00, 127.74, 125.68, 120.59, 120.33, 50.43, 46.79, 34.78, 28.70, 25.35, 24.44, 21.82, 21.36.

**HRMS** (ESI<sup>+</sup>) calculated for [C<sub>19</sub>H<sub>22</sub>N]<sup>+</sup> ([M+H]<sup>+</sup>). Requires  $m/z$  264.1747; found  $m/z$  264.1743.

$[\alpha]_D^{22}$ : +51.1° (*c*2.01, EtOH, 95% ee).

**X-Ray:** see below.



**2-((1S,6R,8R)-8-(4-(*tert*-butoxy)phenyl)bicyclo[4.2.0]octan-1-yl)pyridine**

**(2.3):** Prepared according to General Procedure 2B using racemic Ir(dtbbpy)<sub>2</sub>(dMeObpy)PF<sub>6</sub> (3.7 mg, 0.0034 mmol, 0.01 equiv.), (*R*)-biphenyl SPINOL phosphoric acid (19.3 mg, 0.031 mmol, 0.10 equiv.), 2-(cyclohex-1-en-1-yl)pyridine (**2.1**, 50.2 mg, 0.32 mmol, 1 equiv.), dry toluene (20.9 mL), pentane

(10.5 mL), and 4-*tert*-butoxystyrene (0.59 mL, 3.1 mmol, 10.0 equiv.). The crude material was purified by flash column chromatography on silica gel with 15:1 hexanes:EtOAc to afford the cyclobutane as a colorless oil (92.6 mg, 0.28 mmol, 88% yield). 93% ee.

**SFC:** Daicel CHIRALCEL<sup>®</sup> AD-H, 5% MeOH, 3 g/min, t<sub>1</sub> = 6.67 min, t<sub>2</sub> = 9.83 min; Area% = 96.28 : 3.72 (93% ee).

Prepared according to General Procedure 2B using Δ-Ir(dtbbpy)<sub>2</sub>(dMeObpy)PF<sub>6</sub> (3.4 mg, 0.0031 mmol, 0.01 equiv.), (*R*)-biphenyl SPINOL phosphoric acid (19.5 mg, 0.031 mmol, 0.10 equiv.), 2-(cyclohex-1-en-1-yl)pyridine (**2.1**, 49.4 mg, 0.31 mmol, 1 equiv.), dry toluene (20.9 mL), pentane (10.5 mL), and 4-*tert*-butoxystyrene (0.59 mL, 3.1 mmol, 10.0 equiv.). The crude material was purified by flash column chromatography on silica gel with 15:1 hexanes:EtOAc to afford the cyclobutane as a colorless oil (99.3 mg, 0.30 mmol, 95% yield). 95% ee.

**SFC:** Daicel CHIRALCEL<sup>®</sup> AD-H, 5% MeOH, 3 g/min, t<sub>1</sub> = 6.68 min, t<sub>2</sub> = 9.62 min; Area% = 97.52 : 2.48 (95% ee).

Prepared according to General Procedure 2B using Λ-[Ir(dtbbpy)<sub>2</sub>(dMeObpy)]PF<sub>6</sub> (3.1 mg, 0.0031 mmol, 0.01 equiv.), (*R*)-biphenyl SPINOL phosphoric acid (19.4 mg, 0.031 mmol, 0.10

equiv.), 2-(cyclohex-1-en-1-yl)pyridine (**2.1**, 53.0 mg, 0.31 mmol, 1 equiv.), dry toluene (20.9 mL), pentane (10.5 mL), and 4-*tert*-butoxystyrene (0.59 mL, 3.1 mmol, 10.0 equiv.). The crude material was purified by flash column chromatography on silica gel with 15:1 hexanes:EtOAc to afford the cyclobutane as a colorless oil (13.8 mg, 0.041 mmol, 12% yield). 42% ee. 16:1 d.r.

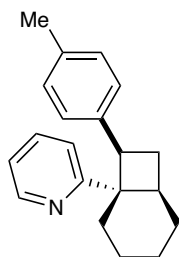
**SFC:** Daicel CHIRALCEL<sup>®</sup> AD-H, 5% MeOH, 3 g/min,  $t_1 = 6.74$  min,  $t_2 = 8.95$  min; Area% = 71.05 : 28.95 (42% ee).

**<sup>1</sup>H NMR** (500 MHz, CDCl<sub>3</sub>)  $\delta$  8.65 (ddd,  $J = 4.8, 2.0, 0.9$  Hz, 1H), 7.63 (td,  $J = 7.7, 1.9$  Hz, 1H), 7.30 (dt,  $J = 8.0, 1.0$  Hz, 1H), 7.15 (d,  $J = 8.2$  Hz, 2H), 7.11 (ddd,  $J = 7.5, 4.8, 1.1$  Hz, 1H), 6.89 (d,  $J = 8.2$  Hz, 2H), 3.74 (dd,  $J = 10.6, 7.6$  Hz, 1H), 2.97 – 2.91 (m, 1H), 2.30 (q,  $J = 10.6$  Hz, 1H), 2.15 (dt,  $J = 10.0, 7.9$  Hz, 1H), 1.77 – 1.72 (m, 1H), 1.64 – 1.57 (m, 4H), 1.53 – 1.44 (m, 2H), 1.33 (s, 9H), 1.15 – 1.00 (m, 1H).

**<sup>13</sup>C NMR** (126 MHz, CDCl<sub>3</sub>)  $\delta$  167.44, 153.28, 149.14, 136.51, 135.84, 128.31, 123.49, 120.57, 120.38, 78.02, 50.40, 46.37, 34.69, 28.89, 28.63, 25.40, 24.69, 21.85, 21.36.

**HRMS** (ESI<sup>+</sup>) calculated for [C<sub>23</sub>H<sub>30</sub>NO]<sup>+</sup> ([M+H]<sup>+</sup>). Requires  $m/z$  336.2322; found  $m/z$  336.2317.

$[\alpha]_D^{22}$ : +76.5° (*c*6.46, EtOH, 95% ee).



**2-((1*S*,6*R*,8*R*)-8-(*p*-tolyl)bicyclo[4.2.0]octan-1-yl)pyridine (**2.4**):** Prepared according to General Procedure 2B using racemic Ir(dtbbpy)<sub>2</sub>(dMeObpy)PF<sub>6</sub> (3.1 mg, 0.0029 mmol, 0.01 equiv.), (*R*)-biphenyl SPINOL phosphoric acid (20.0 mg, 0.032 mmol, 0.10 equiv.), 2-(cyclohex-1-en-1-yl)pyridine (**2.1**, 49.2 mg, 0.31

mmol, 1 equiv.), dry toluene (20.9 mL), pentane (10.5 mL), and 4-methylstyrene (0.41 mL, 3.1 mmol, 10.0 equiv.). The crude material was purified by flash column chromatography on silica gel with 15:1 hexanes:EtOAc to afford the cyclobutane as a colorless oil (77.5 mg, 0.28 mmol, 90% yield). 92% ee.

**SFC:** Daicel CHIRALCEL<sup>®</sup> OD-H, 5% *i*-PrOH, 3 g/min,  $t_1 = 8.93$  min,  $t_2 = 10.08$  min; Area% = 96.17 : 3.83 (92% ee).

Prepared according to General Procedure 2B using  $\Delta$ -Ir(dtbbpy)<sub>2</sub>(dMeObpy)PF<sub>6</sub> (3.6 mg, 0.0033 mmol, 0.01 equiv.), (*R*)-biphenyl SPINOL phosphoric acid (19.2 mg, 0.031 mmol, 0.10 equiv.), 2-(cyclohex-1-en-1-yl)pyridine (**2.1**, 49.4 mg, 0.31 mmol, 1 equiv.), dry toluene (20.9 mL), pentane (10.5 mL), and 4-methylstyrene (0.41 mL, 3.1 mmol, 10.0 equiv.). The crude material was purified by flash column chromatography on silica gel with 15:1 hexanes:EtOAc to afford the cyclobutane as a colorless oil (80.1 mg, 0.29 mmol, 93% yield). 94% ee.

**SFC:** Daicel CHIRALCEL<sup>®</sup> OD-H, 5% *i*-PrOH, 3 g/min,  $t_1 = 9.02$  min,  $t_2 = 10.13$  min; Area% = 97.18 : 2.82 (94% ee).

Prepared according to General Procedure 2B using  $\Lambda$ -[Ir(dtbbpy)<sub>2</sub>(dMeObpy)]PF<sub>6</sub> (3.4 mg, 0.0031 mmol, 0.01 equiv.), (*R*)-biphenyl SPINOL phosphoric acid (19.5 mg, 0.031 mmol, 0.10 equiv.), 2-(cyclohex-1-en-1-yl)pyridine (**2.1**, 52.4 mg, 0.31 mmol, 1 equiv.), dry toluene (20.9 mL), pentane (10.5 mL), and 4-methylstyrene (0.41 mL, 3.1 mmol, 10.0 equiv.). The crude material was purified by flash column chromatography on silica gel with 15:1 hexanes:EtOAc to afford the cyclobutane as a colorless oil (22.4 mg, 0.081 mmol, 25% yield). 35% ee. >20:1 d.r.

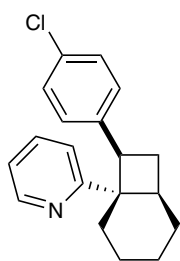
**SFC:** Daicel CHIRALCEL<sup>®</sup> OD-H, 5% *i*-PrOH, 3 g/min,  $t_1 = 9.70$  min,  $t_2 = 10.83$  min; Area% = 67.54 : 32.46 (35% ee).

**<sup>1</sup>H NMR** (500 MHz, CDCl<sub>3</sub>)  $\delta$  8.66 (ddd,  $J = 4.8, 1.9, 0.9$  Hz, 1H), 7.63 (td,  $J = 7.7, 1.9$  Hz, 1H), 7.32 – 7.29 (m, 1H), 7.15 (d,  $J = 8.0$  Hz, 2H), 7.13 – 7.10 (m, 1H), 7.09 (d,  $J = 8.0$  Hz, 2H), 3.74 (dd,  $J = 10.6, 7.6$  Hz, 1H), 2.99 – 2.92 (m, 1H), 2.34 – 2.30 (m, 1H), 2.32 (s, 3H), 2.14 (dt,  $J = 10.1, 7.9$  Hz, 1H), 1.79 – 1.73 (m, 1H), 1.64 – 1.59 (m, 4H), 1.51 – 1.44 (m, 2H), 1.12 – 1.01 (m, 1H).

**<sup>13</sup>C NMR** (126 MHz, CDCl<sub>3</sub>)  $\delta$  167.36, 149.13, 138.51, 135.80, 135.12, 128.48, 127.93, 120.54, 120.32, 50.39, 46.58, 34.65, 28.70, 25.37, 24.47, 21.85, 21.34, 21.03.

**HRMS** (ESI<sup>+</sup>) calculated for [C<sub>20</sub>H<sub>24</sub>N]<sup>+</sup> ([M+H]<sup>+</sup>). Requires  $m/z$  278.1903; found  $m/z$  278.1900.

$[\alpha]_D^{22}$ : +67.4° (*c*5.12, EtOH, 94% ee).



**2-((1*S*,6*R*,8*R*)-8-(4-chlorophenyl)bicyclo[4.2.0]octan-1-yl)pyridine (2.5):**

Prepared according to General Procedure 2B using racemic

Ir(dtbbpy)<sub>2</sub>(dMeObpy)PF<sub>6</sub> (3.5 mg, 0.0032 mmol, 0.01 equiv.), (*R*)-biphenyl

SPINOL phosphoric acid (20.1 mg, 0.032 mmol, 0.10 equiv.), 2-(cyclohex-1-en-

1-yl)pyridine (**2.1**, 49.9 mg, 0.31 mmol, 1 equiv.), dry toluene (20.9 mL), pentane (10.5 mL), and 4-chlorostyrene (0.38 mL, 3.1 mmol, 10.0 equiv.). The crude material was purified by flash column

chromatography on silica gel with 15:1 hexanes:EtOAc to afford the cyclobutane as a colorless oil (75.0 mg, 0.25 mmol, 80% yield). 89% ee.

**SFC:** Daicel CHIRALCEL® OJ-H, 10% MeOH, 3 g/min,  $t_1 = 4.95$  min,  $t_2 = 8.56$  min; Area% = 5.69 : 94.31 (89% ee).

Prepared according to General Procedure 2B using  $\Delta$ -Ir(dtbbpy)<sub>2</sub>(dMeObpy)PF<sub>6</sub> (3.7 mg, 0.0034 mmol, 0.01 equiv.), (*R*)-biphenyl SPINOL phosphoric acid (19.7 mg, 0.032 mmol, 0.10 equiv.), 2-(cyclohex-1-en-1-yl)pyridine (**2.1**, 52.9 mg, 0.33 mmol, 1 equiv.), dry toluene (20.9 mL), pentane (10.5 mL), and 4-chlorostyrene (0.38 mL, 3.1 mmol, 10.0 equiv.). The crude material was purified by flash column chromatography on silica gel with 15:1 hexanes:EtOAc to afford the cyclobutane as a colorless oil (93.0 mg, 0.31 mmol, 94% yield). 96% ee.

**SFC:** Daicel CHIRALCEL® OJ-H, 10% MeOH, 3 g/min,  $t_1 = 5.39$  min,  $t_2 = 9.27$  min; Area% = 2.22 : 97.78 (96% ee).

Prepared according to General Procedure 2B using  $\Lambda$ -[Ir(dtbbpy)<sub>2</sub>(dMeObpy)]PF<sub>6</sub> (3.4 mg, 0.0031 mmol, 0.01 equiv.), (*R*)-biphenyl SPINOL phosphoric acid (19.5 mg, 0.031 mmol, 0.10 equiv.), 2-(cyclohex-1-en-1-yl)pyridine (**2.1**, 54.0 mg, 0.34 mmol, 1 equiv.), dry toluene (20.9 mL), pentane (10.5 mL), and 4-chlorostyrene (0.38 mL, 3.1 mmol, 10.0 equiv.). The crude material was purified by flash column chromatography on silica gel with 15:1 hexanes:EtOAc to afford the cyclobutane as a colorless oil (21.0 mg, 0.071 mmol, 21% yield). 34% ee. 4:1 d.r.



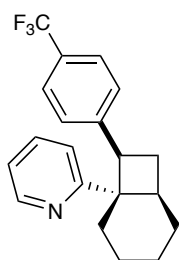
**SFC:** Daicel CHIRALCEL® OJ-H, 10% MeOH, 3 g/min,  $t_1 = 5.13$  min,  $t_2 = 9.00$  min; Area% = 33.07 : 66.93 (34% ee).

**$^1\text{H NMR}$**  (500 MHz,  $\text{CD}_2\text{Cl}_2$ )  $\delta$  8.54 (ddd,  $J = 4.8, 1.9, 1.0$  Hz, 1H), 7.57 (td,  $J = 7.7, 1.9$  Hz, 1H), 7.28 – 7.24 (m, 2H), 7.23 (dt,  $J = 7.9, 1.0$  Hz, 1H), 7.20 – 7.13 (m, 2H), 7.05 (ddd,  $J = 7.5, 4.8, 1.1$  Hz, 1H), 3.63 (dd,  $J = 10.6, 7.6$  Hz, 1H), 2.83 – 2.76 (m, 1H), 2.21 (q,  $J = 10.6$  Hz, 1H), 2.08 (dt,  $J = 10.1, 7.9$  Hz, 1H), 1.65 – 1.59 (m, 1H), 1.59 – 1.53 (m, 2H), 1.44 (td,  $J = 14.0, 3.4$  Hz, 2H), 1.40 – 1.33 (m, 2H), 1.04 – 0.91 (m, 1H).

**$^{13}\text{C NMR}$**  (126 MHz,  $\text{CD}_2\text{Cl}_2$ )  $\delta$  167.22, 148.97, 140.45, 135.75, 131.07, 129.60, 127.51, 120.57, 120.17, 50.39, 45.97, 34.51, 28.99, 25.16, 24.43, 21.62, 21.04.

**HRMS** ( $\text{ESI}^+$ ) calculated for  $[\text{C}_{19}\text{H}_{21}\text{ClN}]^+$  ( $[\text{M}+\text{H}]^+$ ). Requires  $m/z$  298.1357; found  $m/z$  298.1357.

$[\alpha]_D^{22}$ : +75.9° ( $c$ 6.12, EtOH, 96% ee).



**2-((1S,6R,8R)-8-(4-(trifluoromethyl)phenyl)bicyclo[4.2.0]octan-1-**

**yl)pyridine (2.6):** Prepared according to General Procedure 2B using racemic

$\text{Ir}(\text{dtbppy})_2(\text{dMeObpy})\text{PF}_6$  (3.6 mg, 0.0033 mmol, 0.01 equiv.), (*R*)-biphenyl

SPINOL phosphoric acid (19.8 mg, 0.032 mmol, 0.10 equiv.), 2-(cyclohex-1-en-

1-yl)pyridine (**2.1**, 51.2 mg, 0.32 mmol, 1 equiv.), dry toluene (20.9 mL), pentane (10.5 mL), and 4-trifluoromethylstyrene (0.40 mL, 2.7 mmol, 8.4 equiv.). The crude material was purified by flash

column chromatography on silica gel with 7:1 hexanes:EtOAc to afford the cyclobutane as a colorless oil (44.2 mg, 0.13 mmol, 41% yield). 87% ee.

**SFC:** Daicel CHIRALCEL<sup>®</sup> OJ-H, 1% MeOH, 3 g/min,  $t_1 = 5.99$  min,  $t_2 = 11.42$  min; Area% = 6.63 : 93.37 (87% ee).

Prepared according to General Procedure 2B using  $\Delta$ -Ir(dtbbpy)<sub>2</sub>(dMeObpy)PF<sub>6</sub> (2.9 mg, 0.0027 mmol, 0.01 equiv.), (*R*)-biphenyl SPINOL phosphoric acid (19.4 mg, 0.031 mmol, 0.10 equiv.), 2-(cyclohex-1-en-1-yl)pyridine (**2.1**, 52.7 mg, 0.33 mmol, 1 equiv.), dry toluene (20.9 mL), pentane (10.5 mL), and 4-trifluoromethylstyrene (0.46 mL, 3.1 mmol, 10.0 equiv.). The crude material was purified by flash column chromatography on silica gel with 8:1 hexanes:EtOAc to afford the cyclobutane as a colorless oil (40.2 mg, 0.12 mmol, 37% yield). 89% ee.

**SFC:** Daicel CHIRALCEL<sup>®</sup> OJ-H, 1% MeOH, 3 g/min,  $t_1 = 5.84$  min,  $t_2 = 11.36$  min; Area% = 5.42 : 94.58 (89% ee).

Prepared according to General Procedure 2B using  $\Lambda$ -[Ir(dtbbpy)<sub>2</sub>(dMeObpy)]PF<sub>6</sub> (3.5 mg, 0.0031 mmol, 0.01 equiv.), (*R*)-biphenyl SPINOL phosphoric acid (19.6 mg, 0.031 mmol, 0.10 equiv.), 2-(cyclohex-1-en-1-yl)pyridine (**2.1**, 47.0 mg, 0.30 mmol, 1 equiv.), dry toluene (20.9 mL), pentane (10.5 mL), and 4-trifluoromethylstyrene (0.46 mL, 3.1 mmol, 10.0 equiv.). The crude material was purified by flash column chromatography on silica gel with 15:1 hexanes:EtOAc to afford the cyclobutane as a colorless oil (23.3 mg, 0.070 mmol, 24% yield). 33% ee. 8:1 d.r.

**SFC:** Daicel CHIRALCEL® OJ-H, 1% MeOH, 3 g/min,  $t_1 = 6.09$  min,  $t_2 = 11.64$  min; Area% = 33.67 : 66.33 (33% ee).

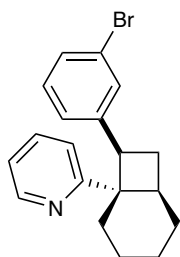
**$^1\text{H NMR}$**  (500 MHz,  $\text{CDCl}_3$ )  $\delta$  8.67 (ddd,  $J = 4.8, 1.9, 0.9$  Hz, 1H), 7.65 (td,  $J = 7.7, 1.9$  Hz, 1H), 7.53 (d,  $J = 8.2$  Hz, 2H), 7.46 (d,  $J = 8.2$  Hz, 2H), 7.30 (dt,  $J = 7.9, 1.1$  Hz, 1H), 7.14 (ddd,  $J = 7.5, 4.8, 1.1$  Hz, 1H), 3.85 (dd,  $J = 10.3, 7.9$  Hz, 1H), 2.98 – 2.89 (m, 1H), 2.34 (q,  $J = 10.6$  Hz, 1H), 2.22 (dt,  $J = 10.1, 7.9$  Hz, 1H), 1.81 – 1.73 (m, 1H), 1.68 – 1.60 (m, 3H), 1.57 – 1.51 (m, 1H), 1.51 – 1.45 (m, 2H), 1.07 (qt,  $J = 13.8, 3.9$  Hz, 1H).

**$^{13}\text{C NMR}$**  (126 MHz,  $\text{CDCl}_3$ )  $\delta$  166.94, 149.30, 146.07, 135.94, 128.37, 127.86 (q,  $J = 32.1$  Hz), 124.62 (q,  $J = 3.8$  Hz), 124.50 (q,  $J = 271.7$  Hz), 120.80, 120.26, 50.59, 46.44, 34.82, 29.07, 25.27, 24.57, 21.70, 21.18.

**$^{19}\text{F NMR}$**  (377 MHz,  $\text{CDCl}_3$ )  $\delta$  –62.23.

**HRMS** (ESI<sup>+</sup>) calculated for  $[\text{C}_{20}\text{H}_{21}\text{F}_3\text{N}]^+$  ( $[\text{M}+\text{H}]^+$ ). Requires  $m/z$  332.1621; found  $m/z$  332.1616.

$[\alpha]_D^{22}$ : +52.0° ( $c$ 1.21, EtOH, 89% ee).



**2-((1S,6R,8R)-8-(3-bromophenyl)bicyclo[4.2.0]octan-1-yl)pyridine (2.7):**

Prepared according to General Procedure 2B using racemic

$\text{Ir}(\text{dtbppy})_2(\text{dMeObpy})\text{PF}_6$  (3.5 mg, 0.0032 mmol, 0.01 equiv.), (*R*)-biphenyl

SPINOL phosphoric acid (19.6 mg, 0.032 mmol, 0.10 equiv.), 2-(cyclohex-1-en-

1-yl)pyridine (**2.1**, 50.5 mg, 0.32 mmol, 1 equiv.), dry toluene (20.9 mL), pentane (10.5 mL), and 3-bromostyrene (0.41 mL, 3.1 mmol, 10.0 equiv.). The crude material was purified by flash column chromatography on silica gel with 15:1 hexanes:EtOAc to afford the cyclobutane as a colorless oil (79.2 mg, 0.23 mmol, 73% yield). 95% ee.

**SFC:** Daicel CHIRALCEL® OJ-H, 5% *i*-PrOH, 3 g/min,  $t_1 = 7.66$  min,  $t_2 = 11.51$  min; Area% = 2.41 : 97.59 (95% ee).

Prepared according to General Procedure 2B using  $\Delta$ -Ir(dtbppy)<sub>2</sub>(dMeObpy)PF<sub>6</sub> (3.4 mg, 0.0031 mmol, 0.01 equiv.), (*R*)-biphenyl SPINOL phosphoric acid (18.8 mg, 0.030 mmol, 0.10 equiv.), 2-(cyclohex-1-en-1-yl)pyridine (**2.1**, 50.4 mg, 0.32 mmol, 1 equiv.), dry toluene (20.9 mL), pentane (10.5 mL), and 3-bromostyrene (0.41 mL, 3.1 mmol, 10.0 equiv.). The crude material was purified by flash column chromatography on silica gel with 15:1 hexanes:EtOAc to afford the cyclobutane as a colorless oil (100.6 mg, 0.29 mmol, 93% yield). 95% ee.

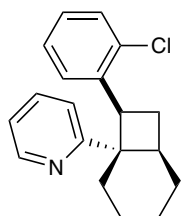
**SFC:** Daicel CHIRALCEL® OJ-H, 5% *i*-PrOH, 3 g/min,  $t_1 = 7.81$  min,  $t_2 = 11.71$  min; Area% = 2.55 : 97.45 (95% ee).

**<sup>1</sup>H NMR** (500 MHz, CDCl<sub>3</sub>)  $\delta$  8.67 (d,  $J = 4.6$  Hz, 1H), 7.64 (td,  $J = 7.7, 1.9$  Hz, 1H), 7.49 – 7.47 (m, 1H), 7.32 – 7.27 (m, 3H), 7.15 – 7.11 (m, 2H), 3.79 (dd,  $J = 10.5, 7.6$  Hz, 1H), 2.94 – 2.88 (m, 1H), 2.29 (q,  $J = 10.5$  Hz, 1H), 2.18 (dt,  $J = 10.1, 7.9$  Hz, 1H), 1.81 – 1.76 (m, 1H), 1.66 – 1.55 (m, 4H), 1.53 – 1.40 (m, 2H), 1.13 – 1.03 (m, 1H).

$^{13}\text{C}$  NMR (126 MHz,  $\text{CDCl}_3$ )  $\delta$  166.93, 149.27, 144.44, 135.92, 131.03, 129.27, 128.73, 126.84, 122.12, 120.75, 120.24, 50.49, 46.25, 34.79, 28.92, 25.27, 24.58, 21.70, 21.21.

**HRMS** (ESI<sup>+</sup>) calculated for  $[\text{C}_{19}\text{H}_{21}\text{BrN}]^+$  ( $[\text{M}+\text{H}]^+$ ). Requires  $m/z$  342.0852; found  $m/z$  342.0848.

$[\alpha]_D^{22}$ : +63.2° ( $c$ 6.31, EtOH, 95% ee).



**2-((1*S*,6*R*,8*S*)-8-(2-chlorophenyl)bicyclo[4.2.0]octan-1-yl)pyridine (2.8):**

Prepared according to General Procedure 2B using racemic  $\text{Ir}(\text{dtbppy})_2(\text{dMeObpy})\text{PF}_6$  (3.6 mg, 0.0033 mmol, 0.01 equiv.), (*R*)-biphenyl SPINOL phosphoric acid (19.4 mg, 0.031 mmol, 0.10 equiv.), 2-(cyclohex-1-en-1-yl)pyridine (**2.1**, 49.3 mg, 0.31 mmol, 1 equiv.), dry toluene (20.9 mL), pentane (10.5 mL), and 2-chlorostyrene (0.40 mL, 3.1 mmol, 10.0 equiv.). The crude material was purified by flash column chromatography on silica gel with 15:1 hexanes:EtOAc to afford the cyclobutane as a colorless oil (41.8 mg, 0.14 mmol, 45% yield). Separation of the two diastereomers was achieved by preparative TLC using 20:1 hexanes:EtOAc. The top band was the minor diastereomer, and the bottom band was the major diastereomer. 69% ee of major diastereomer. 1.4 : 1 d.r.

**SFC:** Daicel CHIRALCEL<sup>®</sup> OD-H, 1% MeOH, 3 g/min,  $t_1 = 27.18$  min,  $t_2 = 36.49$  min; Area% = 15.32 : 84.68 (69% ee).

Prepared according to General Procedure 2B using  $\Delta\text{-Ir}(\text{dtbppy})_2(\text{dMeObpy})\text{PF}_6$  (4.0 mg, 0.0037 mmol, 0.01 equiv.), (*R*)-biphenyl SPINOL phosphoric acid (19.3 mg, 0.031 mmol, 0.10 equiv.),

2-(cyclohex-1-en-1-yl)pyridine (**2.1**, 51.4 mg, 0.32 mmol, 1 equiv.), dry toluene (20.9 mL), pentane (10.5 mL), and 2-chlorostyrene (0.40 mL, 3.1 mmol, 10.0 equiv.). The crude material was purified by flash column chromatography on silica gel with 15:1 hexanes:EtOAc to afford the cyclobutane as a colorless oil (53.7 mg, 0.18 mmol, 56% yield). 69% ee of major diastereomer. 1.1 : 1 d.r.

**SFC:** Daicel CHIRALCEL<sup>®</sup> OD-H, 1% MeOH, 3 g/min,  $t_1 = 27.52$  min,  $t_2 = 36.81$  min; Area% = 15.67 : 84.33 (69% ee).

Characterization for the major diastereomer (Prep TLC bottom spot):

**<sup>1</sup>H NMR** (500 MHz, CD<sub>2</sub>Cl<sub>2</sub>)  $\delta$  8.26 (ddd,  $J = 4.7, 1.9, 1.1$  Hz, 1H), 7.22 (ddd,  $J = 8.0, 7.4, 1.9$  Hz, 1H), 7.14 – 7.09 (m, 1H), 6.90 – 6.76 (m, 5H), 4.11 (dd,  $J = 8.5, 5.4$  Hz, 1H), 3.42 (dt,  $J = 12.7, 7.9$  Hz, 1H), 2.30 – 2.19 (m, 2H), 2.12 (ddd,  $J = 11.3, 8.9, 5.4$  Hz, 1H), 2.00 (ddd,  $J = 13.8, 6.5, 3.6$  Hz, 1H), 1.86 (tdd,  $J = 10.7, 7.8, 4.2$  Hz, 1H), 1.65 – 1.54 (m, 3H), 1.44 – 1.39 (m, 1H), 1.15 – 1.07 (m, 1H).

**<sup>13</sup>C NMR** (126 MHz, CD<sub>2</sub>Cl<sub>2</sub>)  $\delta$  164.63, 147.68, 139.91, 134.83, 134.33, 128.67, 128.13, 126.58, 126.06, 121.69, 120.02, 51.99, 44.83, 37.06, 32.39, 26.99, 26.93, 22.00, 21.67.

**HRMS** (ESI<sup>+</sup>) calculated for [C<sub>19</sub>H<sub>21</sub>ClN]<sup>+</sup> ([M+H]<sup>+</sup>). Requires  $m/z$  298.1357; found  $m/z$  298.1355.

**$[\alpha]_D^{22}$ :** +105.5° (c0.44, EtOH, 69% ee).

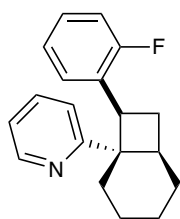
Characterization for the minor diastereomer (Prep TLC top spot):

**<sup>1</sup>H NMR** (500 MHz, CD<sub>2</sub>Cl<sub>2</sub>) δ 8.52 (ddd, *J* = 4.8, 1.9, 1.0 Hz, 1H), 7.53 (td, *J* = 7.7, 1.9 Hz, 1H), 7.34 (dd, *J* = 7.6, 1.5 Hz, 1H), 7.27 (dt, *J* = 8.0, 1.1 Hz, 1H), 7.17 (td, *J* = 7.5, 1.4 Hz, 1H), 7.11 (dd, *J* = 7.9, 1.4 Hz, 1H), 7.07 – 6.98 (m, 2H), 4.03 (dd, *J* = 10.8, 7.4 Hz, 1H), 3.02 (dt, *J* = 12.7, 6.5 Hz, 1H), 2.37 (q, *J* = 10.7 Hz, 1H), 2.14 – 2.05 (m, 1H), 1.91 – 1.85 (m, 1H), 1.55 (td, *J* = 14.1, 3.1 Hz, 1H), 1.51 – 1.45 (m, 4H), 1.36 – 1.27 (m, 1H), 1.08 – 0.97 (m, 1H).

**<sup>13</sup>C NMR** (126 MHz, CD<sub>2</sub>Cl<sub>2</sub>) δ 165.30, 148.59, 138.97, 135.36, 133.97, 129.81, 129.09, 126.98, 125.93, 120.35, 120.27, 50.70, 45.60, 35.65, 25.96, 24.98, 24.33, 21.64, 21.62.

**HRMS** (ESI<sup>+</sup>) calculated for [C<sub>19</sub>H<sub>21</sub>ClN]<sup>+</sup> ([M+H]<sup>+</sup>). Requires *m/z* 298.1357; found *m/z* 298.1355.

[α]<sub>D</sub><sup>22</sup>: +12.6° (c0.38, CDCl<sub>3</sub>).



**2-((1*S*,6*R*,8*S*)-8-(2-fluorophenyl)bicyclo[4.2.0]octan-1-yl)pyridine (2.9):**

Prepared according to General Procedure 2B using racemic Ir(dtbbpy)<sub>2</sub>(dMeObpy)PF<sub>6</sub> (3.3 mg, 0.0030 mmol, 0.01 equiv.), (*R*)-biphenyl SPINOL phosphoric acid (20.4 mg, 0.033 mmol, 0.10 equiv.), 2-(cyclohex-1-en-1-yl)pyridine (**2.1**, 50.7 mg, 0.32 mmol, 1 equiv.), dry toluene (20.9 mL), pentane (10.5 mL), and 2-fluorostyrene (0.37 mL, 3.1 mmol, 10.0 equiv.). The crude material was purified by flash column chromatography on silica gel with 15:1 hexanes:EtOAc to afford the cyclobutane as a colorless oil (66.3 mg, 0.24 mmol, 74% yield). 79% ee.

**SFC:** Daicel CHIRALCEL<sup>®</sup> OJ-H, 5% *i*-PrOH, 3 g/min,  $t_1 = 6.57$  min,  $t_2 = 8.65$  min; Area% = 10.62 : 89.38 (79% ee).

Prepared according to General Procedure 2B using  $\Delta$ -Ir(dtbbpy)<sub>2</sub>(dMeObpy)PF<sub>6</sub> (3.2 mg, 0.0029 mmol, 0.01 equiv.), (*R*)-biphenyl SPINOL phosphoric acid (19.7 mg, 0.032 mmol, 0.10 equiv.), 2-(cyclohex-1-en-1-yl)pyridine (**2.1**, 50.1 mg, 0.31 mmol, 1 equiv.), dry toluene (20.9 mL), pentane (10.5 mL), and 2-fluorostyrene (0.37 mL, 3.1 mmol, 10.0 equiv.). The crude material was purified by flash column chromatography on silica gel with 15:1 hexanes:EtOAc to afford the cyclobutane as a colorless oil (78.4 mg, 0.28 mmol, 89% yield). 88% ee.

**SFC:** Daicel CHIRALCEL<sup>®</sup> OJ-H, 5% *i*-PrOH, 3 g/min,  $t_1 = 6.59$  min,  $t_2 = 8.72$  min; Area% = 5.76 : 94.24 (88% ee).

**<sup>1</sup>H NMR** (500 MHz, CDCl<sub>3</sub>)  $\delta$  8.66 (ddd,  $J = 4.8, 1.9, 0.9$  Hz, 1H), 7.63 (ddd,  $J = 7.9, 7.4, 1.9$  Hz, 1H), 7.34 – 7.30 (m, 2H), 7.17 – 7.07 (m, 3H), 6.86 (ddd,  $J = 10.4, 8.0, 1.4$  Hz, 1H), 4.06 (dd,  $J = 10.7, 7.6$  Hz, 1H), 3.12 – 3.04 (m, 1H), 2.39 (q,  $J = 10.7$  Hz, 1H), 2.21 (dt,  $J = 10.2, 7.9$  Hz, 1H), 1.98 – 1.93 (m, 1H), 1.65 (td,  $J = 14.2, 3.2$  Hz, 1H), 1.60 – 1.53 (m, 3H), 1.51 – 1.43 (m, 2H), 1.20 – 1.09 (m, 1H).

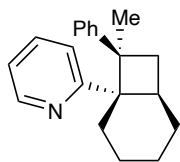
**<sup>13</sup>C NMR** (126 MHz, CDCl<sub>3</sub>)  $\delta$  165.66, 161.23 (d,  $J = 245.8$  Hz), 148.90, 135.66, 129.75 (d,  $J = 5.7$  Hz), 128.50 (d,  $J = 17.0$  Hz), 127.29 (d,  $J = 7.9$  Hz), 123.42 (d,  $J = 3.4$  Hz), 120.56, 120.21 (d,  $J = 2.1$  Hz), 114.81 (d,  $J = 22.2$  Hz), 50.21, 42.23, 36.12, 27.09, 25.21, 24.29, 24.28, 21.73.

**<sup>19</sup>F NMR** (377 MHz, CDCl<sub>3</sub>)  $\delta$  -114.07.



**HRMS** (ESI<sup>+</sup>) calculated for [C<sub>19</sub>H<sub>21</sub>FN]<sup>+</sup> ([M+H]<sup>+</sup>). Requires *m/z* 282.1653; found *m/z* 282.1650.

[ $\alpha$ ]<sub>D</sub><sup>22</sup>: +53.7° (*c*5.28, EtOH, 88% ee).



**2-((1*S*,6*R*,8*R*)-8-methyl-8-phenylbicyclo[4.2.0]octan-1-yl)pyridine (2.10):**

Prepared according to General Procedure 2B using racemic Ir(dtbbpy)<sub>2</sub>(dMeObpy)PF<sub>6</sub> (3.5 mg, 0.0032 mmol, 0.01 equiv.), (*R*)-biphenyl SPINOL phosphoric acid (19.5 mg, 0.032 mmol, 0.10 equiv.), 2-(cyclohex-1-en-1-yl)pyridine (**2.1**, 49.5 mg, 0.31 mmol, 1 equiv.), dry toluene (20.9 mL), pentane (10.5 mL), and  $\alpha$ -methylstyrene (0.41 mL, 3.1 mmol, 10.0 equiv.). The crude material was purified by flash column chromatography on silica gel with 15:1 hexanes:EtOAc to afford the cyclobutane as a colorless oil (31.3 mg, 0.11 mmol, 36% yield). 77% ee.

**SFC:** Daicel CHIRALCEL<sup>®</sup> OD-H, 5% *i*-PrOH, 3 g/min, *t*<sub>1</sub> = 7.02 min, *t*<sub>2</sub> = 17.55 min; Area% = 88.46 : 11.54 (77% ee).

Prepared according to General Procedure 2B using  $\Delta$ -Ir(dtbbpy)<sub>2</sub>(dMeObpy)PF<sub>6</sub> (3.4 mg, 0.0031 mmol, 0.01 equiv.), (*R*)-biphenyl SPINOL phosphoric acid (19.4 mg, 0.031 mmol, 0.10 equiv.), 2-(cyclohex-1-en-1-yl)pyridine (**2.1**, 49.8 mg, 0.31 mmol, 1 equiv.), dry toluene (20.9 mL), pentane (10.5 mL), and  $\alpha$ -methylstyrene (0.41 mL, 3.1 mmol, 10.0 equiv.). The crude material was purified by flash column chromatography on silica gel with 15:1 hexanes:EtOAc to afford the cyclobutane as a colorless oil (51.9 mg, 0.19 mmol, 60% yield). 82% ee.

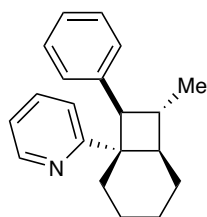
**SFC:** Daicel CHIRALCEL® OD-H, 5% *i*-PrOH, 3 g/min,  $t_1 = 8.17$  min,  $t_2 = 17.87$  min; Area% = 91.17 : 8.83 (82% ee).

**$^1\text{H NMR}$**  (500 MHz,  $\text{CDCl}_3$ )  $\delta$  8.71 (ddd,  $J = 4.8, 2.0, 0.9$  Hz, 1H), 7.73 (d,  $J = 7.4$  Hz, 2H), 7.64 (td,  $J = 7.7, 1.9$  Hz, 1H), 7.38 – 7.30 (m, 3H), 7.22 – 7.15 (m, 1H), 7.11 (ddd,  $J = 7.5, 4.8, 1.1$  Hz, 1H), 3.13 (q,  $J = 8.7, 8.1$  Hz, 1H), 2.49 (t,  $J = 10.6$  Hz, 1H), 2.02 – 1.97 (m, 1H), 1.90 (dd,  $J = 10.1, 8.5$  Hz, 1H), 1.81 – 1.73 (m, 1H), 1.72 – 1.66 (m, 1H), 1.60 – 1.54 (m, 1H), 1.41 (td,  $J = 14.0, 3.2$  Hz, 1H), 1.38 – 1.33 (m, 1H), 1.33 – 1.26 (m, 1H), 1.04 (s, 3H), 0.75 (qt,  $J = 13.6, 3.0$  Hz, 1H).

**$^{13}\text{C NMR}$**  (126 MHz,  $\text{CDCl}_3$ )  $\delta$  165.84, 149.27, 149.17, 135.44, 127.79, 127.40, 125.22, 121.73, 120.38, 52.50, 49.53, 34.44, 31.92, 30.49, 27.37, 25.37, 21.96, 21.34.

**HRMS** (ESI<sup>+</sup>) calculated for  $[\text{C}_{20}\text{H}_{24}\text{N}]^+$  ( $[\text{M}+\text{H}]^+$ ). Requires  $m/z$  278.1903; found  $m/z$  278.1899.

$[\alpha]_D^{22}$ : +60.1° ( $c$ 2.89, EtOH, 82% ee).



**2-((1*S*,6*R*,7*R*,8*R*)-7-methyl-8-phenylbicyclo[4.2.0]octan-1-yl)pyridine**

**(2.11):** Prepared according to General Procedure 2B using racemic

$\text{Ir}(\text{dtbppy})_2(\text{dMeObpy})\text{PF}_6$  (3.3 mg, 0.0030 mmol, 0.01 equiv.), (*R*)-biphenyl SPINOL phosphoric acid (19.4 mg, 0.031 mmol, 0.10 equiv.), 2-(cyclohex-1-en-1-yl)pyridine (**2.1**, 48.8 mg, 0.31 mmol, 1 equiv.), dry toluene (20.9 mL), pentane (10.5 mL), and *trans*- $\beta$ -methylstyrene (0.41 mL, 3.1 mmol, 10.0 equiv.). The crude material was purified by flash column

chromatography on silica gel with 15:1 hexanes:EtOAc to afford the cyclobutane as a colorless oil (27.4 mg, 0.10 mmol, 32% yield). 70% ee.

**SFC:** Daicel CHIRALCEL<sup>®</sup> OJ-H, 5% *i*-PrOH, 3 g/min,  $t_1 = 6.08$  min,  $t_2 = 9.12$  min; Area% = 15.23 : 84.77 (70% ee).

Prepared according to General Procedure 2B using  $\Delta$ -Ir(dtbbpy)<sub>2</sub>(dMeObpy)PF<sub>6</sub> (3.5 mg, 0.0032 mmol, 0.01 equiv.), (*R*)-biphenyl SPINOL phosphoric acid (18.7 mg, 0.030 mmol, 0.10 equiv.), 2-(cyclohex-1-en-1-yl)pyridine (**2.1**, 50.4 mg, 0.32 mmol, 1 equiv.), dry toluene (20.9 mL), pentane (10.5 mL), and trans- $\beta$ -methylstyrene (0.41 mL, 3.1 mmol, 10.0 equiv.). The crude material was purified by flash column chromatography on silica gel with 15:1 hexanes:EtOAc to afford the cyclobutane as a colorless oil (40.7 mg, 0.15 mmol, 46% yield). 83% ee.

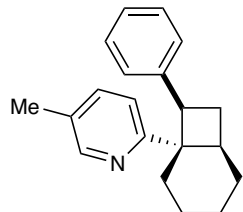
**SFC:** Daicel CHIRALCEL<sup>®</sup> OJ-H, 5% *i*-PrOH, 3 g/min,  $t_1 = 6.28$  min,  $t_2 = 9.42$  min; Area% = 8.45 : 91.55 (83% ee).

**<sup>1</sup>H NMR** (500 MHz, CDCl<sub>3</sub>)  $\delta$  8.65 (ddd,  $J = 4.8, 1.9, 0.9$  Hz, 1H), 7.62 (td,  $J = 7.7, 1.9$  Hz, 1H), 7.32 – 7.27 (m, 5H), 7.19 (ddt,  $J = 8.6, 6.3, 2.0$  Hz, 1H), 7.11 (ddd,  $J = 7.5, 4.8, 1.1$  Hz, 1H), 3.31 (d,  $J = 9.6$  Hz, 1H), 2.66 (tq,  $J = 9.8, 6.4$  Hz, 1H), 2.47 (dd,  $J = 10.2, 5.5$  Hz, 1H), 1.75 – 1.68 (m, 2H), 1.66 – 1.56 (m, 3H), 1.50 – 1.40 (m, 2H), 1.22 (d,  $J = 6.4$  Hz, 3H), 1.14 – 1.01 (m, 1H).

**<sup>13</sup>C NMR** (126 MHz, CDCl<sub>3</sub>)  $\delta$  167.58, 149.11, 140.98, 135.81, 128.11, 127.87, 125.80, 120.54, 120.45, 55.08, 48.63, 42.93, 31.62, 29.73, 23.81, 22.28, 21.67, 19.02.

**HRMS** (ESI<sup>+</sup>) calculated for [C<sub>20</sub>H<sub>24</sub>N]<sup>+</sup> ([M+H]<sup>+</sup>). Requires  $m/z$  278.1903; found  $m/z$  278.1901.

$[\alpha]_D^{22}$ : +19.1° (*c*2.11, EtOH, 83% ee).



**5-methyl-2-((1*S*,6*R*,8*R*)-8-phenylbicyclo[4.2.0]octan-1-yl)pyridine**

**(2.12)**: Prepared according to General Procedure 2B using racemic

Ir(dtbbpy)<sub>2</sub>(dMeObpy)PF<sub>6</sub> (3.2 mg, 0.0029 mmol, 0.01 equiv.), (*R*)-biphenyl SPINOL phosphoric acid (18.9 mg, 0.031 mmol, 0.10 equiv.), 2-(cyclohex-1-en-1-yl)-5-methylpyridine (**S2.1**, 54.0 mg, 0.31 mmol, 1 equiv.), dry toluene (20.9 mL), pentane (10.5 mL), and styrene (0.36 mL, 3.1 mmol, 10.0 equiv.). The crude material was purified by flash column chromatography on silica gel with 15:1 hexanes:EtOAc to afford the cyclobutane as a colorless oil (73.5 mg, 0.26 mmol, 85% yield). 79% ee.

**SFC**: Daicel CHIRALCEL® OJ-H, 5% MeOH, 3 g/min, *t*<sub>1</sub> = 6.65 min, *t*<sub>2</sub> = 7.82 min; Area% = 10.56 : 89.44 (79% ee).

Prepared according to General Procedure 2B using Δ-Ir(dtbbpy)<sub>2</sub>(dMeObpy)PF<sub>6</sub> (3.2 mg, 0.0029 mmol, 0.01 equiv.), (*R*)-biphenyl SPINOL phosphoric acid (19.0 mg, 0.031 mmol, 0.10 equiv.), 2-(cyclohex-1-en-1-yl)-5-methylpyridine (**S2.1**, 54.6 mg, 0.32 mmol, 1 equiv.), dry toluene (20.9 mL), pentane (10.5 mL), and styrene (0.36 mL, 3.1 mmol, 10.0 equiv.). The crude material was purified by flash column chromatography on silica gel with 15:1 hexanes:EtOAc to afford the cyclobutane as a colorless oil (77.7 mg, 0.28 mmol, 89% yield). 86% ee.

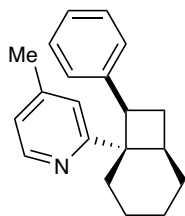
**SFC**: Daicel CHIRALCEL® OJ-H, 5% MeOH, 3 g/min, *t*<sub>1</sub> = 6.67 min, *t*<sub>2</sub> = 7.86 min; Area% = 7.12 : 92.88 (86% ee).

**$^1\text{H}$  NMR** (500 MHz,  $\text{CD}_2\text{Cl}_2$ )  $\delta$  8.38 (dt,  $J = 2.4, 0.8$  Hz, 1H), 7.39 (ddq,  $J = 8.0, 2.3, 0.7$  Hz, 1H), 7.21 – 7.17 (m, 3H), 7.17 – 7.12 (m, 2H), 7.10 – 7.05 (m, 1H), 3.65 (dd,  $J = 10.6, 7.6$  Hz, 1H), 2.86 – 2.78 (m, 1H), 2.28 – 2.20 (m, 1H), 2.24 (s, 3H), 2.05 (dt,  $J = 10.0, 7.9$  Hz, 1H), 1.68 – 1.62 (m, 1H), 1.54 – 1.46 (m, 4H), 1.40 – 1.33 (m, 2H), 0.96 (qt,  $J = 12.6, 2.4$  Hz, 1H).

**$^{13}\text{C}$  NMR** (126 MHz,  $\text{CD}_2\text{Cl}_2$ )  $\delta$  164.17, 149.31, 141.78, 136.23, 129.77, 127.91, 127.49, 125.42, 119.61, 50.00, 46.71, 34.68, 28.64, 25.17, 24.21, 21.72, 21.28, 17.59.

**HRMS** (ESI<sup>+</sup>) calculated for  $[\text{C}_{20}\text{H}_{24}\text{N}]^+$  ( $[\text{M}+\text{H}]^+$ ). Requires  $m/z$  278.1903; found  $m/z$  278.1901.

$[\alpha]_D^{22}$ : +59.9° ( $c$ 4.96, EtOH, 86% ee).



**4-methyl-2-((1*S*,6*R*,8*R*)-8-phenylbicyclo[4.2.0]octan-1-yl)pyridine (2.13):**

Prepared according to General Procedure 2B using racemic  $\text{Ir}(\text{dtbppy})_2(\text{dMeObpy})\text{PF}_6$  (3.9 mg, 0.0036 mmol, 0.01 equiv.), (*R*)-biphenyl SPINOL phosphoric acid (20.0 mg, 0.032 mmol, 0.10 equiv.), 2-(cyclohex-1-en-1-yl)-4-methylpyridine (**S2.2**, 55.7 mg, 0.32 mmol, 1 equiv.), dry toluene (20.9 mL), pentane (10.5 mL), and styrene (0.36 mL, 3.1 mmol, 10.0 equiv.). The crude material was purified by flash column chromatography on silica gel with 12:1 hexanes:EtOAc to afford the cyclobutane as a colorless oil (25.7 mg, 0.09 mmol, 29% yield). 55% ee.

**SFC:** Daicel CHIRALCEL<sup>®</sup> OD-H, 3% *i*-PrOH, 3 g/min,  $t_1 = 13.67$  min,  $t_2 = 15.07$  min; Area% = 77.64 : 22.36 (55% ee).

Prepared according to General Procedure 2B using  $\Delta$ -Ir(dtbppy)<sub>2</sub>(dMeObpy)PF<sub>6</sub> (3.7 mg, 0.0034 mmol, 0.01 equiv.), (*R*)-biphenyl SPINOL phosphoric acid (19.7 mg, 0.032 mmol, 0.10 equiv.), 2-(cyclohex-1-en-1-yl)-4-methylpyridine (**S2.2**, 54.3 mg, 0.31 mmol, 1 equiv.), dry toluene (20.9 mL), pentane (10.5 mL), and styrene (0.36 mL, 3.1 mmol, 10.0 equiv.). The crude material was purified by flash column chromatography on silica gel with 12:1 hexanes:EtOAc to afford the cyclobutane as a colorless oil (39.4 mg, 0.14 mmol, 45% yield). 63% ee.

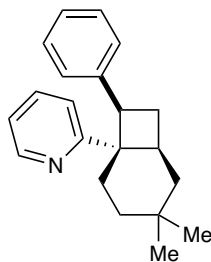
**SFC**: Daicel CHIRALCEL<sup>®</sup> OD-H, 3% *i*-PrOH, 3 g/min,  $t_1 = 13.59$  min,  $t_2 = 14.97$  min; Area% = 81.32 : 18.68 (63% ee).

**<sup>1</sup>H NMR** (500 MHz, CD<sub>2</sub>Cl<sub>2</sub>)  $\delta$  8.39 (dd,  $J = 5.0, 0.8$  Hz, 1H), 7.24 – 7.21 (m, 2H), 7.20 – 7.15 (m, 2H), 7.10 – 7.05 (m, 2H), 6.88 (ddd,  $J = 5.0, 1.6, 0.8$  Hz, 1H), 3.66 (dd,  $J = 10.6, 7.6$  Hz, 1H), 2.81 (ddt,  $J = 11.4, 7.7, 3.6$  Hz, 1H), 2.28 (s, 3H), 2.25 (q,  $J = 10.6$  Hz, 1H), 2.06 (dt,  $J = 10.0, 7.9$  Hz, 1H), 1.68 – 1.62 (m, 1H), 1.56 – 1.47 (m, 4H), 1.42 – 1.33 (m, 2H), 1.06 – 0.93 (m, 1H).

**<sup>13</sup>C NMR** (126 MHz, CD<sub>2</sub>Cl<sub>2</sub>)  $\delta$  167.09, 148.63, 146.71, 141.80, 128.00, 127.47, 125.43, 121.46, 121.07, 50.22, 46.60, 34.62, 28.70, 25.22, 24.28, 21.71, 21.25, 20.85.

**HRMS** (ESI<sup>+</sup>) calculated for [C<sub>20</sub>H<sub>24</sub>N]<sup>+</sup> ([M+H]<sup>+</sup>). Requires  $m/z$  278.1903; found  $m/z$  278.1900.

$[\alpha]_D^{22}$ : +33.8° ( $c$ 2.53, EtOH, 63% ee).



**2-((1S,6S,8R)-4,4-dimethyl-8-phenylbicyclo[4.2.0]octan-1-yl)pyridine**

**(2.14):** Prepared according to General Procedure 2B using racemic

Ir(dtbbpy)<sub>2</sub>(dMeObpy)PF<sub>6</sub> (3.3 mg, 0.0030 mmol, 0.01 equiv.), (*R*)-biphenyl

SPINOL phosphoric acid (19.5 mg, 0.032 mmol, 0.10 equiv.), 2-(4,4-

dimethylcyclohex-1-en-1-yl)pyridine (**S2.3**, 58.7 mg, 0.31 mmol, 1 equiv.), dry toluene (20.9 mL),

pentane (10.5 mL), and styrene (0.36 mL, 3.1 mmol, 10.0 equiv.). The crude material was purified

by flash column chromatography on silica gel with 7:1 hexanes:EtOAc to afford the cyclobutane

as a colorless oil (31.2 mg, 0.11 mmol, 34% yield). 78% ee.

**SFC:** Daicel CHIRALCEL<sup>®</sup> OD-H, 5% *i*-PrOH, 3 g/min, *t*<sub>1</sub> = 7.35 min, *t*<sub>2</sub> = 9.44 min; Area% =

89.00 : 11.00 (78% ee).

Prepared according to General Procedure 2B using Δ-Ir(dtbbpy)<sub>2</sub>(dMeObpy)PF<sub>6</sub> (3.8 mg, 0.0035

mmol, 0.01 equiv.), (*R*)-biphenyl SPINOL phosphoric acid (20.0 mg, 0.032 mmol, 0.10 equiv.),

2-(4,4-dimethylcyclohex-1-en-1-yl)pyridine (**S2.3**, 59.5 mg, 0.32 mmol, 1 equiv.), dry toluene

(20.9 mL), pentane (10.5 mL), and styrene (0.36 mL, 3.1 mmol, 10.0 equiv.). The crude material

was purified by flash column chromatography on silica gel with 12:1 hexanes:EtOAc to afford the

cyclobutane as a colorless oil (38.2 mg, 0.13 mmol, 41% yield). 90% ee.

**SFC:** Daicel CHIRALCEL<sup>®</sup> OD-H, 5% *i*-PrOH, 3 g/min, *t*<sub>1</sub> = 7.14 min, *t*<sub>2</sub> = 9.10 min; Area% =

95.17 : 4.83 (90% ee).

**<sup>1</sup>H NMR** (500 MHz, CD<sub>2</sub>Cl<sub>2</sub>) δ 8.55 (ddd, *J* = 4.8, 1.9, 0.9 Hz, 1H), 7.57 (td, *J* = 7.7, 1.9 Hz, 1H),

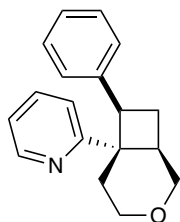
7.25 – 7.16 (m, 5H), 7.12 – 7.07 (m, 1H), 7.05 (ddd, *J* = 7.4, 4.8, 1.1 Hz, 1H), 3.61 (dd, *J* = 9.8,

8.4 Hz, 1H), 2.97 (q,  $J = 8.8$  Hz, 1H), 2.36 (q,  $J = 10.5$  Hz, 1H), 2.21 (dt,  $J = 10.4, 8.3$  Hz, 1H), 1.73 (td,  $J = 14.3, 3.3$  Hz, 1H), 1.56 (dt,  $J = 15.0, 3.5$  Hz, 1H), 1.40 – 1.35 (m, 2H), 1.12 – 1.06 (m, 1H), 1.03 (s, 3H), 0.95 (td,  $J = 13.7, 3.1$  Hz, 1H), 0.77 (s, 3H).

$^{13}\text{C}$  NMR (126 MHz,  $\text{CD}_2\text{Cl}_2$ )  $\delta$  167.00, 148.94, 141.57, 135.70, 127.94, 127.57, 125.53, 120.49, 120.22, 50.40, 47.40, 37.61, 34.26, 33.67, 29.55, 29.36, 27.54, 27.28, 24.26.

HRMS (ESI<sup>+</sup>) calculated for  $[\text{C}_{21}\text{H}_{26}\text{N}]^+$  ( $[\text{M}+\text{H}]^+$ ). Requires  $m/z$  292.2060; found  $m/z$  292.2056.

$[\alpha]_D^{22}$ : +37.5° ( $c$ 0.64, EtOH, 78% ee).



**2-((1*R*,6*R*,7*R*)-7-phenyl-3-oxabicyclo[4.2.0]octan-6-yl)pyridine (2.15):**

Prepared according to General Procedure 2B using racemic  $\text{Ir}(\text{dtbppy})_2(\text{dMeObpy})\text{PF}_6$  (3.8 mg, 0.0035 mmol, 0.01 equiv.), (*R*)-biphenyl SPINOL phosphoric acid (19.9 mg, 0.032 mmol, 0.10 equiv.), 2-(3,6-dihydro-2*H*-pyran-4-yl)pyridine (**S2.4**, 50.1 mg, 0.31 mmol, 1 equiv.), dry toluene (20.9 mL), pentane (10.5 mL), and styrene (0.36 mL, 3.1 mmol, 10.0 equiv.). The crude material was purified by flash column chromatography on silica gel with 4:1 hexanes:EtOAc to afford the cyclobutane as a colorless oil (60.1 mg, 0.23 mmol, 75% yield). 91% ee.

SFC: Daicel CHIRALCEL<sup>®</sup> OJ-H, 5% MeOH, 3 g/min,  $t_1 = 5.60$  min,  $t_2 = 7.41$  min; Area% = 4.37 : 95.63 (91% ee).

Prepared according to General Procedure 2B using  $\Delta\text{-Ir}(\text{dtbppy})_2(\text{dMeObpy})\text{PF}_6$  (3.5 mg, 0.0032 mmol, 0.01 equiv.), (*R*)-biphenyl SPINOL phosphoric acid (20.5 mg, 0.033 mmol, 0.10 equiv.),



2-(3,6-dihydro-2*H*-pyran-4-yl)pyridine (**S2.4**, 51.2 mg, 0.32 mmol, 1 equiv.), dry toluene (20.9 mL), pentane (10.5 mL), and styrene (0.36 mL, 3.1 mmol, 10.0 equiv.). The crude material was purified by flash column chromatography on silica gel with 4:1 hexanes:EtOAc to afford the cyclobutane as a colorless oil (62.4 mg, 0.24 mmol, 74% yield). 95% ee.

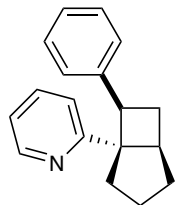
**SFC**: Daicel CHIRALCEL® OJ-H, 5% MeOH, 3 g/min,  $t_1 = 5.62$  min,  $t_2 = 7.38$  min; Area% = 2.53 : 97.47 (95% ee).

**<sup>1</sup>H NMR** (500 MHz, CDCl<sub>3</sub>)  $\delta$  8.66 (ddd,  $J = 4.8, 1.9, 0.9$  Hz, 1H), 7.68 (td,  $J = 7.7, 1.9$  Hz, 1H), 7.32 (dt,  $J = 8.0, 1.1$  Hz, 1H), 7.31 – 7.27 (m, 2H), 7.25 – 7.18 (m, 3H), 7.16 (ddd,  $J = 7.5, 4.8, 1.1$  Hz, 1H), 3.89 – 3.81 (m, 2H), 3.77 (ddd,  $J = 11.5, 4.7, 1.8$  Hz, 1H), 3.68 (dd,  $J = 12.3, 3.6$  Hz, 1H), 3.23 (ddd,  $J = 13.1, 11.4, 1.8$  Hz, 1H), 2.82 (ddd,  $J = 10.8, 8.1, 3.5$  Hz, 1H), 2.64 (q,  $J = 10.7$  Hz, 1H), 2.24 (dt,  $J = 10.2, 7.9$  Hz, 1H), 2.09 (ddd,  $J = 14.8, 13.0, 4.7$  Hz, 1H), 1.71 (d,  $J = 14.9$  Hz, 1H).

**<sup>13</sup>C NMR** (126 MHz, CDCl<sub>3</sub>)  $\delta$  165.95, 149.31, 140.76, 136.25, 127.98, 127.96, 126.10, 121.08, 120.27, 67.16, 63.63, 48.46, 46.60, 34.77, 28.63, 23.36.

**HRMS** (ESI<sup>+</sup>) calculated for [C<sub>18</sub>H<sub>20</sub>NO]<sup>+</sup> ([M+H]<sup>+</sup>). Requires  $m/z$  266.1539; found  $m/z$  266.1535.

$[\alpha]_D^{22}$ : +53.7° ( $c$ 3.98, EtOH, 95% ee).



**2-((1*S*,5*R*,7*R*)-7-phenylbicyclo[3.2.0]heptan-1-yl)pyridine (2.16):** Prepared according to General Procedure 2B using racemic Ir(dtbbpy)<sub>2</sub>(dMeObpy)PF<sub>6</sub> (3.7 mg, 0.0034 mmol, 0.01 equiv.), (*R*)-biphenyl SPINOL phosphoric acid (19.5 mg, 0.032 mmol, 0.10 equiv.), 2-(cyclopent-1-en-1-yl)pyridine (**S2.5**, 45.5 mg, 0.31 mmol, 1 equiv.), dry toluene (20.9 mL), pentane (10.5 mL), and styrene (0.36 mL, 3.1 mmol, 10.0 equiv.). The crude material was purified by flash column chromatography on silica gel with 15:1 hexanes:EtOAc to afford the cyclobutane as a colorless oil (66.2 mg, 0.27 mmol, 85% yield combined). Collected 19.8 mg of the minor diastereomer, and collected 46.4 mg of the major diastereomer. 89% ee of the major diastereomer.

**SFC:** Daicel CHIRALCEL<sup>®</sup> OD-H, 5% *i*-PrOH, 3 g/min, *t*<sub>1</sub> = 7.55 min, *t*<sub>2</sub> = 8.47 min; Area% = 5.39 : 94.61 (89% ee).

Prepared according to General Procedure 2B using Δ-Ir(dtbbpy)<sub>2</sub>(dMeObpy)PF<sub>6</sub> (3.7 mg, 0.0034 mmol, 0.01 equiv.), (*R*)-biphenyl SPINOL phosphoric acid (19.2 mg, 0.031 mmol, 0.10 equiv.), 2-(cyclopent-1-en-1-yl)pyridine (**S2.5**, 49.9 mg, 0.34 mmol, 1 equiv.), dry toluene (20.9 mL), pentane (10.5 mL), and styrene (0.36 mL, 3.1 mmol, 10.0 equiv.). The crude material was purified by flash column chromatography on silica gel with 15:1 hexanes:EtOAc to afford the cyclobutane as a colorless oil (67.1 mg, 0.27 mmol, 78% yield combined). Collected 21.4 mg of the minor diastereomer, and collected 45.7 mg of the major diastereomer. 90% ee of the major diastereomer.

**SFC:** Daicel CHIRALCEL<sup>®</sup> OD-H, 5% *i*-PrOH, 3 g/min, *t*<sub>1</sub> = 7.54 min, *t*<sub>2</sub> = 8.36 min; Area% = 5.17 : 94.83 (90% ee).

Characterization of the major diastereomer:

**<sup>1</sup>H NMR** (500 MHz, CD<sub>2</sub>Cl<sub>2</sub>) δ 8.24 (ddd, *J* = 4.8, 1.9, 1.0 Hz, 1H), 7.18 (td, *J* = 7.7, 1.9 Hz, 1H), 6.95 – 6.87 (m, 2H), 6.85 – 6.81 (m, 3H), 6.75 (ddd, *J* = 7.4, 4.8, 1.2 Hz, 1H), 6.67 (dt, *J* = 7.9, 1.1 Hz, 1H), 3.44 (t, *J* = 8.8 Hz, 1H), 3.42 – 3.36 (m, 1H), 2.48 (ddd, *J* = 12.6, 10.1, 8.0 Hz, 1H), 2.21 – 2.14 (m, 2H), 1.98 – 1.93 (m, 1H), 1.90 (ddd, *J* = 12.6, 9.6, 4.4 Hz, 1H), 1.73 – 1.65 (m, 3H).

**<sup>13</sup>C NMR** (126 MHz, CD<sub>2</sub>Cl<sub>2</sub>) δ 164.09, 147.84, 143.06, 134.76, 127.90, 127.20, 125.07, 122.12, 119.85, 60.83, 47.86, 40.57, 37.90, 32.84, 28.49, 25.65.

**HRMS** (ESI<sup>+</sup>) calculated for [C<sub>18</sub>H<sub>20</sub>N]<sup>+</sup> ([M+H]<sup>+</sup>). Requires *m/z* 250.1590; found 250.1587.

[α]<sub>D</sub><sup>22</sup>: +16.4° (*c*3.00, EtOH, 90% ee).

Characterization of the minor diastereomer:

**<sup>1</sup>H NMR** (500 MHz, CDCl<sub>3</sub>) δ 8.63 (ddd, *J* = 4.9, 1.9, 1.0 Hz, 1H), 7.63 (td, *J* = 7.7, 1.9 Hz, 1H), 7.35 – 7.26 (m, 4H), 7.23 (dt, *J* = 8.0, 1.1 Hz, 1H), 7.21 – 7.17 (m, 1H), 7.10 (ddd, *J* = 7.4, 4.9, 1.1 Hz, 1H), 4.12 (t, *J* = 10.0 Hz, 1H), 3.20 (q, *J* = 6.6 Hz, 1H), 2.48 (ddd, *J* = 12.2, 10.5, 9.0 Hz, 1H), 2.00 (ddd, *J* = 12.1, 9.5, 6.6 Hz, 1H), 1.90 – 1.60 (m, 6H).

**<sup>13</sup>C NMR** (126 MHz, CDCl<sub>3</sub>) δ 169.06, 148.93, 141.39, 136.15, 128.02, 127.78, 125.67, 120.53, 120.12, 59.97, 43.61, 41.92, 34.48, 33.11, 26.38, 25.11.

**HRMS** (ESI<sup>+</sup>) calculated for [C<sub>18</sub>H<sub>20</sub>N]<sup>+</sup> ([M+H]<sup>+</sup>). Requires *m/z* 250.1590; found *m/z* 250.1589.

[α]<sub>D</sub><sup>22</sup>: +90.8° (*c*1.26, EtOH).

## 2.10.8. Unsuccessful Substrates for the Enantioselective [2+2] Photocycloaddition

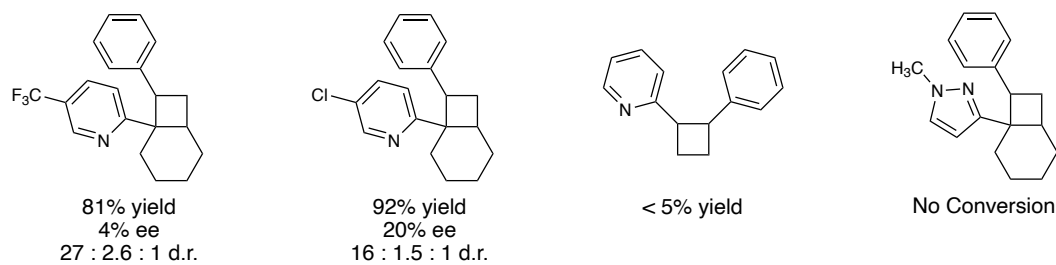


Figure 2.6 Unsuccessful Substrates for the Enantioselective [2+2] Photocycloaddition

## 2.10.9. Screening of CPAs for the Parent [2+2] Photocycloaddition

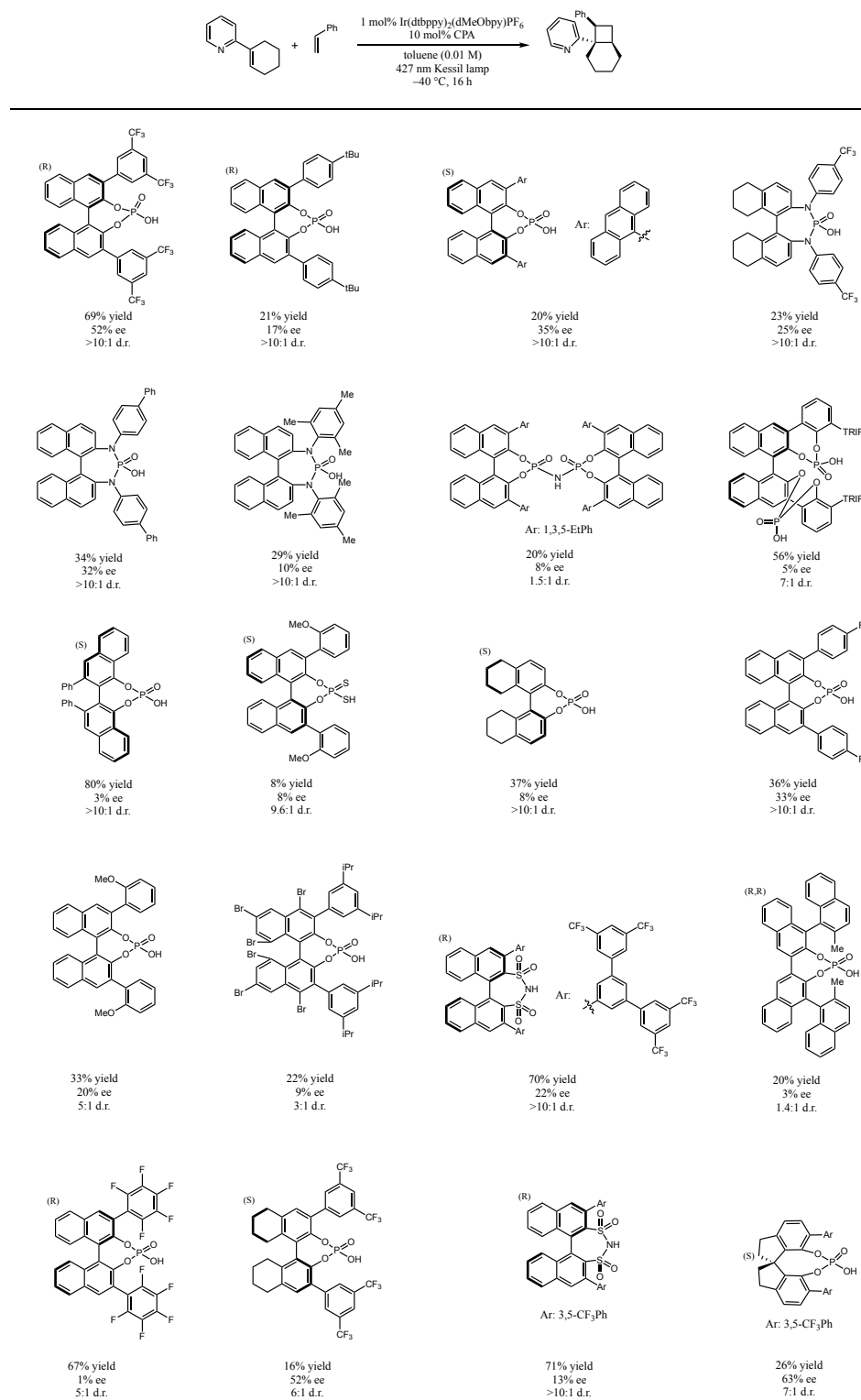
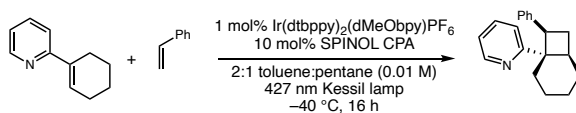


Figure 2.7 Diverse Screen of Chiral Brønsted Acids During Reaction Optimization

The chiral Brønsted acids in Figure 2.7 were synthesized by Christine Le and F. Dean Toste at the University of California – Berkeley. The photochemical reactions with these chiral Brønsted acids were performed by Steven J. Chapman and Tehshik P. Yoon at the University of Wisconsin – Madison.

The SPINOL based CPAs in Figure 2.8 were synthesized and subjected to the photochemical reactions by Steven J. Chapman and Tehshik P. Yoon at the University of Wisconsin – Madison.

## Optimized Reaction Conditions



Screening conditions: Reaction concentrations were 0.005 M and on a 0.044 mmol SM scale unless otherwise noted

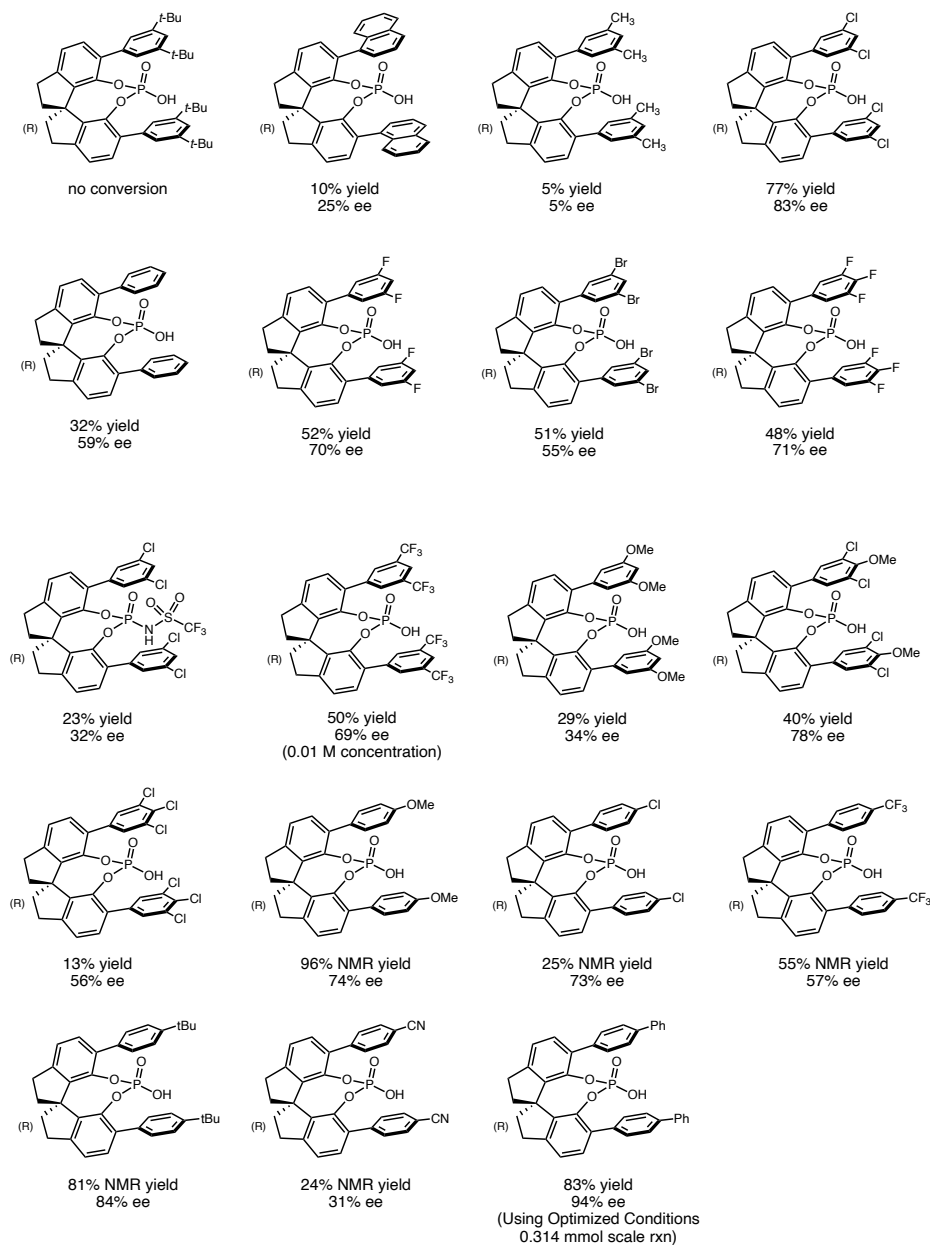
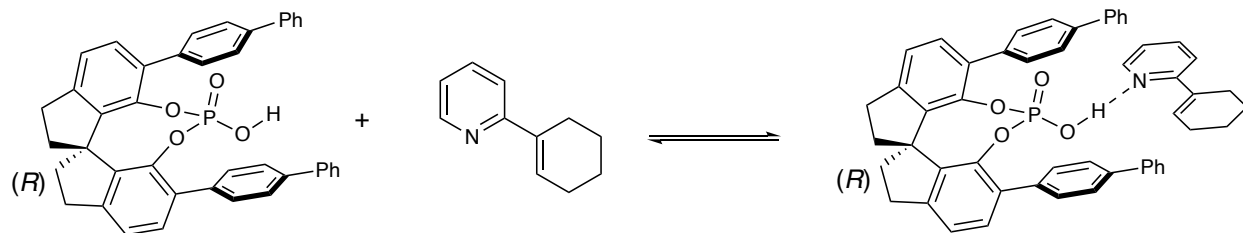


Figure 2.8 Screen of SPINOL CPAs During Reaction Optimization

## 2.10.10. NMR Binding Experiments

Association constants for the binding of the vinyl pyridine substrate with the chiral phosphoric acid were determined through NMR titration studies.



Scheme 2.5 Binding Equilibrium Between (*R*)-CPA3 and **2.1**

A solution of the vinyl pyridine starting material (8.0 mg, 0.050 mmol) was created in toluene-*d*<sub>8</sub> (4.5 mL). A separate solution containing 4-biphenyl SPINOL phosphoric acid (38.7 mg, 0.063 mmol) was created using the above vinyl pyridine solution as the solvent (1.25 mL). This ensured the concentration of the vinyl pyridine remained constant during the experiment. The vinyl pyridine solution (0.5 mL) was transferred to an NMR tube. Increasing amounts of the CPA solution were titrated into the NMR sample, acquiring <sup>1</sup>H NMR spectra between each titration. Started by adding 10 μL of the CPA solution and increased the addition volume toward the end of the experiment.



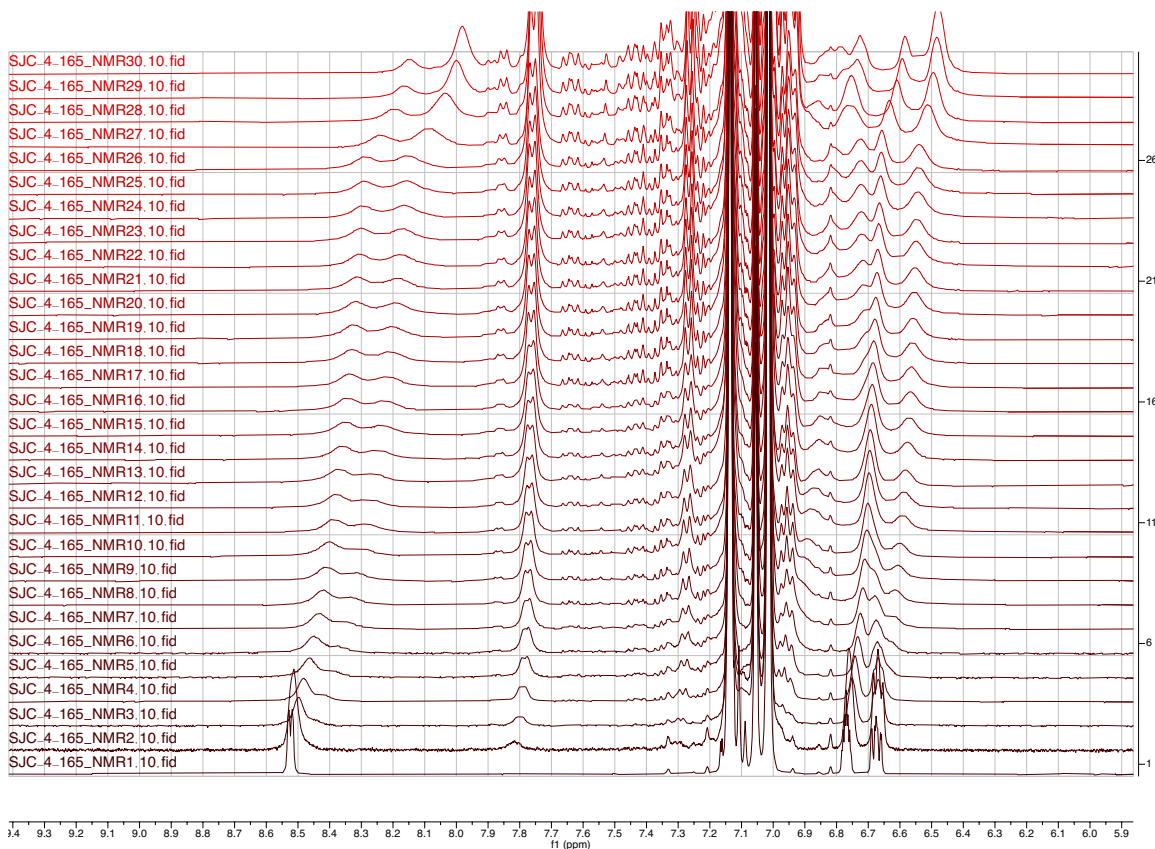


Figure 2.9 NMR Titration with Increasing Quantity of (*R*)-CPA3 from Bottom to Top.

### Significant ppm Shifts Measured from the Vinyl Pyridine **2.1**

These data were fit to a 1:1 binding model using the method developed by Thordarson<sup>63</sup> and his online analysis tool ‘BindFit’.<sup>64</sup> Using the pyridine signal originating at 8.52 ppm, this technique provided the binding isotherm shown in Figure 2.10 and calculated the  $K_a$  to be  $27 \pm 1.6$ .

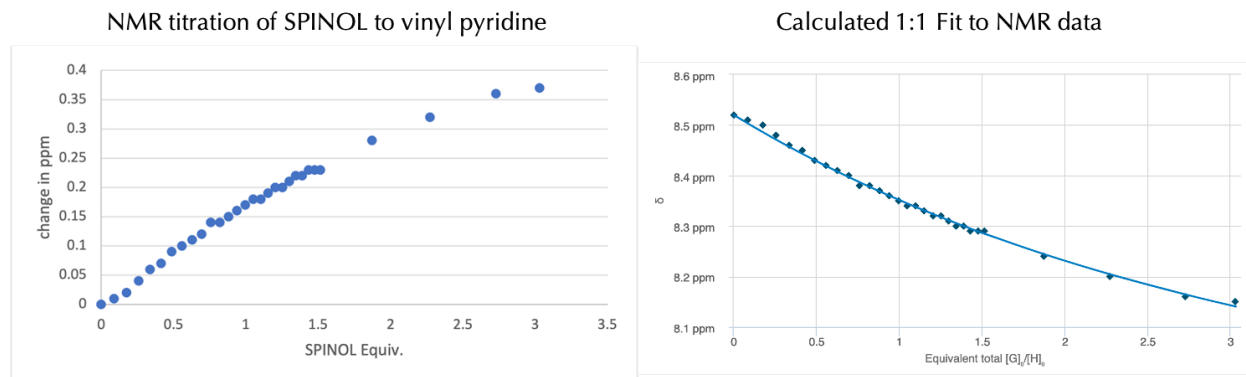
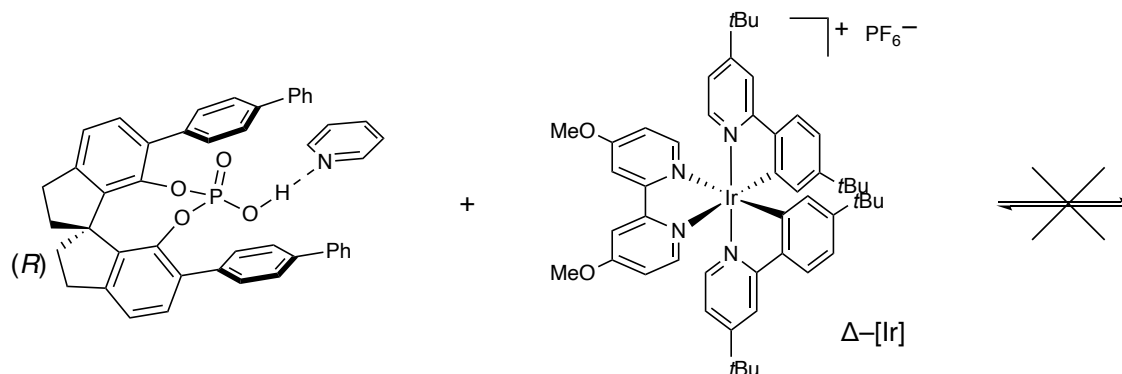


Figure 2.10 1:1 Binding Measured Between (*R*)-CPA3 and **2.1**



Scheme 2.6 No Ground State Interaction or Equilibrium Found Between (*R*)-CPA3–pyridine and  $\Delta$ -[Ir]

A solution of  $\Delta$ -[Ir] (0.6 mg, 0.0006 mmol) was created using toluene- $d_8$  (4.4 mL). A separate solution containing 4-biphenyl SPINOL phosphoric acid (2.4 mg, 0.0039 mmol) and pyridine (3.2  $\mu\text{L}$ , 0.039 mmol) was created using the above  $\Delta$ -[Ir] solution as the solvent (2.0 mL). This ensured the concentration of the  $\Delta$ -[Ir] remained constant during the experiment. Four separate NMR tubes were prepared:

1) 0.5 mL of the  $\Delta$ -[Ir] solution only.

2) 0.5 mL of the  $\Delta$ -[Ir] solution + 0.10 mL of the SPINOL/pyridine solution.

3) 0.5 mL of the  $\Delta$ -[Ir] solution + 0.25 mL of the SPINOL/pyridine solution.

4) 0.5 mL of the  $\Delta$ -[Ir] solution + 0.50 mL of the SPINOL/pyridine solution.

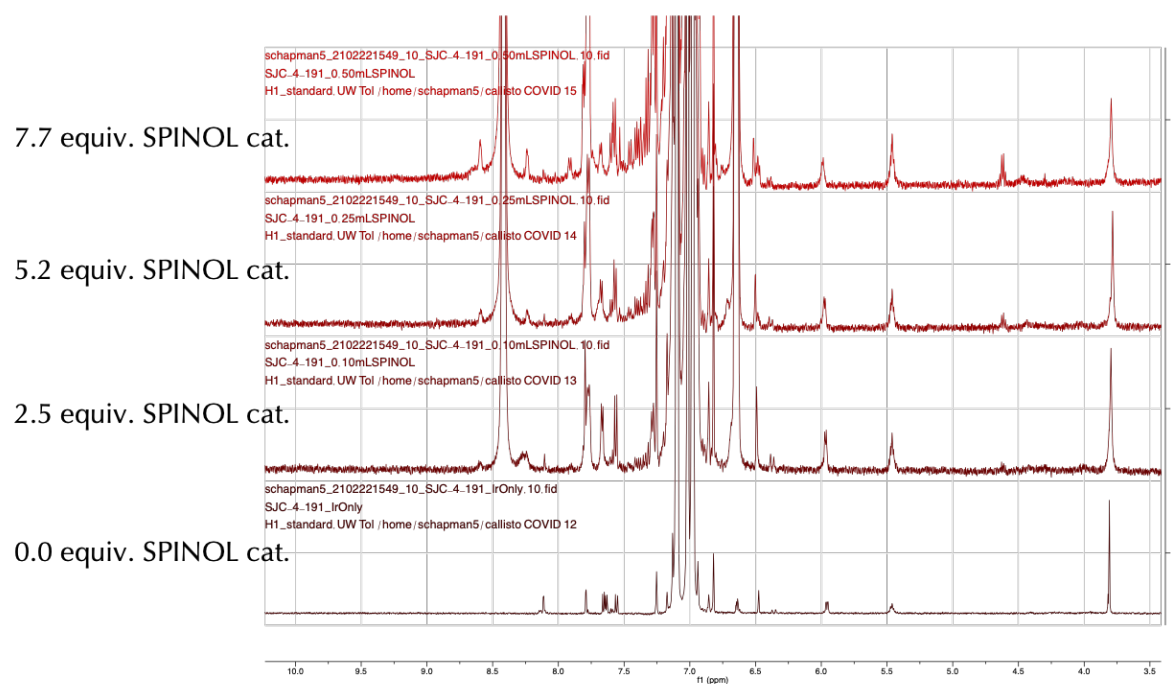


Figure 2.11  $^1\text{H}$  NMR Titration with Increasing (R)-CPA3-Pyridine Quantities Indicating No ppm Shift and No Ground State Interaction

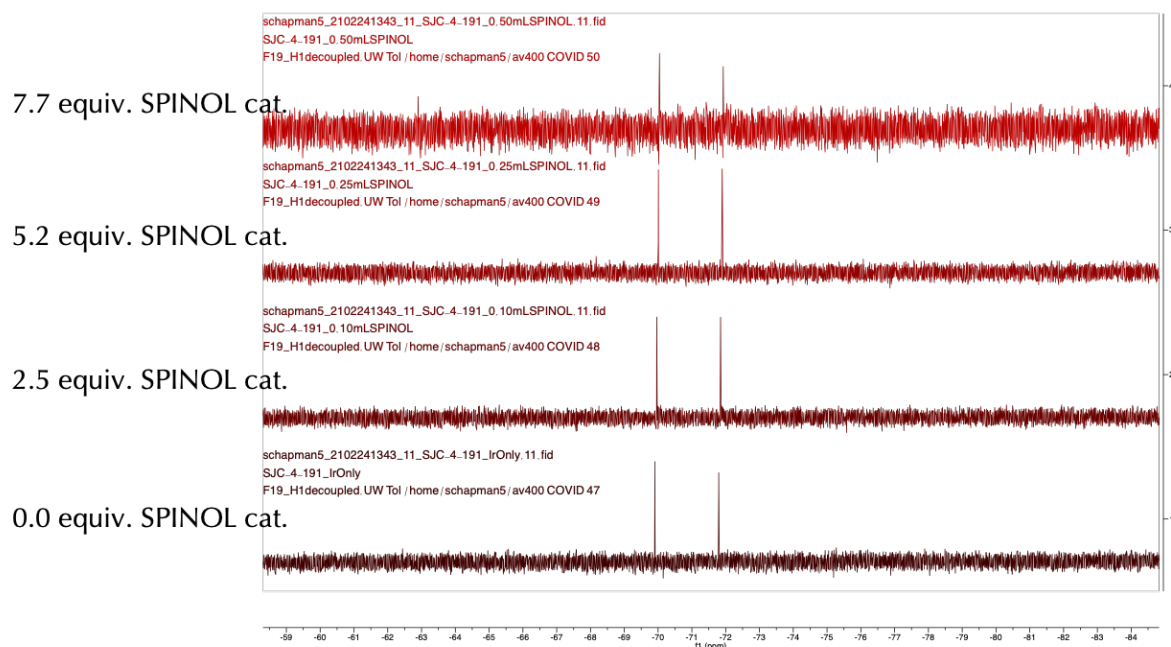


Figure 2.12  $^{19}\text{F}$  NMR Titration with Increasing (R)–CPA3–Pyridine Quantities Indicating No ppm Shift and No Ground State Interaction

No shifts in the  $\Delta$ –[Ir]  $^1\text{H}$  NMR signals were detected, indicating there is no ground state interaction between the  $\Delta$ –[Ir] photocatalyst and the preformed CPA/pyridine complex (Figure 2.11). No shifts in the  $\Delta$ –[Ir]  $^{19}\text{F}$  NMR were detected, indicating the  $\text{PF}_6$  counteranion is not associating with a different complex in solution (Figure 2.12).

## 2.10.11. UV-Vis/Emission Experiments

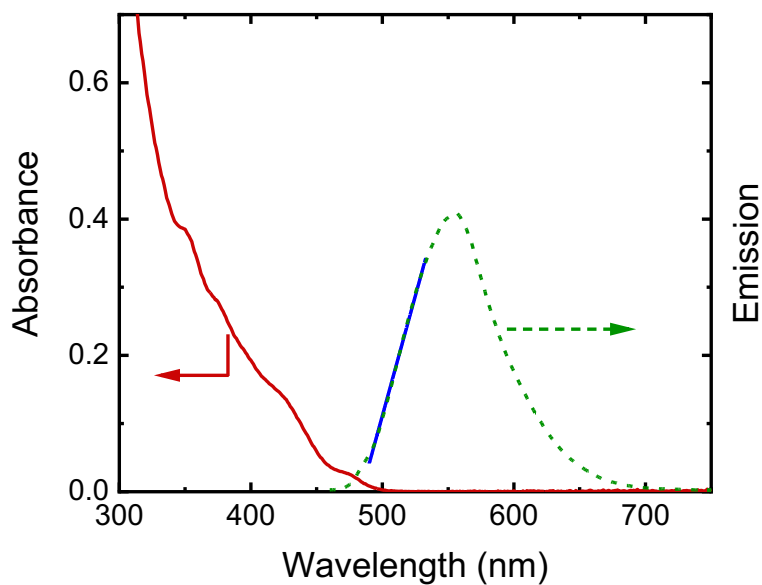


Figure 2.13 UV-visible spectra (red line) and emission spectra (dashed green line) of the Ir photocatalyst. The triplet energy ( $E_T$ ) of the photocatalyst was determined from the X-intercept of a linear regression fit to the blue edge of the emission spectra (solid blue line, X-intercept = 485 nm).  $E_T = 2.55$  eV,  $58.8$  kcal mol<sup>-1</sup>.

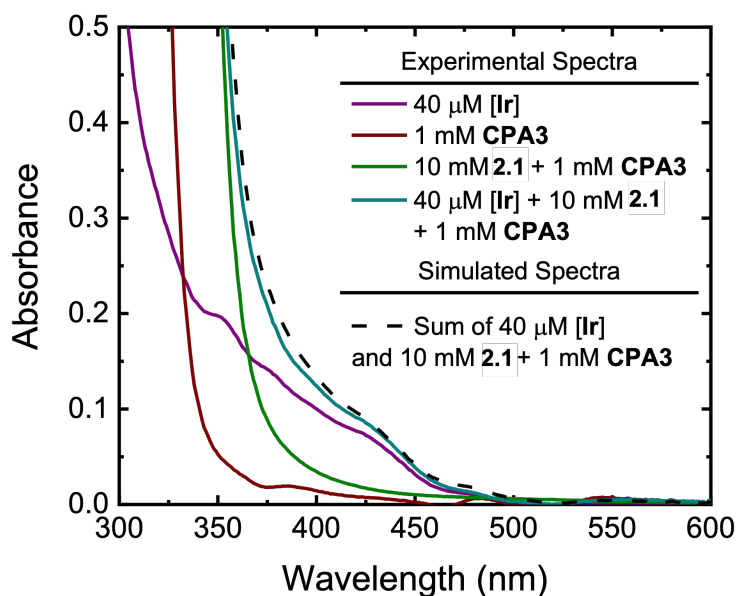


Figure 2.14 UV-visible spectra of the components of the parent reaction.  $[\text{Ir}] = 40 \text{ uM}$ , while the other species are close to reaction concentrations. Notably, there is only a subtle difference between the spectra acquired with all three species present and the sum of individual  $[\text{Ir}]$  and **CPA3+2.1** spectra (dashed line). The slight difference can be ascribed to error in the concentrations of the individual components between the acquisition of the spectra.

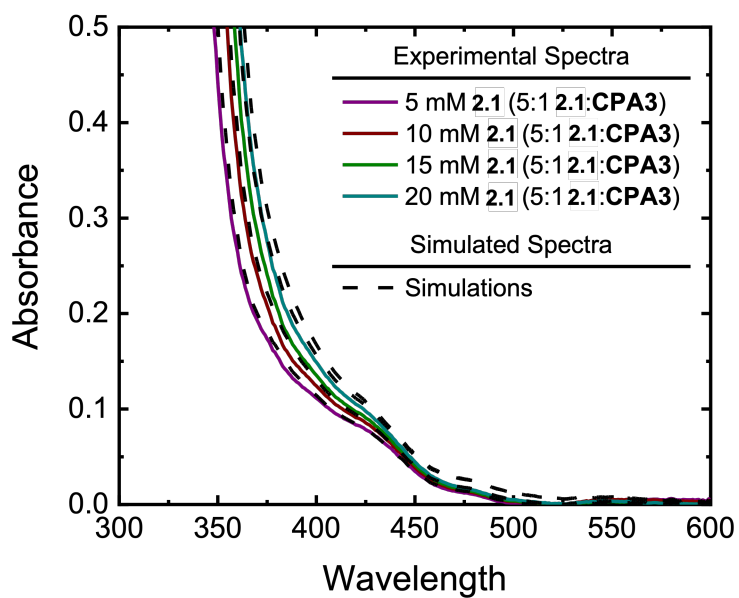


Figure 2.15 Experimental and simulated spectra at different concentrations of 5:1 **2.1:CPA3** mixture. At every concentration, the spectra have little distinction barring that which can be ascribed to subtle concentration variations.

## 2.10.12. Stern–Volmer Experiments

*TFA+vinyl pyridine 2.1 H<sup>+</sup>*: Dissolved 2.0 mg  $\Delta$ -[Ir] in 50.0 mL dry toluene. To a separate vial containing 22.1 mg vinyl pyridine **2.1** was added 7.0 mL of the above  $\Delta$ -[Ir] solution; then 81.2 mg trifluoroacetic acid (TFA) was added to afford a 0.02 M solution of **2.1**. This is a 5:1 TFA:**2.1** solution.

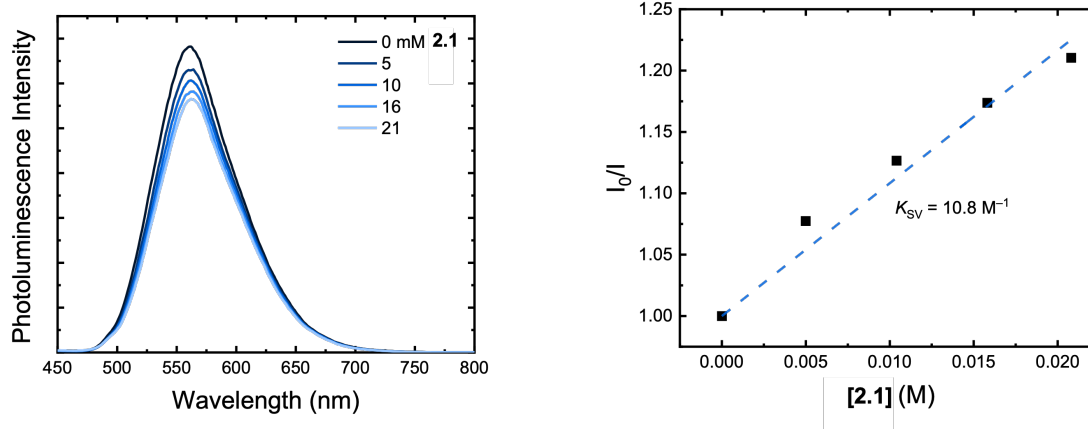


Figure 2.16 Photoluminescence quenching of  $\Delta$ -[Ir] by vinyl pyridine in the presence of excess trifluoroacetic acid. A) Photoluminescence spectra at the indicated concentration of **2.1** and B) Stern–Volmer plot.



## 2.10.13. Time-Resolved Emission

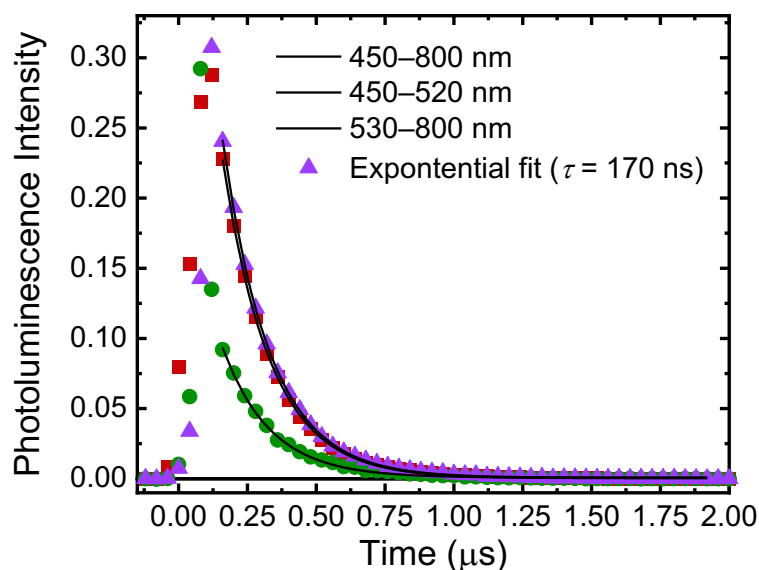
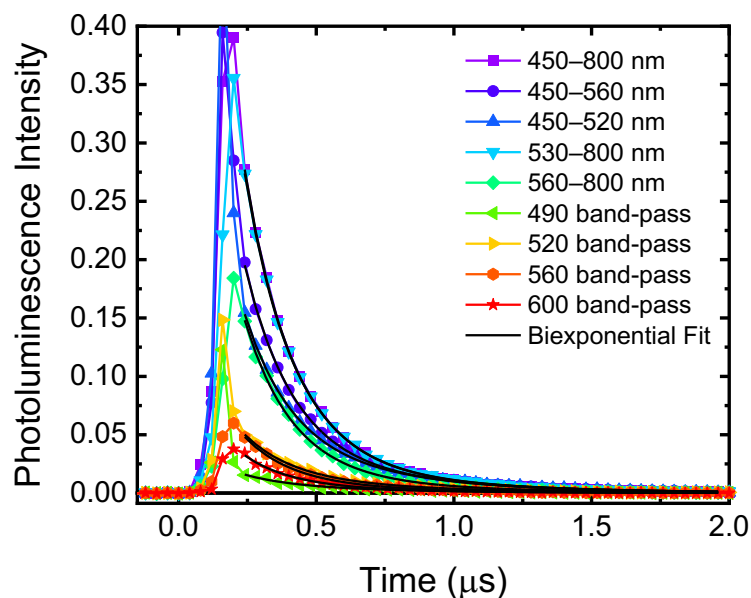


Figure 2.17 Time-resolved emission of Ir photocatalyst in toluene (symbols). Long and short pass filters used to define the range of emission collected. Three ranges were acquired to ensure accuracy of the measured lifetime. Lifetimes were acquired under an argon atmosphere. Excitation at 420 nm. Lifetime of Ir photocatalyst  $\tau = 170$  ns.

## Matched and Mismatched Time-Resolved Experiments

In these experiments, we collected time-resolved emission on the home-built set-up described in the general methods section. Data was collected using different filter combinations or band-pass filters to study the PL at distinct wavelength ranges as noted in the figure legends. Band pass filters significantly lowered the emission intensity and therefore, the higher intensities acquired with the filter combinations were used to corroborate the band pass results. Both the unnormalized and normalized data are shown. Biexponential fitting was required (Figure 2.18 and Figure 2.19). The two lifetimes ( $\tau$ ) could be shared across all wavelength ranges and were allowed

to float while the preexponential values ( $A$ ) were not shared and allowed to float. The fast lifetime ( $\tau_1$ ) in most cases was within 15 ns of the unbound Ir photocatalyst lifetime (and could be fixed to that lifetime without significantly impacting the fit). This lifetime accounted for  $\sim 70$ – $90\%$  of the emission signal across the wavelength ranges studied. Notably, the magnitude of  $A_1$  was lower at higher energy wavelength ranges (450–520 nm or with 490 and 520 nm band pass filters), indicating more signal for  $A_2$  and the longer time-component, which we have proposed as the diastereomeric excited-state complex. The longer lifetime ( $\tau_2$ ) was distinct between the matched and mismatched cases being elongated by  $\sim 50$  ns (matched = 485 ns vs. mismatched = 530 ns). Notably, using these lifetimes to estimate Stern–Volmer quenching constants for the matched and mismatched titrations with styrene enhances the difference between the quenching rates for matched:  $K_{SV,matched} = 5.4 \text{ M}^{-1}$ ;  $k_{q,matched} = 11.1 \times 10^7 \text{ M}^{-1}\text{s}^{-1}$ , and mismatched:  $K_{SV,mismatched} = 3.6 \text{ M}^{-1}$ ;  $k_{q,mismatched} = 6.8 \times 10^6 \text{ M}^{-1}\text{s}^{-1}$ . This is a 1.6 fold larger quenching for the matched reaction.



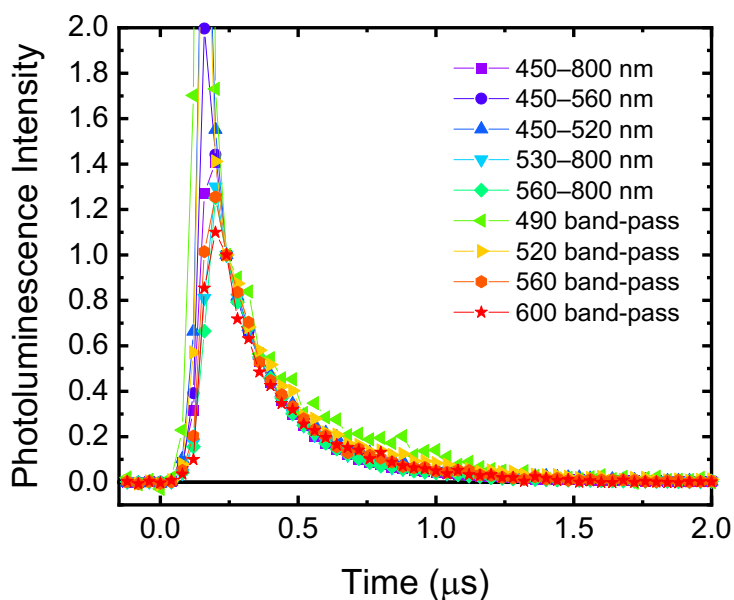


Figure 2.18 Time-resolved photoluminescence decays for the *matched* conditions:  $\Delta\text{-Ir} = 40 \mu\text{M}$ , CPA3 = 1 mM, vinyl pyridine = 10 mM. A) Absolute intensities, B) Normalized intensities, normalized at 200 ns. Wavelength ranges of filter combinations are indicated in the legend. Black lines correspond to the biexponential fitting. Table 2.1 provides the pre-exponential values and lifetimes of the fits.

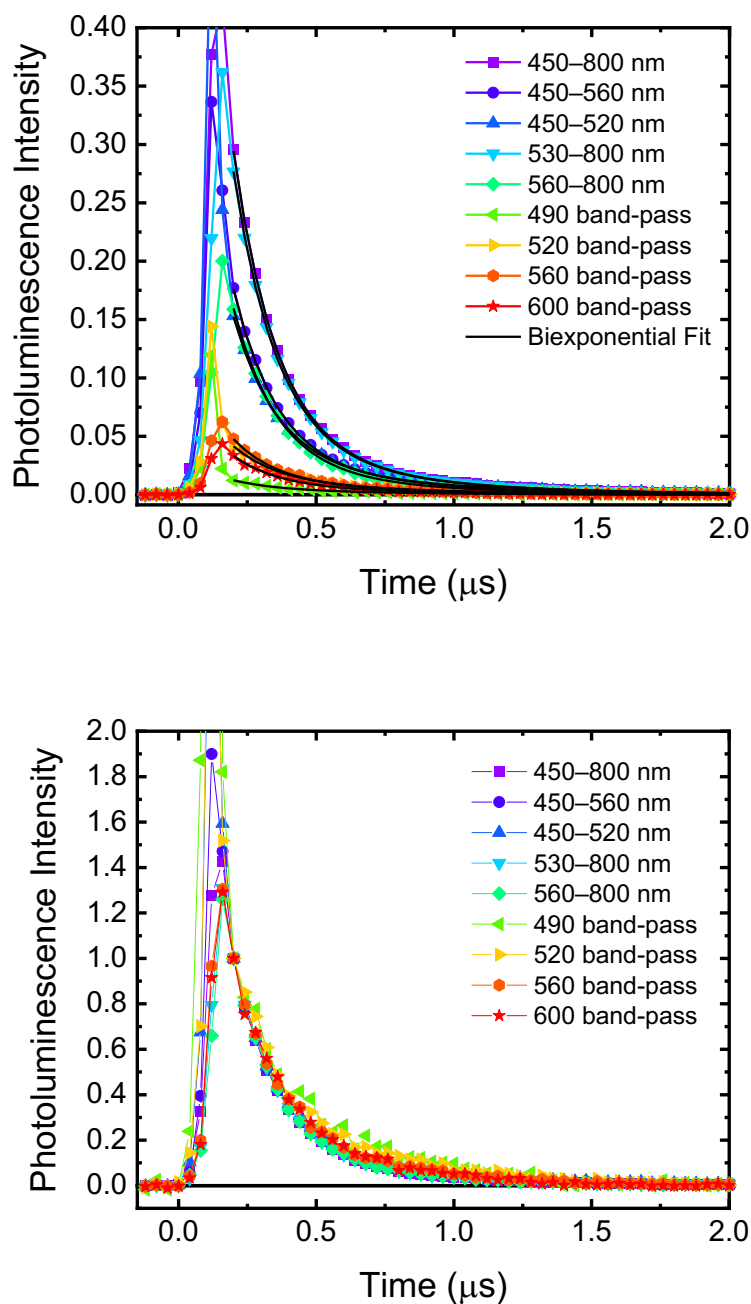
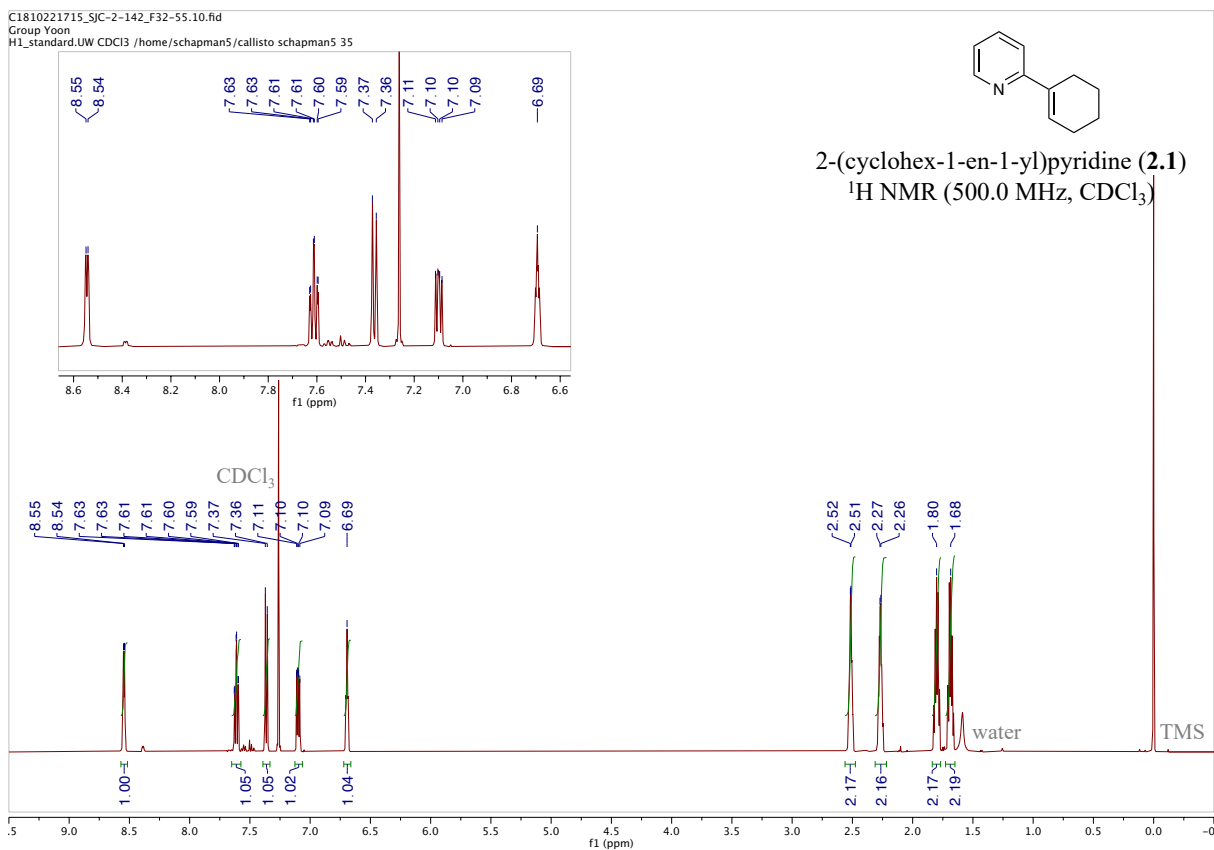


Figure 2.19 Time-resolved photoluminescence decays for the *mismatched* conditions:  $\Lambda$ -Ir = 40  $\mu$ M, CPA3 = 1 mM, vinyl pyridine = 10 mM. Wavelength ranges of filter combinations are indicated in the legend. Black lines correspond to the biexponential fitting. Table 2.1 provides the pre-exponential values and lifetimes of the fits.

Table 2.1 Pre-exponential Values and Lifetimes of the Fits for Both Matched and Mismatched Cases

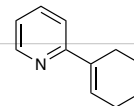
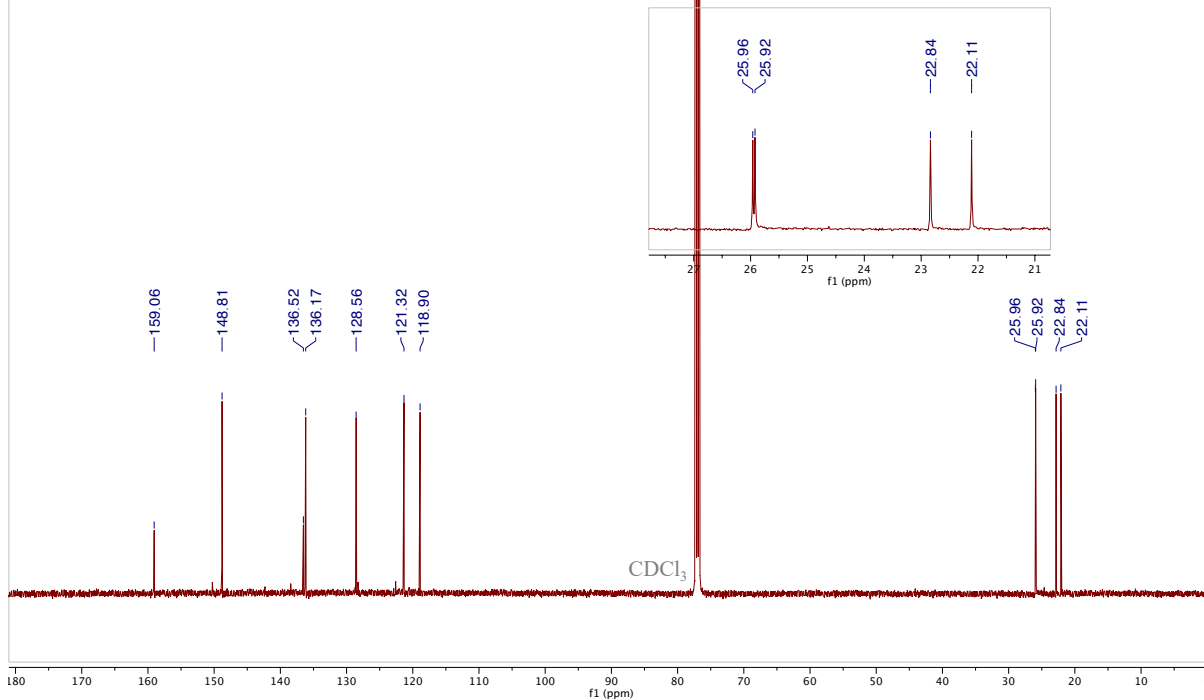
<b>Preexponential Factors</b>	<i>Matched</i>		<i>mismatched</i>	
	A1	A2	A1	A2
Wavelength (nm) range				
450–800	0.97	0.06	0.90	0.06
450–560	0.63	0.06	0.52	0.04
450–520	0.45	0.07	0.43	0.05
530–800	0.95	0.07	0.83	0.06
560–800	0.51	0.04	0.48	0.03
490 band-pass	0.03	0.01	0.03	0.01
520 band-pass	0.14	0.03	0.10	0.02
560 band-pass	0.16	0.02	0.13	0.02
600 band-pass	0.10	0.01	0.09	0.01
<b>Lifetimes</b>				
<i>matched</i>	$\tau_1$ (ns)	170	160	
<i>mismatched</i>	$\tau_2$ (ns)	485	530	

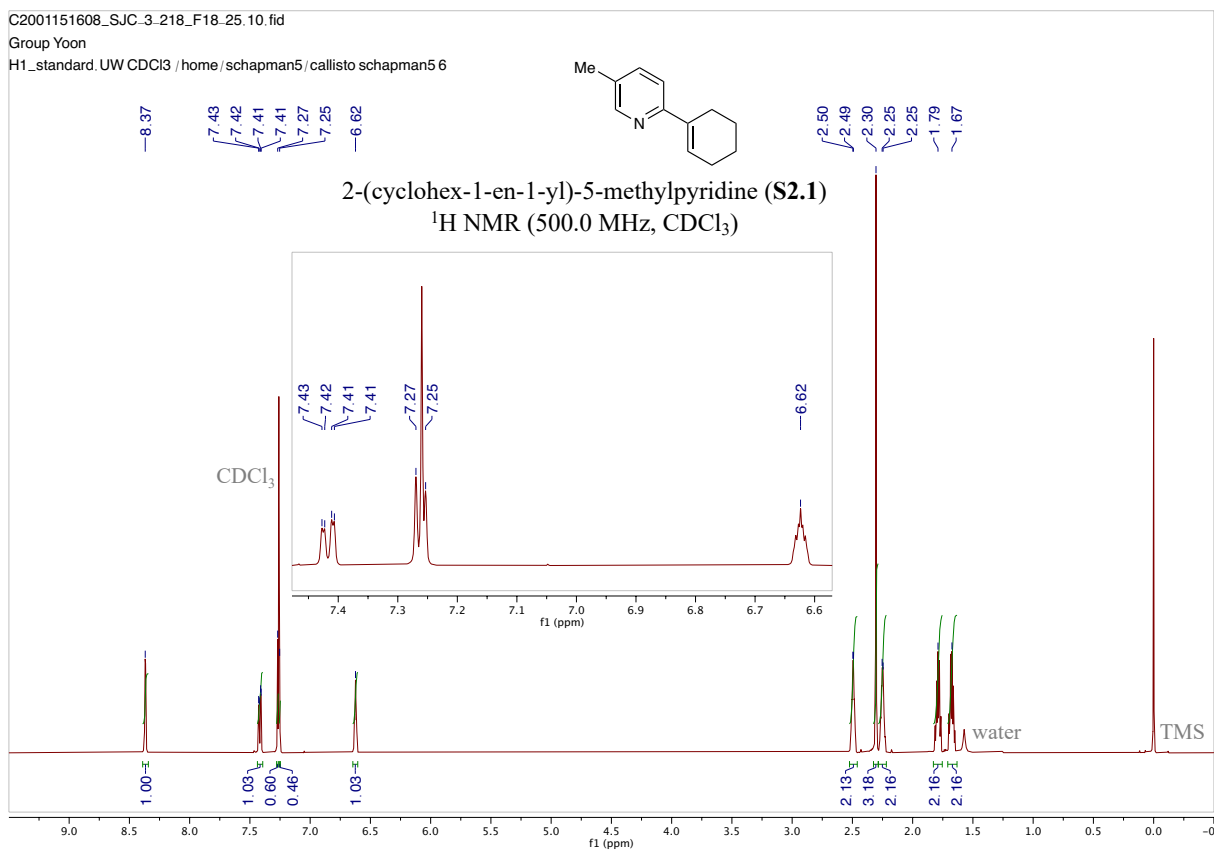
2.10.14.  $^1\text{H}$ ,  $^{13}\text{C}$ ,  $^{19}\text{F}$ , and  $^{31}\text{P}$  NMR Spectra

C1810221715\_SJC-2-142\_F32-55.11.fid

Group Yoon

C13\_H1dec.UW CDCl3 /home/schapman5/callisto schapman5 35

2-(cyclohex-1-en-1-yl)pyridine (**2.1**)  
 $^{13}\text{C}$  NMR (125.7 MHz,  $\text{CDCl}_3$ )

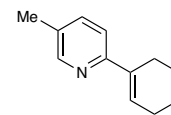




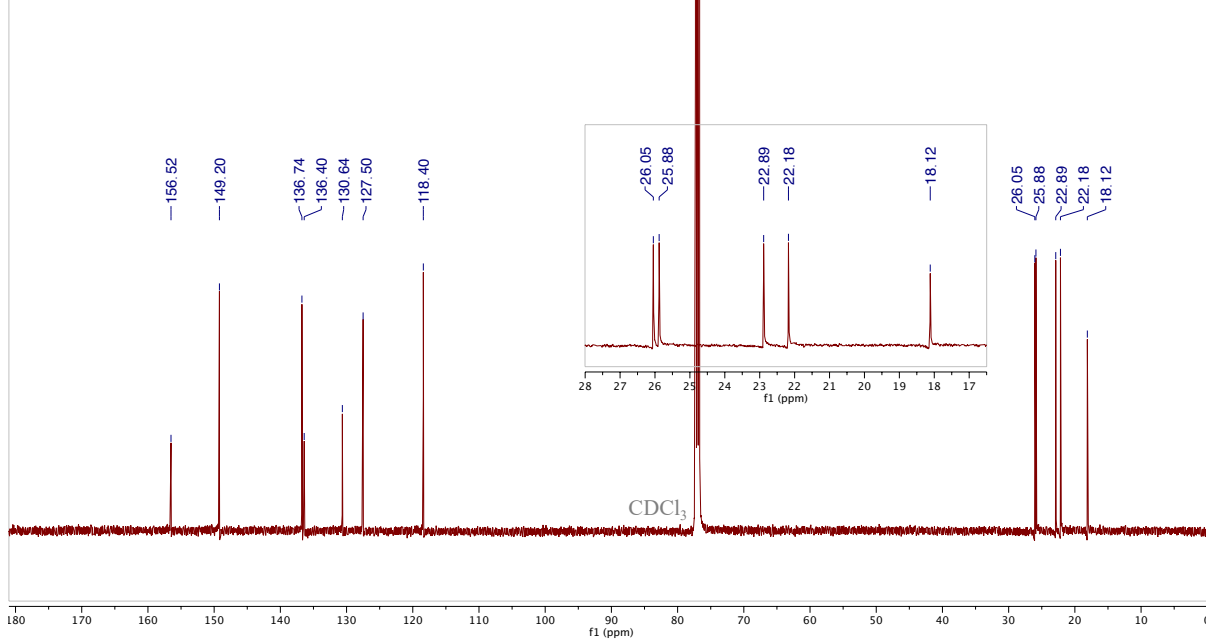
C2001151608\_SJC-3\_218\_F18.25.11.fid

Group Yoon

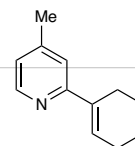
C13\_H1dec.UW CDCl3 /home/schapman5/callisto schapman5 6



2-(cyclohex-1-en-1-yl)-5-methylpyridine (S2.1)  
 $^{13}\text{C}$  NMR (125.7 MHz,  $\text{CDCl}_3$ )

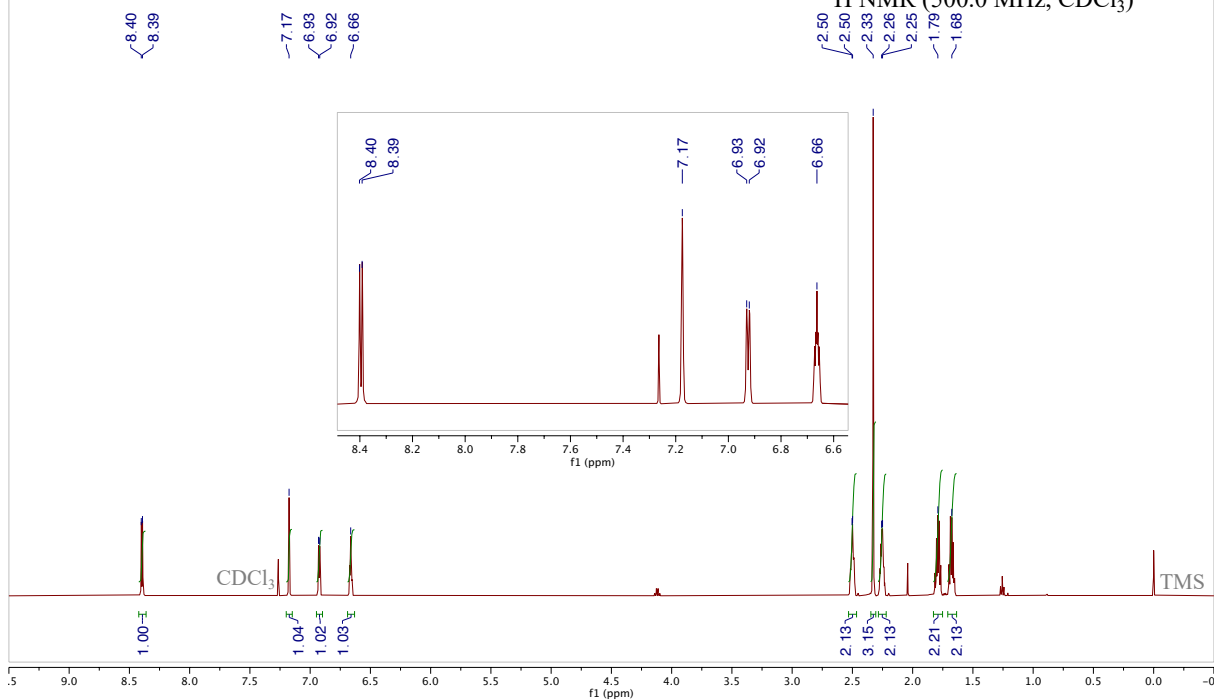


schapman5\_2102151753\_10\_SJC.4-172\_F21-39.10.fid  
SJC.4-172\_F21-39  
H1\_standard.UW CDCl3 /home/schapman5/callisto COVID 47

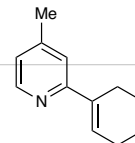


2-(cyclohex-1-en-1-yl)-4-methylpyridine (S2.2)

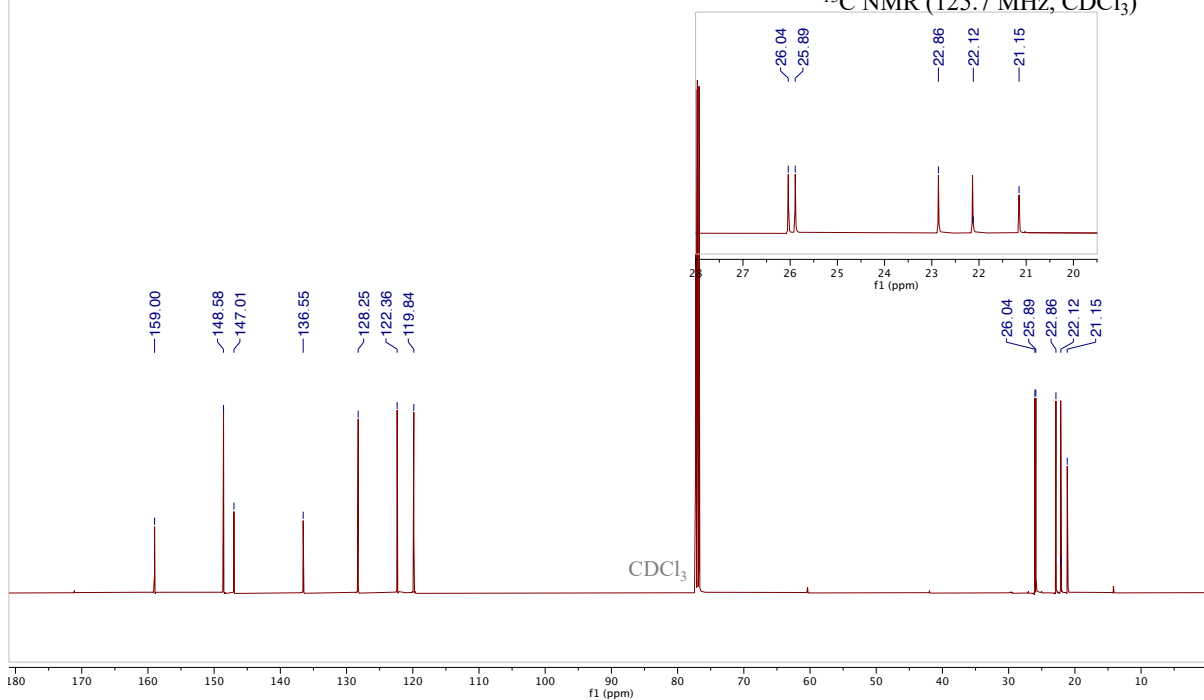
<sup>1</sup>H NMR (500.0 MHz, CDCl<sub>3</sub>)



schapman5\_2102151753\_11\_SJC\_4-172\_F21-39.11.fid  
SJC\_4-172\_F21-39  
C13\_standard.UW CDCl3 /home/schapman5/callisto COVID 47

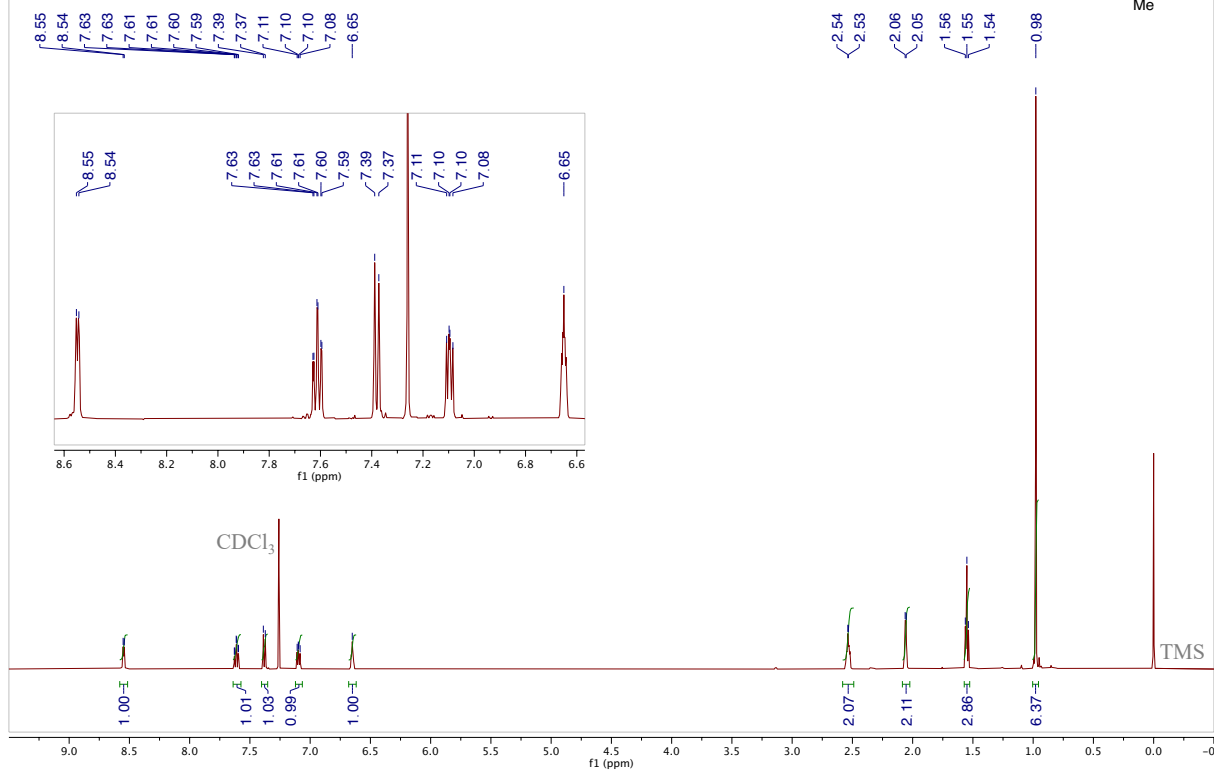
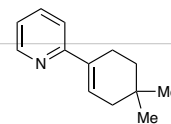


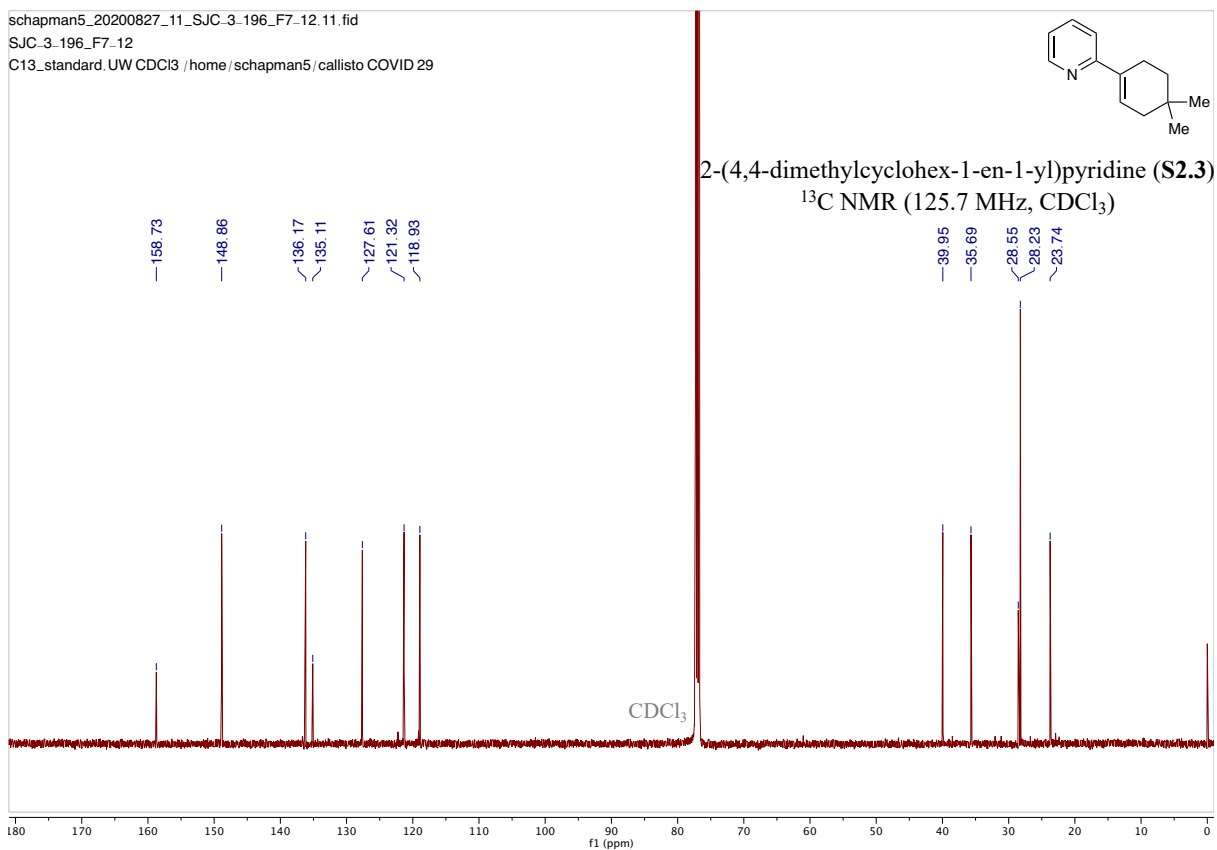
2-(cyclohex-1-en-1-yl)-4-methylpyridine (S2.2)  
 $^{13}\text{C}$  NMR (125.7 MHz,  $\text{CDCl}_3$ )

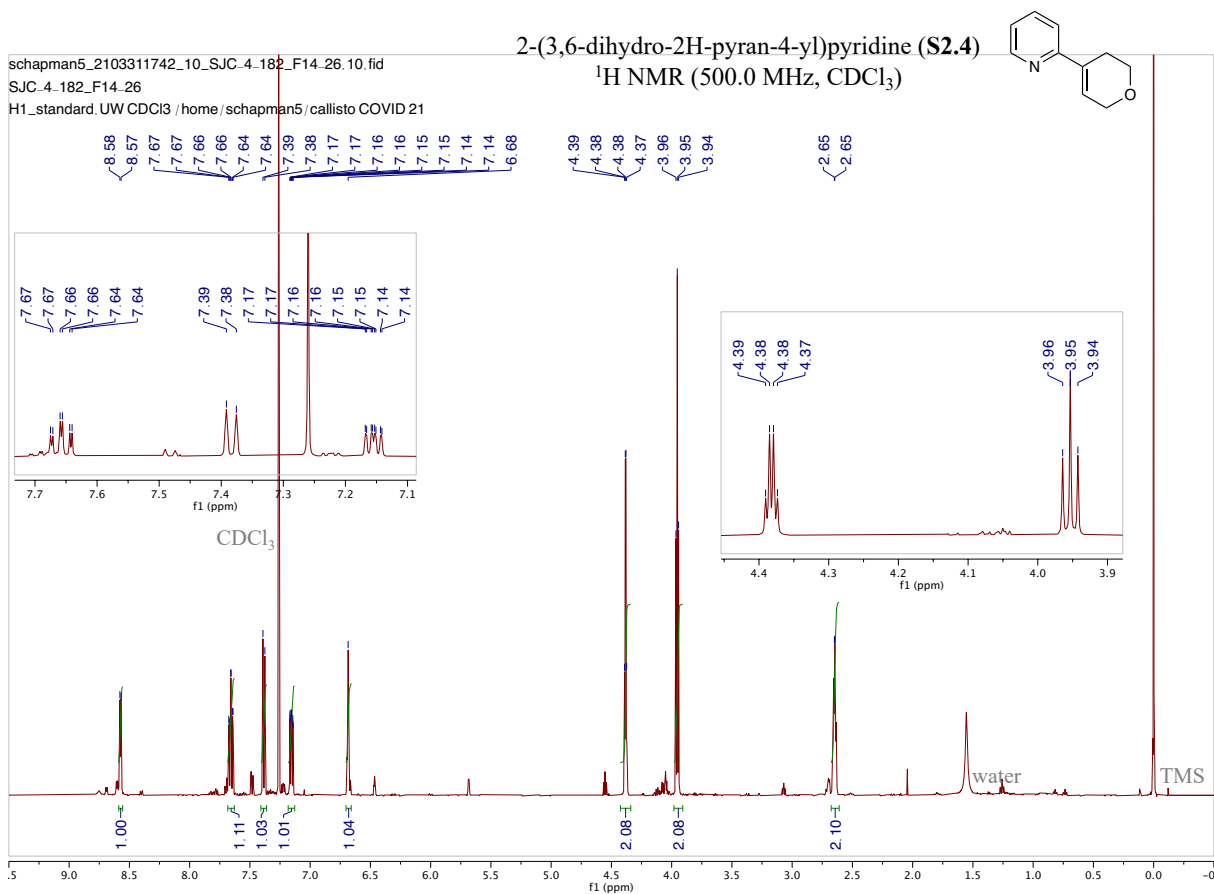


schapman5\_20200827\_10\_SJC.3-196\_F7-12.10.fid  
SJC.3-196\_F7-12  
H1\_standard.UW CDCl3 / home / schapman5 / callisto COVID 29

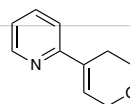
2-(4,4-dimethylcyclohex-1-en-1-yl)pyridine (**S2.3**)  
<sup>1</sup>H NMR (500.0 MHz, CDCl<sub>3</sub>)



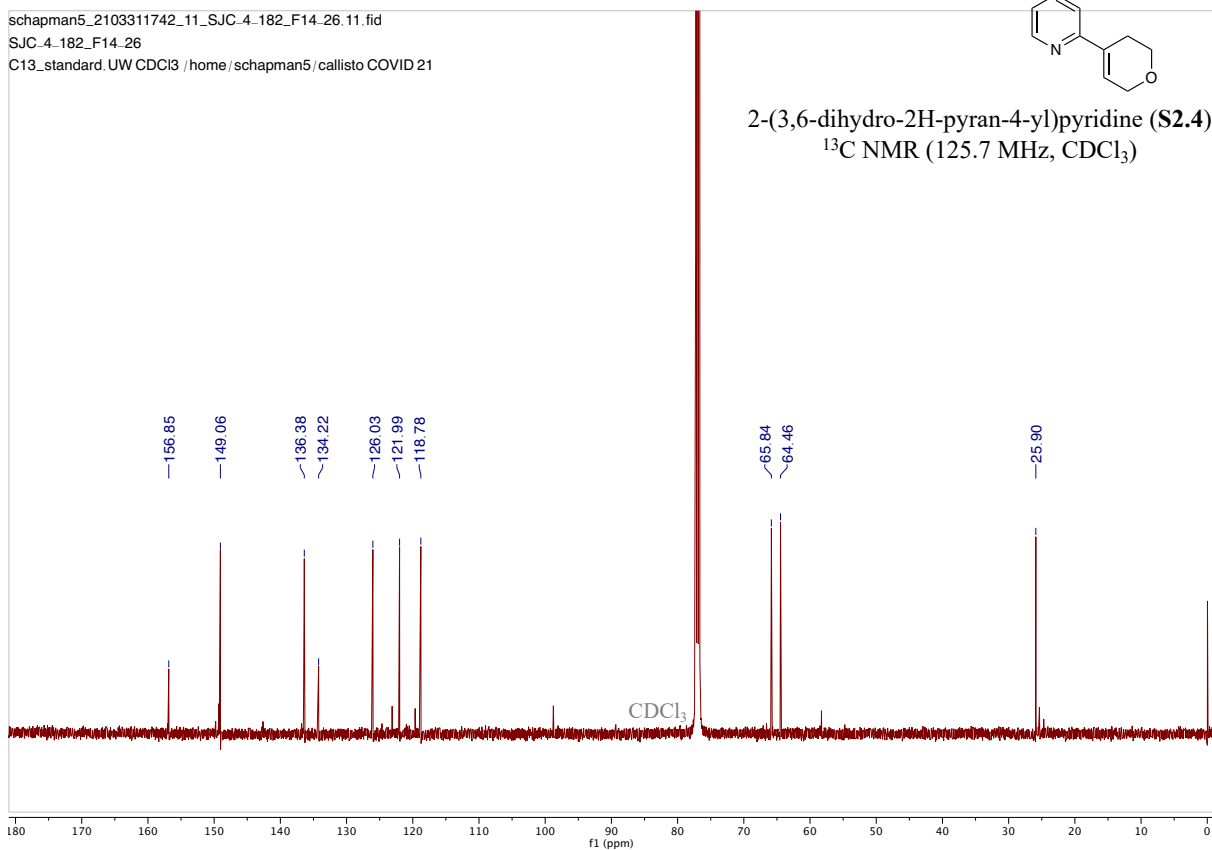




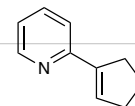
schapman5\_2103311742\_11\_SJC.4-182\_F14.26.11.fid  
SJC.4-182\_F14.26  
C13\_standard.UW CDCl3 /home/schapman5/callisto COVID 21



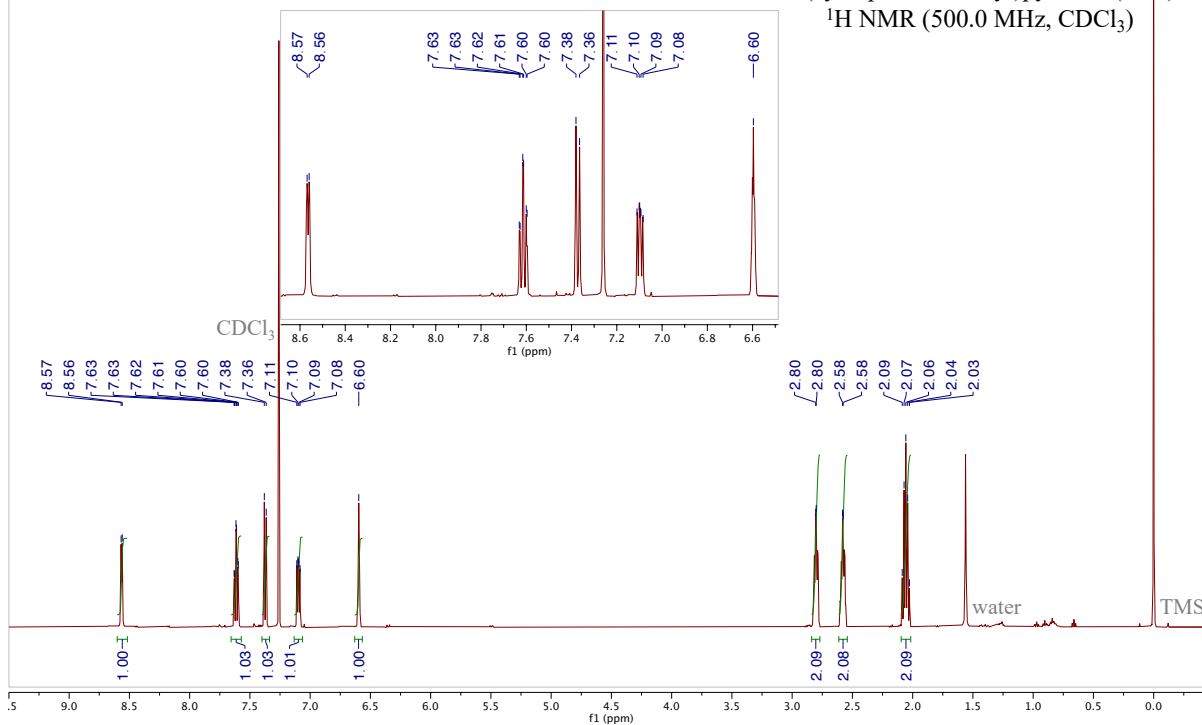
2-(3,6-dihydro-2H-pyran-4-yl)pyridine (**S2.4**)  
 $^{13}\text{C}$  NMR (125.7 MHz,  $\text{CDCl}_3$ )



schapman5\_20200827\_10\_SJC.2-300\_F10.18.10.fid  
SJC.2-300\_F10.18  
H1\_standard.UW CDCl3 /home/schapman5/callisto COVID 30

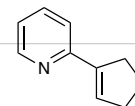


2-(cyclopent-1-en-1-yl)pyridine (S2.5)  
<sup>1</sup>H NMR (500.0 MHz, CDCl<sub>3</sub>)

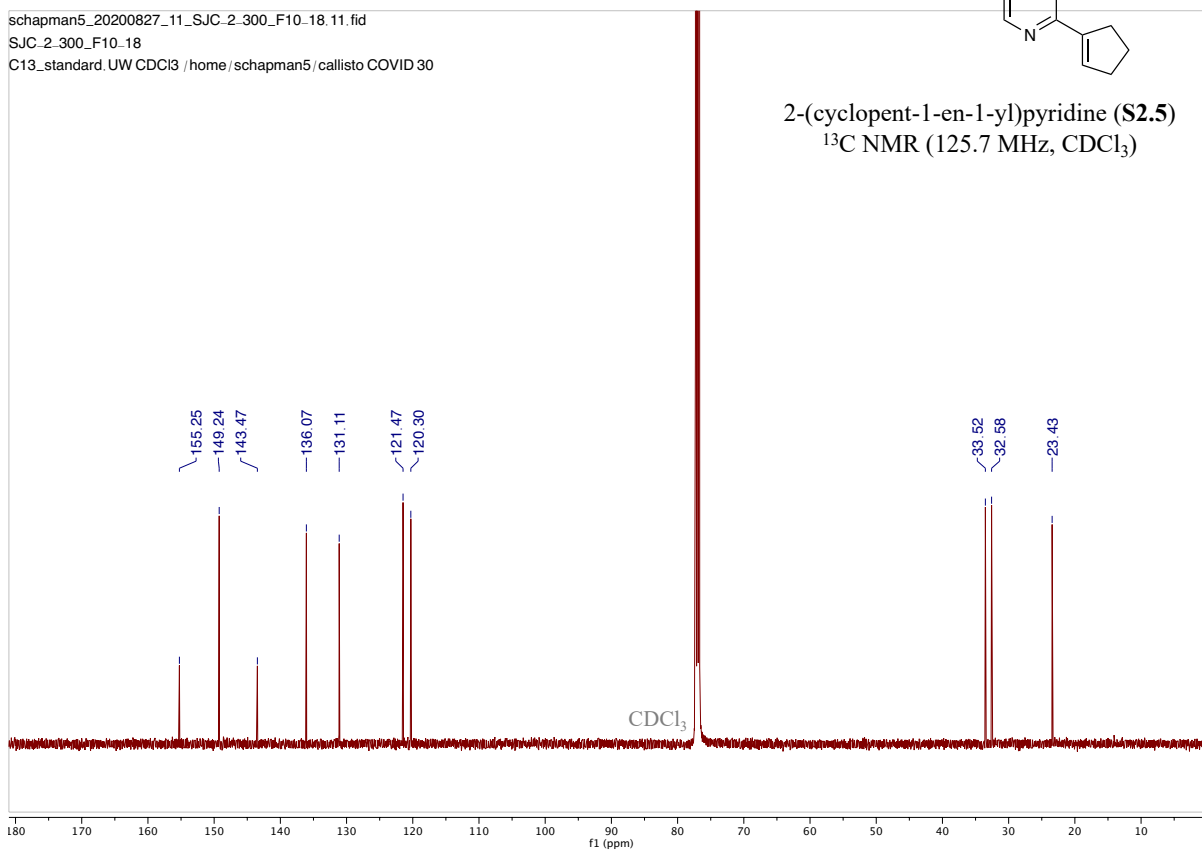


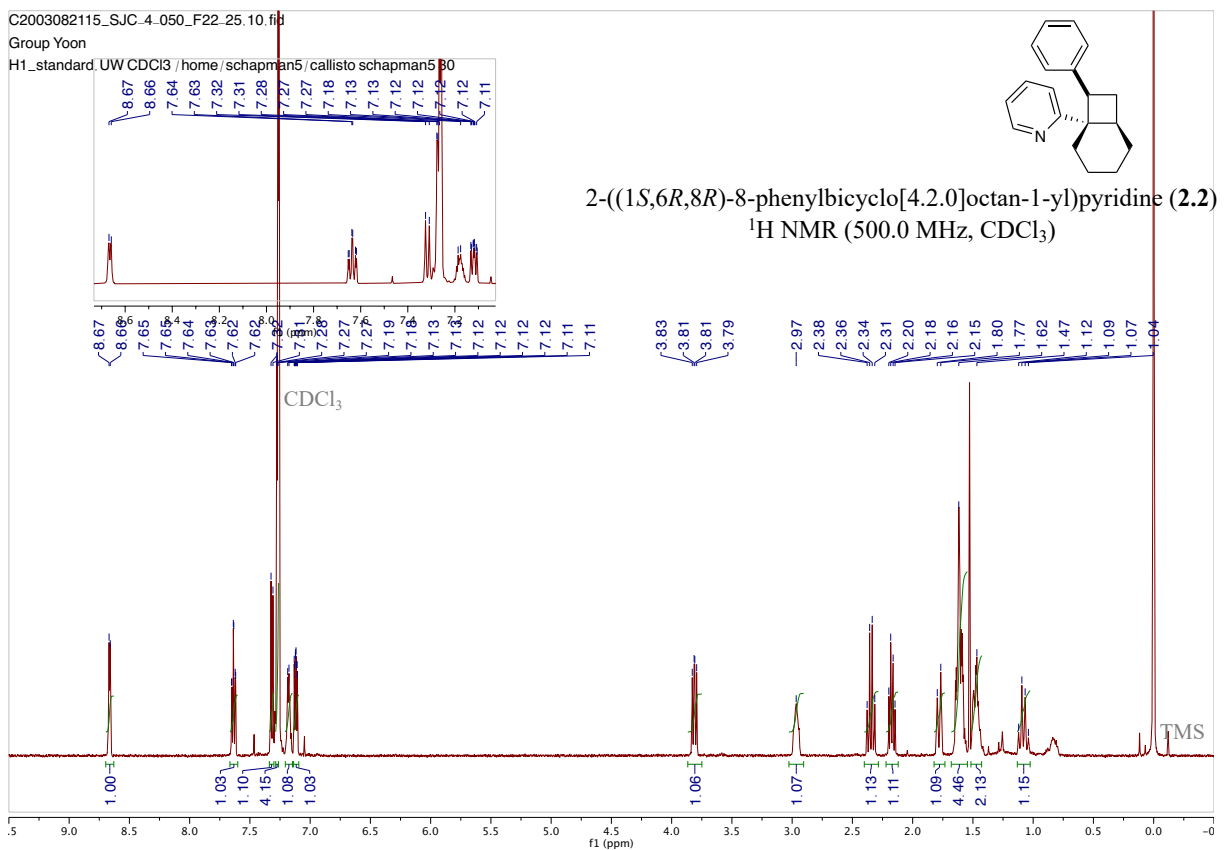


schapman5\_20200827\_11\_SJC.2.300\_F10.18.11.fid  
SJC.2.300\_F10.18  
C13\_standard.UW CDCl3 /home/schapman5/callisto COVID 30



2-(cyclopent-1-en-1-yl)pyridine (**S2.5**)  
 $^{13}\text{C}$  NMR (125.7 MHz,  $\text{CDCl}_3$ )

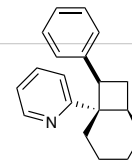




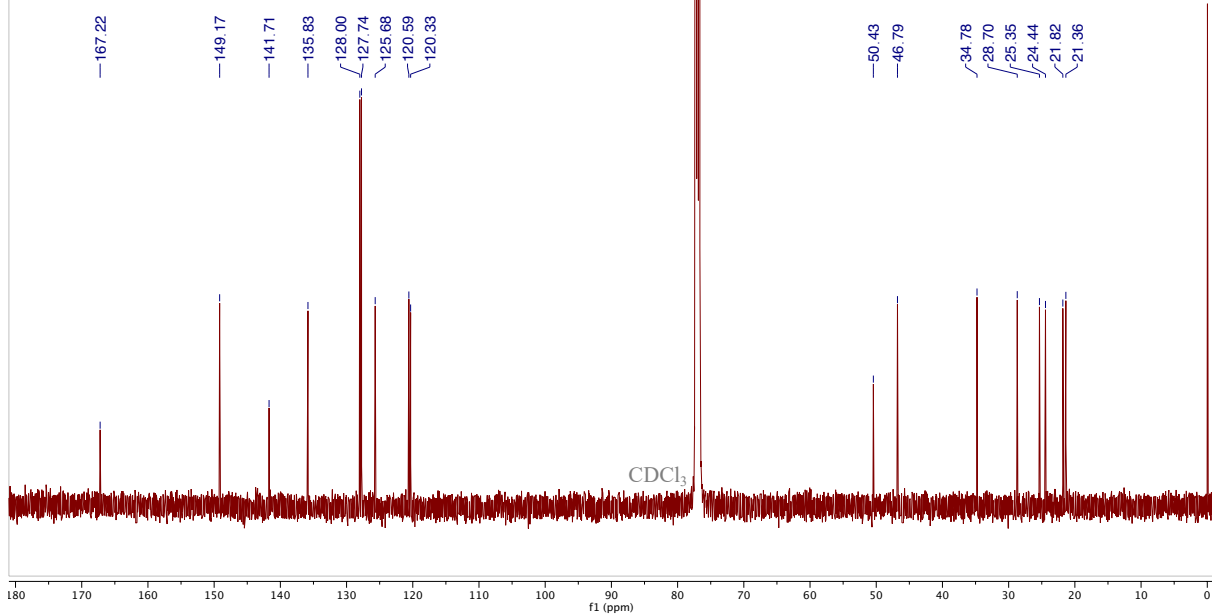
C2003082115\_SJC-4.050\_F22.25.11.fid

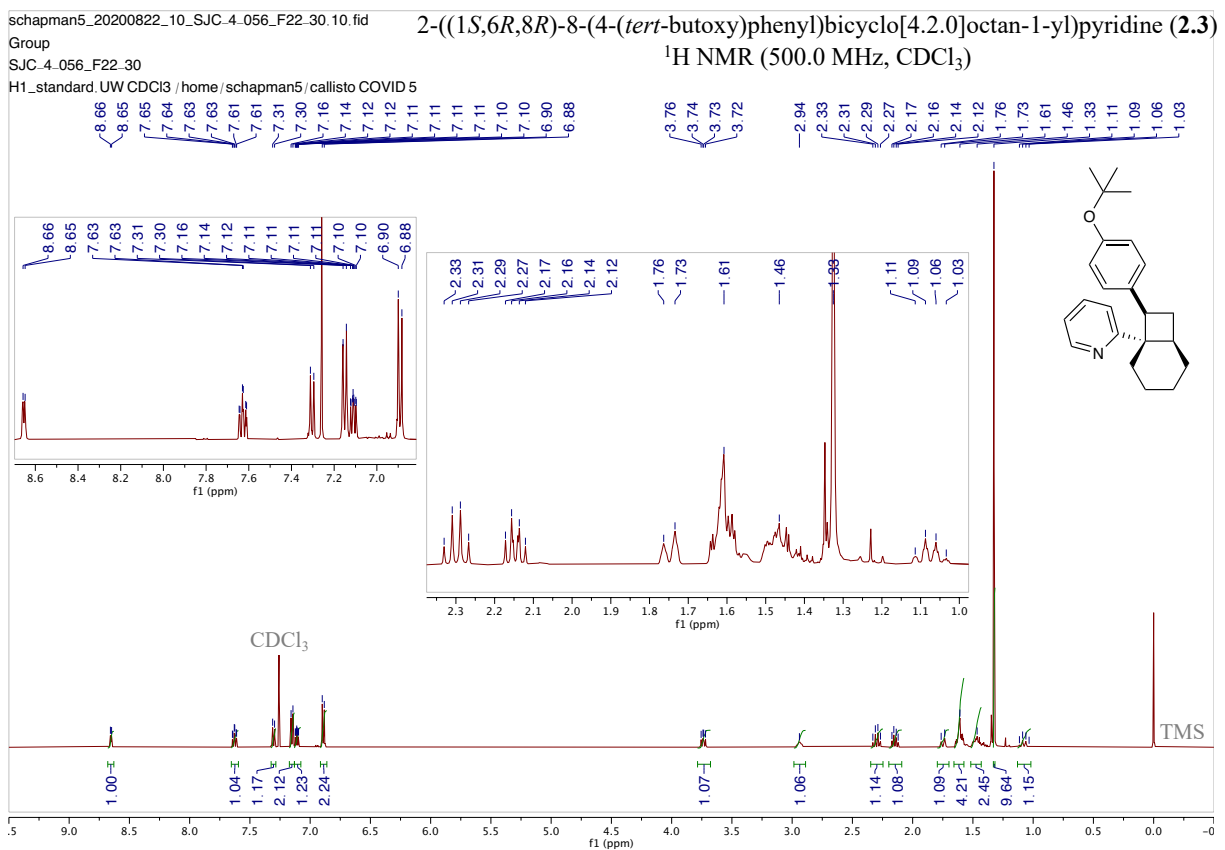
Group Yoon

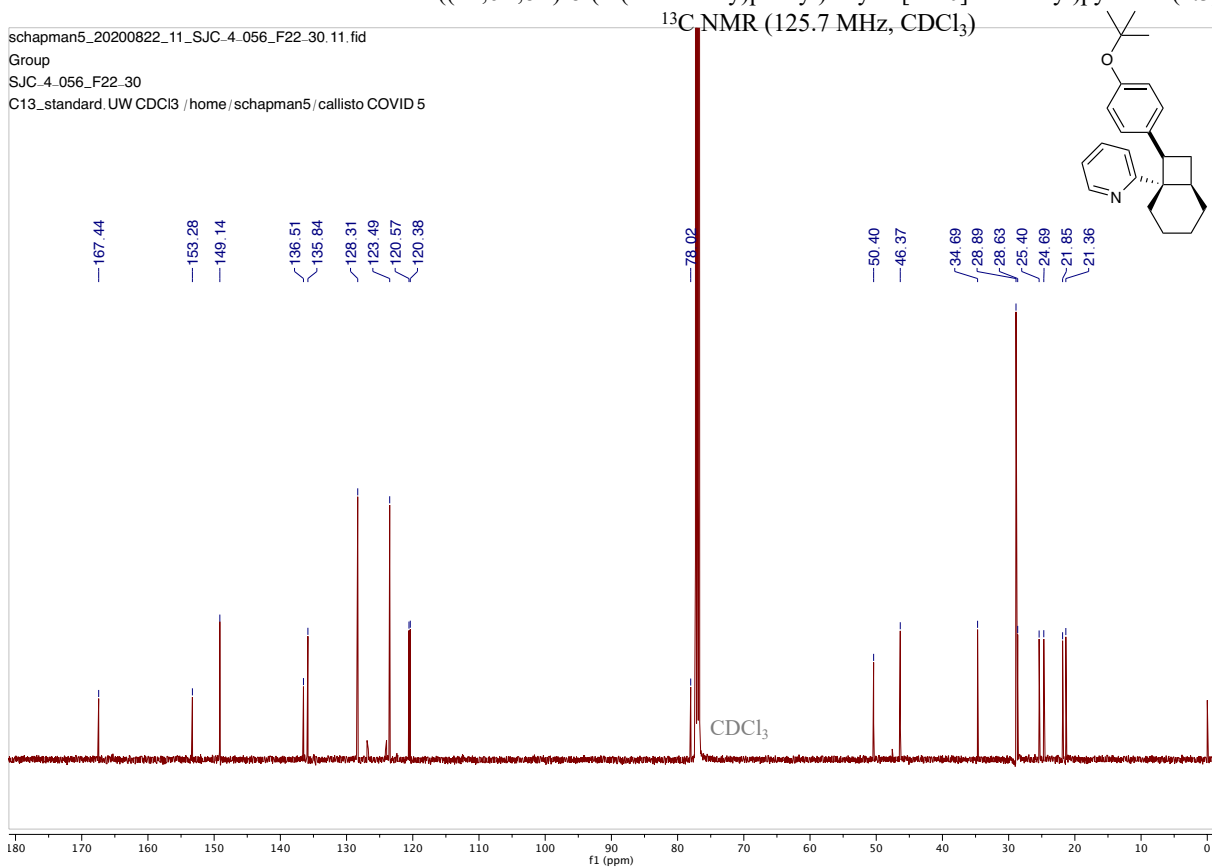
C13\_H1dec.UW CDCl3 /home/schapman5/callisto schapman5.30

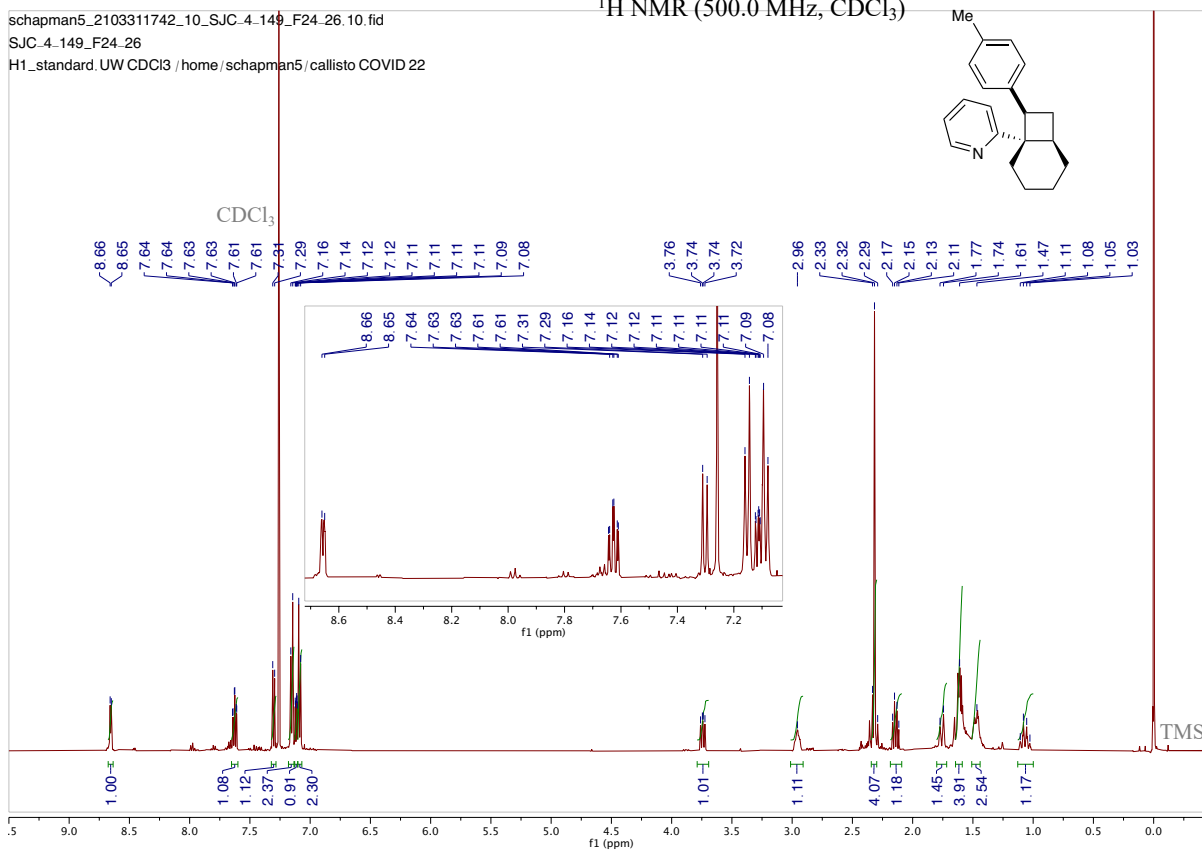


2-((1S,6R,8R)-8-phenylbicyclo[4.2.0]octan-1-yl)pyridine (**2.2**)  
 $^{13}\text{C}$  NMR (125.7 MHz,  $\text{CDCl}_3$ )





2-((1S,6R,8R)-8-(4-(tert-butoxy)phenyl)bicyclo[4.2.0]octan-1-yl)pyridine (**2.3**)

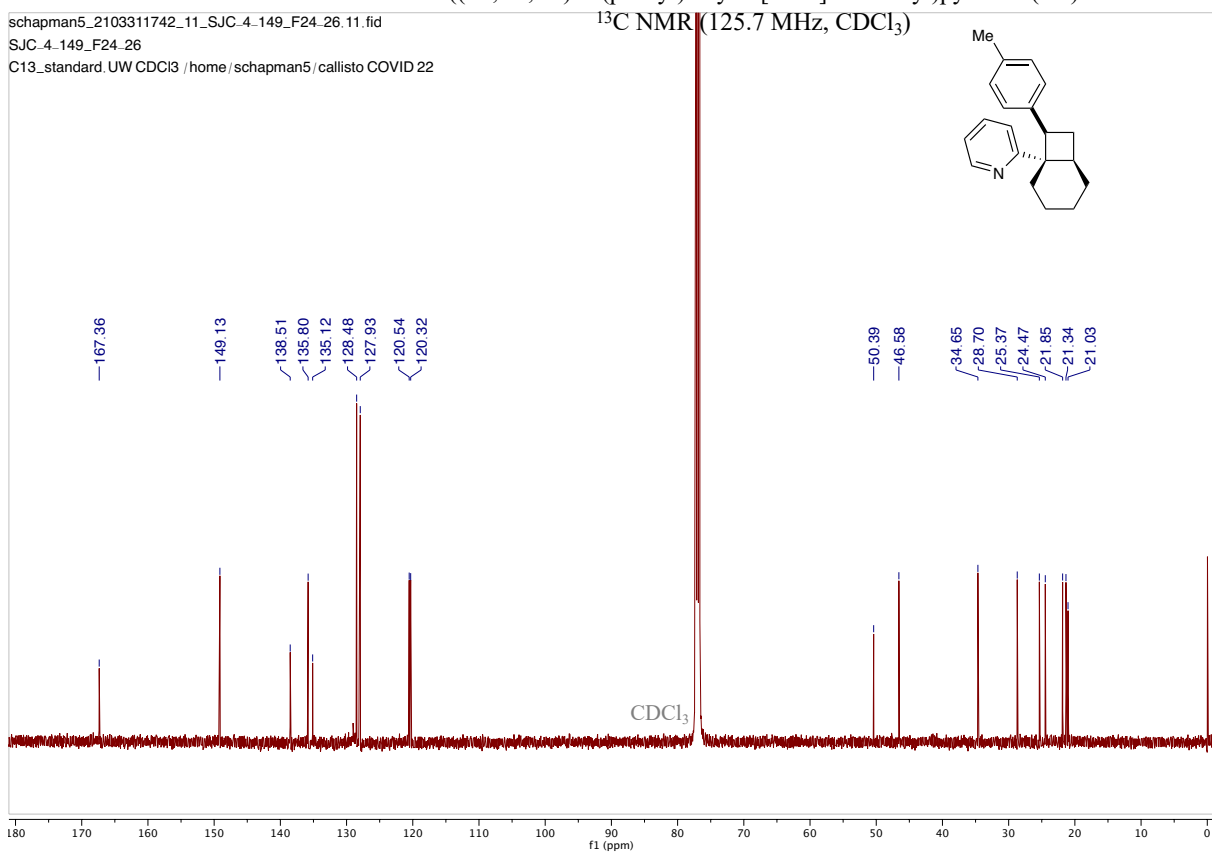
2-((1*S*,6*R*,8*R*)-8-(*p*-tolyl)bicyclo[4.2.0]octan-1-yl)pyridine (**2.4**)<sup>1</sup>H NMR (500.0 MHz, CDCl<sub>3</sub>)

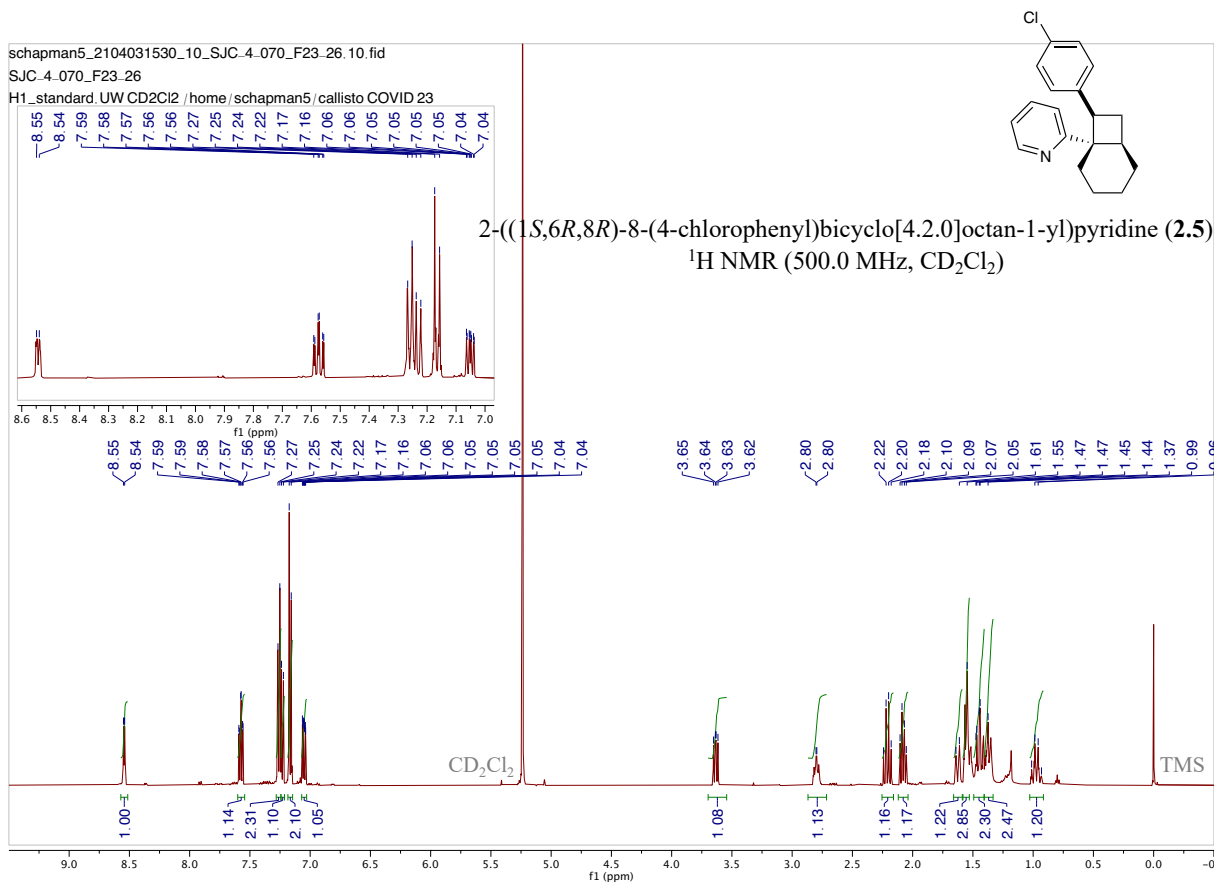
2-((1S,6R,8R)-8-(p-tolyl)bicyclo[4.2.0]octan-1-yl)pyridine (**2.4**)

schapman5\_2103311742\_11\_SJC.4-149\_F24.26.11.fid

SJC.4-149\_F24\_26

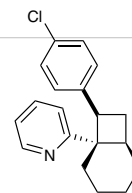
C13\_standard.UW CDCl3 /home/schapman5/callisto COVID 22



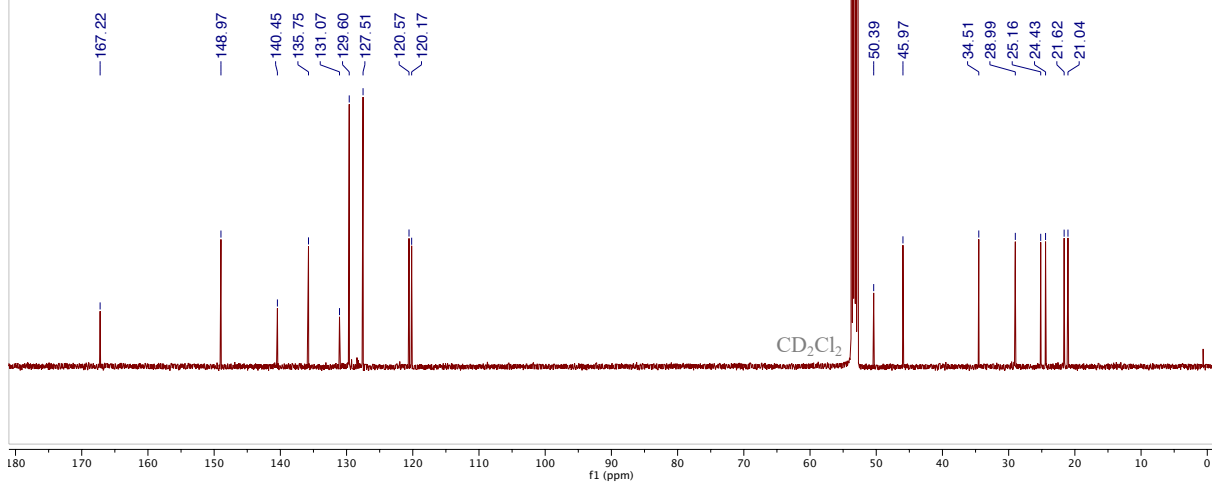


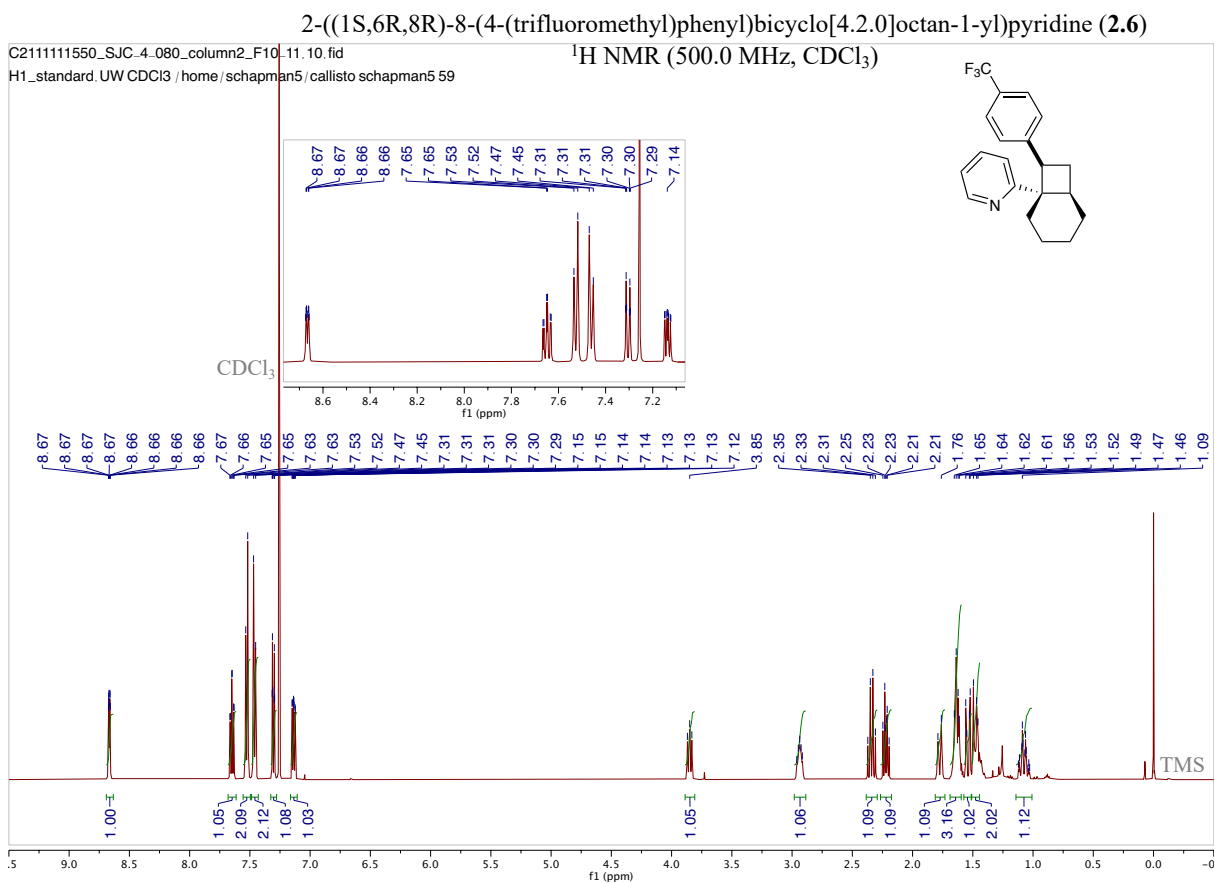


schapman5\_2104031530\_11\_SJC\_4.070\_F23.26.11.fid  
SJC\_4.070\_F23\_26  
C13\_standard.UW CD2Cl2 /home/schapman5/callisto COVID 23

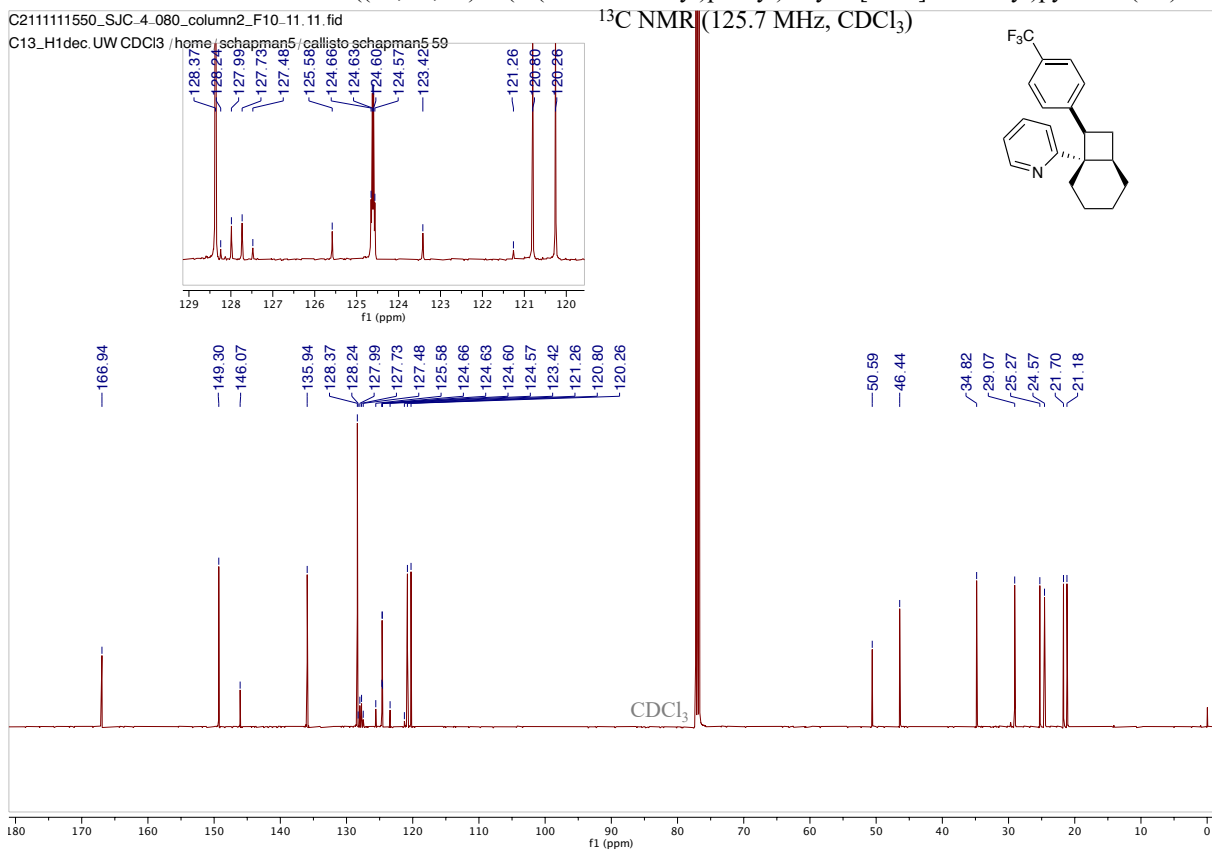


2-((1S,6R,8R)-8-(4-chlorophenyl)bicyclo[4.2.0]octan-1-yl)pyridine (2.5)  
 $^{13}\text{C}$  NMR (125.7 MHz,  $\text{CD}_2\text{Cl}_2$ )





## 2-((1S,6R,8R)-8-(4-(trifluoromethyl)phenyl)bicyclo[4.2.0]octan-1-yl)pyridine (2.6)

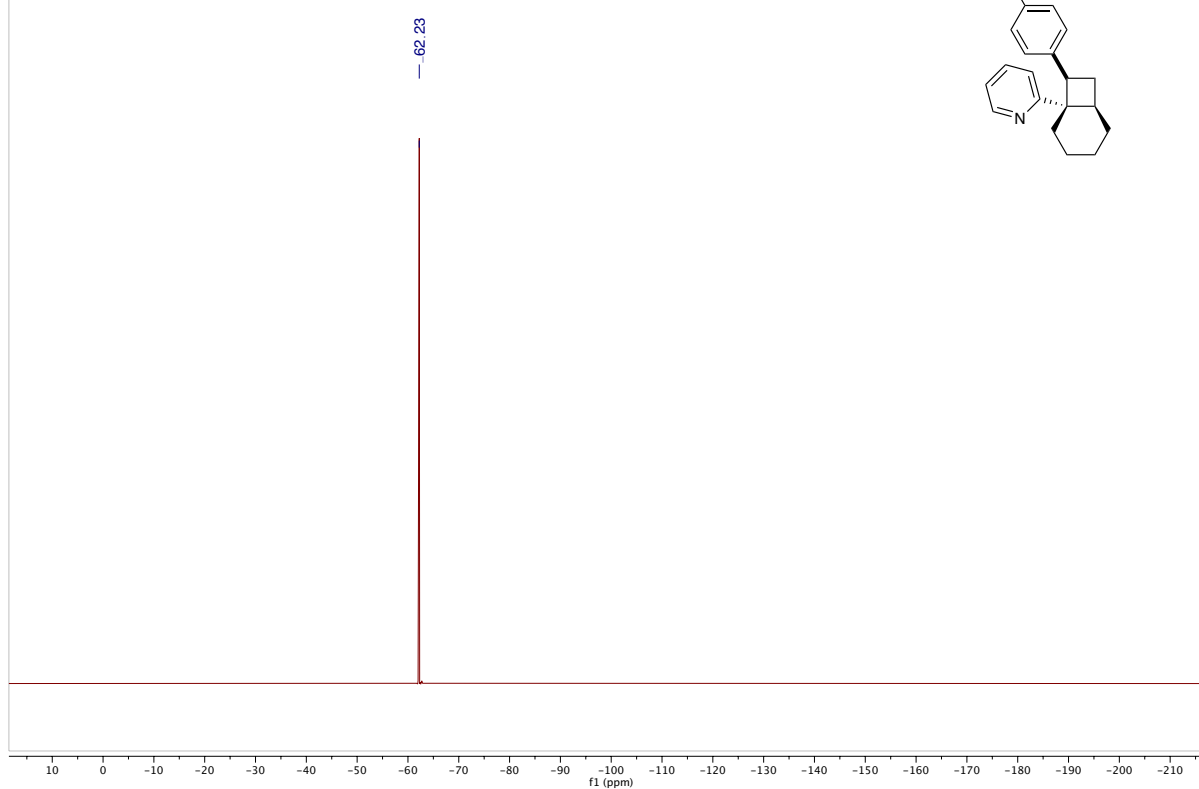


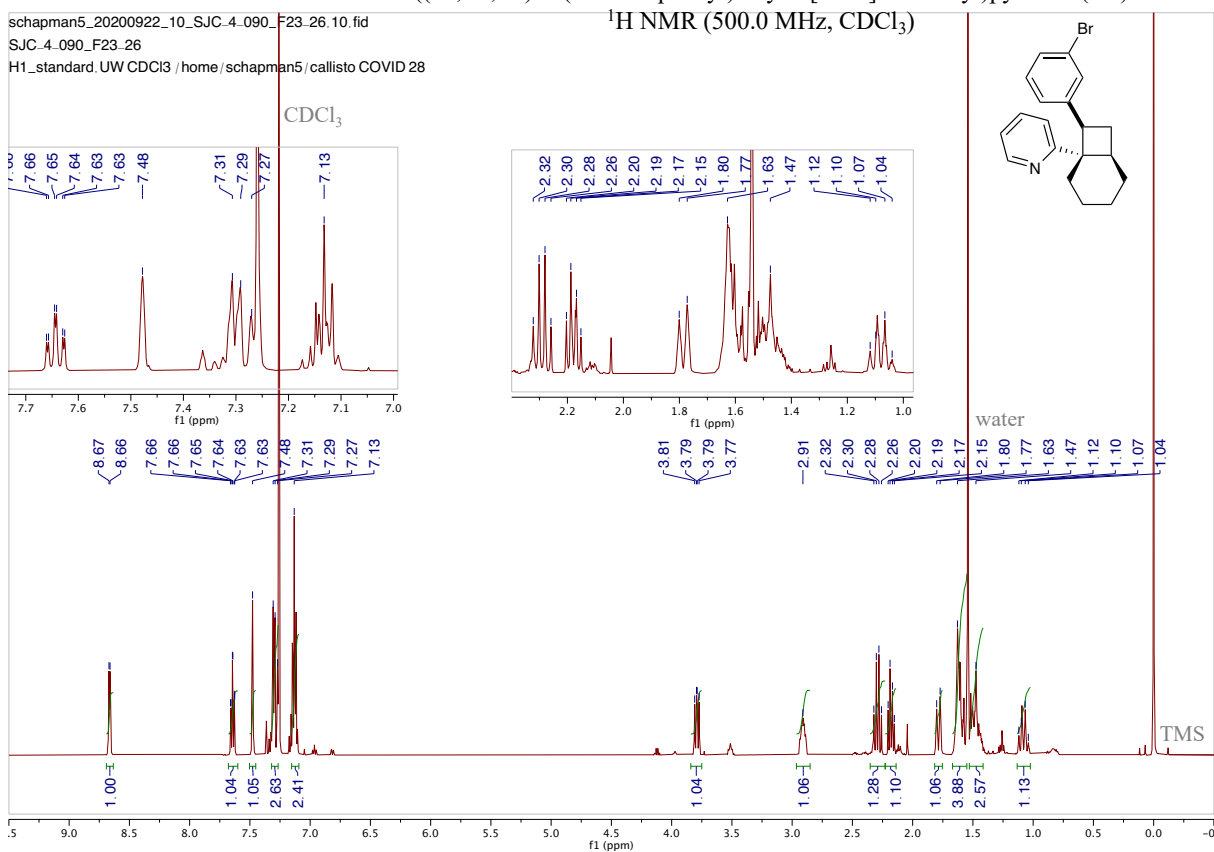
2-((1S,6R,8R)-8-(4-(trifluoromethyl)phenyl)bicyclo[4.2.0]octan-1-yl)pyridine (**2.6**)

D2111121117\_SJC.4.080\_column2\_F10-11.11.fid

 $^{19}\text{F}$  NMR (376.5 MHz,  $\text{CDCl}_3$ )

F19\_H1decoupled.UW.CDCI3 / home / schapman5 / av400 schapman5 5



2-((1*S*,6*R*,8*R*)-8-(3-bromophenyl)bicyclo[4.2.0]octan-1-yl)pyridine (2.7)

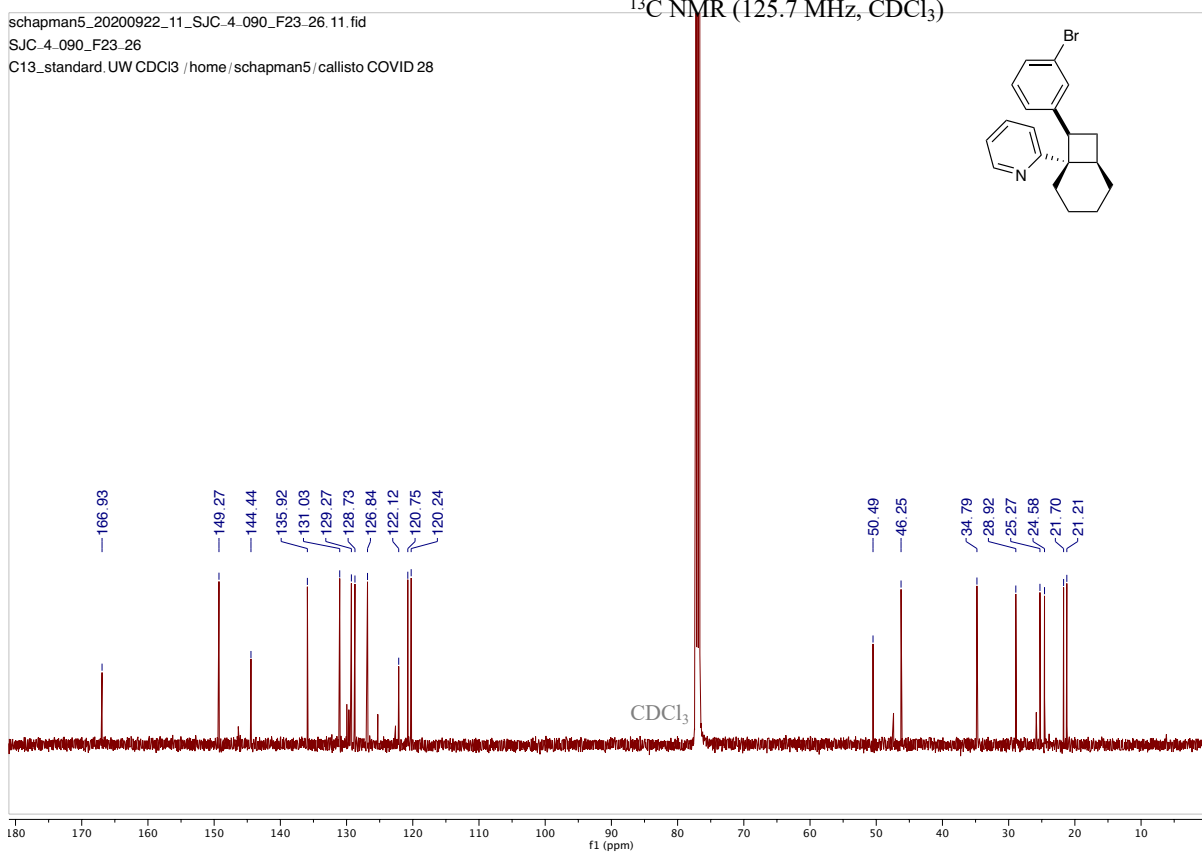
## 2-((1S,6R,8R)-8-(3-bromophenyl)bicyclo[4.2.0]octan-1-yl)pyridine (2.7)

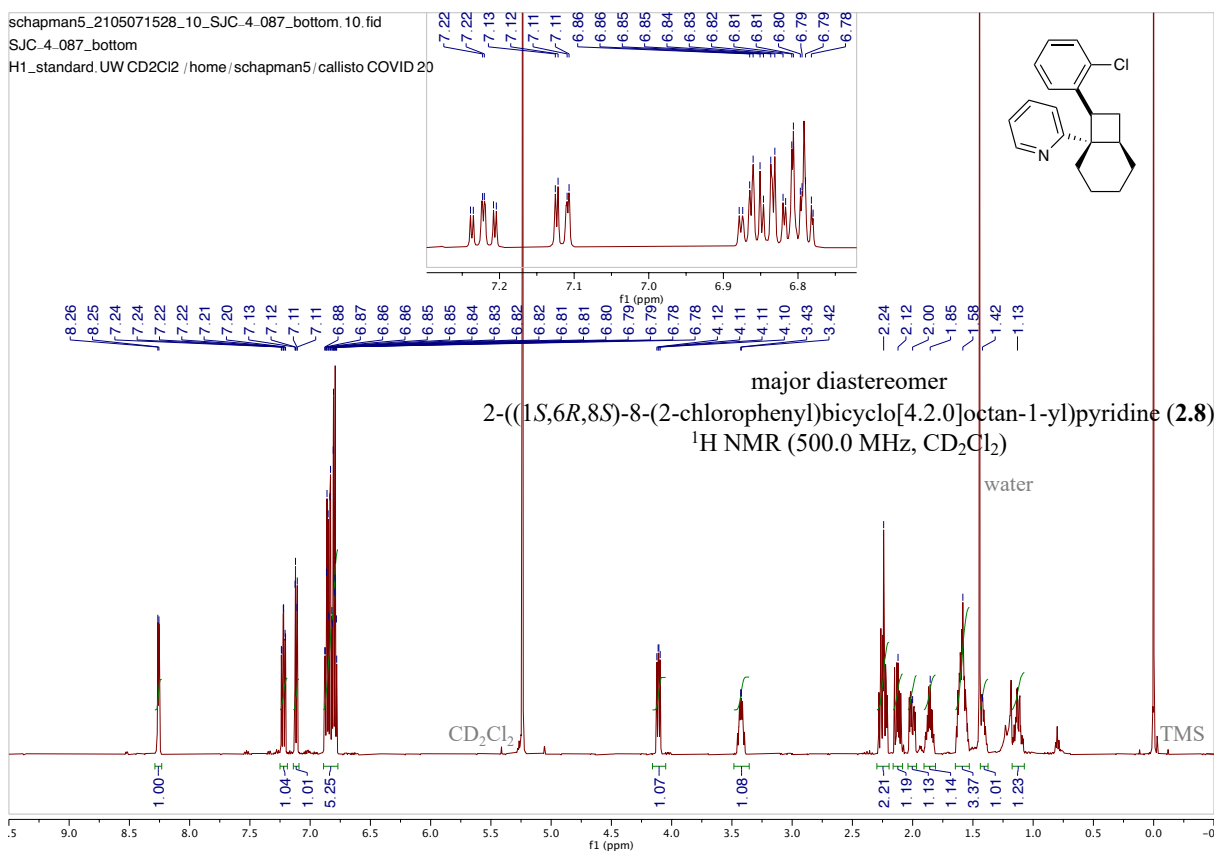
 $^{13}\text{C}$  NMR (125.7 MHz,  $\text{CDCl}_3$ )

schapman5\_20200922\_11\_SJC.4.090\_F23.26.11.fid

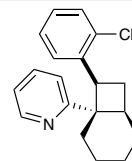
SJC.4.090\_F23.26

C13\_standard.UW CDCl3 /home/schapman5/callisto COVID 28

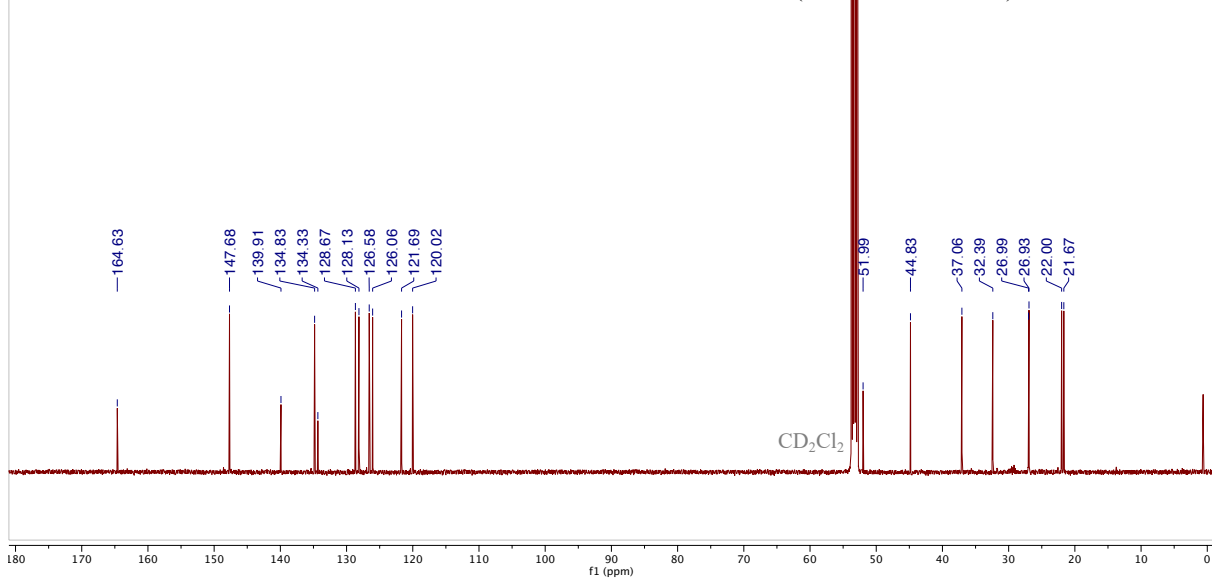




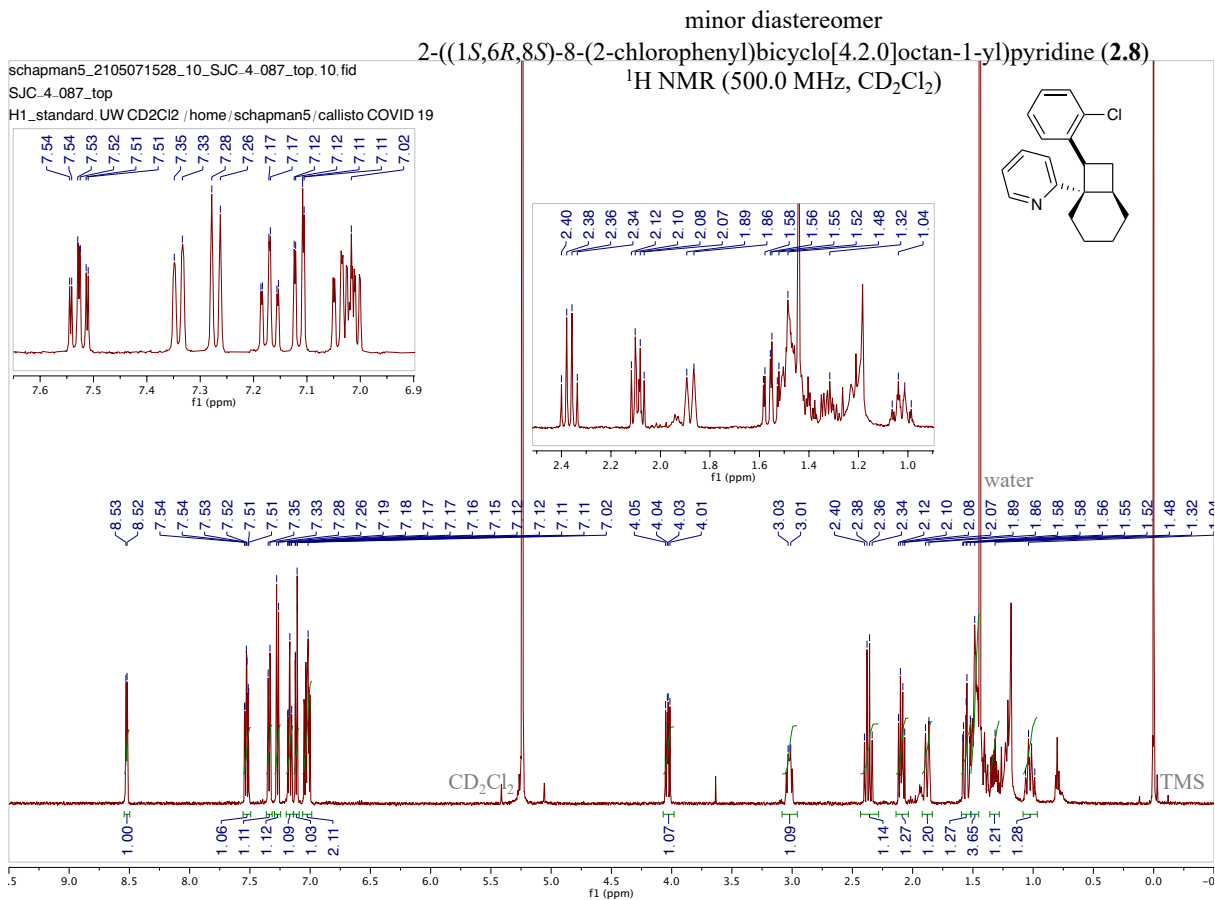
schapman5\_2105071528\_11\_SJC\_4.087\_bottom.11.fid  
SJC\_4.087\_bottom  
C13\_standard.UW CD2Cl2 /home/schapman5/callisto COVID 20

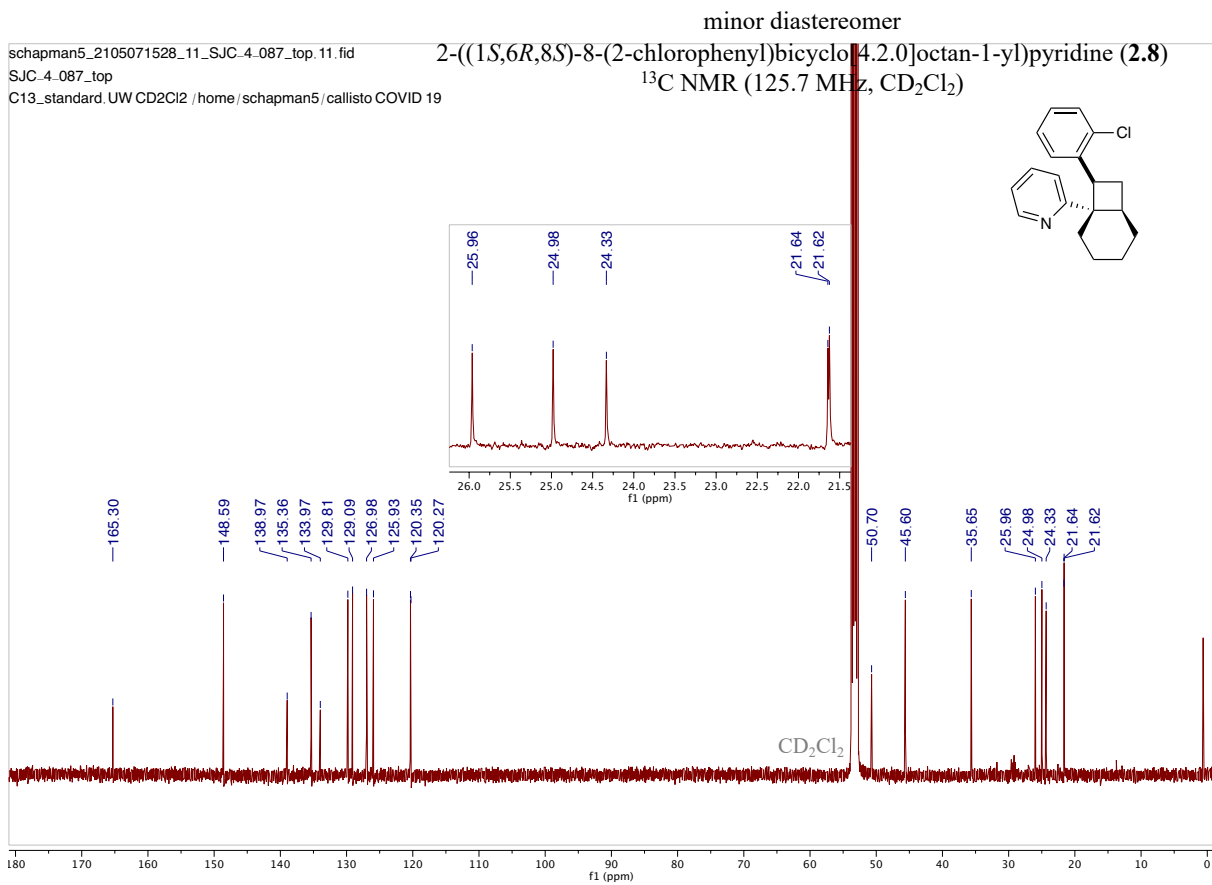


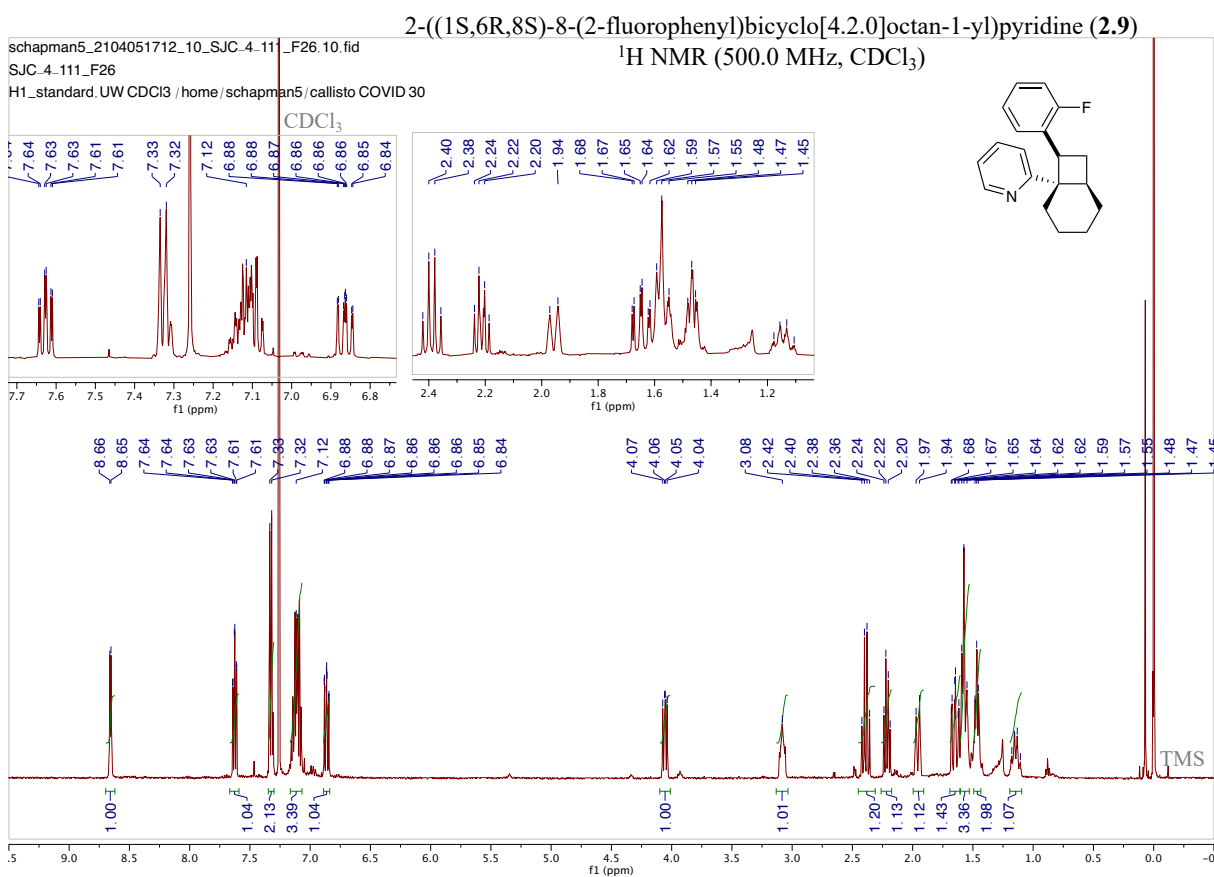
major diastereomer  
2-((1*S*,6*R*,8*S*)-8-(2-chlorophenyl)bicyclo[4.2.0]octan-1-yl)pyridine (**2.8**)  
<sup>13</sup>C NMR (125.7 MHz, CD<sub>2</sub>Cl<sub>2</sub>)



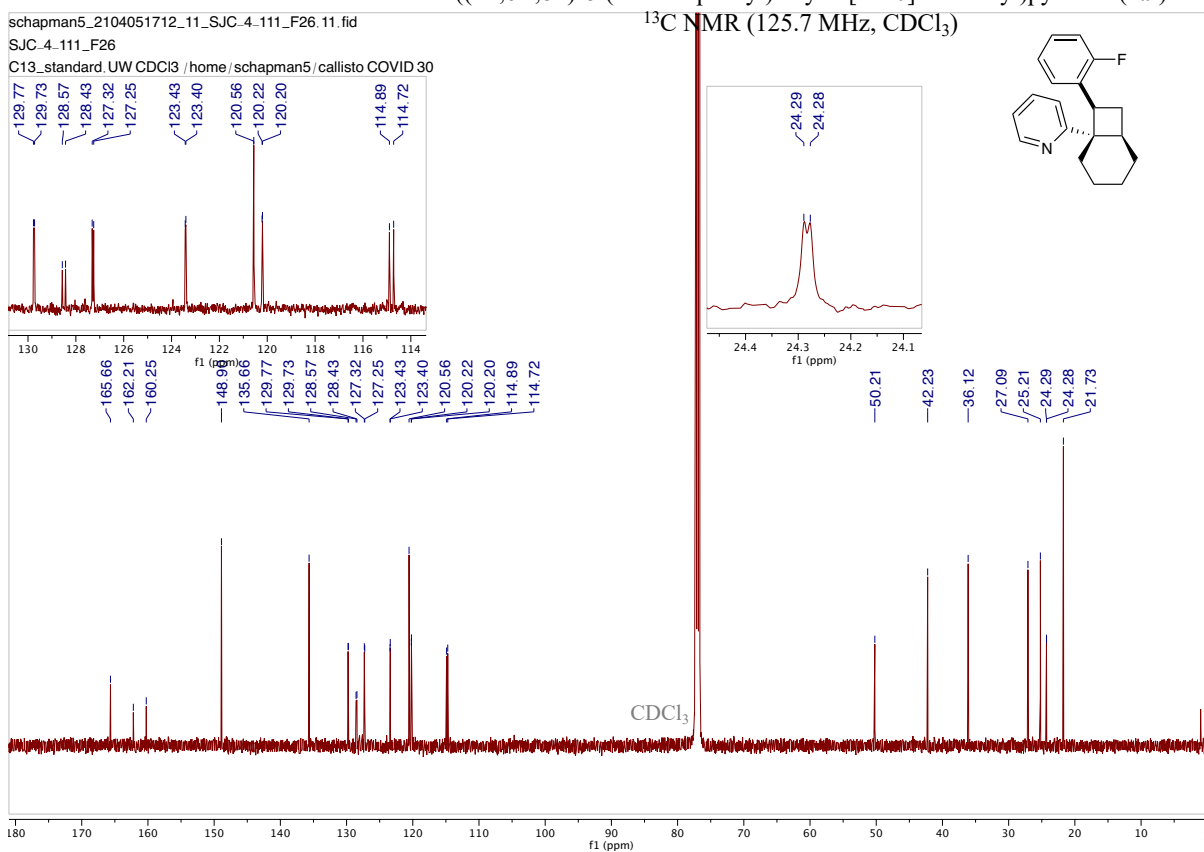


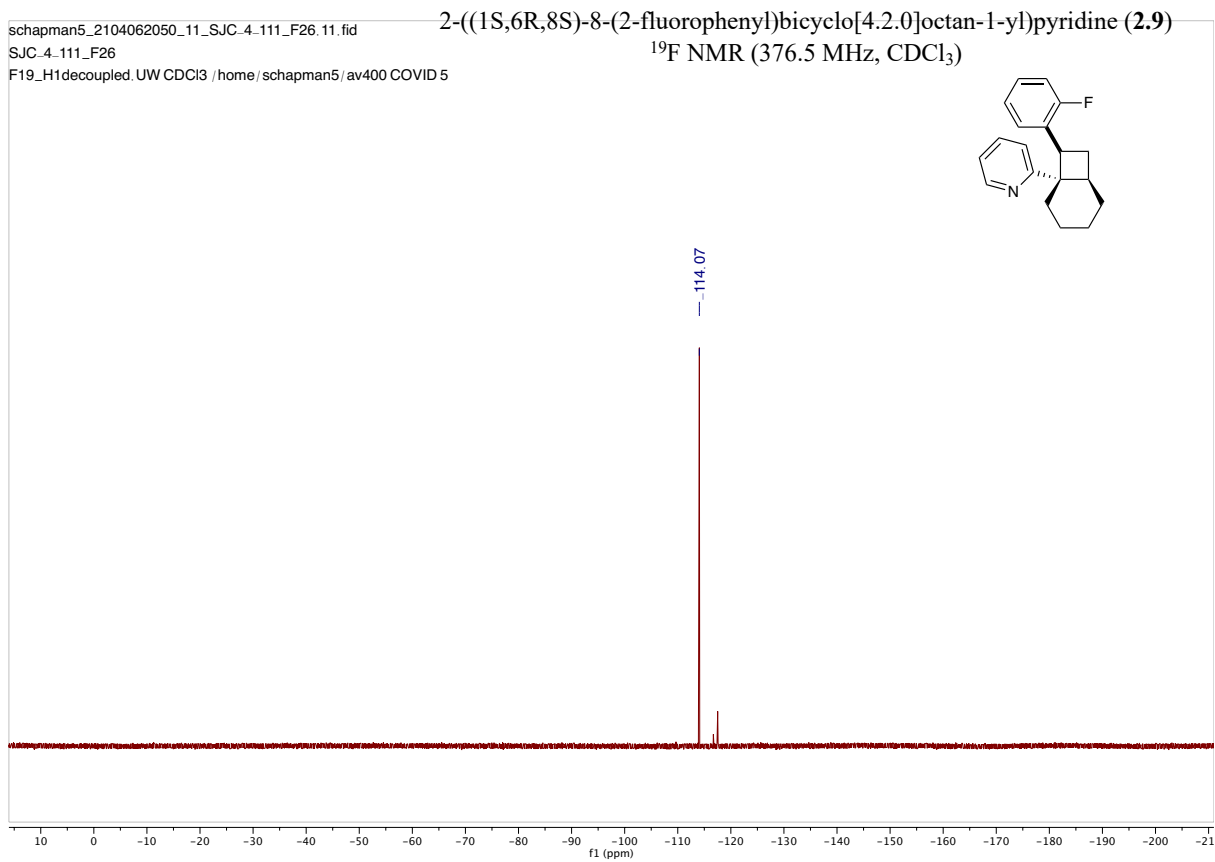


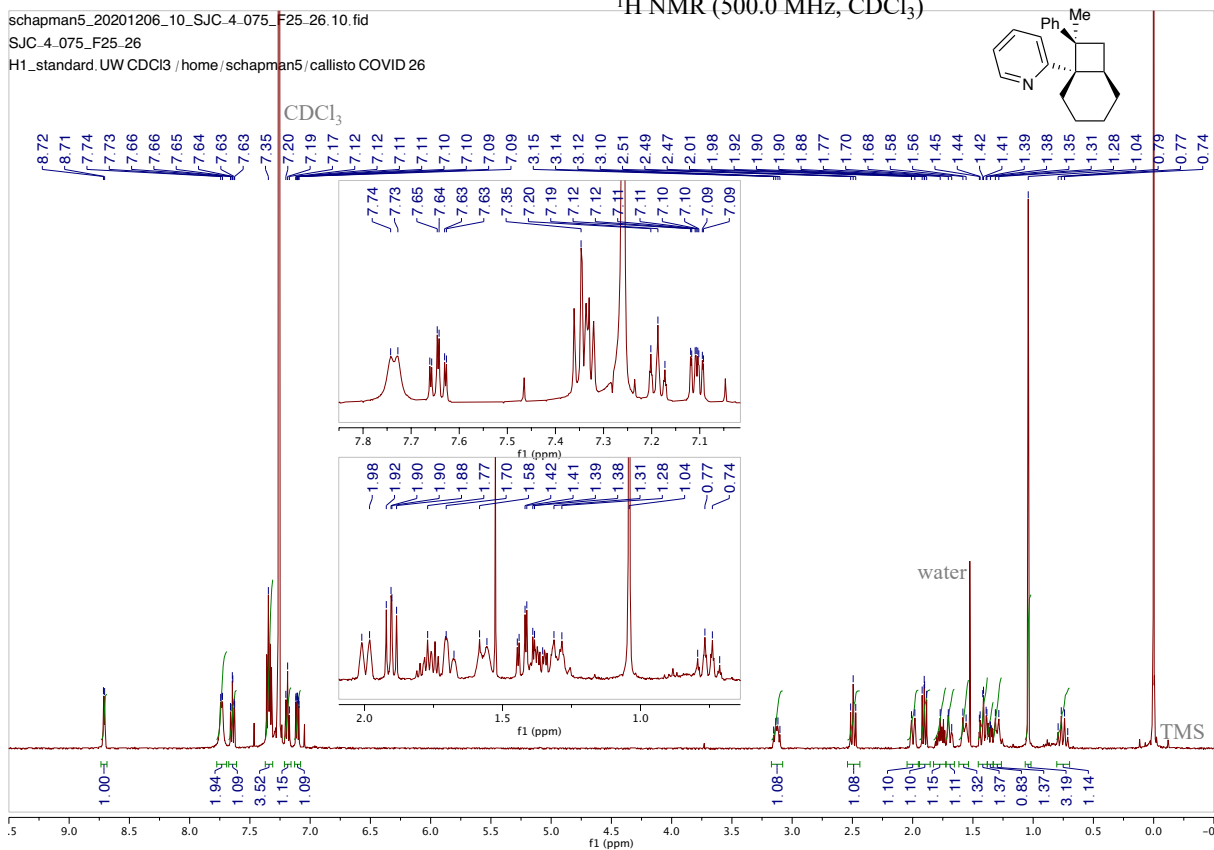




## 2-((1S,6R,8S)-8-(2-fluorophenyl)bicyclo[4.2.0]octan-1-yl)pyridine (2.9)





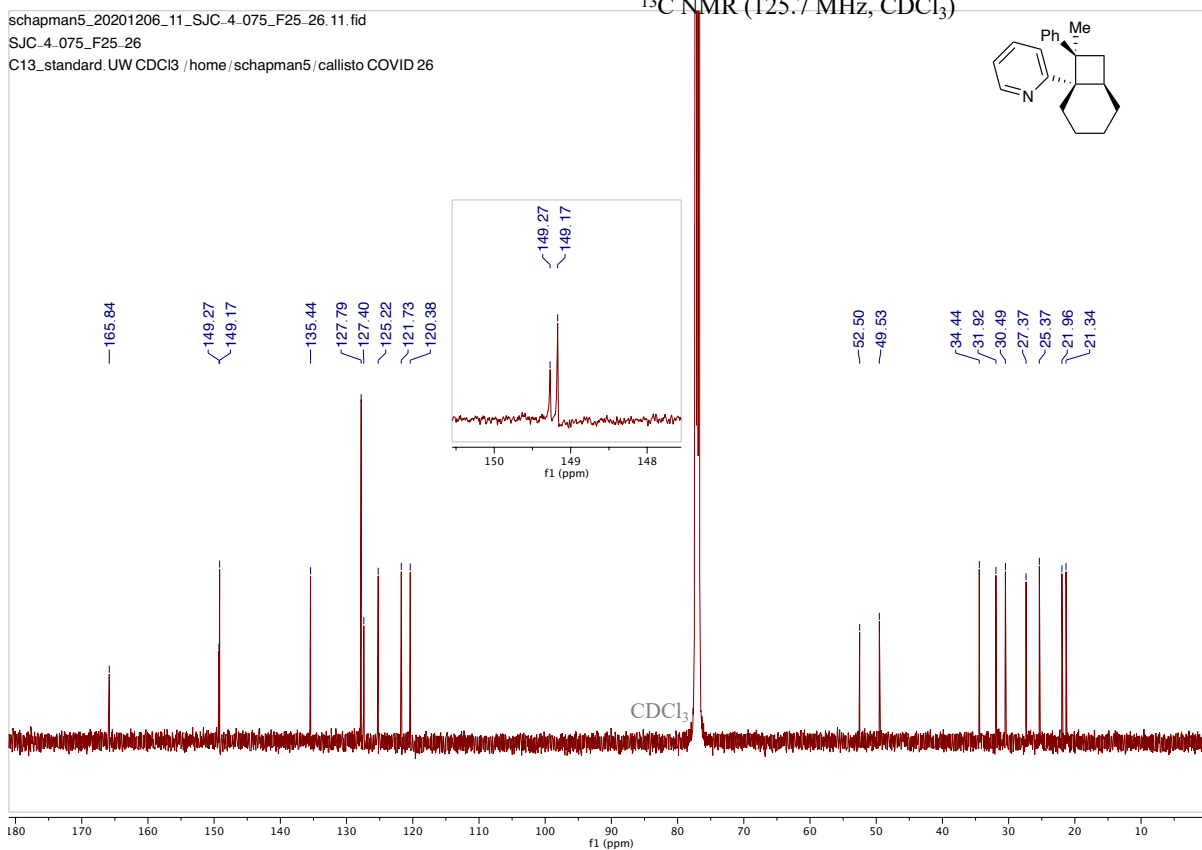
2-((1S,6R,8R)-8-methyl-8-phenylbicyclo[4.2.0]octan-1-yl)pyridine (**2.10**)<sup>1</sup>H NMR (500.0 MHz, CDCl<sub>3</sub>)

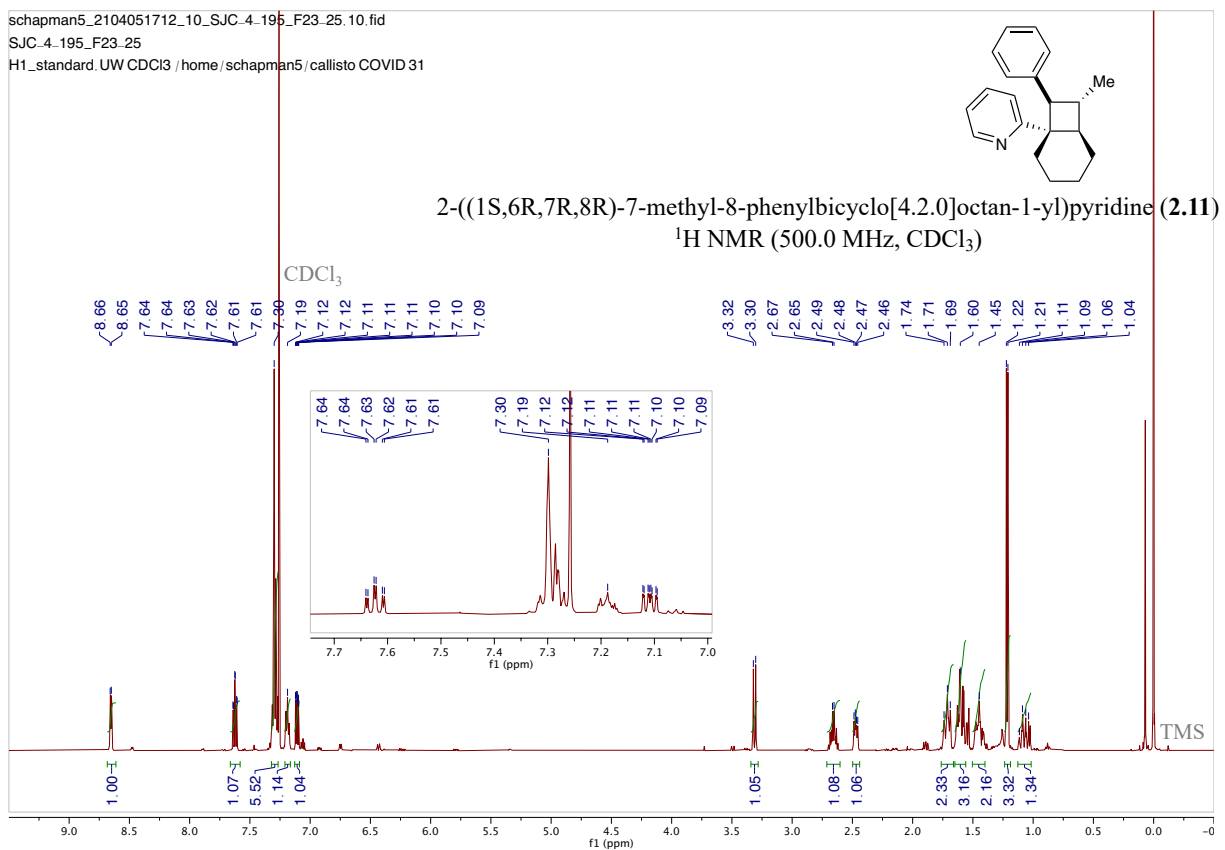
2-((1S,6R,8R)-8-methyl-8-phenylbicyclo[4.2.0]octan-1-yl)pyridine (**2.10**) $^{13}\text{C}$  NMR (125.7 MHz,  $\text{CDCl}_3$ )

schapman5\_20201206\_11\_SJC.4.075\_F25.26.11.fid

SJC.4.075\_F25.26

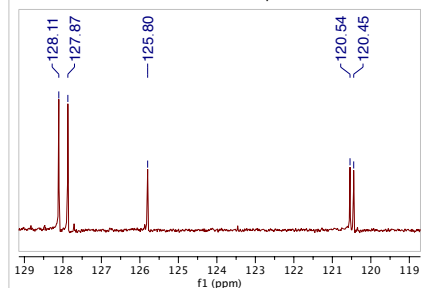
C13\_standard.UW.CDCI3 /home/schapman5/callisto COVID 26



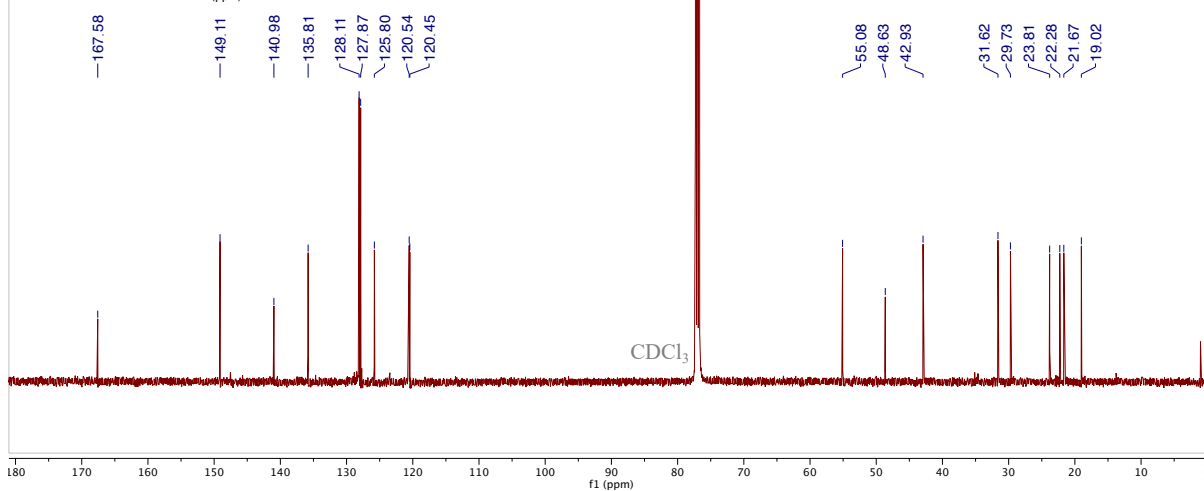
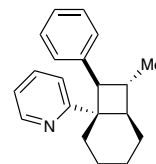


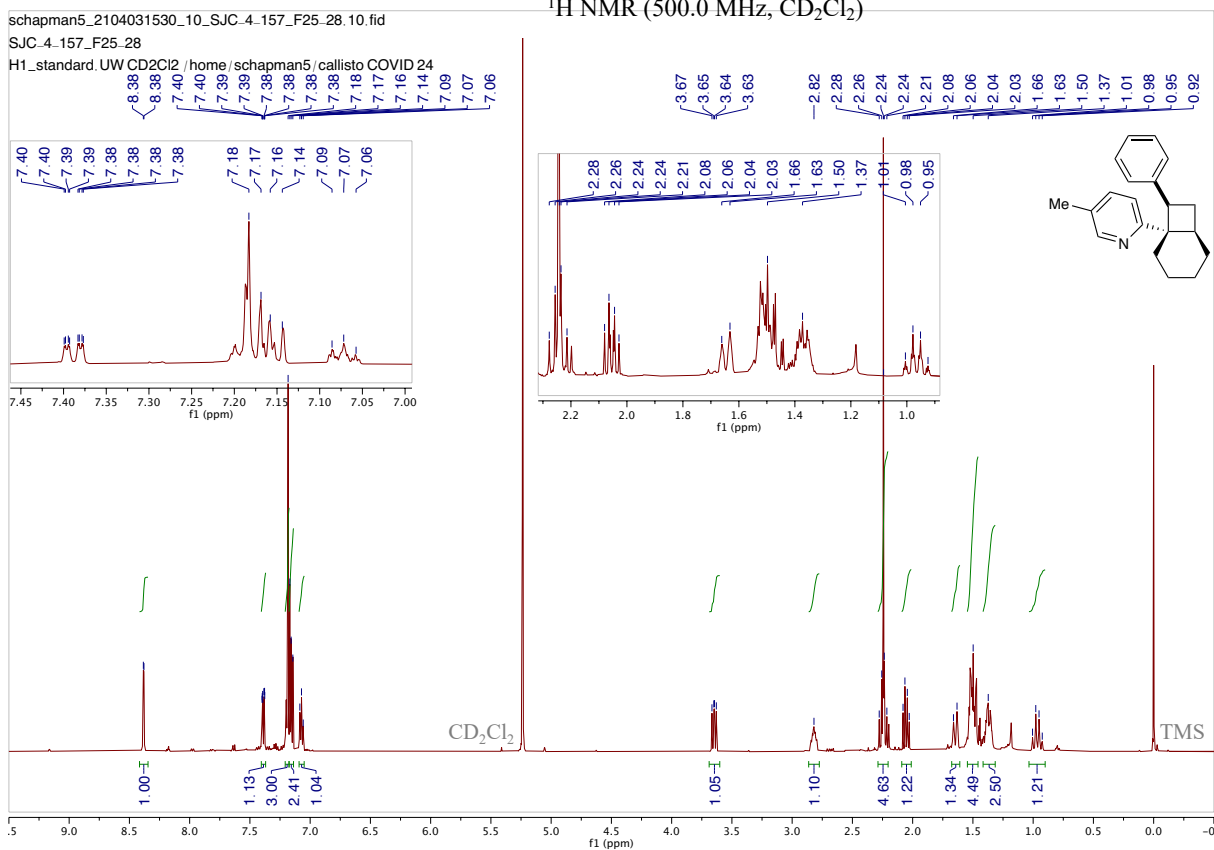


schapman5\_2104051712\_11\_SJC.4.195\_F23.25.11.fid  
SJC.4.195\_F23.25  
C13\_standard.UW CDCl3 /home/schapman5/callisto COVID 31



2-((1S,6R,7R,8R)-7-methyl-8-phenylbicyclo[4.2.0]octan-1-yl)pyridine (**2.11**)  
 $^{13}\text{C}$  NMR (125.7 MHz,  $\text{CDCl}_3$ )



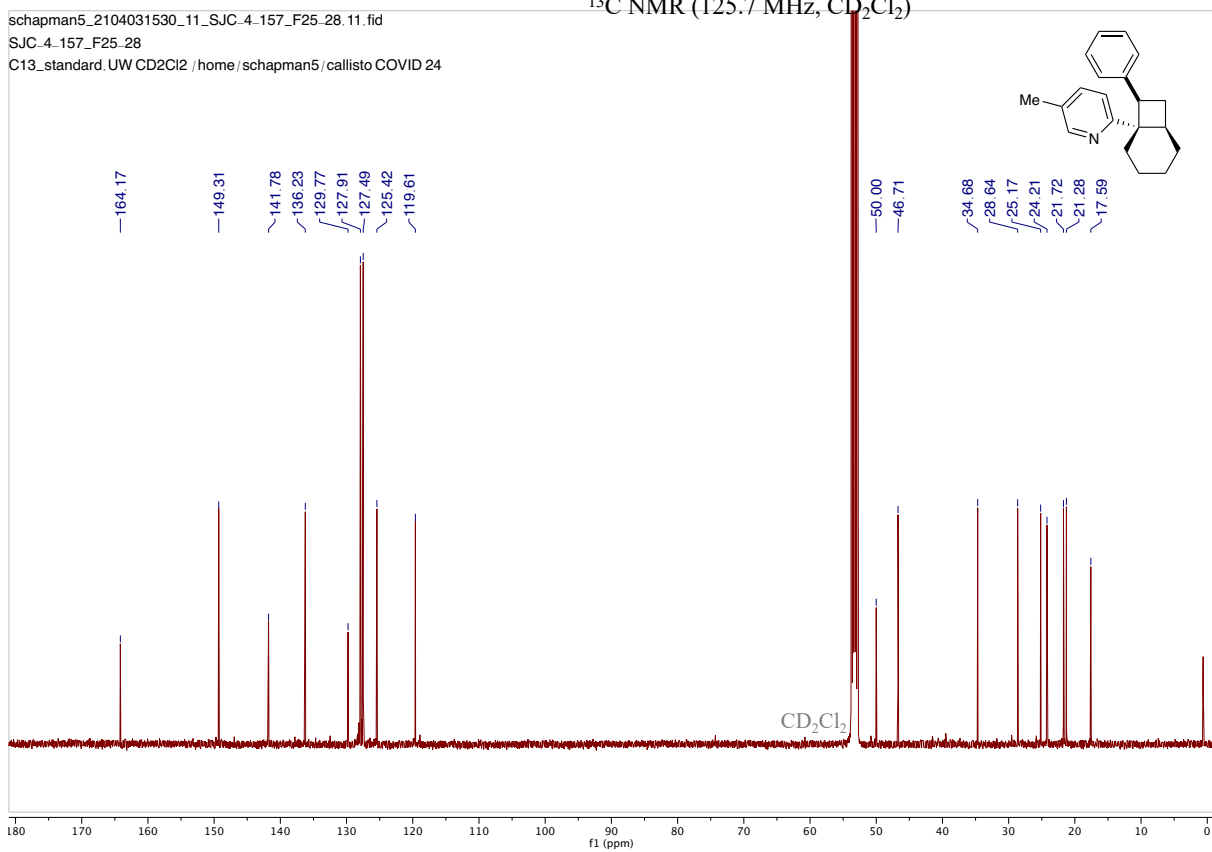
5-methyl-2-((1S,6R,8R)-8-phenylbicyclo[4.2.0]octan-1-yl)pyridine (**2.12**) $^1\text{H}$  NMR (500.0 MHz,  $\text{CD}_2\text{Cl}_2$ )

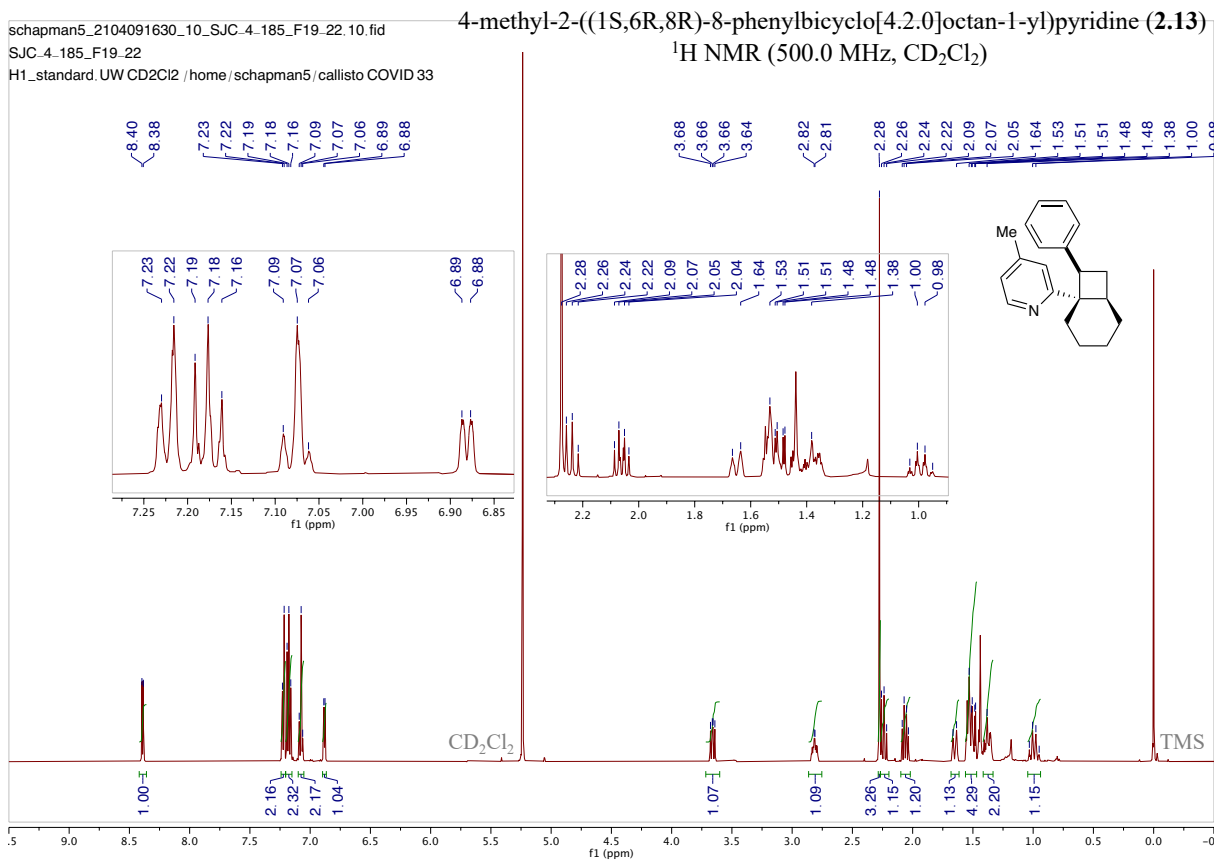
5-methyl-2-((1S,6R,8R)-8-phenylbicyclo[4.2.0]octan-1-yl)pyridine (**2.12**) $^{13}\text{C}$  NMR (125.7 MHz,  $\text{CD}_2\text{Cl}_2$ )

schapman5\_2104031530\_11\_SJC.4.157\_F25.28.11.fid

SJC.4.157\_F25.28

C13\_standard.UW CD2Cl2 /home/schapman5/callisto COVID 24



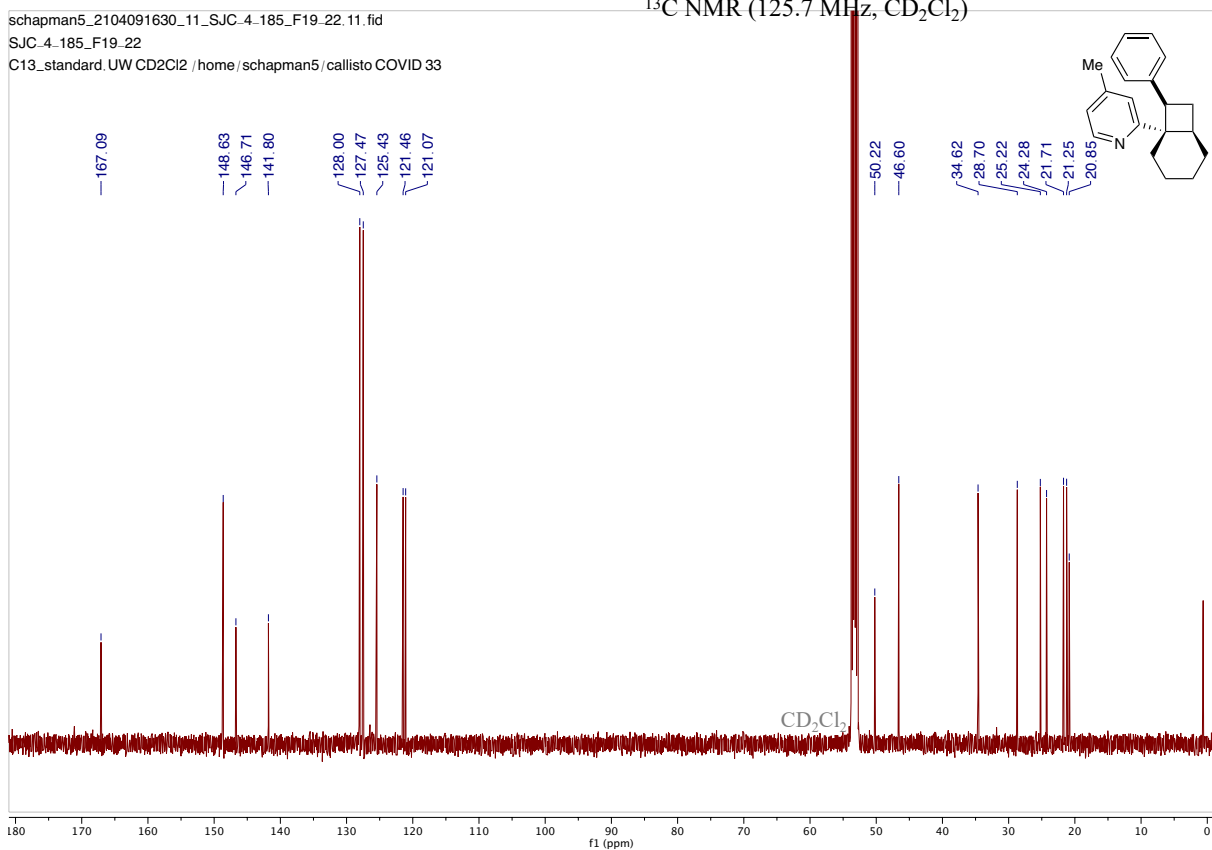


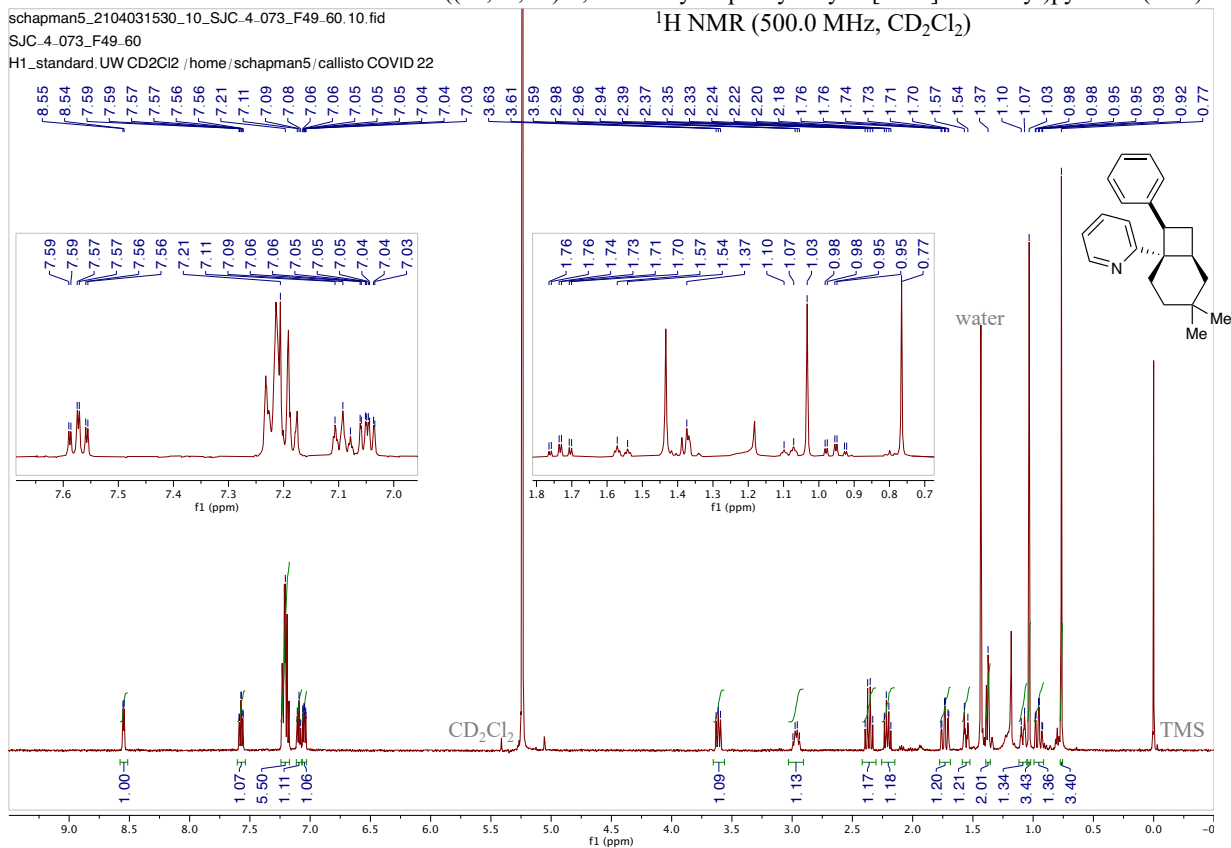
4-methyl-2-((1S,6R,8R)-8-phenylbicyclo[4.2.0]octan-1-yl)pyridine (**2.13**) $^{13}\text{C}$  NMR (125.7 MHz,  $\text{CD}_2\text{Cl}_2$ )

schapman5\_2104091630\_11\_SJC.4-185\_F19.22.11.fid

SJC.4-185\_F19.22

C13\_standard.UW CD2Cl2 /home/schapman5/callisto COVID 33



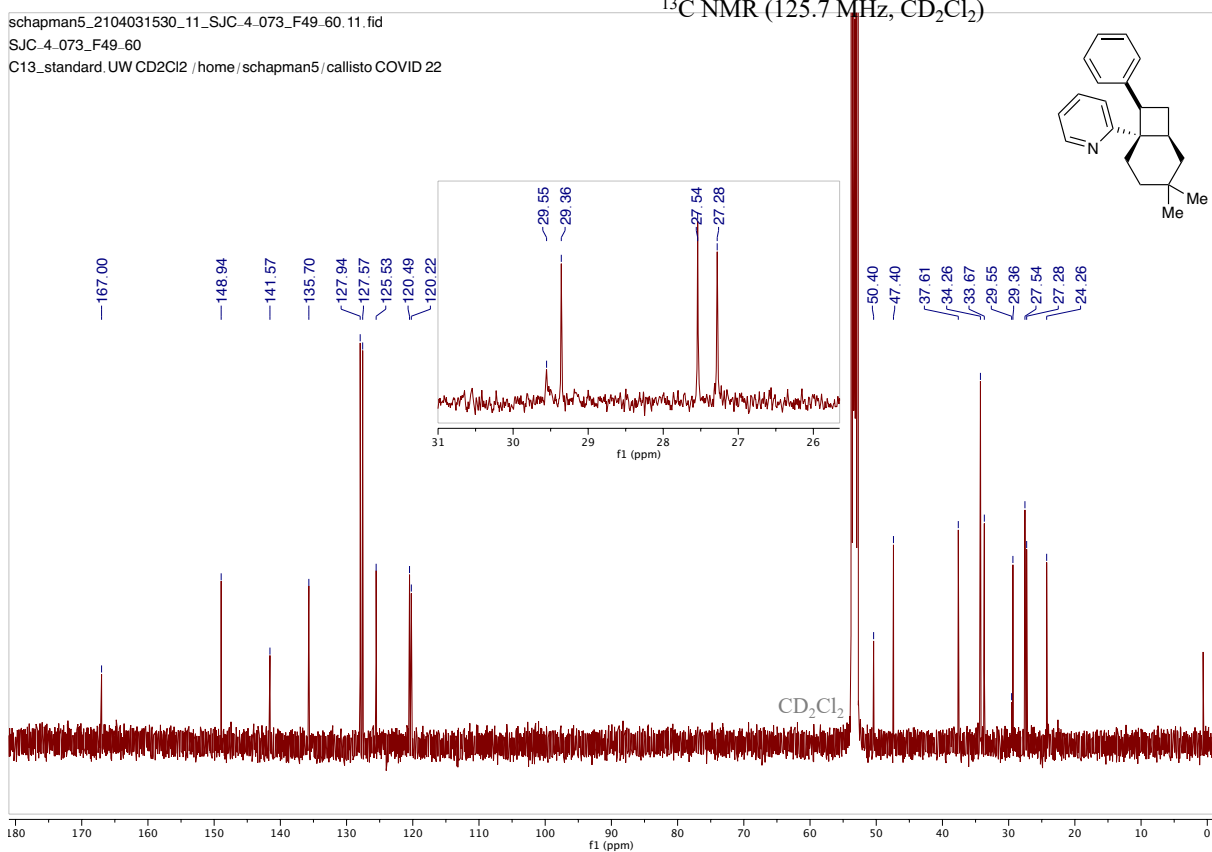
2-((1*S*,6*S*,8*R*)-4,4-dimethyl-8-phenylbicyclo[4.2.0]octan-1-yl)pyridine (**2.14**)

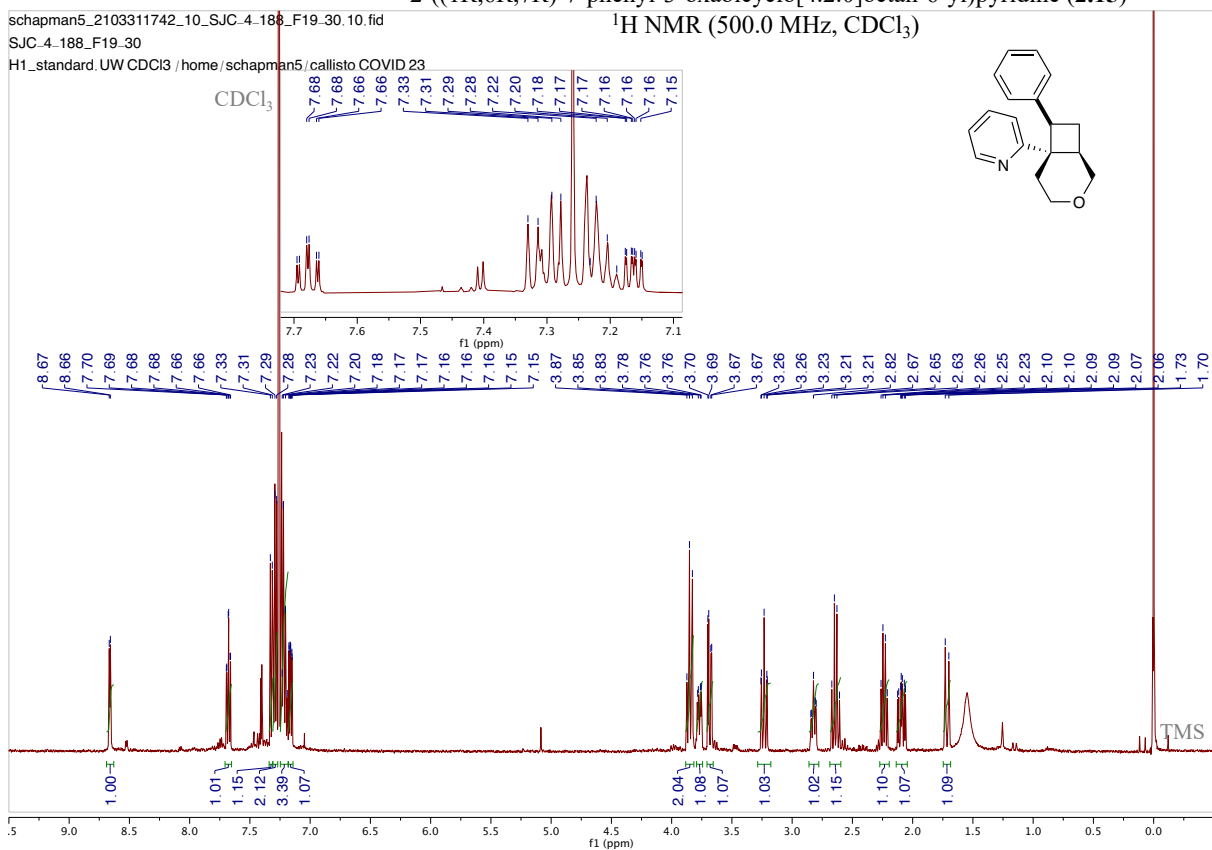
2-((1S,6S,8R)-4,4-dimethyl-8-phenylbicyclo[4.2.0]octan-1-yl)pyridine (**2.14**) $^{13}\text{C}$  NMR (125.7 MHz,  $\text{CD}_2\text{Cl}_2$ )

schapman5\_2104031530\_11\_SJC\_4.073\_F49.60.11.fid

SJC\_4.073\_F49.60

C13\_standard\_UW CD2Cl2 /home/schapman5/callisto COVID 22



2-((1R,6R,7R)-7-phenyl-3-oxabicyclo[4.2.0]octan-6-yl)pyridine (**2.15**)

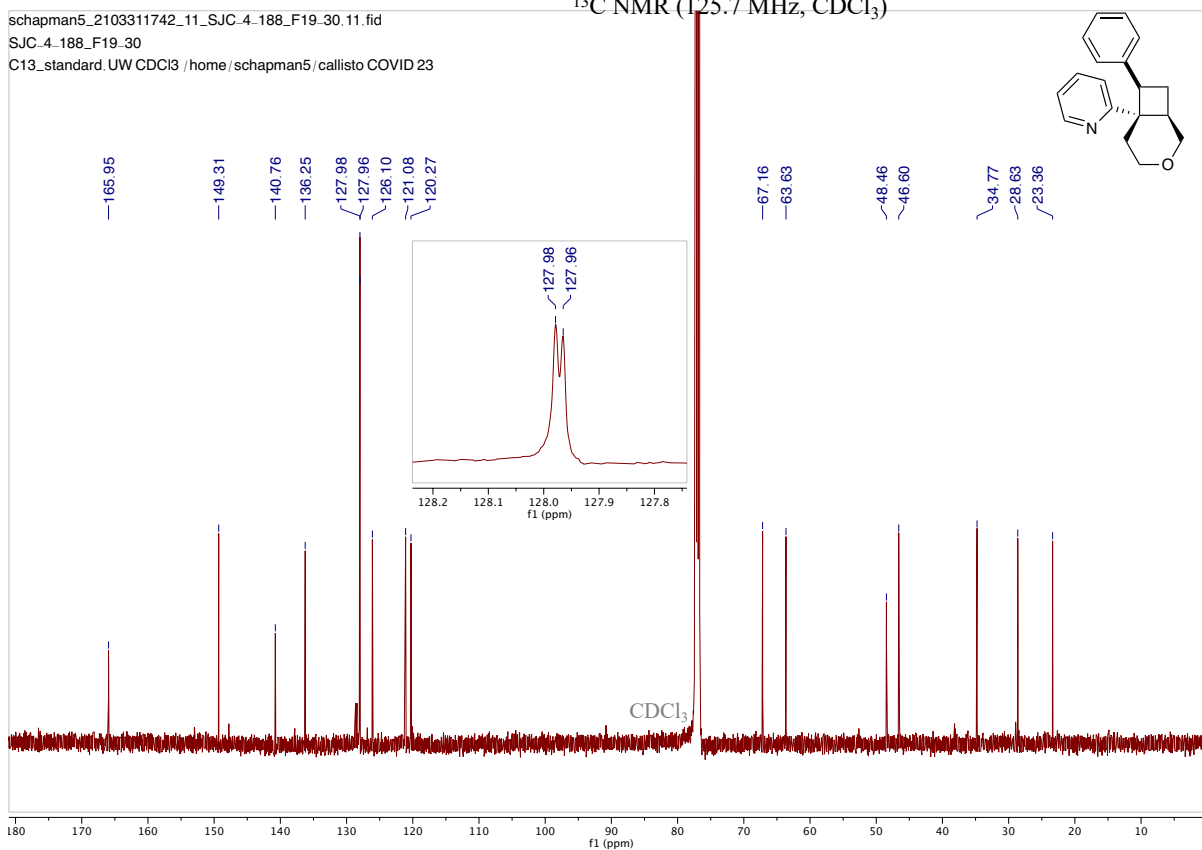


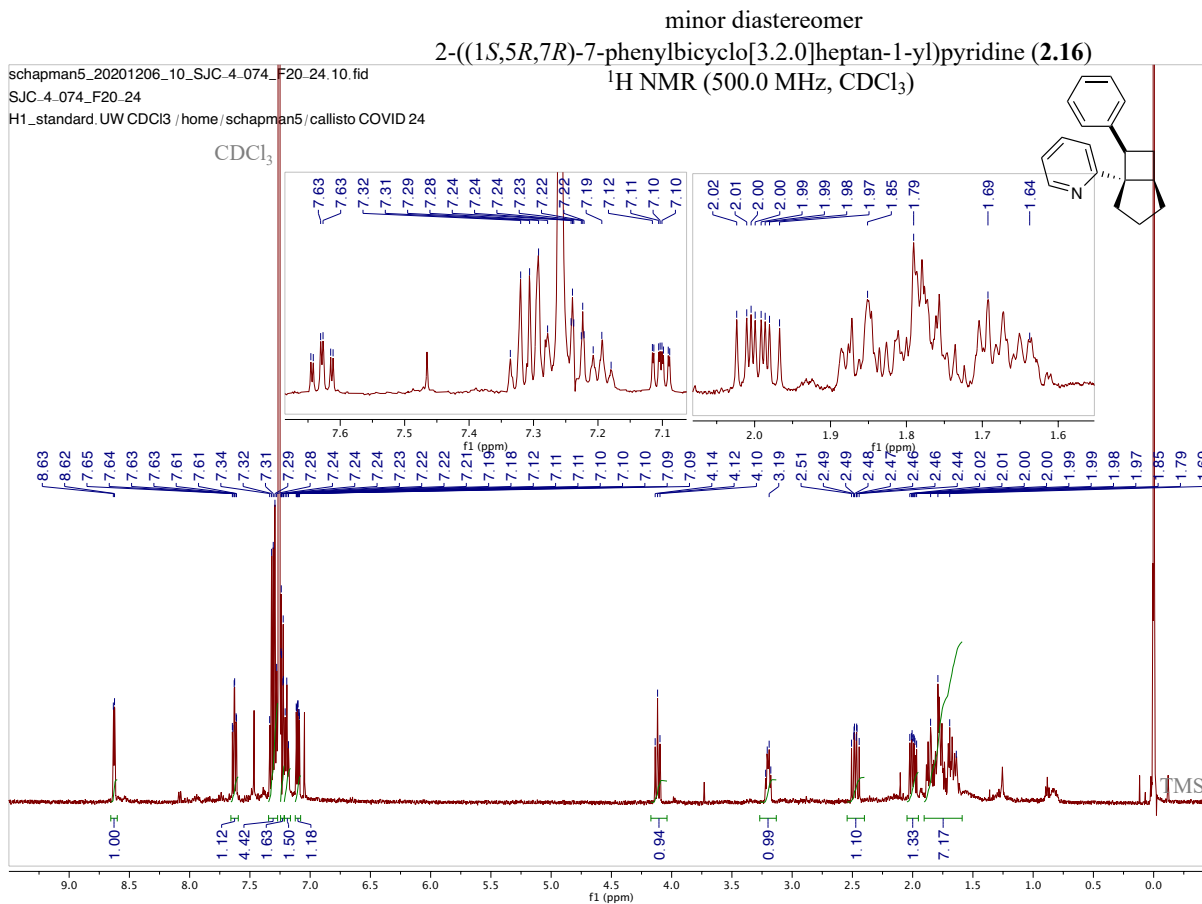
2-((1R,6R,7R)-7-phenyl-3-oxabicyclo[4.2.0]octan-6-yl)pyridine (**2.15**) $^{13}\text{C}$  NMR (125.7 MHz,  $\text{CDCl}_3$ )

schapman5\_2103311742\_11\_SJC.4-188\_F19.30.11.fid

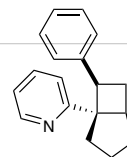
SJC.4-188\_F19.30

C13\_standard.UW CDCl3 /home/schapman5/callisto COVID 23

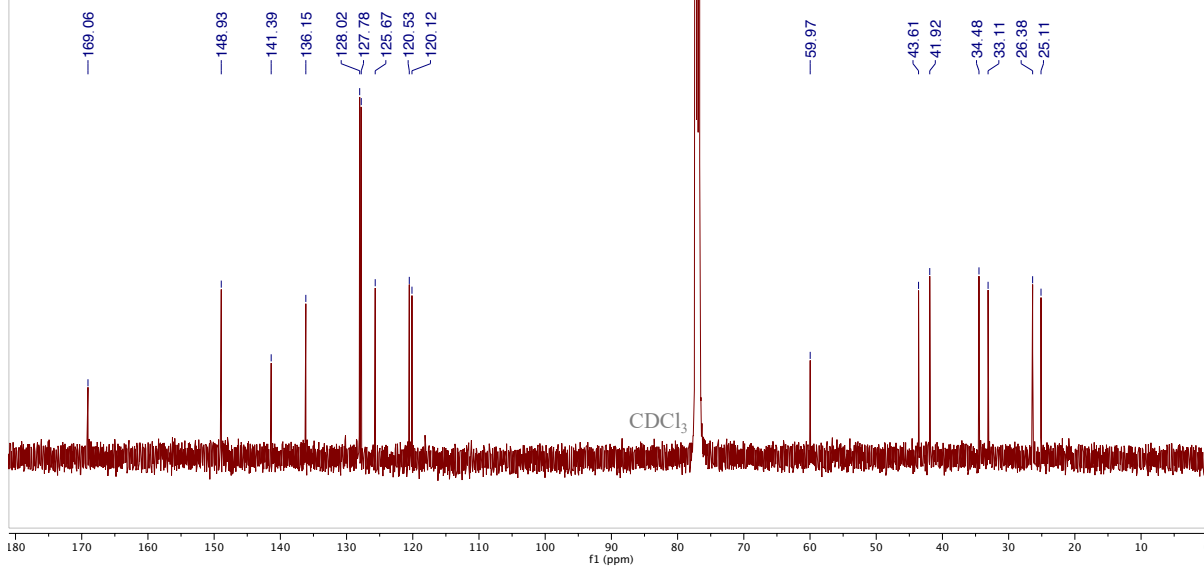


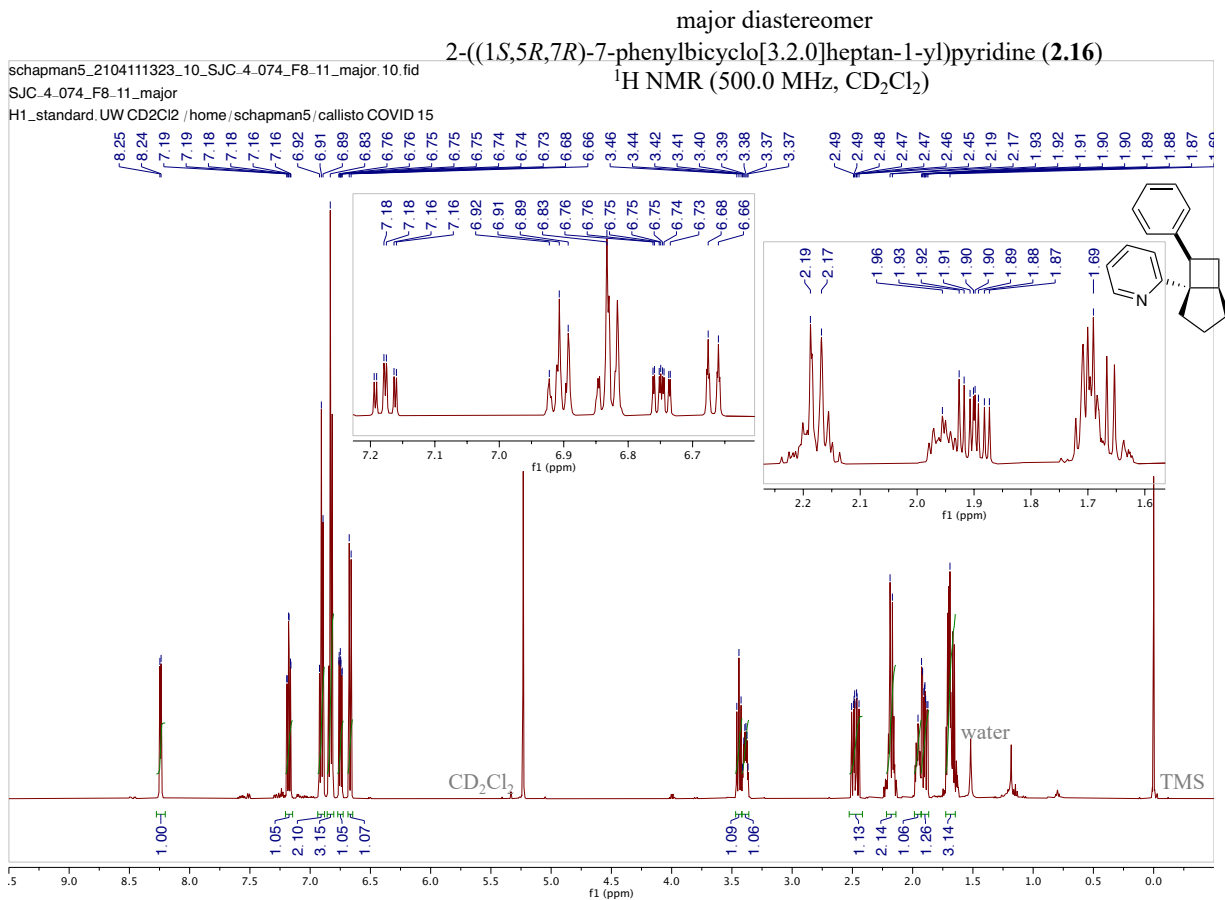


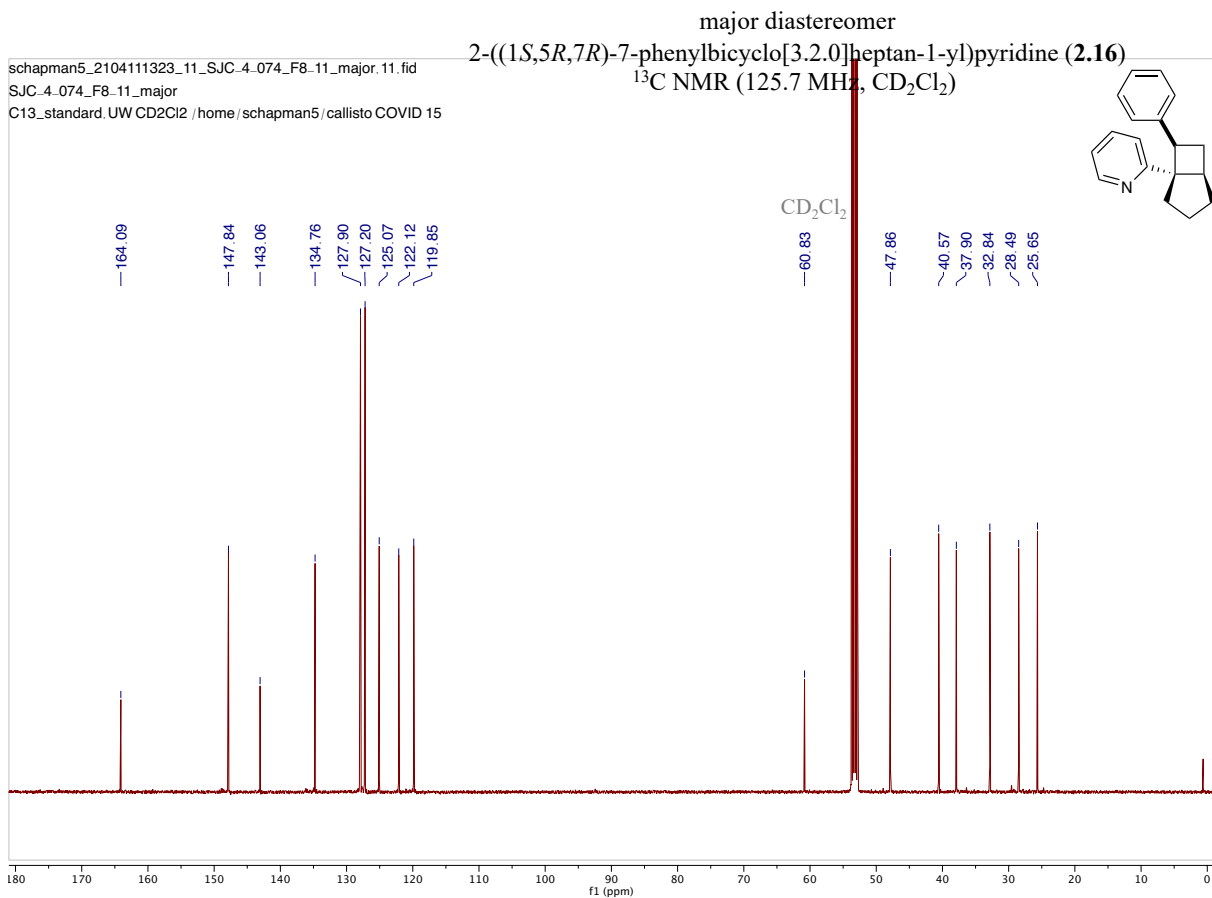
schapman5\_20201206\_11\_SJC.4.074\_F20.24.11.fid  
SJC.4.074\_F20.24  
C13\_standard.UW CDCI3 /home/schapman5/callisto COVID 24

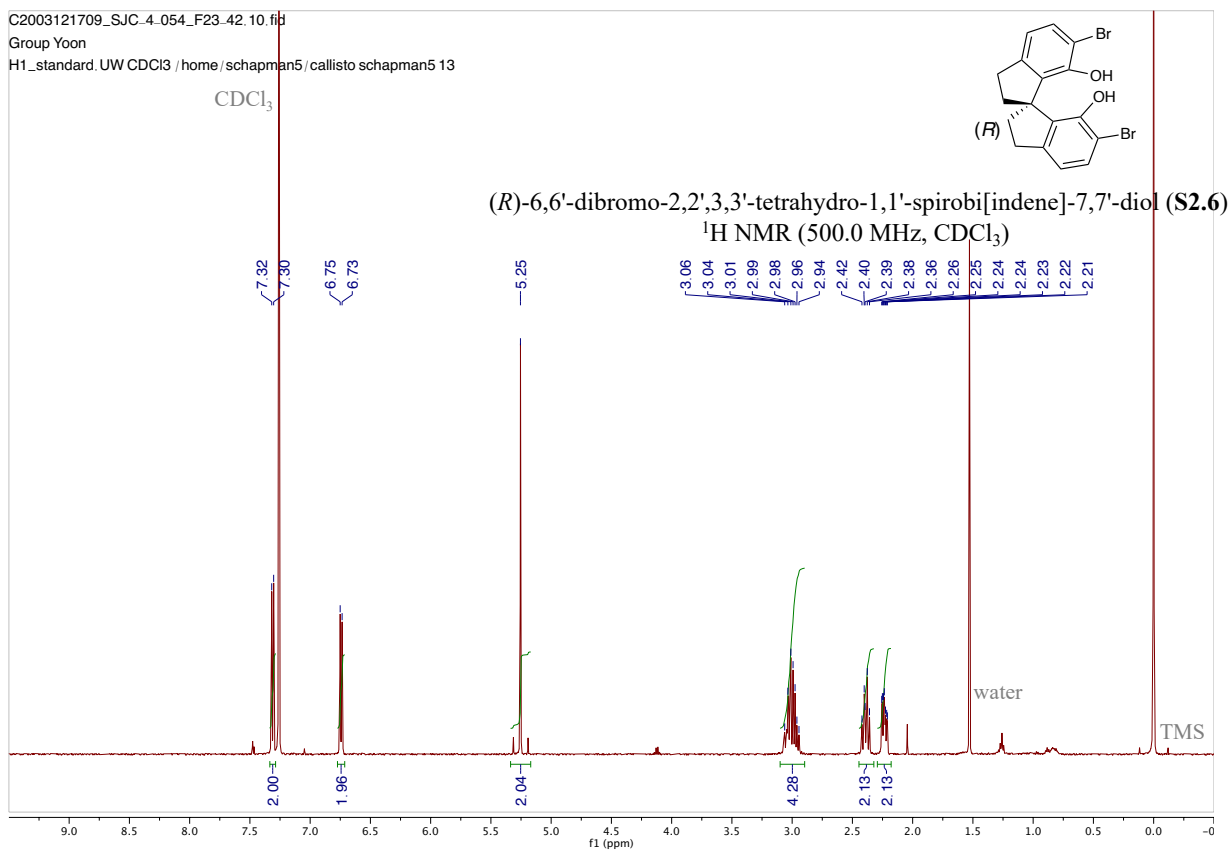


minor diastereomer  
2-((1*S*,5*R*,7*R*)-7-phenylbicyclo[3.2.0]heptan-1-yl)pyridine (**2.16**)  
 $^{13}\text{C}$  NMR (125.7 MHz,  $\text{CDCl}_3$ )





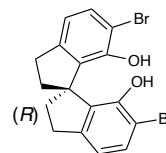




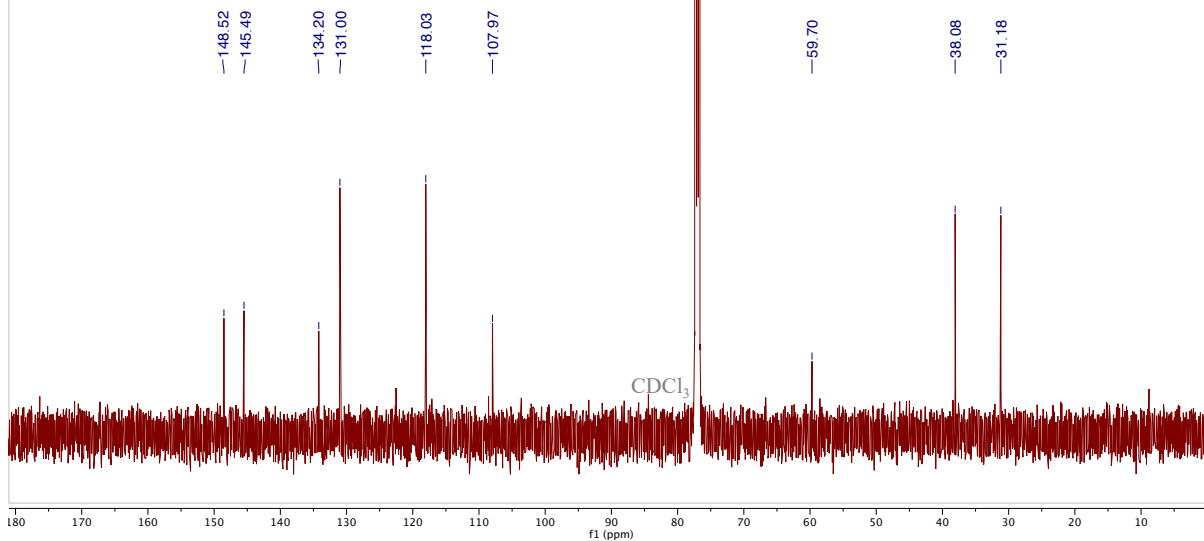
C2003121709\_SJC-4.054\_F23.42.11.fid

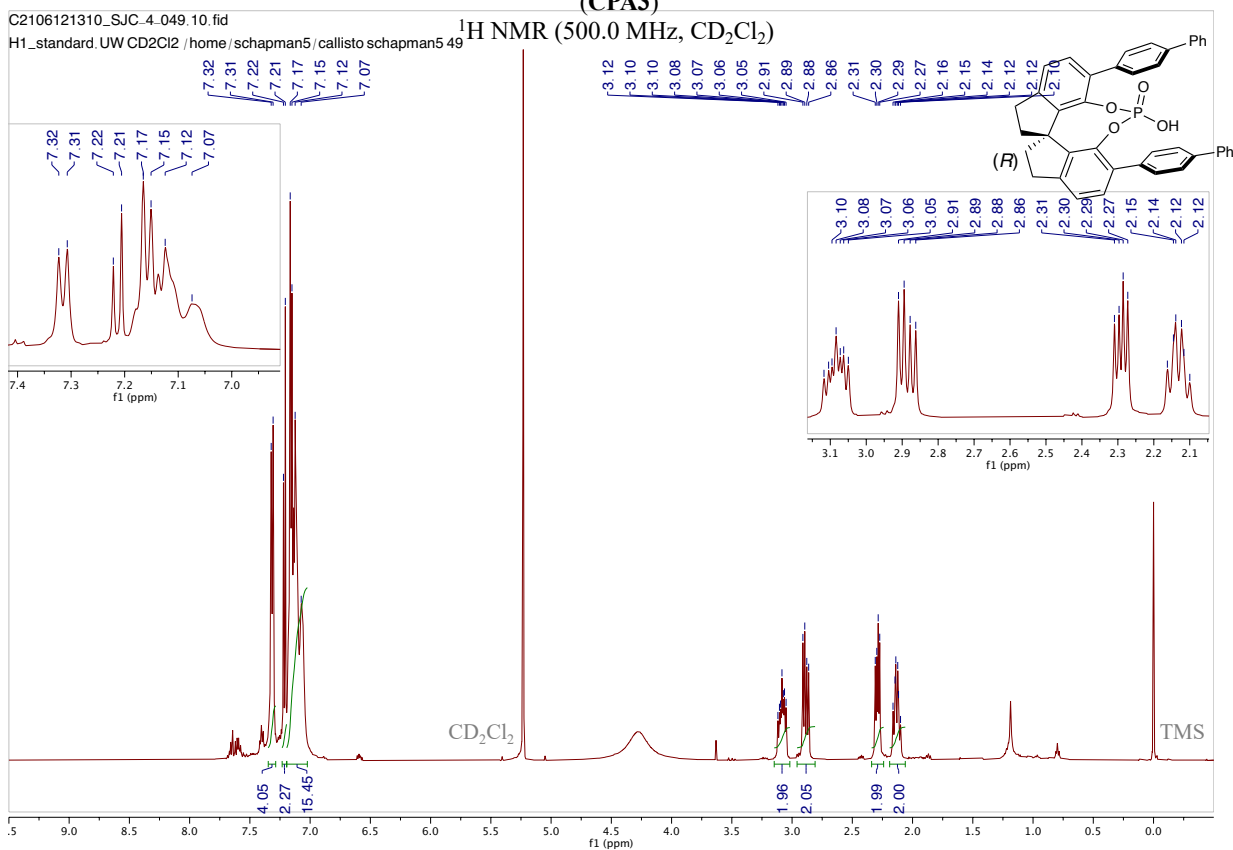
Group Yoon

C13\_H1dec.UW CDCl3 /home/schapman5/callisto schapman5 13



(R)-6,6'-dibromo-2,2',3,3'-tetrahydro-1,1'-spirobi[indene]-7,7'-diol (S2.6)  
<sup>13</sup>C NMR (125.7 MHz, CDCl<sub>3</sub>)



1,10-di([1,1'-biphenyl]-4-yl)-12-hydroxy-4,5,6,7-tetrahydroindeno[7,1-de:1',7'-fg][1,3,2]dioxaphosphocine 12-oxide  
(CPA3)

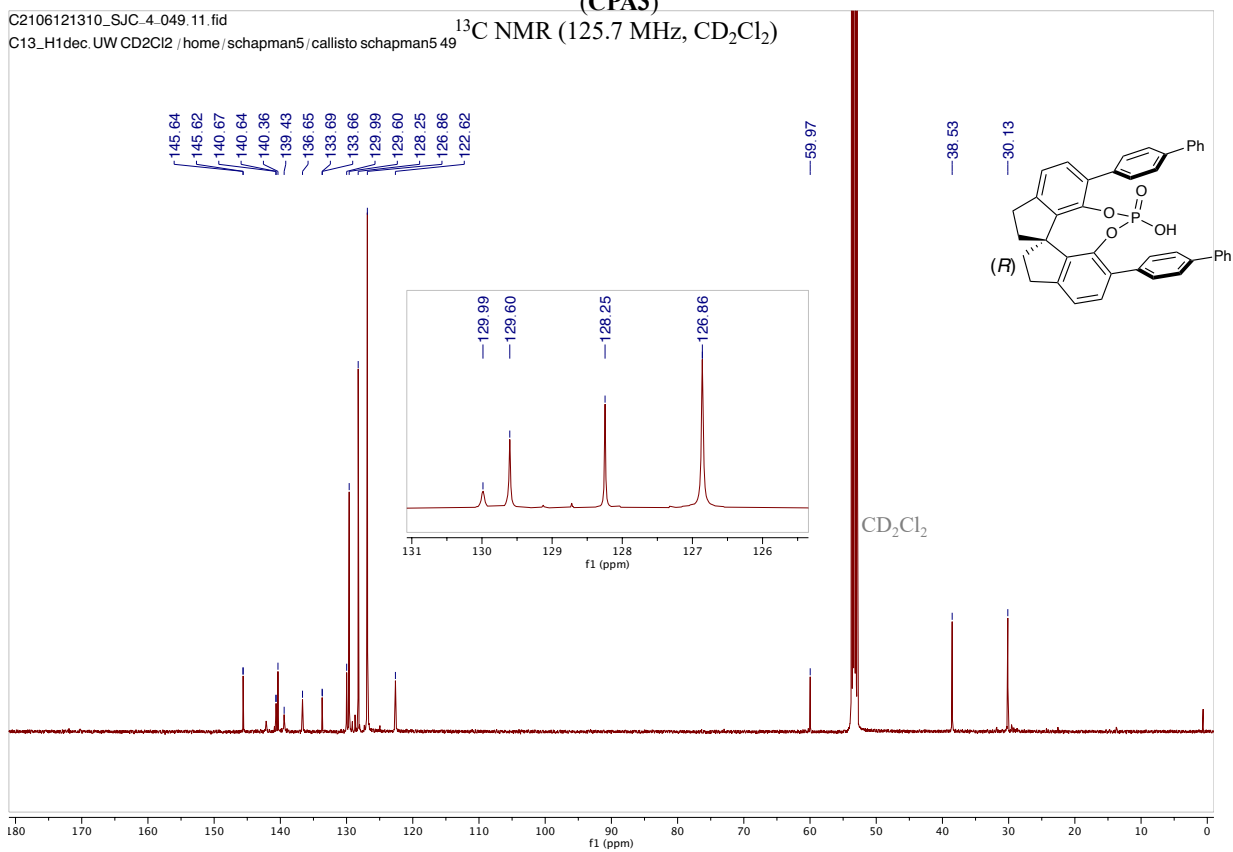


1,10-di([1,1'-biphenyl]-4-yl)-12-hydroxy-4,5,6,7-tetrahydroindeno[7,1-de:1',7'-fg][1,3,2]dioxaphosphocine 12-oxide  
(CPA3)

C2106121310\_SJC-4.049.11.fid

 $^{13}\text{C}$  NMR (125.7 MHz,  $\text{CD}_2\text{Cl}_2$ )

C13\_H1dec.UW CD2Cl2 / home / schapman5 / callisto schapman5 49

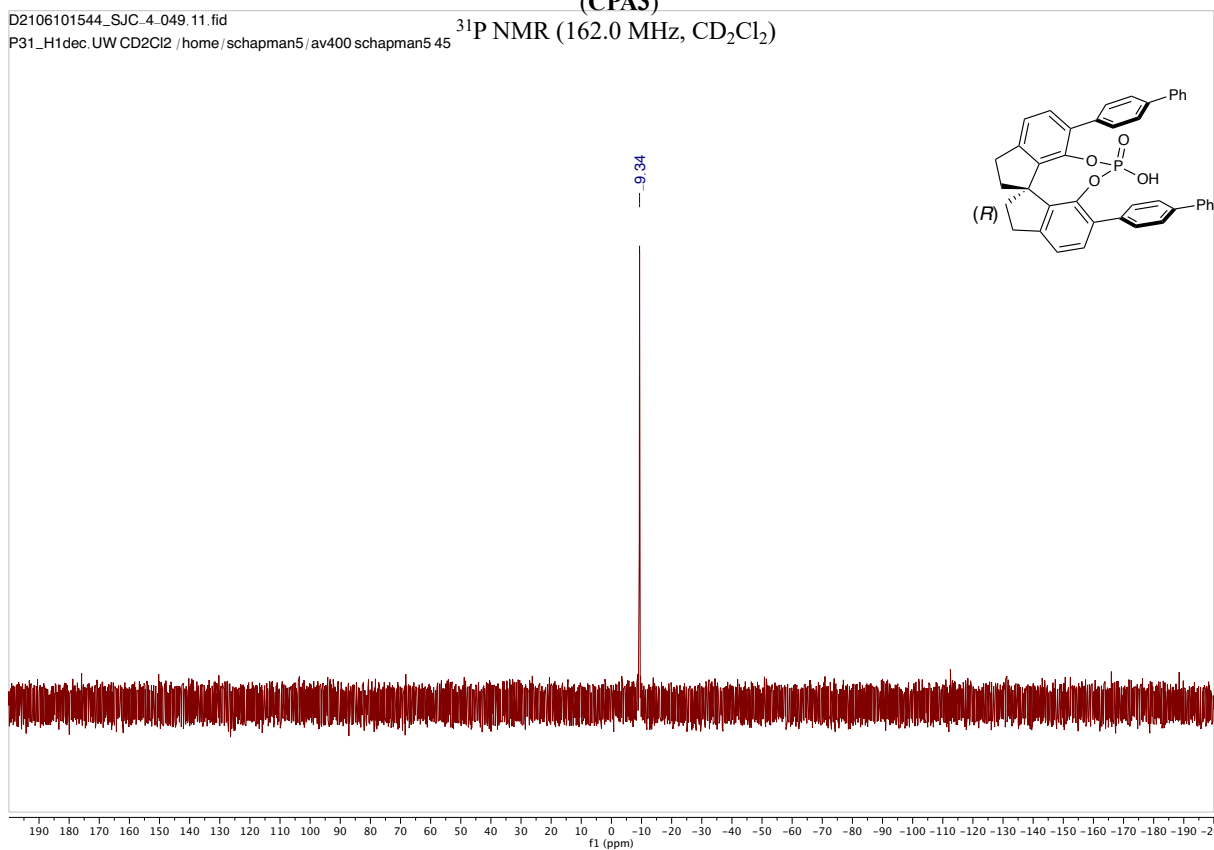


1,10-di([1,1'-biphenyl]-4-yl)-12-hydroxy-4,5,6,7-tetrahydroindeno[7,1-de:1',7'-fg][1,3,2]dioxaphosphocine 12-oxide  
(CPA3)

D2106101544\_SJC-4.049.11.fid

P31\_H1dec.UW CD2Cl2 /home/schapman5/av400 schapman5 45

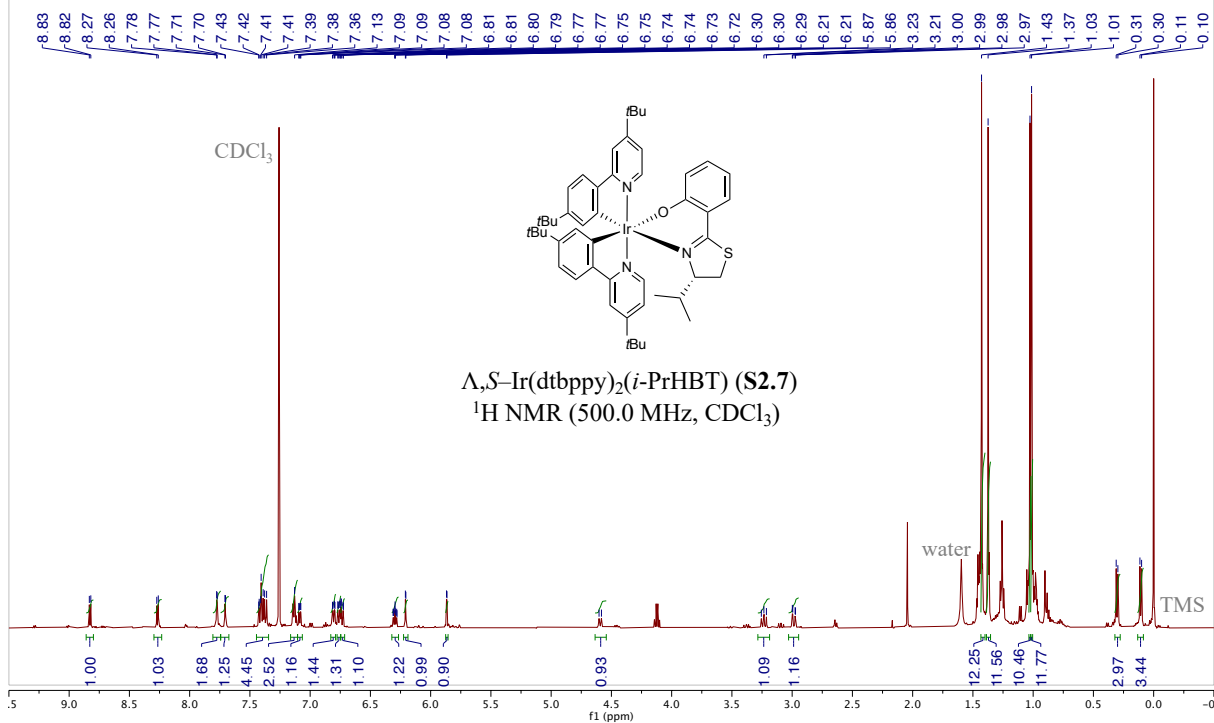
$^{31}\text{P}$  NMR (162.0 MHz,  $\text{CD}_2\text{Cl}_2$ )



schapman5\_2102201339\_10\_SJC.4.117\_F8-20.10.fid

SJC.4.117\_F8-20

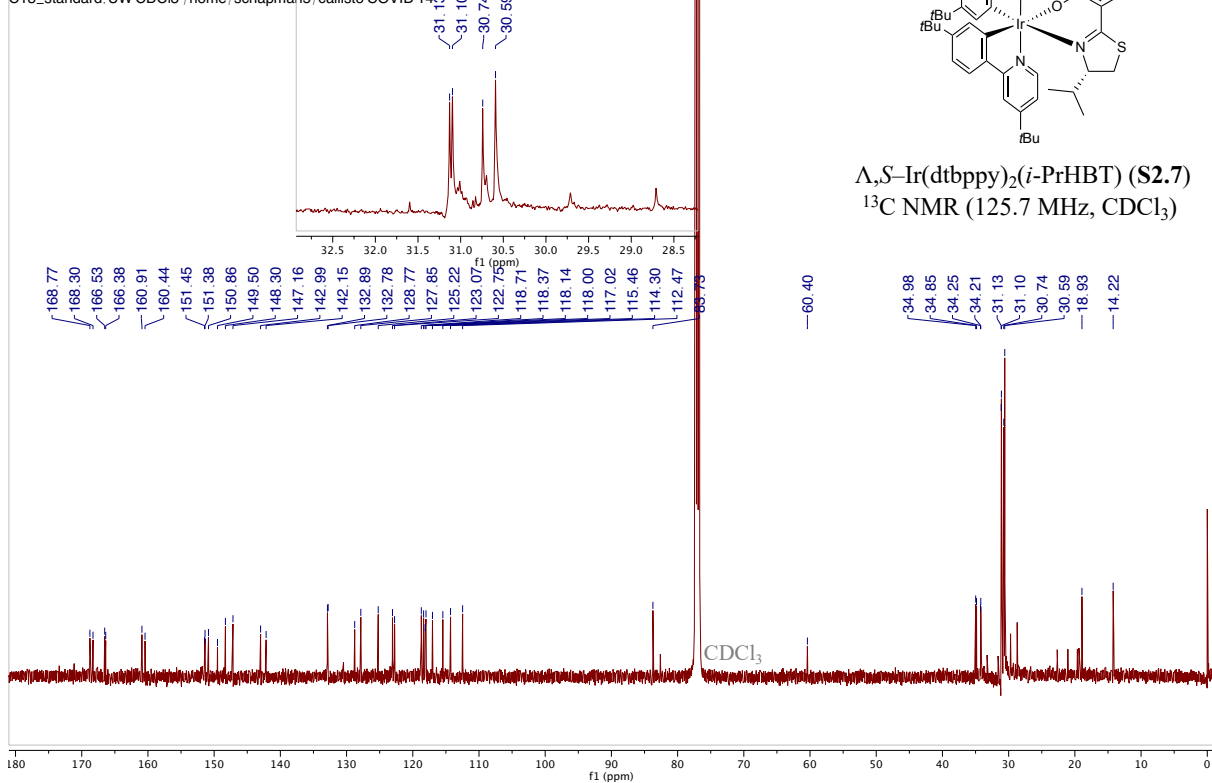
H1\_standard.UW CDCl3 /home/schapman5/callisto COVID 14

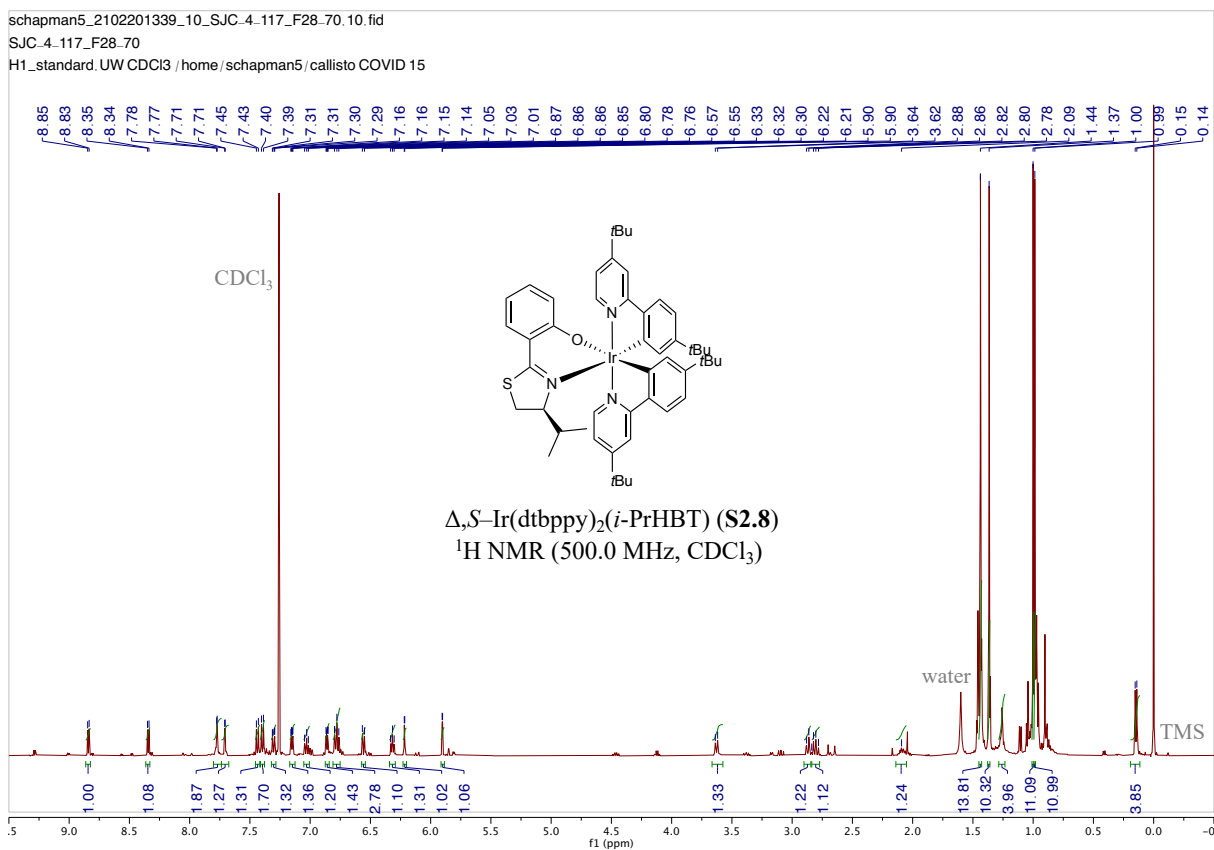


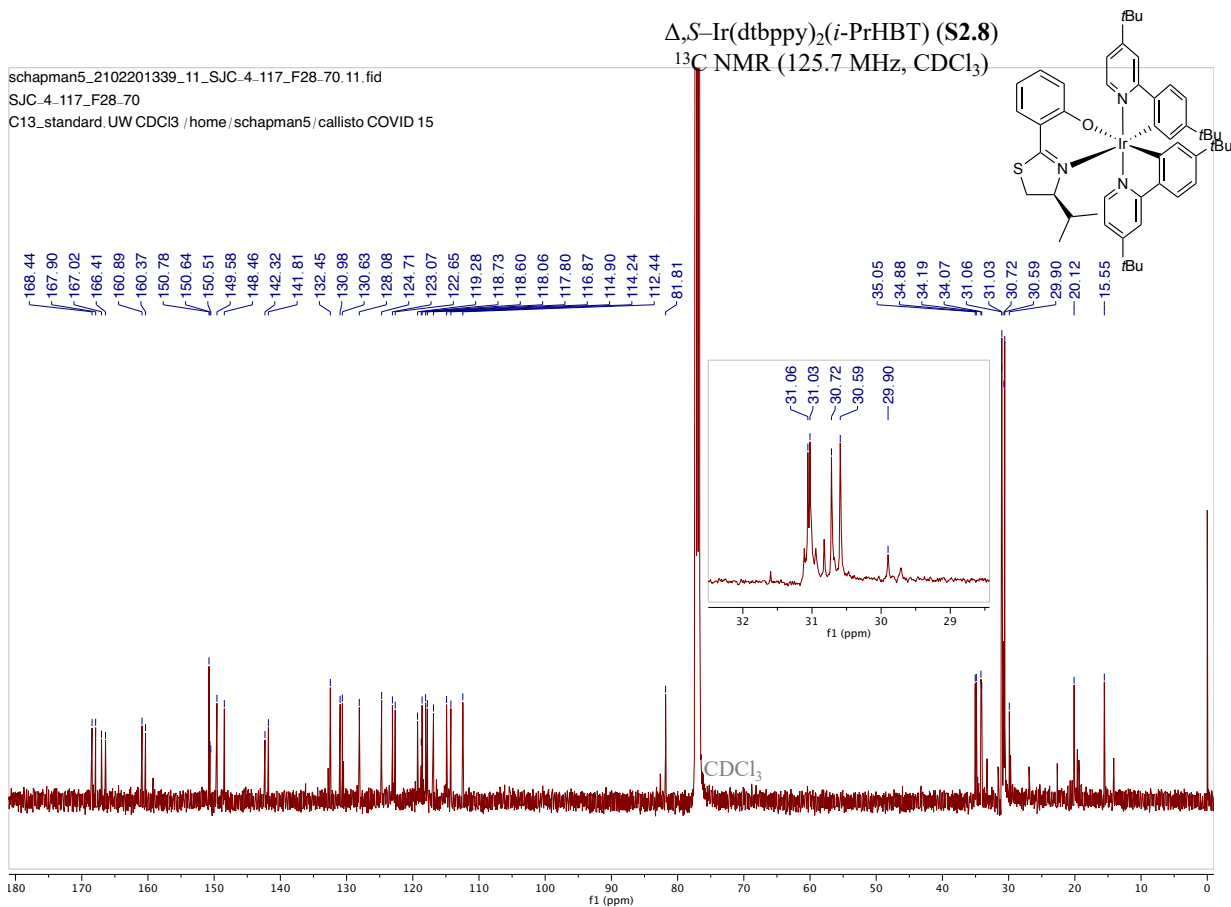
schapman5\_2102201339\_11\_SJC.4-117\_F8-20.11.fid

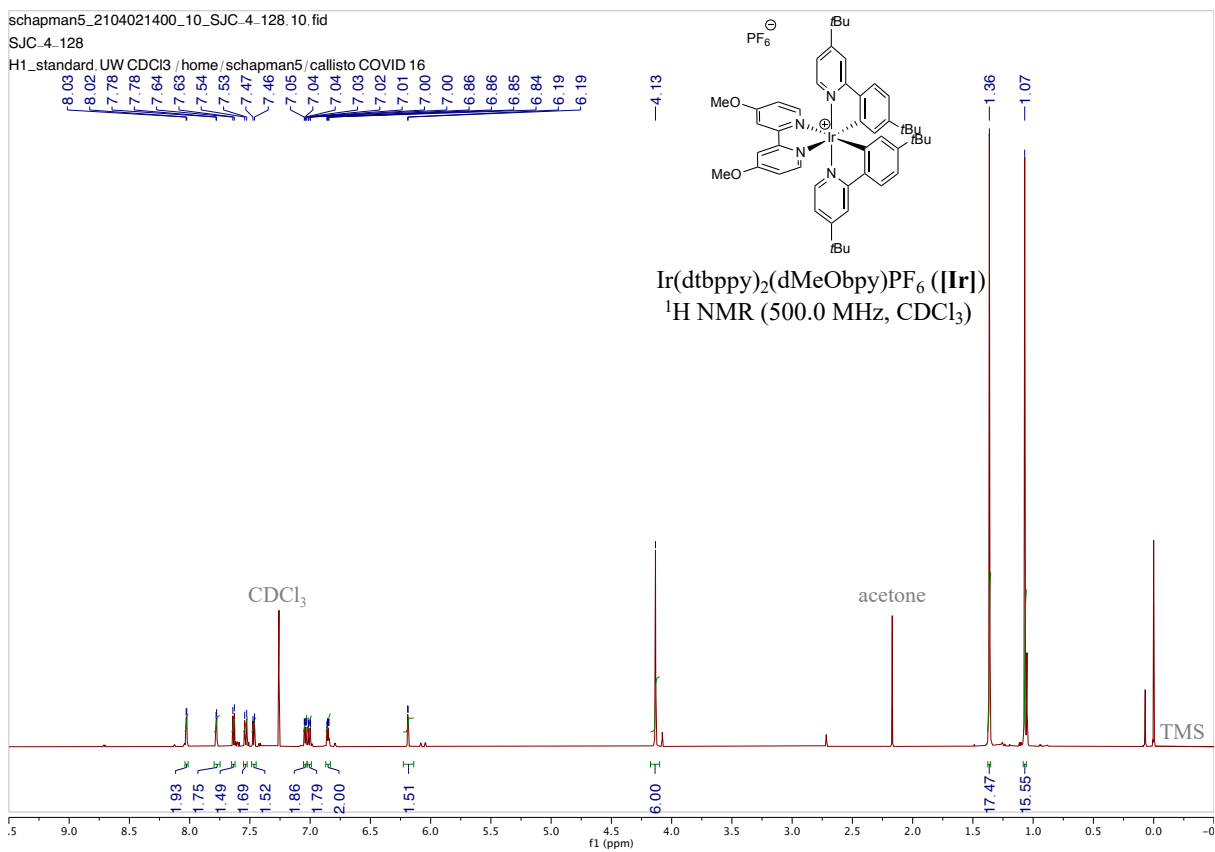
SJC.4-117\_F8.20

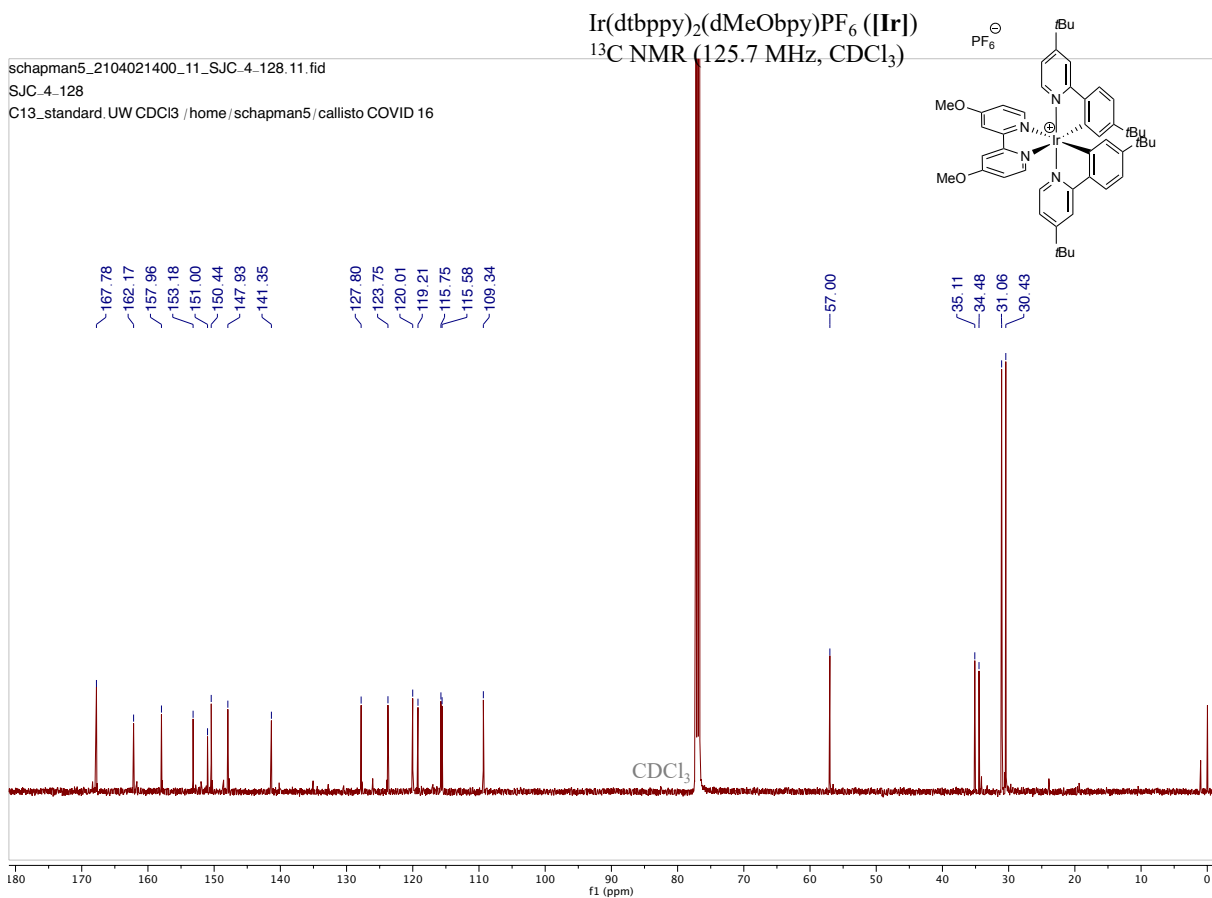
C13\_standard\_UW CDCI3 /home/schapman5/callisto COVID 14









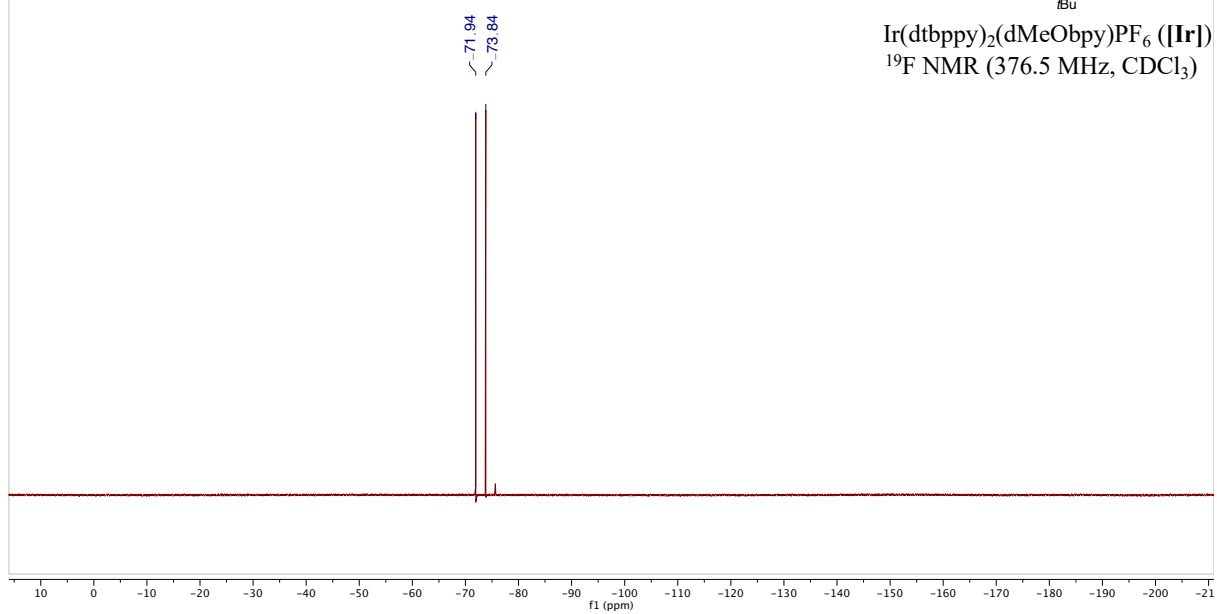




schapman5\_2104011542\_12\_SJC\_4-128.12.fid

SJC\_4-128

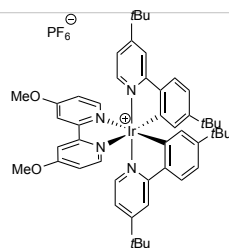
F19\_H1decoupled.UW CDCl3 / home/schapman5 / av400 COVID 44



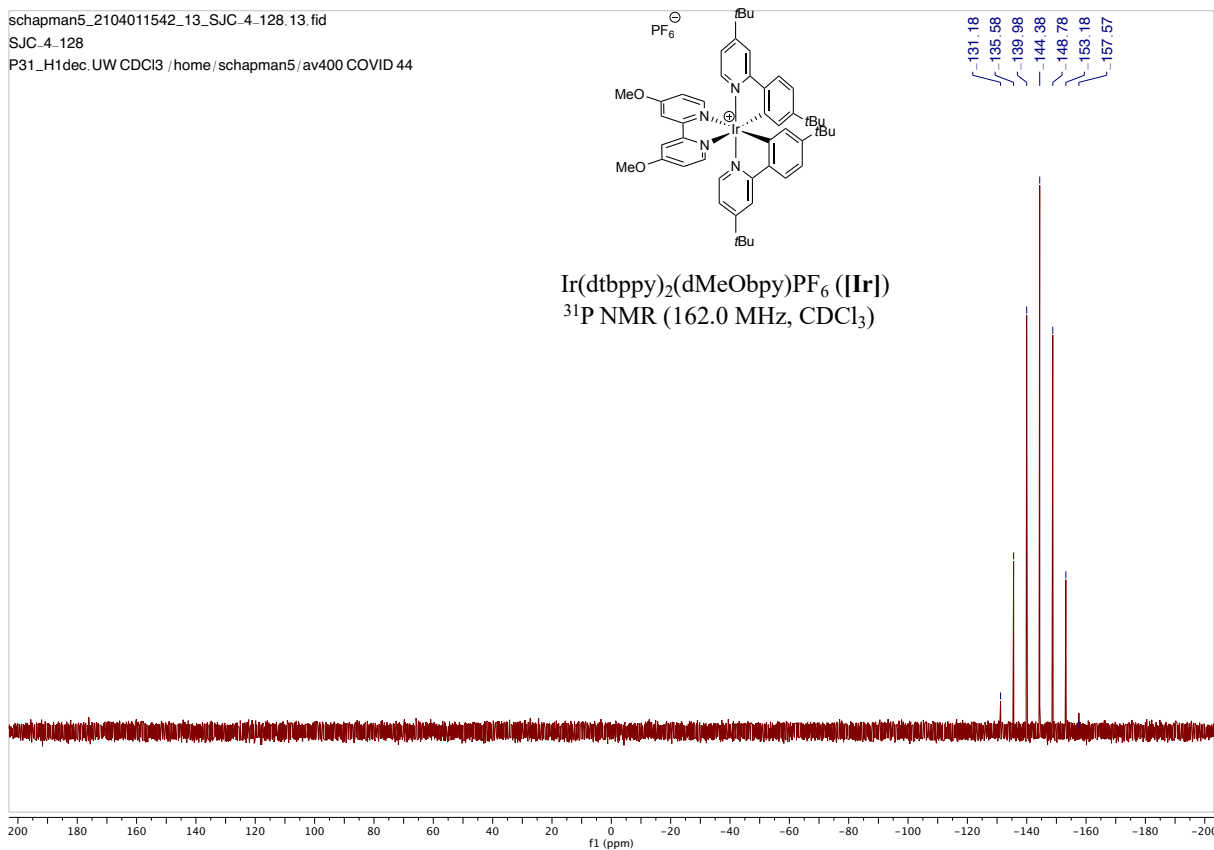
schapman5\_2104011542\_13\_SJC\_4-128.13.fid

SJC\_4-128

P31\_H1dec.UW CDCl3 /home/schapman5/av400 COVID 44



$\text{Ir}(\text{dtbbpy})_2(\text{dMeObpy})\text{PF}_6$  (**IIr**)  
 $^{31}\text{P}$  NMR (162.0 MHz,  $\text{CDCl}_3$ )

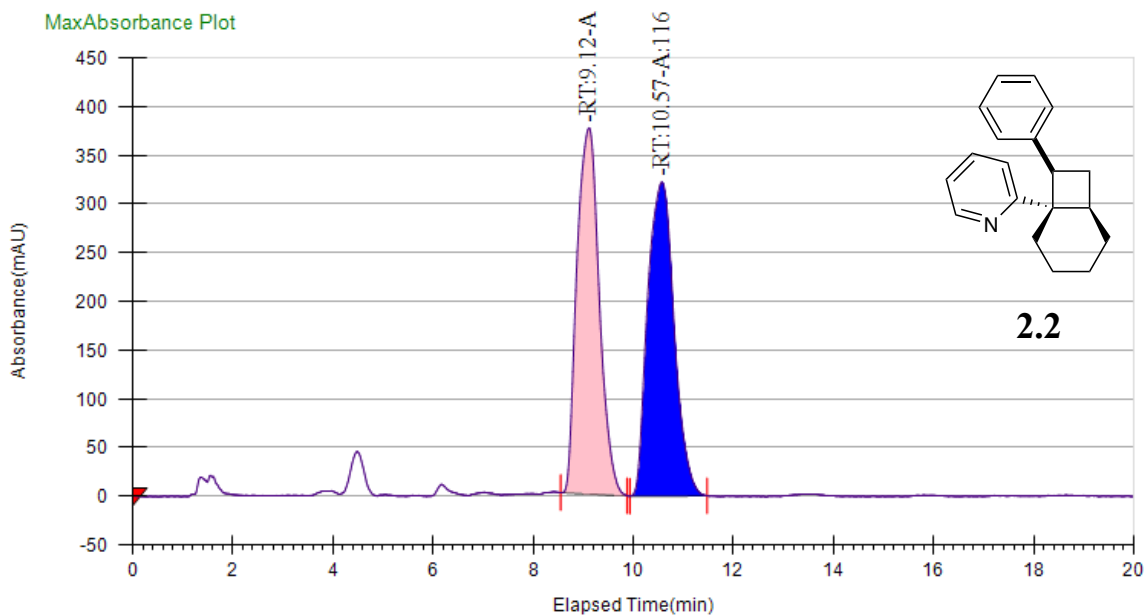


## 2.10.15. SFC Traces



Racemic

C:\Program Files (x86)\ChromScope IE\Investigator\Projects\Steven\DataFiles\3\_11\_2020\SJC-4-046\_F21\_rac ODH\_1.tta



## General Information

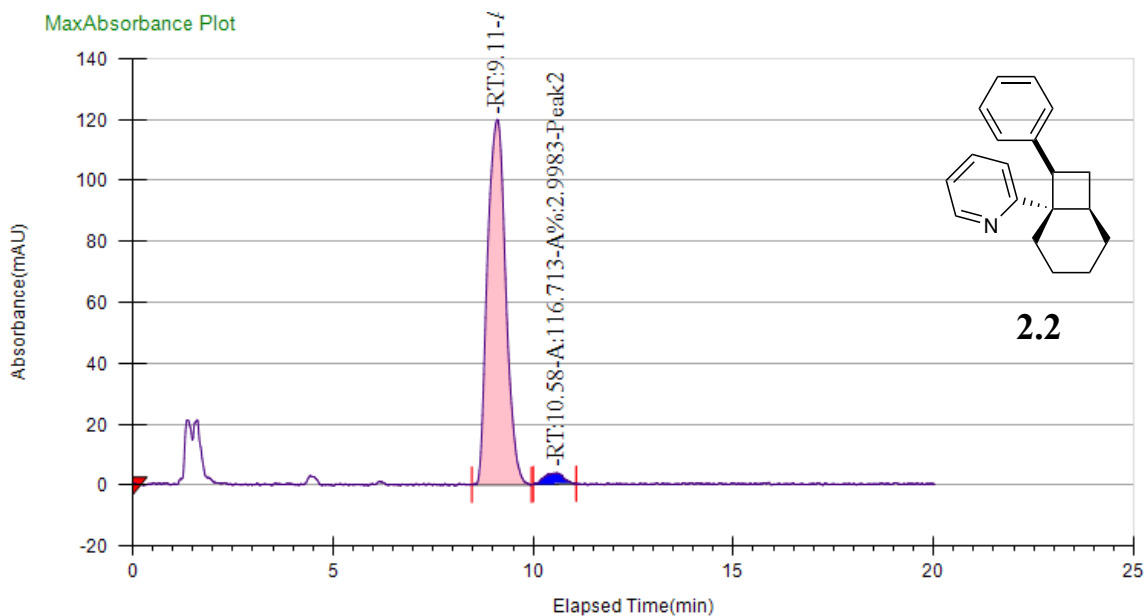
Log Author	Log Date	Report By	Report Date	Notes
Administrator	3/11/2020 2:05:12 PM	Administrator	3/11/2020	

## Run Information

Instrument Method	Inj. Vol.	Solvent	Column	Sample	Well Location	Temp. (C)	Flow (g/min)	% Modifier	Pressure (Bar)
5%IPA-20min	20 uL	IPA	Column 1	SJC-4-046_F21_rac	12F	35	3	5	100

## Peak Information

Peak No	% Area	Area	Ret. Time	Height	Cap. Factor
1	49.7424	11563.1224	9.12 min	375.897	0
2	50.2576	11682.8778	10.57 min	322.1577	0



### General Information

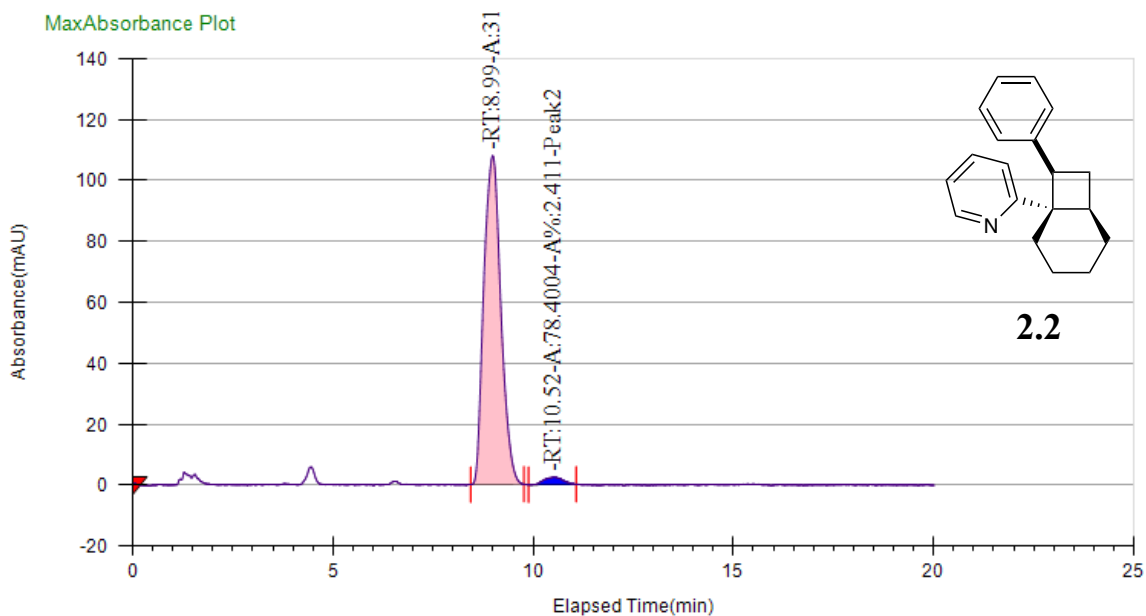
Log Author	Log Date	Report By	Report Date	Notes
Administrator	3/7/2020 4:56:09 PM	Administrator	3/7/2020	

### Run Information

Instrument Method	Inj. Vol.	Solvent	Column	Sample	Well Location	Temp. (C)	Flow (g/min)	% Modifier	Pressure (Bar)
5%IPA-20min	20 uL	IPA	Column 1	SJC-4-050_F22-25	12F	35	3	5	100

### Peak Information

Peak No	% Area	Area	Ret. Time	Height	Cap. Factor
1	97.0017	3775.8923	9.11 min	119.9921	0
2	2.9983	116.713	10.58 min	3.5593	0

**General Information**

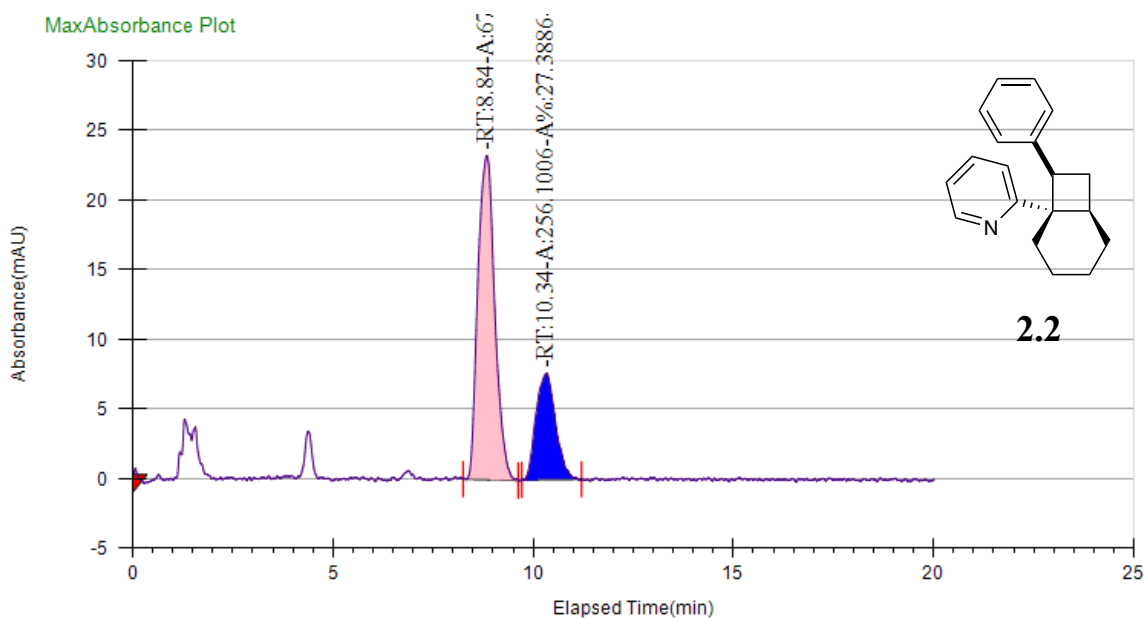
Log Author	Log Date	Report By	Report Date	Notes
Administrator	10/20/2020 2:41:18 PM	Administrator	10/20/2020	

**Run Information**

Instrument Method	Inj. Vol.	Solvent	Column	Sample	Well Location	Temp. (C)	Flow (g/min)	% Modifier	Pressure (Bar)
5%IPA-20min	20 uL	IPA	Column 1	SJC-4-113_F18-21	15F	35	3	5	100

**Peak Information**

Peak No	% Area	Area	Ret. Time	Height	Cap. Factor
1	97.589	3173.3187	8.99 min	107.9728	0
2	2.411	78.4004	10.52 min	2.4527	0



### General Information

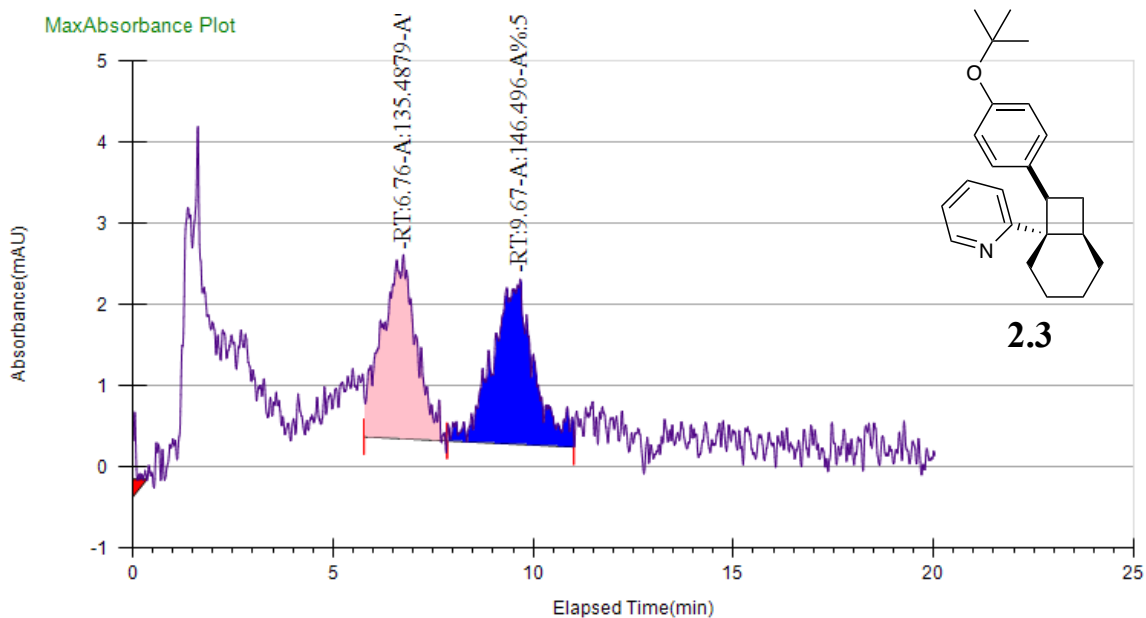
Log Author	Log Date	Report By	Report Date	Notes
Administrator	10/20/2020 1:56:51 PM	Administrator	10/20/2020	

### Run Information

Instrument Method	Inj. Vol.	Solvent	Column	Sample	Well Location	Temp. (C)	Flow (g/min)	% Modifier	Pressure (Bar)
5%IPA-20min	20 uL	IPA	Column 1	SJC-4-112_F19-22	14F	35	3	5	100

### Peak Information

Peak No	% Area	Area	Ret. Time	Height	Cap. Factor
1	72.6114	678.9616	8.84 min	23.2928	0
2	27.3886	256.1006	10.34 min	7.6325	0



### General Information

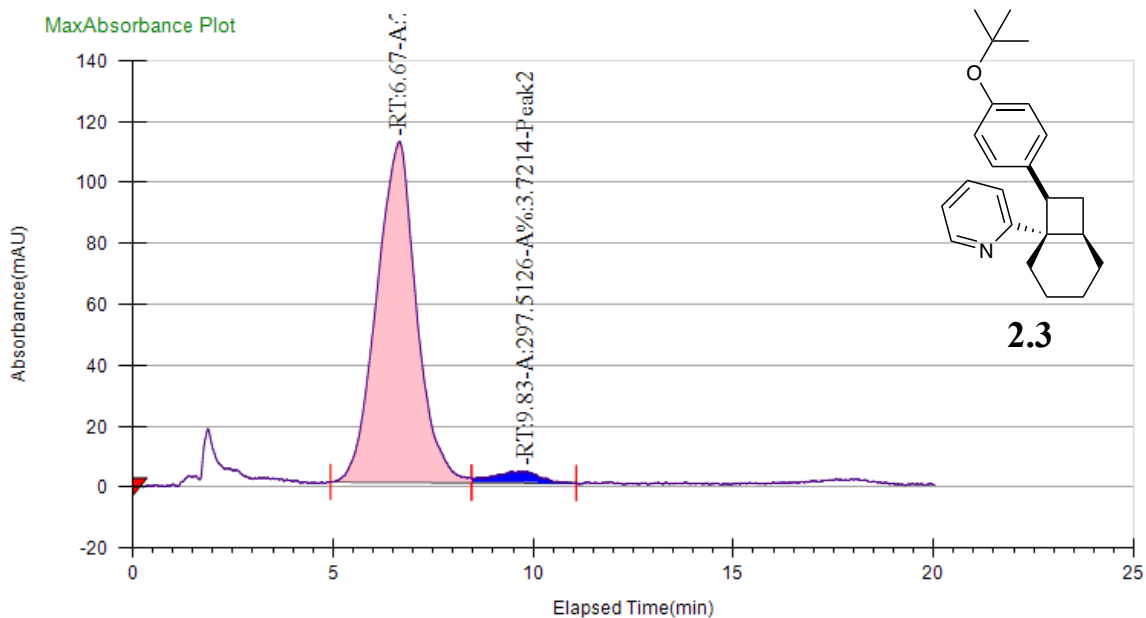
Log Author	Log Date	Report By	Report Date	Notes
Administrator	2/5/2021 11:36:09 AM	Administrator	2/5/2021	

### Run Information

Instrument Method	Inj. Vol.	Solvent	Column	Sample	Well Location	Temp. (C)	Flow (g/min)	% Modifier	Pressure (Bar)
5%MeOH-20min	20 uL	MeOH	Column 2	SJC-3-147_F18-21	16F	35	3	5	100

### Peak Information

Peak No	% Area	Area	Ret. Time	Height	Cap. Factor
1	48.0481	135.4879	6.76 min	2.2665	0
2	51.9519	146.496	9.67 min	2.0347	0



### General Information

Log Author	Log Date	Report By	Report Date	Notes
Administrator	2/5/2021 10:51:43 AM	Administrator	2/5/2021	

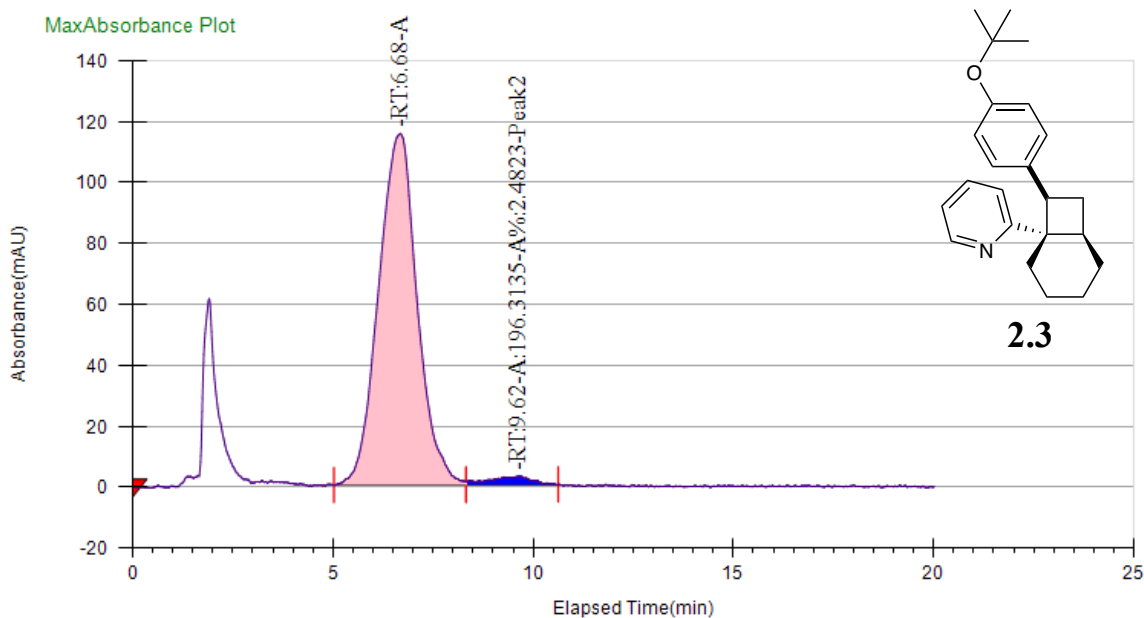
### Run Information

Instrument Method	Inj. Vol.	Solvent	Column	Sample	Well Location	Temp. (C)	Flow (g/min)	% Modifier	Pressure (Bar)
5%MeOH-20min	20 uL	MeOH	Column 2	SJC-4-056_F22-30	17F	35	3	5	100

### Peak Information

Peak No	% Area	Area	Ret. Time	Height	Cap. Factor
1	96.2786	7697.2328	6.67 min	111.9992	0
2	3.7214	297.5126	9.83 min	3.7643	0





### General Information

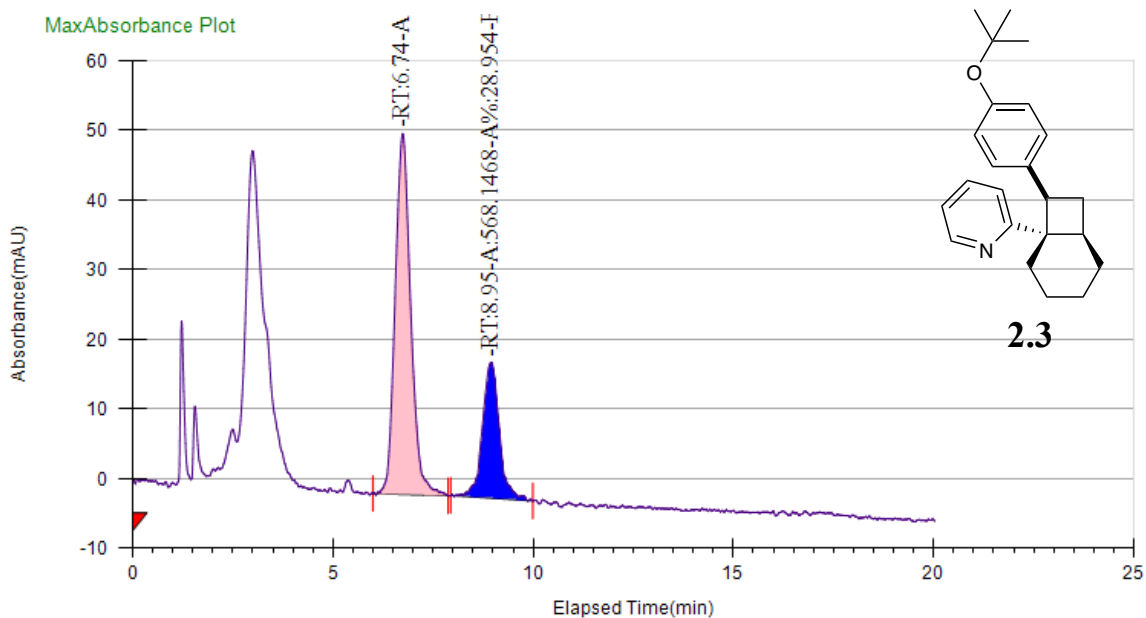
Log Author	Log Date	Report By	Report Date	Notes
Administrator	2/5/2021 11:13:56 AM	Administrator	2/5/2021	

### Run Information

Instrument Method	Inj. Vol.	Solvent	Column	Sample	Well Location	Temp. (C)	Flow (g/min)	% Modifier	Pressure (Bar)
5%MeOH-20min	20 uL	MeOH	Column 2	SJC-4-170_F24-31	18F	35	3	5	100

### Peak Information

Peak No	% Area	Area	Ret. Time	Height	Cap. Factor
1	97.5177	7712.2211	6.68 min	115.3874	0
2	2.4823	196.3135	9.62 min	2.7511	0



### General Information

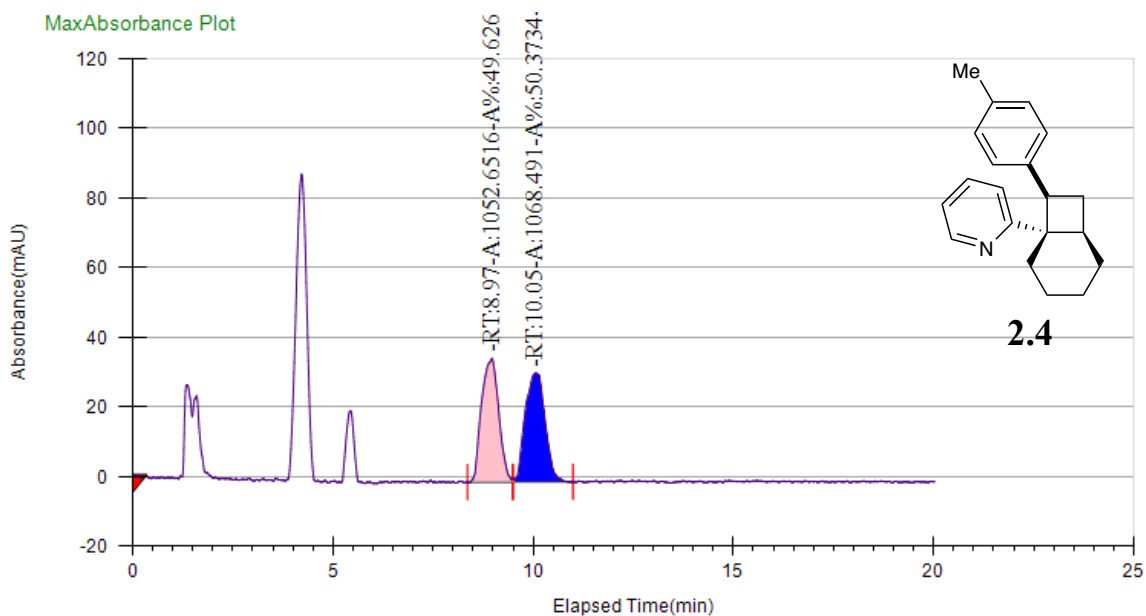
Log Author	Log Date	Report By	Report Date	Notes
Administrator	6/11/2021 11:24:12 AM	Administrator	6/11/2021	

### Run Information

Instrument Method	Inj. Vol.	Solvent	Column	Sample	Well Location	Temp. (C)	Flow (g/min)	% Modifier	Pressure (Bar)
5%MeOH-20min	20 uL	MeOH	Column 2	SJC-4-225_F27-32	14F	35	3	5	100

### Peak Information

Peak No	% Area	Area	Ret. Time	Height	Cap. Factor
1	71.046	1394.0923	6.74 min	51.872	0
2	28.954	568.1468	8.95 min	19.5351	0



### General Information

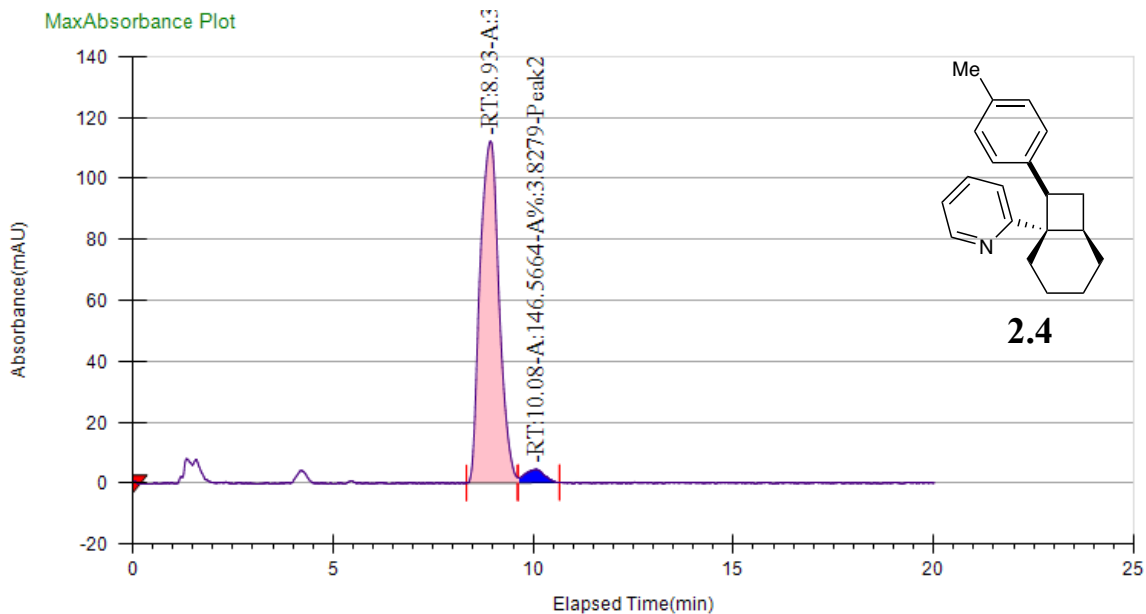
Log Author	Log Date	Report By	Report Date	Notes
Administrator	12/6/2020 11:11:36 AM	Administrator	12/6/2020	

### Run Information

Instrument Method	Inj. Vol.	Solvent	Column	Sample	Well Location	Temp. (C)	Flow (g/min)	% Modifier	Pressure (Bar)
5%IPA-20min	20 uL	IPA	Column 1	SJC-4-150_F21-23	12F	35	3	5	100

### Peak Information

Peak No	% Area	Area	Ret. Time	Height	Cap. Factor
1	49.6266	1052.6516	8.97 min	35.5638	8973.8667
2	50.3734	1068.491	10.05 min	31.1769	10048.85



### General Information

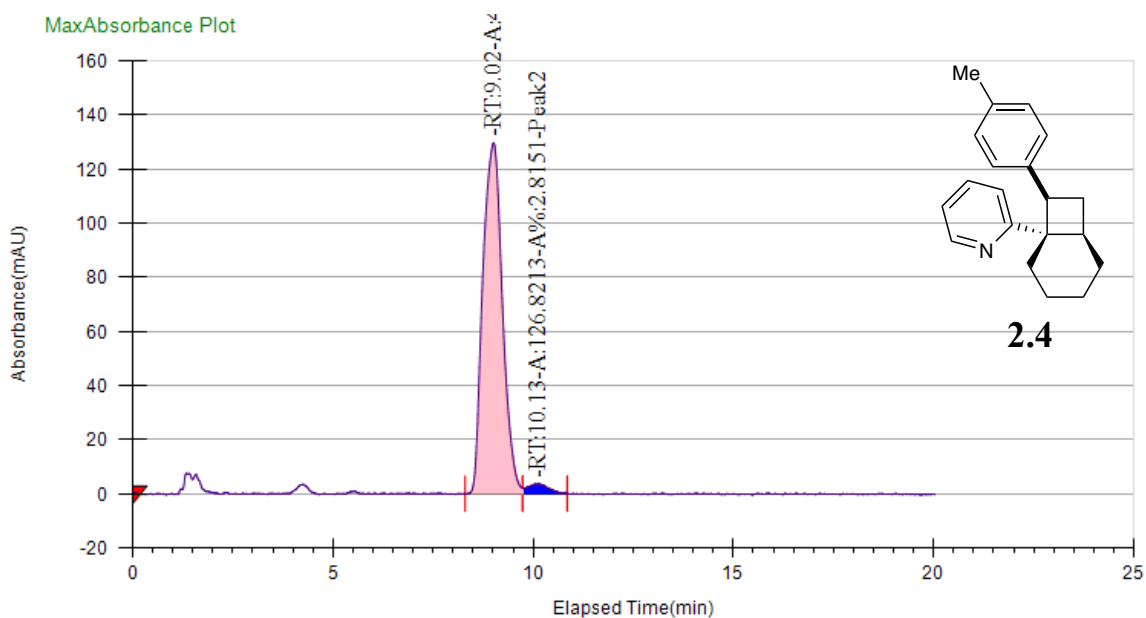
Log Author	Log Date	Report By	Report Date	Notes
Administrator	12/6/2020 2:24:29 PM	Administrator	12/6/2020	

### Run Information

Instrument Method	Inj. Vol.	Solvent	Column	Sample	Well Location	Temp. (C)	Flow (g/min)	% Modifier	Pressure (Bar)
5%IPA-20min	20 uL	IPA	Column 1	SJC-4-149_F24-26	13F	35	3	5	100

### Peak Information

Peak No	% Area	Area	Ret. Time	Height	Cap. Factor
1	96.1721	3682.3345	8.93 min	112.2426	0
2	3.8279	146.5664	10.08 min	4.2981	0



### General Information

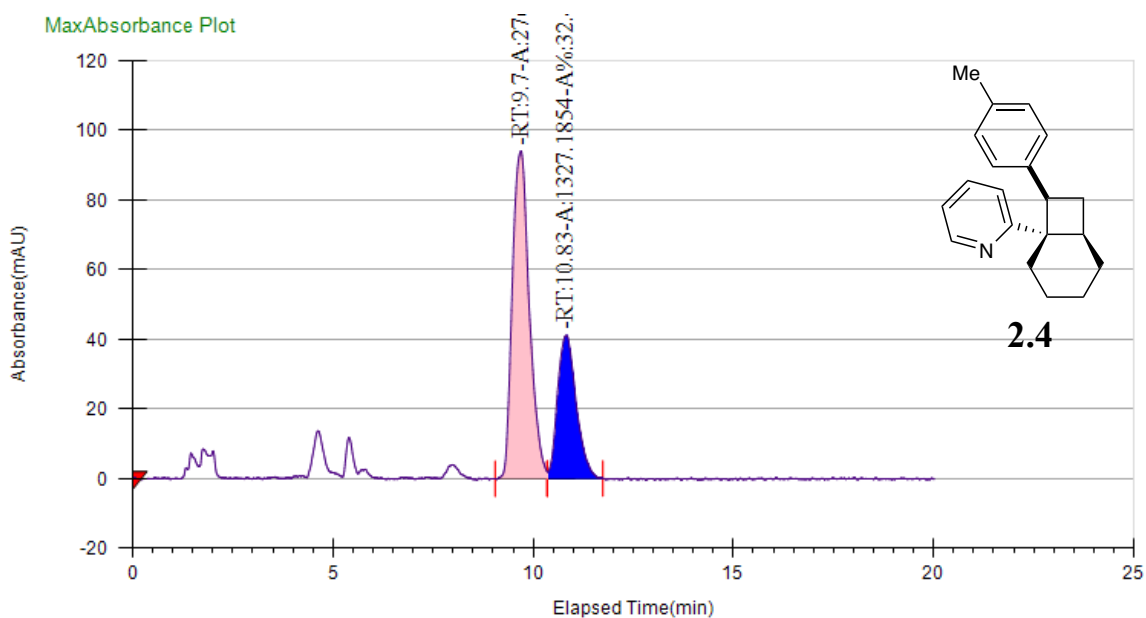
Log Author	Log Date	Report By	Report Date	Notes
Administrator	12/6/2020 3:08:55 PM	Administrator	12/6/2020	

### Run Information

Instrument Method	Inj. Vol.	Solvent	Column	Sample	Well Location	Temp. (C)	Flow (g/min)	% Modifier	Pressure (Bar)
5%IPA-20min	20 uL	IPA	Column 1	SJC-4-152_F26-28	14F	35	3	5	100

### Peak Information

Peak No	% Area	Area	Ret. Time	Height	Cap. Factor
1	97.1849	4378.2208	9.02 min	129.6945	0
2	2.8151	126.8213	10.13 min	3.5385	0



### General Information

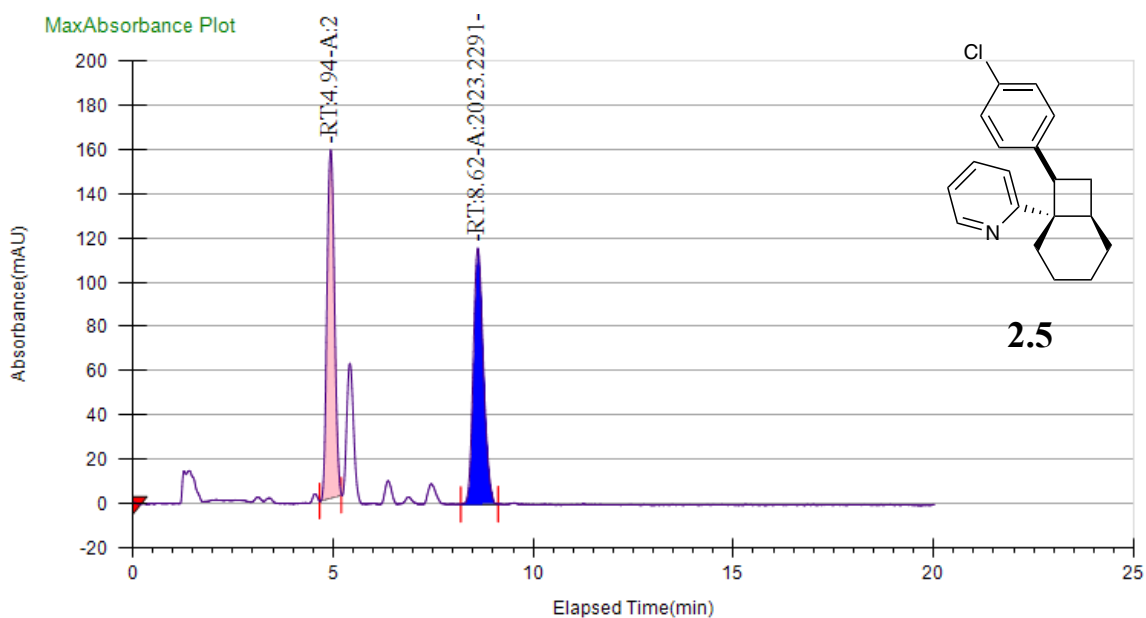
Log Author	Log Date	Report By	Report Date	Notes
Administrator	6/2/2021 5:59:22 PM	Administrator	6/2/2021	

### Run Information

Instrument Method	Inj. Vol.	Solvent	Column	Sample	Well Location	Temp. (C)	Flow (g/min)	% Modifier	Pressure (Bar)
5%IPA-20min	10 uL	IPA	Column 1	SJC-4-223_F21-23	12F	35	3	5	100

### Peak Information

Peak No	% Area	Area	Ret. Time	Height	Cap. Factor
1	67.5429	2761.8557	9.7 min	94.2464	0
2	32.4571	1327.1854	10.83 min	41.1348	0



### General Information

Log Author	Log Date	Report By	Report Date	Notes
Administrator	8/25/2020 12:31:26 PM	Administrator	8/25/2020	

### Run Information

Instrument Method	Inj. Vol.	Solvent	Column	Sample	Well Location	Temp. (C)	Flow (g/min)	% Modifier	Pressure (Bar)
10%MeOH-20min	20 uL	MeOH	Column 3	SJC-4-067_F22_rac	12F	35	3	10	100

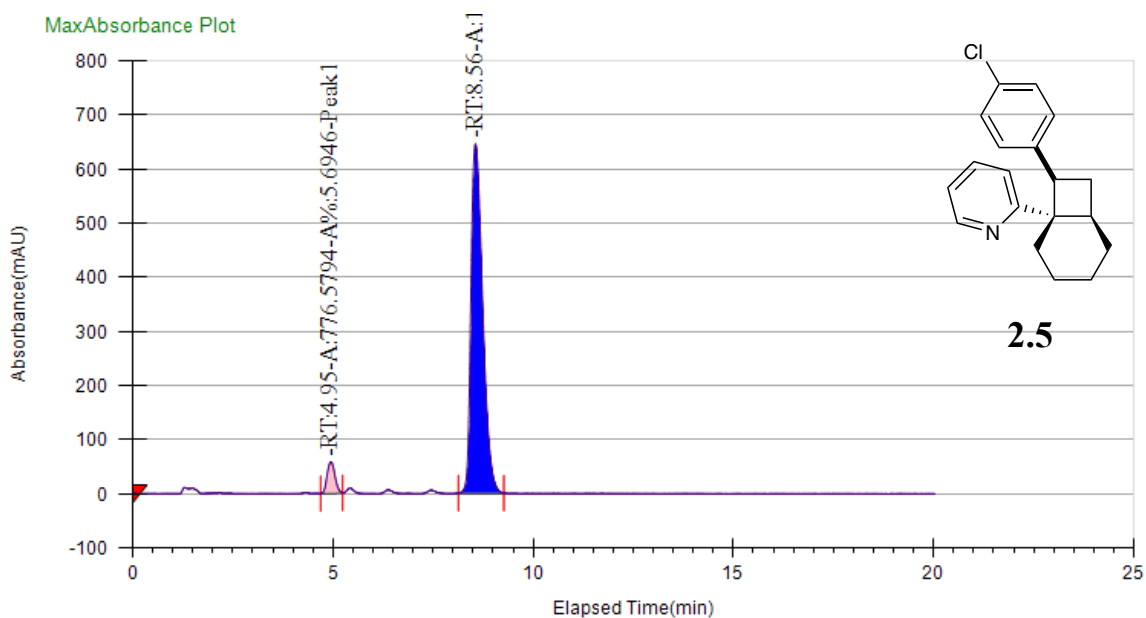
### Peak Information

Peak No	% Area	Area	Ret. Time	Height	Cap. Factor
1	49.9022	2015.3267	4.94 min	157.2368	0
2	50.0978	2023.2291	8.62 min	115.6883	0



## Enantioenriched – using racemic [Ir] – 89% ee

C:\Program Files (x86)\ChromScope IE\Investigator\Projects\Steven\DataFiles\8\_25\_2020\SJC-4-070\_F23-26\_20uL\_OJH\_1.tta



### General Information

Log Author	Log Date	Report By	Report Date	Notes
Administrator	8/25/2020 2:00:17 PM	Administrator	8/25/2020	

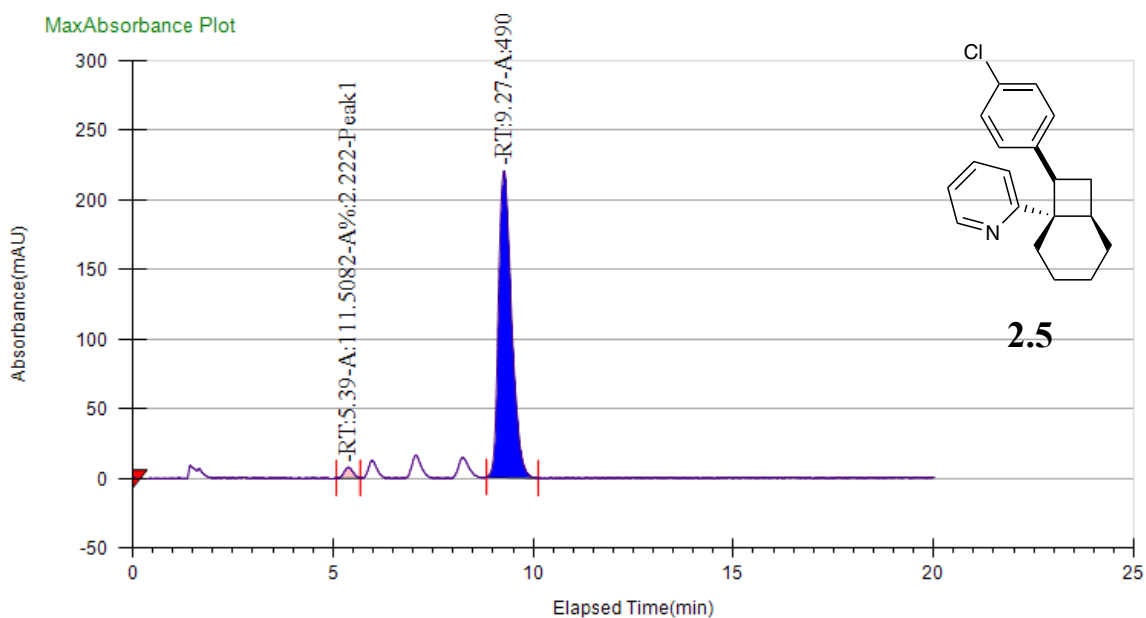
### Run Information

Instrument Method	Inj. Vol.	Solvent	Column	Sample	Well Location	Temp. (C)	Flow (g/min)	% Modifier	Pressure (Bar)
10%MeOH-20min	20 uL	MeOH	Column 3	SJC-4-070_F23-26	13F	35	3	10	100

### Peak Information

Peak No	% Area	Area	Ret. Time	Height	Cap. Factor
1	5.6946	776.5794	4.95 min	58.3312	0
2	94.3054	12860.4796	8.56 min	645.3933	0





### General Information

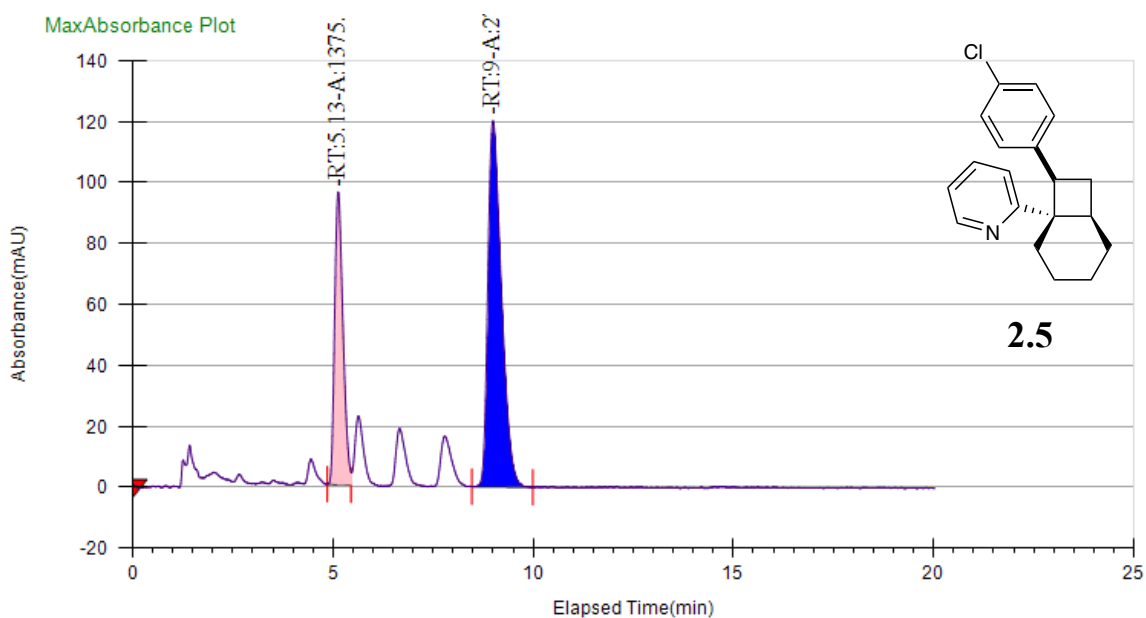
Log Author	Log Date	Report By	Report Date	Notes
Administrator	11/19/2020 1:16:49 PM	Administrator	11/19/2020	

### Run Information

Instrument Method	Inj. Vol.	Solvent	Column	Sample	Well Location	Temp. (C)	Flow (g/min)	% Modifier	Pressure (Bar)
10%MeOH-20min	20 uL	MeOH	Column 3	SJC-4-141_F27-30	12F	35	3	10	100

### Peak Information

Peak No	% Area	Area	Ret. Time	Height	Cap. Factor
1	2.222	111.5082	5.39 min	7.4753	0
2	97.778	4906.8675	9.27 min	220.2536	0



### General Information

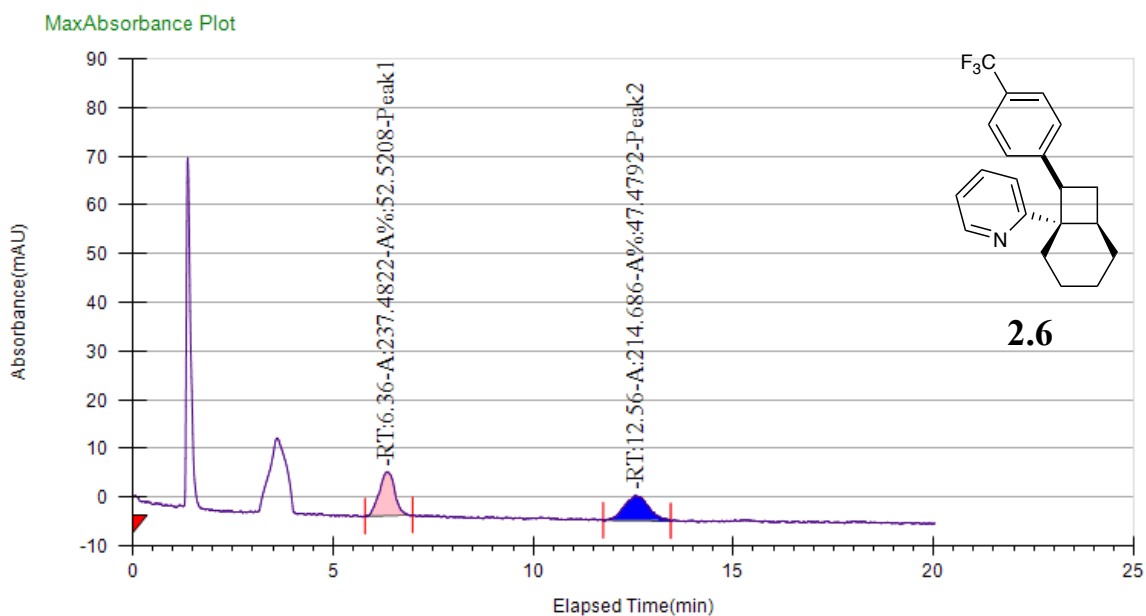
Log Author	Log Date	Report By	Report Date	Notes
Administrator	6/24/2021 10:39:59 AM	Administrator	6/24/2021	

### Run Information

Instrument Method	Inj. Vol.	Solvent	Column	Sample	Well Location	Temp. (C)	Flow (g/min)	% Modifier	Pressure (Bar)
10%MeOH-20min	20 $\mu$ L	MeOH	Column 3	SJC-4-238_F31-32	12F	35	3	10	100

### Peak Information

Peak No	% Area	Area	Ret. Time	Height	Cap. Factor
1	33.0743	1375.6532	5.13 min	96.1195	0
2	66.9257	2783.6294	9 min	120.2062	0



### General Information

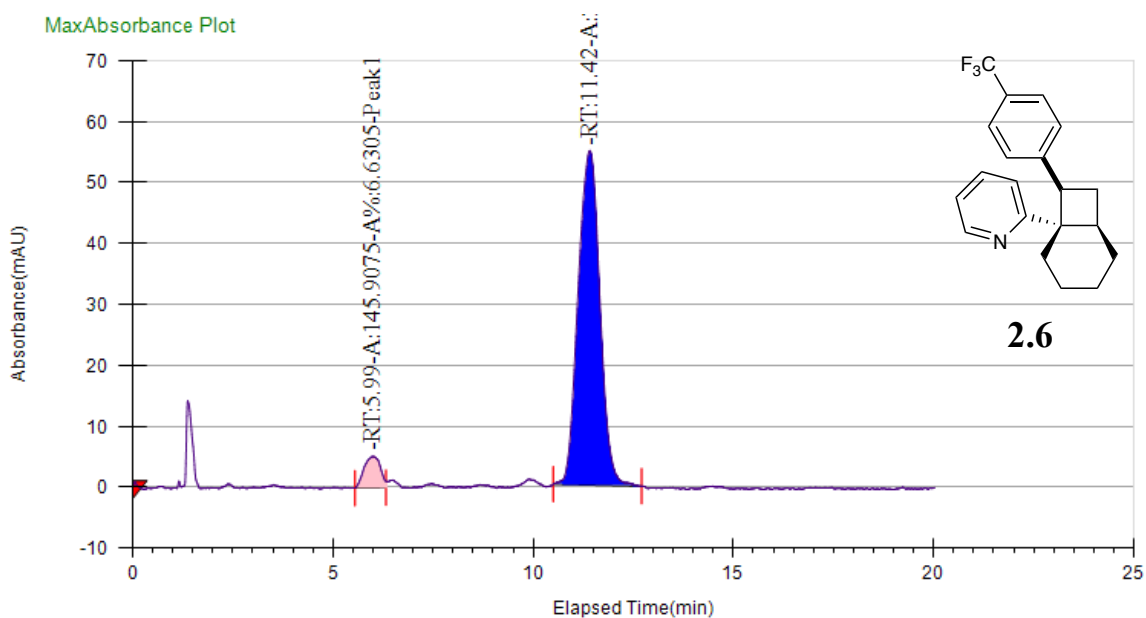
Log Author	Log Date	Report By	Report Date	Notes
Administrator	9/10/2020 2:33:11 PM	Administrator	4/1/2021	

### Run Information

Instrument Method	Inj. Vol.	Solvent	Column	Sample	Well Location	Temp. (C)	Flow (g/min)	% Modifier	Pressure (Bar)
1%MeOH-20min	10 uL	MeOH	Column 3	SJC-4-081_F16_rac	12F	35	3	1	100

### Peak Information

Peak No	% Area	Area	Ret. Time	Height	Cap. Factor
1	52.5208	237.4822	6.36 min	8.9932	6357.25
2	47.4792	214.686	12.56 min	5.0736	12557.15



### General Information

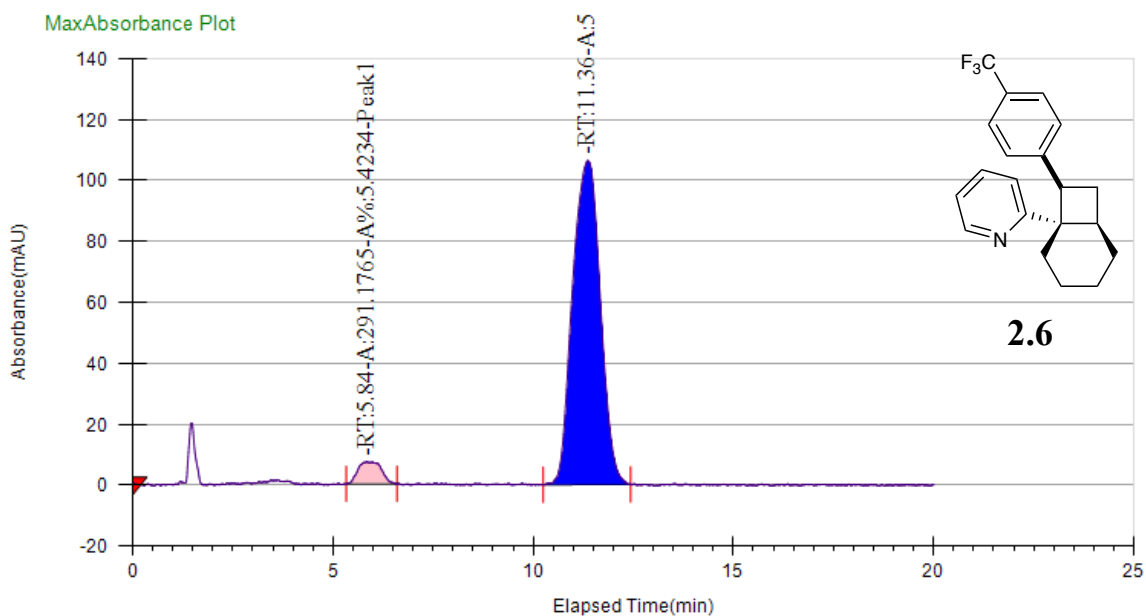
Log Author	Log Date	Report By	Report Date	Notes
Administrator	9/10/2020 5:31:11 PM	Administrator	9/11/2020	

### Run Information

Instrument Method	Inj. Vol.	Solvent	Column	Sample	Well Location	Temp. (C)	Flow (g/min)	% Modifier	Pressure (Bar)
1%MeOH-20min	10 uL	MeOH	Column 3	SJC-4-080_F24-25	13F	35	3	1	100

### Peak Information

Peak No	% Area	Area	Ret. Time	Height	Cap. Factor
1	6.6305	145.9075	5.99 min	5.1607	0
2	93.3695	2054.6526	11.42 min	54.9374	0



### General Information

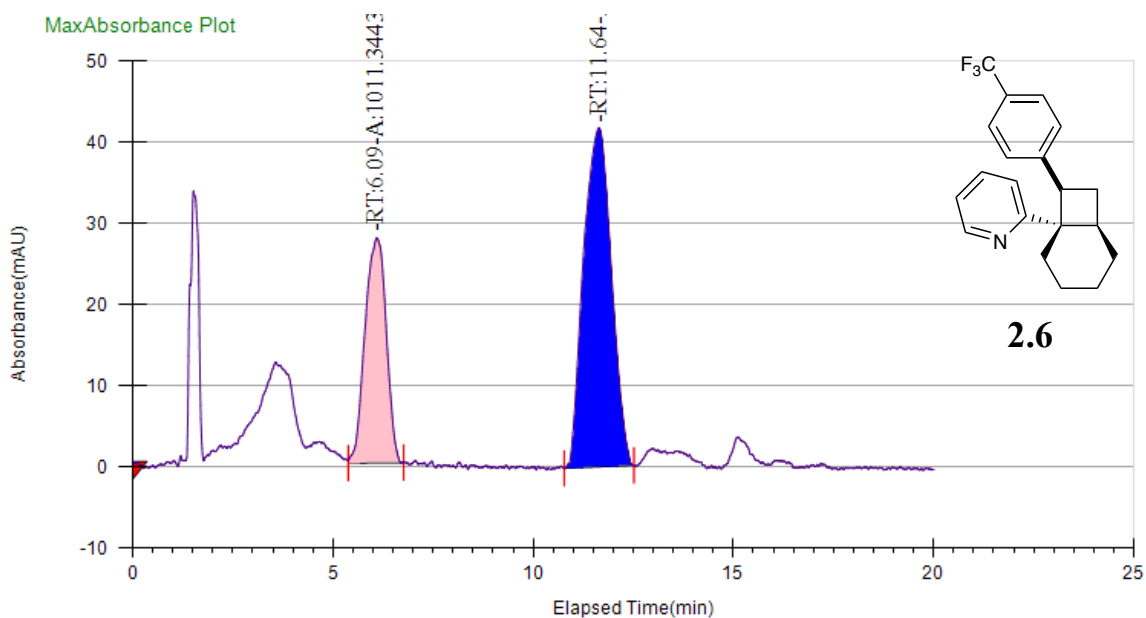
Log Author	Log Date	Report By	Report Date	Notes
Administrator	12/8/2020 2:44:59 PM	Administrator	12/8/2020	

### Run Information

Instrument Method	Inj. Vol.	Solvent	Column	Sample	Well Location	Temp. (C)	Flow (g/min)	% Modifier	Pressure (Bar)
1%MeOH-20min	20 uL	MeOH	Column 3	SJC-4-155_F21	12F	35	3	1	100

### Peak Information

Peak No	% Area	Area	Ret. Time	Height	Cap. Factor
1	5.4234	291.1765	5.84 min	7.2413	0
2	94.5766	5077.6695	11.36 min	106.4354	0



### General Information

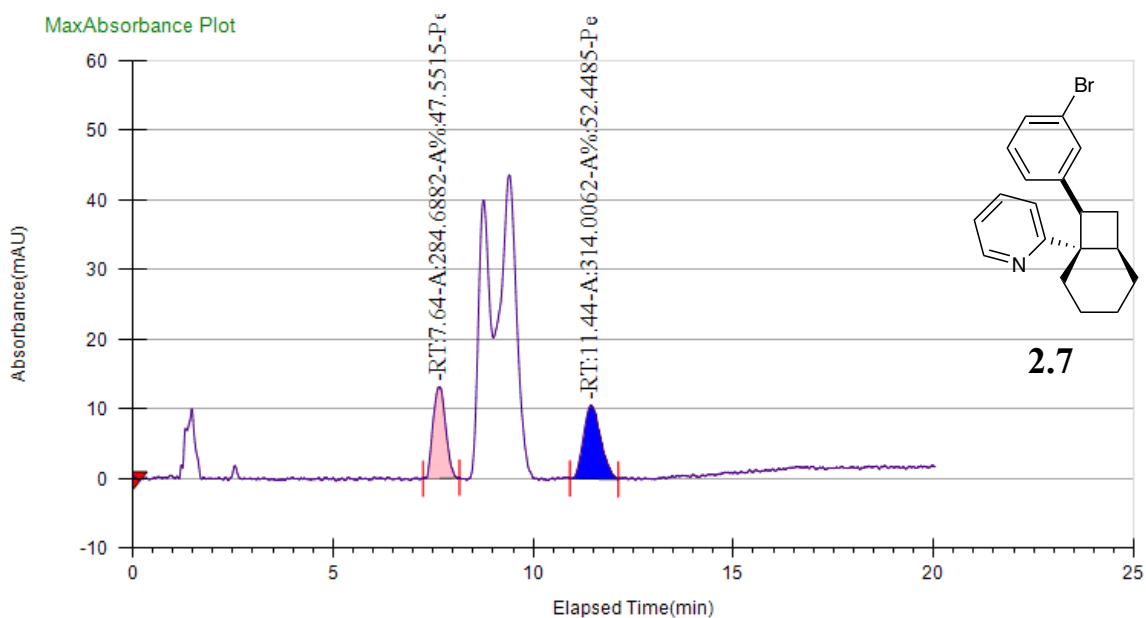
Log Author	Log Date	Report By	Report Date	Notes
Administrator	6/10/2021 3:29:14 PM	Administrator	6/10/2021	

### Run Information

Instrument Method	Inj. Vol.	Solvent	Column	Sample	Well Location	Temp. (C)	Flow (g/min)	% Modifier	Pressure (Bar)
1%MeOH-20min	20 uL	MeOH	Column 3	SJC-4-227_F27	12F	35	3	1	100

### Peak Information

Peak No	% Area	Area	Ret. Time	Height	Cap. Factor
1	33.669	1011.3443	6.09 min	27.7181	0
2	66.331	1992.4371	11.64 min	41.7871	0



### General Information

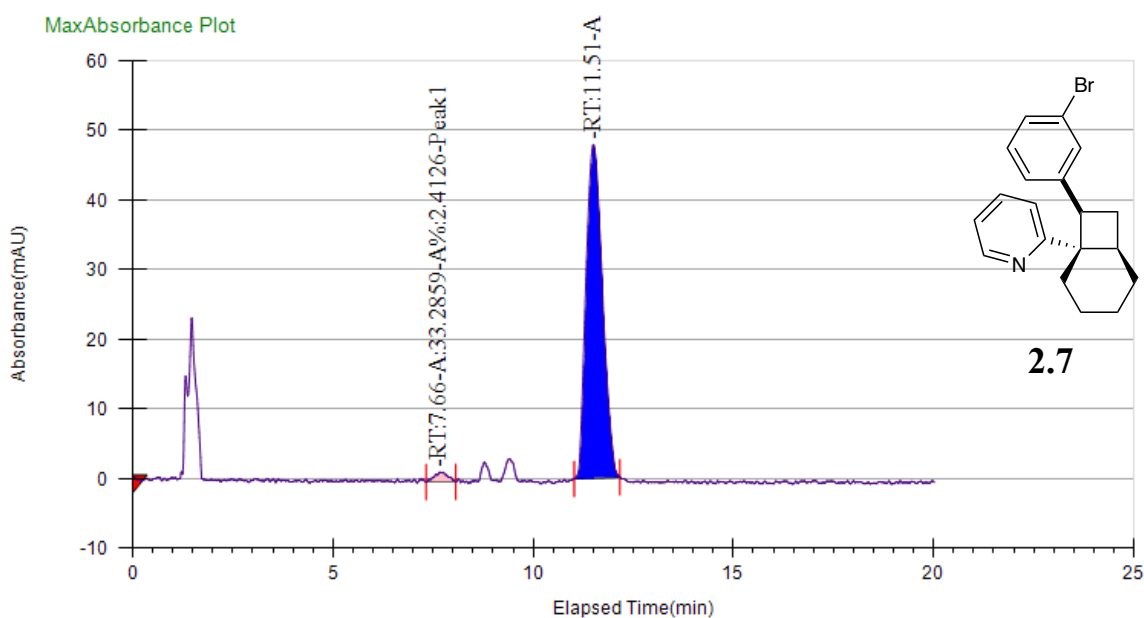
Log Author	Log Date	Report By	Report Date	Notes
Administrator	9/22/2020 4:58:51 PM	Administrator	9/24/2020	

### Run Information

Instrument Method	Inj. Vol.	Solvent	Column	Sample	Well Location	Temp. (C)	Flow (g/min)	% Modifier	Pressure (Bar)
5%IPA-20min	10 uL	IPA	Column 3	SJC-4-089_21-23_rac	12F	35	3	5	100

### Peak Information

Peak No	% Area	Area	Ret. Time	Height	Cap. Factor
1	47.5515	284.6882	7.64 min	13.0902	7640.55
2	52.4485	314.0062	11.44 min	10.6305	11440.5



### General Information

Log Author	Log Date	Report By	Report Date	Notes
Administrator	9/22/2020 8:14:26 PM	Administrator	1/13/2021	

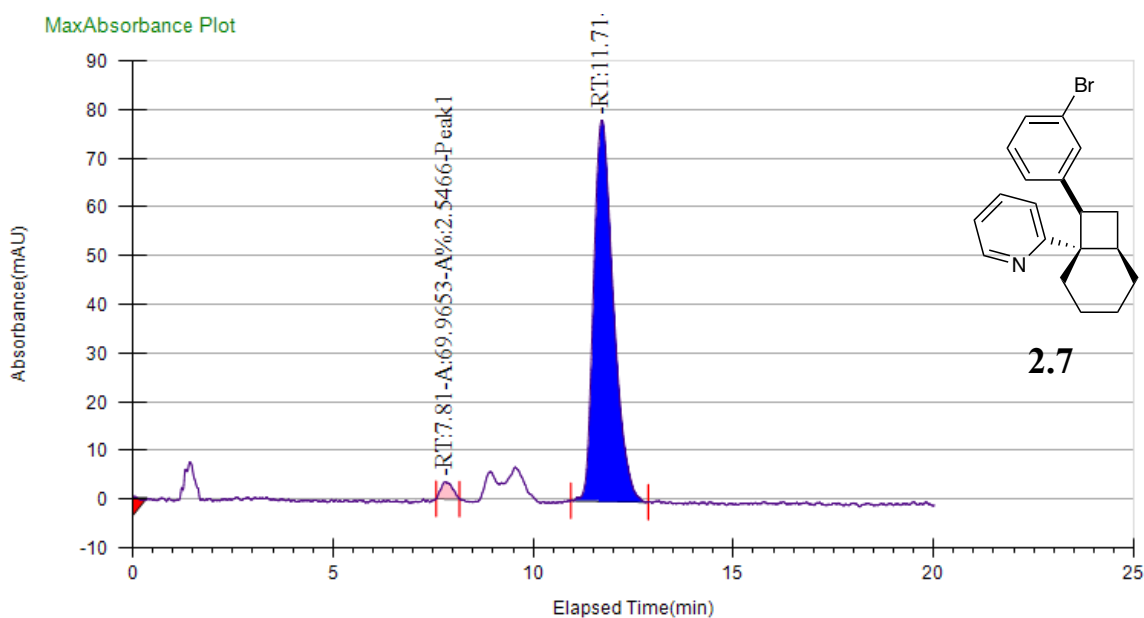
### Run Information

Instrument Method	Inj. Vol.	Solvent	Column	Sample	Well Location	Temp. (C)	Flow (g/min)	% Modifier	Pressure (Bar)
5%IPA-20min	10 uL	IPA	Column 3	SJC-4-090_F23-26	13F	35	3	5	100

### Peak Information

Peak No	% Area	Area	Ret. Time	Height	Cap. Factor
1	2.4126	33.2859	7.66 min	1.4051	7657.2167
2	97.5874	1346.3918	11.51 min	47.9505	11507.1667





### General Information

Log Author	Log Date	Report By	Report Date	Notes
Administrator	1/13/2021 2:00:17 PM	Administrator	1/13/2021	

### Run Information

Instrument Method	Inj. Vol.	Solvent	Column	Sample	Well Location	Temp. (C)	Flow (g/min)	% Modifier	Pressure (Bar)
5%IPA-20min	10 uL	IPA	Column 3	SJC-4-166_F17-19	12F	35	3	5	100

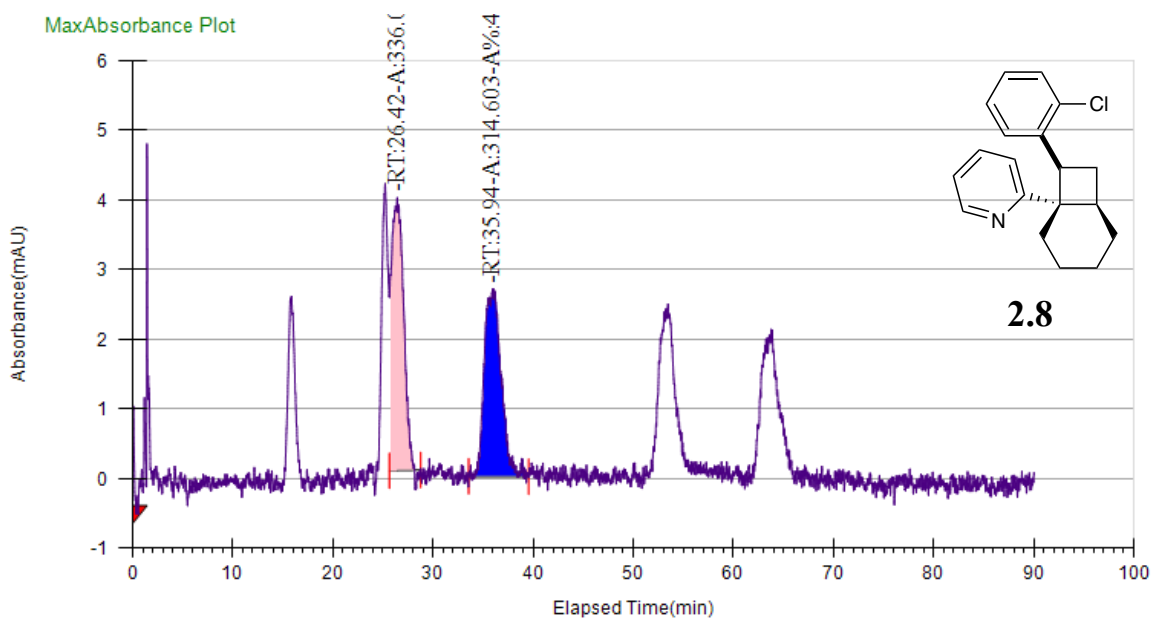
### Peak Information

Peak No	% Area	Area	Ret. Time	Height	Cap. Factor
1	2.5466	69.9653	7.81 min	3.5447	7807.2167
2	97.4534	2677.4587	11.71 min	78.2318	11707.1667



Racemic

C:\Program Files (x86)\ChromScope IE\Investigator\Projects\Steven\DataFiles\11\_6\_2020\SJC-4-086\_F23-25\_rac  
ODH\_7.tta



### General Information

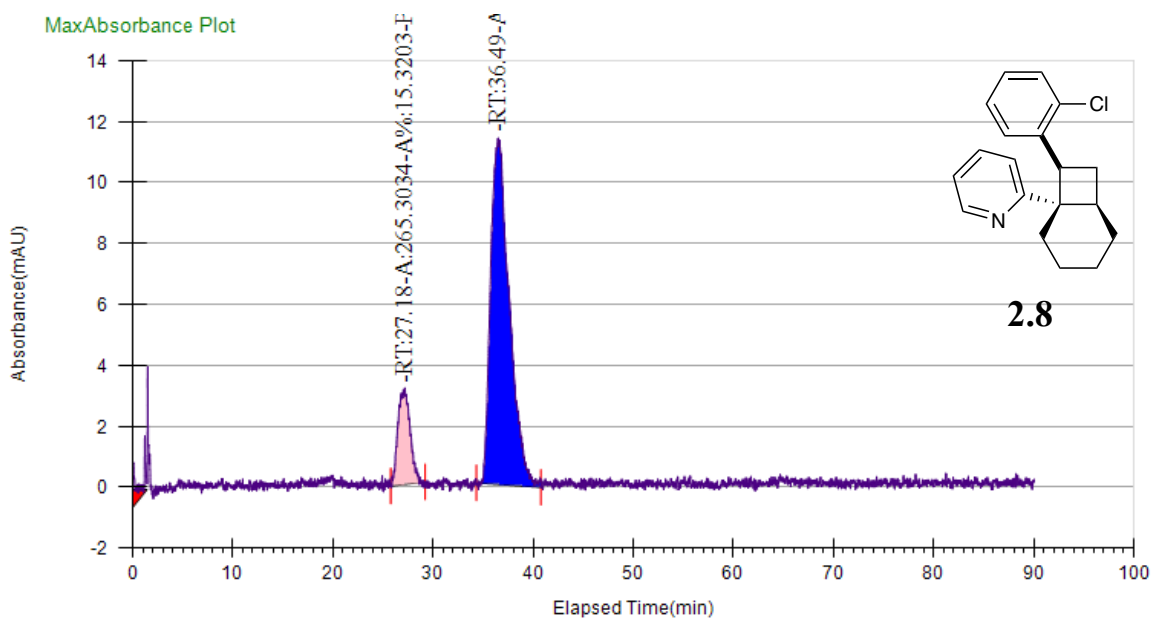
Log Author	Log Date	Report By	Report Date	Notes
Administrator	11/6/2020 6:38:24 PM	Administrator	6/24/2021	

### Run Information

Instrument Method	Inj. Vol.	Solvent	Column	Sample	Well Location	Temp. (C)	Flow (g/min)	% Modifier	Pressure (Bar)
1%MeOH-90min	20 uL	MeOH	Column 1	SJC-4-086_F23-25_rac	12F	35	3	1	100

### Peak Information

Peak No	% Area	Area	Ret. Time	Height	Cap. Factor
1	51.6471	336.0365	26.42 min	3.9232	26415.2667
2	48.3529	314.603	35.94 min	2.6929	35941.0333



### General Information

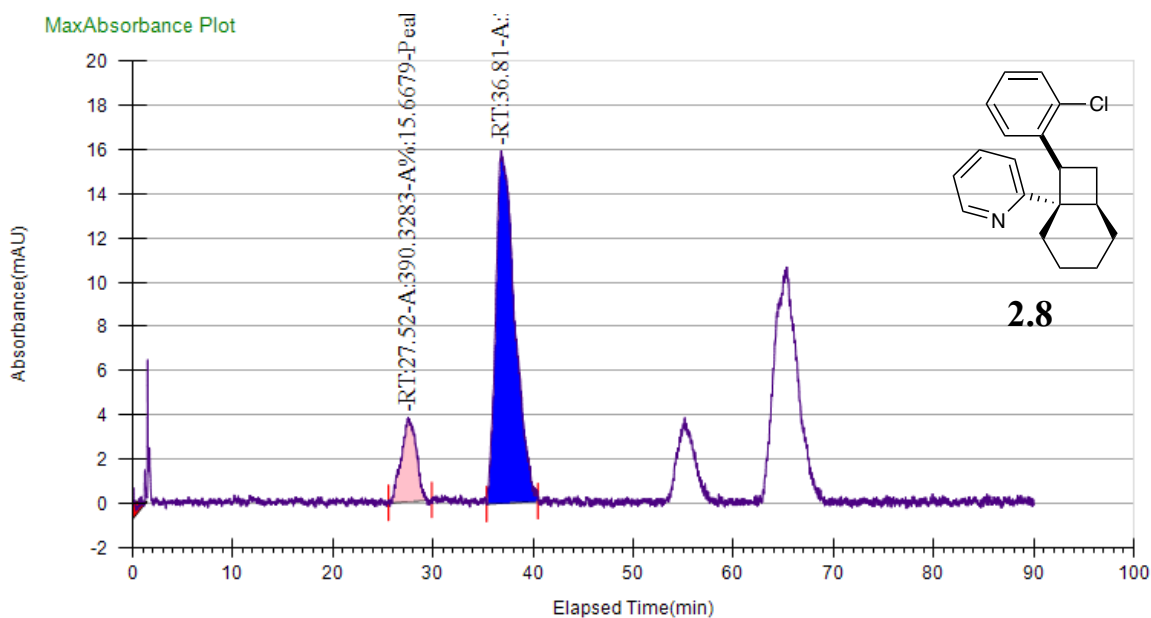
Log Author	Log Date	Report By	Report Date	Notes
Administrator	5/6/2021 7:54:18 PM	Administrator	5/7/2021	

### Run Information

Instrument Method	Inj. Vol.	Solvent	Column	Sample	Well Location	Temp. (C)	Flow (g/min)	% Modifier	Pressure (Bar)
1%MeOH-90min	20 uL	MeOH	Column 1	SJC-4-087_bottom	13F	35	3	1	100

### Peak Information

Peak No	% Area	Area	Ret. Time	Height	Cap. Factor
1	15.3203	265.3034	27.18 min	3.1656	27181.9333
2	84.6797	1466.4106	36.49 min	11.37	36491.15



### General Information

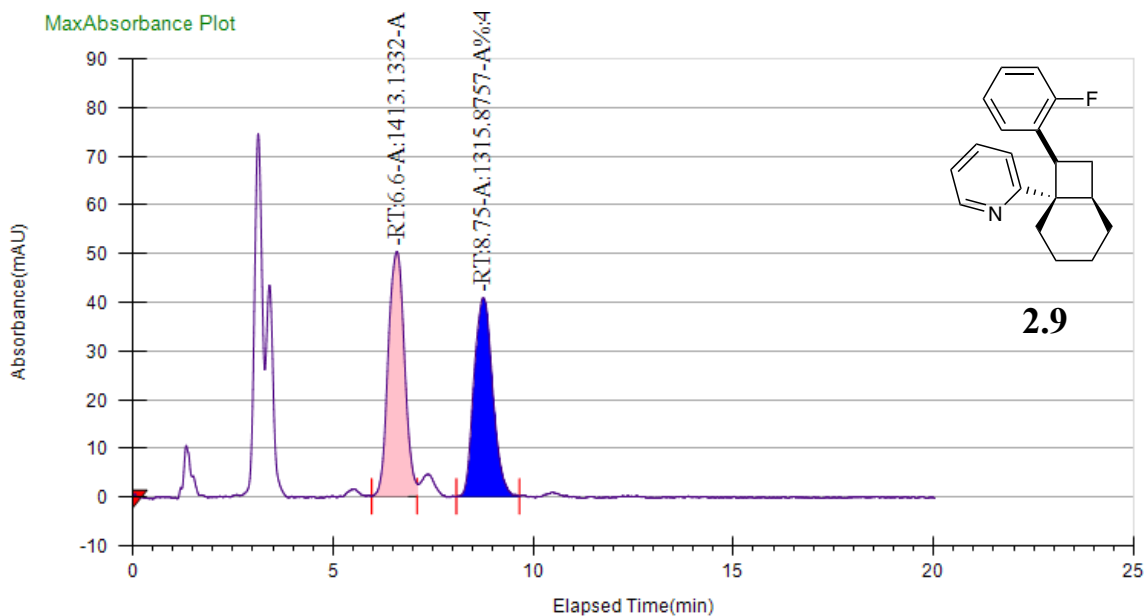
Log Author	Log Date	Report By	Report Date	Notes
Administrator	11/7/2020 7:26:26 PM	Administrator	6/28/2021	

### Run Information

Instrument Method	Inj. Vol.	Solvent	Column	Sample	Well Location	Temp. (C)	Flow (g/min)	% Modifier	Pressure (Bar)
1%MeOH-90min	20 uL	MeOH	Column 1	SJC-4-129_F25-29	14F	35	3	1	100

### Peak Information

Peak No	% Area	Area	Ret. Time	Height	Cap. Factor
1	15.6679	390.3283	27.52 min	3.7953	27515.25
2	84.3321	2100.9261	36.81 min	15.9049	36807.8833



### General Information

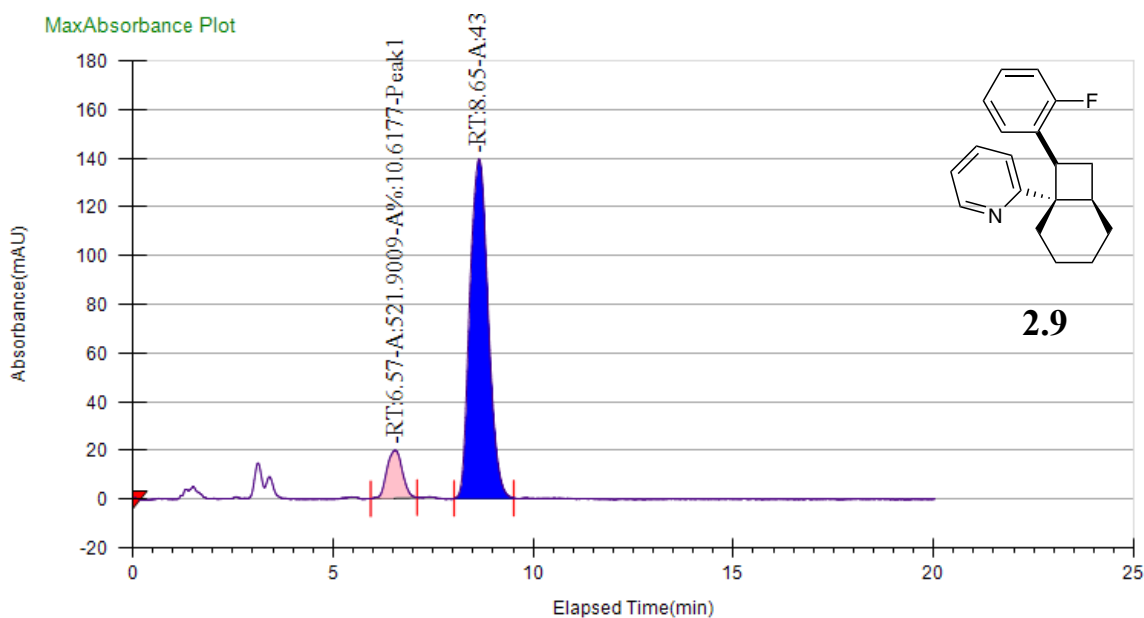
Log Author	Log Date	Report By	Report Date	Notes
Administrator	10/20/2020 10:14:16 AM	Administrator	10/20/2020	

### Run Information

Instrument Method	Inj. Vol.	Solvent	Column	Sample	Well Location	Temp. (C)	Flow (g/min)	% Modifier	Pressure (Bar)
5%IPA-20min	20 uL	IPA	Column 3	SJC-4-110_F26_rac	12F	35	3	5	100

### Peak Information

Peak No	% Area	Area	Ret. Time	Height	Cap. Factor
1	51.7819	1413.1332	6.6 min	50.2328	6598.9
2	48.2181	1315.8757	8.75 min	40.7994	8748.8667

**General Information**

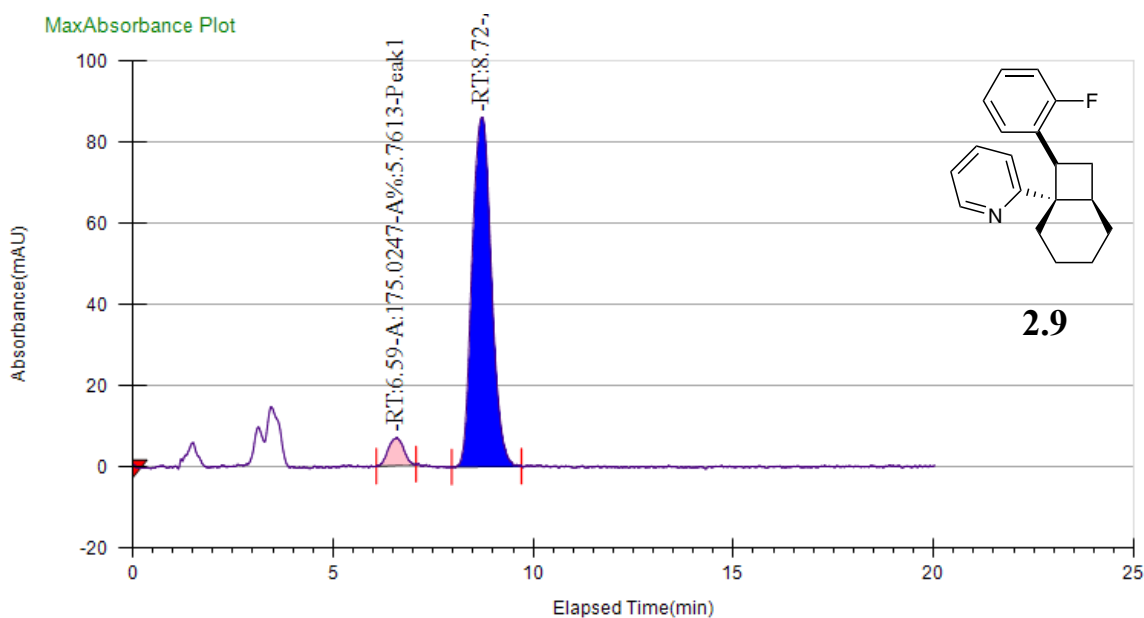
Log Author	Log Date	Report By	Report Date	Notes
Administrator	10/20/2020 12:27:46 PM	Administrator	10/20/2020	

**Run Information**

Instrument Method	Inj. Vol.	Solvent	Column	Sample	Well Location	Temp. (C)	Flow (g/min)	% Modifier	Pressure (Bar)
5%IPA-20min	20 uL	IPA	Column 3	SJC-4-111_F26	13F	35	3	5	100

**Peak Information**

Peak No	% Area	Area	Ret. Time	Height	Cap. Factor
1	10.6177	521.9009	6.57 min	19.5765	0
2	89.3823	4393.4832	8.65 min	139.3221	0



### General Information

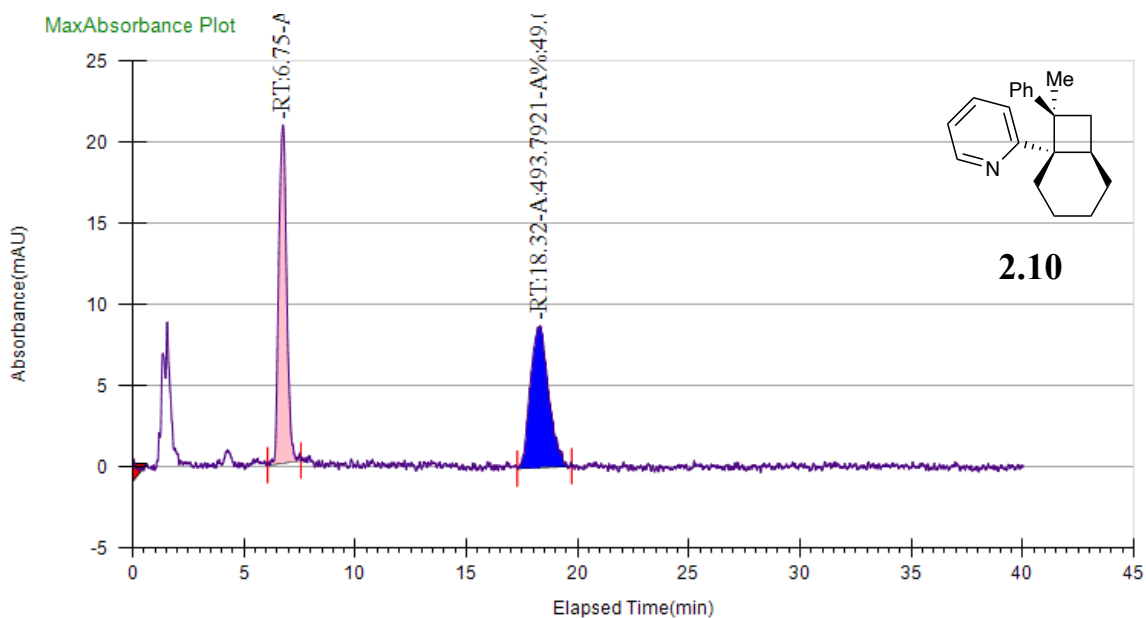
Log Author	Log Date	Report By	Report Date	Notes
Administrator	10/31/2020 11:10:41 AM	Administrator	10/31/2020	

### Run Information

Instrument Method	Inj. Vol.	Solvent	Column	Sample	Well Location	Temp. (C)	Flow (g/min)	% Modifier	Pressure (Bar)
5%IPA-20min	20 uL	IPA	Column 3	SJC-4-124_F22-27	12F	35	3	5	100

### Peak Information

Peak No	% Area	Area	Ret. Time	Height	Cap. Factor
1	5.7613	175.0247	6.59 min	6.7293	0
2	94.2387	2862.9165	8.72 min	86.104	0



### General Information

Log Author	Log Date	Report By	Report Date	Notes
Administrator	10/30/2019 10:24:56 PM	Administrator	10/31/2019	

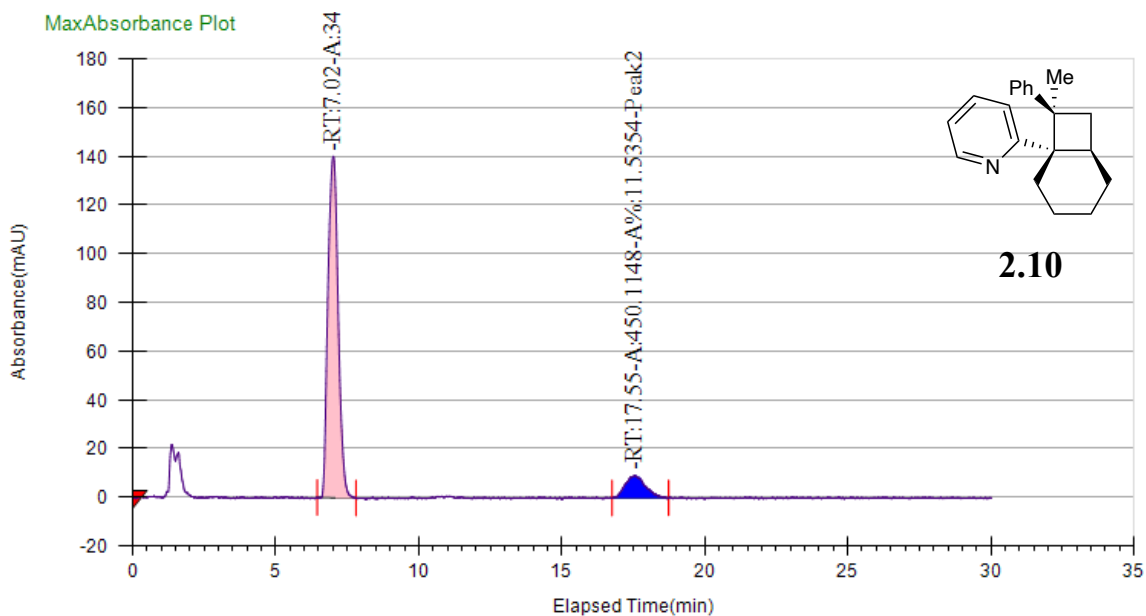
### Run Information

Instrument Method	Inj. Vol.	Solvent	Column	Sample	Well Location	Temp. (C)	Flow (g/min)	% Modifier	Pressure (Bar)
5%IPA-40min	20 uL	IPA	Column 1	SJC-3-149_F24	12F	35	3	5	100

### Peak Information

Peak No	% Area	Area	Ret. Time	Height	Cap. Factor
1	50.914	512.1822	6.75 min	20.7988	0
2	49.086	493.7921	18.32 min	8.7233	0





### General Information

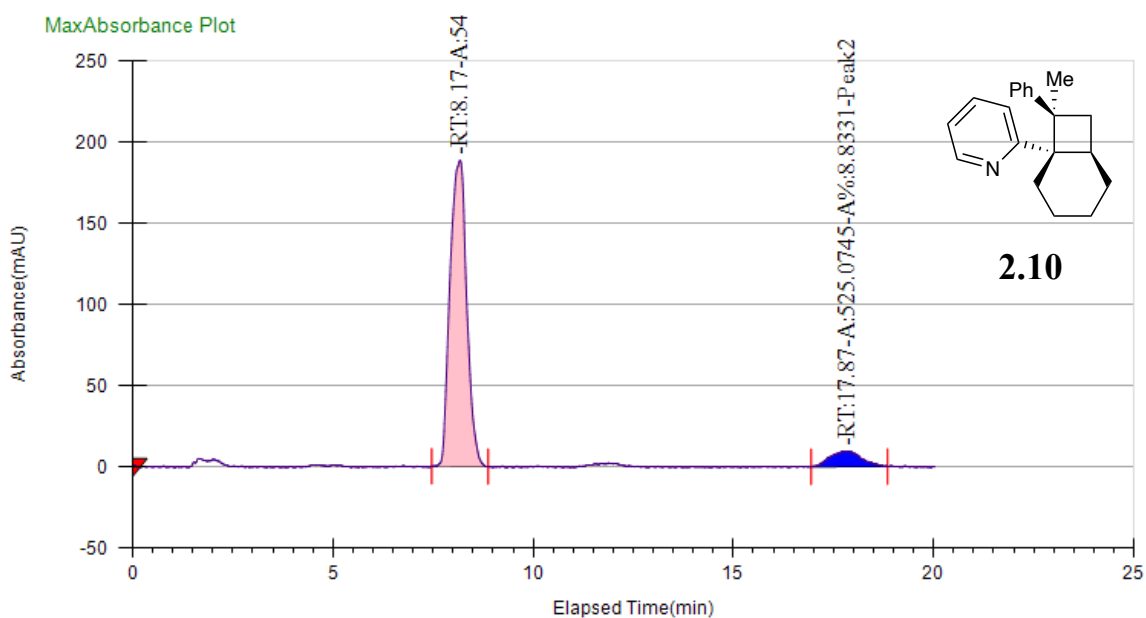
Log Author	Log Date	Report By	Report Date	Notes
Administrator	9/8/2020 9:08:34 AM	Administrator	9/8/2020	

### Run Information

Instrument Method	Inj. Vol.	Solvent	Column	Sample	Well Location	Temp. (C)	Flow (g/min)	% Modifier	Pressure (Bar)
5%IPA-30min	20 uL	IPA	Column 1	SJC-4-075_F25-26	12F	35	3	5	100

### Peak Information

Peak No	% Area	Area	Ret. Time	Height	Cap. Factor
1	88.4646	3451.9197	7.02 min	140.1652	0
2	11.5354	450.1148	17.55 min	9.2688	0



### General Information

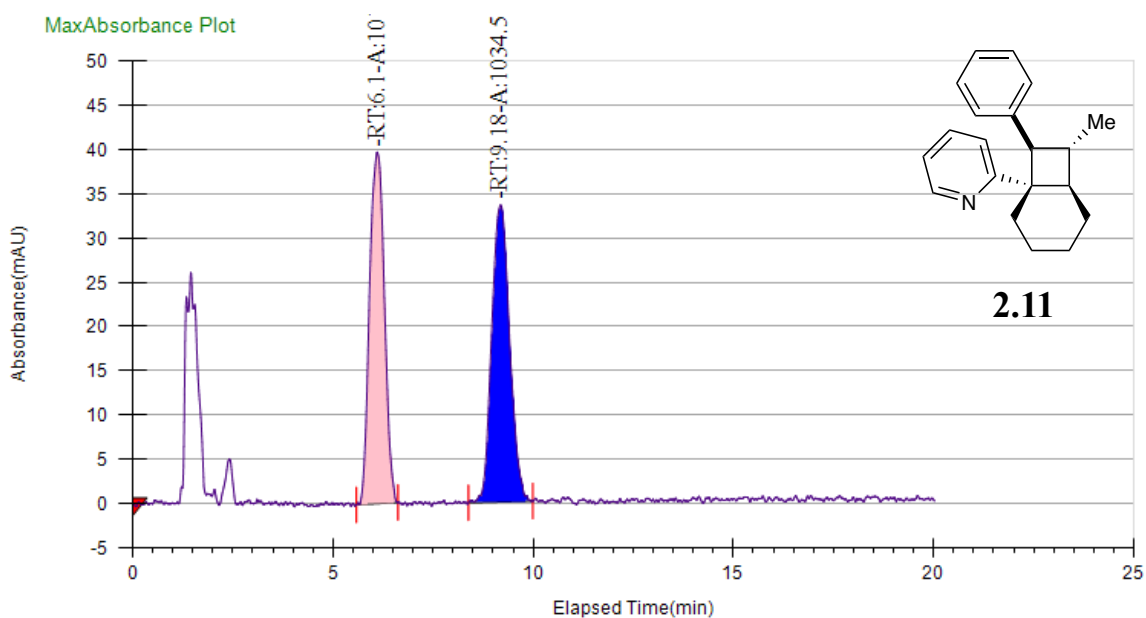
Log Author	Log Date	Report By	Report Date	Notes
Administrator	11/21/2020 3:17:22 PM	Administrator	11/21/2020	

### Run Information

Instrument Method	Inj. Vol.	Solvent	Column	Sample	Well Location	Temp. (C)	Flow (g/min)	% Modifier	Pressure (Bar)
5%IPA-20min	20 uL	IPA	Column 1	SJC-4-144_F24-26	12F	35	3	5	100

### Peak Information

Peak No	% Area	Area	Ret. Time	Height	Cap. Factor
1	91.1669	5419.3132	8.17 min	188.5208	0
2	8.8331	525.0745	17.87 min	9.5874	0



### General Information

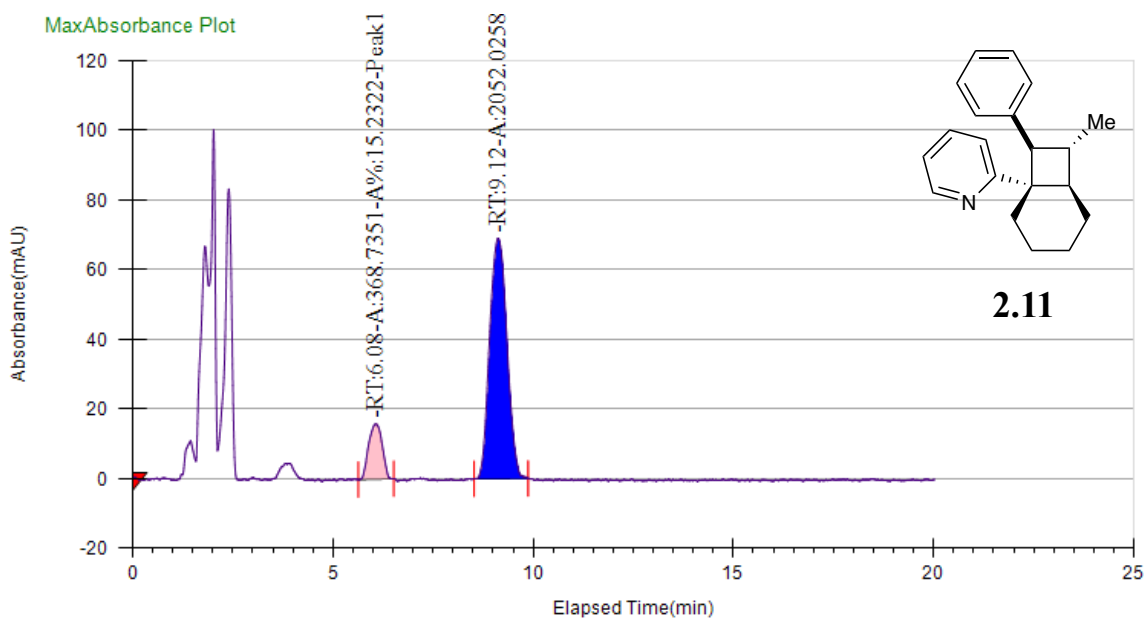
Log Author	Log Date	Report By	Report Date	Notes
Administrator	10/6/2020 10:48:58 PM	Administrator	10/7/2020	

### Run Information

Instrument Method	Inj. Vol.	Solvent	Column	Sample	Well Location	Temp. (C)	Flow (g/min)	% Modifier	Pressure (Bar)
5%IPA-20min	20 uL	IPA	Column 3	SJC-4-098_20-23_rac	12F	35	3	5	100

### Peak Information

Peak No	% Area	Area	Ret. Time	Height	Cap. Factor
1	49.4382	1011.5671	6.1 min	39.6929	6098.9167
2	50.5618	1034.5576	9.18 min	33.5106	9182.2



### General Information

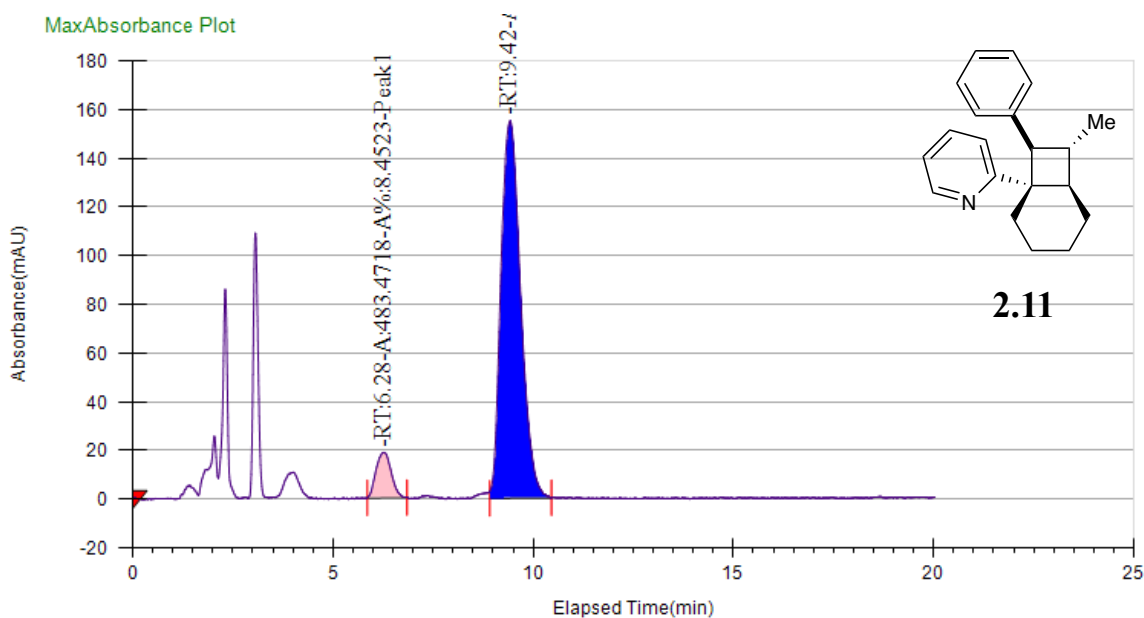
Log Author	Log Date	Report By	Report Date	Notes
Administrator	10/7/2020 3:11:40 PM	Administrator	10/7/2020	

### Run Information

Instrument Method	Inj. Vol.	Solvent	Column	Sample	Well Location	Temp. (C)	Flow (g/min)	% Modifier	Pressure (Bar)
5%IPA-20min	20 uL	IPA	Column 3	SJC-4-099_F18-21	13F	35	3	5	100

### Peak Information

Peak No	% Area	Area	Ret. Time	Height	Cap. Factor
1	15.2322	368.7351	6.08 min	15.8175	0
2	84.7678	2052.0258	9.12 min	69.1526	0



### General Information

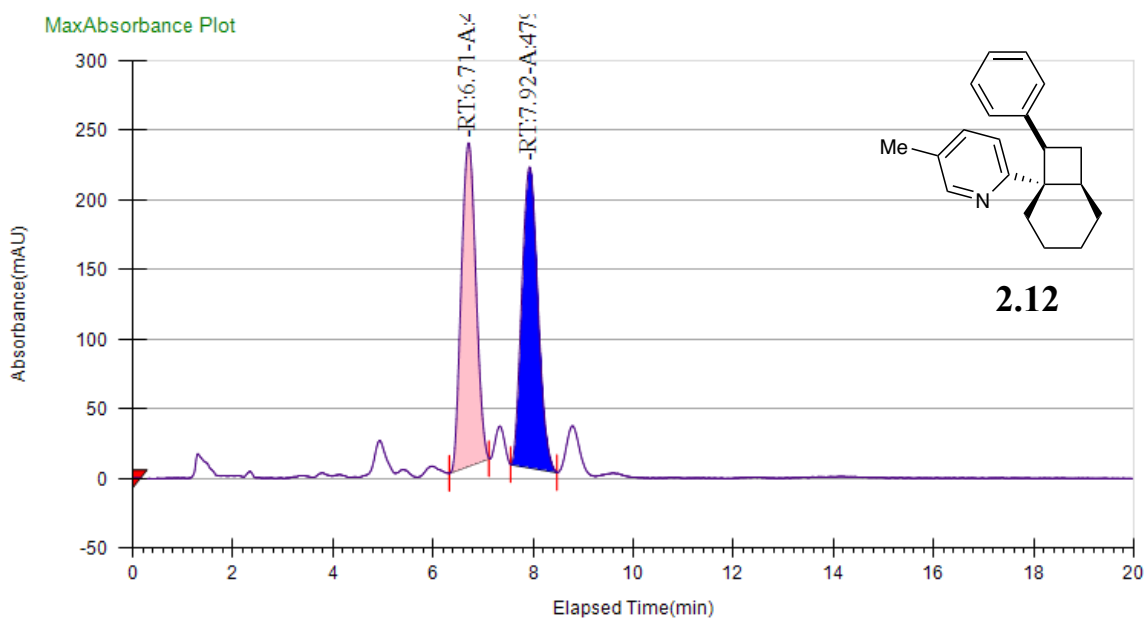
Log Author	Log Date	Report By	Report Date	Notes
Administrator	3/3/2021 5:14:10 PM	Administrator	3/4/2021	

### Run Information

Instrument Method	Inj. Vol.	Solvent	Column	Sample	Well Location	Temp. (C)	Flow (g/min)	% Modifier	Pressure (Bar)
5%IPA-20min	20 uL	IPA	Column 3	SJC-4-195_F23-25	12F	35	3	5	100

### Peak Information

Peak No	% Area	Area	Ret. Time	Height	Cap. Factor
1	8.4523	483.4718	6.28 min	18.5741	0
2	91.5477	5236.556	9.42 min	154.9108	0



### General Information

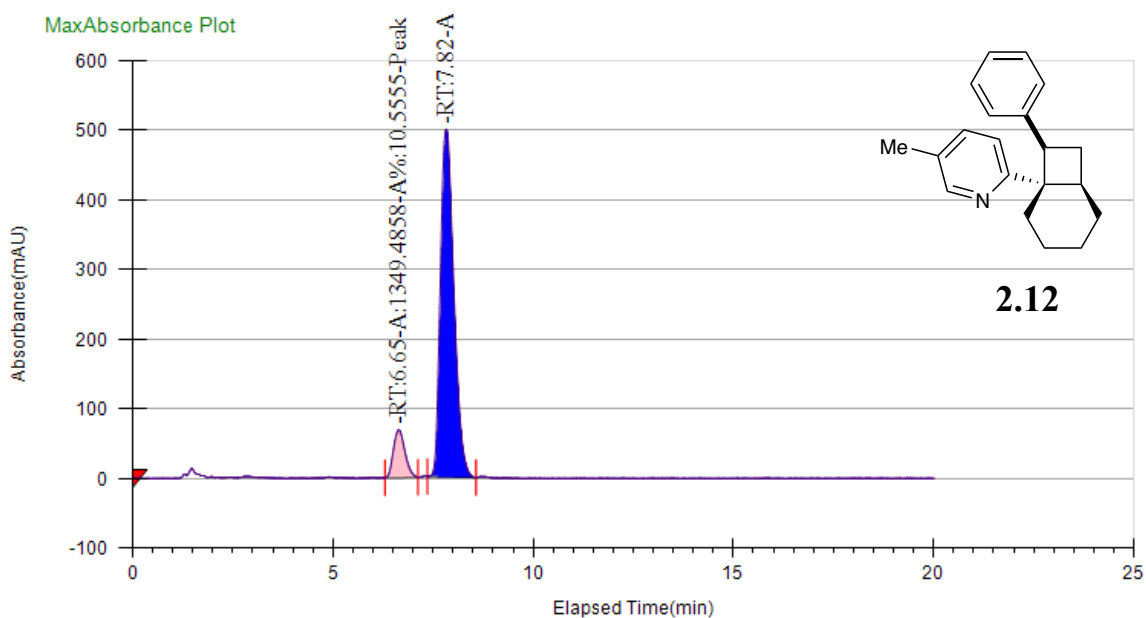
Log Author	Log Date	Report By	Report Date	Notes
Administrator	1/22/2020 7:46:49 PM	Administrator	1/22/2020	

### Run Information

Instrument Method	Inj. Vol.	Solvent	Column	Sample	Well Location	Temp. (C)	Flow (g/min)	% Modifier	Pressure (Bar)
5%MeOH-20min	20 uL	MeOH	Column 3	SJC-3-225_F20-22	12F	35	3	5	100

### Peak Information

Peak No	% Area	Area	Ret. Time	Height	Cap. Factor
1	49.252	4650.1893	6.71 min	232.4478	0
2	50.748	4791.4313	7.92 min	215.9898	0



### General Information

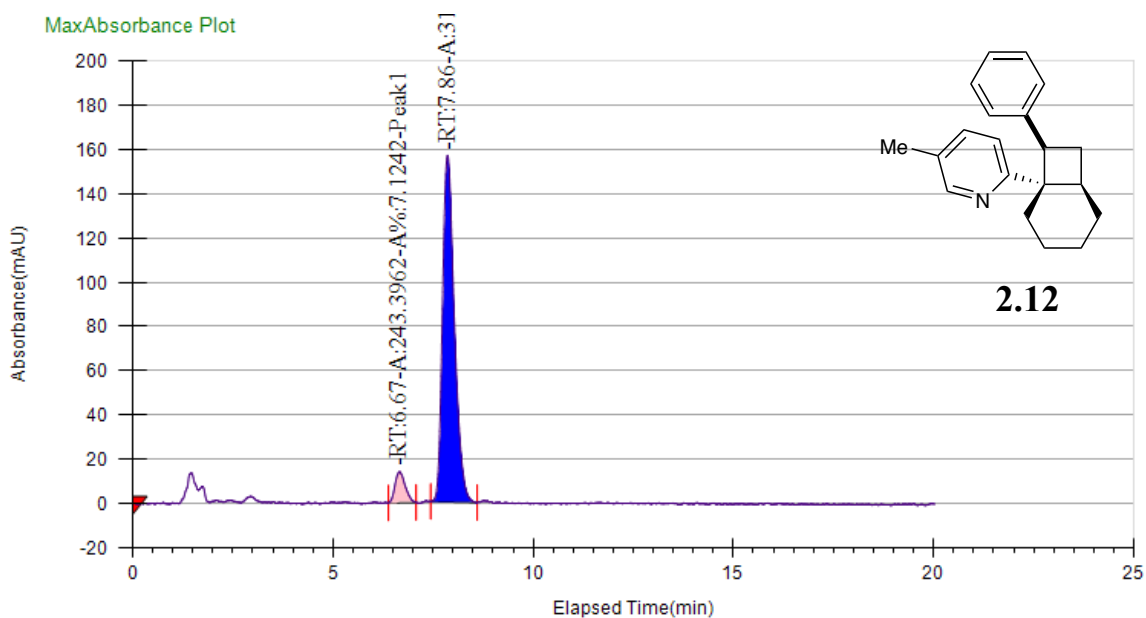
Log Author	Log Date	Report By	Report Date	Notes
Administrator	12/11/2020 12:02:32 PM	Administrator	12/11/2020	

### Run Information

Instrument Method	Inj. Vol.	Solvent	Column	Sample	Well Location	Temp. (C)	Flow (g/min)	% Modifier	Pressure (Bar)
5%MeOH-20min	20 uL	MeOH	Column 3	SJC-4-157_F25-28	12F	35	3	5	100

### Peak Information

Peak No	% Area	Area	Ret. Time	Height	Cap. Factor
1	10.5555	1349.4858	6.65 min	68.5314	0
2	89.4445	11435.2197	7.82 min	499.7785	0



### General Information

Log Author	Log Date	Report By	Report Date	Notes
Administrator	12/12/2020 11:26:26 AM	Administrator	12/12/2020	

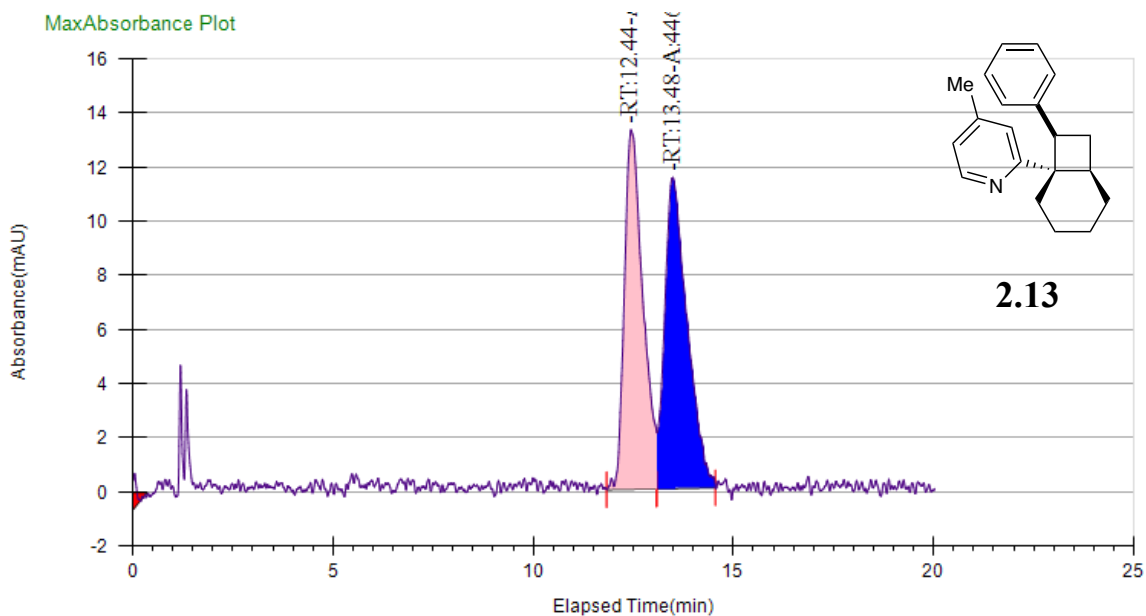
### Run Information

Instrument Method	Inj. Vol.	Solvent	Column	Sample	Well Location	Temp. (C)	Flow (g/min)	% Modifier	Pressure (Bar)
5%MeOH-20min	10 uL	MeOH	Column 3	SJC-4-159_F24-27	12F	35	3	5	100

### Peak Information

Peak No	% Area	Area	Ret. Time	Height	Cap. Factor
1	7.1242	243.3962	6.67 min	13.9688	0
2	92.8758	3173.0636	7.86 min	156.5075	0





### General Information

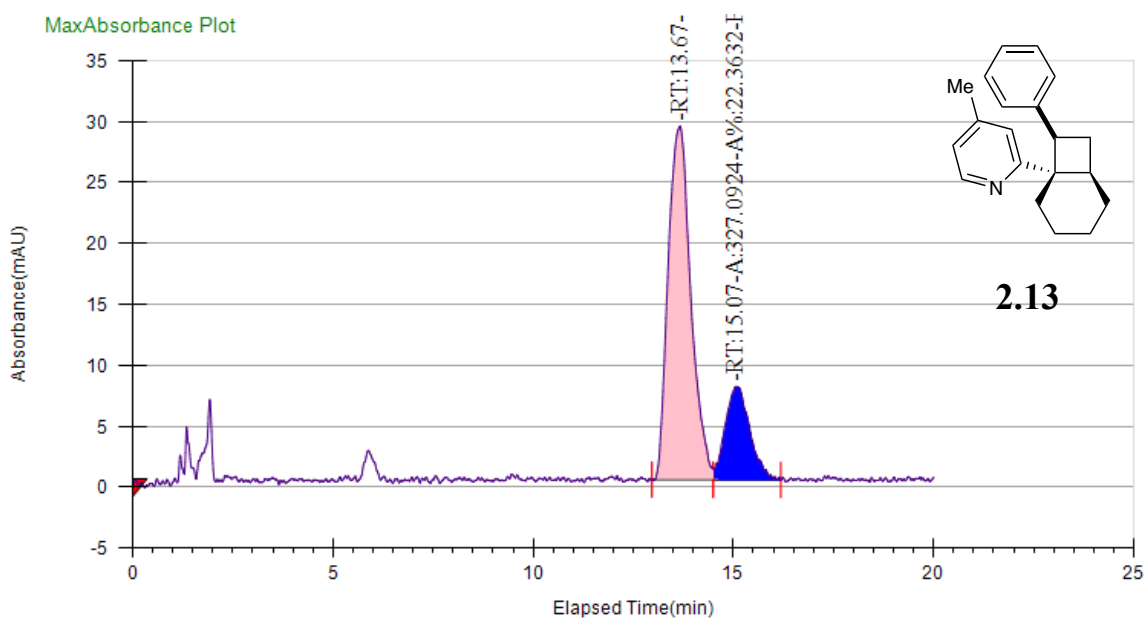
Log Author	Log Date	Report By	Report Date	Notes
Administrator	2/17/2021 9:57:05 PM	Administrator	2/18/2021	

### Run Information

Instrument Method	Inj. Vol.	Solvent	Column	Sample	Well Location	Temp. (C)	Flow (g/min)	% Modifier	Pressure (Bar)
3%IPA-20min	5 uL	IPA	Column 1	SJC-3-004_F12_rac	12F	35	3	3	100

### Peak Information

Peak No	% Area	Area	Ret. Time	Height	Cap. Factor
1	48.7764	425.3495	12.44 min	13.289	0
2	51.2236	446.6906	13.48 min	11.4957	0



### General Information

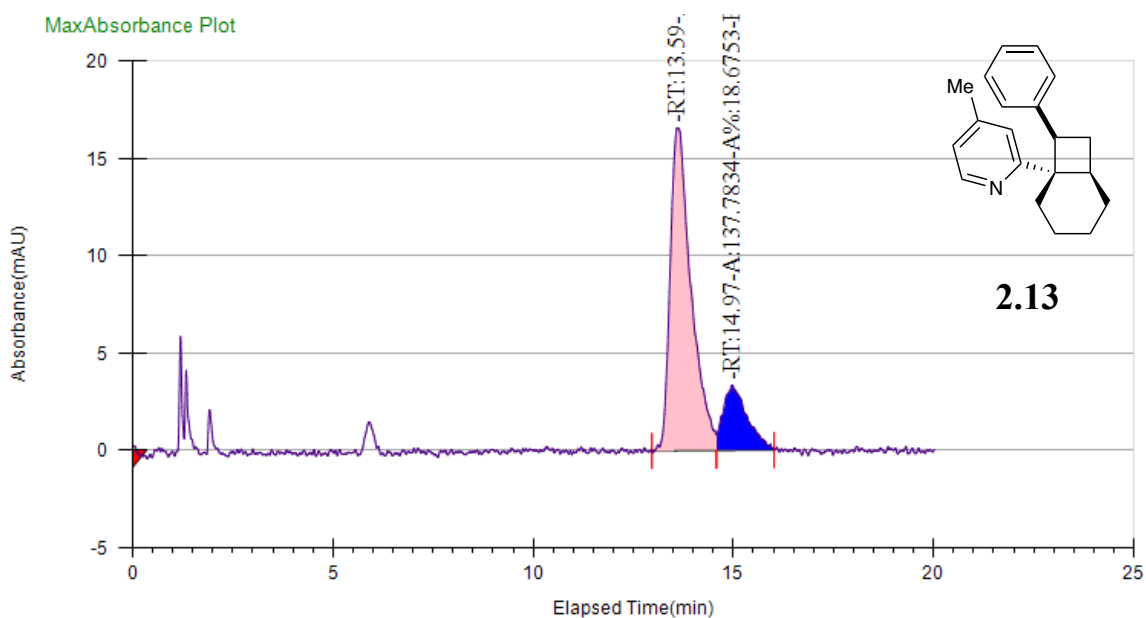
Log Author	Log Date	Report By	Report Date	Notes
Administrator	2/2/2021 8:16:29 PM	Administrator	2/3/2021	

### Run Information

Instrument Method	Inj. Vol.	Solvent	Column	Sample	Well Location	Temp. (C)	Flow (g/min)	% Modifier	Pressure (Bar)
3%IPA-20min	10 uL	IPA	Column 1	SJC-4-175_F26-27	12F	35	3	3	100

### Peak Information

Peak No	% Area	Area	Ret. Time	Height	Cap. Factor
1	77.6368	1135.5418	13.67 min	29.0413	0
2	22.3632	327.0924	15.07 min	7.6558	0



### General Information

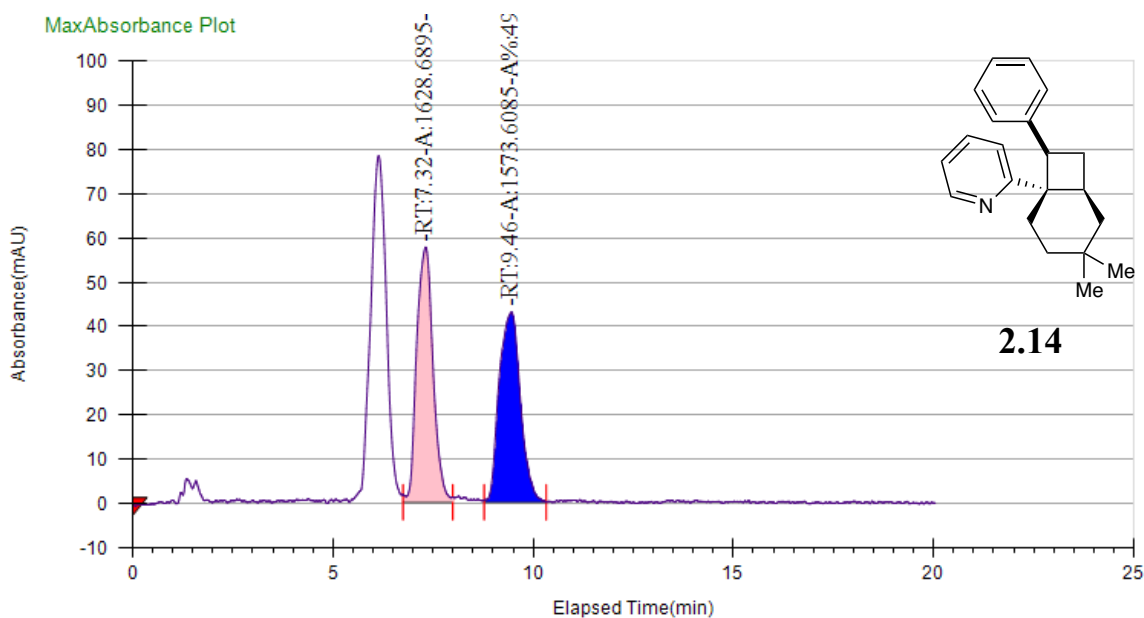
Log Author	Log Date	Report By	Report Date	Notes
Administrator	2/17/2021 10:41:34 PM	Administrator	2/18/2021	

### Run Information

Instrument Method	Inj. Vol.	Solvent	Column	Sample	Well Location	Temp. (C)	Flow (g/min)	% Modifier	Pressure (Bar)
3%IPA-20min	5 uL	IPA	Column 1	SJC-4-185_F19-22	13F	35	3	3	100

### Peak Information

Peak No	% Area	Area	Ret. Time	Height	Cap. Factor
1	81.3247	600.0008	13.59 min	16.5729	13590.4667
2	18.6753	137.7834	14.97 min	3.3436	14973.7833



### General Information

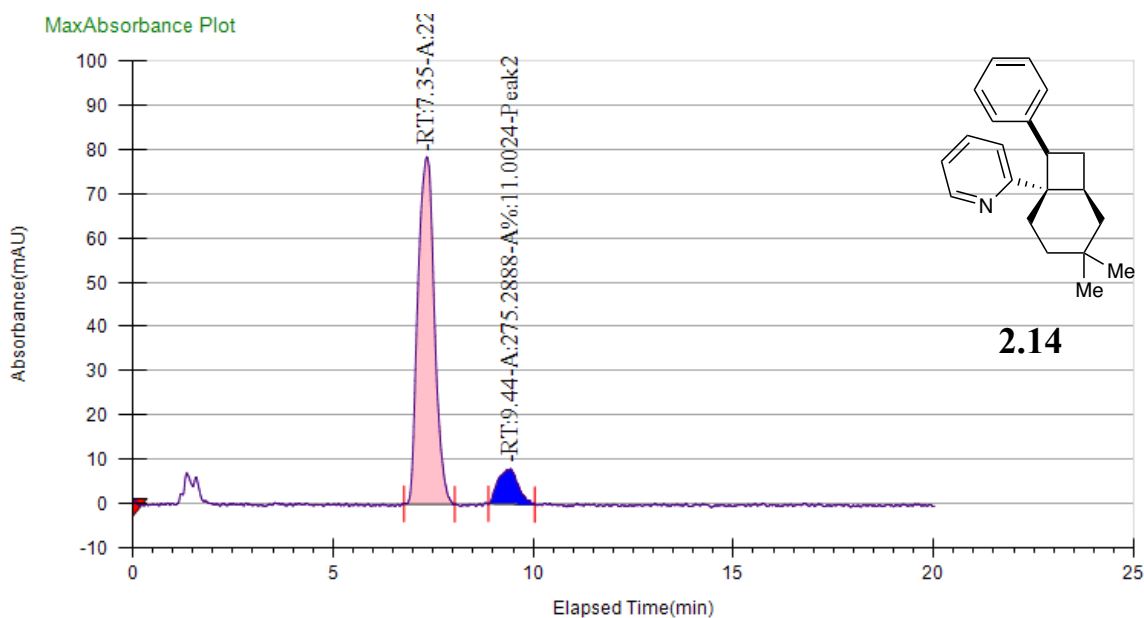
Log Author	Log Date	Report By	Report Date	Notes
Administrator	3/7/2021 2:54:42 PM	Administrator	3/7/2021	

### Run Information

Instrument Method	Inj. Vol.	Solvent	Column	Sample	Well Location	Temp. (C)	Flow (g/min)	% Modifier	Pressure (Bar)
5%IPA-20min	20 uL	IPA	Column 1	SJC-3-198_F10	12F	35	3	5	100

### Peak Information

Peak No	% Area	Area	Ret. Time	Height	Cap. Factor
1	50.86	1628.6895	7.32 min	57.6445	0
2	49.14	1573.6085	9.46 min	42.9652	0



### General Information

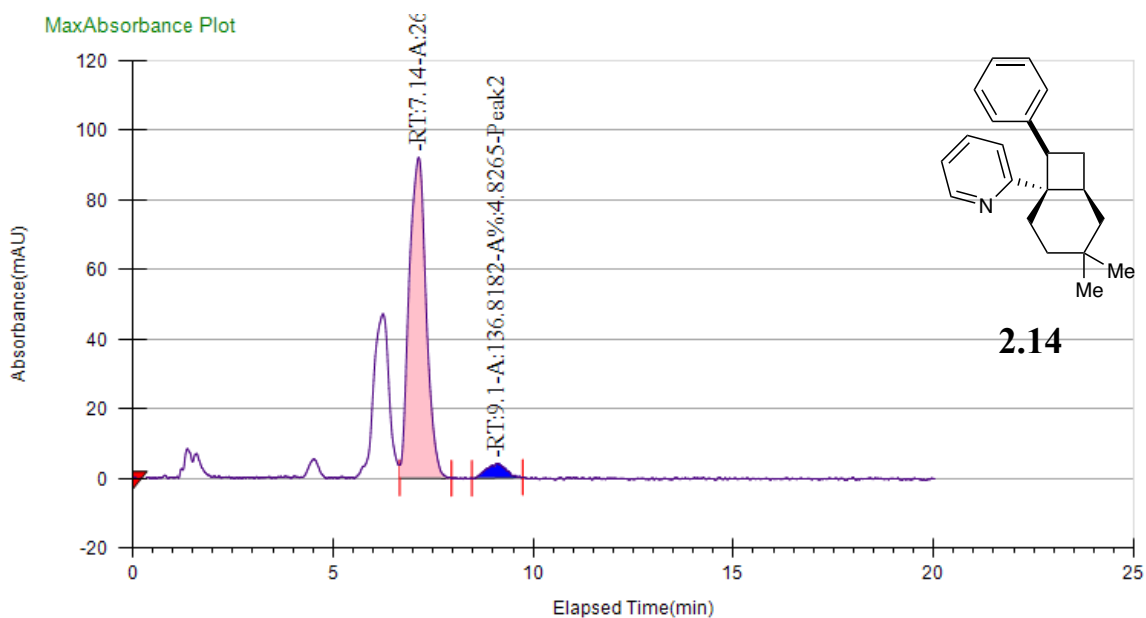
Log Author	Log Date	Report By	Report Date	Notes
Administrator	4/1/2021 2:52:01 PM	Administrator	4/1/2021	

### Run Information

Instrument Method	Inj. Vol.	Solvent	Column	Sample	Well Location	Temp. (C)	Flow (g/min)	% Modifier	Pressure (Bar)
5%IPA-20min	20 uL	IPA	Column 1	SJC-4-073_F49-60	12F	35	3	5	100

### Peak Information

Peak No	% Area	Area	Ret. Time	Height	Cap. Factor
1	88.9976	2226.7897	7.35 min	78.4303	0
2	11.0024	275.2888	9.44 min	7.9795	0



### General Information

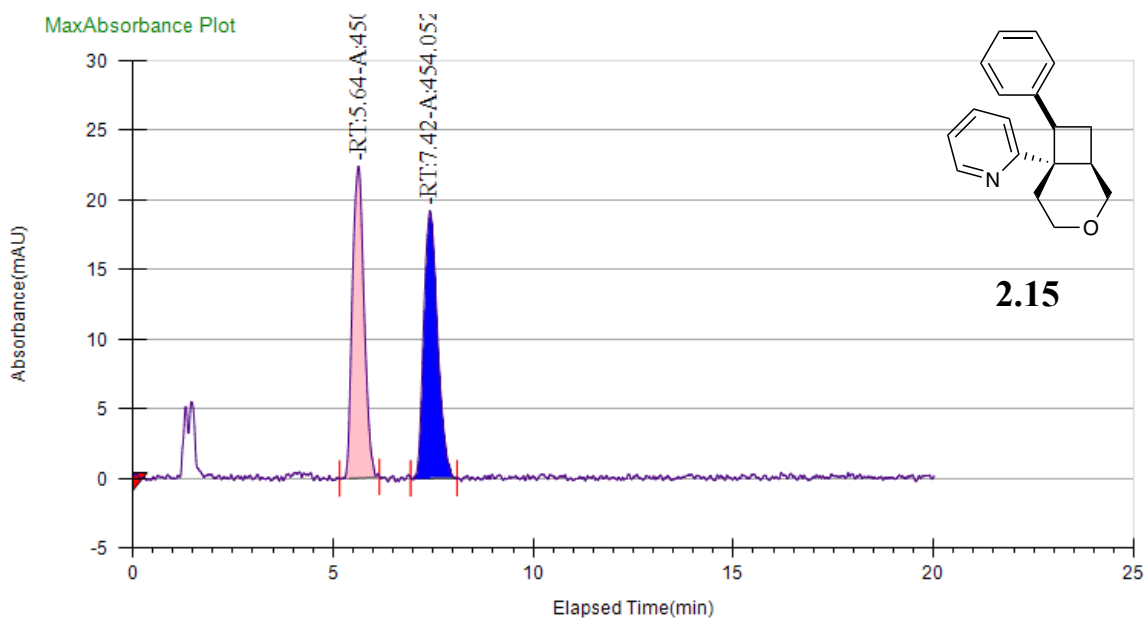
Log Author	Log Date	Report By	Report Date	Notes
Administrator	2/20/2021 1:40:42 PM	Administrator	2/22/2021	

### Run Information

Instrument Method	Inj. Vol.	Solvent	Column	Sample	Well Location	Temp. (C)	Flow (g/min)	% Modifier	Pressure (Bar)
5%IPA-20min	20 uL	IPA	Column 1	SJC-4-190_F16-17	12F	35	3	5	100

### Peak Information

Peak No	% Area	Area	Ret. Time	Height	Cap. Factor
1	95.1735	2697.9396	7.14 min	92.141	0
2	4.8265	136.8182	9.1 min	4.1342	0

**General Information**

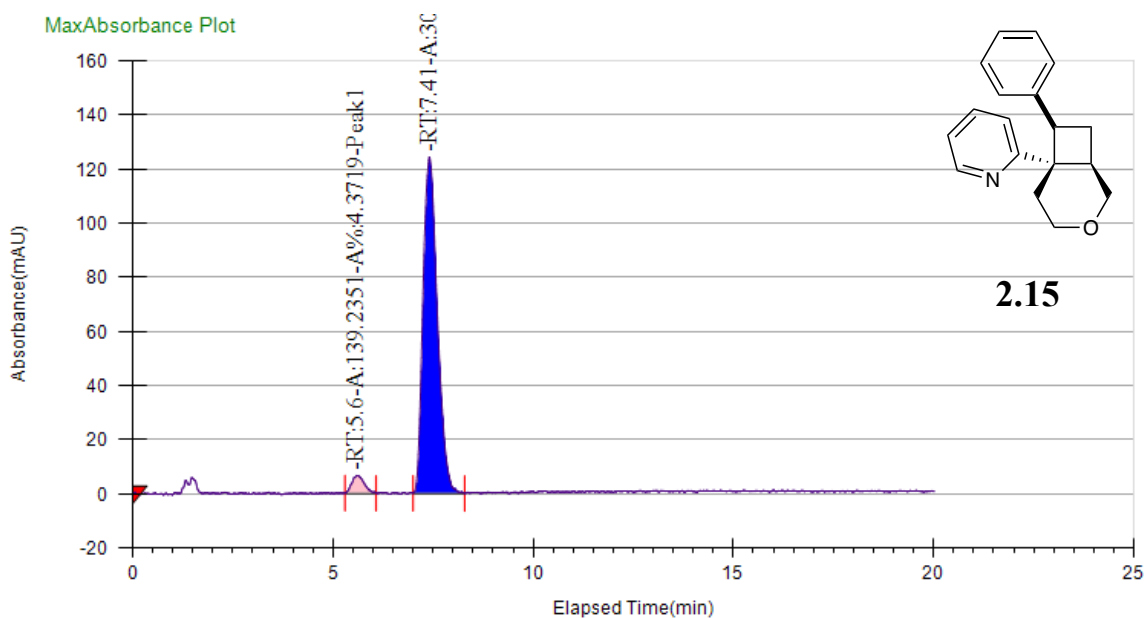
Log Author	Log Date	Report By	Report Date	Notes
Administrator	2/17/2021 7:42:45 PM	Administrator	2/18/2021	

**Run Information**

Instrument Method	Inj. Vol.	Solvent	Column	Sample	Well Location	Temp. (C)	Flow (g/min)	% Modifier	Pressure (Bar)
5%MeOH-20min	20 uL	MeOH	Column 3	SJC-4-187_F17-20	14F	35	3	5	100

**Peak Information**

Peak No	% Area	Area	Ret. Time	Height	Cap. Factor
1	49.8248	450.882	5.64 min	22.3771	5640.5833
2	50.1752	454.052	7.42 min	19.2198	7423.9



### General Information

Log Author	Log Date	Report By	Report Date	Notes
Administrator	2/18/2021 11:15:32 AM	Administrator	2/18/2021	

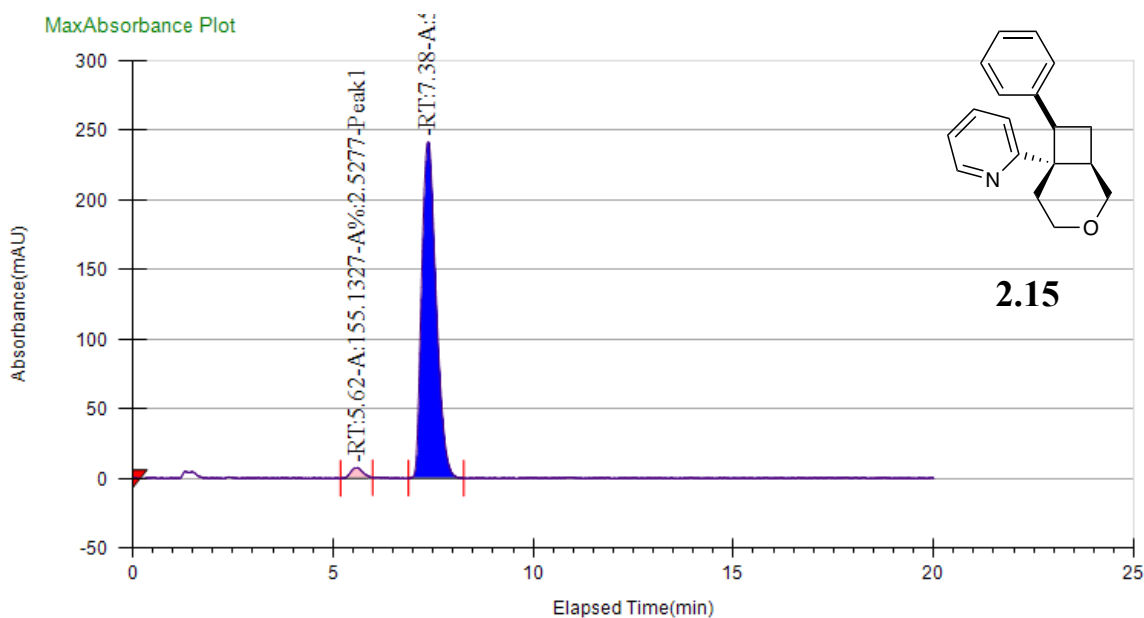
### Run Information

Instrument Method	Inj. Vol.	Solvent	Column	Sample	Well Location	Temp. (C)	Flow (g/min)	% Modifier	Pressure (Bar)
5%MeOH-20min	20 uL	MeOH	Column 3	SJC-4-188_F19-30	14F	35	3	5	100

### Peak Information

Peak No	% Area	Area	Ret. Time	Height	Cap. Factor
1	4.3719	139.2351	5.6 min	6.5221	5598.9167
2	95.6281	3045.5141	7.41 min	124.3246	7407.2333





### General Information

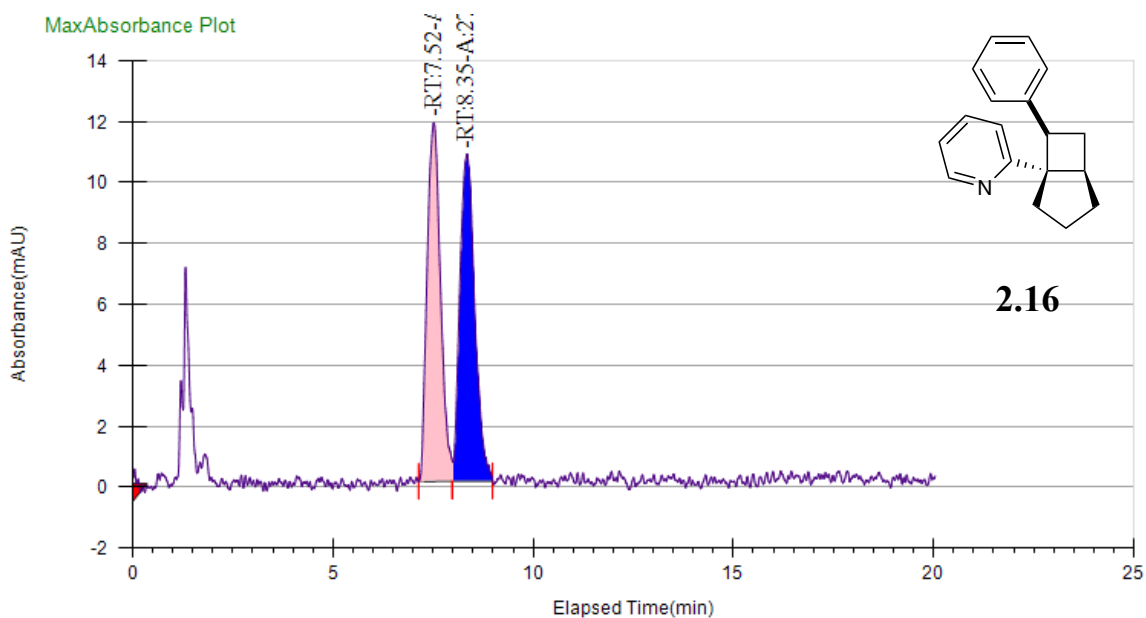
Log Author	Log Date	Report By	Report Date	Notes
Administrator	2/19/2021 1:21:00 PM	Administrator	2/19/2021	

### Run Information

Instrument Method	Inj. Vol.	Solvent	Column	Sample	Well Location	Temp. (C)	Flow (g/min)	% Modifier	Pressure (Bar)
5%MeOH-20min	20 uL	MeOH	Column 3	SJC-4-189_F19-29	14F	35	3	5	100

### Peak Information

Peak No	% Area	Area	Ret. Time	Height	Cap. Factor
1	2.5277	155.1327	5.62 min	7.417	0
2	97.4723	5982.152	7.38 min	241.6265	0



### General Information

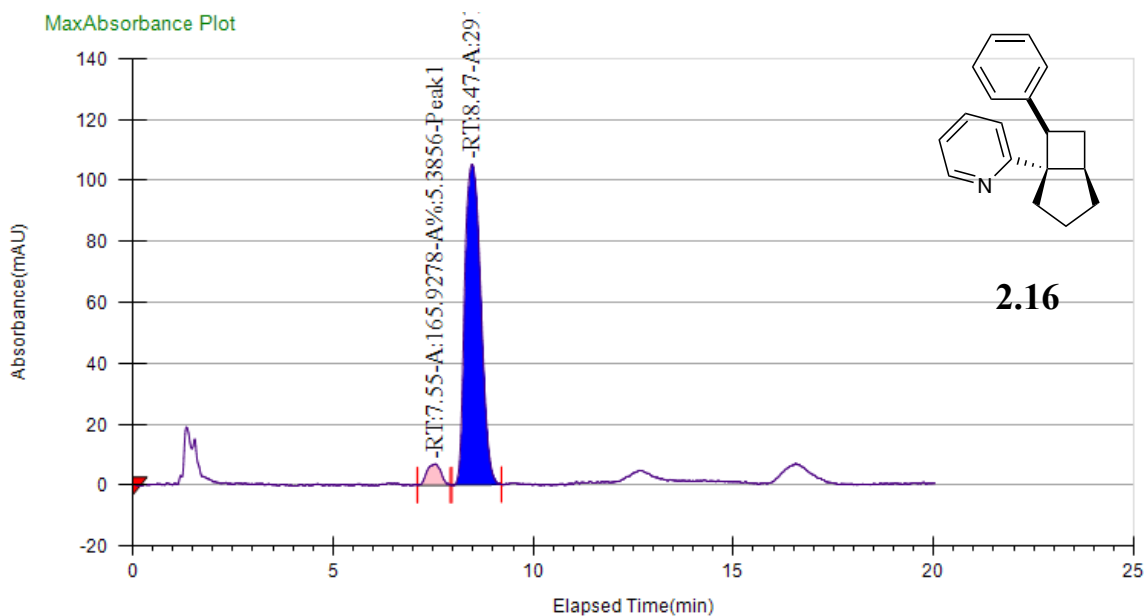
Log Author	Log Date	Report By	Report Date	Notes
Administrator	5/6/2021 10:40:50 AM	Administrator	5/6/2021	

### Run Information

Instrument Method	Inj. Vol.	Solvent	Column	Sample	Well Location	Temp. (C)	Flow (g/min)	% Modifier	Pressure (Bar)
5%IPA-20min	10 uL	IPA	Column 1	SJC-4-218_F18-21	12F	35	3	5	100

### Peak Information

Peak No	% Area	Area	Ret. Time	Height	Cap. Factor
1	49.7032	271.2864	7.52 min	11.7777	0
2	50.2968	274.5261	8.35 min	10.7491	0

**General Information**

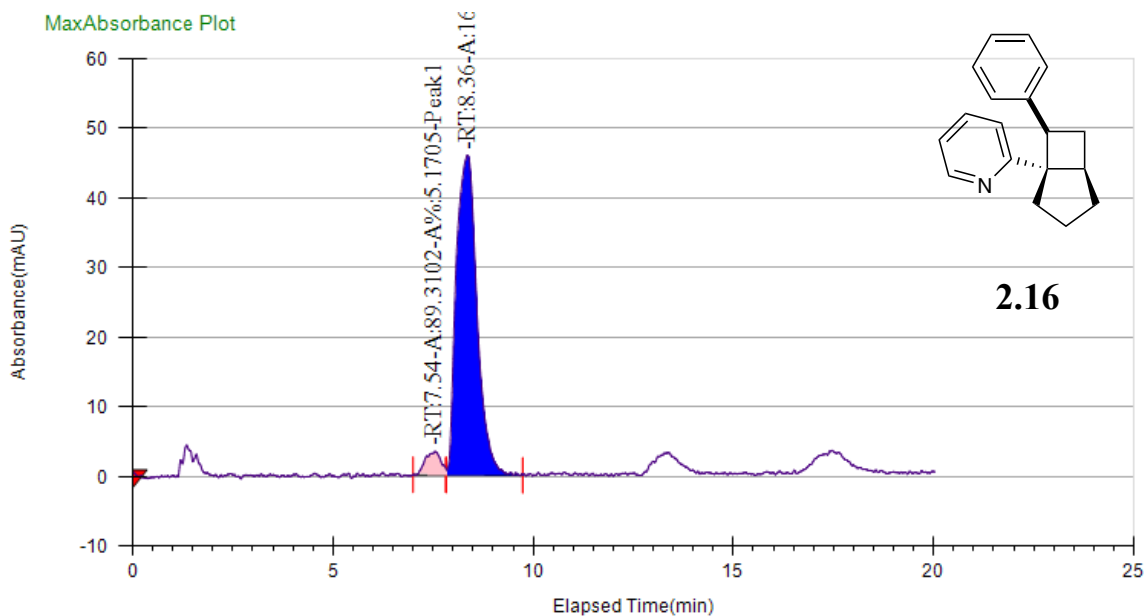
Log Author	Log Date	Report By	Report Date	Notes
Administrator	9/5/2020 11:45:41 AM	Administrator	9/5/2020	

**Run Information**

Instrument Method	Inj. Vol.	Solvent	Column	Sample	Well Location	Temp. (C)	Flow (g/min)	% Modifier	Pressure (Bar)
5%IPA-20min	10 uL	IPA	Column 1	SJC-4-074_F28-40	14F	35	3	5	100

**Peak Information**

Peak No	% Area	Area	Ret. Time	Height	Cap. Factor
1	5.3856	165.9278	7.55 min	6.9207	0
2	94.6144	2915.0199	8.47 min	105.2623	0



### General Information

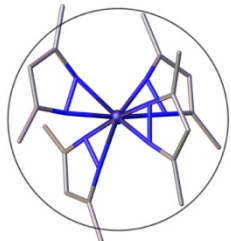
Log Author	Log Date	Report By	Report Date	Notes
Administrator	3/5/2021 2:09:29 PM	Administrator	3/5/2021	

### Run Information

Instrument Method	Inj. Vol.	Solvent	Column	Sample	Well Location	Temp. (C)	Flow (g/min)	% Modifier	Pressure (Bar)
5%IPA-20min	20 uL	IPA	Column 1	SJC-4-198_F38-55	13F	35	3	5	100

### Peak Information

Peak No	% Area	Area	Ret. Time	Height	Cap. Factor
1	5.1705	89.3102	7.54 min	3.332	0
2	94.8295	1637.977	8.36 min	45.9618	0

2.10.16. X-Ray Structure of **2.2**.

## Molecular Structure Laboratory

ILIA A. GUZEI, PH.D.

---

University of Wisconsin-Madison

☎ 608-263-4694

2124 Chemistry Department

Fax 608-262-0381

1101 University Ave

Madison, WI 53706

E-mail: [iguzei@chem.wisc.edu](mailto:iguzei@chem.wisc.edu)

---

## Structural report on Yoon60

December 12, 2019

Crystallographic Experimental Section

Data Collection

A colorless crystal with approximate dimensions  $0.07 \times 0.06 \times 0.04 \text{ mm}^3$  was selected under oil under ambient conditions and attached to the tip of a MiTeGen MicroMount<sup>®</sup>. The crystal was mounted in a stream of cold nitrogen at 100(1) K and centered in the X-ray beam by using a video camera.

The crystal evaluation and data collection were performed on a Bruker Quazar SMART APEXII diffractometer with Mo K $\alpha$  ( $\lambda = 0.71073 \text{ \AA}$ ) radiation and the detector to crystal distance of 4.96 cm.<sup>65</sup>

The initial cell constants were obtained from three series of  $\omega$  scans at different starting angles. Each series consisted of 12 frames collected at intervals of  $0.5^\circ$  in a  $6^\circ$  range about  $\omega$  with the exposure time of 20 seconds per frame. The reflections were successfully indexed by an automated indexing routine built in the APEX3 program suite. The final cell constants were calculated from a set of 5289 strong reflections from the actual data collection.

The data were collected by using the full sphere data collection routine to survey the reciprocal space to the extent of a full sphere to a resolution of  $0.68 \text{ \AA}$ . A total of 31983 data were harvested by collecting 4 sets of frames with  $0.5^\circ$  scans in  $\omega$  and  $\phi$  with exposure times of 90 sec per frame. These highly redundant datasets were corrected for Lorentz and polarization effects. The absorption correction was based on fitting a function to the empirical transmission surface as sampled by multiple equivalent measurements.<sup>66</sup>

### Structure Solution and Refinement

The systematic absences in the diffraction data were uniquely consistent for the space group  $P2_12_12_1$  that yielded chemically reasonable and computationally stable results of refinement.<sup>67,68,69,70,71,72</sup>

A successful solution by the direct methods provided most non-hydrogen atoms from the  $E$ -map. The remaining non-hydrogen atoms were located in an alternating series of least-squares cycles and difference Fourier maps. All non-hydrogen atoms were refined with anisotropic displacement coefficients. All hydrogen atoms were included in the structure factor calculation at idealized positions and were allowed to ride on the neighboring atoms with relative isotropic displacement coefficients.

The absolute configuration was unequivocally established based on resonant scattering effects: C6 –  $S$ , C7 –  $R$ , C15 –  $R$ . There may be a 5(3) % contribution to the diffraction pattern from the other enantiomer.

The final least-squares refinement of 193 parameters against 5215 data resulted in residuals  $R$  (based on  $F^2$  for  $I \geq 2\sigma$ ) and  $wR$  (based on  $F^2$  for all data) of 0.0516 and 0.1100, respectively. The final difference Fourier map was featureless.

### Summary

**Crystal Data** for  $C_{19}H_{22}ClN$  ( $M=299.82$  g/mol): orthorhombic, space group  $P2_12_12_1$  (no. 19),  $a = 6.986(3)$  Å,  $b = 8.603(3)$  Å,  $c = 26.046(9)$  Å,  $V = 1565.2(10)$  Å<sup>3</sup>,  $Z = 4$ ,  $T = 100.02$  K,  $\mu(\text{Mo K}\alpha) = 0.238$  mm<sup>-1</sup>,  $D_{\text{calc}} = 1.272$  g/cm<sup>3</sup>, 31983 reflections measured ( $3.128^\circ \leq 2\theta \leq 63.036^\circ$ ), 5215 unique ( $R_{\text{int}} = 0.0721$ ,  $R_{\text{sigma}} = 0.0559$ ) which were used in all calculations. The final  $R_1$  was 0.0516 ( $I > 2\sigma(I)$ ) and  $wR_2$  was 0.1100 (all data).

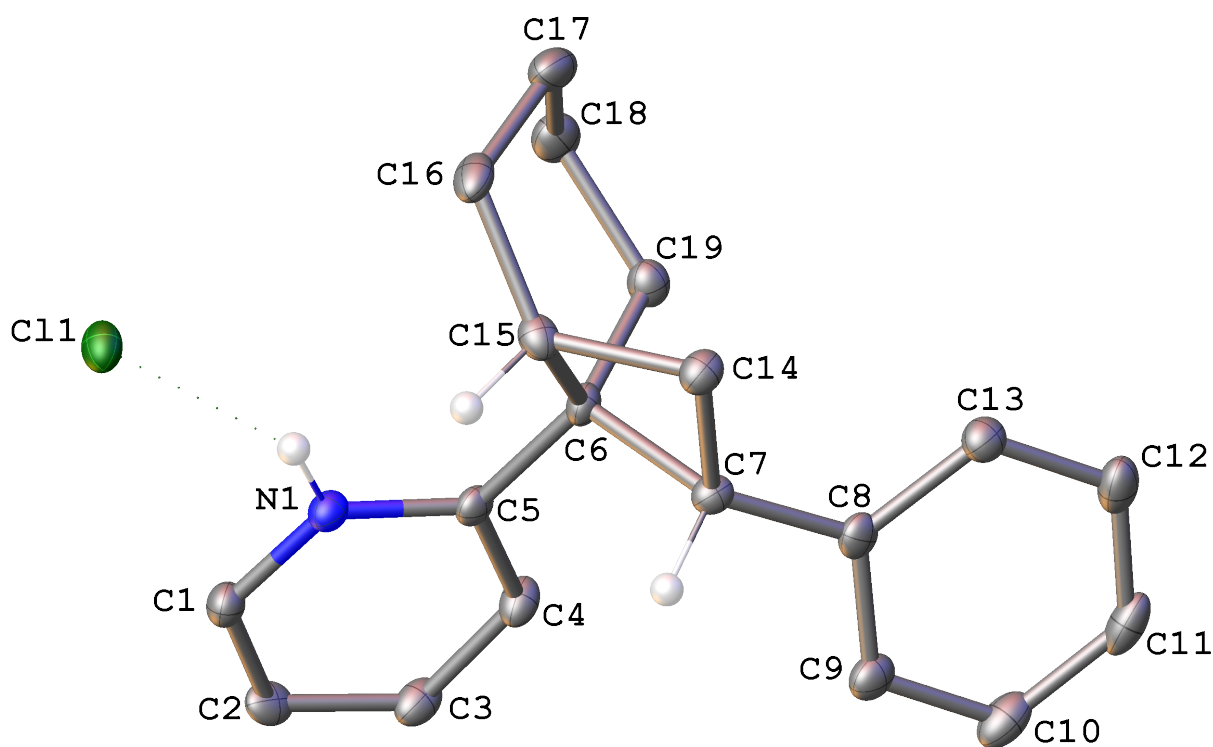


Figure 2.20 A molecular drawing of Yoon60 shown with 50% probability ellipsoids. Only selected H atoms are shown.

**Crystal Table 1 Crystal data and structure refinement for yoon60.**

Identification code	yoon60
Empirical formula	C <sub>19</sub> H <sub>22</sub> ClN
Formula weight	299.82
Temperature/K	100.02
Crystal system	orthorhombic
Space group	P2 <sub>1</sub> 2 <sub>1</sub> 2 <sub>1</sub>
a/Å	6.986(3)
b/Å	8.603(3)
c/Å	26.046(9)
$\alpha$ /°	90
$\beta$ /°	90
$\gamma$ /°	90
Volume/Å <sup>3</sup>	1565.2(10)
Z	4
$\rho_{\text{calc}}/\text{cm}^3$	1.272
$\mu/\text{mm}^{-1}$	0.238



F(000)	640.0
Crystal size/mm <sup>3</sup>	0.07 × 0.06 × 0.04
Radiation	Mo K $\alpha$ ( $\lambda$ = 0.71073)
2 $\Theta$ range for data collection/ $^{\circ}$	3.128 to 63.036
Index ranges	-10 $\leq$ h $\leq$ 10, -12 $\leq$ k $\leq$ 12, -38 $\leq$ l $\leq$ 38
Reflections collected	31983
Independent reflections	5215 [R <sub>int</sub> = 0.0721, R <sub>sigma</sub> = 0.0559]
Data/restraints/parameters	5215/0/193
Goodness-of-fit on F <sup>2</sup>	1.094
Final R indexes [I $\geq$ 2 $\sigma$ (I)]	R <sub>1</sub> = 0.0516, wR <sub>2</sub> = 0.1049
Final R indexes [all data]	R <sub>1</sub> = 0.0669, wR <sub>2</sub> = 0.1100
Largest diff. peak/hole / e $\text{\AA}^{-3}$	0.59/-0.33
Flack parameter	0.05(3)

**Crystal Table 2 Fractional Atomic Coordinates ( $\times 10^4$ ) and Equivalent Isotropic Displacement Parameters ( $\text{\AA}^2 \times 10^3$ ) for yoon60.  $U_{eq}$  is defined as 1/3 of of the trace of the orthogonalised  $U_{ij}$  tensor.**

<b>Atom</b>	<b>x</b>	<b>y</b>	<b>z</b>	<b>U(eq)</b>
C11	7555.9(10)	1343.3(7)	7324.1(2)	18.98(14)
N1	6414(3)	4503(3)	6932.0(9)	14.7(5)
C1	7654(4)	5292(3)	7232.6(10)	17.1(5)
C2	7823(4)	6868(3)	7185.7(11)	18.0(6)
C3	6750(4)	7625(3)	6814.9(12)	19.1(6)
C4	5542(4)	6784(3)	6499.9(11)	17.0(5)
C5	5340(4)	5186(3)	6567.1(10)	13.9(5)
C6	3923(4)	4249(3)	6264.1(10)	13.8(5)
C7	1754(4)	4747(3)	6363.8(10)	13.7(5)
C8	815(4)	5986(3)	6048.7(10)	16.0(5)
C9	844(4)	7522(3)	6222.9(11)	18.9(6)
C10	-20(4)	8697(4)	5946.1(12)	23.9(6)
C11	-939(4)	8379(4)	5490.0(12)	23.7(6)

C12	-1022(4)	6870(4)	5313.0(12)	23.2(6)
C13	-149(4)	5665(3)	5589.7(11)	17.6(5)
C14	1235(4)	3010(3)	6317.9(11)	16.6(5)
C15	3334(4)	2608(3)	6461.4(11)	16.1(5)
C16	4345(4)	1195(3)	6237.6(11)	20.4(6)
C17	4693(4)	1327(4)	5663.7(11)	24.1(6)
C18	5703(4)	2864(4)	5544.5(12)	22.9(6)
C19	4431(4)	4239(3)	5689.3(11)	17.5(5)

**Crystal Table 3 Anisotropic Displacement Parameters ( $\text{\AA}^2 \times 10^3$ ) for yoon60. The Anisotropic displacement factor exponent takes the form:  $-2\pi^2[h^2a^{*2}U_{11}+2hka^*b^*U_{12}+\dots]$ .**

Atom	$U_{11}$	$U_{22}$	$U_{33}$	$U_{23}$	$U_{13}$	$U_{12}$
Cl1	19.2(3)	14.8(3)	22.9(3)	3.1(2)	-5.6(3)	-0.9(3)
N1	13.2(10)	12.4(11)	18.5(11)	-0.3(9)	-0.7(9)	0.1(9)
C1	14.4(11)	17.6(11)	19.3(13)	-0.2(9)	-2.7(11)	2.1(11)
C2	10.9(12)	19.0(13)	23.9(14)	-5.3(10)	-0.1(9)	-5.0(10)
C3	13.6(12)	13.8(13)	30.0(15)	-0.8(11)	0.1(11)	-1.0(10)

C4	13.0(11)	12.9(12)	25.2(14)	3.6(10)	-2.2(10)	-1.0(10)
C5	9.2(10)	14.8(12)	17.7(12)	-1.0(10)	0.6(9)	1.4(9)
C6	10.4(11)	13.7(12)	17.4(12)	1.2(9)	-1.5(10)	1.3(9)
C7	12.4(11)	12.3(12)	16.5(12)	-0.1(10)	1.6(10)	-0.9(10)
C8	9.4(10)	19.2(13)	19.3(12)	0.6(10)	1.3(9)	1.4(10)
C9	12.4(11)	18.4(14)	25.7(14)	-1.9(11)	0.7(11)	1.1(11)
C10	18.2(13)	15.5(13)	38.1(16)	3.6(13)	3.7(12)	1.4(11)
C11	16.0(12)	23.8(16)	31.3(16)	10.7(12)	4.5(11)	7.1(11)
C12	15.9(13)	31.4(17)	22.2(14)	3.2(12)	-0.8(11)	6.2(12)
C13	14.9(12)	16.5(13)	21.5(14)	-1.2(10)	-1.0(11)	-1.2(10)
C14	14.2(12)	14.2(13)	21.6(13)	0.5(10)	0.3(10)	-0.8(10)
C15	16.6(12)	14.3(13)	17.3(12)	1.5(10)	-3.0(10)	-3.4(11)
C16	19.6(13)	11.8(12)	29.9(14)	-0.1(11)	-8.2(11)	1.7(11)
C17	18.3(12)	24.0(15)	30.1(15)	-9.5(13)	-3.0(11)	5.6(12)
C18	16.2(12)	29.6(16)	23.0(14)	-3.1(12)	1.6(11)	3.4(12)
C19	14.8(12)	20.5(14)	17.1(12)	0.7(10)	-0.3(10)	-0.5(10)

**Crystal Table 4 Bond Lengths for yoon60.**

<b>Atom Atom Length/Å</b>			<b>Atom Atom Length/Å</b>		
N1	C1	1.351(4)	C8	C9	1.397(4)
N1	C5	1.346(3)	C8	C13	1.400(4)
C1	C2	1.367(4)	C9	C10	1.381(4)
C2	C3	1.385(4)	C10	C11	1.378(4)
C3	C4	1.381(4)	C11	C12	1.379(5)
C4	C5	1.393(4)	C12	C13	1.402(4)
C5	C6	1.501(4)	C14	C15	1.552(4)
C6	C7	1.595(4)	C15	C16	1.522(4)
C6	C15	1.558(4)	C16	C17	1.519(4)
C6	C19	1.539(4)	C17	C18	1.531(5)
C7	C8	1.497(4)	C18	C19	1.526(4)
C7	C14	1.542(4)			

**Crystal Table 5 Bond Angles for yoon60.**

<b>Atom Atom Atom Angle/°</b>	<b>Atom Atom Atom Angle/°</b>
-------------------------------	-------------------------------

C5	N1	C1	123.2(2)	C9	C8	C7	119.3(2)
N1	C1	C2	120.2(3)	C9	C8	C13	118.1(3)
C1	C2	C3	118.8(3)	C13	C8	C7	122.6(3)
C4	C3	C2	119.9(3)	C10	C9	C8	121.1(3)
C3	C4	C5	120.3(3)	C11	C10	C9	120.5(3)
N1	C5	C4	117.6(2)	C10	C11	C12	119.7(3)
N1	C5	C6	120.3(2)	C11	C12	C13	120.4(3)
C4	C5	C6	122.1(2)	C8	C13	C12	120.2(3)
C5	C6	C7	113.4(2)	C7	C14	C15	88.6(2)
C5	C6	C15	119.2(2)	C14	C15	C6	88.2(2)
C5	C6	C19	111.3(2)	C16	C15	C6	118.4(2)
C15	C6	C7	86.49(19)	C16	C15	C14	121.6(2)
C19	C6	C7	112.3(2)	C17	C16	C15	113.1(2)
C19	C6	C15	112.1(2)	C16	C17	C18	109.7(2)
C8	C7	C6	121.2(2)	C19	C18	C17	110.6(2)
C8	C7	C14	123.0(2)	C18	C19	C6	112.3(2)
C14	C7	C6	87.2(2)				

**Crystal Table 6 Hydrogen Bonds for yoon60.**

<b>D</b>	<b>H</b>	<b>A</b>	<b>d(D-H)/Å</b>	<b>d(H-A)/Å</b>	<b>d(D-A)/Å</b>	<b>D-H-A/°</b>
N1	H1	C11	0.85(4)	2.24(4)	3.011(3)	152(3)

**Crystal Table 7 Torsion Angles for yoon60.**

<b>A</b>	<b>B</b>	<b>C</b>	<b>D</b>	<b>Angle/°</b>	<b>A</b>	<b>B</b>	<b>C</b>	<b>D</b>	<b>Angle/°</b>
N1	C1	C2	C3	-2.1(4)	C7	C6	C19	C18	-140.1(2)
N1	C5	C6	C7	114.7(3)	C7	C8	C9	C10	-179.4(3)
N1	C5	C6	C15	15.2(4)	C7	C8	C13	C12	179.3(3)
N1	C5	C6	C19	-117.6(3)	C7	C14	C15	C6	-23.6(2)
C1	N1	C5	C4	0.3(4)	C7	C14	C15	C16	-146.2(3)
C1	N1	C5	C6	-177.1(3)	C8	C7	C14	C15	148.9(2)
C1	C2	C3	C4	-0.3(4)	C8	C9	C10	C11	0.1(4)
C2	C3	C4	C5	2.6(4)	C9	C8	C13	C12	1.2(4)
C3	C4	C5	N1	-2.6(4)	C9	C10	C11	C12	1.1(4)
C3	C4	C5	C6	174.7(3)	C10	C11	C12	C13	-1.1(4)
C4	C5	C6	C7	-62.6(3)	C11	C12	C13	C8	0.0(4)

C4 C5 C6 C15-162.1(2)	C13 C8 C9 C10-1.2(4)
C4 C5 C6 C19 65.1(3)	C14 C7 C8 C9 158.0(3)
C5 N1 C1 C2 2.1(4)	C14 C7 C8 C13 -20.0(4)
C5 C6 C7 C8 89.2(3)	C14 C15 C16 C17 66.9(3)
C5 C6 C7 C14 -143.4(2)	C15 C6 C7 C8 -150.4(3)
C5 C6 C15 C14 137.7(2)	C15 C6 C7 C14 -23.0(2)
C5 C6 C15 C16 -96.9(3)	C15 C6 C19 C18 -44.6(3)
C5 C6 C19 C18 91.6(3)	C15 C16 C17 C18 52.2(3)
C6 C7 C8 C9 -93.0(3)	C16 C17 C18 C19 -63.2(3)
C6 C7 C8 C13 88.9(3)	C17 C18 C19 C6 60.1(3)
C6 C7 C14 C15 23.1(2)	C19 C6 C7 C8 -37.9(3)
C6 C15 C16 C17 -39.9(3)	C19 C6 C7 C14 89.5(2)
C7 C6 C15 C14 22.8(2)	C19 C6 C15 C14 -89.8(2)
C7 C6 C15 C16 148.2(2)	C19 C6 C15 C16 35.5(3)

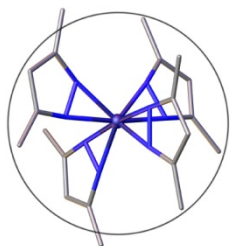
**Crystal Table 8 Hydrogen Atom Coordinates ( $\text{\AA} \times 10^4$ ) and Isotropic Displacement Parameters ( $\text{\AA}^2 \times 10^3$ ) for yoon60.**



<b>Atom</b>	<b>x</b>	<b>y</b>	<b>z</b>	<b>U(eq)</b>
H1	6420(50)	3520(40)	6966(12)	18
H1A	8410.09	4750.3	7477.2	20
H2	8662.16	7435.01	7403.4	22
H3	6844.38	8720.6	6777.27	23
H4	4847.15	7297.96	6236.29	20
H7	1633.89	5048.01	6733.2	16
H9	1469.36	7761.26	6537.06	23
H10	19.4	9734.2	6071.23	29
H11	-1511.82	9194.87	5298.43	28
H12	-1674.99	6645.11	5001.7	28
H13	-212.01	4627.65	5465.36	21
H14A	867.76	2686.7	5966.66	20
H14B	281.67	2655.09	6573.41	20
H15	3455.63	2583.73	6843.83	19
H16A	5588.38	1057.44	6413.98	25
H16B	3560.8	258.56	6305.46	25

H17A 3457.12	1280.71	5478.26	29
H17B 5494.78	446.68	5546.39	29
H18A 6918.51	2921.29	5738.95	28
H18B 6010.43	2913.06	5173.83	28
H19A 3236.74	4194.5	5485.26	21
H19B 5099.73	5218.35	5601.83	21

#### 2.10.17. X-Ray Structure of $\Delta$ -[Ir]



## Molecular Structure Laboratory

ILIA A. GUZEI, PH.D.

---

University of Wisconsin-Madison

☎ 608-263-4694

2124 Chemistry Department

Fax 608-262-0381

1101 University Ave

Madison, WI 53706

E-mail: [iguzei@chem.wisc.edu](mailto:iguzei@chem.wisc.edu)

---

# Structural report on Yoon77

March 29, 2021

## Crystallographic Experimental Section

### Data Collection

A yellow crystal with approximate dimensions  $0.109 \times 0.08 \times 0.024 \text{ mm}^3$  was selected under oil under ambient conditions and attached to the tip of a MiTeGen MicroMount©. The crystal was mounted in a stream of cold nitrogen at 100(1) K and centered in the X-ray beam by using a video camera.

The crystal evaluation and data collection were performed on a Bruker Quazar SMART APEXII diffractometer with Mo  $K_\alpha$  ( $\lambda = 0.71073 \text{ \AA}$ ) radiation and the diffractometer to crystal distance of 4.96 cm.<sup>65</sup>

The initial cell constants were obtained from three series of  $\omega$  scans at different starting angles. Each series consisted of 12 frames collected at intervals of  $0.5^\circ$  in a  $6^\circ$  range about  $\omega$  with the exposure time of 10 seconds per frame. The reflections were successfully indexed by an automated indexing routine built in the APEXII program suite. The final cell constants were calculated from a set of 9863 strong reflections from the actual data collection.

The data were collected by using the full sphere data collection routine to survey the reciprocal space to the extent of a full sphere to a resolution of  $0.70 \text{ \AA}$ . A total of 22130 data were harvested by collecting 6 sets of frames with  $0.5^\circ$  scans in  $\omega$  and  $\varphi$  with exposure times of 45 sec per frame. These highly redundant datasets were corrected for Lorentz and polarization effects. The absorption correction was based on fitting a function to the empirical transmission surface as sampled by multiple equivalent measurements.<sup>66</sup>

## Structure Solution and Refinement

The systematic absences in the diffraction data were consistent for the space groups  $P\bar{1}$  and  $P1$ . The  $E$ -statistics strongly suggested the non-centrosymmetric space group  $P1$  that yielded chemically reasonable and computationally stable results of refinement.<sup>67,68,69,70,71,72</sup>

A successful solution by the direct methods provided most non-hydrogen atoms from the  $E$ -map. The remaining non-hydrogen atoms were located in an alternating series of least-squares cycles and difference Fourier maps. All non-hydrogen atoms were refined with anisotropic displacement coefficients unless specified otherwise. All hydrogen atoms were included in the structure factor calculation at idealized positions and were allowed to ride on the neighboring atoms with relative isotropic displacement coefficients.

The composition of the asymmetric unit (in this case it is the unit cell) is two Ir complexes, two  $PF_6^-$  anions, and 3.91 molecules of solvent acetone.

There is positional disorder in all moieties except acetone O1.

Complex Ir1. The t-Bu group at C28 is disordered over two positions with the major component occupancy factor of 0.740(11). The bidentate ligand is disordered over two positions with the major component occupancy factor of 0.876(10); the minor component was refined isotropically.

Complex Ir2. The t-Bu group at C59 is disordered over two positions with the major component occupancy factor of 0.599(12). The t-Bu group at C72 is disordered over two positions with the major component occupancy factor of 0.749(12). The bidentate ligand is disordered over two positions with the major component occupancy factor of 0.514(12).

Anion P1 is disordered over two positions with the major component occupancy factor of 0.812(9).

Anion P2 is disordered over two positions with the major component occupancy factor of 0.739(10).

Three acetone molecules O6–O11 are disordered over six positions with occupancy factors for molecules O6, O7, O8, O9, O10, and O11: 0.496(4), 0.504(4), 0.504(4), 0.406(14), 0.580(15), 0.420(15), respectively.

The disordered moieties were refined with restraints and constraints.

The final least-squares refinement of 1685 parameters against 27002 data resulted in residuals  $R$  (based on  $F^2$  for  $I \geq 2\sigma$ ) and  $wR$  (based on  $F^2$  for all data) of 0.0384 and 0.0831, respectively. The final difference Fourier map contained several small peaks near the Ir atoms; these peaks were considered noise.

## Summary

**Crystal Data** for  $C_{55.865}H_{71.73}F_6IrN_4O_{3.955}P$  ( $M = 1199.73$  g/mol): triclinic, space group P1 (no. 1),  $a = 11.077(3)$  Å,  $b = 12.096(3)$  Å,  $c = 23.894(6)$  Å,  $\alpha = 76.572(14)^\circ$ ,  $\beta = 80.483(16)^\circ$ ,  $\gamma = 63.548(14)^\circ$ ,  $V = 2780.9(14)$  Å<sup>3</sup>,  $Z = 2$ ,  $T = 100.0$  K,  $\mu(\text{Mo K}\alpha) = 2.497$  mm<sup>-1</sup>,  $D_{\text{calc}} = 1.433$  g/cm<sup>3</sup>, 67079 reflections measured ( $1.756^\circ \leq 2\Theta \leq 56.626^\circ$ ), 27002 unique ( $R_{\text{int}} = 0.0230$ ,  $R_{\text{sigma}} = 0.0320$ ) which were used in all calculations. The final  $R_1$  was 0.0384 ( $I > 2\sigma(I)$ ) and  $wR_2$  was 0.0831 (all data).

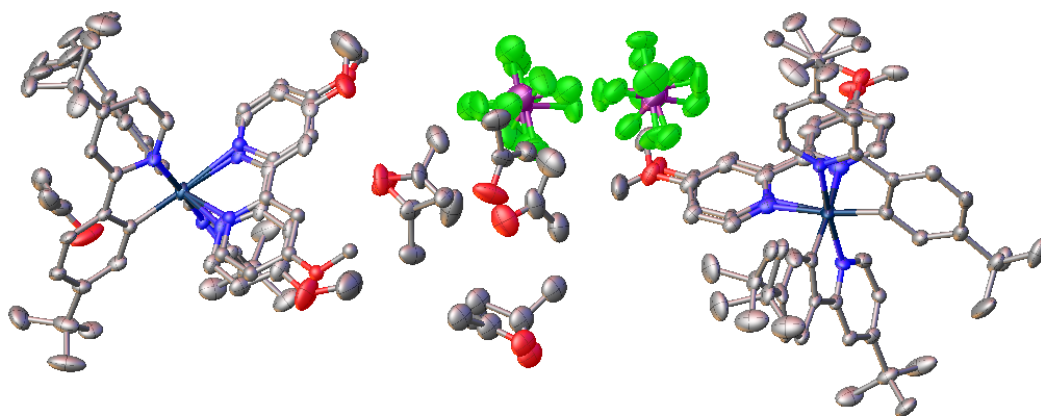


Figure 2.21 A molecular drawing of the unit cell content of Yoon77 shown with 50% probability ellipsoids. All H atoms are omitted but all disordered atoms are shown.

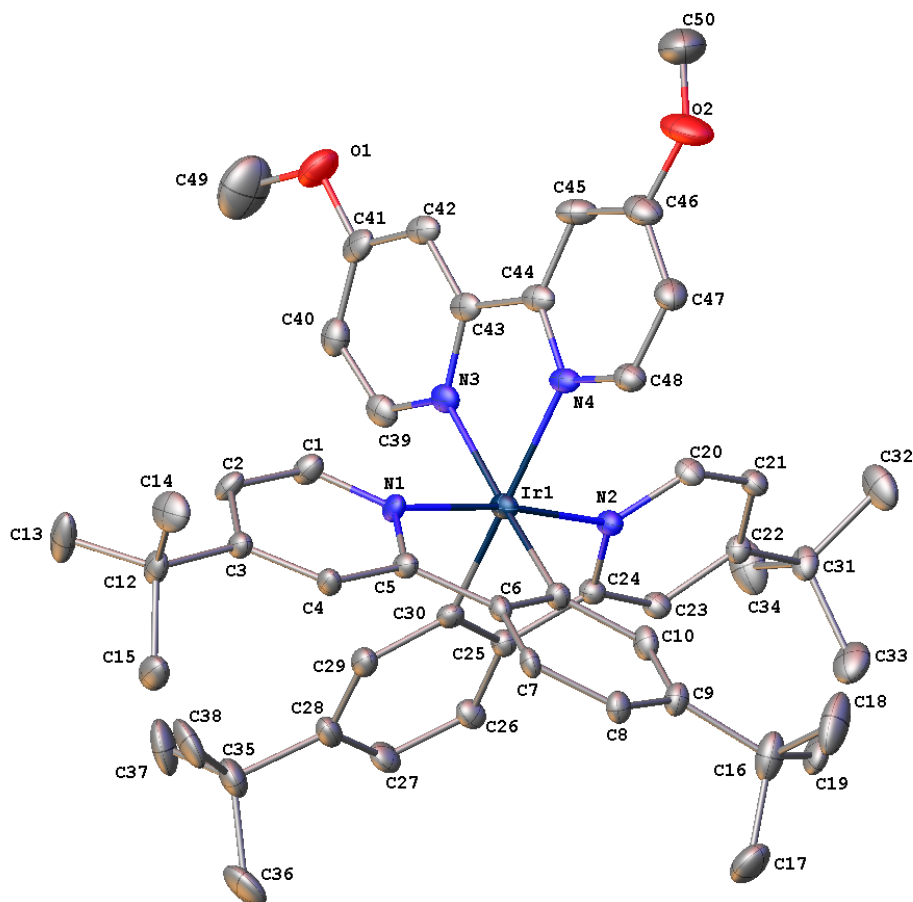


Figure 2.22 A molecular drawing of the Ir1 complex of Yoon77 shown with 30% probability ellipsoids. All H atoms and minor disorder components are omitted.

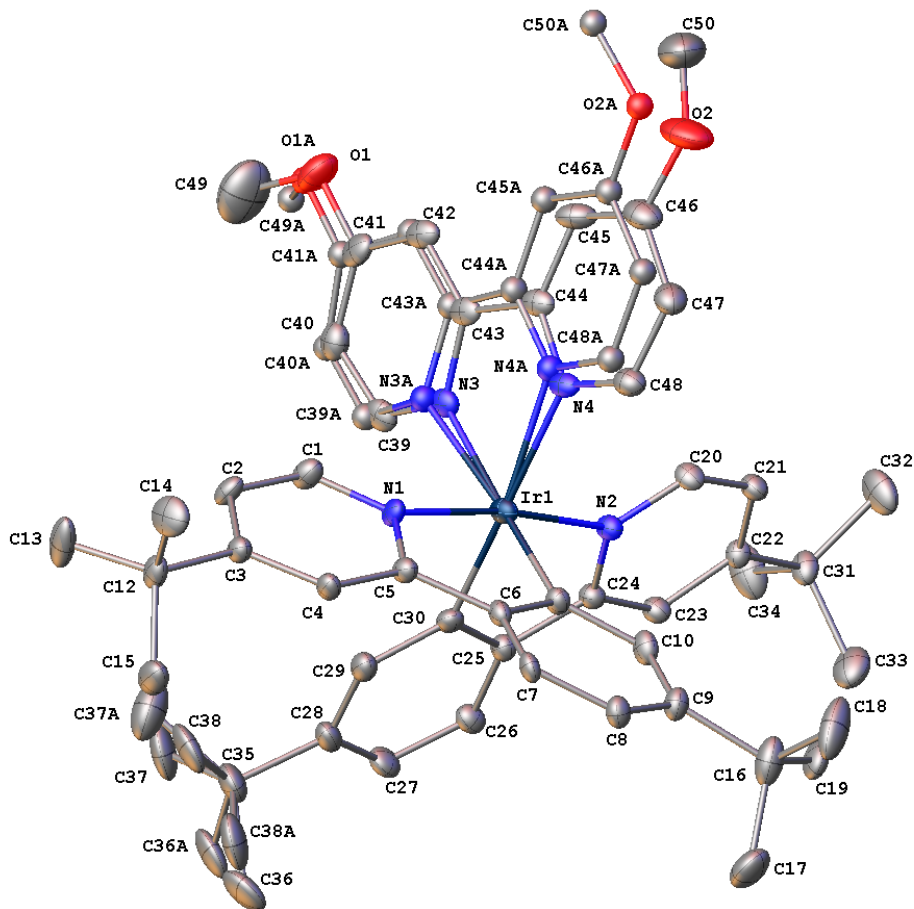


Figure 2.23 A molecular drawing of the Ir1 complex of Yoon77 shown with 30% probability ellipsoids. All H atoms are omitted but all disorder components are shown.



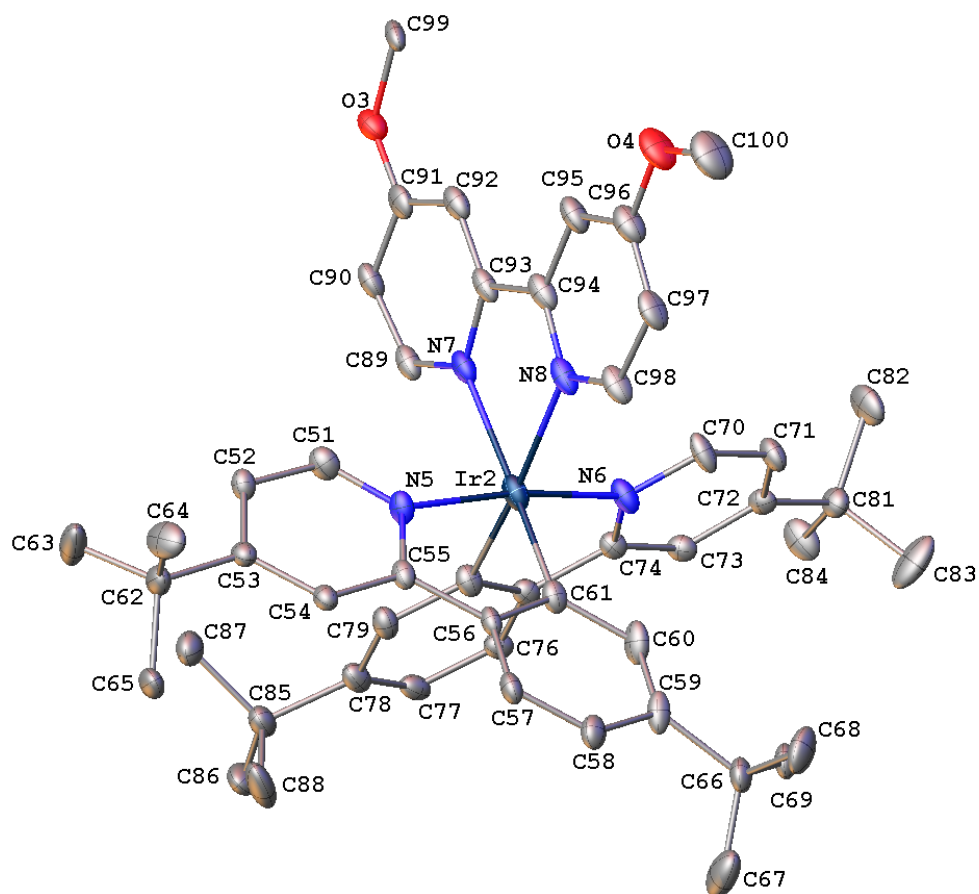


Figure 2.24 A molecular drawing of the Ir<sub>2</sub> complex of Yoon77 shown with 30% probability ellipsoids. All H atoms and minor disorder components are omitted.

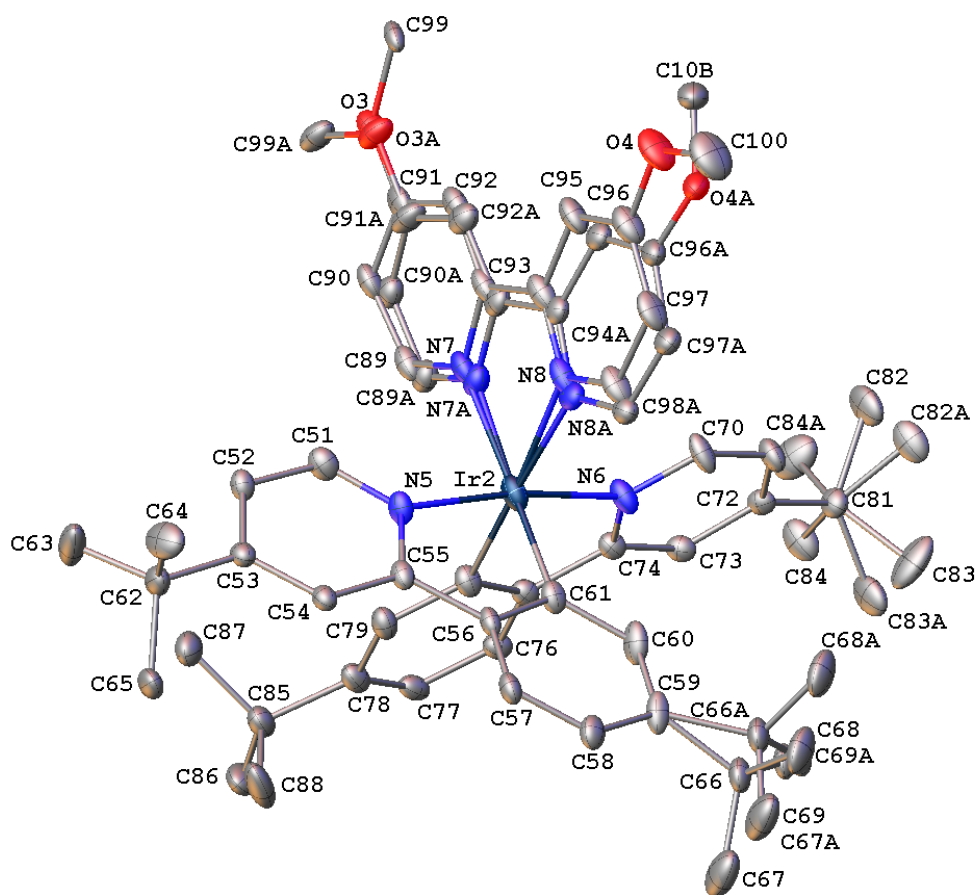


Figure 2.25 A molecular drawing of the Ir complex of Yoon77 shown with 30% probability ellipsoids. All H atoms are omitted but all disorder components are shown.

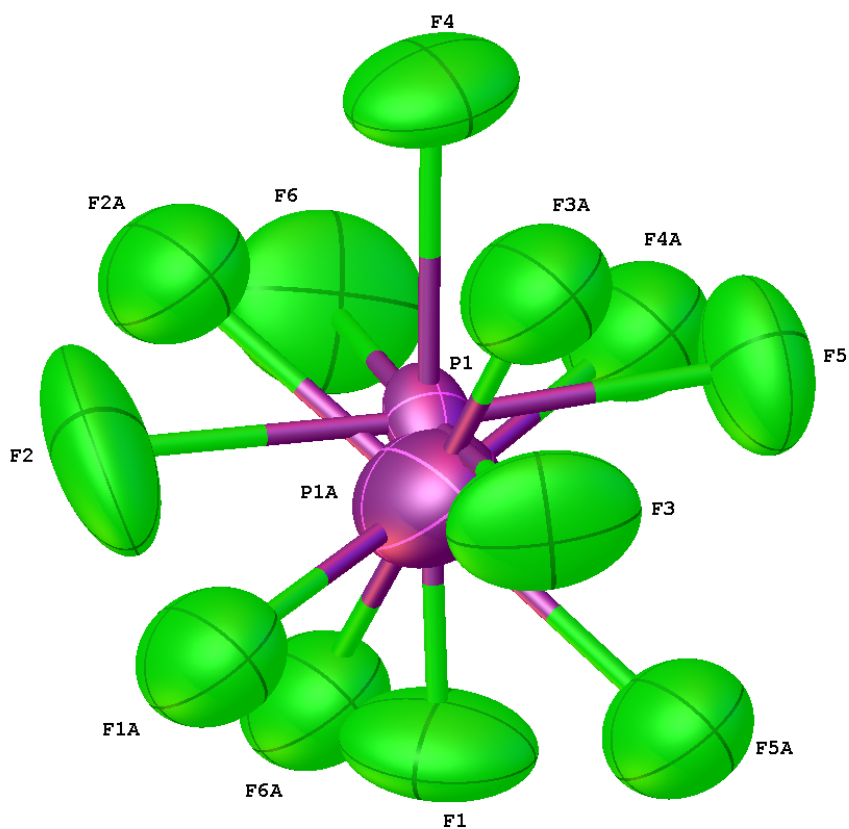


Figure 2.26 A molecular drawing of the disordered P1 anion of Yoon77 shown with 50% probability ellipsoids. Both disorder components are shown.

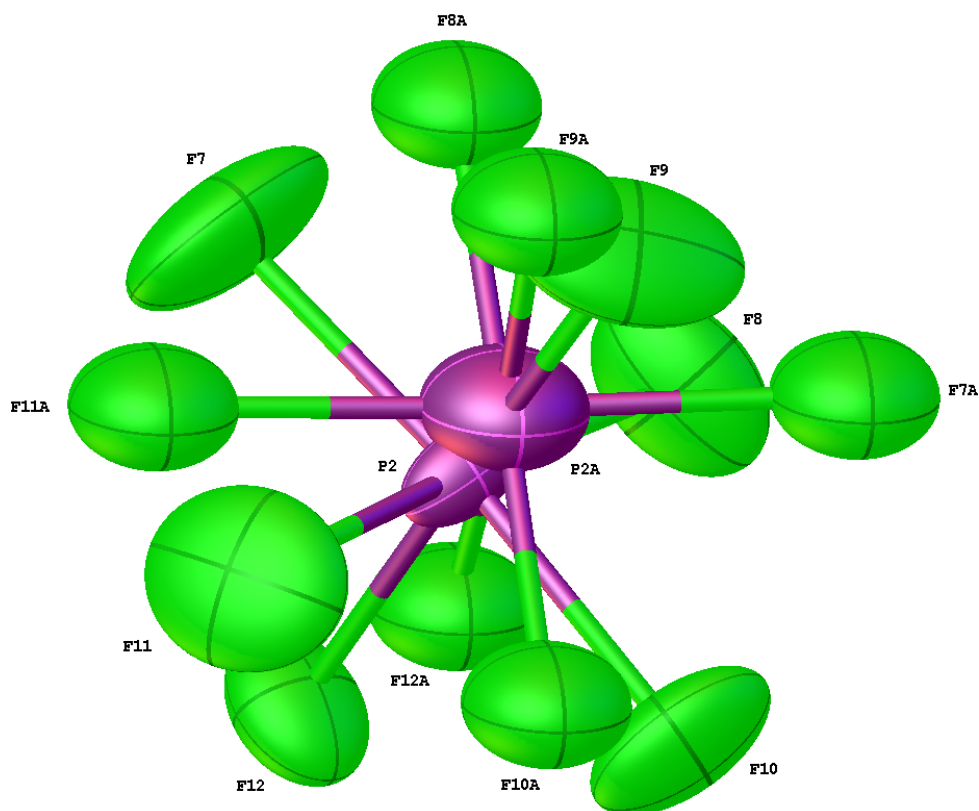


Figure 2.27 A molecular drawing of the disordered P2 anion of Yoon77 shown with 50% probability ellipsoids. Both disorder components are shown.

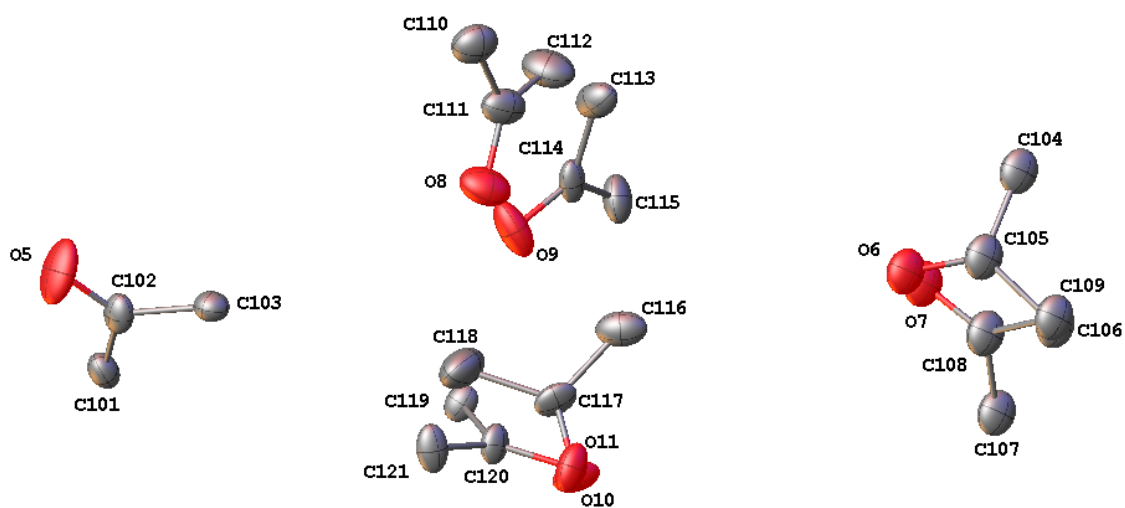


Figure 2.28 A molecular drawing of the acetone solvent molecules in structure Yoon77 shown with 50% probability ellipsoids. All H atoms are omitted but all disordered atoms are shown. All molecules except O5 have partial occupancy. The total number of solvent molecules is 3.91.

### Crystal Table 1 Crystal data and structure refinement for yoon77.

Identification code	yoon77
Empirical formula	$C_{55.87}H_{71.73}F_6IrN_4O_{3.96}P$
Formula weight	1199.73
Temperature/K	100.0
Crystal system	triclinic
Space group	P1

a/Å	11.077(3)
b/Å	12.096(3)
c/Å	23.894(6)
$\alpha$ /°	76.572(14)
$\beta$ /°	80.483(16)
$\gamma$ /°	63.548(14)
Volume/Å <sup>3</sup>	2780.9(14)
Z	2
$\rho_{\text{calc}}$ /cm <sup>3</sup>	1.433
$\mu$ /mm <sup>-1</sup>	2.497
F(000)	1225.0
Crystal size/mm <sup>3</sup>	0.109 × 0.08 × 0.024
Radiation	Mo K $\alpha$ ( $\lambda$ = 0.71073)
2 $\Theta$ range for data collection/°	1.756 to 56.626
Index ranges	-14 ≤ h ≤ 14, -16 ≤ k ≤ 16, -31 ≤ l ≤ 31
Reflections collected	67079
Independent reflections	27002 [R <sub>int</sub> = 0.0230, R <sub>sigma</sub> = 0.0320]

Data/restraints/parameters	27002/1918/1685
Goodness-of-fit on $F^2$	1.099
Final R indexes [ $I \geq 2\sigma(I)$ ]	$R_1 = 0.0384$ , $wR_2 = 0.0812$
Final R indexes [all data]	$R_1 = 0.0422$ , $wR_2 = 0.0831$
Largest diff. peak/hole / $e \text{ \AA}^{-3}$	3.11/-3.20
Flack parameter	-0.007(2)

**Crystal Table 2 Fractional Atomic Coordinates ( $\times 10^4$ ) and Equivalent Isotropic Displacement Parameters ( $\text{\AA}^2 \times 10^3$ ) for yoon77.  $U_{eq}$  is defined as 1/3 of of the trace of the orthogonalised  $U_{IJ}$  tensor.**

Atom	$x$	$y$	$z$	$U(eq)$
Ir1	6632.3(2)	9938.9(2)	7523.9(2)	26.46(7)
O1	2578(10)	9981(10)	6004(4)	63(3)
O2	9850(12)	7689(10)	5337(4)	81(3)
N3	5184(8)	9846(9)	7085(3)	29.5(18)
N4	7785(8)	9248(10)	6768(3)	28.0(15)

**Crystal Table 2 Fractional Atomic Coordinates ( $\times 10^4$ ) and Equivalent Isotropic Displacement Parameters ( $\text{\AA}^2 \times 10^3$ ) for yoon77.  $U_{\text{eq}}$  is defined as 1/3 of of the trace of the orthogonalised  $U_{\text{IJ}}$  tensor.**

Atom	$x$	$y$	$z$	$U(\text{eq})$
C39	3886(9)	10219(15)	7244(5)	35(2)
C40	2925(11)	10290(13)	6909(4)	40(2)
C41	3382(11)	9945(10)	6376(4)	41(2)
C42	4737(11)	9561(9)	6189(4)	35.0(18)
C43	5619(10)	9523(10)	6548(4)	31.9(17)
C44	7095(9)	9096(8)	6399(3)	31.9(18)
C45	7729(12)	8583(11)	5910(4)	41(2)
C46	9104(12)	8222(10)	5801(4)	47(2)
C47	9816(10)	8369(9)	6182(4)	41(2)
C48	9111(9)	8882(10)	6660(4)	34.1(19)
C49	1216(15)	10533(19)	6173(10)	112(6)
C50	9328(18)	7231(16)	5010(7)	103(6)
O1A	2160(30)	9970(60)	6110(16)	26



**Crystal Table 2 Fractional Atomic Coordinates ( $\times 10^4$ ) and Equivalent Isotropic Displacement Parameters ( $\text{\AA}^2 \times 10^3$ ) for yoon77.  $U_{\text{eq}}$  is defined as 1/3 of of the trace of the orthogonalised  $U_{\text{IJ}}$  tensor.**

Atom	$x$	$y$	$z$	$U(\text{eq})$
O2A	9220(30)	8100(40)	5155(13)	26
N3A	4890(30)	10040(90)	7050(20)	26
N4A	7490(30)	9290(90)	6700(20)	26
C39A	3620(40)	10360(130)	7260(30)	26
C40A	2650(40)	10280(90)	6990(20)	26
C41A	3010(30)	10010(70)	6430(20)	26
C42A	4360(30)	9530(70)	6230(20)	26
C43A	5280(30)	9560(80)	6550(20)	26
C44A	6700(30)	9270(70)	6330(18)	26
C45A	7240(30)	8820(60)	5818(17)	26
C46A	8600(30)	8480(60)	5667(16)	26
C47A	9400(30)	8560(60)	6029(18)	26
C48A	8800(30)	8970(80)	6540(20)	26

**Crystal Table 2 Fractional Atomic Coordinates ( $\times 10^4$ ) and Equivalent Isotropic Displacement Parameters ( $\text{\AA}^2 \times 10^3$ ) for yoon77.  $U_{\text{eq}}$  is defined as 1/3 of of the trace of the orthogonalised  $U_{\text{IJ}}$  tensor.**

Atom	$x$	$y$	$z$	$U(\text{eq})$
C49A	1180(40)	9630(60)	6440(20)	26
C50A	8480(40)	8300(50)	4705(15)	26
N1	6206(7)	11769(5)	7160(3)	27.3(13)
N2	6974(7)	8194(5)	7990(3)	24.7(12)
C1	5092(8)	12572(7)	6886(3)	34.0(16)
C2	4704(9)	13859(7)	6737(3)	29.8(17)
C3	5534(7)	14351(6)	6869(3)	27.5(14)
C4	6703(7)	13514(6)	7133(3)	27.5(14)
C5	7032(7)	12234(6)	7290(3)	25.7(13)
C6	8166(7)	11284(6)	7622(3)	24.4(13)
C7	9191(7)	11526(6)	7758(3)	27.1(14)
C8	10172(7)	10598(6)	8115(3)	31.3(15)
C9	10134(7)	9444(7)	8342(3)	31.9(15)

**Crystal Table 2 Fractional Atomic Coordinates ( $\times 10^4$ ) and Equivalent Isotropic Displacement Parameters ( $\text{\AA}^2 \times 10^3$ ) for yoon77.  $U_{\text{eq}}$  is defined as 1/3 of of the trace of the orthogonalised  $U_{\text{IJ}}$  tensor.**

<b>Atom</b>	<b><i>x</i></b>	<b><i>y</i></b>	<b><i>z</i></b>	<b>U(eq)</b>
C10	9117(7)	9220(6)	8190(3)	33.0(15)
C11	8112(7)	10112(6)	7831(3)	26.3(14)
C12	5171(8)	15768(6)	6717(3)	34.8(16)
C13	3728(12)	16508(10)	6556(7)	62(4)
C14	6116(11)	15975(8)	6207(4)	53(2)
C15	5382(10)	16203(7)	7228(4)	51(2)
C16	11177(10)	8498(10)	8773(5)	55(3)
C17	11156(14)	9118(13)	9278(6)	67(4)
C18	12557(11)	8099(13)	8484(6)	81(4)
C19	10865(9)	7397(8)	9064(4)	47(2)
C20	7790(9)	7084(9)	7832(4)	27.6(19)
C21	7898(7)	5950(6)	8150(3)	27.7(14)
C22	7125(6)	5900(6)	8668(3)	24.4(13)

**Crystal Table 2 Fractional Atomic Coordinates ( $\times 10^4$ ) and Equivalent Isotropic Displacement Parameters ( $\text{\AA}^2 \times 10^3$ ) for yoon77.  $U_{\text{eq}}$  is defined as 1/3 of of the trace of the orthogonalised  $U_{\text{IJ}}$  tensor.**

<b>Atom</b>	<b><i>x</i></b>	<b><i>y</i></b>	<b><i>z</i></b>	<b>U(eq)</b>
C23	6303(7)	7046(6)	8848(3)	27.0(13)
C24	6214(7)	8183(6)	8510(3)	25.1(13)
C25	5347(7)	9423(6)	8646(3)	26.7(13)
C26	4468(7)	9639(7)	9144(3)	31.5(15)
C27	3663(8)	10850(8)	9229(4)	37.4(17)
C28	3700(8)	11882(7)	8828(4)	37.8(18)
C29	4608(8)	11643(7)	8339(3)	33.9(16)
C30	5432(7)	10433(7)	8234(3)	28.6(15)
C31	7143(8)	4670(7)	9040(3)	33.8(16)
C32	7928(11)	3575(8)	8734(5)	58(3)
C33	7828(11)	4475(10)	9598(4)	59(3)
C34	5715(11)	4813(9)	9219(5)	65(3)
C35	2800(8)	13228(8)	8909(4)	53(2)

**Crystal Table 2 Fractional Atomic Coordinates ( $\times 10^4$ ) and Equivalent Isotropic Displacement Parameters ( $\text{\AA}^2 \times 10^3$ ) for yoon77.  $U_{\text{eq}}$  is defined as 1/3 of of the trace of the orthogonalised  $U_{\text{IJ}}$  tensor.**

Atom	$x$	$y$	$z$	$U(\text{eq})$
C36	3044(16)	13422(12)	9486(5)	67(4)
C37	1335(12)	13492(14)	8857(8)	74(4)
C38	3142(14)	14211(10)	8425(6)	64(3)
C36A	1860(30)	13170(30)	9477(11)	64(3)
C37A	1850(40)	14000(40)	8416(14)	88(14)
C38A	3640(30)	13890(30)	9000(17)	74(4)
Ir2	3338.5(3)	108.2(2)	2489.9(2)	34.25(9)
O3	-2142(15)	109(16)	3897(6)	38(3)
O4	2325(16)	2093(13)	4830(6)	57(3)
N7	1400(20)	100(20)	2954(7)	31(3)
N8	3077(18)	760(20)	3309(8)	35(3)
C89	600(20)	-312(17)	2792(7)	34(3)
C90	-580(20)	-395(17)	3122(7)	36(3)

**Crystal Table 2 Fractional Atomic Coordinates ( $\times 10^4$ ) and Equivalent Isotropic Displacement Parameters ( $\text{\AA}^2 \times 10^3$ ) for yoon77.  $U_{\text{eq}}$  is defined as 1/3 of of the trace of the orthogonalised  $U_{\text{IJ}}$  tensor.**

Atom	$x$	$y$	$z$	$U(\text{eq})$
C91	-947(17)	70(19)	3622(8)	36(3)
C92	-135(17)	480(20)	3810(8)	35(3)
C93	1033(19)	460(20)	3482(8)	33(3)
C94	1966(19)	850(20)	3664(8)	37(3)
C95	1700(20)	1308(17)	4177(8)	39(3)
C96	2583(19)	1681(18)	4325(7)	45(3)
C97	3710(20)	1612(19)	3962(8)	42(3)
C98	3930(20)	1120(20)	3457(8)	39(3)
C99	-2598(16)	517(12)	4459(5)	32(3)
C100	3220(20)	2450(20)	5007(10)	72(5)
O3A	-1725(15)	17(18)	3963(8)	46(2)
O4A	2726(13)	2463(12)	4620(5)	41(3)
N7A	1560(20)	210(30)	2891(9)	38(2)

**Crystal Table 2 Fractional Atomic Coordinates ( $\times 10^4$ ) and Equivalent Isotropic Displacement Parameters ( $\text{\AA}^2 \times 10^3$ ) for yoon77.  $U_{\text{eq}}$  is defined as 1/3 of of the trace of the orthogonalised  $U_{\text{IJ}}$  tensor.**

Atom	$x$	$y$	$z$	$U(\text{eq})$
N8A	3330(20)	790(20)	3220(8)	32(3)
C89A	710(20)	-130(20)	2704(10)	38(2)
C90A	-470(20)	-180(20)	3053(9)	38(2)
C91A	-630(20)	70(30)	3587(10)	46(2)
C92A	190(20)	470(30)	3784(10)	40(3)
C93A	1280(20)	540(30)	3427(10)	35(3)
C94A	2220(20)	960(20)	3585(8)	33(3)
C95A	1950(20)	1540(20)	4061(8)	35(3)
C96A	2891(19)	1900(16)	4172(7)	35(3)
C97A	4044(19)	1704(18)	3800(7)	35(3)
C98A	4230(20)	1140(20)	3333(8)	31(3)
C99A	-2558(16)	-419(17)	3736(8)	46(2)
C10B	1470(20)	2833(19)	4964(8)	50(4)

**Crystal Table 2 Fractional Atomic Coordinates ( $\times 10^4$ ) and Equivalent Isotropic Displacement Parameters ( $\text{\AA}^2 \times 10^3$ ) for yoon77.  $U_{\text{eq}}$  is defined as 1/3 of of the trace of the orthogonalised  $U_{\text{IJ}}$  tensor.**

Atom	$x$	$y$	$z$	$U(\text{eq})$
N5	4482(6)	-1727(5)	2840(3)	29.5(13)
N6	2295(7)	1865(6)	2031(3)	33.8(15)
C51	3966(8)	-2535(7)	3109(4)	36.9(17)
C52	4752(8)	-3825(7)	3262(3)	28.7(16)
C53	6158(8)	-4293(7)	3136(3)	28.6(14)
C54	6673(7)	-3433(6)	2866(3)	27.1(13)
C55	5829(7)	-2158(6)	2715(3)	26.8(14)
C56	6253(7)	-1187(6)	2384(3)	26.2(13)
C57	7605(8)	-1387(6)	2244(3)	31.8(15)
C58	7901(9)	-440(7)	1901(3)	35.9(16)
C59	6903(9)	731(7)	1687(3)	39.6(19)
C60	5558(9)	905(7)	1853(4)	43(2)
C61	5193(7)	-18(6)	2191(3)	30.4(15)



**Crystal Table 2 Fractional Atomic Coordinates ( $\times 10^4$ ) and Equivalent Isotropic Displacement Parameters ( $\text{\AA}^2 \times 10^3$ ) for yoon77.  $U_{\text{eq}}$  is defined as 1/3 of of the trace of the orthogonalised  $U_{\text{IJ}}$  tensor.**

Atom	$x$	$y$	$z$	$U(\text{eq})$
C62	7092(8)	-5695(7)	3297(4)	39.9(18)
C63	6316(13)	-6504(12)	3430(8)	74(5)
C64	7794(11)	-5867(9)	3836(4)	59(3)
C65	8179(9)	-6122(7)	2809(4)	44(2)
C66	7404(17)	1613(13)	1255(6)	39(2)
C67	8460(20)	1060(20)	804(13)	79(7)
C68	8070(20)	2127(18)	1606(8)	62(4)
C69	6100(20)	2640(17)	915(10)	39(2)
C66A	7014(19)	1966(12)	1439(8)	39(2)
C67A	8410(30)	1550(30)	1210(14)	79(7)
C68A	6850(30)	2790(20)	1832(11)	62(4)
C69A	6220(30)	2800(20)	961(13)	39(2)
C70	1946(10)	2953(9)	2199(5)	38(2)

**Crystal Table 2 Fractional Atomic Coordinates ( $\times 10^4$ ) and Equivalent Isotropic Displacement Parameters ( $\text{\AA}^2 \times 10^3$ ) for yoon77.  $U_{\text{eq}}$  is defined as 1/3 of of the trace of the orthogonalised  $U_{\text{IJ}}$  tensor.**

Atom	$x$	$y$	$z$	$U(\text{eq})$
C71	1196(8)	4104(7)	1882(3)	35.3(17)
C72	722(6)	4161(6)	1361(3)	27.7(14)
C73	1113(7)	3032(7)	1182(3)	29.2(14)
C74	1889(6)	1885(6)	1515(3)	26.7(13)
C75	2359(7)	645(6)	1365(3)	27.9(14)
C76	2057(7)	433(7)	863(3)	31.1(15)
C77	2566(7)	-782(7)	764(3)	34.0(16)
C78	3368(7)	-1812(7)	1150(4)	35.3(16)
C79	3633(7)	-1571(7)	1651(3)	34.9(16)
C80	3162(7)	-369(7)	1766(3)	31.1(15)
C81	-169(8)	5404(7)	1004(3)	33.6(16)
C82	-1338(17)	6181(12)	1399(6)	56(4)
C83	671(16)	6109(16)	710(7)	74(5)

**Crystal Table 2 Fractional Atomic Coordinates ( $\times 10^4$ ) and Equivalent Isotropic Displacement Parameters ( $\text{\AA}^2 \times 10^3$ ) for yoon77.  $U_{\text{eq}}$  is defined as 1/3 of of the trace of the orthogonalised  $U_{\text{IJ}}$  tensor.**

Atom	$x$	$y$	$z$	$U(\text{eq})$
C84	-828(12)	5238(11)	529(5)	49(3)
C82A	-540(40)	6470(30)	1313(16)	49(3)
C83A	490(40)	5660(30)	423(12)	56(4)
C84A	-1500(30)	5360(40)	1000(20)	69(13)
C85	3930(9)	-3179(8)	1062(4)	42.1(19)
C86	3548(13)	-3253(10)	492(4)	63(3)
C87	3390(10)	-3928(8)	1555(4)	48(2)
C88	5480(11)	-3726(9)	1032(7)	76(4)
P1	664(3)	4249(3)	6656.7(13)	39.4(9)
F1	1124(10)	5227(8)	6782(5)	92(3)
F2	-749(8)	4850(12)	6985(5)	114(4)
F3	118(9)	5096(8)	6064(3)	86(3)
F4	253(10)	3240(9)	6513(4)	84(3)

**Crystal Table 2 Fractional Atomic Coordinates ( $\times 10^4$ ) and Equivalent Isotropic Displacement Parameters ( $\text{\AA}^2 \times 10^3$ ) for yoon77.  $U_{\text{eq}}$  is defined as 1/3 of of the trace of the orthogonalised  $U_{\text{IJ}}$  tensor.**

Atom	$x$	$y$	$z$	$U(\text{eq})$
F5	2108(7)	3542(9)	6342(4)	83(3)
F6	1264(11)	3319(9)	7238(3)	108(4)
P1A	560(20)	4613(19)	6598(10)	97(7)
F1A	-830(20)	5820(20)	6596(17)	97(7)
F2A	-130(30)	3880(30)	7071(13)	97(7)
F3A	100(30)	4230(30)	6109(13)	97(7)
F4A	1920(30)	3390(20)	6619(17)	97(7)
F5A	1260(30)	5360(30)	6144(14)	97(7)
F6A	1000(40)	5000(30)	7094(13)	97(7)
P2	997(3)	5819(4)	3368.2(16)	40.6(11)
F7	406(13)	5239(14)	3032(6)	119(4)
F8	876(10)	4955(9)	3951(4)	92(3)
F9	2491(8)	4871(10)	3229(5)	108(4)

**Crystal Table 2 Fractional Atomic Coordinates ( $\times 10^4$ ) and Equivalent Isotropic Displacement Parameters ( $\text{\AA}^2 \times 10^3$ ) for yoon77.  $U_{\text{eq}}$  is defined as 1/3 of of the trace of the orthogonalised  $U_{\text{IJ}}$  tensor.**

Atom	$x$	$y$	$z$	$U(\text{eq})$
F10	1524(10)	6526(10)	3681(4)	83(3)
F11	1106(11)	6756(9)	2789(3)	107(4)
F12	-495(8)	6835(9)	3501(4)	74(3)
P2A	1177(16)	5503(14)	3407(7)	89(5)
F7A	1990(20)	4837(19)	3961(8)	89(5)
F8A	890(20)	4325(19)	3422(12)	89(5)
F9A	2500(20)	4910(30)	3007(11)	89(5)
F10A	1490(30)	6673(18)	3370(11)	89(5)
F11A	400(30)	6120(20)	2839(9)	89(5)
F12A	-180(20)	6140(20)	3773(10)	89(5)
O5	7409(10)	8266(7)	9917(4)	96(3)
C101	7010(9)	10388(10)	9550(4)	54(2)
C102	6819(9)	9362(9)	9981(4)	51(2)

**Crystal Table 2 Fractional Atomic Coordinates ( $\times 10^4$ ) and Equivalent Isotropic Displacement Parameters ( $\text{\AA}^2 \times 10^3$ ) for yoon77.  $U_{\text{eq}}$  is defined as 1/3 of of the trace of the orthogonalised  $U_{\text{IJ}}$  tensor.**

<b>Atom</b>	<b><i>x</i></b>	<b><i>y</i></b>	<b><i>z</i></b>	<b>U(eq)</b>
C103	5832(10)	9726(9)	10490(4)	50(2)
O6	9320(20)	1309(16)	5061(8)	65(2)
C104	6970(20)	1850(20)	5171(8)	65(2)
C105	8210(20)	1920(20)	5274(8)	65(2)
C106	7910(20)	2900(20)	5628(8)	65(2)
O7	9090(20)	1728(15)	5024(8)	65(2)
C107	8930(20)	3674(19)	5139(8)	65(2)
C108	8760(20)	2506(19)	5327(7)	65(2)
C109	8190(30)	2280(20)	5936(7)	65(2)
O8	5450(20)	4460(20)	5156(9)	83(6)
C110	4880(30)	2680(20)	5392(10)	75(6)
C111	4600(30)	4050(30)	5146(10)	69(6)
C112	3360(30)	4840(30)	4867(14)	87(8)

**Crystal Table 2 Fractional Atomic Coordinates ( $\times 10^4$ ) and Equivalent Isotropic Displacement Parameters ( $\text{\AA}^2 \times 10^3$ ) for yoon77.  $U_{\text{eq}}$  is defined as 1/3 of of the trace of the orthogonalised  $U_{\text{IJ}}$  tensor.**

<b>Atom</b>	<b><i>x</i></b>	<b><i>y</i></b>	<b><i>z</i></b>	<b>U(eq)</b>
O9	4997(17)	5740(30)	4862(10)	85(9)
C113	3100(30)	5300(20)	5152(14)	67(8)
C114	3757(18)	6140(20)	4873(9)	53(6)
C115	2870(20)	7430(20)	4586(11)	68(8)
O10	5770(30)	8640(30)	4928(13)	58(6)
C116	3959(18)	8168(19)	4838(9)	71(5)
C117	5363(17)	8039(16)	4725(6)	54(4)
C118	6240(30)	7100(30)	4351(12)	105(10)
O11	5830(40)	8420(40)	4975(19)	65(12)
C119	6200(20)	7890(20)	4062(7)	44(5)
C120	6560(20)	7674(19)	4660(7)	47(5)
C121	7760(20)	6500(20)	4850(9)	59(7)

**Crystal Table 3 Anisotropic Displacement Parameters ( $\text{\AA}^2 \times 10^3$ ) for yoon77. The Anisotropic displacement factor exponent takes the form:  $-2\pi^2[h^2a^{*2}U_{11}+2hka^*b^*U_{12}+\dots]$ .**

Atom	$U_{11}$	$U_{22}$	$U_{33}$	$U_{23}$	$U_{13}$	$U_{12}$
Ir1	39.63(18)	17.67(15)	23.39(14)	-1.59(11)	-1.81(12)	-14.49(14)
O1	73(5)	61(5)	62(5)	-1(4)	-37(4)	-27(4)
O2	132(9)	75(6)	38(4)	-26(4)	10(5)	-44(6)
N3	44(4)	17(4)	29(3)	-1(3)	-3(3)	-15(4)
N4	47(4)	21(3)	19(3)	0(3)	-1(3)	-19(4)
C39	50(5)	21(6)	36(4)	-3(3)	2(4)	-19(6)
C40	40(5)	26(4)	49(5)	3(4)	-8(4)	-13(5)
C41	62(6)	21(4)	41(5)	9(3)	-24(4)	-18(5)
C42	61(5)	22(4)	28(4)	3(3)	-9(4)	-24(4)
C43	55(5)	17(4)	27(4)	3(3)	-7(4)	-20(5)
C44	56(5)	21(4)	24(4)	1(3)	-2(4)	-23(5)
C45	68(6)	44(6)	25(4)	-6(4)	-2(4)	-37(6)
C46	70(6)	41(5)	28(4)	-7(4)	6(4)	-25(5)
C47	45(5)	41(5)	30(4)	-5(4)	4(4)	-14(4)



**Crystal Table 3 Anisotropic Displacement Parameters ( $\text{\AA}^2 \times 10^3$ ) for yoon77. The Anisotropic displacement factor exponent takes the form:  $-2\pi^2[h^2a^2U_{11}+2hka*b*U_{12}+\dots]$ .**

Atom	$U_{11}$	$U_{22}$	$U_{33}$	$U_{23}$	$U_{13}$	$U_{12}$
C48	47(5)	30(5)	26(4)	-4(4)	0(4)	-18(5)
C49	88(8)	114(12)	150(13)	2(10)	-44(9)	-56(9)
C50	125(12)	95(10)	67(8)	-31(7)	-34(8)	-11(9)
N1	37(3)	15(3)	28(3)	2(2)	-13(3)	-8(3)
N2	34(3)	18(3)	22(3)	-1(2)	-2(2)	-13(3)
C1	43(4)	29(4)	36(4)	1(3)	-14(3)	-19(3)
C2	37(5)	27(4)	29(4)	6(3)	-17(3)	-18(4)
C3	34(4)	19(3)	27(3)	-3(3)	-8(3)	-8(3)
C4	32(3)	18(3)	33(3)	-6(3)	-9(3)	-8(3)
C5	34(3)	19(3)	24(3)	-2(2)	-6(3)	-11(3)
C6	28(3)	16(3)	24(3)	-2(2)	0(2)	-6(2)
C7	26(3)	15(3)	34(4)	-5(3)	0(3)	-3(2)
C8	26(3)	25(3)	38(4)	-5(3)	-3(3)	-7(3)
C9	27(3)	25(3)	35(4)	1(3)	-5(3)	-7(3)

**Crystal Table 3 Anisotropic Displacement Parameters ( $\text{\AA}^2 \times 10^3$ ) for yoon77. The Anisotropic displacement factor exponent takes the form:  $-2\pi^2[h^2a^{*2}U_{11}+2hka^*b^*U_{12}+\dots]$ .**

Atom	$U_{11}$	$U_{22}$	$U_{33}$	$U_{23}$	$U_{13}$	$U_{12}$
C10	35(4)	19(3)	38(4)	1(3)	-1(3)	-9(3)
C11	28(3)	20(3)	30(3)	-5(3)	-5(3)	-9(3)
C12	39(4)	18(3)	45(4)	1(3)	-17(3)	-9(3)
C13	53(7)	21(5)	113(11)	-2(6)	-43(7)	-9(5)
C14	80(7)	27(4)	50(5)	7(4)	-5(5)	-28(4)
C15	68(6)	24(4)	59(6)	-8(4)	-28(5)	-10(4)
C16	38(5)	39(5)	76(7)	12(5)	-16(5)	-12(4)
C17	72(8)	64(8)	66(8)	-1(6)	-41(6)	-23(6)
C18	33(5)	74(7)	91(8)	31(6)	-4(5)	-4(5)
C19	48(5)	31(4)	43(5)	10(3)	-13(4)	-3(4)
C20	35(4)	26(4)	22(4)	-3(3)	7(3)	-16(3)
C21	33(4)	24(3)	25(3)	-6(3)	2(3)	-11(3)
C22	25(3)	21(3)	26(3)	1(2)	-1(2)	-11(3)
C23	32(3)	25(3)	23(3)	-4(3)	2(3)	-14(3)

**Crystal Table 3 Anisotropic Displacement Parameters ( $\text{\AA}^2 \times 10^3$ ) for yoon77. The Anisotropic displacement factor exponent takes the form:  $-2\pi^2[h^2a^2U_{11}+2hka*b*U_{12}+\dots]$ .**

Atom	$U_{11}$	$U_{22}$	$U_{33}$	$U_{23}$	$U_{13}$	$U_{12}$
C24	30(3)	22(3)	23(3)	-4(2)	-1(3)	-12(3)
C25	30(3)	21(3)	28(3)	-4(3)	-4(3)	-10(3)
C26	29(3)	33(4)	35(4)	-11(3)	2(3)	-13(3)
C27	32(4)	39(4)	38(4)	-17(4)	7(3)	-10(3)
C28	36(4)	28(4)	45(4)	-16(3)	-9(3)	-3(3)
C29	40(4)	22(3)	37(4)	-5(3)	-11(3)	-8(3)
C30	35(4)	27(3)	26(3)	-6(3)	-9(3)	-12(3)
C31	35(4)	26(3)	30(4)	5(3)	3(3)	-10(3)
C32	76(7)	24(4)	61(6)	-1(4)	12(5)	-20(4)
C33	65(6)	54(6)	39(5)	12(4)	-4(4)	-17(5)
C34	59(6)	34(5)	95(8)	-2(5)	23(6)	-27(4)
C35	52(5)	31(4)	60(5)	-18(4)	0(4)	1(4)
C36	89(10)	38(7)	77(7)	-35(6)	13(7)	-24(7)
C37	39(6)	39(7)	118(14)	-21(8)	1(7)	7(5)

**Crystal Table 3 Anisotropic Displacement Parameters ( $\text{\AA}^2 \times 10^3$ ) for yoon77. The Anisotropic displacement factor exponent takes the form:  $-2\pi^2[h^2a^{*2}U_{11}+2hka^*b^*U_{12}+\dots]$ .**

Atom	$U_{11}$	$U_{22}$	$U_{33}$	$U_{23}$	$U_{13}$	$U_{12}$
C38	65(8)	22(5)	87(8)	-22(5)	17(6)	-5(5)
C36A	65(8)	22(5)	87(8)	-22(5)	17(6)	-5(5)
C37A	60(30)	80(30)	101(17)	20(30)	-22(17)	-10(20)
C38A	39(6)	39(7)	118(14)	-21(8)	1(7)	7(5)
Ir2	38.18(19)	20.22(17)	39.3(2)	-4.22(14)	-21.40(15)	-2.21(14)
O3	49(6)	29(5)	30(5)	-7(4)	-8(5)	-8(5)
O4	77(7)	48(6)	48(6)	-20(5)	-23(5)	-16(5)
N7	40(6)	17(5)	31(5)	-4(4)	-17(4)	-2(4)
N8	45(6)	21(5)	35(6)	-6(5)	-27(5)	-2(5)
C89	47(6)	20(6)	30(6)	-3(5)	-21(4)	-4(5)
C90	42(6)	21(5)	41(5)	-9(4)	-18(4)	-4(4)
C91	46(6)	15(5)	35(5)	0(4)	-15(4)	-2(5)
C92	46(6)	20(4)	31(5)	-3(4)	-17(4)	-2(4)
C93	43(6)	18(5)	30(5)	-5(4)	-21(4)	-1(4)

**Crystal Table 3 Anisotropic Displacement Parameters ( $\text{\AA}^2 \times 10^3$ ) for yoon77. The Anisotropic displacement factor exponent takes the form:  $-2\pi^2[h^2a^{*2}U_{11}+2hka^*b^*U_{12}+\dots]$ .**

Atom	$U_{11}$	$U_{22}$	$U_{33}$	$U_{23}$	$U_{13}$	$U_{12}$
C94	45(6)	22(5)	35(5)	-6(4)	-24(5)	0(4)
C95	51(6)	25(5)	38(5)	-10(4)	-21(5)	-5(4)
C96	55(6)	34(6)	41(6)	-11(5)	-23(5)	-7(5)
C97	55(6)	33(5)	44(6)	-13(5)	-26(5)	-13(5)
C98	48(7)	28(6)	37(6)	-8(5)	-28(5)	-4(5)
C99	54(8)	16(5)	25(6)	-3(5)	-9(5)	-11(5)
C100	89(12)	67(11)	68(11)	-25(9)	-33(10)	-25(9)
O3A	28(4)	43(4)	50(4)	9(3)	5(3)	-11(3)
O4A	60(6)	34(5)	32(5)	-8(4)	9(4)	-26(4)
N7A	36(4)	27(4)	44(4)	1(3)	-4(3)	-12(3)
N8A	35(5)	22(5)	29(5)	4(4)	-2(4)	-8(4)
C89A	36(4)	27(4)	44(4)	1(3)	-4(3)	-12(3)
C90A	36(4)	27(4)	44(4)	1(3)	-4(3)	-12(3)
C91A	28(4)	43(4)	50(4)	9(3)	5(3)	-11(3)

**Crystal Table 3 Anisotropic Displacement Parameters ( $\text{\AA}^2 \times 10^3$ ) for yoon77. The Anisotropic displacement factor exponent takes the form:  $-2\pi^2[h^2a^{*2}U_{11}+2hka^*b^*U_{12}+\dots]$ .**

Atom	$U_{11}$	$U_{22}$	$U_{33}$	$U_{23}$	$U_{13}$	$U_{12}$
C92A	34(5)	32(5)	42(5)	6(4)	-2(4)	-8(4)
C93A	36(5)	24(5)	38(5)	6(4)	-4(4)	-10(4)
C94A	38(5)	22(5)	31(5)	3(4)	-2(4)	-10(4)
C95A	41(5)	25(5)	30(5)	1(4)	1(4)	-12(4)
C96A	46(6)	24(5)	30(5)	-3(4)	4(4)	-13(4)
C97A	44(6)	29(5)	29(5)	-1(4)	2(4)	-16(5)
C98A	37(6)	24(6)	27(6)	-1(5)	-1(5)	-9(5)
C99A	28(4)	43(4)	50(4)	9(3)	5(3)	-11(3)
C10B	66(9)	43(9)	40(8)	-14(7)	17(7)	-26(8)
N5	27(3)	20(3)	37(3)	0(2)	-16(3)	-4(3)
N6	34(4)	22(3)	39(4)	-9(2)	-19(3)	0(3)
C51	30(4)	33(4)	43(4)	-7(3)	-11(3)	-6(3)
C52	32(4)	23(3)	32(4)	-2(3)	-12(3)	-10(3)
C53	34(4)	25(3)	23(3)	-5(3)	0(3)	-10(3)

**Crystal Table 3 Anisotropic Displacement Parameters ( $\text{\AA}^2 \times 10^3$ ) for yoon77. The Anisotropic displacement factor exponent takes the form:  $-2\pi^2[h^2a^{*2}U_{11}+2hka^*b^*U_{12}+\dots]$ .**

Atom	$U_{11}$	$U_{22}$	$U_{33}$	$U_{23}$	$U_{13}$	$U_{12}$
C54	33(3)	22(3)	23(3)	-4(2)	-4(3)	-8(3)
C55	36(4)	20(3)	23(3)	-1(2)	-12(3)	-8(3)
C56	36(4)	15(3)	25(3)	-2(2)	-11(3)	-7(3)
C57	42(4)	18(3)	33(4)	-5(3)	-10(3)	-9(3)
C58	48(4)	30(4)	37(4)	-5(3)	-11(3)	-21(3)
C59	59(5)	25(3)	43(4)	7(3)	-33(4)	-21(4)
C60	53(5)	23(3)	51(5)	9(3)	-32(4)	-13(3)
C61	35(4)	24(3)	34(4)	-4(3)	-15(3)	-10(3)
C62	41(4)	22(3)	47(5)	-4(3)	6(4)	-9(3)
C63	50(7)	29(6)	127(13)	-8(7)	27(8)	-17(6)
C64	64(6)	41(5)	40(5)	10(4)	-11(4)	-1(4)
C65	48(5)	22(4)	53(5)	-11(3)	11(4)	-10(3)
C66	56(5)	24(4)	43(5)	-5(3)	-8(4)	-22(3)
C67	63(11)	44(11)	105(19)	20(10)	3(12)	-21(9)

**Crystal Table 3 Anisotropic Displacement Parameters ( $\text{\AA}^2 \times 10^3$ ) for yoon77. The Anisotropic displacement factor exponent takes the form:  $-2\pi^2[h^2a^{*2}U_{11}+2hka^*b^*U_{12}+\dots]$ .**

Atom	$U_{11}$	$U_{22}$	$U_{33}$	$U_{23}$	$U_{13}$	$U_{12}$
C68	92(8)	56(7)	64(7)	3(5)	-18(6)	-57(6)
C69	56(5)	24(4)	43(5)	-5(3)	-8(4)	-22(3)
C66A	56(5)	24(4)	43(5)	-5(3)	-8(4)	-22(3)
C67A	63(11)	44(11)	105(19)	20(10)	3(12)	-21(9)
C68A	92(8)	56(7)	64(7)	3(5)	-18(6)	-57(6)
C69A	56(5)	24(4)	43(5)	-5(3)	-8(4)	-22(3)
C70	42(5)	21(4)	49(6)	-11(4)	-27(4)	-1(4)
C71	43(4)	20(3)	36(4)	-7(3)	-14(3)	-3(3)
C72	20(3)	26(3)	28(3)	-2(3)	-3(2)	-3(3)
C73	24(3)	31(3)	27(3)	-5(3)	-5(3)	-6(3)
C74	22(3)	28(3)	29(3)	-6(3)	-7(3)	-7(3)
C75	22(3)	30(3)	31(3)	-8(3)	-3(3)	-9(3)
C76	28(3)	35(4)	31(4)	-9(3)	-1(3)	-13(3)
C77	30(4)	43(4)	37(4)	-20(3)	5(3)	-18(3)



**Crystal Table 3 Anisotropic Displacement Parameters ( $\text{\AA}^2 \times 10^3$ ) for yoon77. The Anisotropic displacement factor exponent takes the form:  $-2\pi^2[h^2a^*^2U_{11}+2hka^*b^*U_{12}+\dots]$ .**

Atom	$U_{11}$	$U_{22}$	$U_{33}$	$U_{23}$	$U_{13}$	$U_{12}$
C78	30(4)	34(4)	46(4)	-17(3)	1(3)	-14(3)
C79	32(4)	25(3)	46(4)	-7(3)	-6(3)	-9(3)
C80	30(4)	28(3)	36(4)	-7(3)	-12(3)	-10(3)
C81	38(4)	26(3)	29(4)	2(3)	-7(3)	-9(3)
C82	65(9)	25(6)	51(7)	-1(5)	-20(6)	6(6)
C83	78(10)	84(10)	61(9)	47(8)	-38(7)	-54(8)
C84	47(6)	35(5)	51(7)	-5(5)	-31(5)	3(5)
C82A	47(6)	35(5)	51(7)	-5(5)	-31(5)	3(5)
C83A	65(9)	25(6)	51(7)	-1(5)	-20(6)	6(6)
C84A	49(19)	70(20)	60(20)	28(17)	-22(16)	-12(16)
C85	44(4)	33(4)	52(5)	-18(4)	7(4)	-18(4)
C86	97(8)	54(6)	52(6)	-30(5)	22(5)	-45(6)
C87	67(6)	39(5)	48(5)	-12(4)	2(4)	-31(4)
C88	54(6)	37(5)	138(12)	-41(7)	16(7)	-15(5)

**Crystal Table 3 Anisotropic Displacement Parameters ( $\text{\AA}^2 \times 10^3$ ) for yoon77. The Anisotropic displacement factor exponent takes the form:  $-2\pi^2[h^2a^{*2}U_{11}+2hka^*b^*U_{12}+\dots]$ .**

Atom	$U_{11}$	$U_{22}$	$U_{33}$	$U_{23}$	$U_{13}$	$U_{12}$
P1	30.6(15)	55.8(19)	40.3(17)	-25.0(13)	1.4(11)	-19.2(13)
F1	102(6)	74(5)	132(7)	-28(5)	-40(6)	-48(5)
F2	71(6)	171(10)	109(7)	-98(7)	27(5)	-33(6)
F3	110(7)	64(5)	82(6)	26(4)	-52(5)	-37(5)
F4	104(8)	88(7)	99(8)	-19(6)	-19(6)	-70(6)
F5	44(4)	110(7)	85(6)	-42(6)	8(4)	-17(4)
F6	141(10)	124(9)	65(6)	-3(5)	-54(6)	-54(7)
P1A	82(11)	88(12)	132(16)	-31(10)	17(10)	-48(9)
F1A	82(11)	88(12)	132(16)	-31(10)	17(10)	-48(9)
F2A	82(11)	88(12)	132(16)	-31(10)	17(10)	-48(9)
F3A	82(11)	88(12)	132(16)	-31(10)	17(10)	-48(9)
F4A	82(11)	88(12)	132(16)	-31(10)	17(10)	-48(9)
F5A	82(11)	88(12)	132(16)	-31(10)	17(10)	-48(9)
F6A	82(11)	88(12)	132(16)	-31(10)	17(10)	-48(9)

**Crystal Table 3 Anisotropic Displacement Parameters ( $\text{\AA}^2 \times 10^3$ ) for yoon77. The Anisotropic displacement factor exponent takes the form:  $-2\pi^2[h^2a^{*2}U_{11}+2hka^*b^*U_{12}+\dots]$ .**

Atom	$U_{11}$	$U_{22}$	$U_{33}$	$U_{23}$	$U_{13}$	$U_{12}$
P2	32.4(17)	63(2)	44(2)	-30.5(16)	13.0(13)	-30.8(16)
F7	120(7)	164(9)	132(8)	-95(6)	8(6)	-88(6)
F8	80(7)	79(6)	97(6)	22(5)	11(5)	-41(5)
F9	50(4)	87(6)	174(12)	-54(7)	55(6)	-25(4)
F10	95(6)	119(8)	84(6)	-51(6)	18(5)	-82(6)
F11	127(9)	119(8)	59(5)	-13(5)	45(5)	-56(6)
F12	46(4)	76(7)	68(6)	-14(5)	8(4)	-1(4)
P2A	93(8)	68(7)	95(9)	-36(6)	-1(6)	-16(6)
F7A	93(8)	68(7)	95(9)	-36(6)	-1(6)	-16(6)
F8A	93(8)	68(7)	95(9)	-36(6)	-1(6)	-16(6)
F9A	93(8)	68(7)	95(9)	-36(6)	-1(6)	-16(6)
F10A	93(8)	68(7)	95(9)	-36(6)	-1(6)	-16(6)
F11A	93(8)	68(7)	95(9)	-36(6)	-1(6)	-16(6)
F12A	93(8)	68(7)	95(9)	-36(6)	-1(6)	-16(6)

**Crystal Table 3 Anisotropic Displacement Parameters ( $\text{\AA}^2 \times 10^3$ ) for yoon77. The Anisotropic displacement factor exponent takes the form:  $-2\pi^2[h^2a^2U_{11}+2hka*b*U_{12}+\dots]$ .**

Atom	$U_{11}$	$U_{22}$	$U_{33}$	$U_{23}$	$U_{13}$	$U_{12}$
O5	106(7)	51(5)	66(5)	-9(4)	-14(5)	26(4)
C101	42(5)	79(7)	47(5)	-20(5)	5(4)	-28(5)
C102	36(4)	57(6)	49(5)	-15(4)	-9(4)	-4(4)
C103	54(6)	53(6)	53(6)	-11(5)	1(4)	-32(5)
O6	83(5)	75(6)	32(3)	-8(3)	1(3)	-31(5)
C104	83(5)	75(6)	32(3)	-8(3)	1(3)	-31(5)
C105	83(5)	75(6)	32(3)	-8(3)	1(3)	-31(5)
C106	83(5)	75(6)	32(3)	-8(3)	1(3)	-31(5)
O7	83(5)	75(6)	32(3)	-8(3)	1(3)	-31(5)
C107	83(5)	75(6)	32(3)	-8(3)	1(3)	-31(5)
C108	83(5)	75(6)	32(3)	-8(3)	1(3)	-31(5)
C109	83(5)	75(6)	32(3)	-8(3)	1(3)	-31(5)
O8	94(14)	110(15)	66(11)	2(10)	-3(10)	-71(13)
C110	95(18)	89(13)	58(13)	-18(11)	-12(12)	-49(13)

**Crystal Table 3 Anisotropic Displacement Parameters ( $\text{\AA}^2 \times 10^3$ ) for yoon77. The Anisotropic displacement factor exponent takes the form:  $-2\pi^2[h^2a^{*2}U_{11}+2hka^*b^*U_{12}+\dots]$ .**

Atom	$U_{11}$	$U_{22}$	$U_{33}$	$U_{23}$	$U_{13}$	$U_{12}$
C111	90(16)	103(15)	41(11)	-18(10)	2(10)	-64(13)
C112	89(18)	86(18)	100(20)	7(15)	-13(15)	-58(16)
O9	38(9)	130(20)	55(13)	4(14)	-1(9)	-21(11)
C113	54(14)	57(15)	90(20)	-21(12)	-26(14)	-13(12)
C114	39(10)	76(14)	30(10)	-24(9)	-1(8)	-7(9)
C115	57(14)	70(14)	53(15)	-15(11)	17(11)	-13(11)
O10	102(16)	74(13)	24(7)	-3(8)	-13(9)	-61(12)
C116	86(11)	68(12)	70(12)	7(9)	-34(10)	-43(10)
C117	80(11)	61(10)	34(8)	-10(7)	-22(7)	-34(9)
C118	140(20)	120(20)	100(20)	-65(17)	37(17)	-86(18)
O11	81(19)	56(16)	35(15)	-14(13)	3(13)	-10(12)
C119	56(13)	38(11)	31(9)	-2(8)	-11(8)	-13(9)
C120	53(13)	53(12)	24(8)	-11(8)	3(8)	-13(9)
C121	50(13)	77(15)	28(10)	-7(10)	-4(8)	-7(10)

**Crystal Table 4 Bond Lengths for yoon77.**

<b>Atom</b>	<b>Atom</b>	<b>Length/Å</b>	<b>Atom</b>	<b>Atom</b>	<b>Length/Å</b>
Ir1	N3	2.111(8)	O3A	C91A	1.403(16)
Ir1	N4	2.139(7)	O3A	C99A	1.47(2)
Ir1	N3A	2.34(3)	O4A	C96A	1.343(15)
Ir1	N4A	2.20(3)	O4A	C10B	1.430(17)
Ir1	N1	2.047(6)	N7A	C89A	1.352(17)
Ir1	N2	2.044(6)	N7A	C93A	1.374(17)
Ir1	C11	2.010(7)	N8A	C94A	1.349(16)
Ir1	C30	2.004(7)	N8A	C98A	1.332(17)
O1	C41	1.341(10)	C89A	C90A	1.445(18)
O1	C49	1.384(17)	C90A	C91A	1.346(18)
O2	C46	1.372(10)	C91A	C92A	1.379(19)
O2	C50	1.374(15)	C92A	C93A	1.388(17)
N3	C39	1.318(10)	C93A	C94A	1.470(17)
N3	C43	1.377(9)	C94A	C95A	1.400(17)
N4	C44	1.350(10)	C95A	C96A	1.374(19)

**Crystal Table 4 Bond Lengths for yoon77.**

<b>Atom</b>	<b>Atom</b>	<b>Length/Å</b>	<b>Atom</b>	<b>Atom</b>	<b>Length/Å</b>
N4	C48	1.330(10)	C96A	C97A	1.389(18)
C39	C40	1.397(11)	C97A	C98A	1.380(17)
C40	C41	1.376(12)	N5	C51	1.335(10)
C41	C42	1.387(13)	N5	C55	1.348(10)
C42	C43	1.382(11)	N6	C70	1.336(11)
C43	C44	1.485(11)	N6	C74	1.371(9)
C44	C45	1.386(10)	C51	C52	1.400(11)
C45	C46	1.381(14)	C52	C53	1.405(10)
C46	C47	1.385(14)	C53	C54	1.385(10)
C47	C48	1.381(11)	C53	C62	1.536(10)
O1A	C41A	1.341(12)	C54	C55	1.398(9)
O1A	C49A	1.385(18)	C55	C56	1.471(9)
O2A	C46A	1.370(12)	C56	C57	1.400(10)
O2A	C50A	1.373(17)	C56	C61	1.410(9)
N3A	C39A	1.318(12)	C57	C58	1.378(10)

**Crystal Table 4 Bond Lengths for yoon77.**

<b>Atom Atom</b>	<b>Length/Å</b>	<b>Atom Atom</b>	<b>Length/Å</b>
N3A C43A	1.378(11)	C58 C59	1.395(10)
N4A C44A	1.350(12)	C59 C60	1.409(12)
N4A C48A	1.330(12)	C59 C66	1.528(13)
C39A C40A	1.397(13)	C59 C66A	1.526(14)
C40A C41A	1.378(13)	C60 C61	1.392(11)
C41A C42A	1.387(14)	C62 C63	1.521(14)
C42A C43A	1.383(12)	C62 C64	1.540(13)
C43A C44A	1.485(13)	C62 C65	1.529(11)
C44A C45A	1.386(12)	C66 C67	1.49(3)
C45A C46A	1.380(15)	C66 C68	1.58(2)
C46A C47A	1.385(15)	C66 C69	1.62(2)
C47A C48A	1.382(13)	C66A C67A	1.45(2)
N1 C1	1.341(9)	C66A C68A	1.45(2)
N1 C5	1.373(9)	C66A C69A	1.45(2)
N2 C20	1.343(11)	C70 C71	1.374(12)



**Crystal Table 4 Bond Lengths for yoon77.**

<b>Atom</b>	<b>Atom</b>	<b>Length/Å</b>	<b>Atom</b>	<b>Atom</b>	<b>Length/Å</b>
N2	C24	1.380(9)	C71	C72	1.405(10)
C1	C2	1.391(10)	C72	C73	1.385(10)
C2	C3	1.402(10)	C72	C81	1.524(9)
C3	C4	1.381(9)	C73	C74	1.396(9)
C3	C12	1.542(9)	C74	C75	1.464(9)
C4	C5	1.394(9)	C75	C76	1.402(9)
C5	C6	1.466(9)	C75	C80	1.406(10)
C6	C7	1.392(10)	C76	C77	1.383(10)
C6	C11	1.414(9)	C77	C78	1.394(11)
C7	C8	1.394(9)	C78	C79	1.398(11)
C8	C9	1.392(10)	C78	C85	1.538(10)
C9	C10	1.390(10)	C79	C80	1.388(10)
C9	C16	1.540(12)	C81	C82	1.541(17)
C10	C11	1.399(10)	C81	C83	1.516(15)
C12	C13	1.508(13)	C81	C84	1.541(13)

**Crystal Table 4 Bond Lengths for yoon77.**

<b>Atom</b>	<b>Atom</b>	<b>Length/Å</b>	<b>Atom</b>	<b>Atom</b>	<b>Length/Å</b>
C12	C14	1.523(12)	C81	C82A	1.50(2)
C12	C15	1.524(11)	C81	C83A	1.49(2)
C16	C17	1.554(17)	C81	C84A	1.49(2)
C16	C18	1.482(15)	C85	C86	1.523(13)
C16	C19	1.509(13)	C85	C87	1.523(12)
C20	C21	1.369(11)	C85	C88	1.537(13)
C21	C22	1.389(9)	P1	F1	1.581(6)
C22	C23	1.400(9)	P1	F2	1.562(7)
C22	C31	1.539(9)	P1	F3	1.574(6)
C23	C24	1.394(9)	P1	F4	1.598(7)
C24	C25	1.455(9)	P1	F5	1.593(6)
C25	C26	1.402(10)	P1	F6	1.596(7)
C25	C30	1.410(10)	P1A	F1A	1.578(11)
C26	C27	1.377(10)	P1A	F2A	1.577(11)
C27	C28	1.399(12)	P1A	F3A	1.577(11)

**Crystal Table 4 Bond Lengths for yoon77.**

<b>Atom</b>	<b>Atom</b>	<b>Length/Å</b>	<b>Atom</b>	<b>Atom</b>	<b>Length/Å</b>
C28	C29	1.403(11)	P1A	F4A	1.573(11)
C28	C35	1.522(11)	P1A	F5A	1.574(11)
C29	C30	1.394(10)	P1A	F6A	1.580(11)
C31	C32	1.503(12)	P2	F7	1.553(8)
C31	C33	1.560(12)	P2	F8	1.561(7)
C31	C34	1.511(12)	P2	F9	1.571(7)
C35	C36	1.536(11)	P2	F10	1.586(6)
C35	C37	1.529(11)	P2	F11	1.597(7)
C35	C38	1.585(11)	P2	F12	1.594(7)
C35	C36A	1.572(13)	P2A	F7A	1.568(10)
C35	C37A	1.548(13)	P2A	F8A	1.586(11)
C35	C38A	1.540(14)	P2A	F9A	1.578(10)
Ir2	N7	2.248(18)	P2A	F10A	1.578(11)
Ir2	N8	2.205(17)	P2A	F11A	1.576(10)
Ir2	N7A	2.00(2)	P2A	F12A	1.571(10)

**Crystal Table 4 Bond Lengths for yoon77.**

Atom	Atom	Length/Å	Atom	Atom	Length/Å
Ir2	N8A	2.09(2)	O5	C102	1.224(11)
Ir2	N5	2.053(6)	C101	C102	1.489(13)
Ir2	N6	2.050(6)	C102	C103	1.498(11)
Ir2	C61	2.010(8)	O6	C105	1.214(19)
Ir2	C80	2.009(7)	C104	C105	1.48(2)
O3	C91	1.364(16)	C105	C106	1.504(19)
O3	C99	1.470(17)	O7	C108	1.211(18)
O4	C96	1.353(15)	C107	C108	1.470(19)
O4	C100	1.397(19)	C108	C109	1.501(18)
N7	C89	1.341(15)	O8	C111	1.25(3)
N7	C93	1.370(15)	C110	C111	1.53(4)
N8	C94	1.350(16)	C111	C112	1.45(4)
N8	C98	1.329(16)	O9	C114	1.234(19)
C89	C90	1.440(17)	C113	C114	1.47(2)
C90	C91	1.362(16)	C114	C115	1.49(2)

**Crystal Table 4 Bond Lengths for yoon77.**

<b>Atom Atom</b>	<b>Length/Å</b>	<b>Atom Atom</b>	<b>Length/Å</b>
C91 C92	1.376(17)	O10 C117	1.229(19)
C92 C93	1.391(17)	C116 C117	1.477(18)
C93 C94	1.469(16)	C117 C118	1.498(19)
C94 C95	1.396(16)	O11 C120	1.23(2)
C95 C96	1.368(18)	C119 C120	1.481(18)
C96 C97	1.38(2)	C120 C121	1.491(19)
C97 C98	1.405(16)		

**Crystal Table 5 Bond Angles for yoon77.**

<b>Atom Atom Atom</b>	<b>Angle/°</b>	<b>Atom Atom Atom</b>	<b>Angle/°</b>
N3 Ir1 N4	77.5(3)	C96 C97 C98	118.1(14)
N4A Ir1 N3A	71.7(9)	N8 C98 C97	122.6(16)
N1 Ir1 N3	94.5(3)	C91A O3A C99A	114.4(16)
N1 Ir1 N4	93.3(3)	C96A O4A C10B	119.6(14)
N1 Ir1 N3A	90(2)	C89A N7A Ir2	125.5(14)

**Crystal Table 5 Bond Angles for yoon77.**

Atom	Atom	Atom	Angle/°	Atom	Atom	Atom	Angle/°
N1	Ir1	N4A	93(3)	C89A	N7A	C93A	118.8(15)
N2	Ir1	N3	89.0(3)	C93A	N7A	Ir2	115.4(12)
N2	Ir1	N4	94.1(3)	C94A	N8A	Ir2	114.0(11)
N2	Ir1	N3A	93(2)	C98A	N8A	Ir2	127.3(11)
N2	Ir1	N4A	95(3)	C98A	N8A	C94A	118.4(14)
N2	Ir1	N1	172.3(2)	N7A	C89A	C90A	122.3(17)
C11	Ir1	N3	171.9(3)	C91A	C90A	C89A	115.8(16)
C11	Ir1	N4	96.2(3)	C90A	C91A	O3A	120.1(16)
C11	Ir1	N1	80.7(3)	C90A	C91A	C92A	123.3(15)
C11	Ir1	N2	96.5(3)	C92A	C91A	O3A	116.4(16)
C30	Ir1	N3	96.5(3)	C91A	C92A	C93A	118.5(16)
C30	Ir1	N4	172.3(3)	N7A	C93A	C92A	121.0(15)
C30	Ir1	N1	92.1(3)	N7A	C93A	C94A	115.3(13)
C30	Ir1	N2	80.7(3)	C92A	C93A	C94A	123.6(15)
C30	Ir1	C11	90.2(3)	N8A	C94A	C93A	114.7(13)

**Crystal Table 5 Bond Angles for yoon77.**

<b>Atom Atom Atom</b>	<b>Angle/°</b>	<b>Atom Atom Atom</b>	<b>Angle/°</b>
C41 O1 C49	113.7(11)	N8A C94A C95A	122.5(14)
C46 O2 C50	120.8(12)	C95A C94A C93A	122.7(14)
C39 N3 Ir1	126.1(5)	C96A C95A C94A	118.2(15)
C39 N3 C43	117.7(7)	O4A C96A C95A	122.6(14)
C43 N3 Ir1	115.6(6)	O4A C96A C97A	118.3(14)
C44 N4 Ir1	115.5(5)	C95A C96A C97A	119.1(14)
C48 N4 Ir1	125.6(5)	C98A C97A C96A	119.5(15)
C48 N4 C44	118.8(7)	N8A C98A C97A	122.3(15)
N3 C39 C40	124.5(8)	C51 N5 Ir2	124.0(5)
C41 C40 C39	116.9(9)	C51 N5 C55	119.1(6)
O1 C41 C40	123.8(9)	C55 N5 Ir2	116.3(5)
O1 C41 C42	115.7(8)	C70 N6 Ir2	126.2(6)
C40 C41 C42	120.5(8)	C70 N6 C74	118.8(7)
C43 C42 C41	118.8(7)	C74 N6 Ir2	115.0(5)
N3 C43 C42	121.5(8)	N5 C51 C52	123.2(7)

**Crystal Table 5 Bond Angles for yoon77.**

<b>Atom Atom Atom</b>	<b>Angle/°</b>	<b>Atom Atom Atom</b>	<b>Angle/°</b>
N3 C43 C44	115.0(7)	C51 C52 C53	118.5(7)
C42 C43 C44	123.5(7)	C52 C53 C62	121.7(7)
N4 C44 C43	115.7(7)	C54 C53 C52	117.2(7)
N4 C44 C45	121.8(8)	C54 C53 C62	121.1(7)
C45 C44 C43	122.5(8)	C53 C54 C55	121.5(7)
C46 C45 C44	118.6(9)	N5 C55 C54	120.5(6)
O2 C46 C45	124.3(10)	N5 C55 C56	113.5(6)
O2 C46 C47	116.0(10)	C54 C55 C56	125.9(6)
C45 C46 C47	119.7(8)	C57 C56 C55	123.8(6)
C48 C47 C46	118.1(9)	C57 C56 C61	120.8(6)
N4 C48 C47	123.0(9)	C61 C56 C55	115.4(6)
C41A O1A C49A	112.8(16)	C58 C57 C56	119.5(7)
C46A O2A C50A	121.0(17)	C57 C58 C59	122.7(8)
C39AN3A Ir1	126.2(15)	C58 C59 C60	115.9(7)
C39AN3A C43A	117.5(11)	C58 C59 C66	115.8(9)



**Crystal Table 5 Bond Angles for yoon77.**

<b>Atom Atom Atom</b>	<b>Angle/°</b>	<b>Atom Atom Atom</b>	<b>Angle/°</b>
C43A N3A Ir1	115.6(13)	C58 C59 C66A	129.4(10)
C44A N4A Ir1	121.1(12)	C60 C59 C66	128.1(9)
C48A N4A Ir1	120.0(13)	C60 C59 C66A	112.4(9)
C48A N4A C44A	118.7(12)	C61 C60 C59	124.2(7)
N3A C39A C40A	124.2(13)	C56 C61 Ir2	114.2(5)
C41A C40A C39A	116.5(14)	C60 C61 Ir2	128.8(6)
O1A C41A C40A	123.3(15)	C60 C61 C56	116.9(7)
O1A C41A C42A	115.5(14)	C53 C62 C64	107.5(7)
C40A C41A C42A	120.0(13)	C63 C62 C53	112.1(8)
C43A C42A C41A	118.2(11)	C63 C62 C64	109.0(9)
N3A C43A C42A	121.7(12)	C63 C62 C65	109.4(8)
N3A C43A C44A	114.8(12)	C65 C62 C53	110.3(6)
C42A C43A C44A	122.8(13)	C65 C62 C64	108.4(7)
N4A C44A C43A	115.7(11)	C59 C66 C68	107.4(11)
N4A C44A C45A	121.7(13)	C59 C66 C69	105.3(13)

**Crystal Table 5 Bond Angles for yoon77.**

<b>Atom Atom Atom</b>	<b>Angle/°</b>	<b>Atom Atom Atom</b>	<b>Angle/°</b>
C45A C44A C43A	121.9(12)	C67 C66 C59	117.0(13)
C46A C45A C44A	118.4(12)	C67 C66 C68	105.0(17)
O2A C46A C45A	123.7(14)	C67 C66 C69	105.9(15)
O2A C46A C47A	116.2(14)	C68 C66 C69	116.7(13)
C45A C46A C47A	120.0(11)	C67A C66A C59	102.6(17)
C48A C47A C46A	117.9(12)	C67A C66A C68A	105.0(13)
N4A C48A C47A	123.0(13)	C68A C66A C59	118.8(16)
C1 N1 Ir1	125.0(5)	C69A C66A C59	119.0(16)
C1 N1 C5	118.5(6)	C69A C66A C67A	105.3(13)
C5 N1 Ir1	115.7(4)	C69A C66A C68A	104.5(12)
C20 N2 Ir1	127.1(5)	N6 C70 C71	123.5(8)
C20 N2 C24	117.8(6)	C70 C71 C72	119.4(7)
C24 N2 Ir1	115.0(4)	C71 C72 C81	121.9(6)
N1 C1 C2	123.7(7)	C73 C72 C71	116.8(6)
C1 C2 C3	118.5(7)	C73 C72 C81	121.3(6)

**Crystal Table 5 Bond Angles for yoon77.**

Atom	Atom	Atom	Angle/°	Atom	Atom	Atom	Angle/°
C2	C3	C12	121.5(6)	C72	C73	C74	121.8(6)
C4	C3	C2	117.4(6)	N6	C74	C73	119.7(6)
C4	C3	C12	121.0(6)	N6	C74	C75	114.3(6)
C3	C4	C5	122.1(6)	C73	C74	C75	126.1(6)
N1	C5	C4	119.7(6)	C76	C75	C74	124.4(6)
N1	C5	C6	113.5(6)	C76	C75	C80	120.3(6)
C4	C5	C6	126.7(6)	C80	C75	C74	115.2(6)
C7	C6	C5	123.1(6)	C77	C76	C75	119.4(7)
C7	C6	C11	121.5(6)	C76	C77	C78	122.0(7)
C11	C6	C5	115.3(6)	C77	C78	C79	117.2(7)
C6	C7	C8	119.2(6)	C77	C78	C85	123.7(7)
C9	C8	C7	121.2(7)	C79	C78	C85	119.1(7)
C8	C9	C16	118.7(7)	C80	C79	C78	122.9(7)
C10	C9	C8	118.3(6)	C75	C80	Ir2	114.4(5)
C10	C9	C16	122.9(7)	C79	C80	Ir2	127.2(6)

**Crystal Table 5 Bond Angles for yoon77.**

Atom	Atom	Atom	Angle/°	Atom	Atom	Atom	Angle/°
C9	C10	C11	123.0(6)	C79	C80	C75	118.1(6)
C6	C11	Ir1	114.1(5)	C72	C81	C82	109.4(7)
C10	C11	Ir1	129.0(5)	C72	C81	C84	113.0(7)
C10	C11	C6	116.8(6)	C82	C81	C84	106.3(9)
C13	C12	C3	110.8(7)	C83	C81	C72	109.8(8)
C13	C12	C14	109.4(8)	C83	C81	C82	111.1(11)
C13	C12	C15	110.0(8)	C83	C81	C84	107.3(9)
C14	C12	C3	107.7(6)	C82A	C81	C72	110.9(13)
C14	C12	C15	109.0(7)	C83A	C81	C72	112.2(14)
C15	C12	C3	109.9(6)	C83A	C81	C82A	109(2)
C9	C16	C17	110.6(8)	C83A	C81	C84A	115(3)
C18	C16	C9	109.9(9)	C84A	C81	C72	106.3(15)
C18	C16	C17	106.8(10)	C84A	C81	C82A	103(3)
C18	C16	C19	112.3(10)	C86	C85	C78	111.5(8)
C19	C16	C9	112.9(8)	C86	C85	C88	106.9(9)

**Crystal Table 5 Bond Angles for yoon77.**

<b>Atom Atom Atom</b>	<b>Angle/°</b>	<b>Atom Atom Atom</b>	<b>Angle/°</b>
C19 C16 C17	104.2(10)	C87 C85 C78	110.0(7)
N2 C20 C21	123.9(7)	C87 C85 C86	109.1(7)
C20 C21 C22	120.1(7)	C87 C85 C88	111.4(9)
C21 C22 C23	116.6(6)	C88 C85 C78	107.8(7)
C21 C22 C31	123.5(6)	F1 P1 F4	177.7(6)
C23 C22 C31	120.0(6)	F1 P1 F5	90.5(5)
C24 C23 C22	121.6(6)	F1 P1 F6	90.7(5)
N2 C24 C23	120.0(6)	F2 P1 F1	92.5(5)
N2 C24 C25	114.3(6)	F2 P1 F3	92.2(6)
C23 C24 C25	125.7(6)	F2 P1 F4	89.7(5)
C26 C25 C24	124.2(6)	F2 P1 F5	176.0(7)
C26 C25 C30	120.7(6)	F2 P1 F6	90.3(6)
C30 C25 C24	115.1(6)	F3 P1 F1	91.6(5)
C27 C26 C25	119.9(7)	F3 P1 F4	87.9(5)
C26 C27 C28	121.4(7)	F3 P1 F5	90.4(5)

**Crystal Table 5 Bond Angles for yoon77.**

Atom	Atom	Atom	Angle/°	Atom	Atom	Atom	Angle/°
C27	C28	C29	117.7(7)	F3	P1	F6	176.5(5)
C27	C28	C35	122.1(7)	F5	P1	F4	87.2(5)
C29	C28	C35	120.2(7)	F5	P1	F6	87.0(5)
C30	C29	C28	122.8(7)	F6	P1	F4	89.7(5)
C25	C30	Ir1	114.6(5)	F1A	P1A	F6A	89.6(10)
C29	C30	Ir1	127.6(6)	F2A	P1A	F1A	88.1(10)
C29	C30	C25	117.5(7)	F2A	P1A	F6A	89.2(11)
C22	C31	C33	105.8(7)	F3A	P1A	F1A	89.8(10)
C32	C31	C22	111.6(6)	F3A	P1A	F2A	90.0(11)
C32	C31	C33	110.3(7)	F3A	P1A	F6A	179.0(14)
C32	C31	C34	111.3(8)	F4A	P1A	F1A	177.8(12)
C34	C31	C22	110.0(6)	F4A	P1A	F2A	89.7(10)
C34	C31	C33	107.6(8)	F4A	P1A	F3A	90.5(10)
C28	C35	C36	109.7(8)	F4A	P1A	F5A	90.3(10)
C28	C35	C37	108.3(8)	F4A	P1A	F6A	90.2(10)

**Crystal Table 5 Bond Angles for yoon77.**

<b>Atom Atom Atom</b>	<b>Angle/°</b>	<b>Atom Atom Atom</b>	<b>Angle/°</b>
C28 C35 C38	111.9(7)	F5A P1A F1A	91.9(10)
C36 C35 C38	106.2(8)	F5A P1A F2A	177.9(16)
C37 C35 C36	113.7(9)	F5A P1A F3A	92.1(18)
C37 C35 C38	107.1(9)	F5A P1A F6A	88.7(11)
C37A C35 C36A	106.4(13)	F7 P2 F8	92.7(6)
C38A C35 C36A	106.9(13)	F7 P2 F9	92.6(6)
C38A C35 C37A	111.3(15)	F7 P2 F10	175.1(7)
N8 Ir2 N7	72.6(6)	F7 P2 F11	89.6(7)
N7A Ir2 N8A	79.8(7)	F7 P2 F12	89.3(6)
N7A Ir2 N5	96.9(9)	F8 P2 F9	92.1(6)
N7A Ir2 N6	87.5(9)	F8 P2 F10	90.9(6)
N7A Ir2 C61	172.5(7)	F8 P2 F11	177.1(6)
N7A Ir2 C80	97.1(6)	F8 P2 F12	89.8(5)
N5 Ir2 N7	93.6(6)	F9 P2 F10	90.6(5)
N5 Ir2 N8	93.0(7)	F9 P2 F11	89.3(6)

**Crystal Table 5 Bond Angles for yoon77.**

<b>Atom Atom Atom</b>	<b>Angle/°</b>	<b>Atom Atom Atom</b>	<b>Angle/°</b>
N5 Ir2 N8A	93.7(7)	F9 P2 F12	177.2(6)
N6 Ir2 N7	90.7(6)	F10 P2 F11	86.6(5)
N6 Ir2 N8	94.8(7)	F10 P2 F12	87.4(5)
N6 Ir2 N8A	93.6(7)	F12 P2 F11	88.7(5)
N6 Ir2 N5	172.0(3)	F7A P2A F8A	91.3(9)
C61 Ir2 N7	171.3(5)	F7A P2A F9A	91.1(11)
C61 Ir2 N8	101.4(5)	F7A P2A F10A	89.9(9)
C61 Ir2 N8A	93.3(5)	F7A P2A F11A	177.6(13)
C61 Ir2 N5	80.2(3)	F7A P2A F12A	92.1(10)
C61 Ir2 N6	96.1(3)	F9A P2A F8A	88.6(9)
C80 Ir2 N7	96.4(4)	F9A P2A F10A	89.7(9)
C80 Ir2 N8	168.2(5)	F10A P2A F8A	178.0(11)
C80 Ir2 N8A	173.7(7)	F11A P2A F8A	87.3(9)
C80 Ir2 N5	92.1(3)	F11A P2A F9A	87.1(16)
C80 Ir2 N6	80.7(3)	F11A P2A F10A	91.5(9)



**Crystal Table 5 Bond Angles for yoon77.**

<b>Atom Atom Atom</b>	<b>Angle/°</b>	<b>Atom Atom Atom</b>	<b>Angle/°</b>
C80 Ir2 C61	90.0(3)	F12A P2A F8A	91.8(9)
C91 O3 C99	120.4(14)	F12A P2A F9A	176.8(15)
C96 O4 C100	120.5(17)	F12A P2A F10A	89.8(9)
C89 N7 Ir2	127.2(11)	F12A P2A F11A	89.8(10)
C89 N7 C93	114.6(13)	O5 C102 C101	121.6(9)
C93 N7 Ir2	118.0(10)	O5 C102 C103	121.0(9)
C94 N8 Ir2	118.5(10)	C101 C102 C103	117.4(8)
C98 N8 Ir2	122.9(12)	O6 C105 C104	123.4(19)
C98 N8 C94	118.6(14)	O6 C105 C106	125(2)
N7 C89 C90	125.7(13)	C104 C105 C106	111.7(17)
C91 C90 C89	116.3(13)	O7 C108 C107	123.2(17)
O3 C91 C92	124.6(13)	O7 C108 C109	120.4(18)
C90 C91 O3	115.5(14)	C107 C108 C109	116.3(16)
C90 C91 C92	119.9(14)	O8 C111 C110	121(3)
C91 C92 C93	120.1(13)	O8 C111 C112	121(3)

**Crystal Table 5 Bond Angles for yoon77.**

Atom	Atom	Atom	Angle/°	Atom	Atom	Atom	Angle/°
N7	C93	C92	123.1(13)	C112	C111	C110	118(2)
N7	C93	C94	113.8(13)	O9	C114	C113	120(2)
C92	C93	C94	123.1(12)	O9	C114	C115	123(2)
N8	C94	C93	117.0(12)	C113	C114	C115	117.4(18)
N8	C94	C95	121.9(14)	O10	C117	C116	122.6(18)
C95	C94	C93	121.1(14)	O10	C117	C118	123.2(19)
C96	C95	C94	119.1(16)	C116	C117	C118	114.2(15)
O4	C96	C95	118.3(16)	O11	C120	C119	119(2)
O4	C96	C97	122.0(14)	O11	C120	C121	124(2)
C95	C96	C97	119.6(13)	C119	C120	C121	116.6(15)

**Crystal Table 6 Torsion Angles for yoon77.**

A	B	C	D	Angle/°	A	B	C	D	Angle/°
Ir1	N3	C39	C40	171.6(11)	Ir2	N7A	C93A	C92A	-171(2)
Ir1	N3	C43	C42	-172.8(8)	Ir2	N7A	C93A	C94A	9(3)

**Crystal Table 6 Torsion Angles for yoon77.**

<b>A</b>	<b>B</b>	<b>C</b>	<b>D</b>	<b>Angle/°</b>	<b>A</b>	<b>B</b>	<b>C</b>	<b>D</b>	<b>Angle/°</b>
Ir1	N3	C43	C44	9.1(11)	Ir2	N8A	C94A	C93A	5(3)
Ir1	N4	C44	C43	4.5(11)	Ir2	N8A	C94A	C95A	-172.2(18)
Ir1	N4	C44	C45	-175.9(8)	Ir2	N8A	C98A	C97A	172.8(18)
Ir1	N4	C48	C47	175.7(8)	Ir2	N5	C51	C52	169.3(6)
Ir1	N3A	C39A	C40A	-173(8)	Ir2	N5	C55	C54	-171.3(5)
Ir1	N3A	C43A	C42A	179(6)	Ir2	N5	C55	C56	4.8(7)
Ir1	N3A	C43A	C44A	-11(9)	Ir2	N6	C70	C71	-177.2(8)
Ir1	N4A	C44A	C43A	-7(10)	Ir2	N6	C74	C73	176.8(5)
Ir1	N4A	C44A	C45A	-178(6)	Ir2	N6	C74	C75	-4.2(8)
Ir1	N4A	C48A	C47A	-180(6)	O3	C91	C92	C93	-177(2)
Ir1	N1	C1	C2	167.6(6)	O4	C96	C97	C98	177.3(18)
Ir1	N1	C5	C4	-170.6(5)	N7	C89	C90	C91	5(3)
Ir1	N1	C5	C6	6.0(8)	N7	C93	C94	N8	-3(3)
Ir1	N2	C20	C21	-175.2(6)	N7	C93	C94	C95	176.5(19)
Ir1	N2	C24	C23	176.2(5)	N8	C94	C95	C96	0(3)

**Crystal Table 6 Torsion Angles for yoon77.**

<b>A</b>	<b>B</b>	<b>C</b>	<b>D</b>	<b>Angle/°</b>	<b>A</b>	<b>B</b>	<b>C</b>	<b>D</b>	<b>Angle/°</b>
Ir1	N2	C24	C25	-2.8(7)	C89	N7	C93	C92	-4(3)
O1	C41	C42	C43	178.9(10)	C89	N7	C93	C94	177.3(18)
O2	C46	C47	C48	-179.0(10)	C89	C90	C91	O3	173.2(16)
N3	C39	C40	C41	0(2)	C89	C90	C91	C92	-6(3)
N3	C43	C44	N4	-9.1(13)	C90	C91	C92	C93	2(3)
N3	C43	C44	C45	171.4(10)	C91	C92	C93	N7	3(3)
N4	C44	C45	C46	-0.1(16)	C91	C92	C93	C94	-178(2)
C39	N3	C43	C42	-1.2(16)	C92	C93	C94	N8	179(2)
C39	N3	C43	C44	-179.3(11)	C92	C93	C94	C95	-2(3)
C39	C40	C41	O1	-179.0(12)	C93	N7	C89	C90	0(3)
C39	C40	C41	C42	-0.7(16)	C93	C94	C95	C96	-178.9(19)
C40	C41	C42	C43	0.5(14)	C94	N8	C98	C97	-1(3)
C41	C42	C43	N3	0.5(15)	C94	C95	C96	O4	-178.4(17)
C41	C42	C43	C44	178.3(9)	C94	C95	C96	C97	1(3)
C42	C43	C44	N4	173.0(10)	C95	C96	C97	C98	-2(3)

**Crystal Table 6 Torsion Angles for yoon77.**

<b>A</b>	<b>B</b>	<b>C</b>	<b>D</b>	<b>Angle/°</b>	<b>A</b>	<b>B</b>	<b>C</b>	<b>D</b>	<b>Angle/°</b>
C42	C43	C44	C45	-6.6(15)	C96	C97	C98	N8	2(3)
C43	N3	C39	C40	1(2)	C98	N8	C94	C93	179(2)
C43	C44	C45	C46	179.3(9)	C98	N8	C94	C95	0(3)
C44	N4	C48	C47	0.9(17)	C99	O3	C91	C90	176.1(17)
C44	C45	C46	O2	179.2(10)	C99	O3	C91	C92	-5(3)
C44	C45	C46	C47	0.6(16)	C100	O4	C96	C95	178.3(18)
C45	C46	C47	C48	-0.3(15)	C100	O4	C96	C97	-1(3)
C46	C47	C48	N4	-0.5(16)	O3A	C91A	C92A	C93A	180(2)
C48	N4	C44	C43	179.9(10)	O4A	C96A	C97A	C98A	-179.2(18)
C48	N4	C44	C45	-0.6(16)	N7A	C89A	C90A	C91A	-3(3)
C49	O1	C41	C40	7.0(18)	N7A	C93A	C94A	N8A	-9(3)
C49	O1	C41	C42	-171.4(13)	N7A	C93A	C94A	C95A	168(2)
C50	O2	C46	C45	-14.0(18)	N8A	C94A	C95A	C96A	-3(3)
C50	O2	C46	C47	164.6(12)	C89A	N7A	C93A	C92A	3(4)
O1A	C41A	C42A	C43A	180(7)	C89A	N7A	C93A	C94A	-177(2)

**Crystal Table 6 Torsion Angles for yoon77.**

<b>A</b>	<b>B</b>	<b>C</b>	<b>D</b>	<b>Angle/°</b>	<b>A</b>	<b>B</b>	<b>C</b>	<b>D</b>	<b>Angle/°</b>
O2A	C46A	C47A	C48A	178(6)	C89A	C90A	C91A	O3A	-179(2)
N3A	C39A	C40A	C41A	-9(15)	C89A	C90A	C91A	C92A	6(4)
N3A	C43A	C44A	N4A	12(10)	C90A	C91A	C92A	C93A	-4(4)
N3A	C43A	C44A	C45A	-178(8)	C91A	C92A	C93A	N7A	0(4)
N4A	C44A	C45A	C46A	-5(11)	C91A	C92A	C93A	C94A	179(2)
C39A	N3A	C43A	C42A	7(14)	C92A	C93A	C94A	N8A	171(2)
C39A	N3A	C43A	C44A	178(9)	C92A	C93A	C94A	C95A	-12(4)
C39A	C40A	C41A	O1A	-177(9)	C93A	N7A	C89A	C90A	-1(4)
C39A	C40A	C41A	C42A	16(10)	C93A	C94A	C95A	C96A	180(2)
C40A	C41A	C42A	C43A	-12(10)	C94A	N8A	C98A	C97A	-2(4)
C41A	C42A	C43A	N3A	0(12)	C94A	C95A	C96A	O4A	-179.7(18)
C41A	C42A	C43A	C44A	-170(7)	C94A	C95A	C96A	C97A	2(3)
C42A	C43A	C44A	N4A	-178(8)	C95A	C96A	C97A	C98A	-1(3)
C42A	C43A	C44A	C45A	-7(11)	C96A	C97A	C98A	N8A	1(3)
C43A	N3A	C39A	C40A	-2(17)	C98A	N8A	C94A	C93A	-180(2)

**Crystal Table 6 Torsion Angles for yoon77.**

<b>A</b>	<b>B</b>	<b>C</b>	<b>D</b>	<b>Angle/°</b>	<b>A</b>	<b>B</b>	<b>C</b>	<b>D</b>	<b>Angle/°</b>
C43A	C44A	C45A	C46A	-175(7)	C98A	N8A	C94A	C95A	3(4)
C44A	N4A	C48A	C47A	-4(14)	C99A	O3A	C91A	C90A	4(3)
C44A	C45A	C46A	O2A	-176(6)	C99A	O3A	C91A	C92A	-180(2)
C44A	C45A	C46A	C47A	1(10)	C10B	O4A	C96A	C95A	-7(3)
C45A	C46A	C47A	C48A	1(10)	C10B	O4A	C96A	C97A	171.5(16)
C46A	C47A	C48A	N4A	0(12)	N5	C51	C52	C53	1.3(12)
C48A	N4A	C44A	C43A	177(8)	N5	C55	C56	C57	174.8(6)
C48A	N4A	C44A	C45A	6(13)	N5	C55	C56	C61	-7.4(8)
C49A	O1A	C41A	C40A	-28(9)	N6	C70	C71	C72	2.2(16)
C49A	O1A	C41A	C42A	139(6)	N6	C74	C75	C76	179.2(7)
C50A	O2A	C46A	C45A	14(9)	N6	C74	C75	C80	-0.7(9)
C50A	O2A	C46A	C47A	-163(5)	C51	N5	C55	C54	-0.1(10)
N1	C1	C2	C3	1.4(13)	C51	N5	C55	C56	176.1(6)
N1	C5	C6	C7	174.3(6)	C51	C52	C53	C54	0.0(10)
N1	C5	C6	C11	-9.5(9)	C51	C52	C53	C62	179.3(7)

**Crystal Table 6 Torsion Angles for yoon77.**

<b>A</b>	<b>B</b>	<b>C</b>	<b>D</b>	<b>Angle/°</b>	<b>A</b>	<b>B</b>	<b>C</b>	<b>D</b>	<b>Angle/°</b>
N2	C20	C21	C22	0.8(13)	C52	C53	C54	C55	-1.2(10)
N2	C24	C25	C26	178.6(6)	C52	C53	C62	C63	16.7(12)
N2	C24	C25	C30	-0.8(9)	C52	C53	C62	C64	-103.0(9)
C1	N1	C5	C4	-0.4(10)	C52	C53	C62	C65	138.9(8)
C1	N1	C5	C6	176.2(7)	C53	C54	C55	N5	1.3(10)
C1	C2	C3	C4	0.8(11)	C53	C54	C55	C56	-174.3(6)
C1	C2	C3	C12	-179.9(7)	C54	C53	C62	C63	-164.0(9)
C2	C3	C4	C5	-2.8(11)	C54	C53	C62	C64	76.2(9)
C2	C3	C12	C13	13.3(12)	C54	C53	C62	C65	-41.8(10)
C2	C3	C12	C14	-106.3(9)	C54	C55	C56	C57	-9.3(10)
C2	C3	C12	C15	135.1(8)	C54	C55	C56	C61	168.5(6)
C3	C4	C5	N1	2.7(11)	C55	N5	C51	C52	-1.2(11)
C3	C4	C5	C6	-173.4(7)	C55	C56	C57	C58	176.0(6)
C4	C3	C12	C13	-167.5(9)	C55	C56	C61	Ir2	6.5(7)
C4	C3	C12	C14	72.9(9)	C55	C56	C61	C60	-177.1(6)



**Crystal Table 6 Torsion Angles for yoon77.**

<b>A</b>	<b>B</b>	<b>C</b>	<b>D</b>	<b>Angle/°</b>	<b>A</b>	<b>B</b>	<b>C</b>	<b>D</b>	<b>Angle/°</b>
C4	C3	C12	C15	-45.7(10)	C56	C57	C58	C59	0.4(11)
C4	C5	C6	C7	-9.4(11)	C57	C56	C61	Ir2	-175.6(5)
C4	C5	C6	C11	166.8(7)	C57	C56	C61	C60	0.8(10)
C5	N1	C1	C2	-1.6(12)	C57	C58	C59	C60	1.5(11)
C5	C6	C7	C8	174.8(6)	C57	C58	C59	C66	-172.8(8)
C5	C6	C11	Ir1	8.6(8)	C57	C58	C59	C66A	162.7(12)
C5	C6	C11	C10	-174.8(6)	C58	C59	C60	C61	-2.4(12)
C6	C7	C8	C9	-0.7(11)	C58	C59	C66	C67	43.2(19)
C7	C6	C11	Ir1	-175.1(5)	C58	C59	C66	C68	-74.5(14)
C7	C6	C11	C10	1.5(10)	C58	C59	C66	C69	160.5(10)
C7	C8	C9	C10	2.0(11)	C58	C59	C66A	C67A	27.8(18)
C7	C8	C9	C16	-175.1(8)	C58	C59	C66A	C68A	-87.3(17)
C8	C9	C10	C11	-1.7(12)	C58	C59	C66A	C69A	143.5(16)
C8	C9	C16	C17	53.3(11)	C59	C60	C61	Ir2	177.1(6)
C8	C9	C16	C18	-64.3(13)	C59	C60	C61	C56	1.3(11)

**Crystal Table 6 Torsion Angles for yoon77.**

<b>A</b>	<b>B</b>	<b>C</b>	<b>D</b>	<b>Angle/°</b>	<b>A</b>	<b>B</b>	<b>C</b>	<b>D</b>	<b>Angle/°</b>
C8	C9	C16	C19	169.6(8)	C60	C59	C66	C67	-130.3(17)
C9	C10	C11	Ir1	176.0(6)	C60	C59	C66	C68	112.0(14)
C9	C10	C11	C6	-0.1(11)	C60	C59	C66	C69	-13.0(15)
C10	C9	C16	C17	-123.7(10)	C60	C59	C66A	C67A	-170.4(14)
C10	C9	C16	C18	118.7(11)	C60	C59	C66A	C68A	74.4(16)
C10	C9	C16	C19	-7.4(13)	C60	C59	C66A	C69A	-54.7(19)
C11	C6	C7	C8	-1.2(10)	C61	C56	C57	C58	-1.6(10)
C12	C3	C4	C5	177.9(7)	C62	C53	C54	C55	179.5(6)
C16	C9	C10	C11	175.4(8)	C66	C59	C60	C61	171.0(10)
C20	N2	C24	C23	-0.4(10)	C66A	C59	C60	C61	-166.8(10)
C20	N2	C24	C25	-179.3(7)	C70	N6	C74	C73	-0.7(12)
C20	C21	C22	C23	-2.8(11)	C70	N6	C74	C75	178.3(8)
C20	C21	C22	C31	177.5(7)	C70	C71	C72	C73	-3.5(12)
C21	C22	C23	C24	3.3(10)	C70	C71	C72	C81	177.1(8)
C21	C22	C31	C32	-8.5(11)	C71	C72	C73	C74	2.8(11)

**Crystal Table 6 Torsion Angles for yoon77.**

<b>A</b>	<b>B</b>	<b>C</b>	<b>D</b>	<b>Angle/°</b>	<b>A</b>	<b>B</b>	<b>C</b>	<b>D</b>	<b>Angle/°</b>
C21	C22	C31	C33	111.5(8)	C71	C72	C81	C82	-48.9(11)
C21	C22	C31	C34	-132.5(8)	C71	C72	C81	C83	73.2(12)
C22	C23	C24	N2	-1.7(10)	C71	C72	C81	C84	-167.1(9)
C22	C23	C24	C25	177.1(6)	C71	C72	C81	C82A	-5(2)
C23	C22	C31	C32	171.8(7)	C71	C72	C81	C83A	117(2)
C23	C22	C31	C33	-68.2(8)	C71	C72	C81	C84A	-116(2)
C23	C22	C31	C34	47.8(10)	C72	C73	C74	N6	-0.7(11)
C23	C24	C25	C26	-0.3(11)	C72	C73	C74	C75	-179.7(7)
C23	C24	C25	C30	-179.7(7)	C73	C72	C81	C82	131.7(10)
C24	N2	C20	C21	0.8(13)	C73	C72	C81	C83	-106.3(11)
C24	C25	C26	C27	-178.5(7)	C73	C72	C81	C84	13.5(11)
C24	C25	C30	Ir1	4.1(8)	C73	C72	C81	C82A	175(2)
C24	C25	C30	C29	179.1(6)	C73	C72	C81	C83A	-62(2)
C25	C26	C27	C28	0.0(12)	C73	C72	C81	C84A	64(2)
C26	C25	C30	Ir1	-175.3(5)	C73	C74	C75	C76	-1.8(11)

**Crystal Table 6 Torsion Angles for yoon77.**

<b>A</b>	<b>B</b>	<b>C</b>	<b>D</b>	<b>Angle/°</b>	<b>A</b>	<b>B</b>	<b>C</b>	<b>D</b>	<b>Angle/°</b>
C26	C25	C30	C29	-0.4(10)	C73	C74	C75	C80	178.3(7)
C26	C27	C28	C29	-1.3(12)	C74	N6	C70	C71	0.0(15)
C26	C27	C28	C35	178.9(8)	C74	C75	C76	C77	179.5(7)
C27	C28	C29	C30	1.9(11)	C74	C75	C80	Ir2	5.4(8)
C27	C28	C35	C36	56.9(11)	C74	C75	C80	C79	179.6(7)
C27	C28	C35	C37	-67.7(11)	C75	C76	C77	C78	0.4(11)
C27	C28	C35	C38	174.4(9)	C76	C75	C80	Ir2	-174.6(5)
C28	C29	C30	Ir1	173.1(6)	C76	C75	C80	C79	-0.3(11)
C28	C29	C30	C25	-1.0(11)	C76	C77	C78	C79	0.6(11)
C29	C28	C35	C36	-122.9(9)	C76	C77	C78	C85	178.7(7)
C29	C28	C35	C37	112.5(10)	C77	C78	C79	C80	-1.5(12)
C29	C28	C35	C38	-5.3(11)	C77	C78	C85	C86	2.3(11)
C30	C25	C26	C27	0.9(11)	C77	C78	C85	C87	-118.9(9)
C31	C22	C23	C24	-177.1(6)	C77	C78	C85	C88	119.5(10)
C35	C28	C29	C30	-178.4(7)	C78	C79	C80	Ir2	174.8(6)

**Crystal Table 6 Torsion Angles for yoon77.**

A	B	C	D	Angle/°	A	B	C	D	Angle/°
Ir2	N7	C89	C90	174.9(14)	C78	C79	C80	C75	1.4(12)
Ir2	N7	C93	C92	-179.5(18)	C79	C78	C85	C86	-179.5(8)
Ir2	N7	C93	C94	2(3)	C79	C78	C85	C87	59.3(10)
Ir2	N8	C94	C93	2(3)	C79	C78	C85	C88	-62.4(11)
Ir2	N8	C94	C95	-177.0(16)	C80	C75	C76	C77	-0.5(11)
Ir2	N8	C98	C97	175.8(17)	C81	C72	C73	C74	-177.8(6)
Ir2	N7A	C89A	C90A	171.8(18)	C85	C78	C79	C80	-179.8(7)

**Crystal Table 7 Hydrogen Atom Coordinates ( $\text{\AA} \times 10^4$ ) and Isotropic Displacement Parameters ( $\text{\AA}^2 \times 10^3$ ) for yoon77.**

Atom	x	y	z	U(eq)
H39	3582.19	10455.61	7612.41	42
H40	1998.18	10563.9	7041.98	48
H42	5053.59	9328.68	5820.21	42
H45	7227.9	8480.79	5654.4	49

**Crystal Table 7 Hydrogen Atom Coordinates ( $\text{\AA}\times 10^4$ ) and Isotropic Displacement Parameters ( $\text{\AA}^2\times 10^3$ ) for yoon77.**

<b>Atom</b>	<b><i>x</i></b>	<b><i>y</i></b>	<b><i>z</i></b>	<b>U(eq)</b>
H47	10763.15	8122.44	6115.39	49
H48	9595.78	8979.32	6924.67	41
H49A	722.48	10240.47	5982.79	168
H49B	874.16	11447.67	6064.75	168
H49C	1085.16	10302.65	6592.52	168
H50A	9928.81	7021.91	4662.98	154
H50B	8432.05	7868.42	4898.7	154
H50C	9249.51	6475.1	5236.12	154
H39A	3353.67	10659.76	7610.75	31
H40A	1780.19	10395.62	7170.99	31
H42A	4637.69	9199.78	5886.82	31
H45A	6681.26	8756.85	5576.81	31
H47A	10335.16	8338.04	5928.62	31
H48A	9336.33	9039.46	6790.48	31

**Crystal Table 7 Hydrogen Atom Coordinates ( $\text{\AA}\times 10^4$ ) and Isotropic Displacement Parameters ( $\text{\AA}^2\times 10^3$ ) for yoon77.**

<b>Atom</b>	<b><i>x</i></b>	<b><i>y</i></b>	<b><i>z</i></b>	<b>U(eq)</b>
H49D	586.23	9607.09	6178.04	39
H49E	1614.32	8791.63	6671.11	39
H49F	639.75	10237.46	6687.36	39
H50D	9095.48	8036.71	4366.54	39
H50E	7871.94	9188.91	4613.19	39
H50F	7952.21	7801.71	4814.42	39
H1	4536.34	12241.73	6787.9	41
H2	3894.96	14393.96	6550.34	36
H4	7302.1	13819.85	7210.44	33
H7	9222.25	12312.74	7608.04	32
H8	10877.75	10756.03	8204.71	38
H10	9102.94	8425.28	8336	40
H13A	3622.9	16282.57	6204.58	93
H13B	3498.89	17407.16	6488.56	93

**Crystal Table 7 Hydrogen Atom Coordinates ( $\text{\AA}\times 10^4$ ) and Isotropic Displacement Parameters ( $\text{\AA}^2\times 10^3$ ) for yoon77.**

<b>Atom</b>	<b><i>x</i></b>	<b><i>y</i></b>	<b><i>z</i></b>	<b>U(eq)</b>
H13C	3123.08	16313.67	6870.97	93
H14A	7056.03	15449.44	6301.1	79
H14B	5956.4	16859.91	6120.52	79
H14C	5944.79	15748.48	5869.19	79
H15A	4844.47	15996.01	7569.18	77
H15B	5096.77	17113.47	7138.02	77
H15C	6341.09	15780.58	7304.53	77
H17A	11560.74	9714.94	9139.59	100
H17B	11674	8468.08	9587.25	100
H17C	10219.88	9561.73	9427.18	100
H18A	12623.62	7678.08	8168.14	122
H18B	13218.1	7517.95	8763.22	122
H18C	12743.34	8836.42	8329.04	122
H19A	9997.85	7696.09	9293.01	71



**Crystal Table 7 Hydrogen Atom Coordinates ( $\text{\AA}\times 10^4$ ) and Isotropic Displacement Parameters ( $\text{\AA}^2\times 10^3$ ) for yoon77.**

<b>Atom</b>	<b><i>x</i></b>	<b><i>y</i></b>	<b><i>z</i></b>	<b>U(eq)</b>
H19B	11581.19	6806.22	9318.04	71
H19C	10813.04	6974.96	8771.34	71
H20	8323.22	7086.3	7476.98	33
H21	8503.1	5195.56	8016.82	33
H23	5794	7049.15	9209.66	32
H26	4427.58	8951.02	9422.21	38
H27	3071.26	10987.2	9568.05	45
H29	4662.91	12334.73	8068.48	41
H32A	7549.65	3752.04	8363	87
H32B	7868.52	2820.65	8971.25	87
H32C	8876.82	3439.76	8666.68	87
H33A	8626.6	4649.98	9493.51	89
H33B	8099.69	3605.04	9800.35	89
H33C	7186.17	5045.85	9850.33	89

**Crystal Table 7 Hydrogen Atom Coordinates ( $\text{\AA}\times 10^4$ ) and Isotropic Displacement Parameters ( $\text{\AA}^2\times 10^3$ ) for yoon77.**

<b>Atom</b>	<b><i>x</i></b>	<b><i>y</i></b>	<b><i>z</i></b>	<b>U(eq)</b>
H34A	5253.63	5483.19	9446.94	98
H34B	5736.2	4022.3	9450.67	98
H34C	5228.09	5025.81	8873.79	98
H36A	2453.06	14284.63	9540.36	100
H36B	3990.03	13270.7	9484.54	100
H36C	2843.36	12833.9	9802.07	100
H37A	1086.27	12899.52	9151.1	110
H37B	1241.12	13393.75	8473.09	110
H37C	738.01	14351.59	8914.12	110
H38A	2555.63	15062.37	8496.21	96
H38B	2992.87	14131.74	8046.39	96
H38C	4089.63	14045.75	8434.34	96
H36D	2420.64	12625.37	9796.17	96
H36E	1236.76	12845.31	9421.03	96

**Crystal Table 7 Hydrogen Atom Coordinates ( $\text{\AA}\times 10^4$ ) and Isotropic Displacement Parameters ( $\text{\AA}^2\times 10^3$ ) for yoon77.**

<b>Atom</b>	<b><i>x</i></b>	<b><i>y</i></b>	<b><i>z</i></b>	<b>U(eq)</b>
H36F	1349.33	14021.4	9566.18	96
H37D	1072.02	14707.04	8553.96	132
H37E	1530.88	13464.59	8291.72	132
H37F	2340.04	14320.98	8090	132
H38D	3045.97	14769.4	9023.03	110
H38E	4319.26	13851.65	8674.53	110
H38F	4098.04	13470.73	9358.4	110
H89	818.66	-569.45	2427.42	41
H90	-1077.47	-753.67	2997.95	43
H92	-373.75	779.97	4164.79	42
H95	911.36	1360.06	4420.96	47
H97	4328.25	1888.07	4051.02	51
H98	4722.33	1045.14	3211.16	46
H99A	-2934.45	1431.84	4402.21	48

**Crystal Table 7 Hydrogen Atom Coordinates ( $\text{\AA}\times 10^4$ ) and Isotropic Displacement Parameters ( $\text{\AA}^2\times 10^3$ ) for yoon77.**

<b>Atom</b>	<b><i>x</i></b>	<b><i>y</i></b>	<b><i>z</i></b>	<b>U(eq)</b>
H99B	-1839.22	119.14	4706.55	48
H99C	-3324.13	273.67	4641.8	48
H10A	3545.06	2918.89	4673.81	108
H10B	3984.04	1705.83	5174.26	108
H10C	2746.94	2991.1	5296.72	108
H89A	891.67	-337.32	2330.54	45
H90A	-1087.91	-378.07	2913.31	45
H92A	0.68	692.88	4154.69	48
H95A	1138.1	1691.75	4300.94	42
H97A	4699.93	1954.89	3867.39	42
H98A	5024.66	1004.91	3082.8	38
H99D	-2184.86	-606.32	3349.87	69
H99E	-3485.64	236.9	3713.85	69
H99F	-2559.24	-1179.42	3992.43	69

**Crystal Table 7 Hydrogen Atom Coordinates ( $\text{\AA}\times 10^4$ ) and Isotropic Displacement Parameters ( $\text{\AA}^2\times 10^3$ ) for yoon77.**

<b>Atom</b>	<b><i>x</i></b>	<b><i>y</i></b>	<b><i>z</i></b>	<b>U(eq)</b>
H10D	779.49	3573.84	4748.74	75
H10E	1583.97	3033.23	5321.18	75
H10F	1192	2143.81	5058.2	75
H51	3017.59	-2218.16	3201.49	44
H52	4344.87	-4373.32	3446.8	34
H54	7621.63	-3717.13	2782.3	32
H57	8312.56	-2170.58	2384.08	38
H58	8822.29	-591.33	1807.86	43
H60	4855.65	1704.08	1726.18	51
H63A	6955.2	-7392.26	3489.04	111
H63B	5774.83	-6318.94	3106.81	111
H63C	5718.72	-6322.1	3780.71	111
H64A	7108.54	-5553.54	4147.59	88
H64B	8350.31	-5397.8	3745.27	88

**Crystal Table 7 Hydrogen Atom Coordinates ( $\text{\AA}\times 10^4$ ) and Isotropic Displacement Parameters ( $\text{\AA}^2\times 10^3$ ) for yoon77.**

<b>Atom</b>	<b><i>x</i></b>	<b><i>y</i></b>	<b><i>z</i></b>	<b>U(eq)</b>
H64C	8368.17	-6760.25	3959.91	88
H65A	8785.2	-7009.37	2922.29	66
H65B	8698.62	-5618.78	2731.01	66
H65C	7748.25	-6009.99	2460.43	66
H67A	9209.62	307.6	986.01	118
H67B	8805.54	1672.22	595.19	118
H67C	8079.52	825.07	533.86	118
H68A	7410.66	2531.78	1907.04	93
H68B	8347.69	2739.83	1344.6	93
H68C	8860.37	1429.3	1784.33	93
H69A	5922.24	2264.48	632.39	59
H69B	6265.44	3367.01	715.13	59
H69C	5306.12	2908.65	1190.77	59
H67D	9007.35	980.13	1514.57	118

**Crystal Table 7 Hydrogen Atom Coordinates ( $\text{\AA}\times 10^4$ ) and Isotropic Displacement Parameters ( $\text{\AA}^2\times 10^3$ ) for yoon77.**

<b>Atom</b>	<b><i>x</i></b>	<b><i>y</i></b>	<b><i>z</i></b>	<b>U(eq)</b>
H67E	8555.34	1113.64	890.81	118
H67F	8620.05	2280.6	1069.79	118
H68D	5931.88	3076.33	2017.27	93
H68E	7006.06	3512.6	1615.87	93
H68F	7505.03	2325.99	2127.34	93
H69D	6152.68	2300.17	708.5	59
H69E	6662.96	3328.06	742.94	59
H69F	5315.37	3329.88	1109.54	59
H70	2230.41	2931.34	2556.75	45
H71	999.88	4852.86	2013.75	42
H73	844.54	3038.49	823.38	35
H76	1508.06	1117.48	594.24	37
H77	2362.35	-918.64	421.91	41
H79	4159.81	-2261.76	1923.76	42

**Crystal Table 7 Hydrogen Atom Coordinates ( $\text{\AA}\times 10^4$ ) and Isotropic Displacement Parameters ( $\text{\AA}^2\times 10^3$ ) for yoon77.**

<b>Atom</b>	<b><i>x</i></b>	<b><i>y</i></b>	<b><i>z</i></b>	<b>U(eq)</b>
H82A	-1726.72	5640.44	1652.23	83
H82B	-2036.18	6865.84	1161.84	83
H82C	-995.91	6531.51	1632.99	83
H83A	1092.03	6246.43	1001.65	111
H83B	88.45	6920.68	492.27	111
H83C	1376.48	5616.04	446.04	111
H84A	-123.77	4805.8	247.42	73
H84B	-1444.54	6062.98	334.96	73
H84C	-1334.58	4738.24	702.27	73
H82D	-809.79	6231.15	1718.16	73
H82E	-1301.2	7208.22	1132.66	73
H82F	233.27	6665.18	1288.88	73
H83D	970.66	6167.08	438.6	83
H83E	-195.24	6120.07	141.79	83



**Crystal Table 7 Hydrogen Atom Coordinates ( $\text{\AA}\times 10^4$ ) and Isotropic Displacement Parameters ( $\text{\AA}^2\times 10^3$ ) for yoon77.**

<b>Atom</b>	<b><i>x</i></b>	<b><i>y</i></b>	<b><i>z</i></b>	<b>U(eq)</b>
H83F	1139.8	4865.4	306.86	83
H84D	-1414.68	4841.59	724.23	104
H84E	-2185.83	6217.15	882.75	104
H84F	-1755.72	5007.91	1385.33	104
H86A	2561.55	-2865.08	485.28	94
H86B	3906.48	-4133.91	452.74	94
H86C	3930.98	-2806.37	172.48	94
H87A	3774.1	-4018.9	1912.79	72
H87B	3646.07	-4760.9	1468.06	72
H87C	2402.63	-3487.62	1600.24	72
H88A	5791.23	-3181.52	734.49	114
H88B	5865.99	-4566.93	934.76	114
H88C	5772.03	-3778.23	1406.09	114
H10G	7790.97	10024.47	9281.4	81

**Crystal Table 7 Hydrogen Atom Coordinates ( $\text{\AA}\times 10^4$ ) and Isotropic Displacement Parameters ( $\text{\AA}^2\times 10^3$ ) for yoon77.**

<b>Atom</b>	<b><i>x</i></b>	<b><i>y</i></b>	<b><i>z</i></b>	<b>U(eq)</b>
H10H	7167	10930.7	9748.16	81
H10I	6198.67	10883.26	9334.75	81
H10J	5530.15	9062.3	10654.03	76
H10K	5051.22	10511.79	10365.81	76
H10L	6269.33	9843.01	10781.9	76
H10M	6319.11	2688.8	5001.04	98
H10N	6564.13	1556.82	5537.64	98
H10O	7187.14	1269.75	4905.88	98
H10P	7949.8	2519.49	6038.12	98
H10Q	6999.8	3570.7	5559.81	98
H10R	8574.26	3251.92	5517.35	98
H10S	9520.72	3701.23	5396.45	98
H10T	8052.54	4395.53	5151.9	98
H10U	9350.55	3704.32	4743.84	98

**Crystal Table 7 Hydrogen Atom Coordinates ( $\text{\AA}\times 10^4$ ) and Isotropic Displacement Parameters ( $\text{\AA}^2\times 10^3$ ) for yoon77.**

<b>Atom</b>	<b><i>x</i></b>	<b><i>y</i></b>	<b><i>z</i></b>	<b>U(eq)</b>
H10V	7813.4	1670.24	5975.21	98
H10W	7469.68	3075.93	6029	98
H10X	8905.47	1962.61	6200.01	98
H11A	5853.69	2178.71	5436.45	113
H11B	4591.46	2346.79	5127.14	113
H11C	4383.29	2621.42	5768.19	113
H11D	2588.54	4990.41	5156.27	131
H11E	3265.67	4426.46	4580.26	131
H11F	3370.7	5646.68	4675.35	131
H11G	2932.54	4953.08	4858.76	100
H11H	2242.66	5784.51	5353.41	100
H11I	3694.75	4621.74	5429.85	100
H11J	3270.94	8003.39	4596.17	102
H11K	1974.75	7709.36	4790.19	102

**Crystal Table 7 Hydrogen Atom Coordinates ( $\text{\AA}\times 10^4$ ) and Isotropic Displacement Parameters ( $\text{\AA}^2\times 10^3$ ) for yoon77.**

<b>Atom</b>	<b><i>x</i></b>	<b><i>y</i></b>	<b><i>z</i></b>	<b>U(eq)</b>
H11L	2798.19	7419.38	4184.91	102
H11M	3952.85	7390.19	5072.95	106
H11N	3570.85	8333.62	4470.62	106
H11O	3420.65	8866.94	5044.09	106
H11P	7160.23	7045.99	4304.55	158
H11Q	5875.13	7352.36	3972.29	158
H11R	6267.9	6271.41	4532.03	158
H11S	5285.42	8560.18	4014.45	66
H11T	6229.48	7114.66	3983.94	66
H11U	6844.38	8129.4	3791.1	66
H12A	7886.56	6442.64	5254.23	89
H12B	8569.09	6507.59	4609.73	89
H12C	7631.65	5771.8	4811.13	89

**Crystal Table 8 Atomic Occupancy for yoon77.**

<b>Atom</b>	<b>Occupancy</b>	<b>Atom</b>	<b>Occupancy</b>	<b>Atom</b>	<b>Occupancy</b>
O1	0.876(10)	O2	0.876(10)	N3	0.876(10)
N4	0.876(10)	C39	0.876(10)	H39	0.876(10)
C40	0.876(10)	H40	0.876(10)	C41	0.876(10)
C42	0.876(10)	H42	0.876(10)	C43	0.876(10)
C44	0.876(10)	C45	0.876(10)	H45	0.876(10)
C46	0.876(10)	C47	0.876(10)	H47	0.876(10)
C48	0.876(10)	H48	0.876(10)	C49	0.876(10)
H49A	0.876(10)	H49B	0.876(10)	H49C	0.876(10)
C50	0.876(10)	H50A	0.876(10)	H50B	0.876(10)
H50C	0.876(10)	O1A	0.124(10)	O2A	0.124(10)
N3A	0.124(10)	N4A	0.124(10)	C39A	0.124(10)
H39A	0.124(10)	C40A	0.124(10)	H40A	0.124(10)
C41A	0.124(10)	C42A	0.124(10)	H42A	0.124(10)
C43A	0.124(10)	C44A	0.124(10)	C45A	0.124(10)
H45A	0.124(10)	C46A	0.124(10)	C47A	0.124(10)

**Crystal Table 8 Atomic Occupancy for yoon77.**

<i>Atom</i>	<i>Occupancy</i>	<i>Atom</i>	<i>Occupancy</i>	<i>Atom</i>	<i>Occupancy</i>
H47A	0.124(10)	C48A	0.124(10)	H48A	0.124(10)
C49A	0.124(10)	H49D	0.124(10)	H49E	0.124(10)
H49F	0.124(10)	C50A	0.124(10)	H50D	0.124(10)
H50E	0.124(10)	H50F	0.124(10)	C36	0.740(11)
H36A	0.740(11)	H36B	0.740(11)	H36C	0.740(11)
C37	0.740(11)	H37A	0.740(11)	H37B	0.740(11)
H37C	0.740(11)	C38	0.740(11)	H38A	0.740(11)
H38B	0.740(11)	H38C	0.740(11)	C36A	0.260(11)
H36D	0.260(11)	H36E	0.260(11)	H36F	0.260(11)
C37A	0.260(11)	H37D	0.260(11)	H37E	0.260(11)
H37F	0.260(11)	C38A	0.260(11)	H38D	0.260(11)
H38E	0.260(11)	H38F	0.260(11)	O3	0.514(12)
O4	0.514(12)	N7	0.514(12)	N8	0.514(12)
C89	0.514(12)	H89	0.514(12)	C90	0.514(12)
H90	0.514(12)	C91	0.514(12)	C92	0.514(12)

**Crystal Table 8 Atomic Occupancy for yoon77.**

<i>Atom</i>	<i>Occupancy</i>	<i>Atom</i>	<i>Occupancy</i>	<i>Atom</i>	<i>Occupancy</i>
H92	0.514(12)	C93	0.514(12)	C94	0.514(12)
C95	0.514(12)	H95	0.514(12)	C96	0.514(12)
C97	0.514(12)	H97	0.514(12)	C98	0.514(12)
H98	0.514(12)	C99	0.514(12)	H99A	0.514(12)
H99B	0.514(12)	H99C	0.514(12)	C100	0.514(12)
H10A	0.514(12)	H10B	0.514(12)	H10C	0.514(12)
O3A	0.486(12)	O4A	0.486(12)	N7A	0.486(12)
N8A	0.486(12)	C89A	0.486(12)	H89A	0.486(12)
C90A	0.486(12)	H90A	0.486(12)	C91A	0.486(12)
C92A	0.486(12)	H92A	0.486(12)	C93A	0.486(12)
C94A	0.486(12)	C95A	0.486(12)	H95A	0.486(12)
C96A	0.486(12)	C97A	0.486(12)	H97A	0.486(12)
C98A	0.486(12)	H98A	0.486(12)	C99A	0.486(12)
H99D	0.486(12)	H99E	0.486(12)	H99F	0.486(12)
C10B	0.486(12)	H10D	0.486(12)	H10E	0.486(12)

**Crystal Table 8 Atomic Occupancy for yoon77.**

<b>Atom</b>	<b>Occupancy</b>	<b>Atom</b>	<b>Occupancy</b>	<b>Atom</b>	<b>Occupancy</b>
H10F	0.486(12)	C66	0.599(12)	C67	0.599(12)
H67A	0.599(12)	H67B	0.599(12)	H67C	0.599(12)
C68	0.599(12)	H68A	0.599(12)	H68B	0.599(12)
H68C	0.599(12)	C69	0.599(12)	H69A	0.599(12)
H69B	0.599(12)	H69C	0.599(12)	C66A	0.401(12)
C67A	0.401(12)	H67D	0.401(12)	H67E	0.401(12)
H67F	0.401(12)	C68A	0.401(12)	H68D	0.401(12)
H68E	0.401(12)	H68F	0.401(12)	C69A	0.401(12)
H69D	0.401(12)	H69E	0.401(12)	H69F	0.401(12)
C82	0.749(12)	H82A	0.749(12)	H82B	0.749(12)
H82C	0.749(12)	C83	0.749(12)	H83A	0.749(12)
H83B	0.749(12)	H83C	0.749(12)	C84	0.749(12)
H84A	0.749(12)	H84B	0.749(12)	H84C	0.749(12)
C82A	0.251(12)	H82D	0.251(12)	H82E	0.251(12)
H82F	0.251(12)	C83A	0.251(12)	H83D	0.251(12)



**Crystal Table 8 Atomic Occupancy for yoon77.**

<i>Atom</i>	<i>Occupancy</i>	<i>Atom</i>	<i>Occupancy</i>	<i>Atom</i>	<i>Occupancy</i>
H83E	0.251(12)	H83F	0.251(12)	C84A	0.251(12)
H84D	0.251(12)	H84E	0.251(12)	H84F	0.251(12)
P1	0.812(9)	F1	0.812(9)	F2	0.812(9)
F3	0.812(9)	F4	0.812(9)	F5	0.812(9)
F6	0.812(9)	P1A	0.188(9)	F1A	0.188(9)
F2A	0.188(9)	F3A	0.188(9)	F4A	0.188(9)
F5A	0.188(9)	F6A	0.188(9)	P2	0.739(10)
F7	0.739(10)	F8	0.739(10)	F9	0.739(10)
F10	0.739(10)	F11	0.739(10)	F12	0.739(10)
P2A	0.261(10)	F7A	0.261(10)	F8A	0.261(10)
F9A	0.261(10)	F10A	0.261(10)	F11A	0.261(10)
F12A	0.261(10)	O6	0.496(4)	C104	0.496(4)
H10M	0.496(4)	H10N	0.496(4)	H10O	0.496(4)
C105	0.496(4)	C106	0.496(4)	H10P	0.496(4)
H10Q	0.496(4)	H10R	0.496(4)	O7	0.504(4)

**Crystal Table 8 Atomic Occupancy for yoon77.**

<i>Atom</i>	<i>Occupancy</i>	<i>Atom</i>	<i>Occupancy</i>	<i>Atom</i>	<i>Occupancy</i>
C107	0.504(4)	H10S	0.504(4)	H10T	0.504(4)
H10U	0.504(4)	C108	0.504(4)	C109	0.504(4)
H10V	0.504(4)	H10W	0.504(4)	H10X	0.504(4)
O8	0.504(4)	C110	0.504(4)	H11A	0.504(4)
H11B	0.504(4)	H11C	0.504(4)	C111	0.504(4)
C112	0.504(4)	H11D	0.504(4)	H11E	0.504(4)
H11F	0.504(4)	O9	0.406(14)	C113	0.406(14)
H11G	0.406(14)	H11H	0.406(14)	H11I	0.406(14)
C114	0.406(14)	C115	0.406(14)	H11J	0.406(14)
H11K	0.406(14)	H11L	0.406(14)	O10	0.580(15)
C116	0.580(15)	H11M	0.580(15)	H11N	0.580(15)
H11O	0.580(15)	C117	0.580(15)	C118	0.580(15)
H11P	0.580(15)	H11Q	0.580(15)	H11R	0.580(15)
O11	0.420(15)	C119	0.420(15)	H11S	0.420(15)
H11T	0.420(15)	H11U	0.420(15)	C120	0.420(15)

### Crystal Table 8 Atomic Occupancy for yoon77.

Atom	Occupancy	Atom	Occupancy	Atom	Occupancy
C121	0.420(15)	H12A	0.420(15)	H12B	0.420(15)
H12C	0.420(15)				

### 2.11. References

<sup>43</sup> (a) Richards, C. J.; Arthurs, R. A. Catalyst Optimisation for Asymmetric Synthesis by Ligand Chirality Element Addition: A Perspective on Stereochemical Cooperativity. *Chem. – Eur. J.* **2017**, *23*, 11460–11478. (b) Kolodiazhnyi, O. I. Multiple Stereoselectivity and Its Application in Organic Synthesis. *Tetrahedron* **2003**, *59*, 5953–6018. (c) Masamune, S.; Choy, W.; Petersen, J. S.; Sita, L. R. Double Asymmetric Synthesis and a New Strategy for Stereochemical Control in Organic Synthesis. *Angew. Chem. Int. Ed.* **1985**, *24*, 1–30.

<sup>44</sup> (a) Evans, D. A.; Miller, S. J.; Lectka, T. Bis(Oxazoline)Copper(II) Complexes as Chiral Catalysts for the Enantioselective Diels-Alder Reaction. *J. Am. Chem. Soc.* **1993**, *115*, 6460–6461. (b) Jermaks, J.; Tallmadge, E. H.; Keresztes, I.; Collum, D. B. Lithium Amino Alkoxide–Evans Enolate Mixed Aggregates: Aldol Addition with Matched and Mismatched Stereocontrol. *J. Am. Chem. Soc.* **2018**, *140*, 3077–3090. (c) Pizzolato, S. F.; Štacko, P.; Kistemaker, J. C. M.; van Leeuwen, T.; Feringa, B. L. Phosphoramidite-Based Photoresponsive Ligands Displaying Multifold Transfer of Chirality in Dynamic Enantioselective Metal Catalysis. *Nat. Catal.* **2020**, *3*, 488–496. (d) Pujol, A.; Whiting, A. Double Diastereoselective Approach to Chiral Syn- and Anti-1,3-Diol Analogues through Consecutive Catalytic Asymmetric Borylations. *J. Org. Chem.* **2017**, *82*, 7265–7279.

<sup>45</sup> For recent reviews, see: (a) Skubi, K. L.; Blum, T. R.; Yoon, T. P. Dual Catalysis Strategies in Photochemical Synthesis. *Chem. Rev.* **2016**, *116*, 10035–10074. (b) Rigotti, T.; Alemán, J. Visible Light Photocatalysis – from Racemic to Asymmetric Activation Strategies. *Chem. Commun.* **2020**, *56*, 11169–11190. (c) Prentice, C.; Morrisson, J.; Smith, A. D.; Zysman-Colman, E. Recent Developments in Enantioselective Photocatalysis. *Beilstein J. Org. Chem.* **2020**, *16*, 2363–2441. (d) Hong, B.-C. Enantioselective Synthesis Enabled by Visible Light Photocatalysis. *Org. Biomol. Chem.* **2020**, *18*, 4298–4353. (e) Großkopf, J.; Kratz, T.; Rigotti, T.; Bach, T. Enantioselective Photochemical Reactions Enabled by Triplet Energy Transfer. *Chem. Rev.* **2021**, Article ASAP. DOI: 10.1021/acs.chemrev.1c00272 (accessed 2021-11-16). (f) Genzink, M. J.; Kidd, J. B.; Swords, W. B.; Yoon, T. P. Chiral Photocatalyst Structures in Asymmetric Photochemical Synthesis. *Chem. Rev.* **2021**, Article ASAP. DOI: 10.1021/acs.chemrev.1c00467 (accessed 2021-11-16).

- <sup>46</sup> (a) Herrero, S.; Usón, M. A. A Straightforward Method for Assigning Stereochemical  $\Lambda/\Delta$  Descriptors to Octahedral Coordination Compounds. *J. Chem. Educ.* **1995**, *72*, 1065–1066. (b) Bauer, E. B. Chiral-at-Metal Complexes and Their Catalytic Applications in Organic Synthesis. *Chem. Soc. Rev.* **2012**, *41*, 3153–3167. (c) Fontecave, M.; Hamelin, O.; Ménage, S. Chiral-at-Metal Complexes as Asymmetric Catalysts. In *Chiral Diazaligands for Asymmetric Synthesis*; Lemaire, M., Mangeney, P., Eds.; Springer Berlin Heidelberg: Berlin, Heidelberg, 2005; pp 271–288.
- <sup>47</sup> (a) Huo, H.; Shen, X.; Wang, C.; Zhang, L.; Röse, P.; Chen, L.-A.; Harms, K.; Marsch, M.; Hilt, G.; Meggers, E. Asymmetric Photoredox Transition-Metal Catalysis Activated by Visible Light. *Nature* **2014**, *515*, 100–103. (b) Zhang, L.; Meggers, E. Steering Asymmetric Lewis Acid Catalysis Exclusively with Octahedral Metal-Centered Chirality. *Acc. Chem. Res.* **2017**, *50*, 320–330.
- <sup>48</sup> Nicewicz, D. A.; MacMillan, D. W. C. Merging Photoredox Catalysis with Organocatalysis: The Direct Asymmetric Alkylation of Aldehydes. *Science* **2008**, *322*, 77–80.
- <sup>49</sup> (a) Blum, T. R.; Miller, Z. D.; Bates, D. M.; Guzei, I. A.; Yoon, T. P. Enantioselective Photochemistry through Lewis Acid-Catalyzed Triplet Energy Transfer. *Science* **2016**, *354*, 1391–1395. (b) Miller, Z. D.; Lee, B. J.; Yoon, T. P. Enantioselective Crossed Photocycloadditions of Styrenic Olefins by Lewis Acid Catalyzed Triplet Sensitization. *Angew. Chem. Int. Ed.* **2017**, *56*, 11891–11895.
- <sup>50</sup> (a) Uraguchi, D.; Kimura, Y.; Ueoka, F.; Ooi, T. Urea as a Redox-Active Directing Group under Asymmetric Photocatalysis of Iridium-Chiral Borate Ion Pairs. *J. Am. Chem. Soc.* **2020**, *142*, 19462–19467. (b) Kimura, Y.; Uraguchi, D.; Ooi, T. Catalytic Asymmetric Synthesis of 5-Membered Alicyclic  $\alpha$ -Quaternary  $\beta$ -Amino Acids via [3+2]-Photocycloaddition of  $\alpha$ -Substituted Acrylates. *Org. Biomol. Chem.* **2021**, *19*, 1744–1747.
- <sup>51</sup> (a) Poplata, S.; Tröster, A.; Zou, Y.-Q.; Bach, T. Recent Advances in the Synthesis of Cyclobutanes by Olefin [2 + 2] Photocycloaddition Reactions. *Chem. Rev.* **2016**, *116*, 9748–9815. (b) Xu, Y.; Conner, M. L.; Brown, M. K. Cyclobutane and Cyclobutene Synthesis: Catalytic Enantioselective [2+2] Cycloadditions. *Angew. Chem. Int. Ed.* **2015**, *54*, 11918–11928. (c) Wen, K.-G.; Peng, Y.-Y.; Zeng, X.-P. Advances in the Catalytic Asymmetric Synthesis of Quaternary Carbon Containing Cyclobutanes. *Org. Chem. Front.* **2020**, *7*, 2576–2597.
- <sup>52</sup> During the preparation of this manuscript Bach and co-workers reported the [2+2] cycloaddition of sulfonyl-alkenes and styrenes: Jeremias, N.; Mohr, L.-M.; Bach, T. Intermolecular [2+2] Photocycloaddition of  $\alpha,\beta$ -Unsaturated Sulfones: Catalyst-Free Reaction and Catalytic Variants. *Org. Lett.* **2021**, *23*, 5674–5678.
- <sup>53</sup> For select examples, see (a) Hepburn, H. B.; Melchiorre, P. Brønsted Acid-Catalysed Conjugate Addition of Photochemically Generated  $\alpha$ -Amino Radicals to Alkenylpyridines. *Chem. Commun.* **2016**, *52*, 3520–3523. (b) Wang, S.; Li, X.; Liu, H.; Xu, L.; Zhuang, J.; Li, J.; Li, H.; Wang, W. Organocatalytic Enantioselective Direct Additions of Aldehydes to 4-Vinylpyridines and Electron-Deficient Vinylarenes and Their Synthetic Applications. *J. Am. Chem. Soc.* **2015**, *137*, 2303–2310. (c) Wang, Y.-Y.; Kanomata, K.; Korenaga, T.; Terada, M. Enantioselective Aza Michael-Type Addition to Alkenyl Benzimidazoles Catalyzed by a Chiral Phosphoric Acid. *Angew. Chem. Int. Ed.* **2016**, *55*, 927–931.

- 
- <sup>54</sup> Sherbrook, E. M.; Jung, H.; Cho, D.; Baik, M-H.; Yoon, T. P. Brønsted Acid Catalysis of Photosensitized Cycloadditions. *Chem. Sci.*, **2020**, *11*, 856–861.
- <sup>55</sup> (a) Pecho, F.; Sempere, Y.; Gramüller, J.; Hörmann, F. M.; Gschwind, R. M.; Bach, T. Enantioselective [2+2] Photocycloaddition via Iminium Ions: Catalysis by a Sensitizing Chiral Brønsted Acid. *J. Am. Chem. Soc.* **2021**, *143*, 9350–9354. (b) Pecho, F.; Zou, Y.-Q.; Gramüller, J.; Mori, T.; Huber, S. M.; Bauer, A.; Gschwind, R. M.; Bach, T. A Thioxanthone Sensitizer with a Chiral Phosphoric Acid Binding Site: Properties and Applications in Visible Light-Mediated Cycloadditions. *Chem. Eur. J.* **2020**, *26*, 5190–5194.
- <sup>56</sup> (c) Ma, J.; Zhang, X.; Huang, X.; Luo, S.; Meggers, E. Preparation of Chiral-at-Metal Catalysts and Their Use in Asymmetric Photoredox Chemistry. *Nat. Protoc.* **2018**, *13*, 605–632.
- <sup>57</sup> Morton, C. M.; Zhu, Q.; Ripberger, H.; Troian-Gautier, L.; Toa, Z. S. D.; Knowles, R. R.; Alexanian, E. J. C–H Alkylation via Multisite-Proton-Coupled Electron Transfer of an Aliphatic C–H Bond. *J. Am. Chem. Soc.* **2019**, *141*, 13253–13260.
- <sup>58</sup> Deb, A.; Manna, S.; Maji, A.; Dutta, U.; Maiti, D. Iron-Catalyzed Direct C–H Arylation of Heterocycles and Quinones with Arylboronic Acids. *Eur. J. Org. Chem.* **2013**, 5251–5256.
- <sup>59</sup> Lowry, M. S.; Hudson, W. R.; Pascal, Jr., R. A.; Bernhard, S. Accelerated Luminophore Discovery through Combinatorial Synthesis. *J. Am. Chem. Soc.* **2004**, *126*, 14129–14135.
- <sup>60</sup> Shen, X.; Huo, H.; Wang, C.; Zhang, B.; Harms, K.; Meggers, E. Octahedral Chiral-at-Metal Iridium Catalysts: Versatile Chiral Lewis Acids for Asymmetric Conjugate Additions. *Chem. Eur. J.* **2015**, *21*, 9720–9726.
- <sup>61</sup> Chen, L.-A.; Xu, W.; Huang, B.; Ma, J.; Wang, L.; Xi, J.; Harms, K.; Gong, L.; Meggers, E. Asymmetric Catalysis with an Inert Chiral-at-Metal Iridium Complex. *J. Am. Chem. Soc.* **2013**, *135*, 10598–10601.
- <sup>62</sup> Zhou, B.; Hu, Y.; Wang, C. Manganese-Catalyzed Direct Nucleophilic C(sp<sup>2</sup>)-H Addition to Aldehydes and Nitriles. *Angew. Chem. Int. Ed.* **2015**, *54*, 13659–13663.
- <sup>63</sup> Thordarson, P. Determining Association Constants from Titration Experiments in Supramolecular Chemistry. *Chem. Soc. Rev.* **2011**, *40*, 1305–1323.
- <sup>64</sup> <http://supramolecular.org>
- <sup>65</sup> Bruker-AXS (2016). *APEX3*. Version 2016.5-0. Madison, Wisconsin, USA.
- <sup>66</sup> Krause, L.; Herbst-Irmer, R.; Sheldrick, G. M.; Stalke, D. J. Comparison of Silver and Molybdenum Microfocus X-ray Sources for Single-Crystal Structure Determination. *Appl. Cryst.* **2015**, *48*, 3–10.
- <sup>67</sup> Sheldrick, G. M. (2013b). *XPREP*. Version 2013/1. Georg-August-Universität Göttingen, Göttingen, Germany.
- <sup>68</sup> Sheldrick, G. M. (2013a). The *SHELX* homepage, <http://shelx.uni-ac.gwdg.de/SHELX/>.
- <sup>69</sup> Sheldrick, G. M. SHELXT—Integrated Space-Group and Crystal-Structure Determination. *Acta Cryst. A* **2015**, *71*, 3–8.

---

<sup>70</sup> Sheldrick, G. M. Crystal Structure Refinement with SHELXL. *Acta Cryst. C* **2015**, *71*, 3–8.

<sup>71</sup> Dolomanov, O. V.; Bourhis, L. J.; Gildea, R. J.; Howard, J. A. K.; Puschmann, H. J. OLEX2: a Complete Structure Solution, Refinement, and Analysis Program. *Appl. Crystallogr.* **2009**, *42*, 339–341.

<sup>72</sup> Guzei, I. A. (2007-2013). Programs *Gn*. University of Wisconsin-Madison, Madison, Wisconsin, USA.

Chapter 3. Discovery and Elucidation of Counteranion Dependence in Photoredox  
Catalysis

### 3.1. Previous Publication of this Work

This work has been previously published:

Farney, E. P.; Chapman, S. J.; Swords, W. B.; Torelli, M. D.; Hamers, R. J.; Yoon, T. P. Discovery and Elucidation of Counteranion Dependence in Photoredox Catalysis. *J. Am. Chem. Soc.* **2019**, *141*, 15, 6385–6391.

### 3.2. Abstract

Over the past decade, there has been a renewed interest in the use of transition metal polypyridyl complexes as photoredox catalysts for a variety of innovative synthetic applications. Many derivatives of these complexes are known, and the effect of ligand modifications on their efficacy as photoredox catalysts has been the subject of extensive, systematic investigation. However, the influence of the photocatalyst counteranion has received little attention, despite the fact that these complexes are generally cationic in nature. Herein, we demonstrate that counteranion effects exert a surprising, dramatic impact on the rate of a representative photocatalytic radical cation Diels–Alder reaction. A detailed analysis reveals that counteranion identity impacts multiple aspects of the reaction mechanism. Most notably, photocatalysts with more non-coordinating counteranions yield a more powerful triplet excited state oxidant and longer radical cation chain length. It is proposed that this counteranion effect arises from Coulombic ion-pairing interactions between the counteranion and both the cationic photoredox catalyst and the radical cation intermediate, respectively. The comparatively slower rate of reaction with coordinating counteranions can be rescued by using hydrogen-bonding anion binders that attenuate deleterious ion-pairing interactions. These results demonstrate the importance of counteranion identity as a variable in the design and optimization of photoredox transformations



and suggest a novel strategy for the optimization of organic reactions using this class of transition metal photocatalysts.

### 3.3. Introduction

Ruthenium(II) polypyridyl complexes have been among the most widely studied molecular photocatalysts for a variety of applications. The photophysical, electrochemical, and physical properties of this class of luminescent transition metal complexes have been extensively characterized.<sup>73</sup> They generally exhibit strong absorbance in the visible spectrum, feature high intersystem crossing efficiency, and can participate in a diverse range of photoinduced electron- and energy-transfer processes. Because of these attractive features, Ru(II) photocatalysts were instrumental in the early development of solar fuel technologies;<sup>74</sup> in addition, some of the best light-harvesting sensitizers for dye-sensitized solar cells belong to this family of complexes.<sup>75</sup> Over the past decade, the recognition that  $\text{Ru}(\text{bpy})_3^{2+}$  and its analogues are also useful photocatalysts for organic transformations has stimulated a renewal of interest in photochemical synthesis.<sup>76</sup> Because of the exceptional utility of  $\text{Ru}(\text{bpy})_3^{2+}$  in so many diverse applications, numerous structurally varied Ru(II) polypyridyl photocatalysts have been prepared, and the effects of ligand modifications on catalyst properties are well-understood (Figure 3.1).<sup>77</sup>

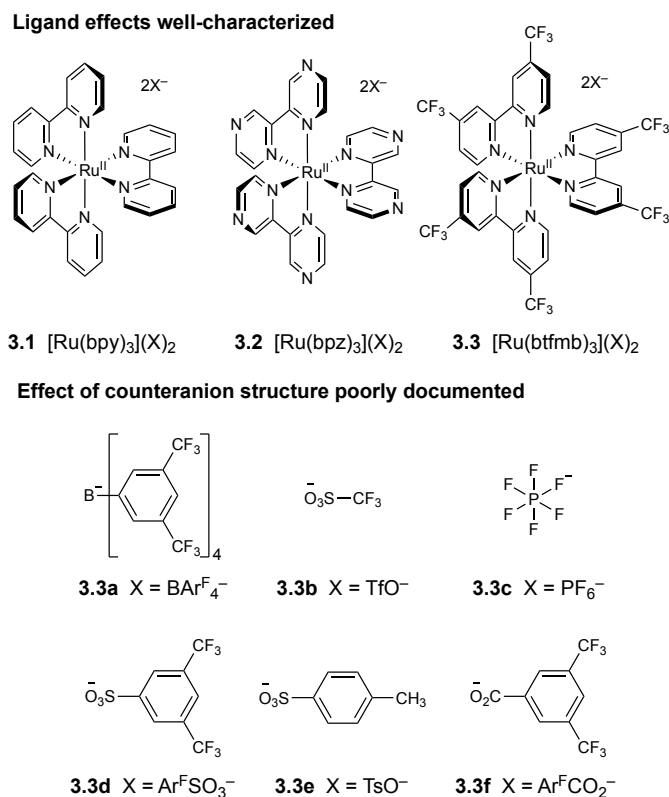


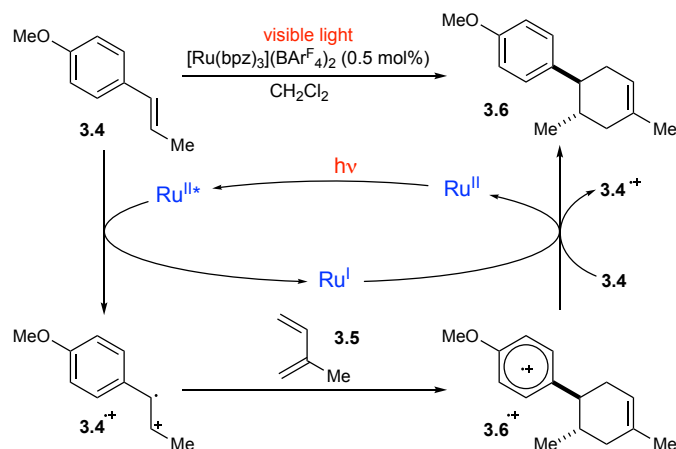
Figure 3.1 Structurally varied Ru(II) photocatalysts.

The effect of counteranion structure on the photoactivity of these cationic complexes, on the other hand, has not been subject to similar systematic study. In this chapter, we document the discovery of the unexpected impact counteranion identity plays on the efficiency of a radical cation Diels–Alder cycloaddition, a representative photoredox transformation. We rationalize the observed rate increase as the consequence of (1) a change in the photocatalyst ground-state electrochemical properties, (2) a significant shift in its triplet-state energy, and (3) an increase in the efficiency of radical cation chain propagation. The results reported herein suggest that this counterion effect may be an under-appreciated but important phenomenon in many photoredox reactions. Understanding the impact of this experimental variable, therefore, should benefit the growing community of scholars interested in the use of these complexes as photoredox catalysts in organic chemistry.

## 3.4. Results and Discussion

### 3.4.1. Counterion Effects in Radical Cation Cycloadditions.

Several years ago, we reported that visible light photoredox catalysis offered an efficient means to conduct radical cation Diels–Alder cycloadditions between a wide range of electron-rich styrenes and diverse dienes.<sup>78</sup> The highly electron-deficient  $[\text{Ru}(\text{bpz})_3](\text{BAr}^{\text{F}_4})_2$  complex<sup>79</sup> proved to be a potent photocatalyst for this transformation, providing excellent rates and yields at ambient temperatures with as little as 0.5 mol % of photocatalyst.<sup>80</sup> Our proposal for the mechanism of this reaction is briefly summarized in Scheme 3.1. Photoexcitation of  $\text{Ru}(\text{bpz})_3^{2+}$  with visible light results in the efficient formation of a long-lived redox-active triplet state. The electron-deficient bpz ligands render the photoexcited catalyst a substantially stronger oxidant (+1.4 V vs SCE) than the parent  $\text{Ru}(\text{bpy})_3^{2+}$  catalyst (+0.89 V vs SCE), enabling the one-electron photooxidation of anethole (**3.4**, +1.1 V vs SCE). The resulting alkene radical cation undergoes rapid [4 + 2] cycloaddition with diene **3.5** to afford product radical cation **3.6**<sup>+</sup>.<sup>81</sup> Formation of the neutral product can occur by one of two mechanisms: either radical chain-propagating oxidation of another equivalent of alkene **3.4** or by chain-terminating oxidation of the reduced  $\text{Ru}(\text{bpz})_3^+$  catalyst.<sup>82</sup> The latter process regenerates the photoactive Ru(II) state of the catalyst and closes the catalytic cycle.



Scheme 3.1 Proposed Photocatalytic Radical Cation Diels–Alder Cycloaddition Mechanism

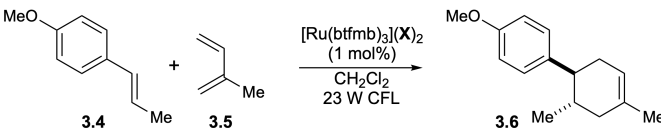
Despite the efficiency and broad scope of this reaction, the  $\text{Ru}(\text{bpz})_3^{2+}$  chromophore suffers from limited solubility in nonpolar organic solvents. Empirical screening indicated that the reaction proceeds more rapidly in these solvents and resulted in the use of  $\text{CH}_2\text{Cl}_2$  in optimized reaction conditions. Nevertheless, the solubility of the bpz complex in  $\text{CH}_2\text{Cl}_2$  is modest, and reactions conducted at moderate catalyst loadings are often visibly heterogeneous. These constraints limited our ability to systematically investigate catalyst structure on the rate of photoredox reactions. We thus became interested in the use of strongly oxidizing photocatalysts with greater lipophilicity that might be freely soluble in low-dielectric solvents.

As a starting point for these studies, Elliot P. Farney prepared a series of photocatalysts based on the  $\text{Ru}(\text{btfmb})_3^{2+}$  chromophore (Figure 3.1, **3.3**; btfmb = 4,4'-bis(trifluoromethyl)-2,2'-bipyridyl). The photophysical and electrochemical properties of the homoleptic  $[\text{Ru}(\text{btfmb})_3](\text{PF}_6)_2$  complex were previously investigated in acetonitrile by Furue and Kamachi.<sup>83</sup> Given the oxidizing potential reported for its excited state (+1.3 V vs SCE), Farney hypothesized that  $\text{Ru}(\text{btfmb})_3^{2+}$  would be an effective photooxidative catalyst for electron-rich styrenes such as **3.4**. Moreover, we hoped that the lipophilic  $\text{CF}_3$  substituents would improve the solubility of the

photocatalyst in nonpolar organic solvents compared to  $\text{Ru}(\text{bpz})_3^{2+}$ . To maximize the organic solubility of this chromophore, Farney prepared a series of salts bearing a variety of lipophilic counteranions (**3.3a–f**) and assessed their activities in a model photoreaction.

The results of this initial catalyst screen for the radical cation Diels–Alder cycloaddition between anethole (**3.4**) and isoprene (**3.5**) are summarized in Table 3.1. In general, these various photocatalysts each promoted the reaction, but surprisingly, the rates of reaction varied dramatically depending on counteranion identity. While the cycloaddition of **3.4** and **3.5** is complete in 20 min using 1 mol %  $\text{BAr}_4^-$  catalyst **3.3a**, the reaction proceeds to only 55% yield after 24 h with the analogous triflate catalyst **3.3b**, 14% yield with the 3,5-bis(trifluoromethyl)benzenesulfonate ( $\text{Ar}^{\text{F}}\text{SO}_3^-$ ) catalyst **3.3d**, and only 2% yield with the tosylate catalyst **3.3e**. No conversion was observed in this time frame using the carboxylate complex **3.3f**. Thus, there appears to be a correlation between the rate of product formation and the noncoordinating nature of the catalyst counteranions.<sup>84</sup> Unaware of any previous report of similarly dramatic counterion effects on the rate of organic photoredox transformations, we elected to investigate the origins of this phenomenon.

Table 3.1 Counteranion Effect on the Rate of Radical Cation Diels–Alder Cycloaddition



entry	catalyst	time	yield 3.6	unreacted 3.4
1	3.3a ( $\text{BAr}_4^-$ )	20 min	98%	0%
2	3.3b ( $\text{TfO}^-$ )	24 h	55%	37%
3	3.3d ( $\text{Ar}^{\text{F}}\text{SO}_3^-$ )	24 h	14%	80%
4	3.3e ( $\text{TsO}^-$ )	24 h	2%	95%
5	3.3f ( $\text{Ar}^{\text{F}}\text{CO}_2^-$ )	24 h	0%	100%

To begin to understand this effect, Farney performed Stern–Volmer analyses of the relationship between the concentration of anethole (**3.4**) in  $\text{CH}_2\text{Cl}_2$  and the photoluminescence intensity of the  $\text{BAr}^{\text{F}}_4^-$ ,  $\text{PF}_6^-$ , and  $\text{Ar}^{\text{F}}\text{SO}_3^-$  complexes of  $\text{Ru}(\text{btfmb})_3^{2+}$ . This investigation demonstrated that the degree of excited-state quenching between the photoexcited catalyst and the organic substrate (i.e., the Stern–Volmer constant,  $K_{\text{SV}}$ ) decreased by 2 orders of magnitude from the least coordinating counteranion,  $\text{BAr}^{\text{F}}_4^-$ , to the most coordinating counteranion in this study,  $\text{Ar}^{\text{F}}\text{SO}_3^-$  (Figure 3.2A). This is consistent with the markedly superior reactivity of the  $\text{BAr}^{\text{F}}_4^-$  complex. The value of  $K_{\text{SV}}$  is dependent on both the excited-state lifetime of the photocatalyst ( $\tau$ ) and the bimolecular electron-transfer rate constant ( $k_{\text{q}}$ );  $K_{\text{SV}} = \tau k_{\text{q}}$ . To deconvolute whether the large change in the Stern–Volmer constant arises primarily from a change in catalyst triplet lifetime or in the electron-transfer rate constant, Marco D. Torelli measured  $\tau$  for each  $\text{Ru}(\text{btfmb})_3^{2+}$  complex (Table 3.2). These results show that while the counteranion does have an influence on triplet lifetime, the effect is relatively small — approximately two-fold over the range of counteranions investigated. The impact on  $k_{\text{q}}$ , therefore, is much larger, spanning two orders of magnitude from  $\text{Ar}^{\text{F}}\text{SO}_3^-$  **3.3d** to  $\text{BAr}^{\text{F}}_4^-$  **3.3a**. Thus, the unanticipated conclusion from these preliminary studies is that the identity of the photocatalyst counteranion can impact a photooxidative reaction by dramatically altering the intrinsic rate constant of bimolecular electron transfer to the photocatalyst excited state.

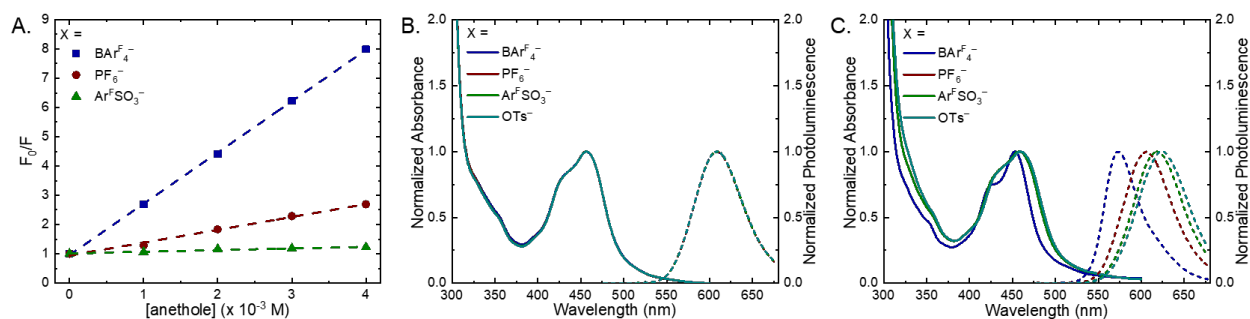


Figure 3.2 (A) Stern–Volmer plots for excited-state quenching of catalysts **3.3a–c** in  $\text{CH}_2\text{Cl}_2$ . (B, C) Effect of counteranion identity on excited-state properties of  $[\text{Ru}(\text{btmb})_3](\text{X})_2$ , where X is indicated in the legend. (B) Absorption (solid line) and photoluminescence (dashed line) spectra in MeCN. (C) Absorption (solid line) and photoluminescence (dashed line) spectra in  $\text{CH}_2\text{Cl}_2$ .

Table 3.2 Spectroscopic Properties and Stern–Volmer Quenching Constants<sup>a</sup>

entry	catalyst	$\lambda_{\text{abs}}$ (nm)	$\lambda_{\text{em}}$ (nm)	$K_{\text{SV}}$ ( $\times 10^2 \text{ M}^{-1}$ )	$\tau$ (ns)	$k_{\text{q}}$ ( $\times 10^8 \text{ M}^{-1} \text{ s}^{-1}$ )
1	3.3a	453	573	17	520	33
2	3.3c	458	605	4.2	860	4.9
3	3.3d	458	618	0.61	950	0.64

<sup>a</sup>Data acquired in  $\text{CH}_2\text{Cl}_2$ .

This finding was surprising. While the importance of the bipyridyl ligand structure in the design and optimization of photocatalytic reactions is well appreciated,<sup>85</sup> the effect of the catalyst counterion on photocatalytic reaction rates has received significantly less attention. Meyer and co-workers have examined ion-pairing effects on the photophysics of Ru(II) polypyridyl chromophores.<sup>86</sup> These investigations show that addition of  $\text{Cl}^-$  to solutions of  $[\text{Ru}(\text{bpy})_2(\text{deeb})](\text{PF}_6)_2$  in  $\text{CH}_2\text{Cl}_2$  results in the formation of tight ion pairs and a concomitant decrease in triplet excited-state energy and lifetime.<sup>87</sup> However, neither the impact of structurally complex organic counteranions on the photochemical properties of Ru(II) complexes nor the

effects of ion pairing on the rate of synthetic photocatalytic applications have been systematically explored.<sup>88</sup>

### 3.4.2. Spectroscopic, Electrochemical, and Quantum Yield Studies.

Farney has collected absorption, emission, and electrochemical data for a representative series of  $\text{Ru}(\text{btfmb})_3^{2+}$  complexes bearing  $\text{BAr}^{\text{F}}_4^-$ ,  $\text{PF}_6^-$ ,  $\text{Ar}^{\text{F}}\text{SO}_3^-$ , and  $\text{TsO}^-$  counteranions. These data are depicted in Figure 3.2B,C. First, Farney obtained spectral data for these complexes in acetonitrile (Figure 3.2B). Both the absorption and emission spectra are superimposable in MeCN, consistent with the attenuated impact of ion pairing in high dielectric solvents. On the other hand, Coulombic effects are more significant in nonpolar solvents, which are often ideal for applications in organic synthesis. Figure 3.2C shows absorption and emission spectra for the same series of catalysts in  $\text{CH}_2\text{Cl}_2$ . The impact of counteranion identity on the absorption spectrum in this relatively nonpolar solvent is modest, suggesting that if differences in Coulombic interactions exert any influence on the ground-state properties of the photocatalyst or on the singlet excited state, it is a small effect. In contrast, the photoluminescence spectra of the various complexes differ markedly. Most notably, the  $\lambda_{\text{max}}$  of photoluminescence varies by 52 nm from the least coordinating ( $\text{BAr}^{\text{F}}_4^-$ , 573 nm) to the most coordinating ( $\text{TsO}^-$ , 625 nm) counteranion, corresponding to a substantial energy difference of 4.2 kcal/mol (0.18 eV).

Thus, altering the identity of the counteranion produces an unexpectedly large change in the energy of the emissive triplet state of  $\text{Ru}^*(\text{btfmb})_3^{2+}$ . One would expect these changes to be reflected in excited-state redox potentials. To quantify this effect, we measured the one-electron reduction potential  $E(\text{Ru}^{2+/+})$  of the  $\text{Ru}(\text{btfmb})_3^{2+}$  complexes in  $\text{CH}_2\text{Cl}_2$ . Each measurement was made using a matching  $n\text{-Bu}_4\text{N}^+\text{X}^-$  salt as a supporting electrolyte to avoid complications arising from counteranion exchange. Counteranions of lower Lewis basicity resulted in significant anodic



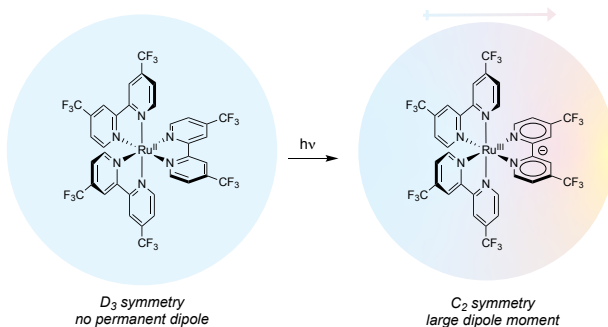
shifts in the ground-state potentials, with the largest and most significant effect observed for the  $\text{BAr}^{\text{F}}_4^-$  counteranion (Table 3.3). This effect can also be rationalized as a consequence of ion pairing where the one-electron reduction of the least electrostatically stabilized  $\text{BAr}^{\text{F}}_4^-$  complex is more energetically favorable than the tightly ion-paired tosylate complex. To calculate the excited-state redox potential, we made the commonly utilized assumption<sup>89,90</sup> that the Gibbs free energy change for the  $S_0$  to  $T_1$  transition is represented by the energy of the corresponding photoluminescence maximum ( $\Delta G_{\text{ES}}$ ). The catalytically relevant first triplet excited-state reduction potential  $E(\text{Ru}^{2+*/+})$  can then be approximated from the sum of  $\Delta G_{\text{ES}}$  and  $E(\text{Ru}^{2+/+})$ . As the data in Table 3.3 show, these potentials span a range of 480 mV (11 kcal/mol), with the  $\text{BAr}^{\text{F}}_4^-$  complex having the most positive reduction potential of +1.52 V vs SCE. The conclusion from these studies, therefore, is that the degree of ion pairing has a synergistic effect on both the excited-state triplet energy and on the ground-state electrochemical potential, leading to a large net dependence of photooxidant strength on the identity of the catalyst counteranion. These results are consistent with the experimentally observed effect of counteranion identity on the radical cation Diels–Alder reaction described above. The most noncoordinating counteranion ( $\text{BAr}^{\text{F}}_4^-$ ) results in the largest driving force for photoinduced electron transfer, consistent with a faster rate of photoinitiation and a shorter reaction time.

Table 3.3 Ground- and Excited-State Redox Potentials for  $\text{Ru}(\text{btfmb})_3^{2+}$  in  $\text{CH}_2\text{Cl}_2$ <sup>a</sup>

entry	catalyst	$\Delta G_{\text{ES}}$	$E(\text{Ru}^{2+/+})$	$E(\text{Ru}^{2+*/+})$
<b>1</b>	3.3a	2.17 eV	−0.65 V	+1.52 V
<b>2</b>	3.3c	2.05 eV	−0.89 V	+1.16 V
<b>3</b>	3.3d	2.01 eV	−0.93 V	+1.08 V
<b>4</b>	3.3e	1.99 eV	−0.95 V	+1.04 V

<sup>a</sup> Electrochemical potentials were measured through cyclic voltammetry in a standard three-electrode setup; scan rate = 100 mV/s. A 100 mM solution of a *n*- $\text{Bu}_4\text{N}^+\text{X}^-$  salt that matched the photocatalyst counteranion was used as a supporting electrolyte. Potentials were corrected to SCE through an external ferrocene reference.

To rationalize the impact of counteranion identity on the triplet excited-state energy of the  $\text{Ru}(\text{btfmb})_3^{2+}$  chromophore, we propose an explanation based upon an empirical physical model for charge redistribution between the ground and electronically excited states of this canonical class of transition metal photocatalysts (Scheme 3.2). The ground state of the  $\text{Ru}(\text{btfmb})_3^{2+}$  chromophore has  $D_3$  symmetry and consequently cannot support a permanent dipole moment. On the other hand, the emissive states of  $\text{Ru}(\text{II})^*$  tris(bipyridyl) complexes are understood to be metal-to-ligand charge-transfer (MLCT) triplets, and considerable experimental evidence supports the contention that the transferred electron is localized to a single ligand without significant delocalization across the other two ligands.<sup>91</sup> Thus, electronically excited  $\text{Ru}^*(\text{btfmb})_3^{2+}$  is best conceptualized as a  $C_2$ -symmetric, charge-separated state with an oxidized  $\text{Ru}(\text{III})$  core and a single reduced  $\text{btfmb}^{\cdot-}$  ligand (Scheme 3.2). This lower symmetry MLCT state would therefore be expected to have a very large dipole moment. Meyer has estimated the dipole moment of the triplet  $\text{Ru}^*(\text{bpy})_3^{2+}$  state to be  $\sim 14$  D.<sup>92</sup> If the photocatalyst exists largely in an ion-paired state in nonpolar solvents, stabilizing charge–dipole interactions should have a larger effect on the triplet excited state than they do on the ground state. One would further expect that more strongly coordinating anions, which produce tighter ion pairs, would better stabilize the triplet excited state. Finally, a strong solvent dependence would be consistent with this model, as charge–dipole interactions are attenuated by increasing solvent dielectric.



Scheme 3.2 Representation of the Ground State (No Dipole) and Triplet Excited State  
(Significant Dipole) for  $[\text{Ru}(\text{btfmtb})_3](\text{X})_2$

In the radical cation Diels–Alder reaction, the radical cation intermediates (**3.4<sup>•+</sup>** and **3.6<sup>•+</sup>**) would also be expected to exist as ion pairs, and the most reasonable counteranion would be that introduced by the photocatalyst.<sup>88</sup> We wondered whether this ion-pairing interaction might also affect the dynamics of the product-forming cycloaddition and chain propagation steps as well as the photoinitiation step. To investigate this question, we utilized the same protocol we previously described for estimating the chain length in radical cation cycloadditions.<sup>82</sup> First, Wesley B. Swords measured the reaction quantum yield with the  $\text{BAr}^{\text{F}_4^-}$  and  $\text{Ar}^{\text{F}\text{SO}_3^-}$  catalysts through chemical actinometry (see the Supporting Information). The quantum yield using the  $\text{BAr}^{\text{F}_4^-}$  catalyst **3.3a** (1 mol %) was measured to be  $\Phi = 26$ , comparable to the value we determined for the corresponding  $[\text{Ru}(\text{bpz})_3](\text{BAr}^{\text{F}_4})_2$  catalyst in previous studies.<sup>82</sup> However, when  $\text{Ar}^{\text{F}\text{SO}_3^-}$  complex **3.3d** was utilized as the photocatalyst, we measured a significantly decreased quantum yield of  $\Phi = 0.35$ . To correct for the differing efficiency of photoinitiation by photocatalysts with different excited-state oxidation potentials, we divided the measured quantum yield values by the quenching fraction. The quenching of **3.3a** by anethole was highly efficient ( $Q > 0.99$ ), and thus the estimated average chain length is the same as the quantum yield ( $\text{CL} = 26$ ). The quenching fraction for **3.3d** was lower ( $Q = 0.83$ ), but the resulting average chain length was still calculated

to be quite low (CL = 0.42). Thus, in addition to influencing the ground and excited states of the photocatalyst, the counteranion impacts the efficiency of the subsequent radical chain reaction.

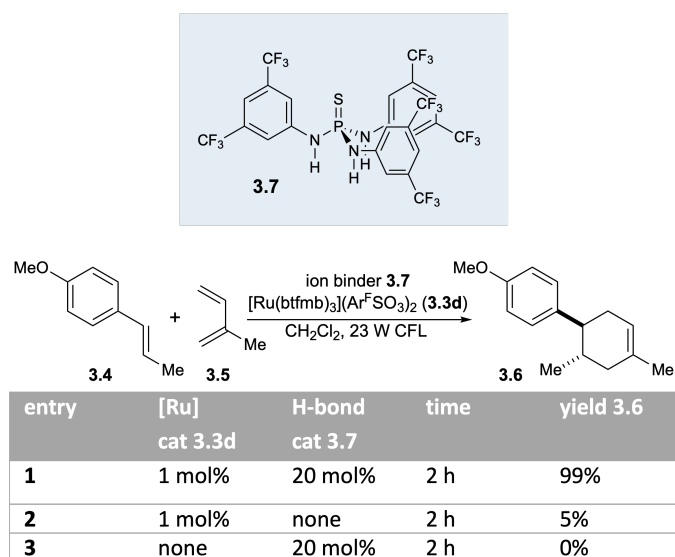
These results have several significant implications. First, counteranion identity is a previously underappreciated variable in the optimization of organic photoredox reactions that has the potential to dramatically impact the success and efficiency of synthetically useful organic reactions. Second, counteranion effects impact multiple aspects of the photocatalytic mechanism, including the energy of the reactive triplet excited state, the rate of the electron-transfer photoinitiation event, and the dynamics of nonphotochemical product-forming radical chain propagation events. Finally, because the strength of ion-pairing interactions is sensitive to solvent dielectric, these counterion effects are expected to be most important in the relatively nonpolar organic solvents that are often optimal for synthetic applications. Such effects may be important in a much wider range of organic photoredox reactions than previously appreciated.

### 3.4.3. Hydrogen-Bonding Anion Binders as Cocatalysts.

The model proposed above suggests that the rate of photocatalytic Diels–Alder cycloaddition is strongly influenced by Coulombic interactions between the counteranion and both the cationic photocatalyst and the radical cation intermediates. As a further test of this model, we hypothesized that other strategies for disrupting ion pairing might be used to exert a similar effect. In particular, we drew inspiration from a concept pioneered by Jacobsen: hydrogen-bonding organocatalysts can accelerate reactions involving various cationic reactive intermediates by binding their associated counteranions.<sup>93,94</sup> We hypothesized that the tight ion pairing between a Lewis basic counteranion and  $\text{Ru}^*(\text{btfmb})_3^{2+}$  could be disrupted by addition of an appropriate hydrogen-bonding anion binder, recapitulating the rate increases we observed using weakly coordinating counteranions.

Our investigations focused on the use of sulfonate complex **3.3d** as a photoredox catalyst for the radical cation Diels–Alder reaction. As described previously, **3.3d** is markedly less reactive than the optimal  $\text{BAr}^{\text{F}}_4^-$  complex **3.3a**. Several recent reports have shown that  $\text{C}_{3\text{V}}$ -symmetric thiophosphotriamide **3.7** is an effective hydrogen-bond donor for binding sulfonate anions,<sup>95</sup> and we imagined that the sequestration of the  $\text{Ar}^{\text{F}}\text{SO}_3^-$  counteranion by **3.7** might attenuate its propensity to participate in tight ion-pairing interactions. To test this hypothesis, Farney conducted Diels–Alder cycloadditions using 1 mol % of **3.3d** in the presence and absence of **3.7** (Table 3.4). These experiments showed a large rate increase for the Diels–Alder cycloaddition upon addition of just 20 mol % of **3.7**. Under these conditions, the reaction is complete within 2 h, while only 5% yield of **3.6** is formed at the same time point in the absence of the anion binder. Notably, there is no observable formation of the cycloadduct upon irradiation in the presence of **3.7** without photocatalyst **3.3d**. This demonstrates that the thiophosphotriamide is not photocatalytically active, and the improvement in photoredox activity thus arises from a synergistic cocatalytic effect.

Table 3.4 Effect of Ion-Binder Cocatalyst **3.7** on Radical Cation Diels–Alder Reaction



We also investigated whether cocatalyst **3.7** had an influence on the photophysical properties of  $\text{Ar}^{\text{F}}\text{SO}_3^-$  photocatalyst **3.3d** consistent with our proposed model (Figure 3.3A). The addition of **3.7** to **3.3d** induced a large hypsochromic shift in the photoluminescence maximum. This shift was in the direction of the emission maximum of  $\text{BAr}^{\text{F}}_4^-$  catalyst **3.3d**, consistent with the expectation that added **3.7** would decrease the extent of ion pairing. In contrast, the addition of **3.7** to the  $\text{BAr}^{\text{F}}_4^-$  complex **3.3a** yielded no change in the emission maximum, even at 50-fold excess of **3.7** relative to **3.3a**. This experiment supports the contention that the effect arises from a specific interaction between the thiophosphotriamide and the sulfate counteranion, rather than an interaction with some other component of the reaction mixture or a general medium effect. To further support this contention, we investigated interaction in  $\text{CD}_2\text{Cl}_2$  using  $^1\text{H}$  NMR spectroscopy. Titration of thiophosphotriamide **3.7** with  $n\text{-Bu}_4\text{N}^+ \text{Ar}^{\text{F}}\text{SO}_3^-$  resulted in a significant shift of the aromatic C–H resonances of **3.7**. A fit of these data to a 1:1 binding model provided an association constant of  $1.3 \times 10^6$ .

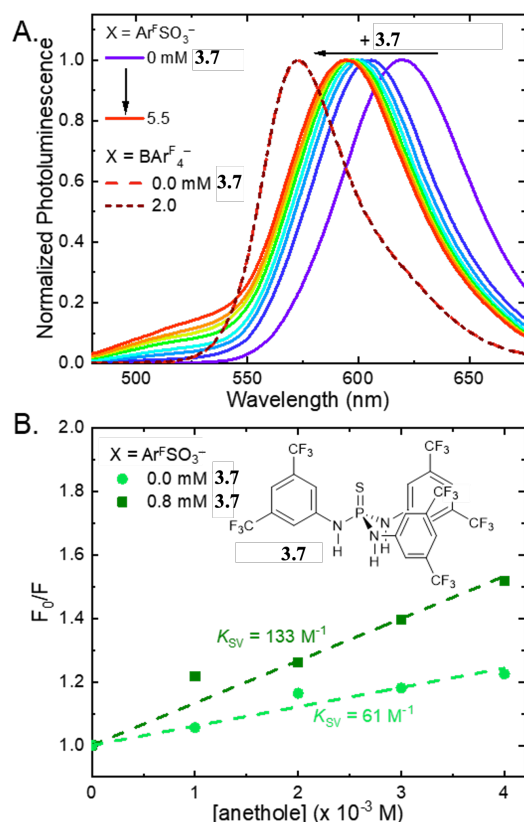


Figure 3.3 (A) Effect of anion-binding cocatalyst **3.7** on photoluminescence of **3.3d**. (B) Stern–Volmer plot in the absence and presence of ion binder **3.7**.

The influence of added thiophosphotriamide **3.7** replicated the effect of weakly coordinating anions in other regards as well. First, Stern–Volmer analysis indicates that the rate of quenching of **3.3d** by anethole is significantly faster upon the addition of the thiophosphotriamide (Figure 3.3B). This is consistent with the observed increase in triplet excited-state energy with greater concentrations of **3.7**. Second, we observed a substantial effect on the radical cation chain length (see the Supporting Information). The addition of 20 mol % of **3.7** yielded a 20-fold increase in both the quantum yield and apparent radical chain length of the

reaction, suggesting that anion binder **3.7** can influence the dynamics of the chain process by disrupting ion pairing.

Thus, we have been able to recapitulate the observed effect of noncoordinating anions on the photocatalytic activity of  $\text{Ar}^{\text{F}}\text{SO}_3^-$  catalyst **3.3d** using hydrogen-bonding cocatalyst **3.7**. The thiophosphotriamide disrupts ion pairing by binding the sulfonate counteranion, which results in significant increases to the photocatalyst's triplet excited-state energy, the rate of photoinduced electron transfer, the length of the radical cation chain process, and the overall efficiency of the photocatalytic Diels–Alder process. These results support the contention that Coulombic effects can be more significant in photoreactions than previously appreciated. Moreover, these results suggest that the use of anion-binding organocatalysts could be a conceptually orthogonal strategy for optimization of the growing class of synthetically useful photoredox transformations.

### 3.5. Conclusions

The studies summarized above suggest several important implications for the design, understanding, and optimization of photocatalytic processes. First, counterion effects can exert a significant impact on the observed rate of radical cation reactions initiated by photoredox catalysis. The degree of ion pairing between the counteranion and both the Ru(II) photoredox catalyst and the oxidized radical cation intermediate can influence the efficiency of multiple steps in the mechanism of these reactions. Thus, these studies indicate that modulating the degree of ion pairing is an important unexplored variable in the optimization of this class of transformations, and we have described two complementary approaches that can successfully increase the overall rate of a radical cation cycloaddition by several orders of magnitude. Second, the Coulombic interactions that are the putative origin of these effects are most significant in relatively nonpolar



solvents such as those that are often optimal for synthetic applications. This could indicate that counteranion identity is a particularly important variable for organic photoredox reactions compared to better established applications of Ru(II) photoredox catalysts in solar energy conversion and biology, where the use of water or other high dielectric solvents might mask the impact of ion pairing. With growing interest in the use of this class of transition metal photoredox catalysts, a deeper understanding of the impact of ion-pairing effects is critical to developing a complete, detailed understanding of the mechanisms in this class of synthetically useful transformations.

### 3.6. Contributions

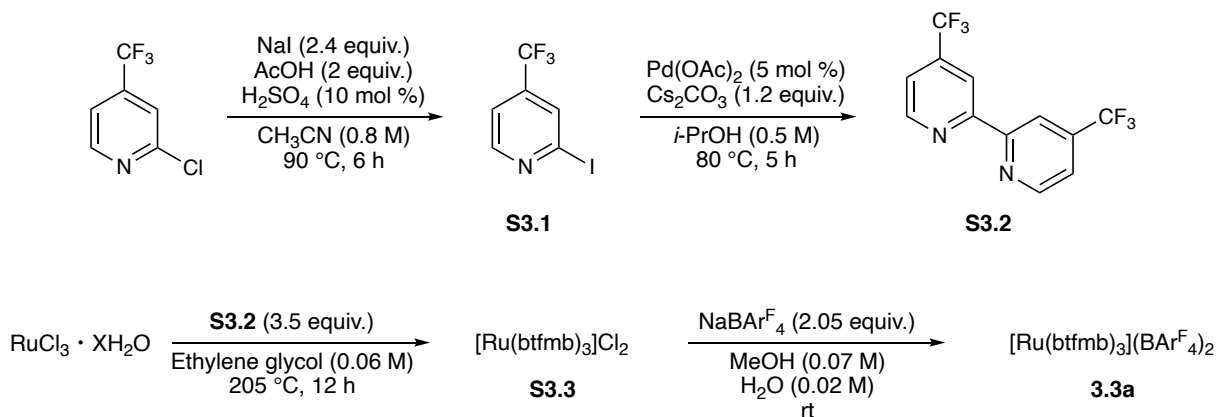
The initial counteranion dependence on the radical cation Diels–Alder reaction was discovered by Elliot P. Farney (University of Wisconsin – Madison). Additionally, E.P.F. performed the Stern–Volmer quenching studies, measured the spectroscopic properties and redox potentials of the photocatalysts, and performed the batch reactions with the ion-binder cocatalyst. Steven J. Chapman (University of Wisconsin – Madison) performed the photoluminescence studies titrating increasing quantities of the ion-binder cocatalyst. Wesley B. Swords (University of Wisconsin – Madison) determined the quantum yields of the reactions using the different photocatalyst salts. Marco D. Torelli (University of Wisconsin – Madison) measured the excited state lifetimes of the different photocatalyst salts. Robert J. Hamers (University of Wisconsin – Madison) provided the equipment and resources for the excited state lifetime measurements. Tehshik P. Yoon (University of Wisconsin – Madison) provided the equipment, resources, and photochemical expertise necessary for this study.

### 3.7. Supporting Information

#### 3.7.1. General Experimental Information for Synthetic Studies

Dichloromethane ( $\text{CH}_2\text{Cl}_2$ ), tetrahydrofuran, diethyl ether ( $\text{Et}_2\text{O}$ ), toluene, and acetonitrile ( $\text{CH}_3\text{CN}$ ) were dried by passage through columns of activated alumina. Ethylene glycol was used as received. Water was purified by a Milli-Q system (Millipore Corporation) to achieve a resistivity of  $18.2 \text{ M}\Omega \text{ cm}^{-1}$  at  $25 \text{ }^\circ\text{C}$ . Reagents were purchased from commercial sources unless otherwise noted. Chromatography was performed with Purasil 60 Å silica gel (230–400 mesh) or with neutral alumina (Aldrich product # 11028). High vacuum refers to a reduced pressure that was measured to be 60 mTorr or lower using a McLeod gauge. Anethole was purified by chromatography on silica gel (hexanes: EtOAc = 20:1) and was subsequently submitted to fractional distillation under high vacuum at  $95 \text{ }^\circ\text{C}$ . Purified anethole was stored at room temperature in a vial wrapped in aluminum foil. Isoprene was fractionally distilled from  $\text{CaH}_2$  under  $\text{N}_2$  at  $45 \text{ }^\circ\text{C}$  and stored at  $5 \text{ }^\circ\text{C}$ .  $^1\text{H}$ ,  $^{13}\text{C}$ ,  $^{19}\text{F}$ ,  $^{11}\text{B}$ , and  $^{31}\text{P}$  NMR data for all previously uncharacterized compounds were obtained using Bruker Avance III 400 MHz and Bruker Avance III 500 MHz spectrometers and are referenced to TMS (0.00 ppm) or residual protio solvent signal. The NMR and mass spectroscopy facilities are supported by the NSF (CHE-1048642), the NIH (S10OD020022-1), the University of Wisconsin, and a generous gift from Paul J. and Margaret M. Bender.

## 3.7.2. Synthesis of Polypyridyl Ru(II) Complexes



**2-Iodo-4-(trifluoromethyl)pyridine (S3.1).** A 250 mL round-bottom flask with a magnetic stirrer was charged with 2-chloro-4-(trifluoromethyl)pyridine (8.00 g, 44.1 mmol, 5.67 mL, 1 equiv.), NaI (15.8 g, 106 mmol, 2.4 equiv.), glacial AcOH (5.04 mL, 88.1 mmol, 2 equiv.), and CH<sub>3</sub>CN (55 mL, 0.8 M). To the resulting faint yellow solution was added conc. H<sub>2</sub>SO<sub>4</sub> (239  $\mu$ L, 4.41 mmol, 0.1 equiv.) in a single portion, and the reaction turned bright red. The reaction vessel was fitted with a water-cooled condenser before being placed in a 90 °C oil bath for 6 h. The resulting brown reaction was allowed to cool to rt, and the solvent was removed *in vacuo*. To the remaining residue was added H<sub>2</sub>O (75 mL) and, with rapid stirring, solid NaHCO<sub>3</sub> until the reaction mixture reached pH = 7. The aqueous mixture was transferred to a separatory funnel and extracted with CH<sub>2</sub>Cl<sub>2</sub> (3 x 100 mL). Residual iodine was removed by washing the combined organic phases with a saturated solution of sodium bisulfite (2 x 75 mL). The organic layer was washed with brine (1 x 50 mL), dried over Na<sub>2</sub>SO<sub>4</sub>, filtered, and concentrated *in vacuo* to afford a yellow oil that was purified via flash column chromatography on silica (hexanes:EtOAc = 20:1) to afford 8.25 g (30.2 mmol, 69% yield) of **S3.1** as a clear oil. <sup>1</sup>H NMR (500.0 MHz, CDCl<sub>3</sub>)  $\delta$  8.57 (d, *J* = 5.1 Hz, 1H), 7.96 (s, 1H), 7.49 (d, *J* = 5.1 Hz, 2H); <sup>13</sup>C NMR (125.7 MHz, CDCl<sub>3</sub>)  $\delta$  151.6, 139.5 (q, *J*<sub>C-F</sub> = 34.3 Hz), 130.7 (q, *J*<sub>C-F</sub> = 3.6 Hz), 121.6 (q, *J*<sub>C-F</sub> = 273.3 Hz), 118.5 (q, *J*<sub>C-F</sub> = 3.6

Hz), 118.0. These data are consistent with previously reported values.<sup>96</sup> Note: the iodopyridine is unstable towards long-term storage and should be used immediately or stored in a cool, dark place.

**4,4'-Bis(trifluoromethyl)-2,2'-bipyridine (S3.2).** A 250 mL round-bottom flask with a magnetic stirrer was charged with Pd(OAc)<sub>2</sub> (339 mg, 1.51 mmol, 0.05 equiv.) and Cs<sub>2</sub>CO<sub>3</sub> (11.8 g, 36.3 mmol, 1.2 equiv.). The flask was equipped with a water-cooled condenser and was purged with N<sub>2</sub>. Subsequently, a solution of **S3.1** (8.25 g, 30.2 mmol, 1 equiv.) in *i*-PrOH (60 mL, 0.5 M) was added. The reaction was heated to an oil bath temperature of 80 °C under N<sub>2</sub> for 5 h. The reaction was allowed to cool to room temperature and was filtered through a pad of Celite. The filter cake was washed with CH<sub>2</sub>Cl<sub>2</sub> (3 x 50 mL), and the volatiles were removed *in vacuo* to afford a brown solid. Insoluble impurities were removed by washing the brown solid with CH<sub>2</sub>Cl<sub>2</sub> and filtering. The solvent was removed *in vacuo*, and the crude product was purified via flash column chromatography on silica (hexanes:EtOAc = 10:1) to afford 2.46 g (8.41 mmol, 56% yield) of **S3.2** as a bright yellow solid. <sup>1</sup>H NMR (500.0 MHz, CDCl<sub>3</sub>) δ 8.89 (d, *J* = 5.0 Hz, 2H), 8.73 (s, 2H), 7.59 (d, *J* = 5.0 Hz, 2H); <sup>13</sup>C NMR (125.7 MHz, CDCl<sub>3</sub>) δ 156.1, 150.3, 139.6 (q, *J*<sub>C-F</sub> = 34.3 Hz), 122.8 (q, *J*<sub>C-F</sub> = 273.3 Hz), 119.9 (q, *J*<sub>C-F</sub> = 3.6 Hz), 117.2 (q, *J*<sub>C-F</sub> = 3.6 Hz). These data are consistent with previously reported values.<sup>97</sup>

**[Ru(btmbfmb)<sub>3</sub>]Cl<sub>2</sub> (S3.3).** A 100 mL round-bottom flask with a magnetic stirrer was charged with RuCl<sub>3</sub>•XH<sub>2</sub>O (Strem Chemicals) (379 mg, 1.83 mmol, 1 equiv.) and **S3.2** (1.87 g, 6.40 mmol, 3.5 equiv.). The flask was equipped with a water-cooled condenser and was purged with N<sub>2</sub>. Subsequently, ethylene glycol (30 mL, 0.06 M) was added, and the reaction was heated to an oil

bath temperature of 205 °C under N<sub>2</sub> for 12 h. The resulting dark red/black mixture was allowed to cool to rt. The crude reaction was added dropwise to a rapidly stirred mixture of Et<sub>2</sub>O/acetone (1:1, 250 mL) over 15 min. The resulting homogeneous mixture was transferred to a dropping funnel and added slowly to a rapidly stirred solution of Et<sub>2</sub>O (1.4 L) over 1 h. A red solid crashed out of solution during the addition and was isolated via slow filtration on a medium-porosity fritted funnel. The solid was washed with Et<sub>2</sub>O (2 x 30 mL), then passed through the fritted funnel with CH<sub>3</sub>CN. The volatiles were removed and the solid was dried under high vacuum. Thereafter, the dry solid was dissolved in CH<sub>3</sub>OH (100 mL) and added dropwise to a rapidly stirred solution of Et<sub>2</sub>O (350 mL) over 45 min. A red solid precipitated throughout the addition and was isolated on a fritted funnel and washed with Et<sub>2</sub>O (2 x 30 mL). The purified solid was dried under high vacuum at 70 °C for 2 h to afford 1.40 g (1.38 mmol, 76% yield) of **S3.3** as a red solid. <sup>1</sup>H NMR (500.0 MHz, CD<sub>3</sub>OD) δ 9.40 (s, 6H), 8.15 (d, *J* = 5.9 Hz, 6H), 7.87 (dd, *J* = 5.9, 1.6 Hz, 6H); <sup>13</sup>C NMR (125.7 MHz, CD<sub>3</sub>OD) δ 159.1, 155.0, 141.1 (q, *J*<sub>C-F</sub> = 35.8 Hz), 125.6 (q, *J*<sub>C-F</sub> = 3.3 Hz), 123.5 (q, *J*<sub>C-F</sub> = 274.6 Hz), 123.3 (q, *J*<sub>C-F</sub> = 3.3 Hz); <sup>19</sup>F NMR (376.5 MHz, CD<sub>3</sub>OD) δ -66.1. HRMS (+ p): calculated for C<sub>36</sub>H<sub>18</sub>ClF<sub>18</sub>N<sub>6</sub>Ru<sup>2+</sup> [M<sup>2+</sup> + A<sup>-</sup>]<sup>+</sup> = 1013.0032. Found = 1013.0039. Calculated for C<sub>36</sub>H<sub>18</sub>F<sub>18</sub>N<sub>6</sub>Ru<sup>2+</sup> [M]<sup>2+</sup> = 489.0169. Found = 489.0166.

**[Ru(btmb)<sub>3</sub>](BAr<sup>F</sup><sub>4</sub>)<sub>2</sub> (3.3a).** A 25 mL round-bottom flask with a magnetic stirrer was charged with **S3.3** (100 mg, 0.0987 mmol, 1 equiv.) and H<sub>2</sub>O (4.2 mL, 0.02 M). To this solution was added a solution of NaBAr<sup>F</sup><sub>4</sub> (Alfa Aesar) (179 mg, 0.202 mmol, 2.05 equiv.) in CH<sub>3</sub>OH (1.4 mL, 0.07 M). An orange precipitate immediately formed, and the solution became difficult to stir. Additional H<sub>2</sub>O (2 mL) was added, stirring was continued for 10 min, and the orange solid was isolated on a fritted funnel, washed with H<sub>2</sub>O (2 x 3 mL), and dried. The dried solid was dissolved

in acetone/CH<sub>2</sub>Cl<sub>2</sub> (1:1, ~5 mL) and purified via gravity elution through a column of neutral Al<sub>2</sub>O<sub>3</sub> using CH<sub>2</sub>Cl<sub>2</sub> as the eluent. The first band that eluted was determined to be the desired product, so these fractions were combined, the volatiles were removed *in vacuo*, and the resulting solid was dried under high vacuum. This residue was dissolved in a minimum volume of CH<sub>2</sub>Cl<sub>2</sub> (5 mL) and passed through a 0.2 μm Whatman PTFE filter to remove residual NaBAR<sup>F</sup><sub>4</sub>. To the filtrate was slowly added hexanes (30 mL) and an orange solid precipitated. The solid was isolated on a fritted funnel and dried under high vacuum to afford 220 mg (0.0819 mmol, 83% yield) of **3.3a** as a reddish/orange solid. <sup>1</sup>H NMR (500.0 MHz, CD<sub>3</sub>OD) δ 9.41 (s, 6H), 8.14 (d, *J* = 5.9 Hz, 6H), 7.86 (dd, *J* = 5.9, 1.6 Hz, 6H), 7.60 (m, 24H); <sup>13</sup>C NMR (125.7 MHz, CD<sub>3</sub>OD) δ 162.9 (q, *J*<sub>C-B</sub> = 49.7 Hz), 159.2, 154.8, 141.4 (q, *J*<sub>C-F</sub> = 35.9 Hz), 135.8, 130.4 (qq, *J*<sub>C-F</sub> = 31.6, 3.1 Hz), 125.7 (q, *J*<sub>C-F</sub> = 271.6 Hz), 125.5 (q, *J*<sub>C-F</sub> = 3.5 Hz), 124.1 (q, *J*<sub>C-F</sub> = 273.8 Hz), 123.3 (q, *J*<sub>C-F</sub> = 3.2 Hz), 118.5 (m); <sup>19</sup>F NMR (376.5 MHz, CD<sub>3</sub>OD) δ -64.3, -66.2; <sup>11</sup>B NMR (128.3 MHz, CD<sub>3</sub>OD) δ -6.77. HRMS (+ p): calculated for C<sub>36</sub>H<sub>18</sub>F<sub>18</sub>N<sub>6</sub>Ru<sup>2+</sup> [M]<sup>2+</sup> = 489.0169. Found = 489.0167. (- p): calculated C<sub>32</sub>H<sub>12</sub>BF<sub>24</sub> [A<sup>-</sup>] = 863.0654. Found = 863.0653.

**[Ru(btffmb)<sub>3</sub>](OTf)<sub>2</sub> (3.3b)**. A 20 mL scintillation vial with a magnetic stirrer was charged with **S3.3** (250 mg, 0.25 mmol, 1 equiv.) and H<sub>2</sub>O (10 mL, 0.025 M). To this solution was added a solution of sodium triflate (NaOTf, 370 mg, 1.7 mmol, 6.9 equiv.) in H<sub>2</sub>O (3 mL, 0.57 M). An orange precipitate immediately formed, and the solution became difficult to stir. Additional H<sub>2</sub>O (4 mL) was added and stirring was continued for 10 min, and the orange solid was isolated on a fritted funnel, washed with H<sub>2</sub>O (2 x 5 mL), and dried. The dried product was sonicated in H<sub>2</sub>O (5 mL) for 2 min and isolated on a fritted funnel. The solid was collected and dried under high vacuum to afford 200 mg (0.157 mmol, 67% yield) of **3.3b** as a reddish/orange solid. <sup>1</sup>H NMR (500.0

MHz, CD<sub>3</sub>OD)  $\delta$  9.34 (s, 6H), 8.14 (d,  $J = 5.9$  Hz, 6H), 7.84 (dd,  $J = 5.9, 1.2$  Hz, 6H); <sup>13</sup>C NMR (125.7 MHz, CD<sub>3</sub>OD)  $\delta$  159.1, 154.9, 141.2 (q,  $J_{C-F} = 35.7$  Hz), 125.5 (q,  $J_{C-F} = 3.4$  Hz), 123.5 (q,  $J_{C-F} = 273.4$  Hz), 123.3 (m), 121.6 (q,  $J_{C-F} = 318.4$  Hz); <sup>19</sup>F NMR (376.5 MHz, CD<sub>3</sub>OD)  $\delta$  -66.13, -80.11. HRMS (+ p): calculated for C<sub>37</sub>H<sub>18</sub>F<sub>21</sub>N<sub>6</sub>O<sub>3</sub>SRu<sup>+</sup> [M<sup>2+</sup> + A<sup>-</sup>]<sup>+</sup> = 11263.9864. Found = 1126.9866. Calculated for C<sub>36</sub>H<sub>18</sub>F<sub>18</sub>N<sub>6</sub>Ru<sup>2+</sup> [M]<sup>2+</sup> = 489.0169. Found = 489.0164. (- p): calculated CF<sub>3</sub>O<sub>3</sub>S<sup>-</sup> [A<sup>-</sup>] = 148.9526. Found = 148.9526.

Note: the mass spectrum of **3.3b** included a signal corresponding to the mass of the monoanionic ruthenium tris(trifluoromethanesulfonate), [[Ru(btmb)<sub>3</sub>](OTf)<sub>3</sub>]<sup>-</sup> complex. This indicates a strong interaction between the ruthenium catalyst and triflate anions, consistent with the conclusions of this paper. Calculated for C<sub>39</sub>H<sub>18</sub>F<sub>27</sub>N<sub>6</sub>O<sub>9</sub>S<sub>3</sub>Ru<sup>-</sup> [M + 3A<sup>-</sup>]<sup>-</sup> = 1424.8915. Found = 1424.8924.

**Sodium 3,5-bis(trifluoromethyl)benzenesulfonate (Ar<sup>F</sup>SO<sub>3</sub>Na) (S3.4).** A 25 mL round-bottom flask with a magnetic stirrer was charged with 3,5-bis(trifluoromethyl)benzenesulfonyl chloride (3.35 g, 10.70 mmol) and millipore H<sub>2</sub>O (12 mL, 0.9 M). A reflux condenser was attached, and the heterogeneous reaction was heated to an oil bath temperature of 107 °C and stirred for 3 h. Thereafter, the reaction was briefly cooled, and a distillation head was attached. The residual H<sub>2</sub>O and dissolved HCl (g) were distilled away, and the resulting pale-yellow solid remaining in the distillation flask was dried *in vacuo*. This solid was dissolved in H<sub>2</sub>O (10 mL), and 4 M NaOH was added to the resulting homogeneous solution to achieve pH = 7. Throughout this process, a white solid precipitated from solution and was isolated. Two successive recrystallizations from boiling H<sub>2</sub>O (~10 mL) followed by drying under high vacuum in a desiccator over P<sub>2</sub>O<sub>5</sub> for 12 h

provided 2.47 g (7.81 mmol, 73% yield) of **S3.4** as colorless needles.  $^1\text{H}$  NMR (500.0 MHz,  $\text{CD}_3\text{OD}$ )  $\delta$  8.34 (s, 2H), 8.06 (s, 1H),  $^{13}\text{C}$  NMR (125.7 MHz,  $\text{CD}_3\text{OD}$ )  $\delta$  149.6, 133.0 (q,  $J_{\text{C-F}} = 33.8$  Hz), 127.7 (q,  $J_{\text{C-F}} = 3.5$  Hz), 124.8 (septet,  $J_{\text{C-F}} = 3.8$  Hz), 124.6 (q,  $J_{\text{C-F}} = 272.4$  Hz);  $^{19}\text{F}$  NMR (376.5 MHz,  $\text{CD}_3\text{OD}$ )  $\delta$  -64.5.

**[Ru(btmb)<sub>3</sub>](Ar<sup>F</sup>SO<sub>3</sub>)<sub>2</sub> (3.3d)**. A 50 mL round-bottom flask with a magnetic stirrer was charged with **S3.3** (450 mg, 0.444 mmol, 1 equiv.), **S3.4** (393 mg, 1.24 mmol, 2.8 equiv.) and MeOH (22 mL, 0.02 M). The flask was fitted with a reflux condenser, and the reaction was heated to an oil bath temperature of 75 °C for 90 min. After cooling to room temperature, MeOH was removed *in vacuo* to afford a red residue that was dissolved in acetone/ $\text{CH}_2\text{Cl}_2$  (1:1, ~8 mL) and subsequently purified via gravity elution through a column of neutral  $\text{Al}_2\text{O}_3$  using acetone/ $\text{CH}_2\text{Cl}_2$  (1:1) as the eluent. The first band that eluted was determined to be the desired product, so these fractions were combined, and the volatiles were removed *in vacuo*. The product was dissolved in a minimum volume of EtOAc and passed through a 0.2  $\mu\text{m}$  Whatman PTFE filter to remove residual **S3.4**. The filtrate was layered hexanes and left to crystallize at 5 °C. The red needles that formed were isolated, washed with hexanes, and dried under high vacuum at 100 °C for 3 h to obtain 593 mg (0.379 mmol, 85% yield) of **3.3d** as a reddish/orange solid.  $^1\text{H}$  NMR (500.0 MHz,  $\text{CD}_3\text{OD}$ )  $\delta$  9.36 (s, 6H), 8.23 (s, 4H), 8.15 (d,  $J = 5.9$  Hz, 6H), 8.05 (s, 2H), 7.85 (d,  $J = 5.9$  Hz, 6H);  $^{13}\text{C}$  NMR (125.7 MHz,  $\text{CD}_3\text{OD}$ )  $\delta$  159.3, 155.1, 149.7, 141.5 (q,  $J_{\text{C-F}} = 35.5$  Hz), 133.0 (q,  $J_{\text{C-F}} = 33.6$  Hz), 127.6 (q,  $J_{\text{C-F}} = 3.6$  Hz), 125.7 (m), 124.8 (m), 124.7 (q,  $J = 277.7$  Hz), 123.9 (q,  $J_{\text{C-F}} = 273.2$  Hz), 123.4 (q,  $J = 3.6$  Hz);  $^{19}\text{F}$  NMR (376.5 MHz,  $\text{CD}_3\text{OD}$ )  $\delta$  -64.5, -66.1. HRMS (+ p): calculated for  $\text{C}_{44}\text{H}_{21}\text{F}_{18}\text{N}_6\text{O}_3\text{SRu}^+ [\text{M}^{2+} + \text{A}^-]^+ = 1271.0051$ . Found = 1271.0053. Calculated for



$C_{36}H_{18}F_{18}N_6Ru^{2+}$   $[M]^{2+} = 489.0169$ . Found = 489.0167. (– p): calculated  $C_8H_3F_6O_3S^-$   $[A^-] = 292.9713$ . Found = 292.9714.

**[Ru(btmb)<sub>3</sub>](OTs)<sub>2</sub> (3.3e)**. Prepared according to the procedure outlined for **3.3d** using **S3.3** (80.5 mg, 0.0795 mmol, 1 equiv.), sodium *p*-toluenesulfonate (61.2 mg, 0.315 mmol, 2.2 equiv.) and MeOH (8.0 mL, 0.01 M). Obtained 90 mg (0.0729 mmol, 51% yield) of **3.3e** as a reddish/orange solid. <sup>1</sup>H NMR (500.0 MHz, CD<sub>3</sub>OD) δ 9.36 (s, 6H), 8.15 (d, *J* = 5.9 Hz, 6H), 7.83 (d, *J* = 5.9 Hz, 6H), 7.64 (d, *J* = 8.1 Hz, 4H), 7.21 (d, *J* = 8.1 Hz, 4H), 2.37 (s, 6H); <sup>13</sup>C NMR (125.7 MHz, CD<sub>3</sub>OD) δ 159.3, 155.1, 143.8, 141.8, 141.5 (q, *J*<sub>C-F</sub> = 35.4 Hz), 129.9, 127.0, 125.7 (q, *J*<sub>C-F</sub> = 3.4 Hz), 123.9 (q, *J*<sub>C-F</sub> = 272.7 Hz), 123.4 (q, *J*<sub>C-F</sub> = 3.4 Hz), 21.4; <sup>19</sup>F NMR (376.5 MHz, CD<sub>3</sub>OD) δ –66.1. HRMS (+ p): calculated for  $C_{43}H_{25}F_{18}N_6O_3SRu^+$   $[M^{2+} + A^-]^+ = 1149.0465$ . Found = 1149.0475. Calculated for  $C_{36}H_{18}F_{18}N_6Ru^{2+}$   $[M]^{2+} = 489.0169$ . Found = 489.0169. (– p): calculated  $C_7H_7O_3S^-$   $[A^-] = 171.0121$ . Found = 171.0122.

**Sodium 3,5-bis(trifluoromethyl)benzenecarboxylate (Ar<sup>F</sup>CO<sub>2</sub>Na) (S3.5)**. To a 250 mL round-bottom flask was added 3,5-bis(trifluoromethyl)benzenecarboxylic acid (1g, 3.90 mmol, 1 equiv.), NaOH (138 mg, 3.45 mmol, 0.95 equiv.), and CH<sub>3</sub>CN (50 mL, 0.08 M). The reaction was stirred for 90 min and the solvent was removed under vacuum. To remove leftover carboxylic acid, the product was suspended in diethyl ether and filtered. The diethyl ether was removed, and 711 mg (2.54 mmol, 74%) of **S3.5** was isolated as a white powder. <sup>1</sup>H NMR (500.0 MHz, CD<sub>3</sub>OD) δ 8.52 (s, 2H), 8.00 (s, 1H); <sup>13</sup>C NMR (125.7 MHz, CD<sub>3</sub>OD) δ 169.7, 140.68, 130.1 (q, *J*<sub>C-F</sub> = 33.3 Hz),

129.1 (q,  $J_{C-F} = 3.2$  Hz), 123.5 (q,  $J_{C-F} = 272.4$  Hz), 122.9 (sept,  $J_{C-F} = 3.9$  Hz);  $^{19}\text{F}$  NMR (376.5 MHz,  $\text{CD}_3\text{OD}$ )  $\delta -64.3$ .

**[Ru(btmb)<sub>3</sub>](Ar<sup>F</sup>CO<sub>2</sub>)<sub>2</sub> (3.3f)**. Prepared according to the procedure outlined for **3.3d** using **S3.3** (150 mg, 0.143 mmol, 1 equiv.), **S3.5** (43.2 mg, 0.222 mmol, 2.8 equiv.), and MeOH (4.0 mL, 0.02 M). Obtained 77.1 mg (0.0584 mmol, 73% yield) of **3.3f** as a reddish/orange solid.  $^1\text{H}$  NMR (500.0 MHz,  $\text{CD}_3\text{OD}$ )  $\delta$  9.31 (s, 6H), 8.36 (s, 4H), 8.07 (d,  $J = 5.9$  Hz, 6H), 7.89 (s, 2H), 7.76 (dd,  $J_{C-F} = 5.9, 1.6$  Hz, 6H);  $^{13}\text{C}$  NMR (125.7 MHz,  $\text{CD}_3\text{OD}$ )  $\delta$  169.3, 157.1, 153.4, 140.7, 139.9 (q,  $J_{C-F} = 35.8$  Hz), 130.8 (q,  $J_{C-F} = 33.1$  Hz), 129.1 (q,  $J_{C-F} = 3.6$  Hz), 124.1 (q,  $J_{C-F} = 3.5$  Hz), 123.5 (q,  $J_{C-F} = 271.9$  Hz), 122.9 (sept,  $J_{C-F} = 123.4$  Hz), 122.1 (q,  $J_{C-F} = 273.3$  Hz), 121.9 (q,  $J_{C-F} = 3.6$  Hz);  $^{19}\text{F}$  NMR (376.5 MHz,  $\text{CD}_3\text{OD}$ )  $\delta -64.3, -66.1$ . HRMS (+ p): calculated for  $\text{C}_{45}\text{H}_{21}\text{F}_{24}\text{N}_6\text{O}_2\text{Ru}^+ [\text{M}^{2+} + \text{A}^-]^+ = 1271.0051$ . Found = 1271.0053. Calculated for  $\text{C}_{36}\text{H}_{18}\text{F}_{18}\text{N}_6\text{Ru}^{2+} [\text{M}]^{2+} = 489.0169$ . Found = 489.0167. (– p): calculated  $\text{C}_9\text{H}_3\text{F}_6\text{O}_2^- [\text{A}^-] = 257.0043$ . Found = 257.0044.

**[Ru(btmb)<sub>3</sub>](PF<sub>6</sub>)<sub>2</sub> (3.3c)**. To a 25 mL round-bottom flask with a magnetic stirrer was charged **S3.3** (261 mg, 0.258 mmol, 1 equiv.) and millipore H<sub>2</sub>O (13 mL, 0.02 M). To the resulting dark red solution was added ammonium hexafluorophosphate (88.2 mg, 0.541 mmol, 2.1 equiv.). A reddish/orange solid immediately precipitated and stirring was continued for 10 min before the solid was isolated on a fritted funnel, washed with H<sub>2</sub>O (2 x 3 mL), and dried. Recrystallization from an acetone/Et<sub>2</sub>O bilayer provided 252 mg (0.199 mmol, 77% yield) of **3.3c** as a reddish/orange solid.  $^1\text{H}$  NMR (500.0 MHz,  $(\text{CD}_3)_2\text{SO}$ )  $\delta$  9.57 (s, 6H), 8.03 (d,  $J = 6.0$  Hz, 6H),

7.88 (dd,  $J = 6.0, 1.4$  Hz, 6H);  $^{13}\text{C}$  NMR (125.7 MHz,  $(\text{CD}_3)_2\text{SO}$ )  $\delta$  157.4, 153.8, 137.9 (q,  $J_{\text{C-F}} = 34.7$  Hz), 124.0 (q,  $J_{\text{C-F}} = 3.4$  Hz), 122.5 (q,  $J_{\text{C-F}} = 273.4$  Hz), 121.9 (q,  $J_{\text{C-F}} = 3.4$  Hz);  $^{19}\text{F}$  NMR (376.5 MHz,  $(\text{CD}_3)_2\text{SO}$ )  $\delta$  -63.0, -70.1 (d,  $J_{\text{F-P}} = 711.2$  Hz);  $^{31}\text{P}$  NMR (162.0 MHz,  $(\text{CD}_3)_2\text{SO}$ )  $\delta$  -144.2 (septet,  $J_{\text{P-F}} = 711.5$  Hz). These data are consistent with previously reported values.<sup>98</sup>  $\text{C}_{36}\text{H}_{18}\text{F}_{24}\text{N}_6\text{PRu}^+ [\text{M}^{2+} + \text{A}^-]^+ = 1122.9990$ . Found = 1123.0004. Calculated for  $\text{C}_{36}\text{H}_{18}\text{F}_{18}\text{N}_6\text{Ru}^{2+} [\text{M}]^{2+} = 489.0169$ . Found = 489.0171. (- p): calculated  $\text{PF}_6^- [\text{A}^-] = 144.9647$ . Found = 144.9648.

### 3.7.3. Visible Light Photocatalysis of Radical Cation [4+2] Diels–Alder Cycloadditions

**General procedure for experiments in Table 3.1:** A stock solution of anethole (54.6 mg, 55.3  $\mu\text{L}$ , 0.368 mmol), isoprene (75.3 mg, 111  $\mu\text{L}$ , 1.11 mmol), and trimethyl(phenyl)silane internal standard (55.4 mg, 63.4  $\mu\text{L}$ , 0.368 mmol) in dry  $\text{CH}_2\text{Cl}_2$  (4.38 mL) was prepared. 810  $\mu\text{L}$  aliquots of this stock solution were added to oven-dried 25 mL Schlenk tubes containing the appropriate ruthenium photocatalyst ( $6.14 \times 10^{-4}$  mmol, 1 mol%). This afforded reaction mixtures containing anethole (9.1 mg, 0.0614 mmol, 1 equiv.), isoprene (12.5 mg, 0.184 mmol, 3 equiv.), and trimethyl(phenyl)silane internal standard (9.2 mg, 0.0614 mmol, 1 equiv.) in  $\text{CH}_2\text{Cl}_2$  (0.77 mL, 0.08 M). A stir bar was added to each reaction. The solutions were submitted to three freeze-pump-thaw cycles, purged with  $\text{N}_2$ , and irradiated at room temperature using a 23 W compact fluorescent light (CFL) bulb. The yields and amount of remaining anethole in Table 3.1 were determined by  $^1\text{H}$  NMR analysis of the unpurified reaction mixtures.  $^1\text{H}$  NMR analysis of the cycloadduct was consistent with previously reported values.<sup>99</sup>

**General procedure for experiments with anion binder 3.7 in Table 3.4:** A stock solution of anethole, isoprene, and trimethyl(phenyl)silane internal standard in dry  $\text{CH}_2\text{Cl}_2$  was added to oven-dried 25 mL Schlenk tubes containing the appropriate ruthenium photocatalyst ( $6.14 \times 10^{-4}$  mmol, 1 mol%) and thiophosphotriamide **3.7** (9.2 mg, 0.0123 mmol, 20 mol%).<sup>100</sup> A stir bar was added to each reaction. The solutions were submitted to three freeze-pump-thaw cycles, purged with  $\text{N}_2$ , and irradiated at room temperature using a 23 W compact fluorescent light (CFL) bulb. The yields in Table 3.4 were determined by  $^1\text{H}$  NMR analysis of the unpurified reaction mixtures.

#### 3.7.4. UV-Vis Spectra, Photoluminescence Spectra, and Chain Length Measurements

*UV-Vis spectroscopy:* Solution spectra were measured in  $\text{CH}_2\text{Cl}_2$  or acetonitrile at a ruthenium photocatalyst concentration of  $3.9 \times 10^{-5}$  M. UV-vis absorption spectra were recorded at room temperature using a Cary 50 spectrophotometer over a scan range of 600 nm $\rightarrow$ 200 nm at a scan rate of 300 nm/min and resolution of 0.5 nm.

*Steady-state photoluminescence spectroscopy:* Steady-state photoluminescence spectra were obtained at room temperature using a Hitachi F4500 fluorescence spectrophotometer with a scan range of 478 nm $\rightarrow$ 678 nm at a scan rate of 240 nm/min and resolution of 0.5 nm. The excitation wavelength was the peak of the MLCT absorbance spectra. Emission and excitation slit widths were maintained at 5 nm.

Solution spectra were measured in  $\text{CH}_2\text{Cl}_2$  or acetonitrile at a ruthenium photocatalyst [Ru] concentration of  $3.9 \times 10^{-5}$  M. The following sample preparation procedure was carried out in the dark. Samples were degassed by three freeze-pump-thaw cycles and subsequently transferred to

fluorescence cuvettes that had been purged with N<sub>2</sub> for 30 min. All photoluminescence spectra were acquired normal to the incident beam.

Excited-state photoluminescence quenching experiments were carried out as follows: the luminescence intensity of a  $3.9 \times 10^{-5}$  M solution of [Ru] in CH<sub>2</sub>Cl<sub>2</sub> was measured. Subsequently, aliquots of a  $1.6 \times 10^{-2}$  M stock solution of anethole quencher in CH<sub>2</sub>Cl<sub>2</sub> were added to 2.0 mL of  $7.8 \times 10^{-5}$  M solutions of [Ru] in CH<sub>2</sub>Cl<sub>2</sub>. The final solution volume was adjusted to 4.0 mL via dilution with CH<sub>2</sub>Cl<sub>2</sub>. Samples were degassed as described above, and the luminescence intensities were determined. The ratio of unquenched (F<sub>0</sub>) to quenched (F) photoluminescence intensity was plotted against [anethole]. The data were linear and followed Stern–Volmer kinetics. A linear regression yielded the Stern–Volmer constants (K<sub>SV</sub>) and division by the unquenched excited-state lifetime provided the bimolecular quenching rate constants (*k<sub>q</sub>*).

The effect of thiophosphotriamide **3.7** on the photoluminescence of the [Ru(bt<sup>F</sup>mb)<sub>3</sub>](Ar<sup>F</sup>SO<sub>3</sub>)<sub>2</sub> photocatalyst was investigated as follows: [Ru(bt<sup>F</sup>mb)<sub>3</sub>](Ar<sup>F</sup>SO<sub>3</sub>)<sub>2</sub> (**3.3d**, 15.3 mg, 9.8 μmol) was dissolved in CH<sub>2</sub>Cl<sub>2</sub> (25 mL) to produce a  $3.9 \times 10^{-4}$  M stock solution. A 10 mL aliquot of the stock solution was diluted to 50 mL with CH<sub>2</sub>Cl<sub>2</sub> to produce a final concentration of  $7.8 \times 10^{-5}$  M. Thiophosphotriamide **3.7** (81.5 mg, 0.109 mmol) was dissolved in CH<sub>2</sub>Cl<sub>2</sub> to produce a 0.0109 M solution. Both solutions were transferred to a respective 25 mL Schlenk tubes (8 mL of solution **3.7**, 14 mL of solution **3.3d**). To another Schlenk tube was added 8 mL CH<sub>2</sub>Cl<sub>2</sub>. The three Schlenk tubes were then subjected to 3 freeze-pump-thaw cycles. Aliquots of each solution were transferred under N<sub>2</sub> to a N<sub>2</sub> sparged cuvette. The ruthenium concentration was maintained at  $4.0 \times 10^{-5}$  M, while the concentration of **3.7** was varied through different addition volumes of the stock solution. The neat CH<sub>2</sub>Cl<sub>2</sub> was used to maintain an overall total volume of 3 mL in the cuvette.

Sample preparation for excited-state lifetime measurements was as follows: a  $3.9 \times 10^{-5}$  M solution of the respective ruthenium photosensitizer in  $\text{CH}_2\text{Cl}_2$  was degassed by 3 freeze-pump-thaw cycles and transferred to a  $\text{N}_2$ -purged cuvette using standard Schlenk technique. Lifetime measurements were collected by the frequency-domain method with an ISS K2 multifrequency cross-correlation phase and modulation fluorometer. The excitation source was intensity modulated through varying MHz frequencies at the sample's absorption maximum, producing shifts in the intensity and phase of fluorescence emission. Comparison to a standard (in this case fluorescein and glycogen) allows lifetime determination. Data was analyzed in Vinci (ISS).

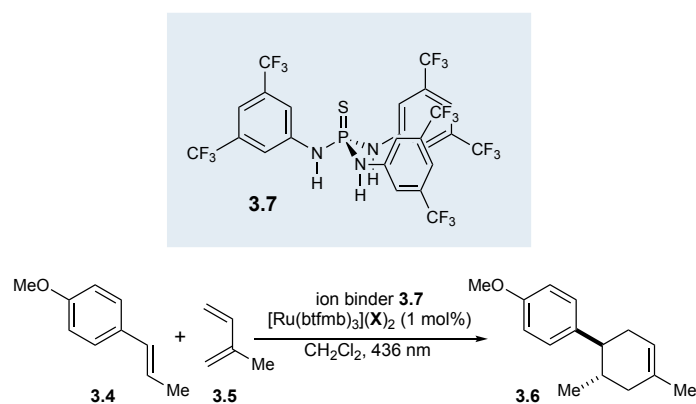
*Chain Length:* Chain lengths of radical cation Diels–Alder cycloadditions were determined as follows. The quantum yields ( $\Phi$ ) for the respective reactions were determined by the method outlined by Cismesia and Yoon.<sup>101</sup> To ascertain chain length, the following formula was employed:

$$\text{chain length} = \frac{\Phi(\tau^{-1} + k_{q,\text{anethole}}[\text{anethole}] + k_{q,\text{isoprene}}[\text{isoprene}] + k_{q,[2+2]}[2+2])}{k_{q,\text{anethole}}[\text{anethole}]}$$

where  $\tau$  is the excited-state lifetime of the respective photocatalyst ( $\tau^{-1} = k_r + k_{nr}$ ),  $k_{q,\text{anethole}}$ ,  $k_{q,\text{isoprene}}$ , and  $k_{q,[2+2]}$  are the rates of excited-state quenching by the designated species, and [anethole], [isoprene], and [2+2] are the concentrations of the designated species. The [2+2] product results from homodimerization of anethole and forms in very small amounts (~2%) at low conversions of anethole. Furthermore, the rate of excited-state quenching by isoprene was very small. Therefore, the final two terms in the numerator were determined to be negligible, and thus

were ignored. Using this formula, chain lengths were determined for radical cation Diels–Alder cycloadditions catalyzed by  $[\text{Ru}(\text{btfmb})_3](\text{BAr}^{\text{F}}_4)_2$  (quantum yield = 26, chain length = 26) and  $[\text{Ru}(\text{btfmb})_3](\text{Ar}^{\text{F}}\text{SO}_3)_2$  (quantum yield = 0.35, chain length = 0.40). Subsequently, a radical cation cycloaddition catalyzed by  $[\text{Ru}(\text{btfmb})_3](\text{Ar}^{\text{F}}\text{SO}_3)_2$  was performed in the presence of thiophosphotriamide **3.7** (20 mol%) (quantum yield = 7, chain length = 8). Therefore, thiophosphotriamide **3.7** exerts its greatest effect on chain length. See Table 3.5.

Table 3.5 Quantum Yield and Chain Length of Diels–Alder Reaction



entry	counteranion (X)	H-bond cat <b>3.7</b>	quantum yield	chain length
1	$\text{BAr}^{\text{F}}_4^-$ ( <b>3.3a</b> )	0 mol%	26	26
2	$\text{Ar}^{\text{F}}\text{SO}_3^-$ ( <b>3.3d</b> )	0 mol%	0.35	0.4
3	$\text{Ar}^{\text{F}}\text{SO}_3^-$ ( <b>3.3d</b> )	20 mol%	7	8

### 3.7.5. Cyclic Voltammetry Experiments

Cyclic voltammetry was performed on a BASi EC Epsilon potentiostat connected to a BASi C3 cell stand and analyzed on a PC using Epsilon software. A three-electrode setup was employed: Pt wire counter electrode, glassy carbon working electrode, and a Ag/AgNO<sub>3</sub> (0.01 M AgNO<sub>3</sub>, 0.1 M *n*-Bu<sub>4</sub>N<sup>+</sup> PF<sub>6</sub><sup>-</sup> in CH<sub>3</sub>CN) quasi-reference electrode containing a polished silver wire immersed in the electrolyte solution. The entire assembly of this electrode was contained in a glass body, the tip of which consisted of a Vycor plug. The electrolyte solution in the electrode was replaced daily to ensure the Vycor plug was free of contaminants. With this setup, Fc/Fc<sup>+</sup> (0.1 M *n*-Bu<sub>4</sub>N<sup>+</sup> PF<sub>6</sub><sup>-</sup> in CH<sub>3</sub>CN) was measured to be 0.093 V vs. Ag/AgNO<sub>3</sub>. A typical experiment was performed as follows: dry solvent and *n*-Bu<sub>4</sub>N<sup>+</sup> X<sup>-</sup> electrolyte (0.1 M) (for example, *n*-Bu<sub>4</sub>N<sup>+</sup> BAr<sup>F</sup><sub>4</sub><sup>-</sup> was used in the analysis of [Ru(btmb)<sub>3</sub>](BAr<sup>F</sup><sub>4</sub>)<sub>2</sub>) were introduced to the cell, the solution was sparged with dry N<sub>2</sub> with stirring for 5 min, and subsequently a voltammogram was recorded to establish background. Thereafter, the appropriate ruthenium catalyst complex (0.001 M) was introduced under N<sub>2</sub> and a second spectrum was collected. Finally, ferrocene internal standard (~0.001 M) was added, and a final voltammogram was collected. After referencing to ferrocene, voltammograms were referenced to SCE by adding 0.30 V to all potentials. Stirring was performed prior to each run to ensure exposure of electrodes to fresh analyte. The scan rate was typically 100 mV/s. Between each catalyst complex analyzed, the glassy carbon working electrode was polished on Al<sub>2</sub>O<sub>3</sub>, sonicated in ultrapure H<sub>2</sub>O, and washed in the organic solvent used for analysis.

For experiments performed in CH<sub>2</sub>Cl<sub>2</sub>, the working and reference electrodes were placed as close as possible without touching to minimize Ohmic drop in the poorly conductive, highly resistive CH<sub>2</sub>Cl<sub>2</sub> solvent. IR compensation experiments were performed in CH<sub>2</sub>Cl<sub>2</sub> in the presence of an



appropriate  $n\text{-Bu}_4\text{N}^+ \text{X}^-$  electrolyte.<sup>102</sup> The uncompensated resistance was found to vary slightly with  $n\text{-Bu}_4\text{N}^+ \text{X}^-$  electrolyte and was typically between 550–850 Ohm. However, when IR compensation was applied, the half-wave potentials of both ferrocene and the catalyst redox couple of interest showed minimal ( $< 30$  mV) shifts, and due to distortions sometimes introduced into the data by using IR compensation, compensation was not employed. It should be noted that all redox couples in  $\text{CH}_2\text{Cl}_2$  exhibited quasi-reversible behavior, with  $90 \text{ mV} < \Delta E_p < 180 \text{ mV}$  (peak separation increased with increasing Lewis basicity of  $\text{X}^-$  in supporting electrolyte and catalyst complex) and  $1.1 < i_{pc}/i_{pa} < 1.4$ . Redox couples in  $\text{CH}_3\text{CN}$  exhibited reversible, Nernstian behavior.

#### Preparation of supporting electrolytes

**Tetrabutylammonium tetrakis-(3,5-bis(trifluoromethyl)phenyl)borate ( $n\text{-Bu}_4\text{N}^+ \text{BAr}^{\text{F}_4-}$ ) (S3.6).** To a 25 mL round-bottom flask with a stir bar was added  $\text{NaBAr}^{\text{F}_4}$  (1.33 g, 1.53 mmol, 1 equiv.) and distilled acetone (5.0 mL, 0.3 M). The solution was stirred until homogeneous, and subsequently, a solution of tetrabutylammonium chloride (426 mg, 1.53 mmol, 1 equiv.) in acetone (1.2 mL) was added.  $\text{NaCl}$  immediately precipitated from solution. The reaction was stirred for an additional 15 min before being filtered through a 0.2  $\mu\text{M}$  Whatman filter. Acetone was removed *in vacuo*, and the resulting viscous oil was dried under high vacuum for 1 h. Thereafter, the oil was dissolved in  $\text{CH}_2\text{Cl}_2$  (10 mL), filtered, and  $\text{CH}_2\text{Cl}_2$  was removed *in vacuo*. The oil was again dried on high vacuum and crystallization was induced by cooling to  $-78$  °C and allowing slow warming to room temperature under high vacuum. The resulting white solid was dried to constant mass to obtain 1.68 g (1.52 mmol, 99% yield) of **S3.6** as a white, hygroscopic solid.  $^1\text{H}$  NMR (500.0 MHz,  $\text{CDCl}_3$ )  $\delta$  7.69 (s, 8H), 7.53 (s, 4H), 2.99 (m, 8H), 1.53 (m, 8H), 1.33 (dq,

$J = 14.8, 7.2$  Hz, 8H), 0.93 (t,  $J = 7.2$  Hz, 12H);  $^{13}\text{C}$  NMR (125.7 MHz,  $\text{CDCl}_3$ )  $\delta$  161.7 (q,  $J_{\text{C-B}} = 49.6$  Hz), 134.8, 128.8 (qq,  $J_{\text{C-F}} = 31.6, 3.1$  Hz), 124.5 (q,  $J_{\text{C-F}} = 271.6$  Hz), 117.4 (m), 58.9, 23.6, 19.5, 13.1;  $^{19}\text{F}$  NMR (376.5 MHz,  $\text{CDCl}_3$ )  $\delta$  -62.4;  $^{11}\text{B}$  NMR (128.3 MHz,  $\text{CDCl}_3$ )  $\delta$  -6.63.

**Tetrabutylammonium 3,5-bis(trifluoromethylbenzenesulfonate ( $n\text{-Bu}_4\text{N}^+ \text{Ar}^{\text{F}}\text{SO}_3^-$ )) (S3.7).**

A 100 mL round-bottom flask with a magnetic stirrer was charged with 3,5-bis(trifluoromethyl)benzenesulfonyl chloride (Matrix Scientific) (1.99 g, 6.35 mmol) and  $\text{H}_2\text{O}$  (15 mL, 0.4 M). A reflux condenser was attached, and the heterogeneous reaction was heated to an oil bath temperature of 107 °C and stirred for 3 h. Thereafter, the reaction was briefly cooled, and a distillation head was attached. The residual  $\text{H}_2\text{O}$  and dissolved  $\text{HCl}$  (g) were distilled off and the resulting pale-yellow solid remaining in the distillation flask was dried *in vacuo*. This solid was dissolved in  $\text{H}_2\text{O}$  (4 mL, 1.6 M) and a 1.0 M solution of tetrabutylammonium hydroxide in MeOH was added to achieve pH = 7. Subsequently,  $\text{H}_2\text{O}$  and MeOH were removed *in vacuo*, the residue obtained was dried on high vacuum and thereafter was dissolved in  $\text{CH}_2\text{Cl}_2$  and filtered to remove insoluble solids. Recrystallization from  $\text{H}_2\text{O}$  followed by drying under high vacuum provided 2.06 g (3.85 mmol, 61% yield) of S3.7 as colorless needles.  $^1\text{H}$  NMR (500.0 MHz,  $\text{CDCl}_3$ )

$\delta$  8.40 (s, 2H), 7.81 (s, 1H), 3.30 (m, 8H), 1.65 (m, 8H), 1.42 (dq,  $J = 14.8, 7.2$  Hz, 8H), 0.99 (t,  $J = 7.2$  Hz, 12H);  $^{13}\text{C}$  NMR (125.7 MHz,  $\text{CDCl}_3$ )  $\delta$  149.4, 131.2 (q,  $J_{\text{C-F}} = 33.4$  Hz), 126.8 (q,  $J_{\text{C-F}} = 3.5$  Hz), 123.0 (q,  $J_{\text{C-F}} = 272.4$  Hz), 122.5 (septet,  $J_{\text{C-F}} = 3.8$  Hz), 58.8, 23.9, 19.7, 13.5;  $^{19}\text{F}$  NMR (376.5 MHz,  $\text{CDCl}_3$ )  $\delta$  -62.8.

**Tetrabutylammonium *p*-toluenesulfonate (*n*-Bu<sub>4</sub>N<sup>+</sup> OTs<sup>-</sup>) (S3.8).** A 25 mL round-bottom flask with a magnetic stirrer was charged with *p*-toluenesulfonic acid monohydrate (1.00 g, 5.26 mmol) and H<sub>2</sub>O (3 mL, 1.8 M). A 1.0 M solution of tetrabutylammonium hydroxide in MeOH was added over 5 min to achieve pH = 7 (5.2 mL added). The exothermic reaction was allowed to stir for 15 min, and subsequently, H<sub>2</sub>O and MeOH were removed *in vacuo*. The residue obtained was dissolved in CH<sub>2</sub>Cl<sub>2</sub>, transferred to a separatory funnel, separated from residual H<sub>2</sub>O, and filtered to remove insoluble solids. Removal of CH<sub>2</sub>Cl<sub>2</sub> *in vacuo* followed by recrystallization from H<sub>2</sub>O and drying under high vacuum provided 1.38 g (3.85 mmol, 63% yield) of **S3.8** as colorless needles. Spectral data were consistent with previously reported values.<sup>103</sup>

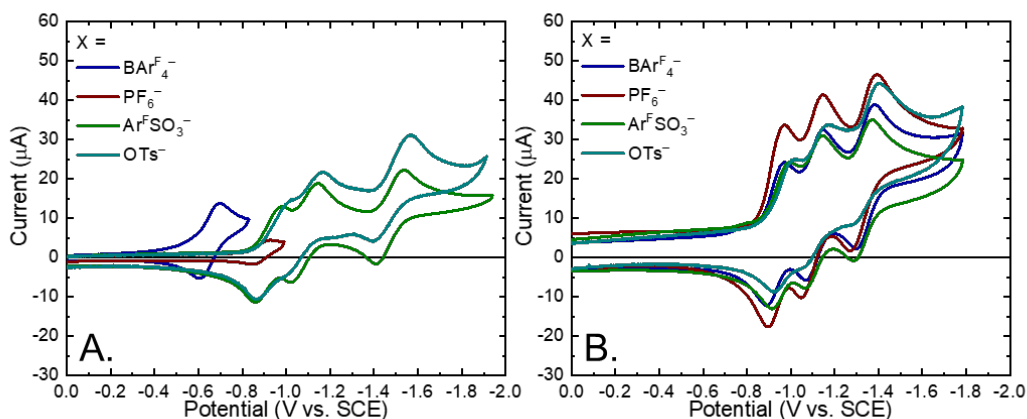


Figure 3.4 Cyclic voltammograms of the [Ru(btmb)<sub>3</sub>](X)<sub>2</sub> catalysts in A. CH<sub>2</sub>Cl<sub>2</sub> and B. CH<sub>3</sub>CN at a scan rate of 100 mV/sec and 0.1 M electrolyte solution composed of the *n*-Bu<sub>4</sub>N<sup>+</sup> salt of the indicated counterion.

Table 3.6 Electrochemical potentials of [Ru(btmb)<sub>3</sub>](X)<sub>2</sub> in CH<sub>3</sub>CN.

entry	catalyst	$\Delta G_{\text{ES}}$ (eV)	Ru <sup>2+/*</sup> (V)	Ru <sup>2+*/+</sup> (V)	Ru <sup>+/0</sup> (V)	Ru <sup>0/-</sup> (V)
1	<b>3.3a</b>	2.04	-0.93	+1.11	-1.11	-1.35
2	<b>3.3c</b>	2.04	-0.93	+1.11	-1.10	-1.33
3	<b>3.3d</b>	2.04	-0.95	+1.09	-1.11	-1.34
4	<b>3.3e</b>	2.04	-0.98	+1.06	-1.11	-1.35

### 3.7.6. <sup>1</sup>H NMR Experiments

#### Hydrogen-Bond Donor Co-Catalyst Titration:

The equilibrium constant for the binding of Ar<sup>F</sup>SO<sub>3</sub><sup>-</sup> to thiophosphotriamide **3.7** was determined through NMR titration studies. A solution of thiophosphotriamide **3.7** (0.16 mg, 0.21 μmol, 1.0 equiv.) in CD<sub>2</sub>Cl<sub>2</sub> (500 μL) was transferred to an NMR tube. Separately, a stock solution containing both *n*-Bu<sub>4</sub>N<sup>+</sup> Ar<sup>F</sup>SO<sub>3</sub><sup>-</sup> (5.6 mg, 10.5 μmol) and thiophosphotriamide **3.7** (1.3 mg, 1.74 μmol) in CD<sub>2</sub>Cl<sub>2</sub> (4.0 mL) was prepared. Increasing amounts of this solution were titrated into the NMR tube in 10 μL aliquots. The titration was quantified by monitoring the chemical shift of the aromatic C–H resonances of **3.7**, which moved downfield with increasing concentration of *n*-Bu<sub>4</sub>N<sup>+</sup> Ar<sup>F</sup>SO<sub>3</sub><sup>-</sup>. The changes in chemical shift (Δppm) were fit to a 1:1 binding model. Microsoft Excel was used to alter *K*<sub>a</sub> to minimize the error between the calculated and experimental chemical shifts. The resulting binding isotherm is shown below. *K*<sub>a</sub> = 1.3 × 10<sup>6</sup>.

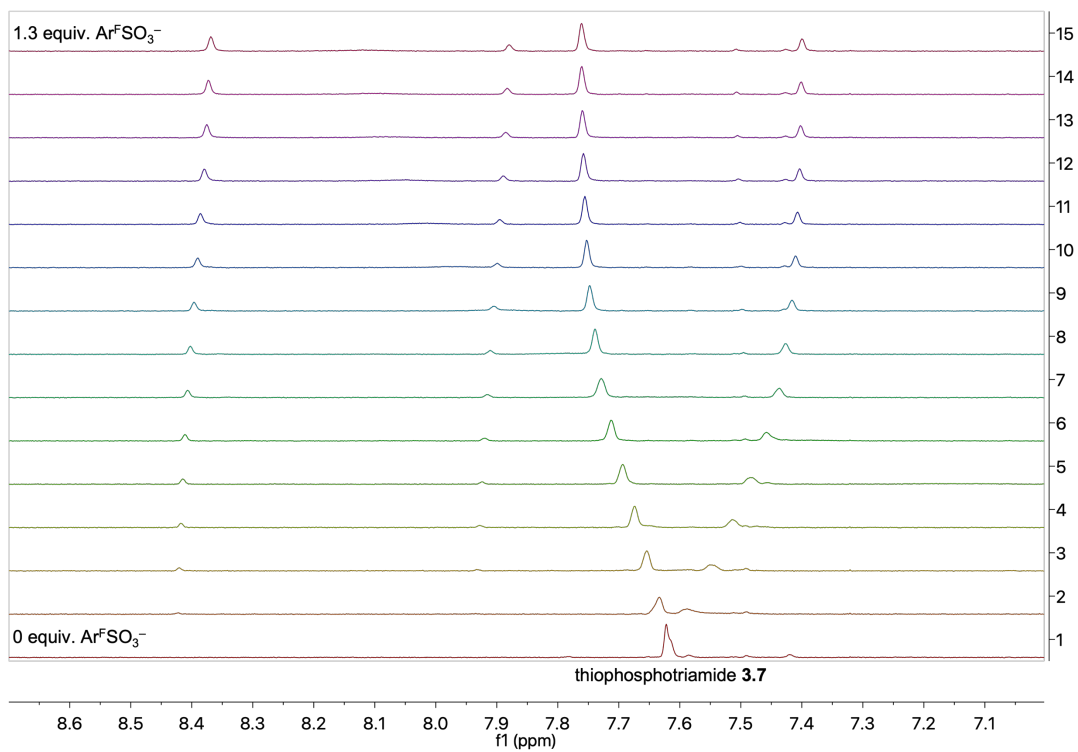


Figure 3.5 Aromatic region of the <sup>1</sup>H NMR titration of thiophosphotriamide **3.7** with *n*-Bu<sub>4</sub>N<sup>+</sup> Ar<sup>F</sup>SO<sub>3</sub><sup>-</sup> in CD<sub>2</sub>Cl<sub>2</sub>. The C–H chemical shift of **3.7** is noted in the figure.

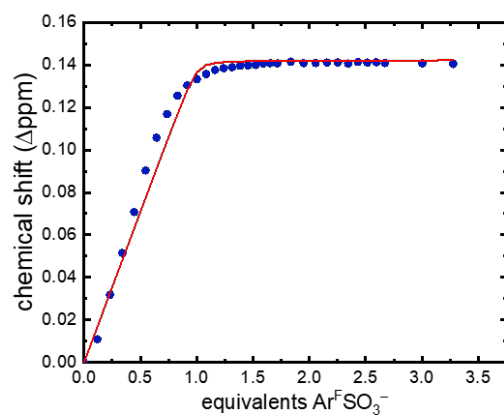
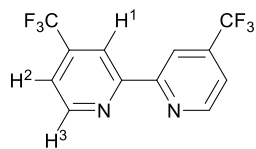


Figure 3.6 Change in chemical shift of the thiophosphotriamide **3.7** C–H resonance, blue circles.

Overlaid is the best fit to a 1:1 binding model, solid line.

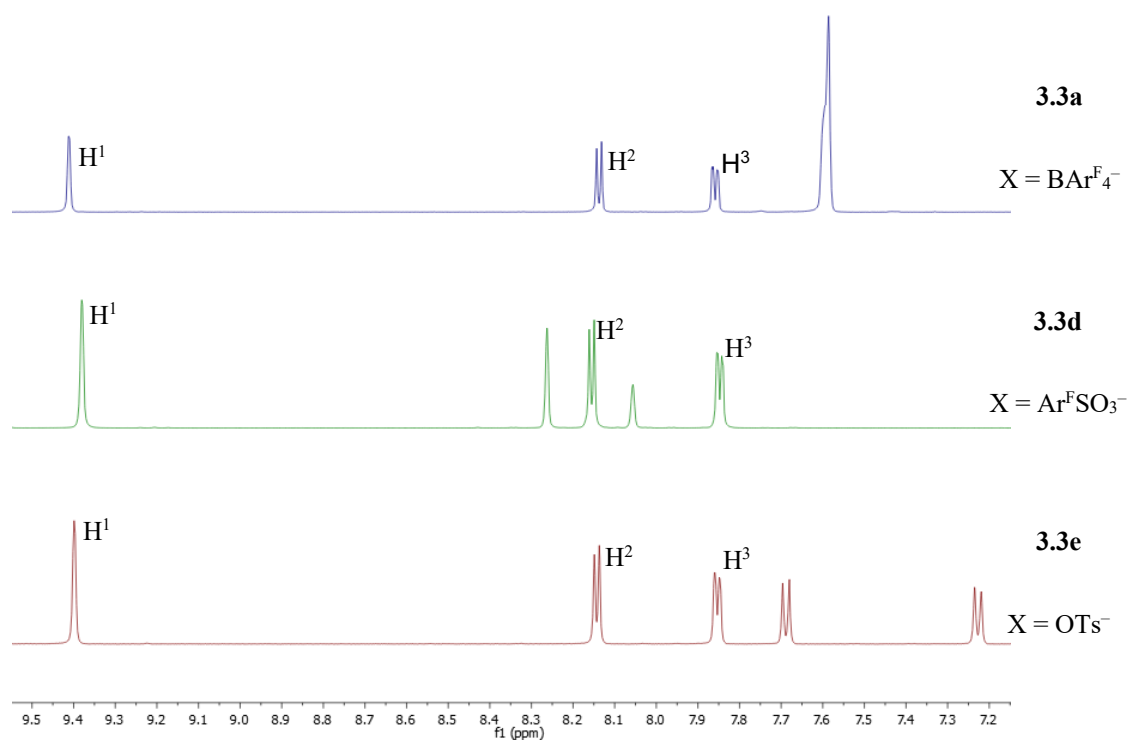
Chemical Shift Dependence on Counteranion Identity:

$^1\text{H}$  NMR Spectra of  $[\text{Ru}(\text{btfmb})_3](\text{X})_2$  (expansions of aromatic regions shown)



$^1\text{H}$  NMR Spectra in  $\text{CD}_3\text{OD}$

**A**



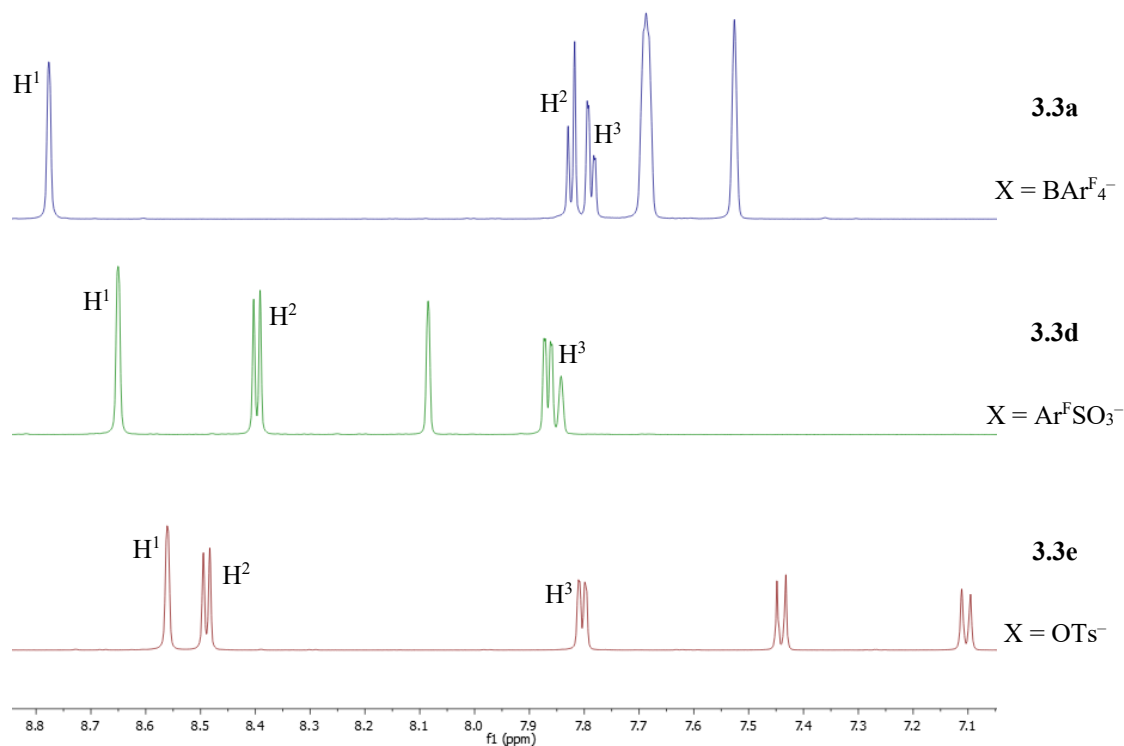
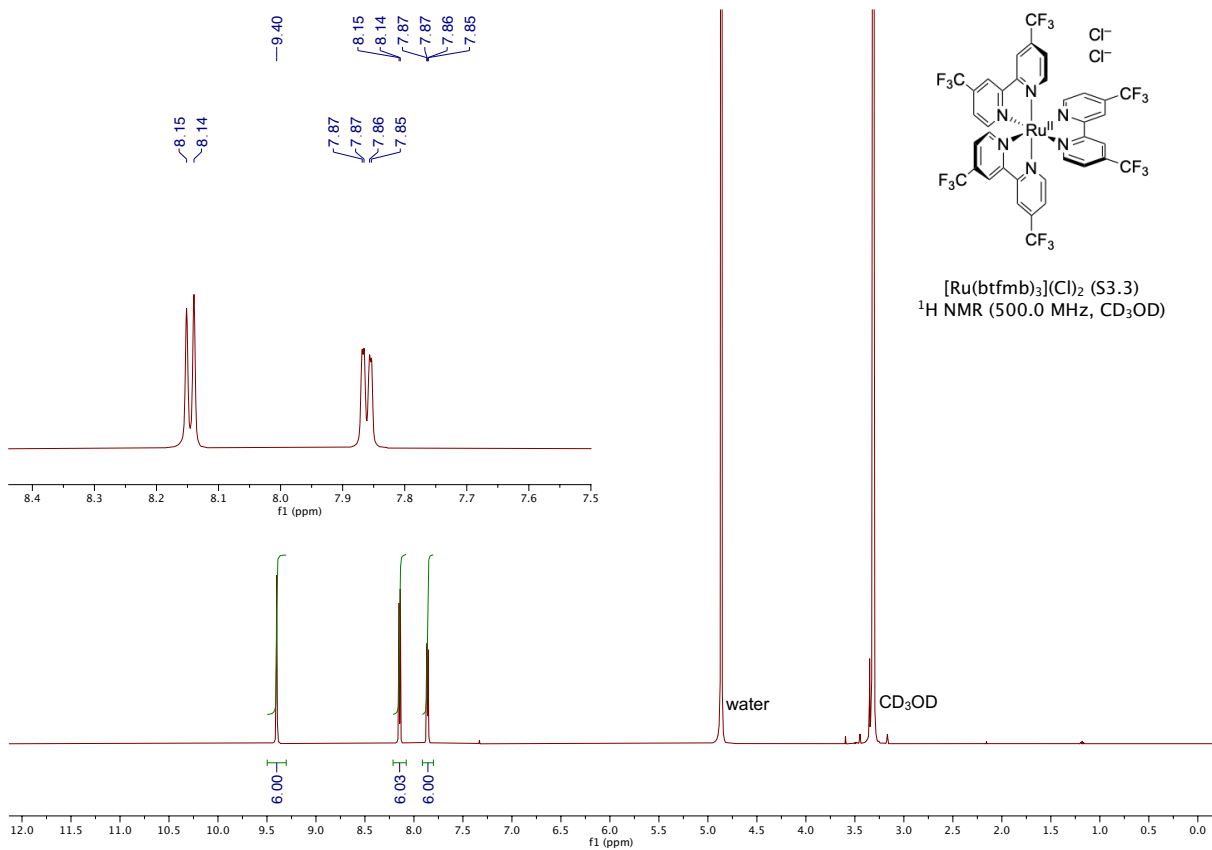
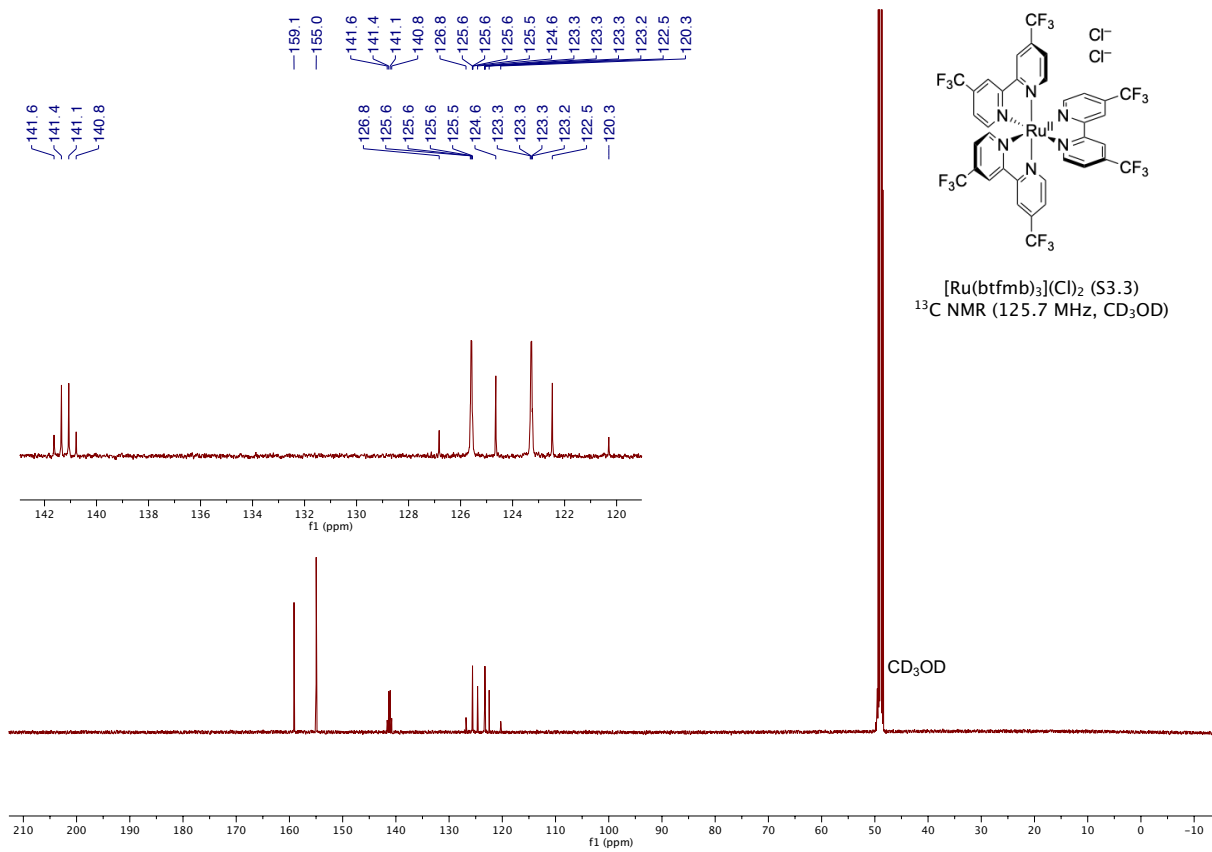
$^1\text{H}$  NMR Spectra in  $\text{CD}_2\text{Cl}_2$ **B**

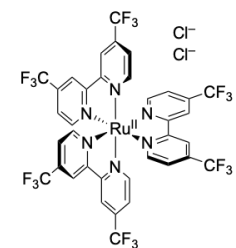
Figure 3.7 The  $^1\text{H}$  NMR chemical shifts for catalysts **3.3a**, **3.3d**, and **3.3e** in  $\text{CD}_3\text{OD}$  (A) and  $\text{CD}_2\text{Cl}_2$  (B). In  $\text{CD}_2\text{Cl}_2$  significant changes in the proton spectra of the btfnb ligands were measured between the photocatalysts. These changes tracked the coordinating ability of the counteranion in good agreement with the hypothesis of Meyer and coworkers of specific interactions between the counteranion and specific positions on the ligands.<sup>104</sup>



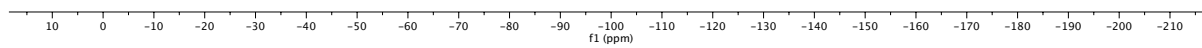
3.7.7.  $^1\text{H}$ ,  $^{13}\text{C}$ ,  $^{19}\text{F}$ ,  $^{11}\text{B}$ , and  $^{31}\text{P}$  NMR spectra

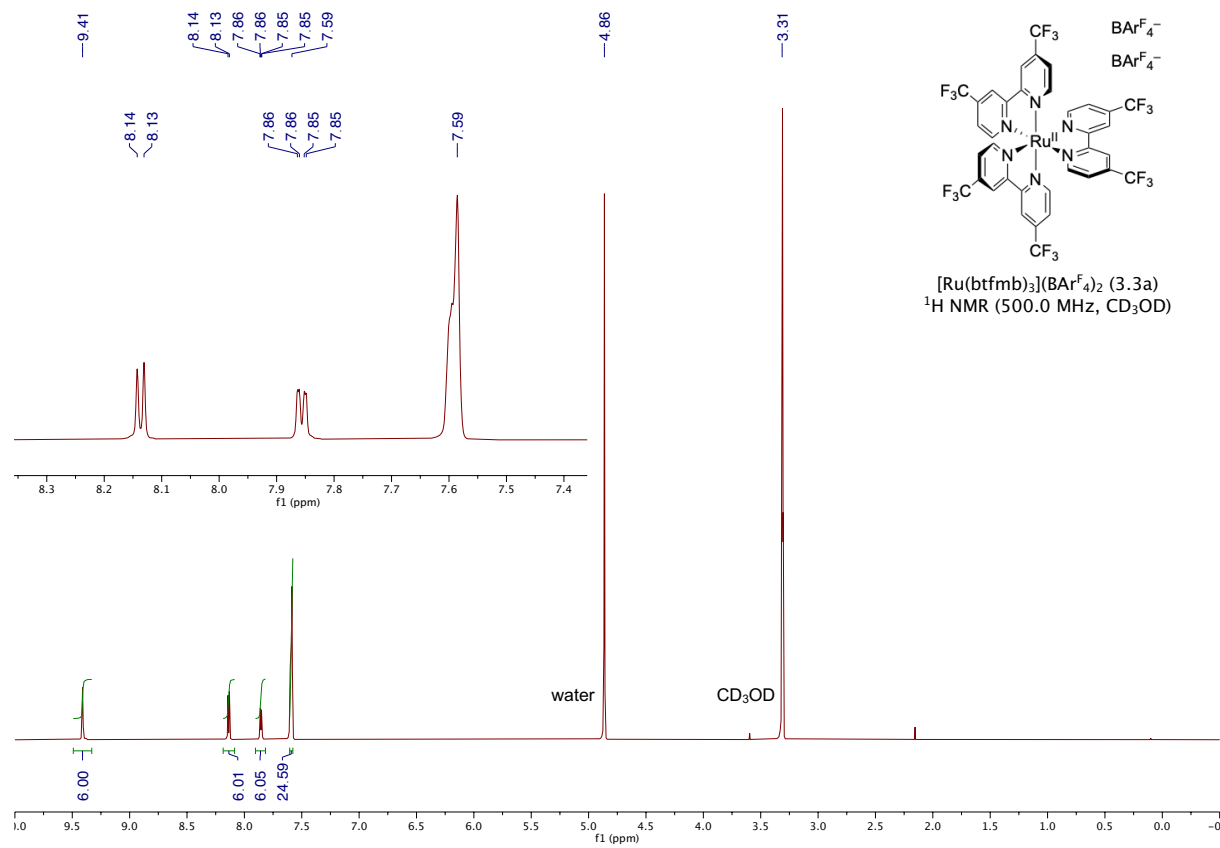


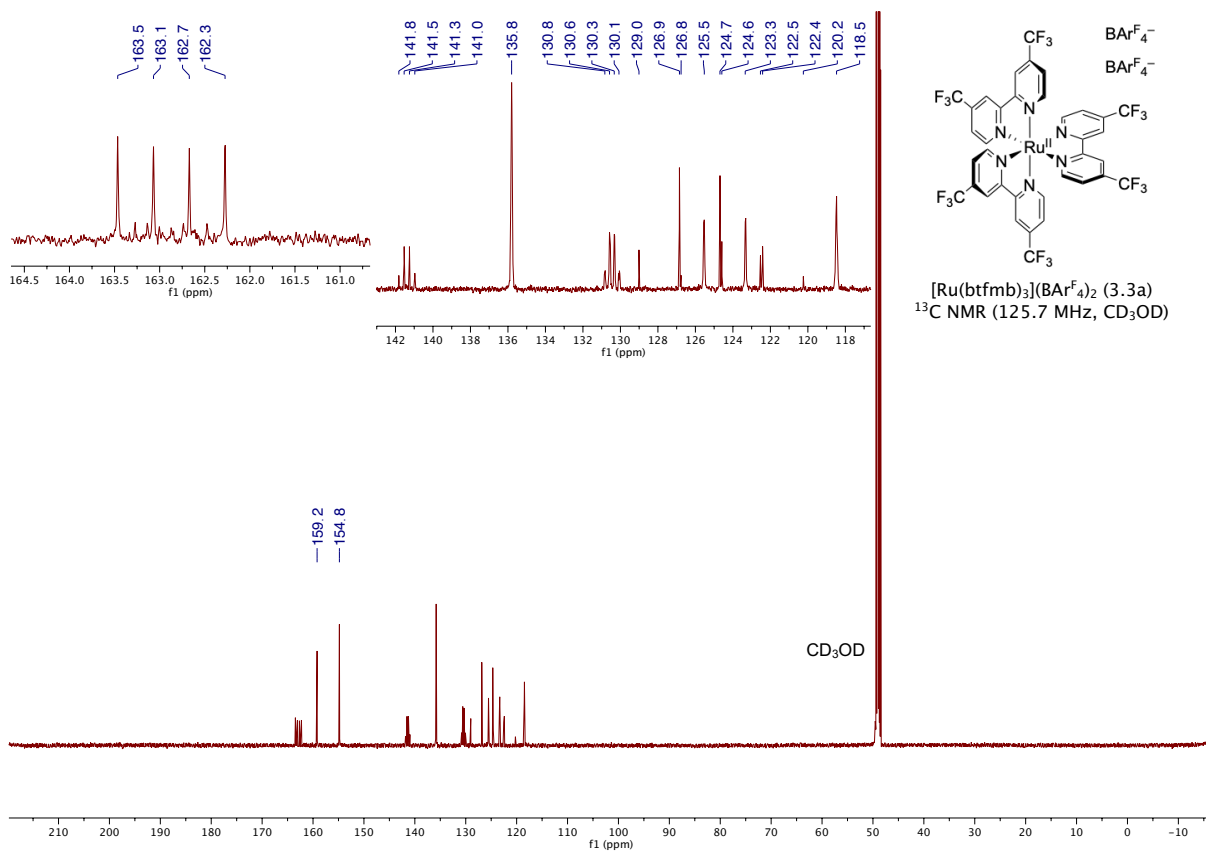
-66.1

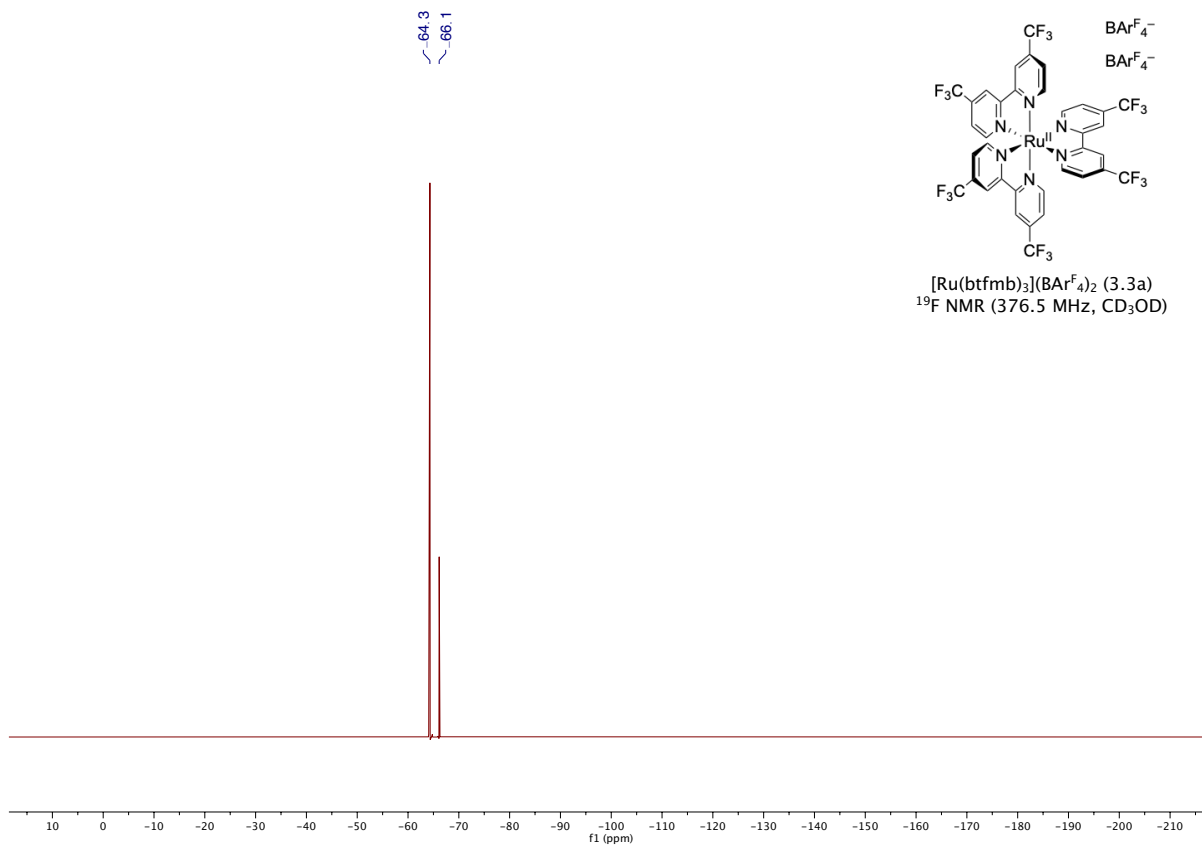


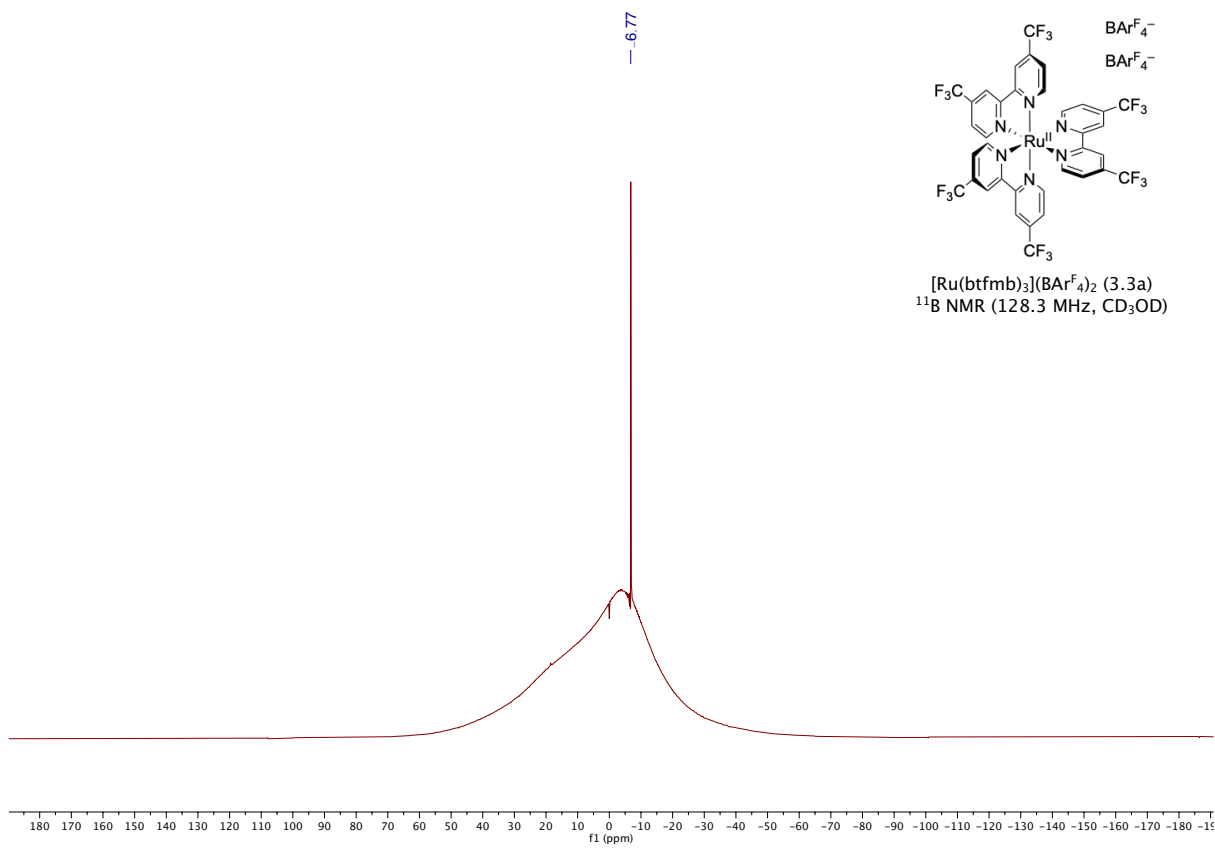
[Ru(btmb)<sub>3</sub>](Cl)<sub>2</sub> (S3.3)  
<sup>19</sup>F NMR (376.5 MHz, CD<sub>3</sub>OD)

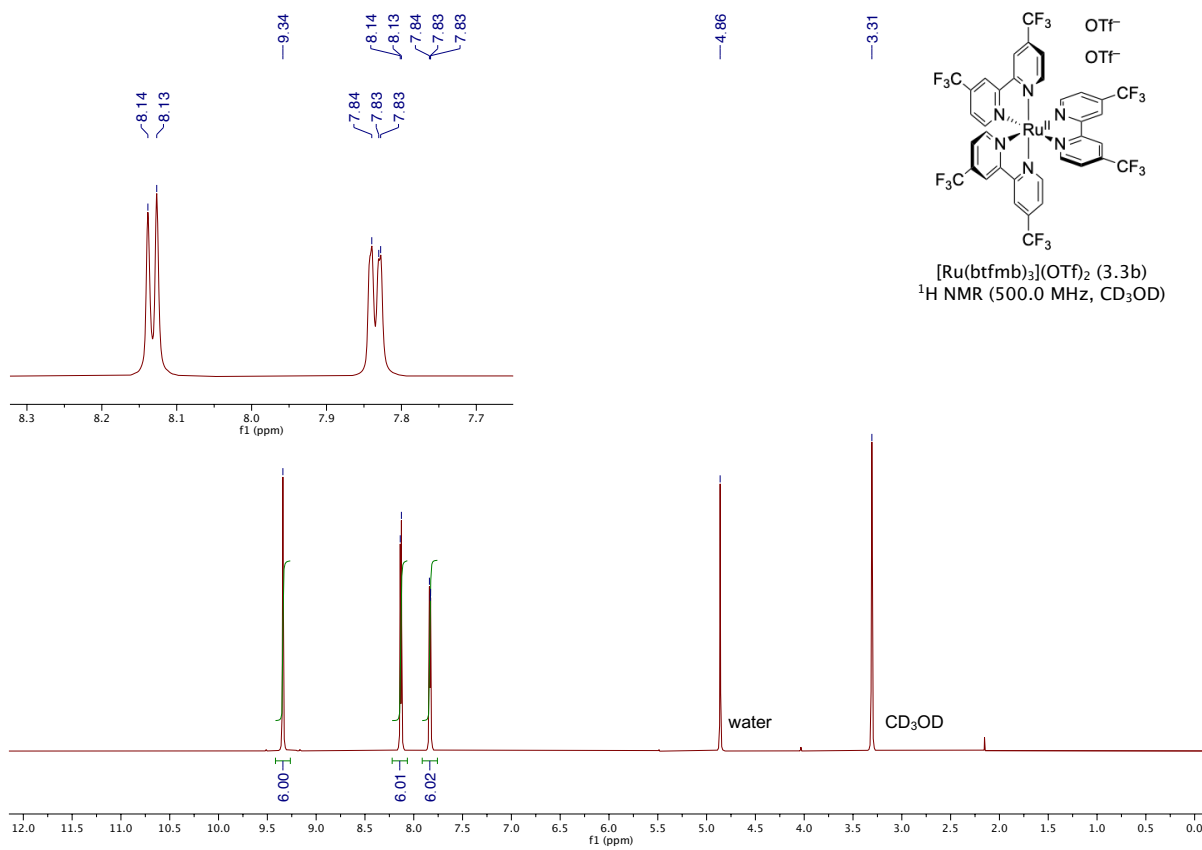




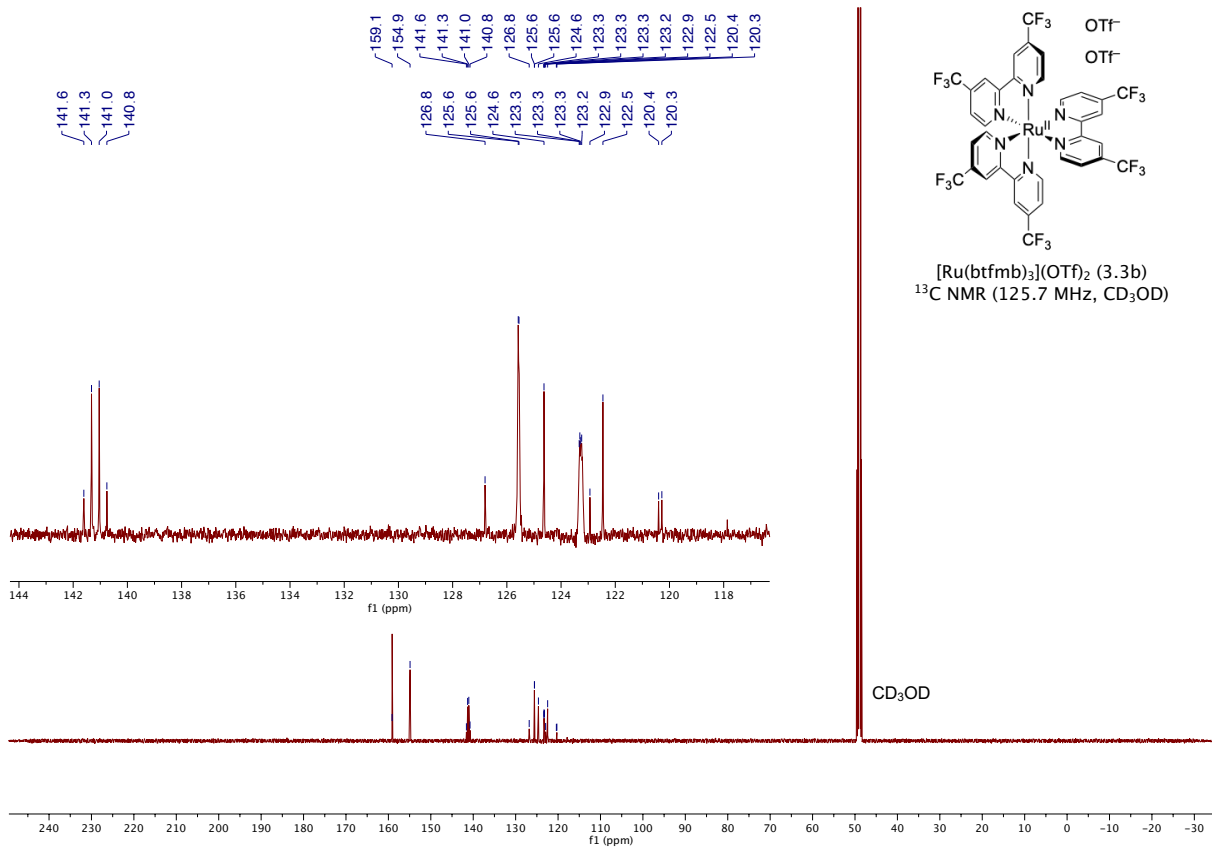


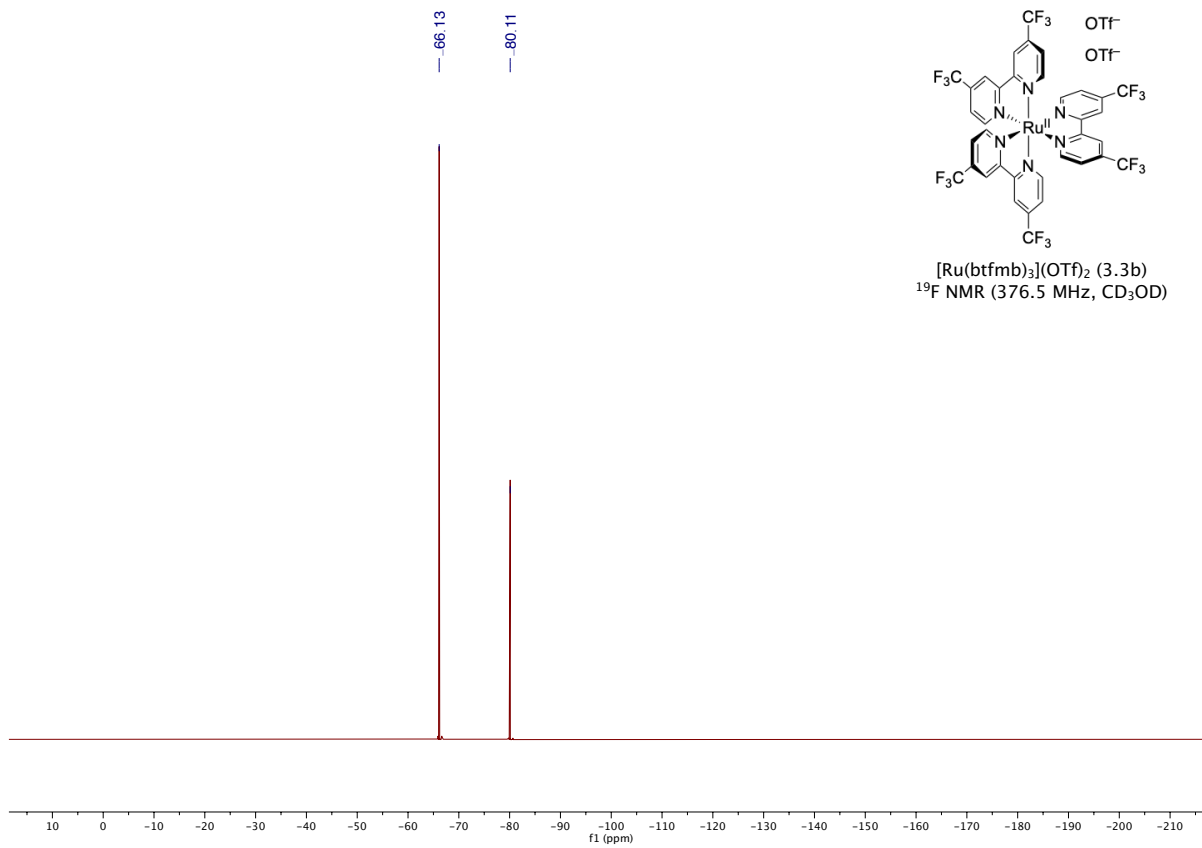


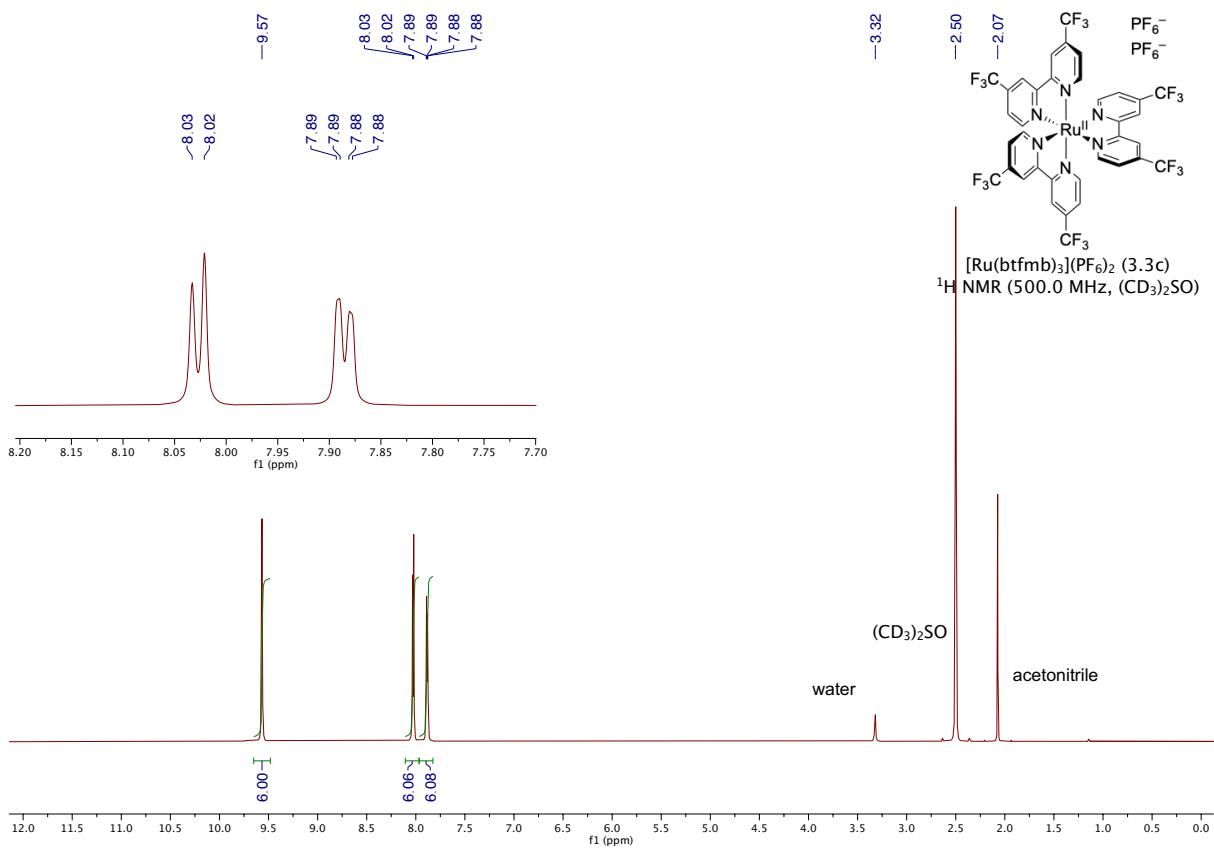


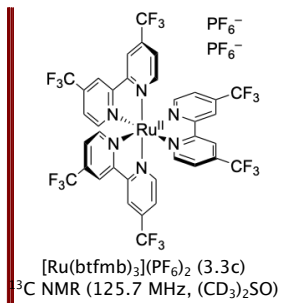
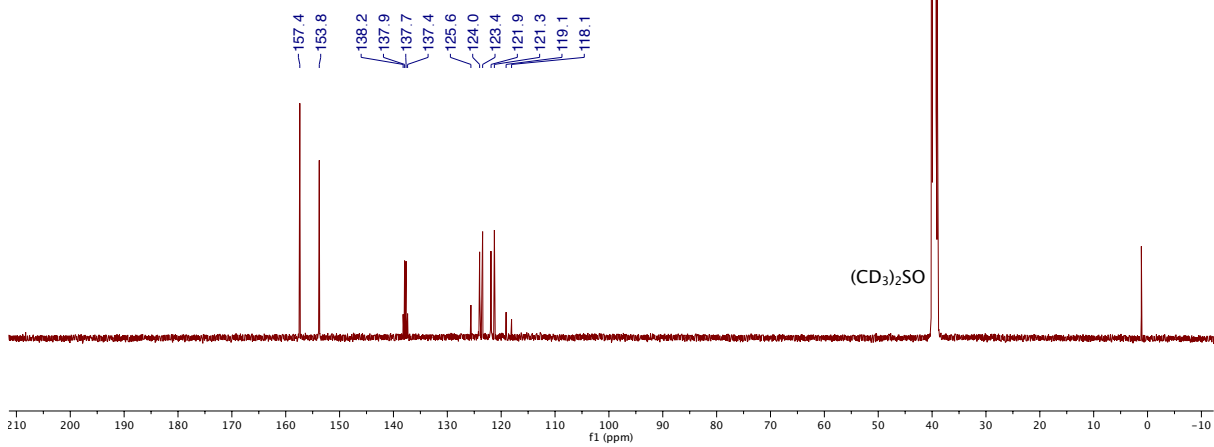
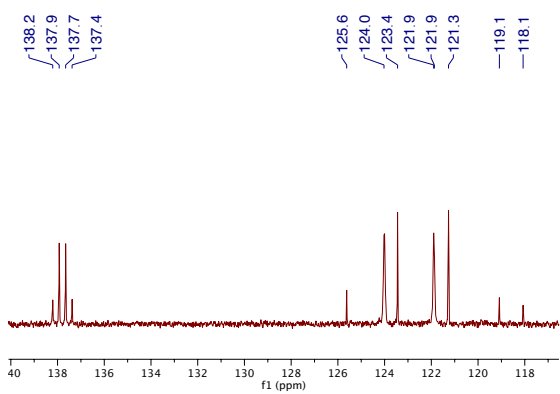


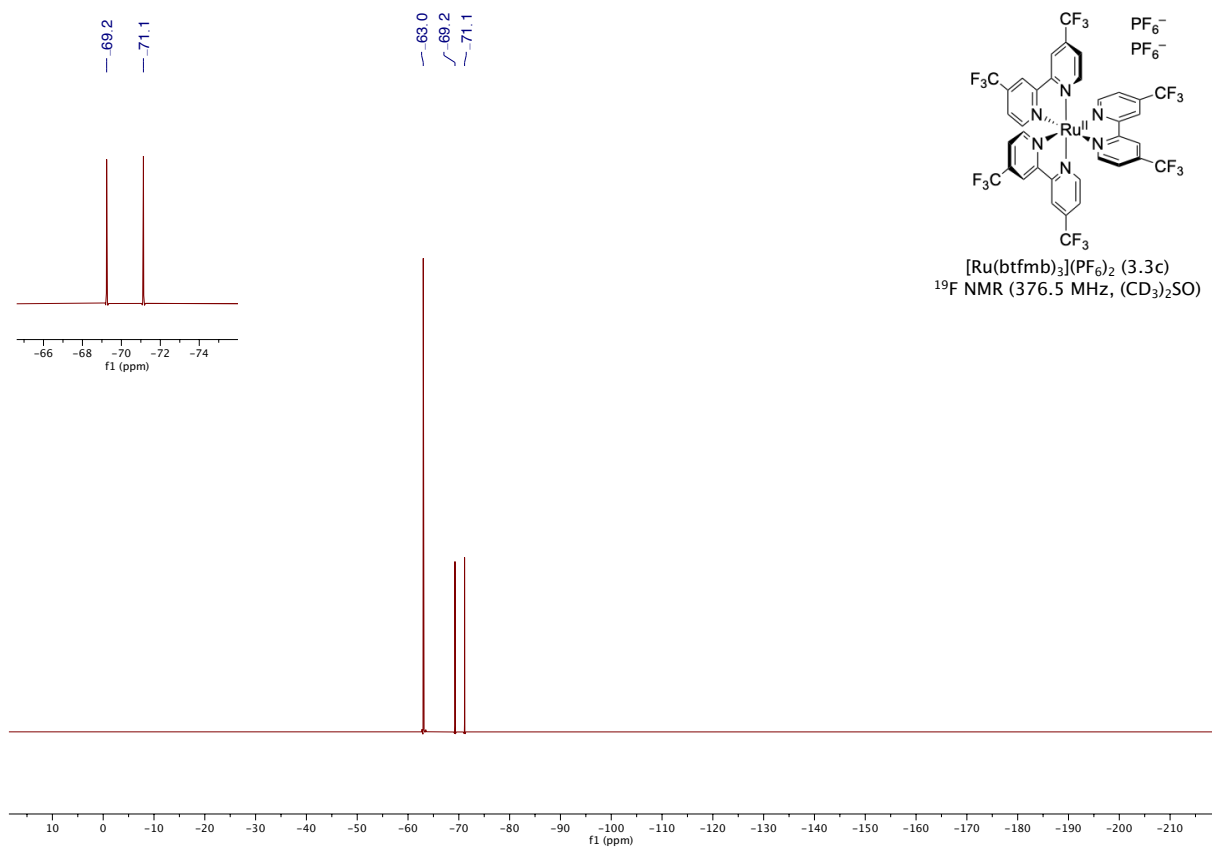


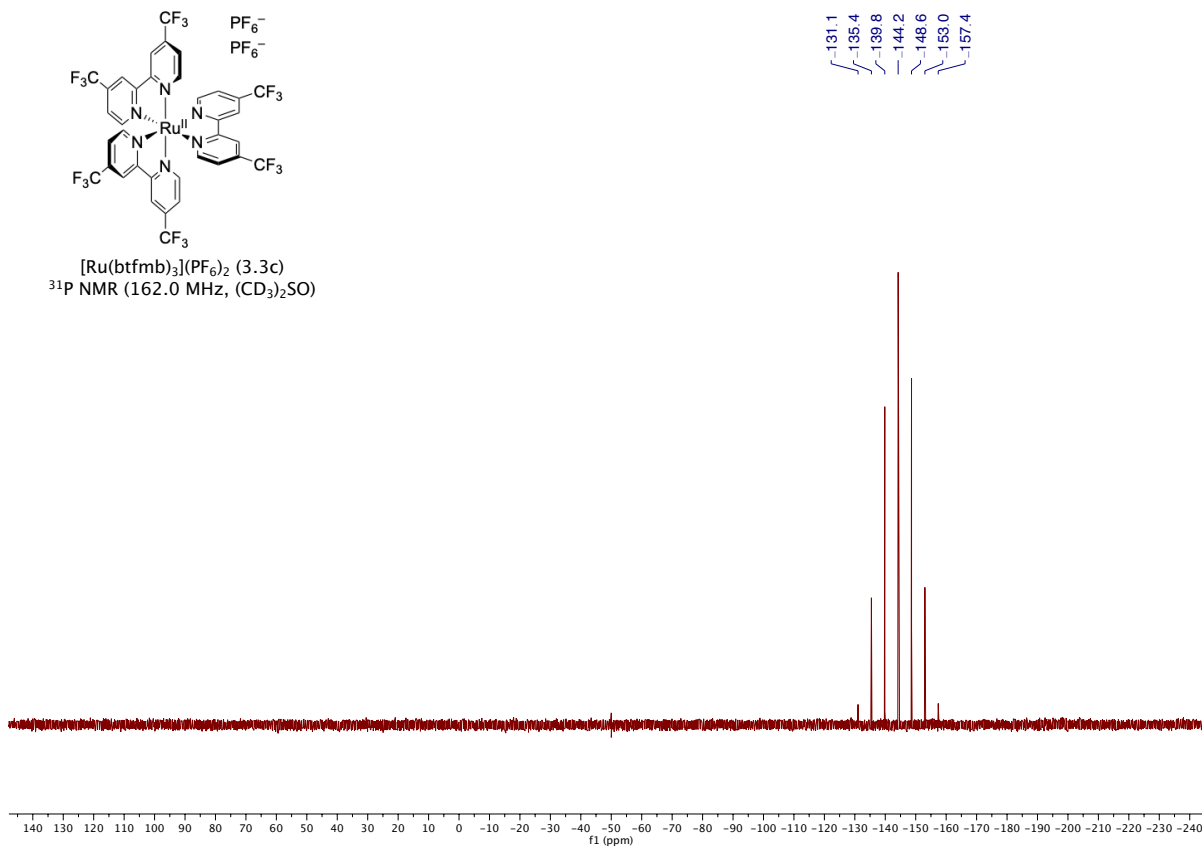
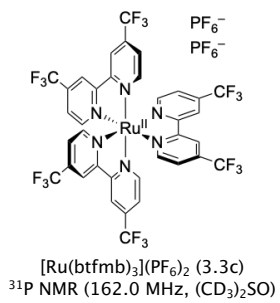


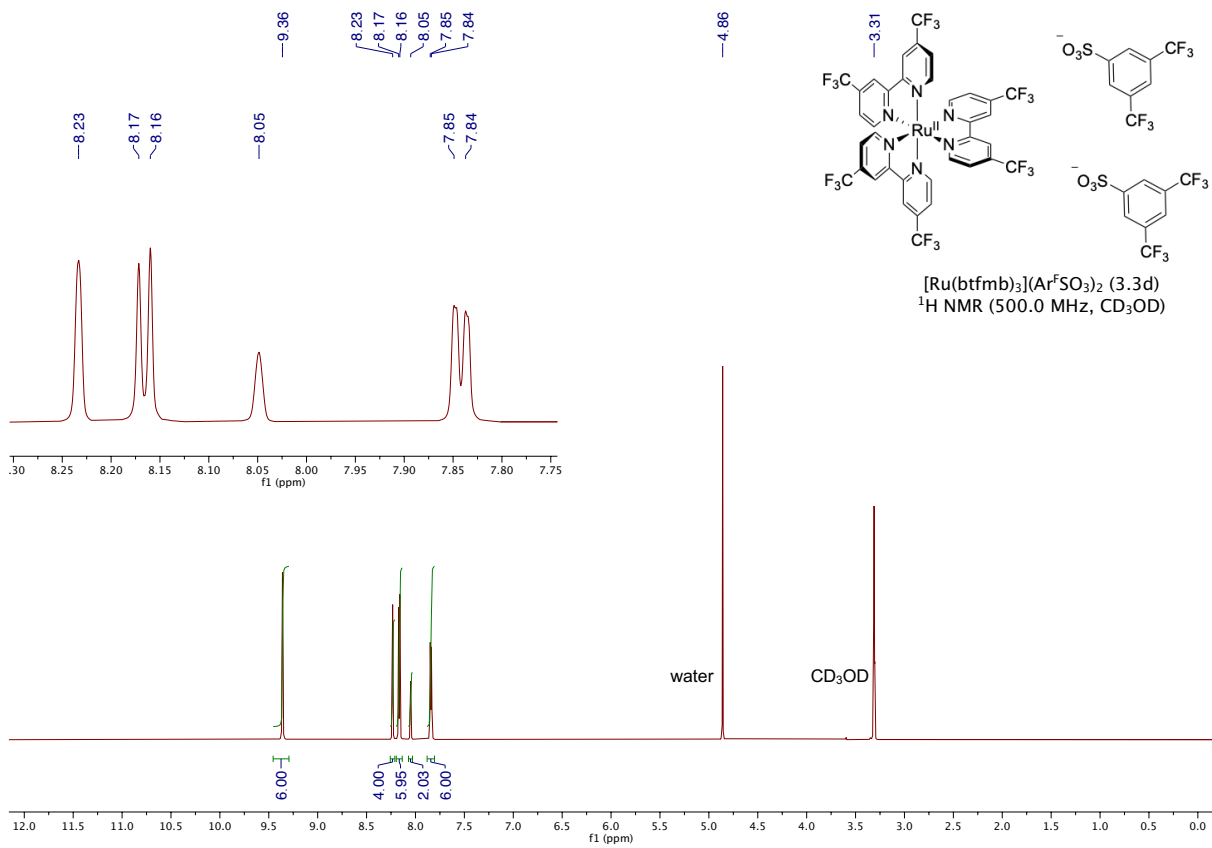


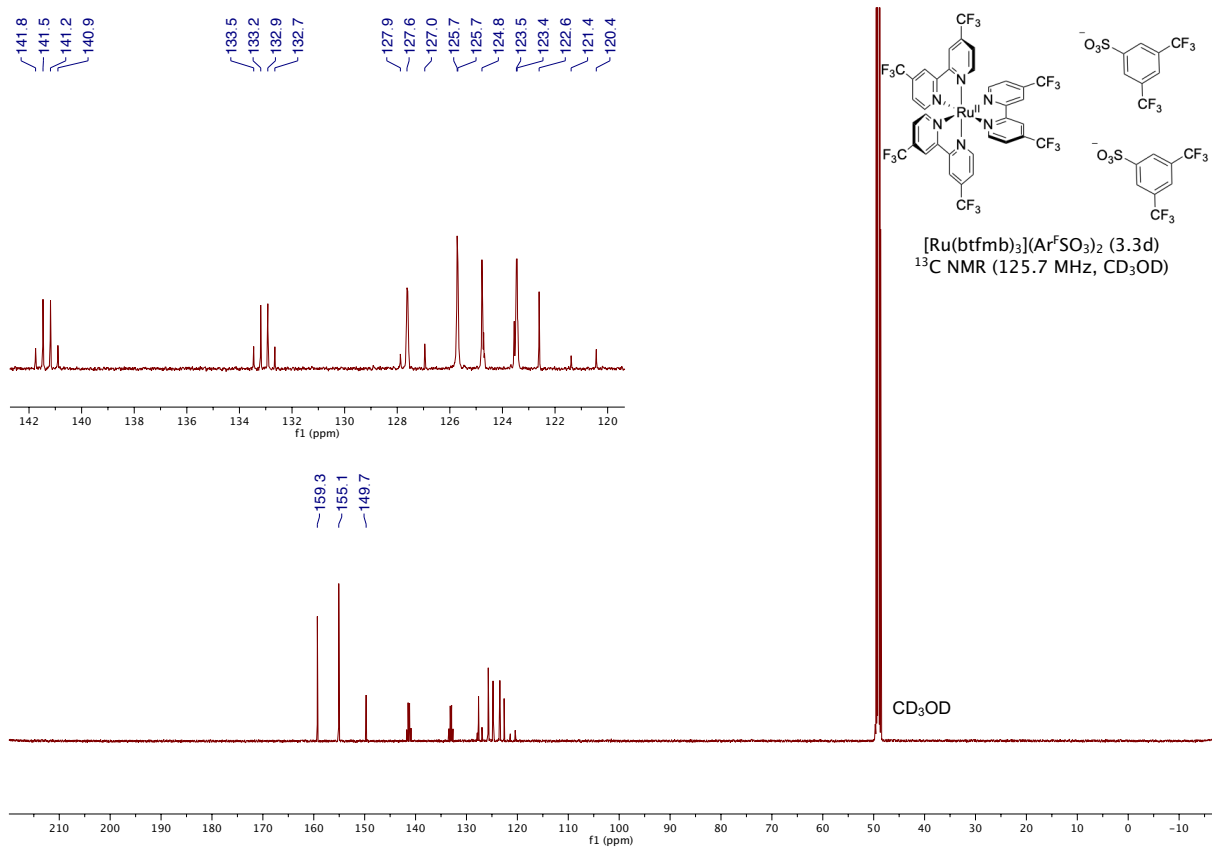




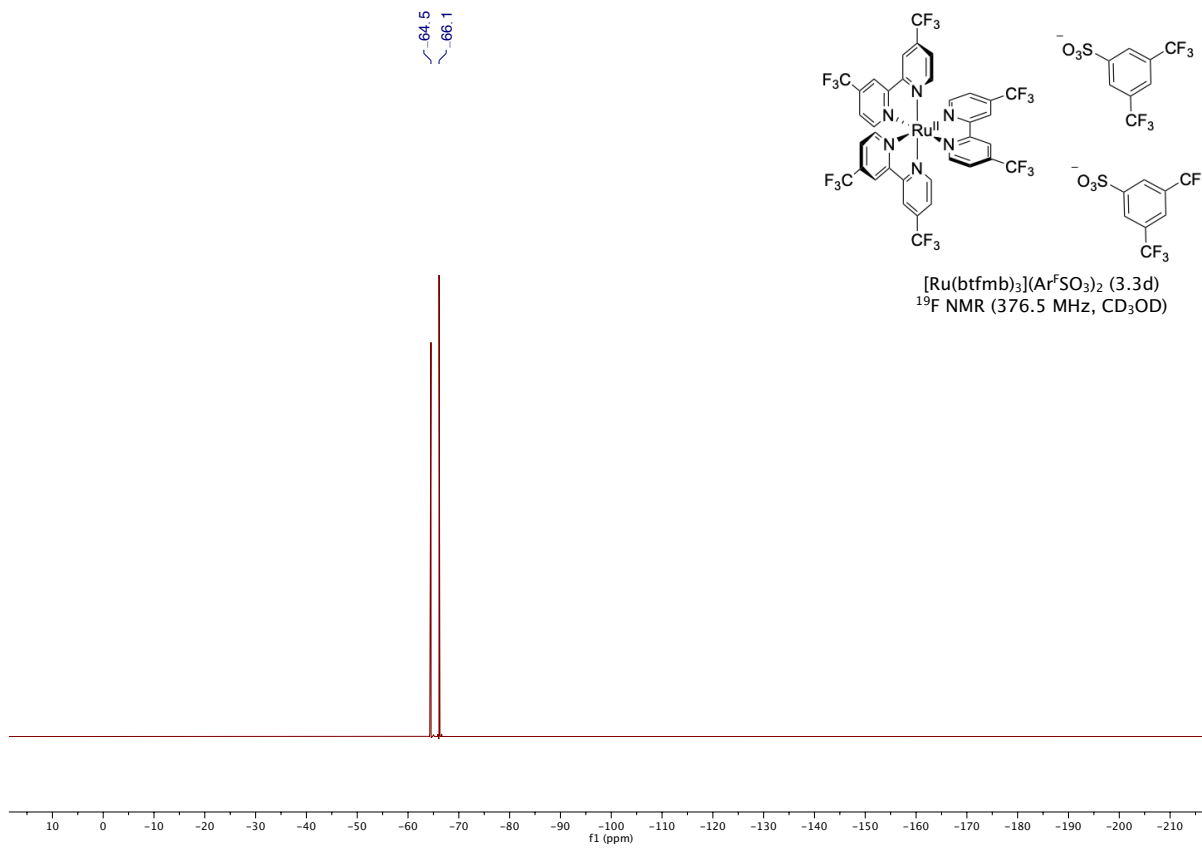


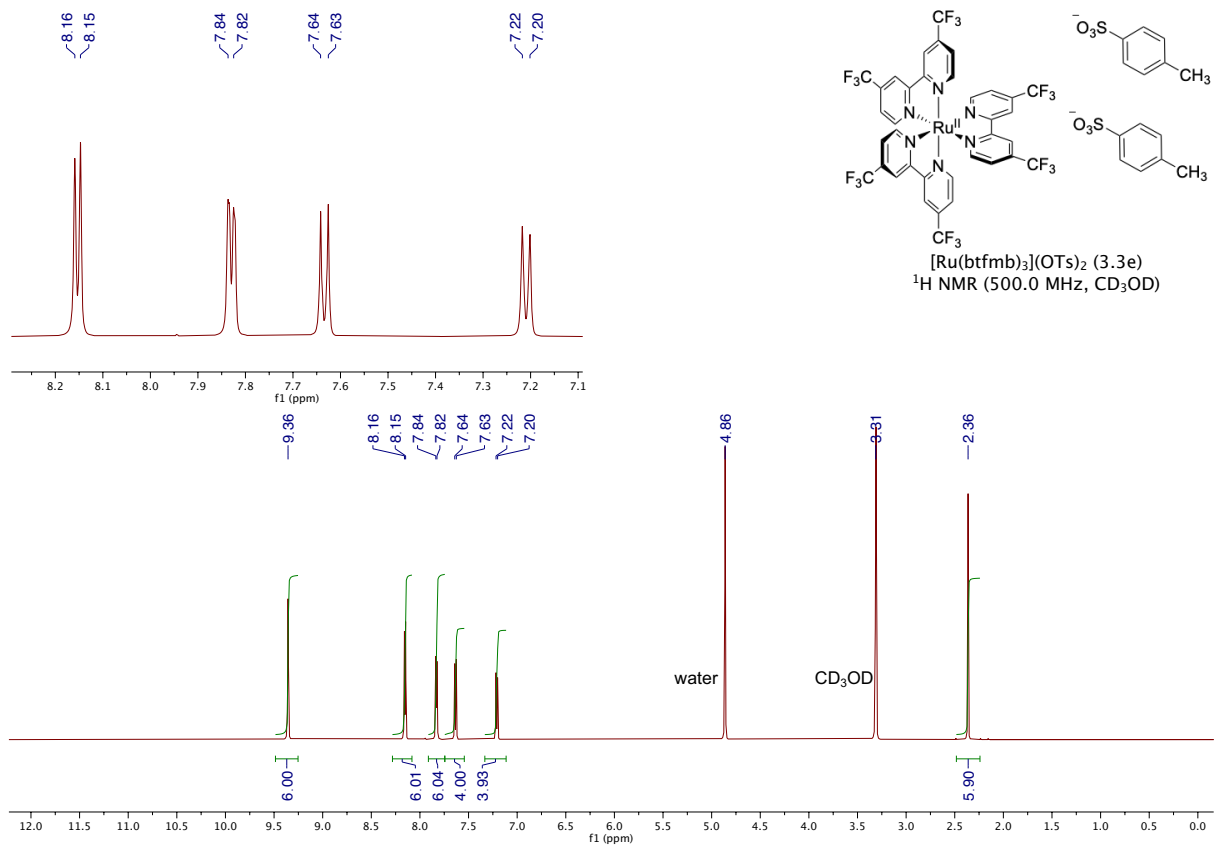


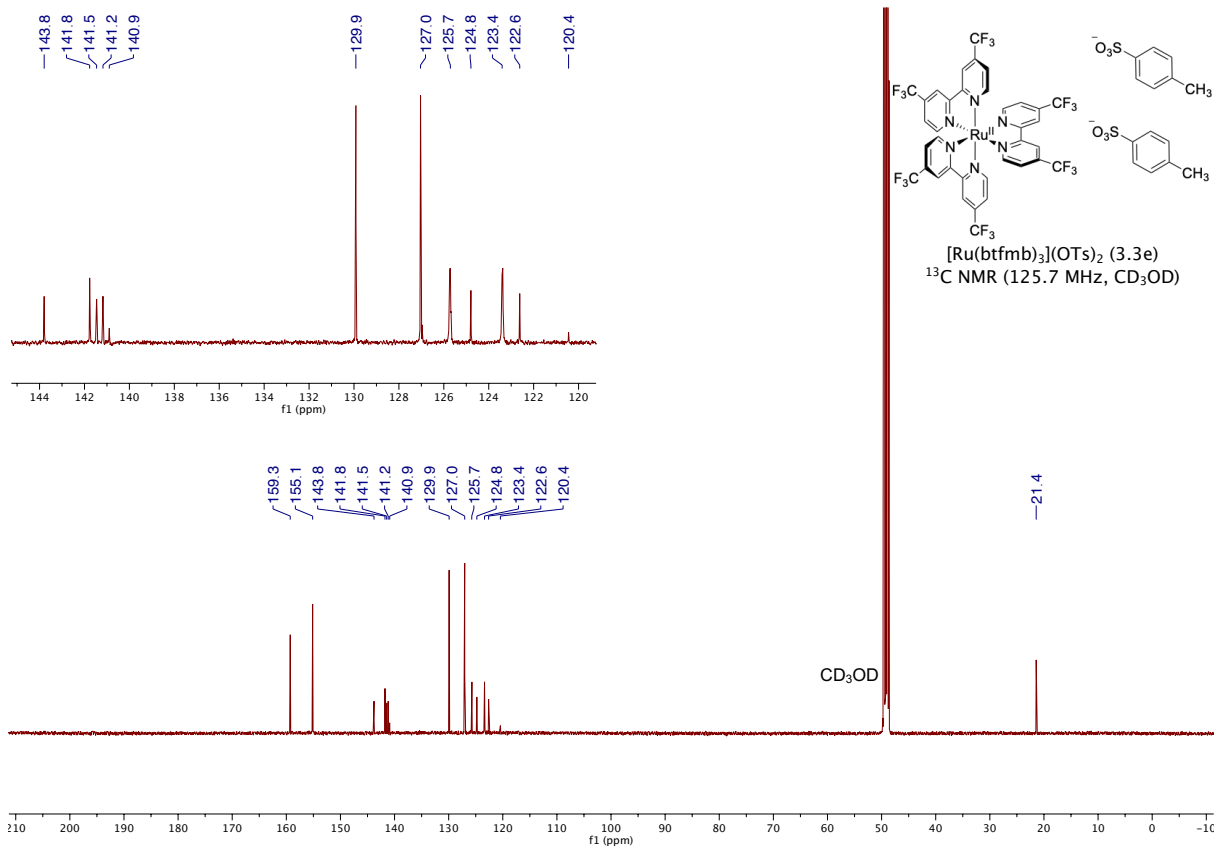


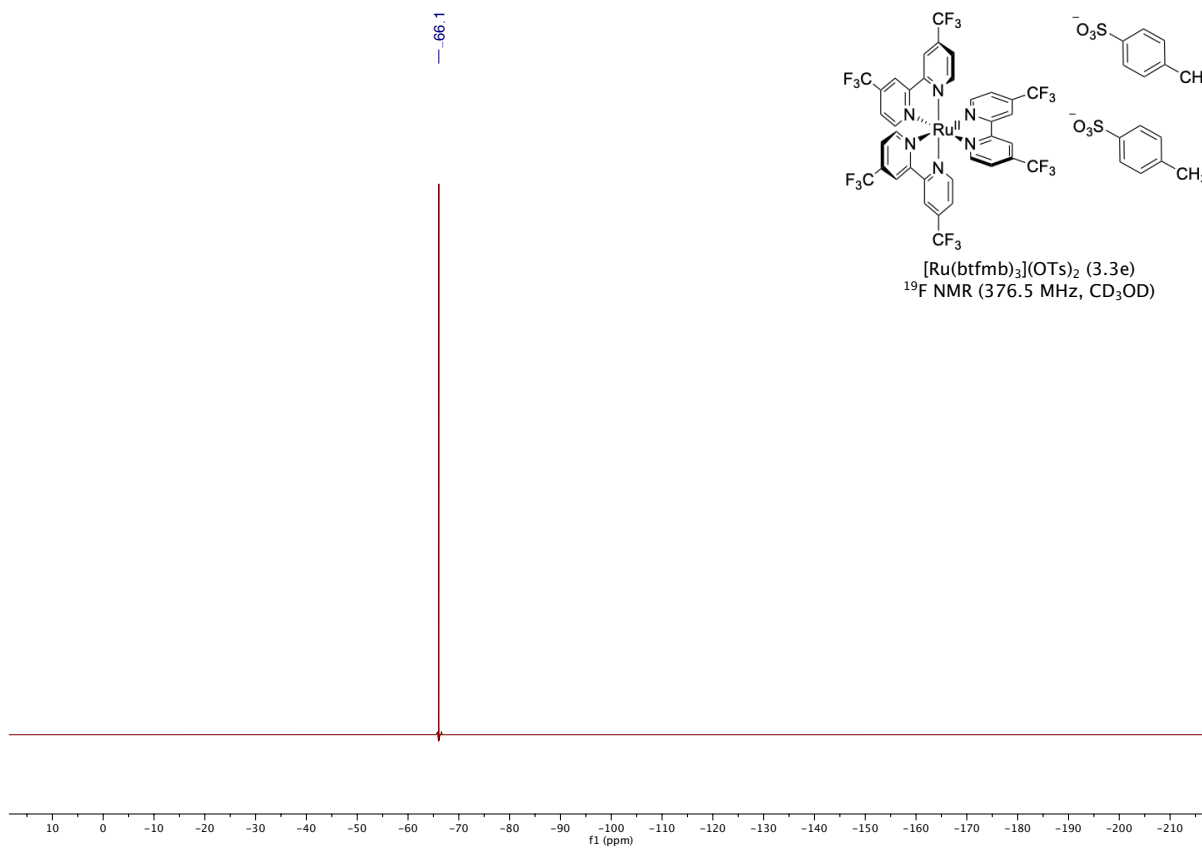


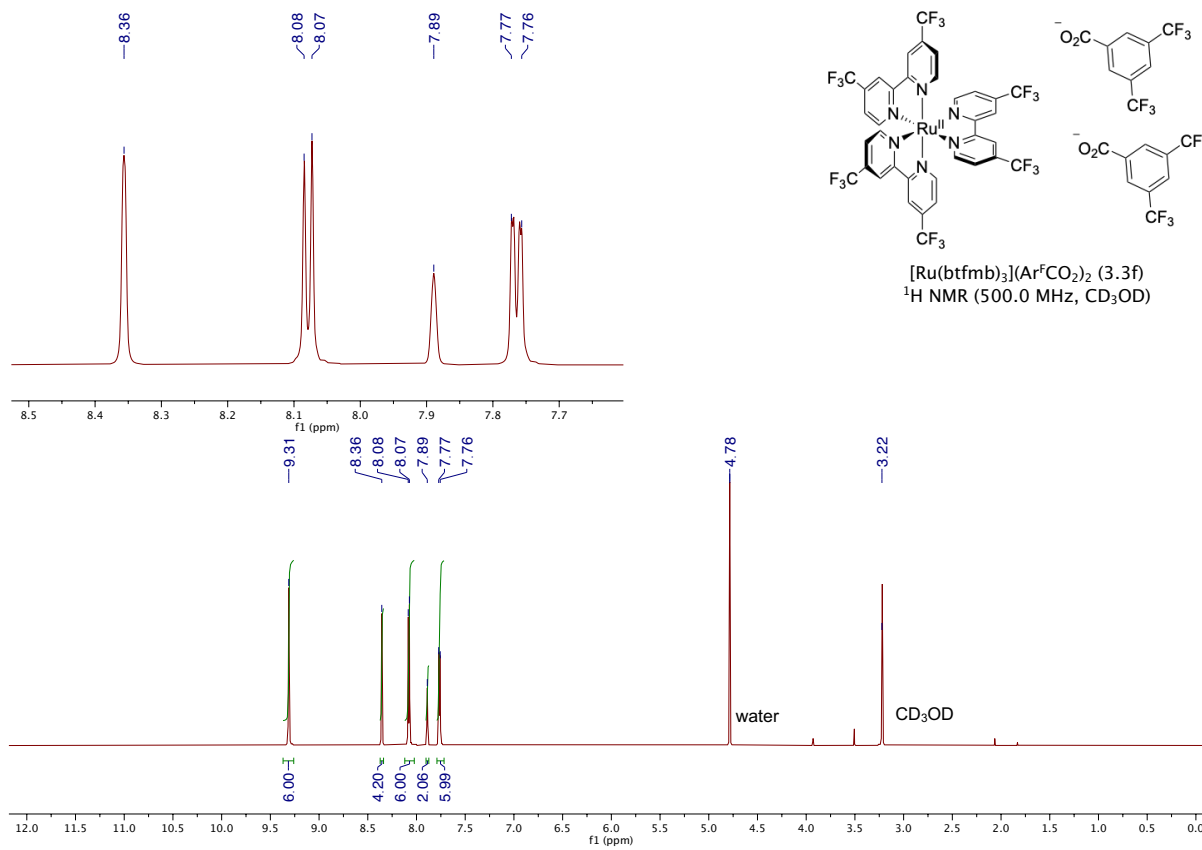


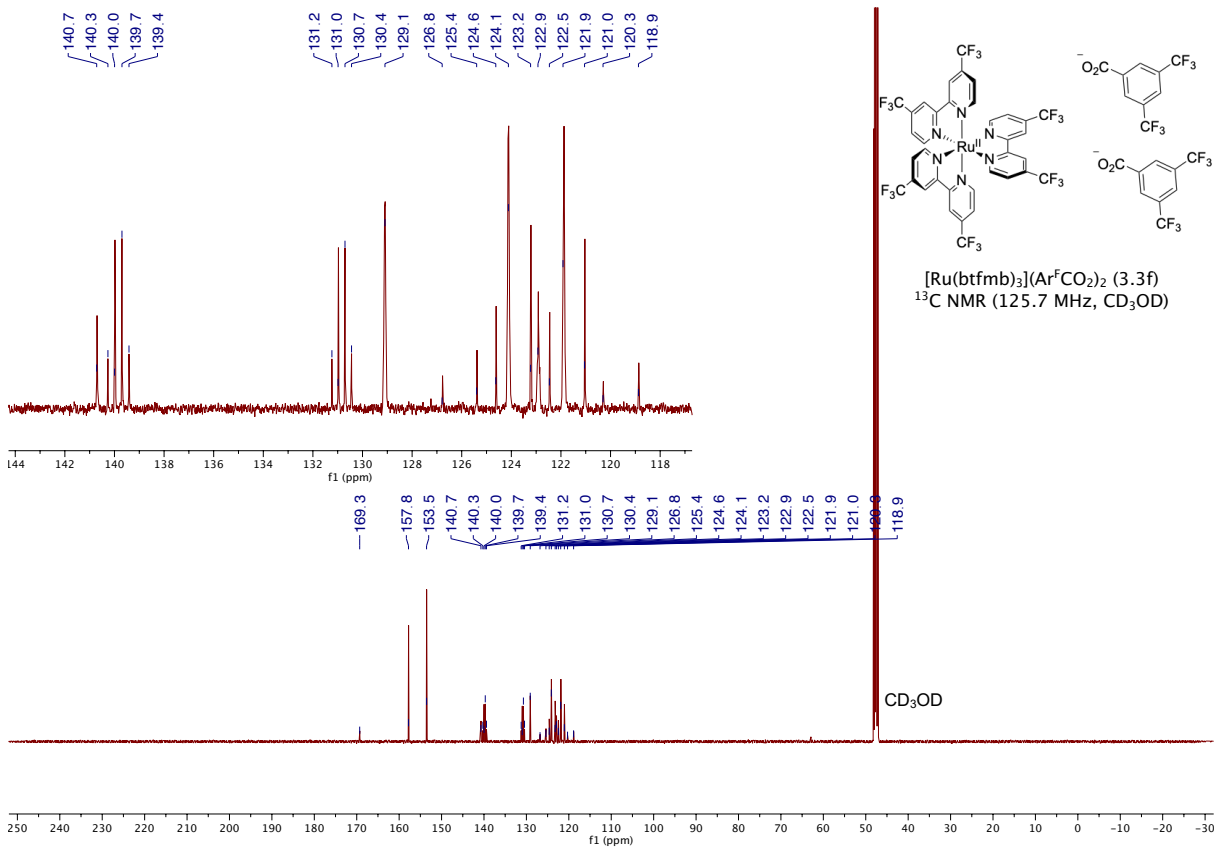


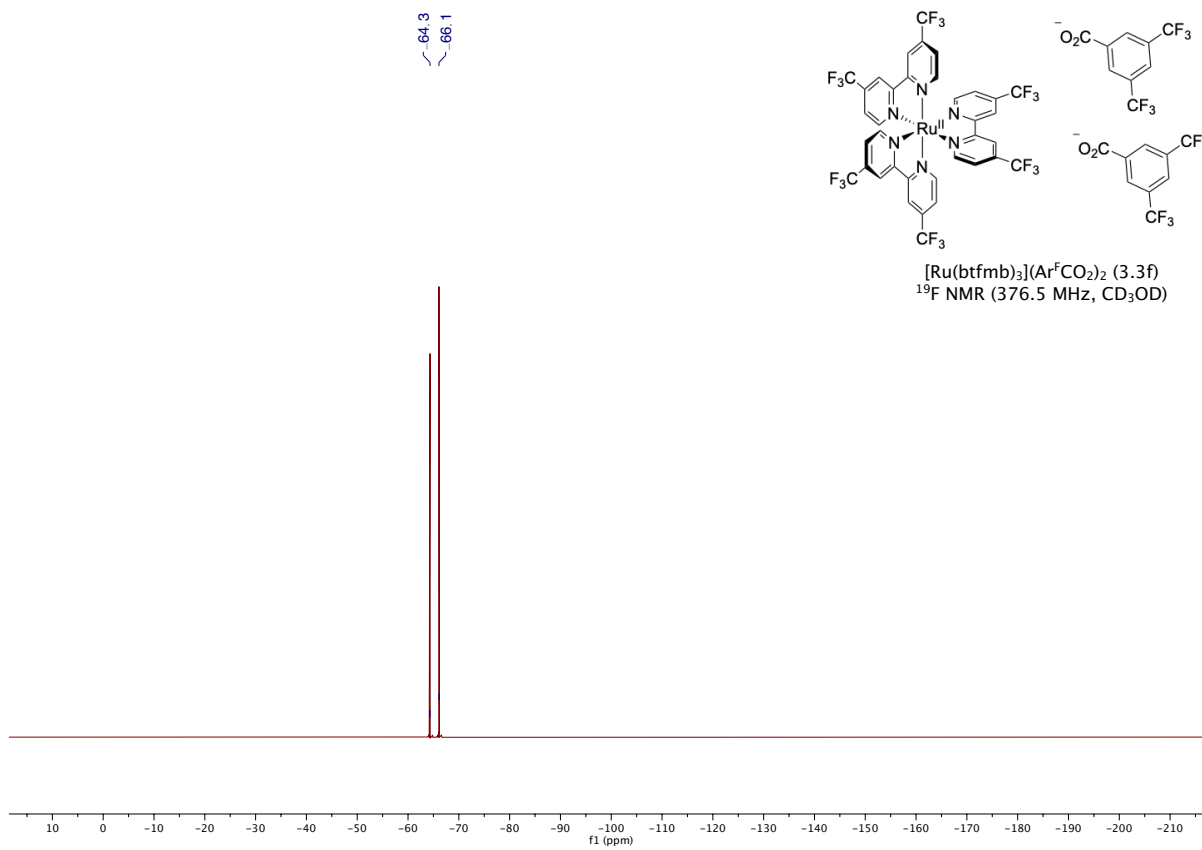


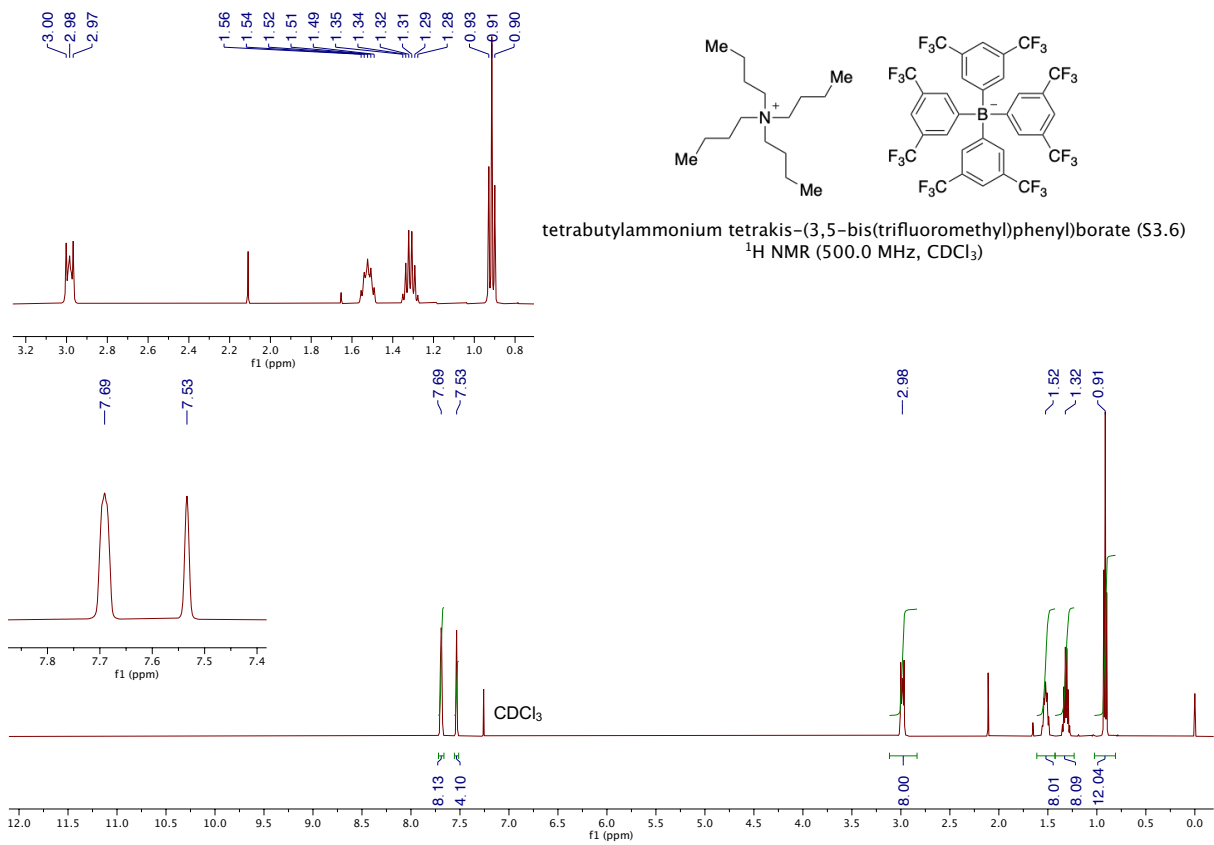




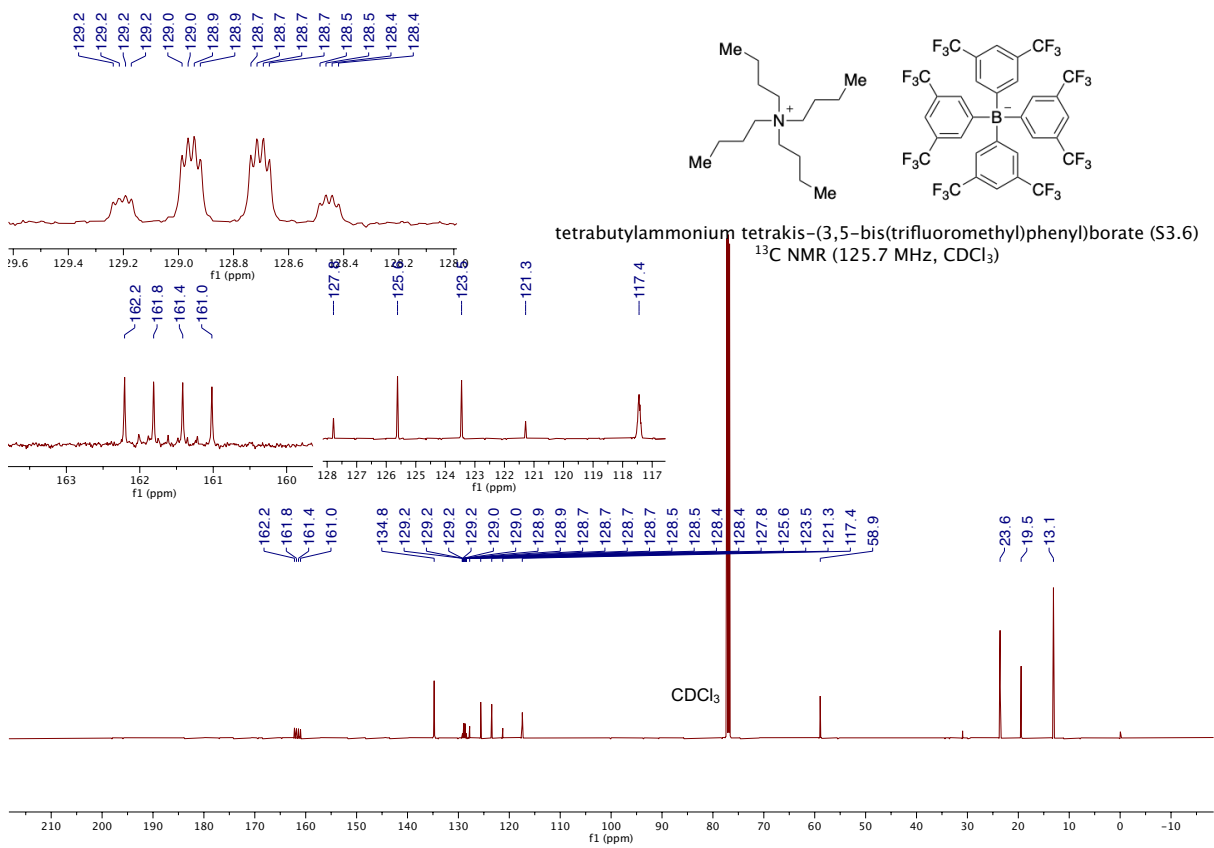




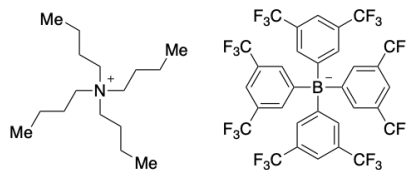




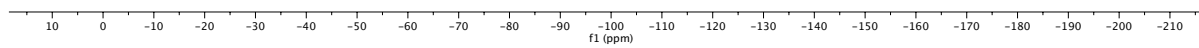


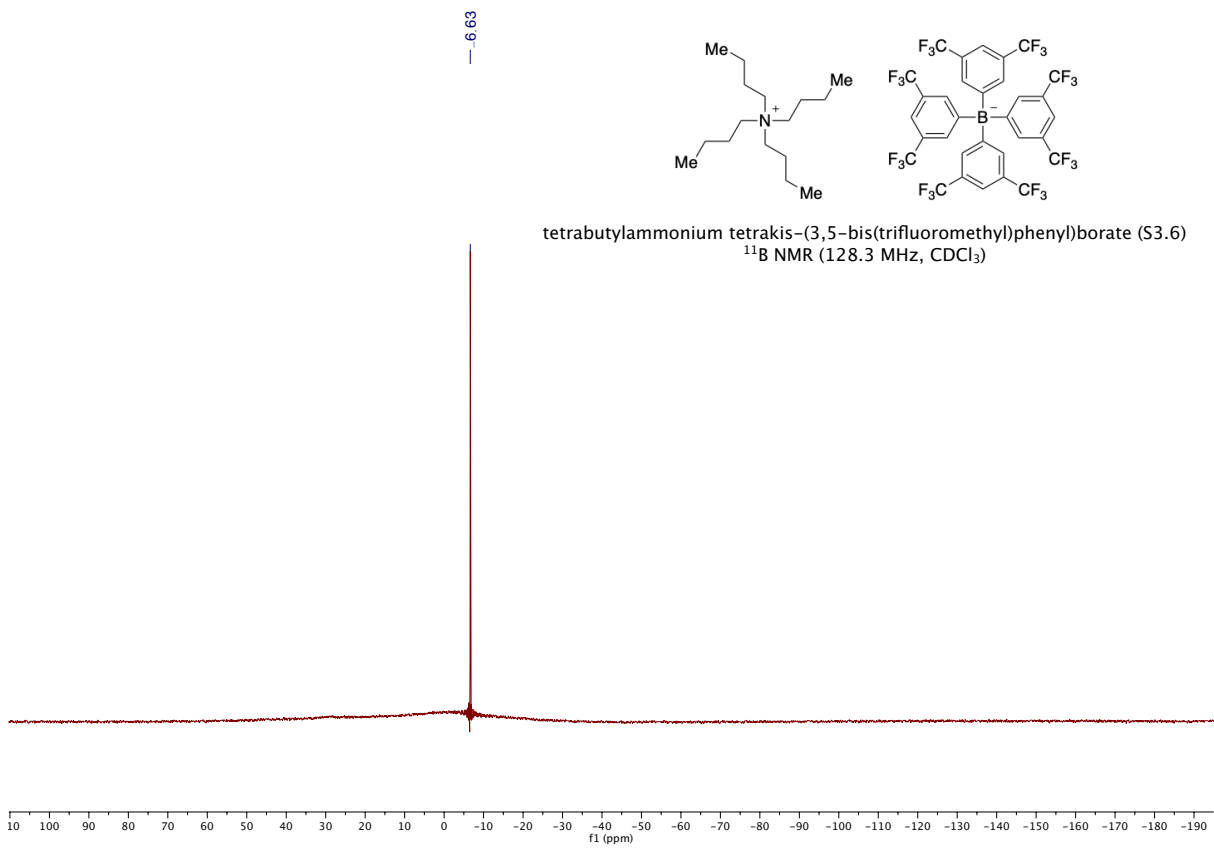


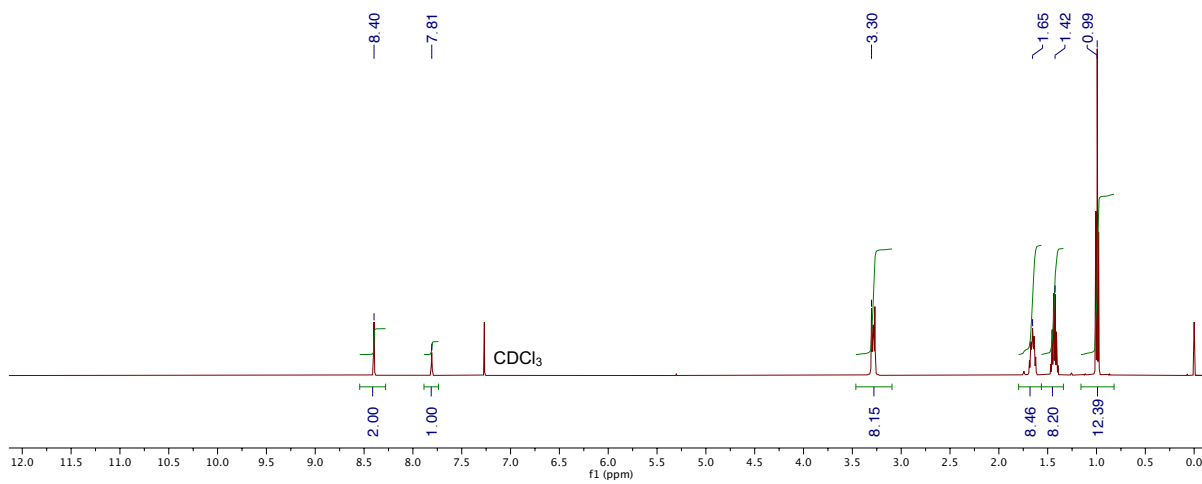
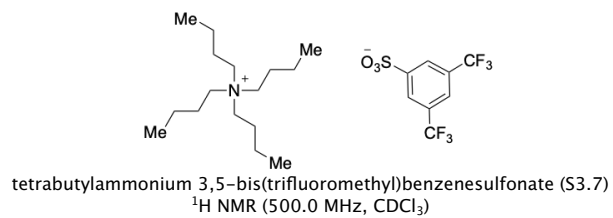
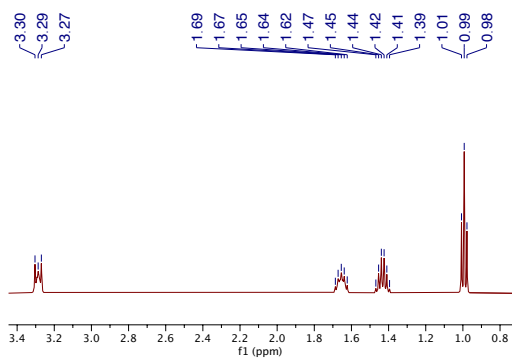
- 62.4

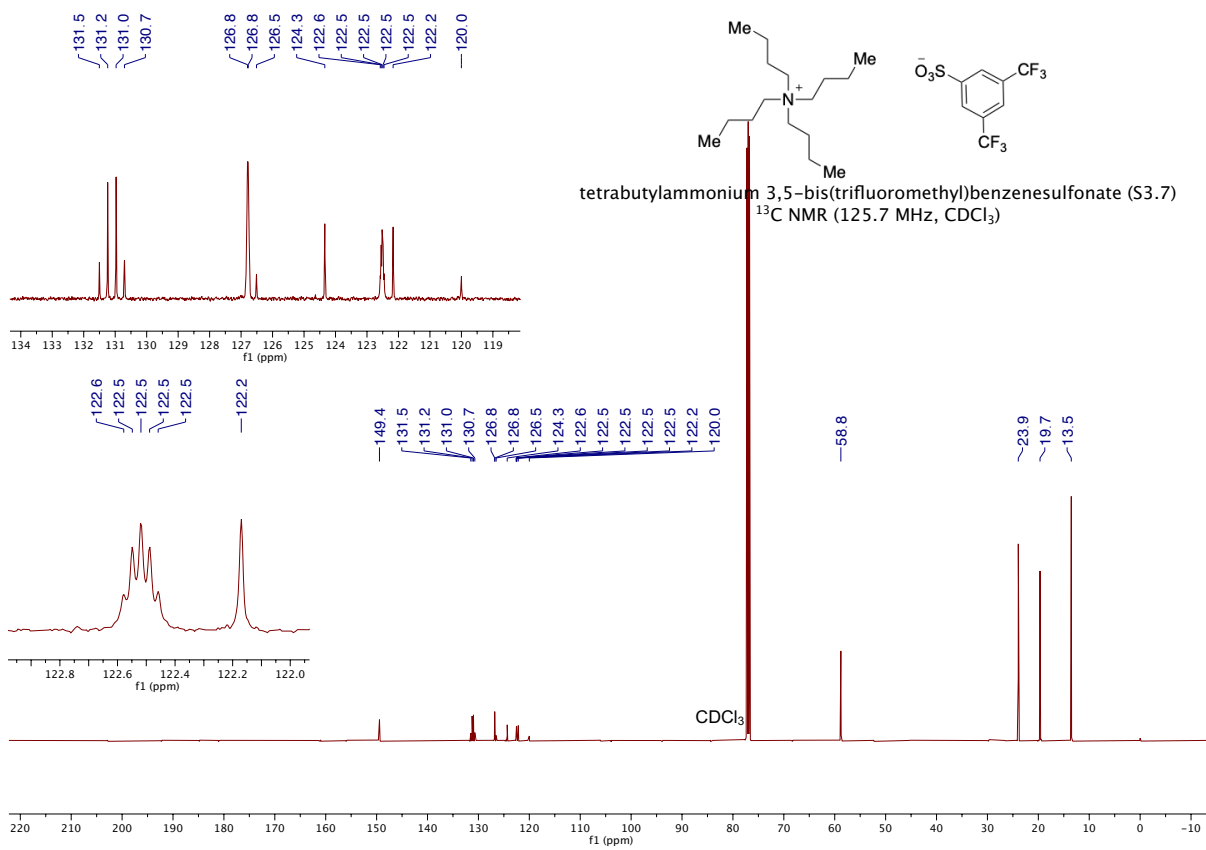


tetrabutylammonium tetrakis-(3,5-bis(trifluoromethyl)phenyl)borate (S3.6)  
<sup>19</sup>F NMR (376.5 MHz, CDCl<sub>3</sub>)

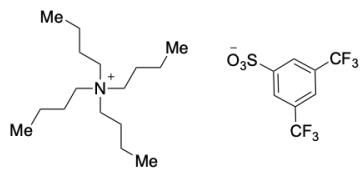




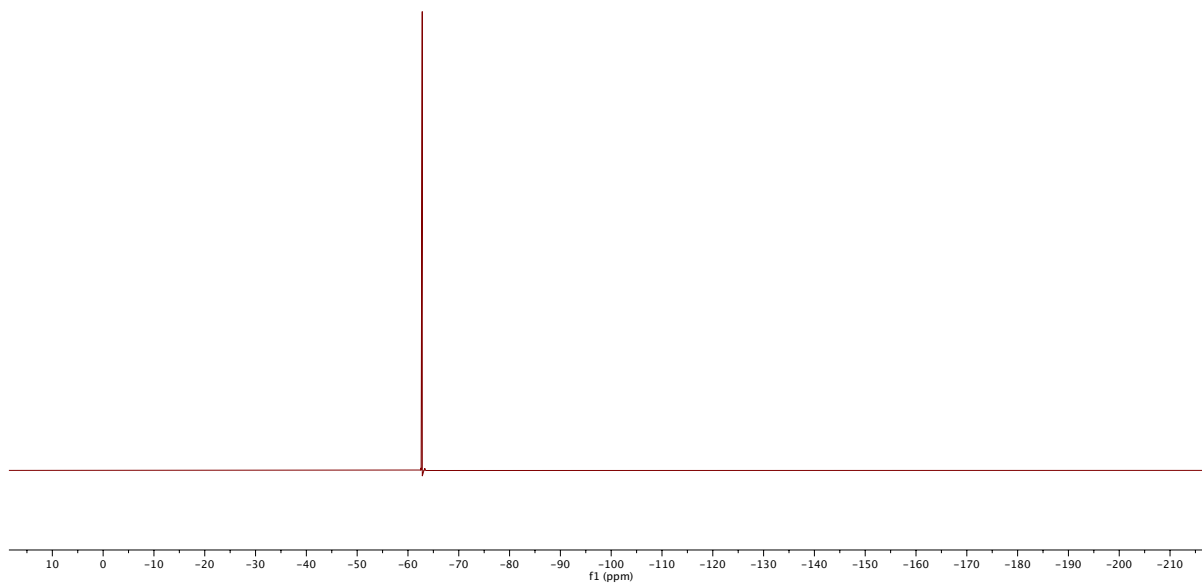


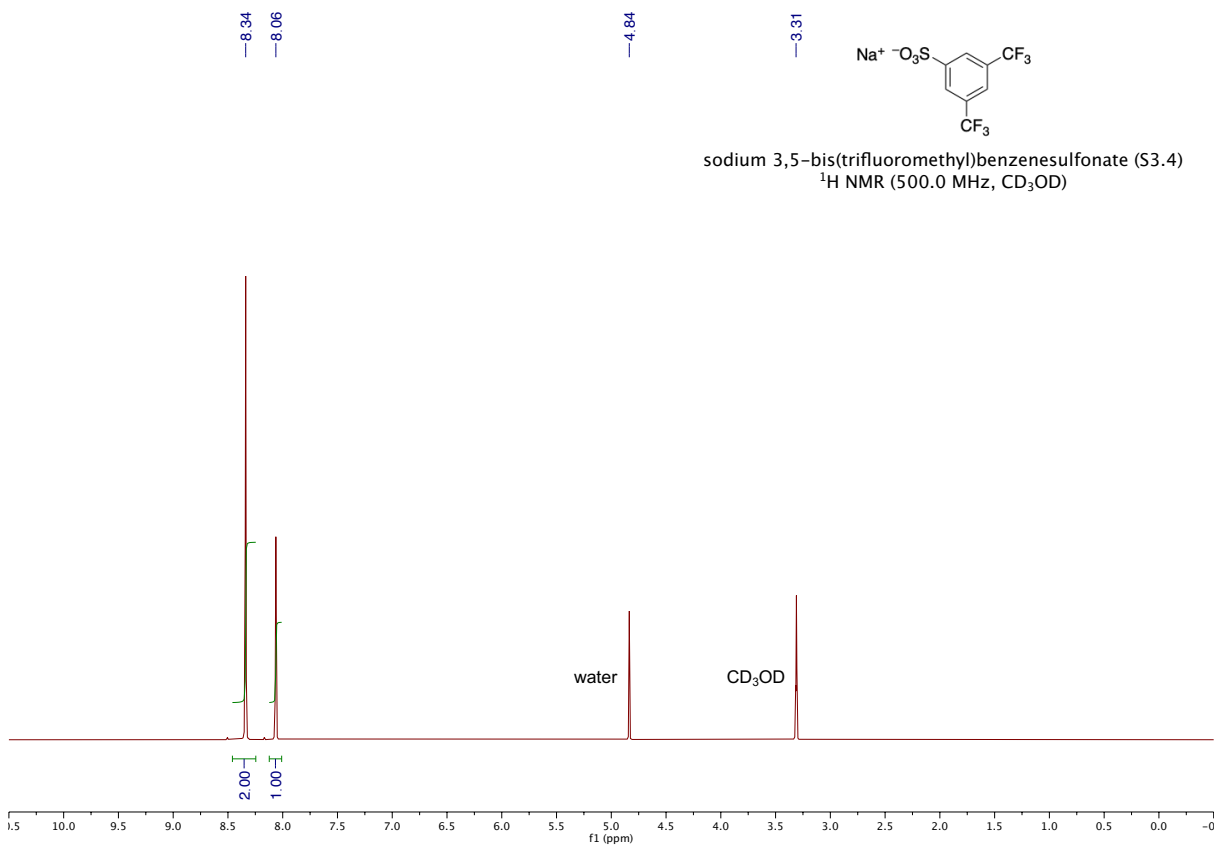


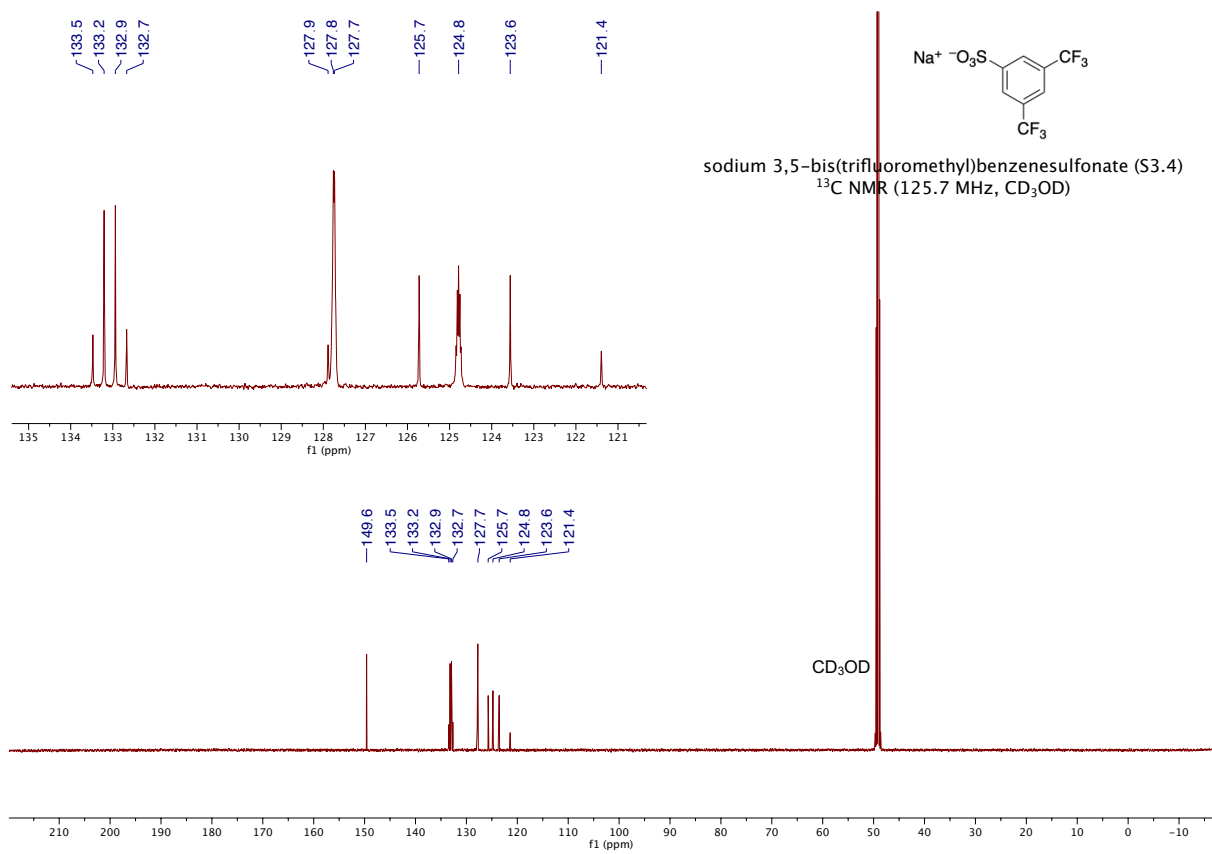
- 62.8



tetrabutylammonium 3,5-bis(trifluoromethyl)benzenesulfonate (S3.7)  
 $^{19}\text{F}$  NMR (376.5 MHz,  $\text{CDCl}_3$ )

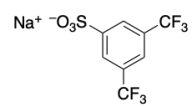




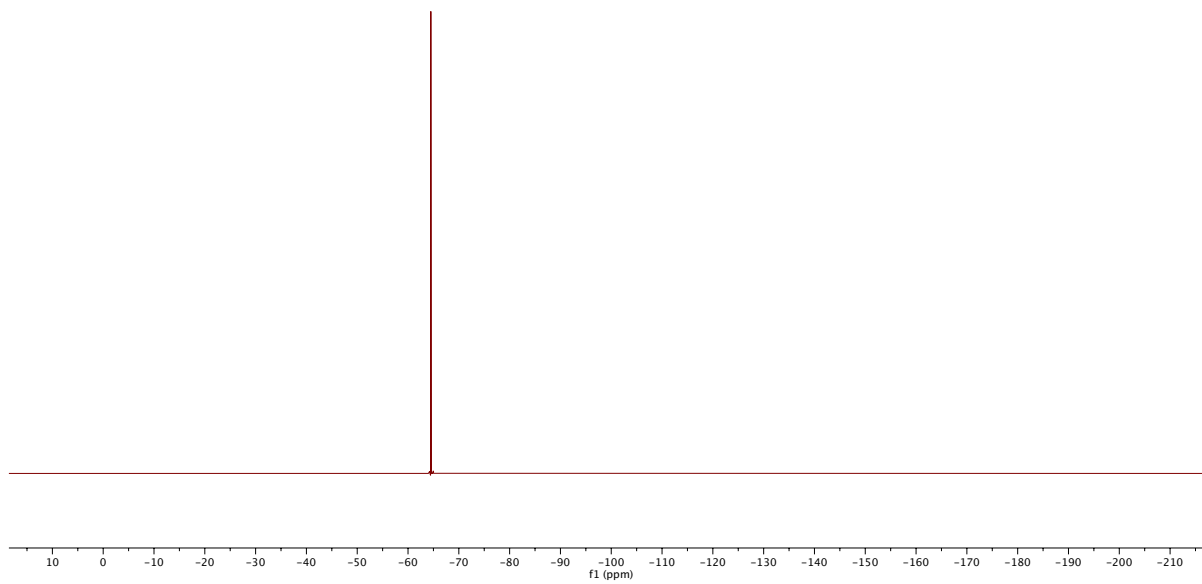


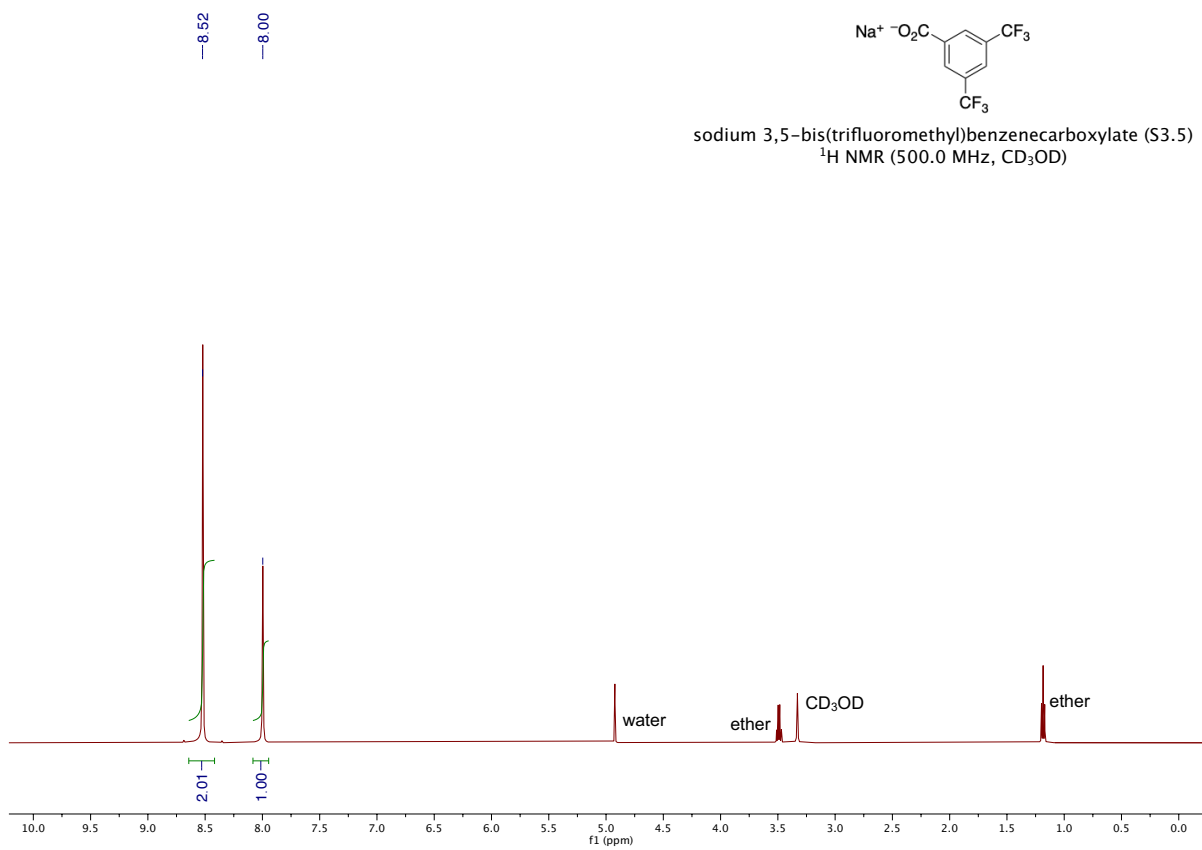


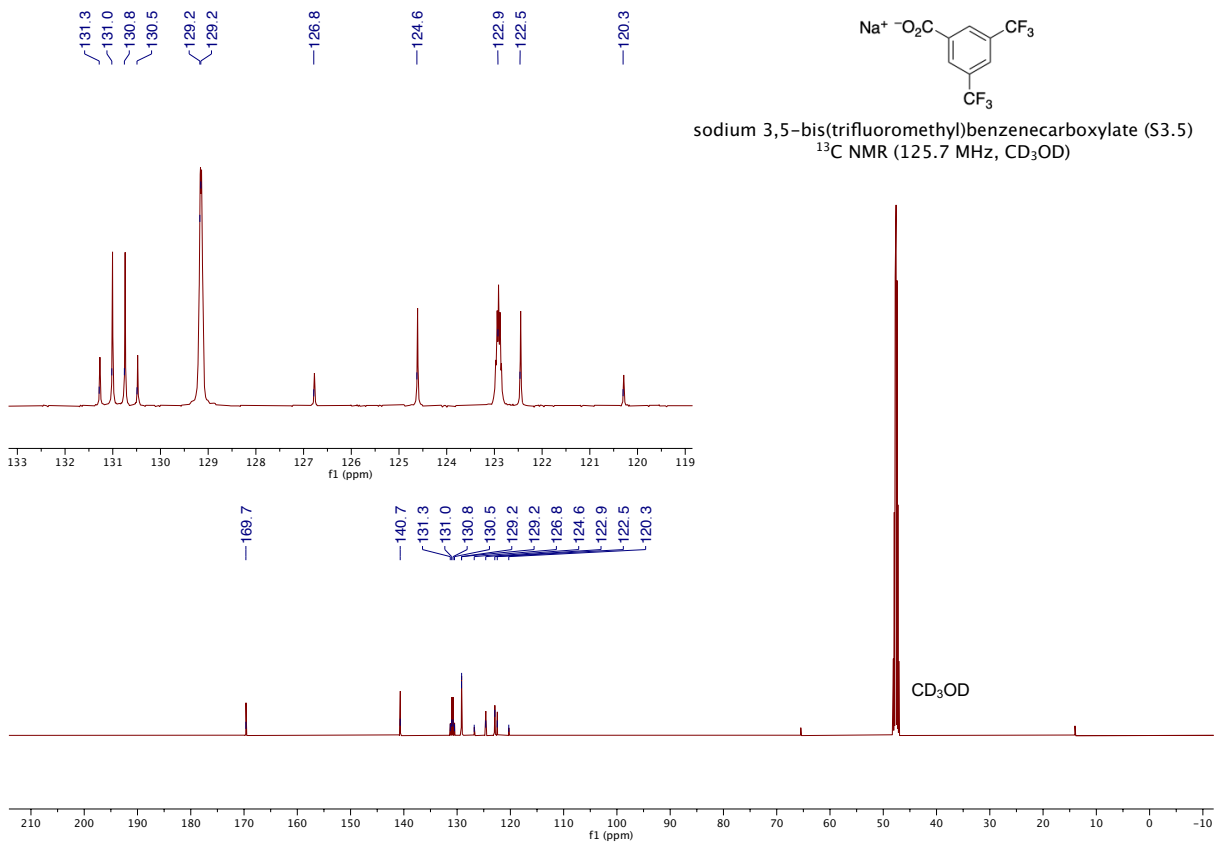
-64.5

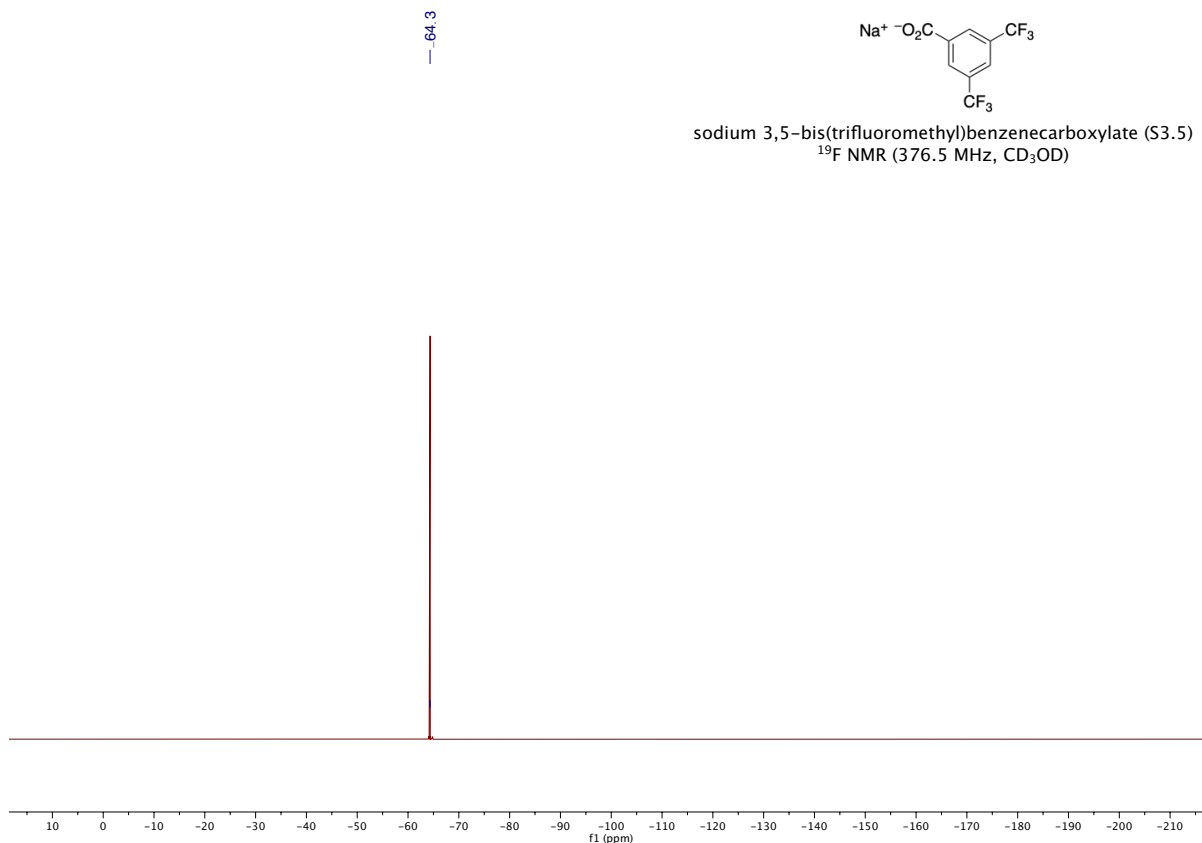


sodium 3,5-bis(trifluoromethyl)benzenesulfonate (S3.4)  
<sup>19</sup>F NMR (376.5 MHz, CD<sub>3</sub>OD)









### 3.8. References

- <sup>73</sup> (a) Kalyanasundaram, K. Photophysics, Photochemistry and Solar Energy Conversion with Tris(bipyridyl)ruthenium(II) and Its Analogues. *Coord. Chem. Rev.* **1982**, *46*, 159–244. (b) Roundhill, D. M. Photochemistry, Photophysics, and Photoredox Reactions of  $\text{Ru}(\text{bpy})_3^{2+}$  and Related Complexes. In *Modern Inorganic Chemistry: Photochemistry and Photophysics of Metal Complexes*; Springer: New York, 1994; pp 165–215.
- <sup>74</sup> Lehn, J. M.; Sauvage, J. P. Chemical Storage of Light Energy. Catalytic Generation of Hydrogen by Visible Light or Sunlight. Irradiation of Neutral Aqueous Solutions. *Nouv. J. Chim.* **1977**, *1*, 449–451.
- <sup>75</sup> O'Regan, B.; Grätzel, M. A Low-Cost, High-Efficiency Solar Cell Based on Dye-Sensitized Colloidal  $\text{TiO}_2$  Films. *Nature* **1991**, *353*, 737–740.
- <sup>76</sup> For reviews, see: (a) Narayanam, J. M. R.; Stephenson, C. R. J. Visible Light Photoredox Catalysis: Applications in Organic Synthesis. *Chem. Soc. Rev.* **2011**, *40*, 102–113. (b) Prier, C. K.; Rankic, D. A.; MacMillan, D. W. C. Visible Light Photoredox Catalysis with Transition Metal

Complexes: Applications in Organic Synthesis. *Chem. Rev.* **2013**, *113*, 5322–5363. (c) Romero, N. A.; Nicewicz, D. A. Organic Photoredox Catalysis. *Chem. Rev.* **2016**, *116*, 10075–10166. (d) Twilton, J.; Le, C.; Zhang, P.; Shaw, M. H.; Evans, R. W.; MacMillan, D. W. C. The Merger of Transition Metal and Photocatalysis. *Nature Rev. Chem.* **2017**, *1*, No. 0052. (e) Zou, Y. Q.; Hörmann, F. M.; Bach, T. Iminium and Enamine Catalysis in Enantioselective Photochemical Reactions. *Chem. Soc. Rev.* **2018**, *47*, 278–290. (f) Silvi, M.; Melchiorre, P. Enhancing the Potential of Enantioselective Organocatalysis with Light. *Nature* **2018**, *554*, 41–49.

<sup>77</sup> Juris, A.; Balzani, V.; Barigelletti, F.; Campagna, S.; Belser, P.; von Zelewsky, A. Ru(II) Polypyridine Complexes: Photophysics, Photochemistry, Electrochemistry, and Chemiluminescence. *Coord. Chem. Rev.* **1988**, *84*, 85–277.

<sup>78</sup> (a) Lin, S.; Ischay, M. A.; Fry, C. G.; Yoon, T. P. Radical Cation Diels–Alder Cycloadditions by Visible Light Photocatalysis. *J. Am. Chem. Soc.* **2011**, *133*, 19350–19353. (b) Lin, S.; Padilla, C. E.; Ischay, M. A.; Yoon, T. P. Visible Light Photocatalysis of Intramolecular Radical Cation Diels–Alder Cycloadditions. *Tetrahedron Lett.* **2012**, *53*, 3073–3076. (c) Lin, S. S.; Lies, S. D.; Gravatt, C. S.; Yoon, T. P. Radical Cation Cycloadditions Using Cleavable Redox Auxiliaries. *Org. Lett.* **2017**, *19*, 368–371.

<sup>79</sup> (a) Crutchley, R. J.; Lever, A. B. P. Ruthenium(II) Tris- (bipyrazyl) Dication – A New Photocatalyst. *J. Am. Chem. Soc.* **1980**, *102*, 7128–7129. (b) Rillema, D. P.; Allen, G.; Meyer, T. J.; Conrad, D. Redox Properties of Ruthenium(II) Tris Chelate Complexes Containing the Ligands 2,2'-bipyrazine, 2,2'-bipyridine, and 2,2'- bipyrimidine. *Inorg. Chem.* **1983**, *22*, 1617–1622.

<sup>80</sup> Several other photocatalytic radical cation Diels–Alder reactions have been reported using alternate photocatalysts. For leading references, see: (a) Stevenson, S. M.; Shores, M. P.; Ferreira, E. M. Photooxidizing Chromium Catalysts for Promoting Radical Cation Cycloadditions. *Angew. Chem., Int. Ed.* **2015**, *54*, 6506–6510. (b) Pitre, S. P.; Scaiano, J. C.; Yoon, T. P. Photocatalytic Indole Diels–Alder Cycloadditions Mediated by Heterogenous Platinum- Modified Titanium Dioxide. *ACS Catal.* **2017**, *7*, 6440–6444. (c) Gieseler, A.; Steckhan, E.; Wiest, O.; Knoch, F. Photochemically Induced Radical Cation Diels–Alder Reaction of Indole and Electron- Rich Dienes. *J. Org. Chem.* **1991**, *56*, 1405–1411.

<sup>81</sup> Bauld, N. L. Cation Radical Cycloadditions and Related Sigmatropic Reactions. *Tetrahedron* **1989**, *45*, 5307–5363.

<sup>82</sup> Cismesia, M. A.; Yoon, T. P. Characterizing Chain Processes in Visible Light Photoredox Catalysis. *Chem. Sci.* **2015**, *6*, 5426–5434.

<sup>83</sup> Furue, M.; Maruyama, K.; Oguni, T.; Naiki, M.; Kamachi, M. Trifluoromethyl-substituted 2,2'-bipyridine Ligands. Synthetic Control of Excited-State Properties of Ruthenium(II) Tris-Chelate Complexes. *Inorg. Chem.* **1992**, *31*, 3792–3795.

<sup>84</sup> Strauss, S. H. The Search for Larger and More Weakly Coordinating Anions. *Chem. Rev.* **1993**, *93*, 927.

<sup>85</sup> (a) Ischay, M. A.; Ament, M. S.; Yoon, T. P. Crossed Intermolecular [2 + 2] Cycloaddition of Styrenes by Visible Light Photocatalysis. *Chem. Sci.* **2012**, *3*, 2087. (b) Douglas, J. J.; Nguyen, J. D.; Cole, K. P.; Stephenson, C. R. J. Enabling Novel Photoredox Reactivity via Photocatalyst Selection. *Aldrichim. Acta* **2014**, *47*, 15–25.

<sup>86</sup> (a) Ward, W. M.; Farnum, B. H.; Siegler, M.; Meyer, G. J. Chloride Ion-Pairing with Ru(II) Polypyridyl Compounds in Dichloromethane. *J. Phys. Chem. A* **2013**, *117*, 8883–8894. (b) Wehlin, S. A. M.; Troian-Gautier, L.; Li, G.; Meyer, G. J. Chloride Oxidation by Ruthenium Excited-States in Solution. *J. Am. Chem. Soc.* **2017**, *139*, 12903–12906. (c) Troian-Gautier, L.; Wehlin, S. A. M.; Meyer, G. J. Photophysical Properties of Tetracationic Ruthenium Complexes and Their Ter-Ionic Assemblies with Chloride. *Inorg. Chem.* **2018**, *57*, 12232–12244.

<sup>87</sup> The chemical shifts associated with the ligands in the <sup>1</sup>H NMR of the photocatalysts vary as a function of counteranion identity and are consistent with observations made by Meyer. These data are summarized in the Supporting Information. See: Li, G.; Swords, W. B.; Meyer, G. J. Bromide Photo-oxidation Sensitized to Visible light in Consecutive Ion Pairs. *J. Am. Chem. Soc.* **2017**, *139*, 14983–14991.

<sup>88</sup> Four recent reports have described the influence of chiral counteranions on the enantioselectivity of photocatalytic radical cation reactions: (a) Morse, P. D.; Nguyen, T. M.; Cruz, C. L.; Nicewicz, D. A. Enantioselective Counter-Anions in Photoredox Catalysis: The Asymmetric Cation Radical Diels–Alder Reaction. *Tetrahedron* **2018**, *74*, 3266–3272. (b) Yang, Z.; Li, H.; Li, S.; Zhang, M.-T.; Luo, S. A Chiral Ion-Pair Photoredox Organocatalyst: Enantioselective Anti-Markovnikov Hydroetherification of Alkenols. *Org. Chem. Front.* **2017**, *4*, 1037–1041. (c) Wang, H.; Ren, Y.; Wang, K.; Man, Y.; Xiang, Y.; Li, N.; Tang, B. Visible Light-Induced Cyclization Reactions for the Synthesis of 1,2,4-Triazolines and 1,2,4-Triazoles. *Chem. Commun.* **2017**, *53*, 9644–9647. (d) Gentry, E. C.; Rono, L. J.; Hale, M. E.; Matsuura, R.; Knowles, R. R. Enantioselective Synthesis of Pyrroloindolines via Noncovalent Stabilization of Indole Radical Cations and Applications to the Synthesis of Alkaloid Natural Products. *J. Am. Chem. Soc.* **2018**, *140*, 3394–3402.

<sup>89</sup> Adamson, Q. W.; Namnath, J.; Shastry, V. J.; Slawson, V. Thermodynamic Inefficiency of Conversion of Solar Energy to Work. *J. Chem. Educ.* **1984**, *61*, 221.

<sup>90</sup> Flamigni, L.; Barbieri, A.; Sabatini, C.; Ventura, B.; Barigelletti, F. Photochemistry and Photophysics of Coordination Compounds: Iridium. *Top. Curr. Chem.* **2007**, *281*, 143–203.

<sup>91</sup> (a) Forster, M.; Hester, R. E. Resonance Raman Investigation of Electronically Excited Ru(bipyridine)<sub>3</sub><sup>2+</sup> Using a CW Laser. *Chem. Phys. Lett.* **1981**, *81*, 42–47. (b) Bradley, P. G.; Kress, N.; Hornberger, B. A.; Dallinger, R. F.; Woodruff, W. H. Vibrational Spectroscopy of the Electronically Excited State. 5. Time-Resolved Resonance Raman Study of Tris(bipyridine) Ruthenium(II) and Related Complexes. Definitive Evidence for the Localized MLCT State. *J. Am. Chem. Soc.* **1981**, *103*, 7441–7446. (c) Ceulemans, A.; Vanquickenborne, L. G. On the Charge-Transfer Spectra of Iron(II)- and Ruthenium(II)-Tris(2,2'-bipyridyl) Complexes. *J. Am. Chem. Soc.* **1981**, *103*, 2238–2241. (d) Ohsawa, Y.; DeArmond, M. K.; Hanck, K. W.; Morris, D. E.; Whitten, D. G.; Neveux, P. E. Spatially Isolated Redox Orbitals: Evidence from Low-Temperature Voltammetry. *J. Am. Chem. Soc.* **1983**, *105*, 6522–6524.

<sup>92</sup> Kober, E. M.; Sullivan, B. P.; Meyer, T. J. Solvent Dependence of Metal-to-Ligand Charge-Transfer Transitions. Evidence for Initial Electron Localization in MLCT Excited States of 2,2'-Bipyridine Complexes of Ruthenium(II) and Osmium(II). *Inorg. Chem.* **1984**, *23*, 2098–2104.

<sup>93</sup> (a) Reisman, S. E.; Doyle, A. G.; Jacobsen, E. N. Enantioselective Thiourea-Catalyzed Additions to Oxocarbenium Ions. *J. Am. Chem. Soc.* **2008**, *130*, 7198–7199. (b) Birrell, J. A.;

Desrosiers, J.-N.; Jacobsen, E. N. Enantioselective Acylation of Silyl Ketene Acetals through Fluoride Anion-Binding Catalysis. *J. Am. Chem. Soc.* **2011**, *133*, 13872–13875. (c) Wasa, M.; Liu, R. Y.; Roche, S. P.; Jacobsen, E. N. Asymmetric Mannich Synthesis of  $\alpha$ -Amino Esters by Anion-Binding Catalysis. *J. Am. Chem. Soc.* **2014**, *136*, 12872–12875.

<sup>94</sup> Gansäuer has recently reported the use of hydrogen bond-donating cocatalysts to influence the rate of titanocene-mediated electron transfer reactions. See: Liedtke, T.; Spanning, P.; Riccardi, L.; Gansäuer, A. Mechanism-Based Condition Screening for Sustainable Catalysis in Single-Electron Steps by Cyclic Voltammetry. *Angew. Chem., Int. Ed.* **2018**, *57*, 5006–5010.

<sup>95</sup> (a) Cranwell, P. B.; Hiscock, R.; Haynes, C. J. E.; Light, M. E.; Wells, N. J.; Gale, P. A. Anion Recognition and Transport Properties of Sulfamide-, Phosphoric Triamide- and Thiophosphoric Triamide- Based Receptors. *Chem. Commun.* **2013**, *49*, 874–876. (b) Borovika, A.; Tang, P. I.; Klapman, S.; Nagorny, P. Thiophosphoramidate-Based Cooperative Catalysts for Brønsted Acid Promoted Ionic Diels–Alder Reactions. *Angew. Chem., Int. Ed.* **2013**, *52*, 13424–13428.

<sup>96</sup> Schlosser, M.; Marull, M. The Direct Metalation and Subsequent Functionalization of Trifluoromethyl-Substituted Pyridines and Quinolones. *Eur. J. Org. Chem.* **2003**, 1569–1575.

<sup>97</sup> Schultz, D.M.; Sawicki, J.W.; Yoon, T.P. An Improved Procedure for the Preparation of Ru(bpz)<sub>3</sub>(PF<sub>6</sub>)<sub>2</sub> Via a High-Yielding Synthesis of 2,2'-Bipyrazine. *Beilstein J. Org. Chem.* **2015**, *11*, 61–65.

<sup>98</sup> Furue, M.; Maruyama, K.; Oguni, T.; Naiki, M.; Kamachi, M. Trifluoromethyl-Substituted 2,2'-Bipyridine ligands. Synthetic Control of Excited-State Properties of Ruthenium(II) Tris-Chelate Complexes. *Inorg. Chem.* **1992**, *31*, 3792–3795.

<sup>99</sup> Lin, S.; Ischay, M.A.; Fry, C.F.; Yoon, T.P. Radical Cation Diels–Alder Cycloadditions by Visible Light Photocatalysis. *J. Am. Chem. Soc.* **2011**, *133*, 19350–19353.

<sup>100</sup> Cranwell, P.B.; Hiscock, J.R.; Haynes, C.J.E.; Light, M.E.; Wells, N.J.; Gale, P.A. Anion Recognition and Transport Properties of Sulfamide-, Phosphoric Triamide- and Thiophosphoric Triamide-Based Receptors. *Chem. Commun.* **2013**, *49*, 874–876.

<sup>101</sup> Cismesia, M. A.; Yoon, T. P. Characterizing Chain Processes in Visible Light Photoredox Catalysis. *Chem. Sci.* **2015**, *6*, 5426–5434.

<sup>102</sup> Bond, A.M.; Oldham, K.B.; Snook, G.A. Use of the Ferrocene Oxidation Process to Provide Both Reference Electrode Potential Calibration and a Simple Measurement (Via Semiintegration) of the Uncompensated Resistance in Cyclic Voltammetric Studies in High-Resistance Organic Solvents. *Anal. Chem.* **2000**, *72*, 3492–3496.

<sup>103</sup> Kohno, Y.; Arai, H.; Saita, S.; Ohno, H. Material Design of Ionic Liquids to Show Temperature-Sensitive LCST-Type Phase Transition After Mixing with Water. *Aust. J. Chem.* **2011**, *64*, 1560–1567.

<sup>104</sup> Li, G.; Swords, W. B.; Meyer, G. J. Bromide Photo-oxidation Sensitized to Visible light in Consecutive Ion Pairs. *J. Am. Chem. Soc.* **2017**, *139*, 14983–14991.

## Chapter 4. Visible Light Photosensitized Di- $\pi$ -Methane Rearrangement

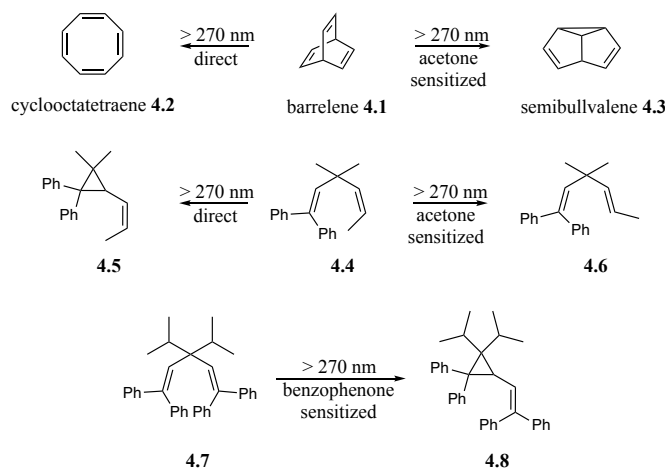


## 4.1. Background

Photochemical rearrangements were among the first photochemical organic reactions to be discovered, and they remain central to research in organic photochemistry. From a synthetic perspective, excited-state rearrangements are valued for their ability to dramatically reshape the connectivity of readily accessible carbocyclic structures into new molecular skeletons that would be difficult to access by other means. One seminal example of such a photorearrangement is the di- $\pi$ -methane rearrangement, which was first reported by Zimmerman in 1966<sup>105</sup> and subsequently the subject of considerable mechanistic and synthetic investigations. The overall transformation involves the rearrangement of a 1,4-diene unit to a vinyl cyclopropane, which Zimmerman rationalized through the intermediacy of a 1,4-diradical. These reactions can be accomplished either via direct irradiation or by triplet sensitization; the sensitivity of the reaction to spin multiplicity has been a subject of significant interest in the study of this reaction (Scheme 4.1).

Our laboratory has been interested in the use of octahedral Ru(II) and Ir(III) polypyridyl complexes as photocatalysts for synthetically useful organic transformations. These complexes have several features that make them ideal for applications in organic synthesis: they are conveniently activated using visible light, they undergo highly efficient intersystem crossing to unusually long-lived triplet excited states, and they possess superior chemical stability compared to many classically utilized organic photosensitizers. Because of these features, this family of transition metal photocatalysts has become widely recognized as useful photoredox catalysts. We have been interested in demonstrating that these same characteristics are beneficial in triplet sensitization reactions as well. We have recently reported that Ru(II) and Ir(III) complexes are valuable triplet sensitizers for a range of cycloadditions and nitrene-generating reactions. We

wondered if di- $\pi$ -methane rearrangements might similarly be amenable to visible light photosensitization using transition metal photosensitizers.<sup>106</sup>



Scheme 4.1 Singlet and Triplet Excited State Reactivity of Di- $\pi$ -Methane Scaffolds

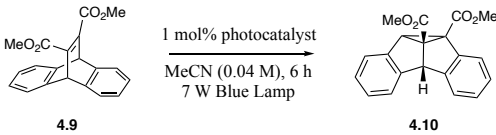
In the 2000s, Armesto *et al.* demonstrated a dependence of the organic sensitizer identity with the outcome of di- $\pi$ -methane reactions.<sup>107,108</sup> He observed that the rearrangement was most efficient when the triplet energy of the sensitizer matched the triplet energy of the substrate. Most substrates Armesto studied had a triplet energy between 53–62 kcal/mol,<sup>109</sup> and we hypothesized that known transition metal photocatalysts with triplet energies reaching 60 kcal/mol would be well suited for these di- $\pi$ -methane transformations. The use of transition metal photocatalysts also enables mild, visible light excitation of the catalyst, allowing for photosensitive functional groups on the substrates to be tolerated.

## 4.2. Reaction Optimization

We began by optimizing reaction conditions with an easily synthesized diarylbarralene compound **4.9** due to its precedent to undergo the di- $\pi$ -methane rearrangement under Zimmerman's conditions (Table 4.1).<sup>110</sup> Entry 1 shows that direct irradiation from a 7 W blue lamp

produces no background reaction. Ruthenium centered photocatalysts also provide no reaction conversion. The yield of this rearrangement tracked with the triplet energy of the photocatalyst. The use of Ir(dFCF<sub>3</sub>ppy)<sub>2</sub>(dtbbpy)PF<sub>6</sub> **4.27** (E<sub>T</sub> = 60 kcal/mol) catalyzed this rearrangement rapidly with full conversion, so we used entry 6 as our optimal reaction conditions.

Table 4.1 Optimization of Reaction Conditions

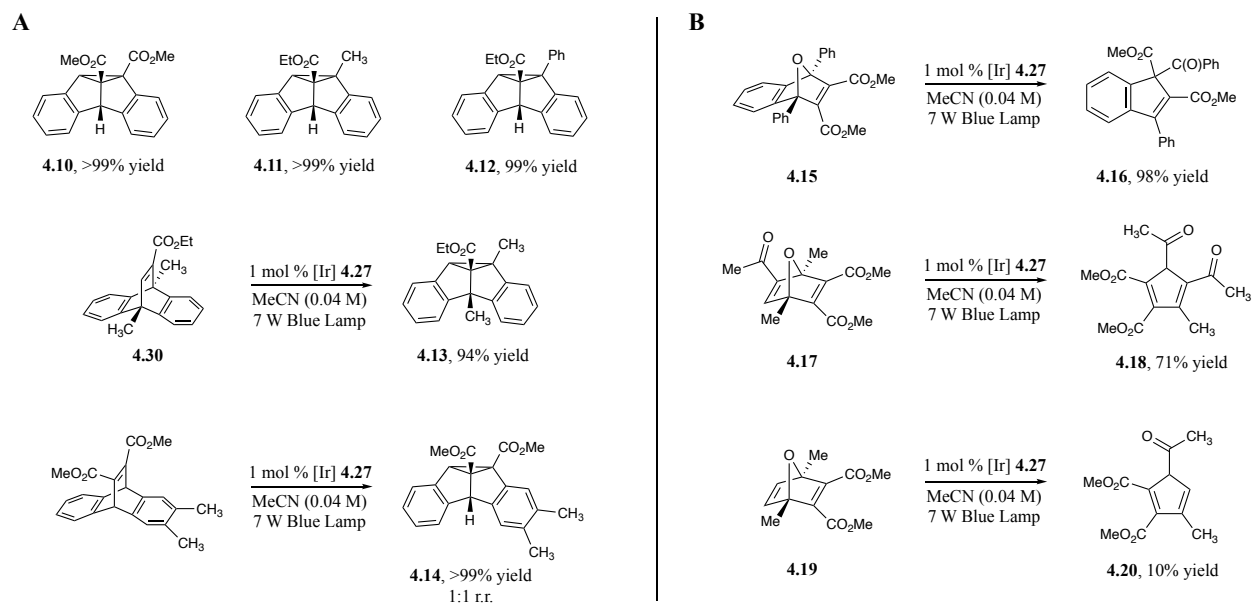


entry	photocatalyst (E <sub>T</sub> , kcal/mol)	% yield <sup>a</sup>	% RSM <sup>a</sup>
1	none	0	100
2	Ru(bpy) <sub>3</sub> (PF <sub>6</sub> ) <sub>2</sub> (47)	0	100
3	Ir(ppy) <sub>2</sub> (dtbbpy)PF <sub>6</sub> (51)	4	91
4	Ir(Fppy) <sub>2</sub> (dtbbpy)PF <sub>6</sub> (53)	47	47
5	Ir(4F 4'tBu ppy) <sub>3</sub> (59)	90	2
6	Ir(dFCF <sub>3</sub> ppy) <sub>2</sub> (dtbbpy)PF <sub>6</sub> (60)	93	0

<sup>a</sup> NMR yields reported using 1,4-bis(trimethylsilyl)benzene as the internal standard.

### 4.3. Scope of the Rearrangement with Visible Light

We started with the scope of this diarylbarralene scaffold and found the rearrangement tolerated steric bulk around the reaction center along with substitution on the aromatic rings. Unsymmetrically substituted barrlenes, however, afforded no regioselectivity in the rearrangement (Scheme 4.2A). Two oxanorbornadiene substrates were reported by Smith and coworkers to undergo di- $\pi$ -methane rearrangements followed by retro [2+2] cycloadditions.<sup>111</sup> We therefore studied the rearrangement of a small scope of oxanorbornadiene scaffolds. (Scheme 4.2B). Increasing yields were obtained using substrates with more electron-stabilizing groups.



Scheme 4.2 A) Scope of substituted diarylbarralene scaffolds. B) Examples of oxanorbornadiene rearrangements.

#### 4.4. Trends with the Electronics of the Substrate

Noting the importance of electron withdrawing groups on the yields of this rearrangement, we systematically compared the rearrangement efficiency to the electronics of the substrate. Upon changing the easily adaptable enone moiety in the substrate, a clear trend emerged in which the rearrangement efficiency increased with the electrophilicity of the enone (Table 4.2).

Table 4.2 Effect of enone electrophilicity on rearrangement efficiency.

entry	R	% yield	time
a		97	6 h
b		92 <sup>a</sup>	6 h
c		96	6 h
d		86	24 h
e		91	72 h
f		1) NR 2) 93 <sup>a</sup>	1) NR 2) 168 h <sup>a</sup>
g		NR	NR

0.2 mmol scale. Isolated yields reported. NR = no reaction. <sup>a</sup> Includes 1 equiv. AlCl<sub>3</sub>.

Substrate **4.21b** highlights the mild reaction conditions and functional group tolerance; this acid chloride rapidly undergoes the rearrangement to **4.22b** without degradation. The piperdyl amide substrate **4.21f**, which was the least electrophilic enone we tested, was unreactive under our standard reaction conditions. Fortunately, reactivity was recovered with the addition of 1 equiv. AlCl<sub>3</sub>. This oxophilic Lewis acid increases the electrophilicity of the piperidyl amide substrate and enables the rearrangement.

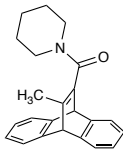
#### 4.5. Effects of a Lewis Acid

Previous work in our lab has illustrated the benefits of dual catalysis with transition metal photosensitizers and chiral Lewis acids to generate asymmetric reactions. The binding of a Lewis

acid has been reported to lower the triplet energy of the substrate, making the bound complex more easily amendable to energy transfer reactions.<sup>112</sup> We hoped this same dual catalytic method would enable efficient energy transfer to di- $\pi$ -methane substrates, allowing for a general, and enantioselective, rearrangement.

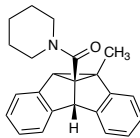
Inspired from substrate **4.21f**, we imagined that the modified piperidyl amide substrate **4.23** would be ideal to study the effect of Lewis acids on the di- $\pi$ -methane rearrangement. Unfortunately, substrate **4.23** did not react under a variety of Lewis acid conditions (Table 4.3).

Table 4.3 Lewis Acid Screen on Piperidyl Amide **4.23**



**4.23**

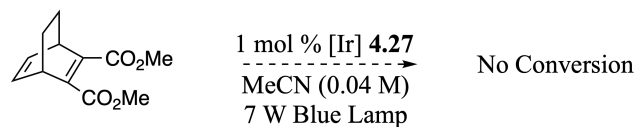
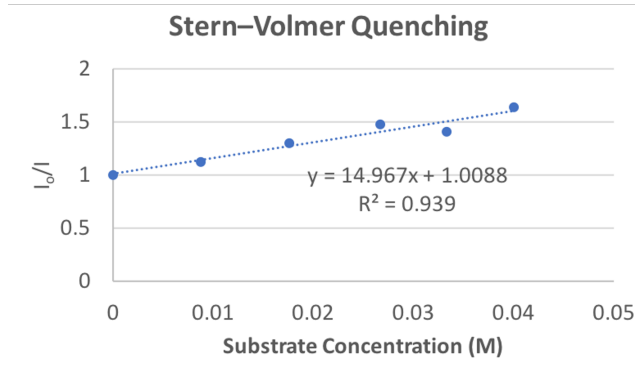
1 mol % [Ir] **4.27**  
 MeCN (0.04 M)  
 Lewis acid (1 equiv.)  
 7 W Blue Lamp



**4.24**

entry	Lewis acid	time	result
1	Al(OTf) <sub>3</sub>	5.5 h	No conversion
2	Sc(OTf) <sub>3</sub>	5.5 h	No conversion
3	AlCl <sub>3</sub>	7 h	No conversion
4	EtAlCl <sub>2</sub>	21 h	No conversion

The additional methyl substituent on substrate **4.23** evidently prevents the reaction. This could be due to a change in substrate triplet energy compared to substrate **4.21f** preventing efficient energy transfer, or the extra methyl substituent could be providing a route for excited state relaxation that outpaces the di- $\pi$ -methane rearrangement. To determine if there was a successful interaction between the photocatalyst and the substrate, we performed Stern–Volmer analysis on the simple cyclic di- $\pi$ -methane scaffold **4.25**. Based on these data, successful energy transfer seems accessible (Scheme 4.3). A first order interaction between the photosensitizer and substrate **4.25** was observed with a quenching constant of  $6.5 \times 10^6 \text{ M}^{-1}\text{s}^{-1}$ .

**4.25**Scheme 4.3 Stern–Volmer Quenching of Substrate **4.25**

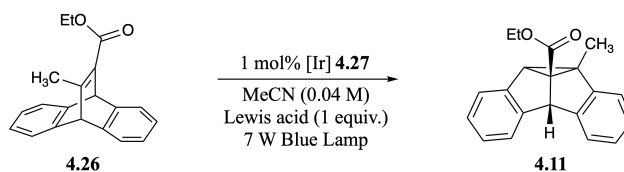
We changed substrates to determine a general effect of a Lewis acid on the rate of the di- $\pi$ -methane rearrangement. Using substrate **4.9**, we screened conditions with various photosensitizers and Lewis acids and found a rate inhibition on the di- $\pi$ -methane rearrangement. Summarized results are shown in Table 4.4.

Table 4.4 Lewis Acid Rate Inhibition on the Di- $\pi$ -Methane Rearrangement Rate

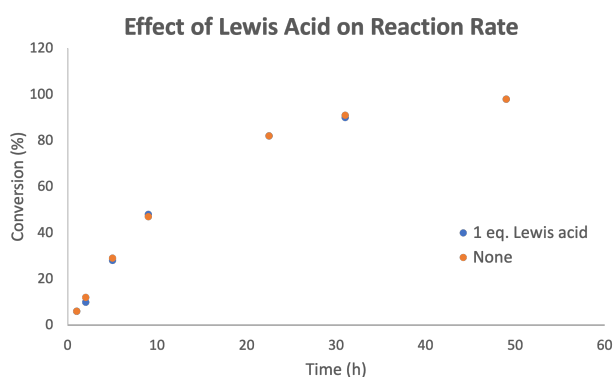
1 mol % photocatalyst  
additive (1 equiv.)  
MeCN, 6 h  
7 W Blue Lamp

entry	photocatalyst	additive	time	conversion (%)
1	Ir(dFCF <sub>3</sub> ppy) <sub>2</sub> (dtbbpy)PF <sub>6</sub>	none	2.5 h	100
2	Ir(dFCF <sub>3</sub> ppy) <sub>2</sub> (dtbbpy)PF <sub>6</sub>	Sc(OTf) <sub>3</sub>	2.5 h	75
3	Ir(dFCF <sub>3</sub> ppy) <sub>2</sub> (dtbbpy)PF <sub>6</sub>	BF <sub>3</sub> · OEt <sub>2</sub>	2.5 h	05
4	Ru(bpy) <sub>3</sub> (PF <sub>6</sub> ) <sub>2</sub>	none	6 h	0
5	Ru(bpy) <sub>3</sub> (PF <sub>6</sub> ) <sub>2</sub>	Sc(OTf) <sub>3</sub> or Al(OTf) <sub>3</sub>	6 h	0
6	Ru(bpy) <sub>3</sub> (PF <sub>6</sub> ) <sub>2</sub>	Ti(OEt) <sub>4</sub> or BF <sub>3</sub> · OEt <sub>2</sub>	6 h	0

The lack of Lewis acid catalysis was also illustrated with substrate **4.26** where the Lewis acid resulted in no rate change for the rearrangement (Scheme 4.4).



entry	Lewis acid	time
1	none	49 h
2	1 eq. AlCl <sub>3</sub>	49 h



Scheme 4.4 Rearrangement Timepoints with Lewis Acid

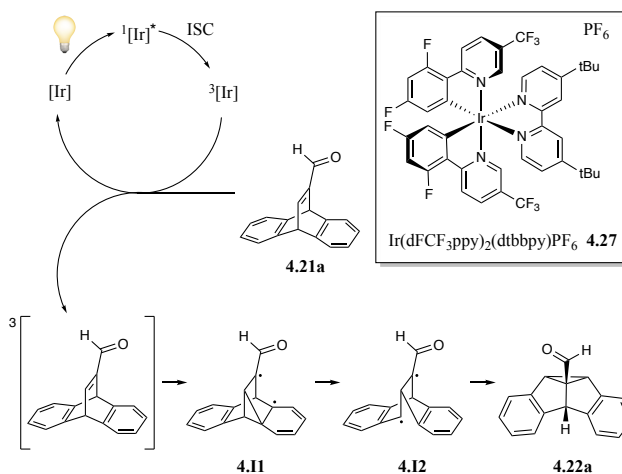
The lack of general Lewis acid catalysis indicates that Lewis acids behave differently in this system than in previously reported systems. We are currently studying if the Lewis acid effects the rate of energy transfer or the downstream radical cascade in the rearrangement reaction.

#### 4.6. Proposed Mechanism

Our proposed mechanism for this rearrangement follows the original mechanistic studies by Zimmerman and coworkers.<sup>113</sup> This mechanism includes Dexter energy transfer between the excited triplet state of the iridium photocatalyst **4.27** and the ground state of the substrate. The process of energy transfer indirectly accesses the excited triplet state of the substrate while regenerating the ground state of the photocatalyst. Then the substrate can undergo an aryl–vinyl C–C bond formation resulting in a biradical intermediate **4.11**. The regeneration of aromaticity is the driving force for accessing intermediate **4.12** prior to the final radical recombination (Scheme



4.5). Presumably, the more efficient rearrangement is caused by the greater stability of  $\alpha$ -carbonyl radicals in more electrophilic enones in **4.11** and **4.12**.



Scheme 4.5 Proposed Mechanism

## 4.7. Conclusion

In summary, we report visible light sensitized di- $\pi$ -methane rearrangements reaching >99% yields. This methodology tolerates sterically bulky reaction centers and photosensitive functional groups, including redox active functionality. Exploration into Lewis acid catalyzed processes reveals a different behavior of the Lewis acid compared to Blum *et al.* Further work is ongoing that examines the role of the Lewis acid either in the photosensitization or in the downstream radical cascade process.

## 4.8. Contributions

Steven J. Chapman (University of Wisconsin – Madison) performed the experimental work. Ilia A. Guzei (University of Wisconsin – Madison) collected and analyzed x-ray crystallographic data.

## 4.9. Supporting Information

### 4.9.1. Reagent Preparation

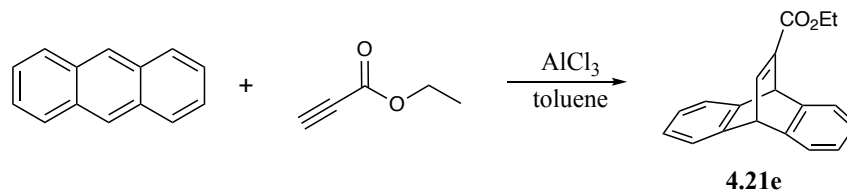
Photocatalyst  $\text{Ir}(\text{dFCF}_3\text{ppy})_2(\text{dtbbpy})\text{PF}_6$  was synthesized using the published route.<sup>114</sup> Photocatalyst  $\text{Ru}(\text{bpy})_3(\text{Cl})_2$  was purchased from Sigma Aldrich. All other chemicals were purchased from chemical suppliers and used without further purification. Except in the case of aqueous reactions, all reaction glassware was flame- or oven-dried prior to use. Flash column chromatography was carried out with Purasil 60 Å silica gel (230–400 mesh).

### 4.9.2. Product Characterization

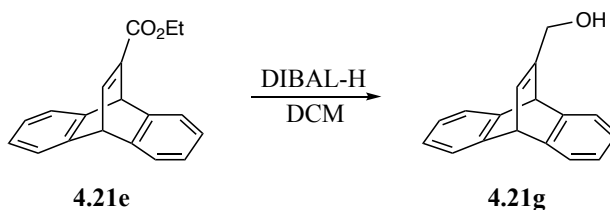
$^1\text{H}$  and  $^{13}\text{C}\{^1\text{H}\}$  NMR spectra were obtained using a Bruker Avance-400 or Avance-500 spectrometer with DCH, Prodigy, BBFO+, or TCI-F probes.  $^1\text{H}$  spectra were internally referenced to tetramethyl silane (0.00 ppm) or the residual protio-solvent peak in acetone- $d_6$  or acetonitrile- $d_3$ .  $^{13}\text{C}\{^1\text{H}\}$  spectra were absolute referenced to the corresponding  $^1\text{H}$  spectrum. Multiplicities are defined using the following abbreviations: s (singlet), d (doublet), t (triplet), q (quartet), p (pentet), sext (sextet), sept (septet), br (broad). The spectrometers used for this work are supported by the NSF (CHE-1048642, CHE-0342998, CHE-9208463), NIH (S10 OD012245, S10 RR13866-01), and a generous gift from Paul J. and Margaret M. Bender.

Mass spectrometry was performed with a Thermo Q Exactive<sup>TM</sup> Plus. This instrumentation is supported by the NIH (1S10 OD020022-1) and the University of Wisconsin.

IR spectra were obtained using a Bruker Alpha Platinum spectrometer (powder). Melting points were obtained using a Stanford Research Systems DigiMelt apparatus.

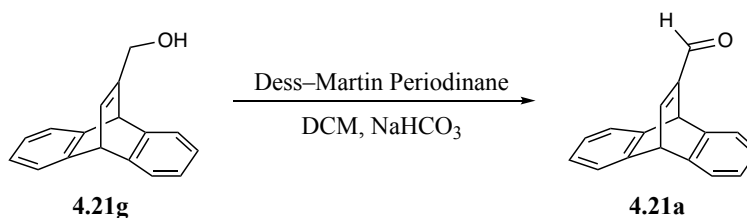
4.9.3. Synthesis of Di- $\pi$ -Methane Substrates

A 25 mL round-bottomed flask was charged with anthracene (1.12 mmol, 1 equiv.), ethyl propiolate (1.12 mmol, 1 equiv.), aluminum chloride (1.12 mmol, 1 equiv.), and anhydrous toluene (1.8 mL, 0.62 M with respect to substrate). The solution was stirred and heated at reflux (130 °C) for 2 h. The reaction was cooled and extracted three times into an equal volume of ethyl acetate. The organic layers were washed with brine, dried over MgSO<sub>4</sub>, filtered, and concentrated *in vacuo*. Isolated pale yellow solid **4.21e** (278 mg, 1.01 mmol, 90% yield). Chemical shifts were consistent with previous reports.<sup>115</sup>



A 25 mL round-bottomed flask was charged with 9,10-dihydro-9,10-ethenoanthracene-11-ethyl carboxylate **4.21e** (1.81 mmol, 1 equiv.) and anhydrous DCM (13 mL). The stirring solution was cooled to -78 °C, and a 1 M solution of DIBAL-H in hexane was added dropwise over 2 min. Solution stirred at -78 °C for 30 min under N<sub>2</sub>. The reaction was warmed to room temperature and 35 mL H<sub>2</sub>O was added. The reaction was extracted three times into an equal volume of DCM, and

the organic layers were washed with a saturated aqueous solution of Rochelle's salt. The combined organic layer was dried over  $\text{MgSO}_4$ , filtered, and concentrated *in vacuo*. Isolated white solid **4.21g** (382 mg, 1.63 mmol, 89% yield). Chemical shifts were consistent with previous reports.<sup>116</sup>



A 100 mL round-bottomed flask was charged with the Dess–Martin Periodinane reagent (3.26 mmol, 2 equiv.) and sodium bicarbonate (8.15 mmol, 5 equiv.), and anhydrous DCM (15 mL). The solution was cooled to 0 °C and was added a solution of 7-hydroxymethyldibenzobicyclo[2.2.2]octatriene **4.21g** (1.63 mmol, 1 equiv.) in anhydrous DCM (15 mL) over 5 min. The reaction was warmed to room temperature and stirred for 30 min under  $\text{N}_2$ . The reaction was quenched with a  $\text{NaHCO}_3:\text{Na}_2\text{S}_2\text{O}_3$  solution (1:1). The reaction was extracted three times into an equal volume of DCM. The combined organic layers were washed with 1 M NaOH and with water. The organic layers were dried over  $\text{MgSO}_4$ , filtered, and concentrated *in vacuo*. The crude product was purified by flash column chromatography on silica gel (9:1 Hexanes:EtOAc), affording a white solid **4.21a** (295 mg, 1.27 mmol, 78% yield).

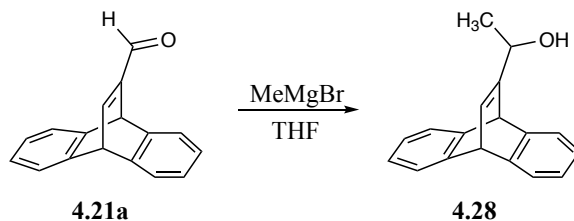
**$^1\text{H}$  NMR** (500 MHz,  $\text{CDCl}_3$ )  $\delta$  9.55 (s, 1H), 7.83 (dd,  $J = 6.1, 1.8$  Hz, 1H), 7.38 – 7.37 (m, 2H), 7.35 – 7.34 (m, 2H), 7.01 – 6.99 (m, 4H), 5.74 (d,  $J = 1.6$  Hz, 1H), 5.34 (d, 6.1 Hz, 1H).

**$^{13}\text{C}$  NMR** (126 MHz,  $\text{CDCl}_3$ )  $\delta$  187.09, 158.05, 153.87, 144.53, 144.03, 125.42, 124.99, 124.00, 123.70, 51.82, 47.07.

**HRMS** (ESI<sup>+</sup>) calculated for [C<sub>17</sub>H<sub>13</sub>O<sup>+</sup>] ([M+H]<sup>+</sup>). Requires *m/z* 233.0961; found *m/z* 233.0958.

**IR** (ATR, powder): 3061, 2974, 2809, 2720, 1666, 1457, 1141, 747 cm<sup>-1</sup>.

**M.P.:** 109–113 °C.



A 25 mL round-bottomed flask was charged with (9*s*,10*s*)-9,10-dihydro-9,10-ethenoanthracene-11-carbaldehyde **4.21a** (0.43 mmol, 1 equiv.) and anhydrous THF (1.75 mL). The solution was cooled to 0 °C and a 3 M solution of methyl magnesium bromide in diethyl ether (0.17 mL) was added dropwise over 2 min. The reaction was warmed to room temperature and stirred for 30 min under N<sub>2</sub>. The reaction was quenched with 0.5 M HCl solution (10 mL) and extracted three times into an equal volume of ethyl acetate. The organic layers were washed with brine, dried over MgSO<sub>4</sub>, filtered, and concentrated *in vacuo*. Isolated a white solid **4.28** (101 mg, 0.41 mmol, 96% yield).

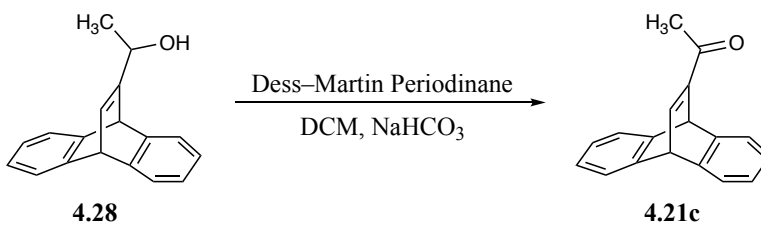
**<sup>1</sup>H NMR** (500 MHz, CDCl<sub>3</sub>) δ 7.32 – 7.29 (m, 2H), 7.28 – 7.27 (m, 2H), 6.96 – 6.94 (m, 4H), 6.70 (dt, *J* = 5.97, 1.60 Hz, 1H), 5.18 (d, *J* = 1.59 Hz, 1H), 5.08 (d, *J* = 5.98 Hz, 1H), 4.54 (br, 1H), 1.30 (d, *J* = 6.42 Hz, 3H).

**<sup>13</sup>C NMR** (126 MHz, CDCl<sub>3</sub>) δ 156.14, 146.59, 146.47, 146.08, 145.96, 132.03, 124.54, 124.50, 124.49, 122.93, 122.88, 122.82, 68.43, 51.67, 50.58, 20.95.

**HRMS** (ESI<sup>+</sup>) calculated for [C<sub>18</sub>H<sub>20</sub>NO<sup>+</sup>] ([M+NH<sub>4</sub>]<sup>+</sup>). Requires *m/z* 266.1539; found *m/z* 266.1536.

**IR** (ATR, powder): 3326, 3061, 3014, 2971, 2926, 2880, 1455, 1061, 744 cm<sup>-1</sup>.

**M.P.:** 95–98 °C.



A 50 mL round-bottomed flask was charged with the Dess–Martin Periodinane reagent (0.74 mmol, 2 equiv.) and sodium bicarbonate (1.86 mmol, 5 equiv.), and anhydrous DCM (3.5 mL). The solution was cooled to 0 °C and was added a solution of 1-((9*s*,10*s*)-9,10-dihydro-9,10-ethenoanthracen-11-yl)ethan-1-ol **4.28** (0.37 mmol, 1 equiv.) in anhydrous DCM (3.5 mL) over 2 min. The reaction was warmed to room temperature and stirred for 30 min under N<sub>2</sub>. The reaction was quenched with a NaHCO<sub>3</sub>:Na<sub>2</sub>S<sub>2</sub>O<sub>3</sub> solution (1:1). The reaction was extracted three times into an equal volume of DCM. The combined organic layers were washed with 1 M NaOH and with water. The organic layers were dried over MgSO<sub>4</sub>, filtered, and concentrated *in vacuo*. The crude product was purified by flash column chromatography on silica gel (9:1 hexanes:EtOAc), affording a white solid **4.21c** (57 mg, 0.23 mmol, 63% yield).

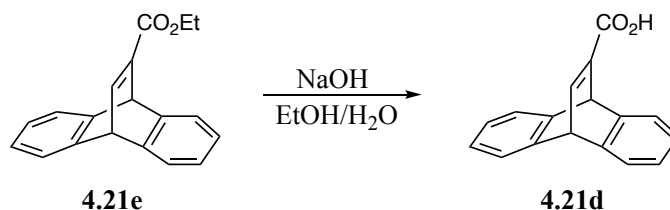
**<sup>1</sup>H NMR** (500 MHz, CDCl<sub>3</sub>) δ 7.80 (dd, *J* = 6.15, 1.85 Hz, 1H), 7.38 – 7.36 (m, 2H), 7.34 – 7.33 (m, 2H), 7.00 – 6.98 (m, 4H), 5.85 (d, *J* = 1.59 Hz, 1H), 5.27 (d, *J* = 6.12 Hz, 1H), 2.23 (s, 3H).

**<sup>13</sup>C NMR** (126 MHz, CDCl<sub>3</sub>) δ 193.95, 152.47, 150.04, 145.19, 144.36, 125.21, 124.81, 123.95, 123.47, 51.56, 48.36, 25.43.

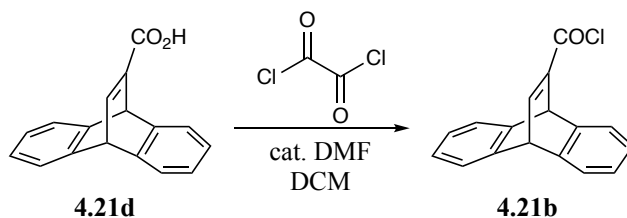
**HRMS** (ESI<sup>+</sup>) calculated for [C<sub>18</sub>H<sub>15</sub>O<sup>+</sup>] ([M+H]<sup>+</sup>). Requires *m/z* 247.1117; found *m/z* 247.1115.

**IR** (ATR, powder): 3068, 3014, 2968, 2923, 2853, 1660, 1456, 743 cm<sup>-1</sup>.

**M.P.:** 141–145 °C.



A 25 mL round-bottomed flask was charged with a solution of sodium hydroxide (11.2 mmol, 15 equiv.) in ethanol (4 mL) and water (1.6 mL). To the solution was added 9,10-dihydro-9,10-ethenoanthracene-11-ethyl carboxylate **4.21e** (0.75 mmol, 1 equiv.). The reaction was refluxed at 104 °C for 1 h open to air. The reaction was cooled to room temperature and added 0.5 M HCl solution until solution was acidic. The reaction was extracted three times into an equal volume of diethyl ether. The organic layers were dried over MgSO<sub>4</sub>, filtered, and concentrated *in vacuo*. Isolated a white solid **4.21d** (169 mg, 0.68 mmol, 91% yield). Chemical shifts were consistent with previous reports.<sup>2</sup>



A 25 mL round-bottomed flask was charged with 9,10-dihydro-9,10-ethenoanthracene-11-carboxylic acid **4.21d** (0.56 mmol, 1 equiv.) and anhydrous DCM (0.56 mL) at room temperature. To the stirring solution was added oxalyl chloride (1.4 mmol, 2.5 equiv.) and anhydrous DMF (0.01 mL). Reaction stirred for 40 min. Residual reagents and solvents removed *in vacuo*. Isolated a pale yellow solid **4.21b** (124 mg, 0.46 mmol, 82% yield).

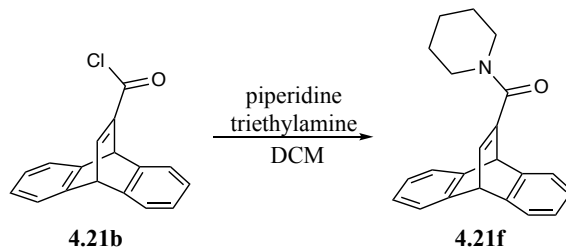
**<sup>1</sup>H NMR** (500 MHz, CDCl<sub>3</sub>) δ 8.25 (dd, *J* = 6.38, 2.01 Hz, 1H), 7.39 – 7.35 (m, 4H), 7.05 – 7.01 (m, 4H), 5.66 (d, *J* = 1.89 Hz, 1H), 5.35 (d, *J* = 6.37 Hz, 1H).

**<sup>13</sup>C NMR** (126 MHz, CDCl<sub>3</sub>) δ 164.76, 159.55, 149.16, 144.14, 143.20, 125.60, 125.39, 123.98, 123.97, 52.16, 50.43.

**IR** (ATR, powder): 3070, 2991, 1731, 1456, 1137, 735 cm<sup>-1</sup>.

**M.P.:** 238–240 °C.





To a solution of piperidine (2.6 mmol, 1 equiv.) and trimethylamine (7.9 mmol, 3 equiv.) at 0 °C was added a solution of 9,10-dihydro-9,10-ethenoanthracene-11-carbonyl chloride **4.21b** (2.6 mmol, 1 equiv.) in anhydrous DCM (5.2 mL). Reaction gradually warmed to room temperature and stirred overnight. Reaction was diluted with 0.5 M HCl and extracted three times into an equal volume of diethyl ether. The organic layers were washed with 2M NaOH (x2), brine (x1), dried over MgSO<sub>4</sub>, filtered, and concentrated *in vacuo*. The crude product was purified by flash column chromatography on silica gel (1:1 hexanes:EtOAc), affording a white solid **4.21f** (347 mg, 1.1 mmol, 42% yield).

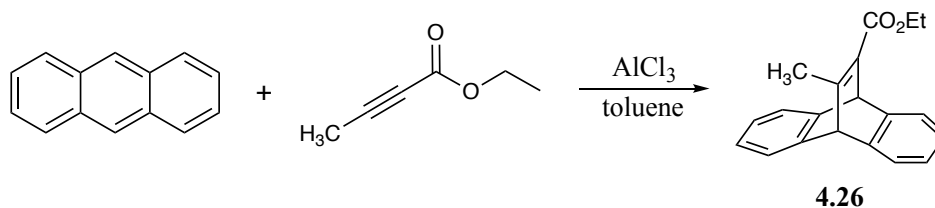
**<sup>1</sup>H NMR** (500 MHz, CDCl<sub>3</sub>) δ 7.34 – 7.33 (m, 2H), 7.30 – 7.28 (m, 2H), 7.04 (dd, *J* = 6.05, 1.84 Hz, 1H), 6.98 – 6.95 (m, 4H), 5.26 (d, *J* = 1.61 Hz, 1H), 5.19 (d, *J* = 6.02 Hz, 1H), 3.37 (br, 4H), 1.63 (br, 2H), 1.51 (br, 4H).

**<sup>13</sup>C NMR** (500 MHz, CDCl<sub>3</sub>) δ 167.84, 147.15, 145.34, 145.05, 139.31, 124.81, 124.74, 123.37, 123.13, 53.28, 50.97, 24.63.

**HRMS** (ESI<sup>+</sup>) calculated for [C<sub>22</sub>H<sub>22</sub>NO<sup>+</sup>] ([M+H]<sup>+</sup>). Requires *m/z* 316.1696; found *m/z* 316.1694.

**IR** (ATR, powder): 3061, 2932, 2851, 1604, 1428, 1221, 756 cm<sup>-1</sup>.

**M.P.:** 129–132 °C.



A 50 mL round-bottomed flask was charged with anthracene (5.61 mmol, 1 equiv.), ethyl-2-butynoate (5.89 mmol, 1.05 equiv.), aluminum chloride (5.89 mmol, 1.05 equiv.), and toluene (9 mL). The reaction was heated to reflux (130 °C) for 16 h open to air. The reaction was extracted three times into an equal volume of diethyl ether, dried over MgSO<sub>4</sub>, filtered over activated charcoal, and concentrated *in vacuo*. The crude product was taken up in diethyl ether, leaving an insoluble solid identified as residual anthracene. The solid was filtered away, and the diethyl ether was removed *in vacuo*. Isolated pale yellow solid **4.26** (1.01 g, 3.48 mmol, 62% yield).

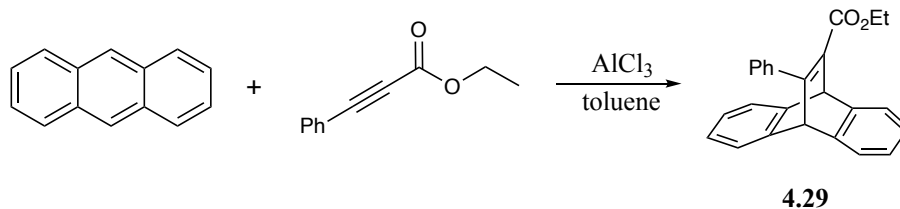
**<sup>1</sup>H NMR** (500 MHz, CDCl<sub>3</sub>) δ 7.36 – 7.35 (m, 2H), 7.32 – 7.30 (m, 2H), 7.02 – 6.96 (m, 4H), 5.68 (s, 1H), 4.91 (s, 1H), 4.20 (q, *J* = 7.13 Hz, 2H), 2.37 (s, 3H), 1.30 (t, 7.13 Hz, 3H).

**<sup>13</sup>C NMR** (126 MHz, CDCl<sub>3</sub>) δ 166.00, 161.69, 145.36, 143.90, 135.30, 125.19, 124.69, 123.19, 123.18, 60.36, 59.87, 51.24, 19.54, 14.35.

**HRMS** (ESI<sup>+</sup>) calculated for [C<sub>20</sub>H<sub>19</sub>O<sub>2</sub><sup>+</sup>] ([M+H]<sup>+</sup>). Requires *m/z* 291.1380; found *m/z* 291.1375.

**IR** (ATR, powder): 2983, 2957, 1690, 1453, 1328, 1219, 1073, 747 cm<sup>-1</sup>.

**M.P.:** 119–120 °C.



A 25 mL round-bottomed flask was charged with anthracene (1.68 mmol, 1 equiv.), ethyl phenylpropiolate (2.52 mmol, 1.5 equiv.), aluminum chloride (2.52 mmol, 1.5 equiv.), and toluene (3.4 mL, 0.5 M). The reaction was heated to reflux (130 °C) for 27 h open to air. The reaction was extracted three times into an equal volume of diethyl ether, dried over MgSO<sub>4</sub>, filtered over activated charcoal, and concentrated *in vacuo*. The crude product was purified by flash column chromatography on silica gel (40:1 hexanes:EtOAc), affording a white solid **4.29** (188 mg, 0.53 mmol, 32% yield).

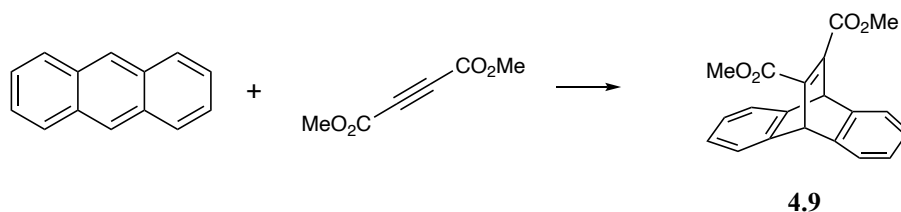
**<sup>1</sup>H NMR** (500 MHz, CDCl<sub>3</sub>) δ 7.44 – 7.43 (m, 2H), 7.36 – 7.31 (m, 5H), 7.20 – 7.18 (m, 2H), 7.04 – 7.01 (m, 4H), 5.77 (s, 1H), 5.28 (s, 1H), 4.01 (q, J = 7.12 Hz, 2H), 0.99 (t, J = 7.13 Hz, 3H).

**<sup>13</sup>C NMR** (126 MHz, CDCl<sub>3</sub>) δ 165.74, 160.64, 145.18, 144.15, 138.63, 136.94, 127.93, 127.68, 127.29, 125.24, 124.94, 123.57, 123.33, 60.47, 60.04, 52.00, 13.71.

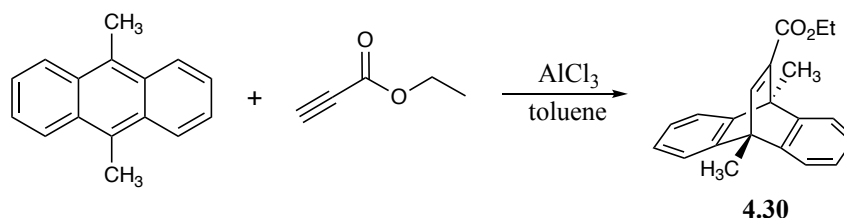
**HRMS** (ESI<sup>+</sup>) calculated for [C<sub>25</sub>H<sub>21</sub>O<sub>2</sub><sup>+</sup>] ([M+H]<sup>+</sup>). Requires *m/z* 353.1536; found *m/z* 353.1527.

**IR** (ATR, powder): 3068.30, 3013.74, 2977.82, 1682.71, 1450.48, 1245.38, 1101.06, 750.76 cm<sup>-1</sup>.

**M.P.:** 129–133 °C.



A 5 mL round-bottomed flask was charged with anthracene (1.12 mmol, 1 equiv.) and dimethyl acetylenedicarboxylate (1.68 mmol, 1.5 equiv.). The neat reaction was refluxed (170 °C) for 45 min. Warm methanol was added to dissolve the residue, and the desired product was crystallized at room temperature. The white crystals were collected by filtration, washed with cold methanol, and dried *in vacuo*, affording a white solid **4.9** (247 mg, 0.77 mmol, 69% yield). Chemical shifts were consistent with previous reports.<sup>117</sup>



A 25 mL round-bottomed flask was charged with 9,10-dimethylanthracene (0.97 mmol, 1 equiv.), ethyl propiolate (1.45 mmol, 1.5 equiv.), aluminum chloride (1.45 mmol, 1.5 equiv.), and toluene (1.6 mL, 0.6 M). The reaction was heated to reflux (130 °C) for 1 h open to air. The reaction was extracted three times into an equal volume of diethyl ether, dried over MgSO<sub>4</sub>, and concentrated *in vacuo* to afford a white solid **4.30** (264 mg, 0.87 mmol, 90% yield).

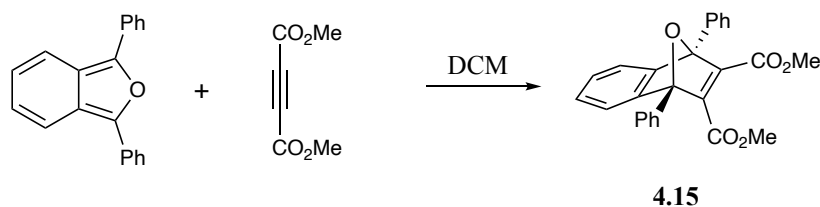
<sup>1</sup>H NMR (500 MHz, CDCl<sub>3</sub>) δ 7.56 (s, 1H), 7.36 – 7.35 (m, 2H), 7.31 – 7.29 (m, 2H), 7.04 – 7.02 (m, 4H), 4.10 (q, J = 7.13 Hz, 2H), 2.43 (s, 3H), 2.20 (s, 3H), 1.22 (t, J = 7.13 Hz, 3H).

$^{13}\text{C}$  NMR (126 MHz,  $\text{CDCl}_3$ )  $\delta$  164.91, 156.14, 149.07, 147.67, 145.91, 124.51, 124.41, 120.75, 120.22, 60.22, 50.08, 49.24, 15.24, 14.50, 14.19.

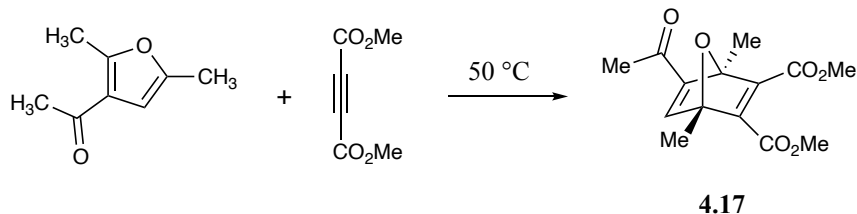
**HRMS** (ESI<sup>+</sup>) calculated for  $[\text{C}_{21}\text{H}_{24}\text{NO}_2]$  ( $[\text{M}+\text{NH}_4]^+$ ). Requires  $m/z$  322.1802; found  $m/z$  322.1800.

**IR** (ATR, powder): 3065.01, 3005.22, 2972.19, 2936.73, 2879.98, 1687.32, 1446.30, 1270.48, 1028.91, 753.30, 725.88  $\text{cm}^{-1}$ .

**M.P.:** 124–126 °C.



A 5 mL round-bottomed flask was charged with 1,3-diphenylisobenzofuran (0.74 mmol, 1 equiv.), dimethyl acetylenedicarboxylate (0.84 mmol, 1.1 equiv.) and DCM (1.5 mL, 0.5 M). The reaction was stirred at room temperature for 1 h. The reaction was concentrated *in vacuo*. The crude product was purified by flash column chromatography on silica gel (4:1 hexanes:EtOAc), affording a white solid **4.15** (263 mg, 0.64 mmol, 86% yield). Chemical shifts were consistent with previous reports.<sup>118</sup>



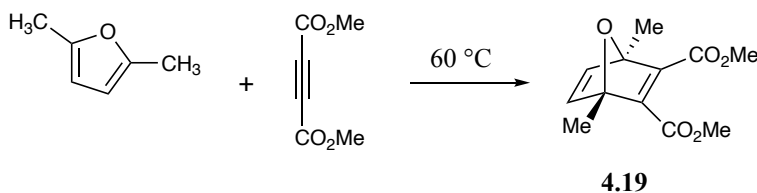
A 5 mL round-bottomed flask was charged with 3-acetyl-2,5-dimethylfuran (1.5 mmol, 1 equiv.) and dimethyl acetylenedicarboxylate (1.5 mmol, 1 equiv.). The reaction was stirred at 50 °C for 74 h. Remaining starting materials were removed *in vacuo* to afford a clear oil **4.17** (264 mg, 0.94 mmol, 63% yield).

**<sup>1</sup>H NMR** (500 MHz, CDCl<sub>3</sub>) δ 7.60 (s, 1H), 3.81 (s, 3H), 3.79 (s, 3H), 2.29 (s, 3H), 1.93 (s, 3H), 1.85 (s, 3H).

**<sup>13</sup>C NMR** (126 MHz, CDCl<sub>3</sub>) δ 193.18, 163.74, 158.19, 156.79, 155.85, 151.61, 92.78, 90.64, 52.38, 52.32, 27.63, 15.17, 15.04.

**HRMS** (ESI<sup>+</sup>) calculated for [C<sub>14</sub>H<sub>17</sub>O<sub>6</sub>] ([M+H]<sup>+</sup>). Requires *m/z* 281.1020; found *m/z* 281.1017.

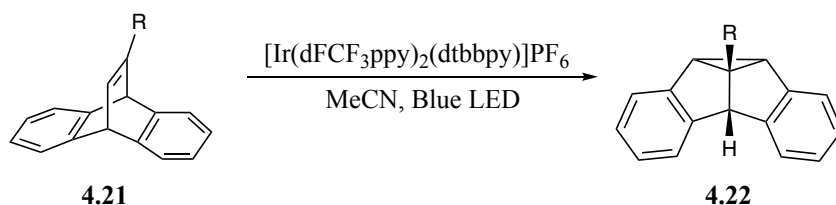
**IR** (ATR, thin film): 3434.82, 2996.67, 2953.37, 1714.71, 1437.11, 1257.71, 1221.56, 1076.60, 1030.24 cm<sup>-1</sup>.



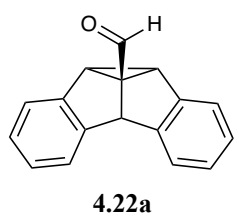
A 5 mL round-bottomed flask was charged with 2,5-dimethylfuran (3.76 mmol, 1 equiv.) and dimethyl acetylenedicarboxylate (4.51 mmol, 1.2 equiv.). The reaction was stirred at 60 °C for 4

h. The crude product was purified by flash column chromatography on silica gel (4:1 hexanes:EtOAc), affording a clear oil **4.19** (570 mg, 2.39 mmol, 64% yield). Chemical shifts were consistent with previous reports.<sup>119</sup>

#### 4.9.4. Di- $\pi$ -Methane Photochemical Rearrangements



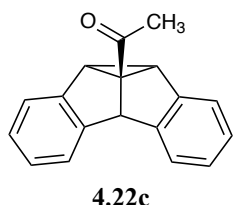
**General Procedure A:** A 25 mL Schlenk flask was charged with a 9,10-dihydro-9,10-ethenoanthracene derivative **4.21** (0.2 mmol, 1 equiv.),  $[\text{Ir}(\text{dFCF}_3\text{ppy})_2(\text{dtbbpy})]\text{PF}_6$  ( $2.1 \times 10^{-3}$  mmol, 0.01 equiv.) and anhydrous MeCN (5.0 mL, 0.04 M). Residual oxygen was removed from solution via three freeze-pump-thaw cycles. Reaction exposed to 7 W blue lamp (10 cm distance). Crude product **4.22** was purified by flash column chromatography on silica gel (9:1 hexanes:EtOAc).



#### **8b,8c-dihydrodibenzo[*a,f*]cyclopropa[*cd*]pentalene-4b<sup>1</sup>(4bH)-**

**carbaldehyde:** Prepared according to General Procedure A using (9*s*,10*s*)-9,10-dihydro-9,10-ethenoanthracene-11-carbaldehyde **4.21a**. Irradiation time

was 6 h. Following workup and purification, a white solid was isolated **4.22a** (52.9 mg, 0.2 mmol, 97% yield). Chemical shifts were consistent with previous reports.<sup>120</sup>



**1-(8b,8c-dihydrodibenzo[*a,f*]cyclopropa[*cd*]pentalen-4b<sup>1</sup>(4bH)-**

**yl)ethan-1-one:** Prepared according to General Procedure A using 1-

((9*s*,10*s*)-9,10-dihydro-9,10-ethenoanthracen-11-yl)ethan-1-one **4.21c**.

Irradiation time was 6 h. Following workup and purification, a white solid was isolated **4.22c** (54.9 mg, 0.22 mmol, 96% yield).

**<sup>1</sup>H NMR** (500 MHz, CDCl<sub>3</sub>) δ 7.25 – 7.24 (m, 2H), 7.17 – 7.15 (m, 2H), 7.09 – 7.03 (m, 4H), 5.05 (s, 1H), 3.86 (s, 2H), 2.17 (s, 3H).

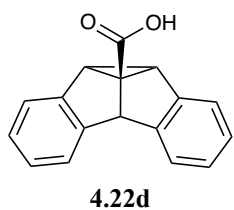
**<sup>13</sup>C NMR** (126 MHz, CDCl<sub>3</sub>) δ 204.01, 149.98, 135.20, 127.13, 126.62, 124.62, 121.44, 72.12, 53.04, 48.00, 25.56.

**HRMS** (ESI<sup>+</sup>) calculated for [C<sub>18</sub>H<sub>15</sub>O<sup>+</sup>] ([M+H]<sup>+</sup>). Requires *m/z* 247.1117; found *m/z* 247.1115.

**IR** (ATR, powder): 3036, 2926, 1670, 1463, 1235, 763 cm<sup>-1</sup>.

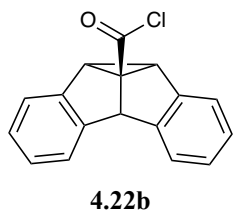
**M.P.:** 192–194 °C.





**8b,8c-dihydrodibenzo[*a,f*]cyclopropa[*cd*]pentalene-4b<sup>1</sup>(4bH)-**

**carboxylic acid:** Prepared according to General Procedure A using 9,10-dihydro-9,10-ethenoanthracene-11-carboxylic acid **4.21d**. Irradiation time was 24 h. Following workup and purification, a white solid was isolated **4.22d** (43.3 mg, 0.17 mmol, 86% yield). Chemical shifts were consistent with previous reports.<sup>121</sup>



**8b,8c-dihydrodibenzo[*a,f*]cyclopropa[*cd*]pentalene-4b<sup>1</sup>(4bH)-**

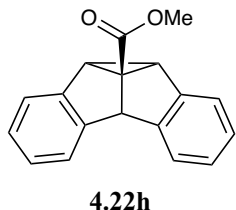
**carbonyl chloride:** Prepared according to General Procedure A using (9*s*,10*s*)-9,10-dihydro-9,10-ethenoanthracene-11-carbonyl chloride **4.21b**. Irradiation time was 6 h. Following workup, a mixture containing the desired di- $\pi$ -methane product **4.22b** and [Ir(dFCF<sub>3</sub>ppy)<sub>2</sub>(dtbbpy)]PF<sub>6</sub> was isolated.

**<sup>1</sup>H NMR** (500 MHz, CDCl<sub>3</sub>)  $\delta$  7.24 (m, 2H), 7.16 – 7.14 (m, 2H), 7.09 – 7.03 (m, 4H), 4.94 (s, 1H), 3.85 (s, 2H).

**<sup>13</sup>C NMR** (126 MHz, CDCl<sub>3</sub>)  $\delta$  177.11, 150.04, 135.10, 127.11, 126.64, 124.73, 121.31, 61.50, 53.54, 47.77.

**IR** (ATR, powder): 3021, 2970, 2854, 2567, 1668, 1436, 1263, 1170, 738 cm<sup>-1</sup>.

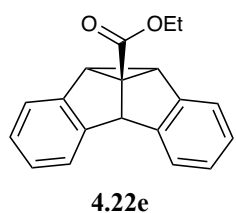
**M.P.:** 215–218 °C.



**methyl 8b,8c-dihydrodibenzo[*a,f*]cyclopropa[*cd*]pentalene-4b<sup>1</sup>(4bH)-**

**carboxylate:** Prepared according to General Procedure A using (9*s*,10*s*)-9,10-dihydro-9,10-ethenoanthracene-11-carbonyl chloride **4.21b**. Irradiation

time was 6 h. Reaction quenched with methanol and concentrated *in vacuo*. Following purification, a white solid was isolated **4.22h** (47.8 mg, 0.18 mmol, 92% yield). Chemical shifts were consistent with previous reports.<sup>122</sup>



**ethyl 8b,8c-dihydrodibenzo[*a,f*]cyclopropa[*cd*]pentalene-4b<sup>1</sup>(4bH)-**

**carboxylate:** Prepared according to General Procedure A using 9,10-dihydro-9,10-ethenoanthracene-11-ethyl carboxylate **4.21e**. Irradiation time was 72 h.

Following workup and purification, a white solid was isolated **4.22e** (50.9 mg, 0.18 mmol, 91% yield).

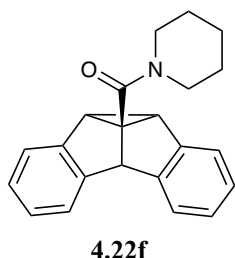
**<sup>1</sup>H NMR** (500 MHz, CDCl<sub>3</sub>) δ 7.24 (m, 2H), 7.16 – 7.14 (m, 2H), 7.08 – 7.03 (m, 4H), 4.96 (s, 1H), 4.19 (q, *J* = 7.13 Hz, 2H), 3.77 (s, 2H), 1.27 (t, *J* = 7.13 Hz, 3H).

**<sup>13</sup>C NMR** (126 MHz, CDCl<sub>3</sub>) δ 171.95, 150.24, 135.56, 126.95, 126.60, 124.75, 121.33, 62.20, 60.86, 53.90, 46.97, 14.33.

**HRMS** (ESI<sup>+</sup>) calculated for [C<sub>19</sub>H<sub>17</sub>O<sub>2</sub><sup>+</sup>] ([M+H]<sup>+</sup>). Requires *m/z* 277.1223; found *m/z* 277.1221.

**IR** (ATR, powder): 2989, 2932, 1708, 1463, 1234, 738 cm<sup>-1</sup>.

**M.P.:** 136–138 °C.



**(8b,8c-dihydrodibenzo[*a,f*]cyclopropa[*cd*]pentalen-4b<sup>1</sup>(4b*H*)-**

**yl)(piperidin-1-yl)methanone:** Prepared according to General Procedure A using ((9*s*,10*s*)-9,10-dihydro-9,10-ethenoanthracen-11-yl)(piperidin-1-

yl)methanone **4.21f** and aluminum chloride (0.2 mmol, 1 equiv.). Irradiation time was 168 h. Following workup and purification by flash column chromatography (1:1 hexanes:EtOAc), a white solid was isolated **4.22f** (58.8 mg, 0.19 mmol, 93% yield).

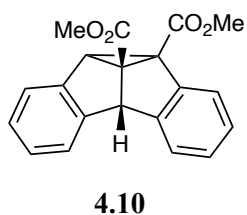
**<sup>1</sup>H NMR** (500 MHz, CD<sub>3</sub>CN) δ 7.30 – 7.27 (m, 2H), 7.24 – 7.21 (m, 2H), 7.09 – 7.06 (m, 4H), 4.64 (s, 1H), 3.49 (s, 2H), 3.31 (br, 4H), 1.62 – 1.57 (m, 2H), 1.44 (br, 4H).

**<sup>13</sup>C NMR** (126 MHz, CD<sub>3</sub>CN) δ 168.49, 150.96, 137.20, 127.54, 127.25, 125.59, 122.10, 64.05, 57.83, 43.26, 24.83.

**HRMS** (ESI<sup>+</sup>) calculated for [C<sub>22</sub>H<sub>22</sub>NO<sup>+</sup>] ([M+H]<sup>+</sup>). Requires *m/z* 316.1696; found *m/z* 316.1694.

**IR** (ATR, powder): 3012.67, 2931.47, 2851.74, 1626.56, 1434.57, 1252.57, 1225.35, 761.36, 739.13 cm<sup>-1</sup>.

**M.P.:** 119–120 °C.



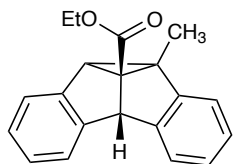
**dimethyl**

**(4b*S*,4b<sup>1</sup>*S*)-4b,8c-**

**dihydrodibenzo[*a,f*]cyclopropa[*cd*]pentalene-4b<sup>1</sup>,8b-dicarboxylate:**

Prepared according to General Procedure A using dimethyl (9*s*,10*s*)-9,10-dihydro-9,10-ethenoanthracene-11,12-dicarboxylate **4.9**. Irradiation time was 48 h. Following workup and purification by flash column chromatography (1:1 hexanes:EtOAc), a clear oil was

isolated **4.10** (63.7 mg, 0.2 mmol, >99% yield). Chemical shifts were consistent with previous reports.<sup>123</sup>



**4.11**

ethyl

(4b*S*,4b<sup>1</sup>*R*)-8b-methyl-8b,8c-

dihydrodibenzo[*a,f*]cyclopropa[*cd*]pentalene-4b<sup>1</sup>(4b*H*)-carboxylate:

Prepared according to General Procedure A using ethyl (9*S*,10*S*)-12-methyl-

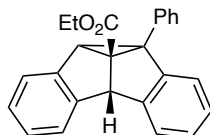
9,10-dihydro-9,10-ethenoanthracene-11-carboxylate **4.26** and 5 mol% Ir(dFCF<sub>3</sub>ppy)<sub>2</sub>(dtbbpy)PF<sub>6</sub>. Irradiation time was 48 h. Following workup and purification by flash column chromatography (1:1 hexanes:EtOAc), a clear oil was isolated **4.11** (57.2 mg, 0.2 mmol, >99% yield).

**<sup>1</sup>H NMR** (500 MHz, CDCl<sub>3</sub>) δ 7.22 – 7.19 (m, 2H), 7.17 – 7.14 (m, 2H), 7.10 – 7.08 (m, 2H), 7.06 – 7.00 (m, 2H), 4.99 (s, 1H), 4.25 – 4.13 (m, 2H), 3.60 (s, 1H), 1.91 (s, 3H), 1.28 (t, J = 7.13 Hz, 3H).

**<sup>13</sup>C NMR** (126 MHz, CDCl<sub>3</sub>) δ 170.86, 150.00, 149.15, 139.10, 136.83, 127.10, 126.70, 126.60, 126.39, 124.67, 123.90, 121.20, 121.14, 66.57, 60.74, 54.84, 53.51, 51.41, 16.30, 14.38.

**HRMS** (ESI<sup>+</sup>) calculated for [C<sub>20</sub>H<sub>18</sub>O<sub>2</sub>Na<sup>+</sup>] ([M+Na]<sup>+</sup>). Requires *m/z* 313.1199; found *m/z* 313.1196.

**IR** (ATR, thin film): 3066.60, 3022.40, 2979.18, 2928.08, 2871.00, 1711.25, 1466.62, 1226.44, 1186.97, 1057.60, 744.64 cm<sup>-1</sup>.



ethyl

**(4bS,4b<sup>1</sup>S)-8b-phenyl-8b,8c-****dihydrodibenzo[*a,f*]cyclopropa[*cd*]pentalene-4b<sup>1</sup>(4bH)-carboxylate:****4.12**Prepared according to General Procedure A using ethyl (9*s*,10*s*)-12-phenyl-9,10-dihydro-9,10-ethenoanthracene-11-carboxylate **4.29** and 5 mol% Ir(dFCF<sub>3</sub>ppy)<sub>2</sub>(dtbbpy)PF<sub>6</sub>.

Irradiation time was 120 h. Following workup and purification by flash column chromatography

(1:1 hexanes:EtOAc), a white solid was isolated **4.12** (69.3 mg, 0.2 mmol, 99% yield).

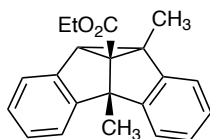
**<sup>1</sup>H NMR** (500 MHz, CDCl<sub>3</sub>) δ 7.60 – 7.58 (m, 1H), 7.38 – 7.36 (m, 1H), 7.29 – 7.28 (m, 4H), 7.25 – 7.24 (m, 1H), 7.21 – 7.19 (m, 1H), 7.15 – 7.11 (m, 3H), 7.08 – 7.07 (m, 2H), 4.72 (s, 1H), 4.55 (s, 1H), 4.09 – 3.97 (m, 2H), 0.97 (t, J = 7.12 Hz, 3H).

**<sup>13</sup>C NMR** (126 MHz, CDCl<sub>3</sub>) δ 168.33, 150.67, 150.43, 136.38, 136.31, 134.06, 128.16, 127.90, 127.51, 127.11, 127.10, 126.68, 125.48, 121.20, 121.17, 72.83, 61.82, 60.83, 55.47, 47.94, 13.90.

**HRMS** (ESI<sup>+</sup>) calculated for [C<sub>25</sub>H<sub>21</sub>O<sub>2</sub><sup>+</sup>] ([M+H]<sup>+</sup>). Requires *m/z* 353.1536; found *m/z* 353.1537.

**IR** (ATR, powder): 3028.65, 2977.89, 1711.46, 1467.56, 1218.14, 1030.95, 740.18, 695.90 cm<sup>-1</sup>.

**M.P.:** 54–56 °C.



ethyl

**(4bS,4b<sup>1</sup>S)-4b,8b-dimethyl-8b,8c-****dihydrodibenzo[*a,f*]cyclopropa[*cd*]pentalene-4b<sup>1</sup>(4bH)-carboxylate:****4.13**Prepared according to General Procedure A using 0.1 mmol ethyl (9*s*,10*s*)-9,10-dimethyl-9,10-dihydro-9,10-ethenoanthracene-11-carboxylate **4.30** and 5 mol%Ir(dFCF<sub>3</sub>ppy)<sub>2</sub>(dtbbpy)PF<sub>6</sub>. Irradiation time was 168 h. Following workup and purification by

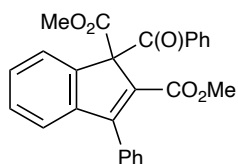
flash column chromatography (1:1 hexanes:EtOAc), a clear oil was isolated **4.13** (28.3 mg, 0.094 mmol, 94% yield).

**<sup>1</sup>H NMR** (500 MHz, CDCl<sub>3</sub>) δ 7.20 – 7.19 (m, 1H), 7.17 – 7.16 (m, 1H), 7.10 – 7.06 (m, 5H), 7.04 – 7.00 (m, 1H), 4.26 – 4.10 (m, 2H), 3.62 (s, 1H), 2.03 (s, 3H), 1.83 (s, 3H), 1.28 (t, J = 7.14 Hz, 3H).

**<sup>13</sup>C NMR** (126 MHz, CDCl<sub>3</sub>) δ 169.61, 153.23, 152.86, 138.57, 136.46, 127.03, 126.72, 126.50, 124.41, 123.61, 119.13, 119.00, 69.97, 60.49, 59.80, 52.07, 49.79, 16.53, 16.40, 14.40.

**HRMS** (ESI<sup>+</sup>) calculated for [C<sub>21</sub>H<sub>21</sub>O<sub>2</sub><sup>+</sup>] ([M+H]<sup>+</sup>). Requires *m/z* 305.1536; found *m/z* 305.1537.

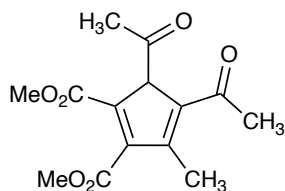
**IR** (ATR, thin film): 3066.47, 3024.92, 2976.84, 2930.35, 2872.07, 1710.77, 1452.28, 1220.73, 1051.92, 749.29 cm<sup>-1</sup>.



**4.16**

**dimethyl 1-benzoyl-3-phenyl-1H-indene-1,2-dicarboxylate:** Prepared according to General Procedure A using dimethyl (1*R*,4*S*)-1,4-diphenyl-1,4-dihydro-1,4-epoxynaphthalene-2,3-dicarboxylate **4.15**. Irradiation time was

48 h. Following workup and purification, a white solid was isolated **4.16** (82.6 mg, 0.2 mmol, 98% yield). Chemical shifts were consistent with previous reports.<sup>111</sup>



**4.18**

**dimethyl 4,5-diacetyl-3-methylcyclopenta-1,3-diene-1,2-dicarboxylate:** Prepared according to General Procedure A using dimethyl (1*S*,4*R*)-5-acetyl-1,4-dimethyl-7-oxabicyclo[2.2.1]hepta-2,5-

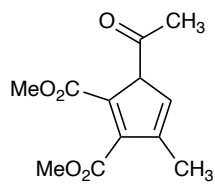
diene-2,3-dicarboxylate **4.17**. Irradiation time was 8 h. Following workup and purification, a white solid was isolated **4.18** (40.1 mg, 0.14 mmol, 71% yield).

$^1\text{H NMR}$  (500 MHz,  $\text{CDCl}_3$ )  $\delta$  3.94 (s, 3H), 3.81 (s, 3H), 2.74 (s, 3H), 2.69 (s, 3H), 2.55 (s, 3H).

$^{13}\text{C NMR}$  (126 MHz,  $\text{CDCl}_3$ )  $\delta$  193.65, 192.56, 169.25, 164.59, 148.79, 141.08, 123.26, 123.04, 119.90, 52.80, 51.63, 28.47, 25.46, 16.80.

**HRMS** ( $\text{ESI}^+$ ) calculated for  $[\text{C}_{14}\text{H}_{17}\text{O}_6]$  ( $[\text{M}+\text{H}]^+$ ). Requires  $m/z$  281.1020; found  $m/z$  281.1020.

**IR** (ATR, powder): 3006.58, 2956.99, 1702.48, 1637.50, 1553.44, 1442.49, 1393.10, 1203.90, 961.56, 932.19  $\text{cm}^{-1}$ .



**4.20**

**dimethyl 5-acetyl-3-methylcyclopenta-1,3-diene-1,2-dicarboxylate:**

Prepared according to General Procedure A using dimethyl (1*R*,4*S*)-1,4-dimethyl-7-oxabicyclo[2.2.1]hepta-2,5-diene-2,3-dicarboxylate **4.19**.

Irradiation time was 72 h. Following workup and purification, a yellow oil was isolated **4.20** (5.2 mg, 0.02 mmol, 10% yield).

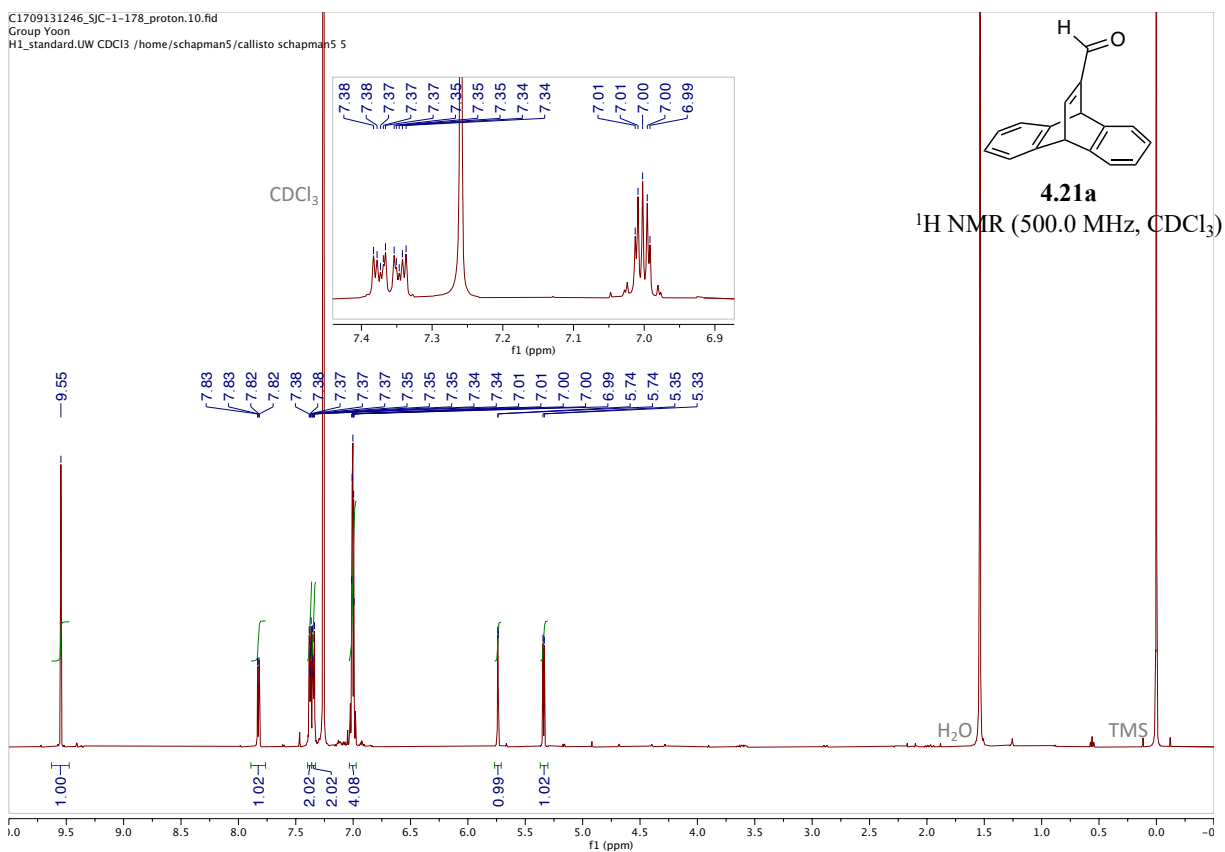
$^1\text{H NMR}$  (500 MHz,  $\text{CDCl}_3$ )  $\delta$  15.71 (s, 1H), 6.73 (d,  $J = 0.86$  Hz, 1H), 3.88 (s, 3H), 3.88 (s, 3H), 2.48 (s, 3H), 2.06 (d,  $J = 0.86$  Hz, 3H).

$^{13}\text{C NMR}$  (126 MHz,  $\text{CDCl}_3$ )  $\delta$  178.96, 168.90, 168.53, 140.53, 130.26, 129.03, 118.38, 113.59, 53.21, 52.09, 21.64, 12.83.

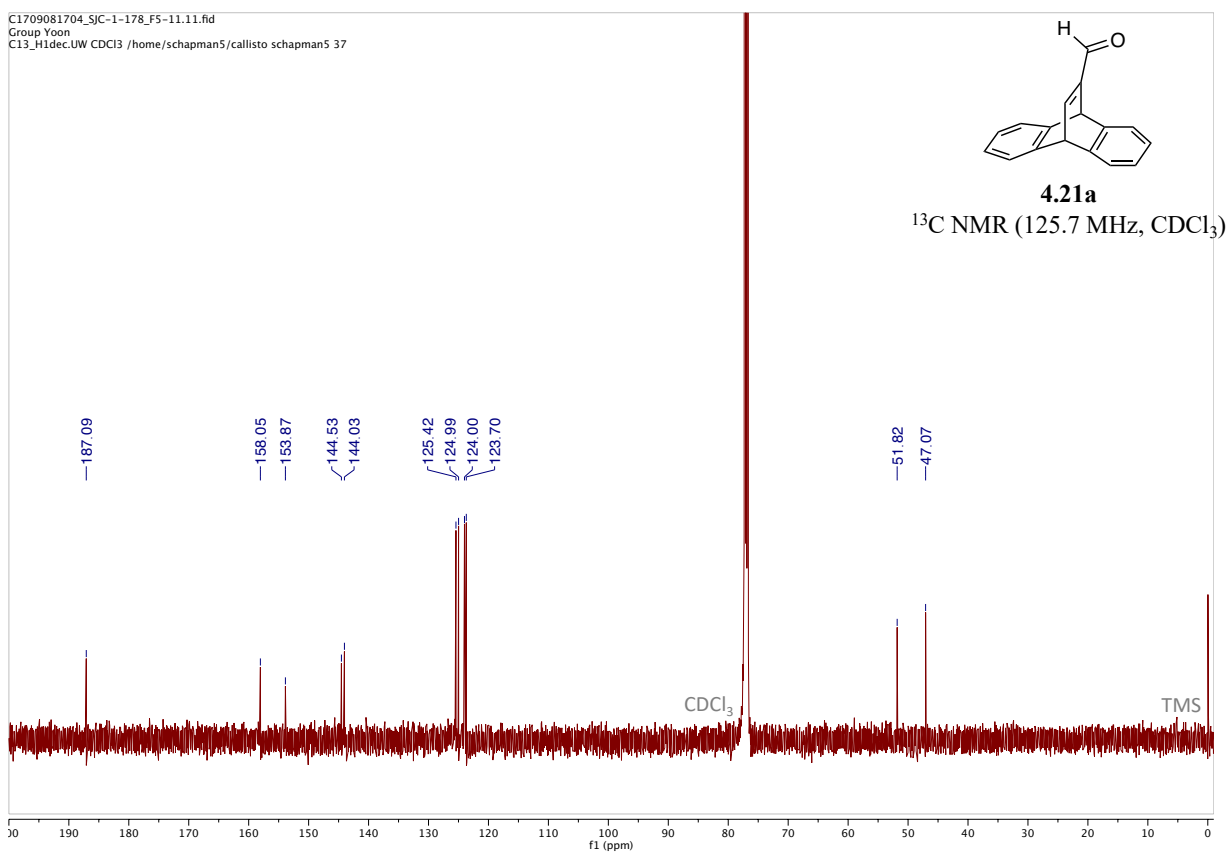
**HRMS** ( $\text{ESI}^+$ ) calculated for  $[\text{C}_{12}\text{H}_{15}\text{O}_5^+]$  ( $[\text{M}+\text{H}]^+$ ). Requires  $m/z$  239.0914; found  $m/z$  239.0912.

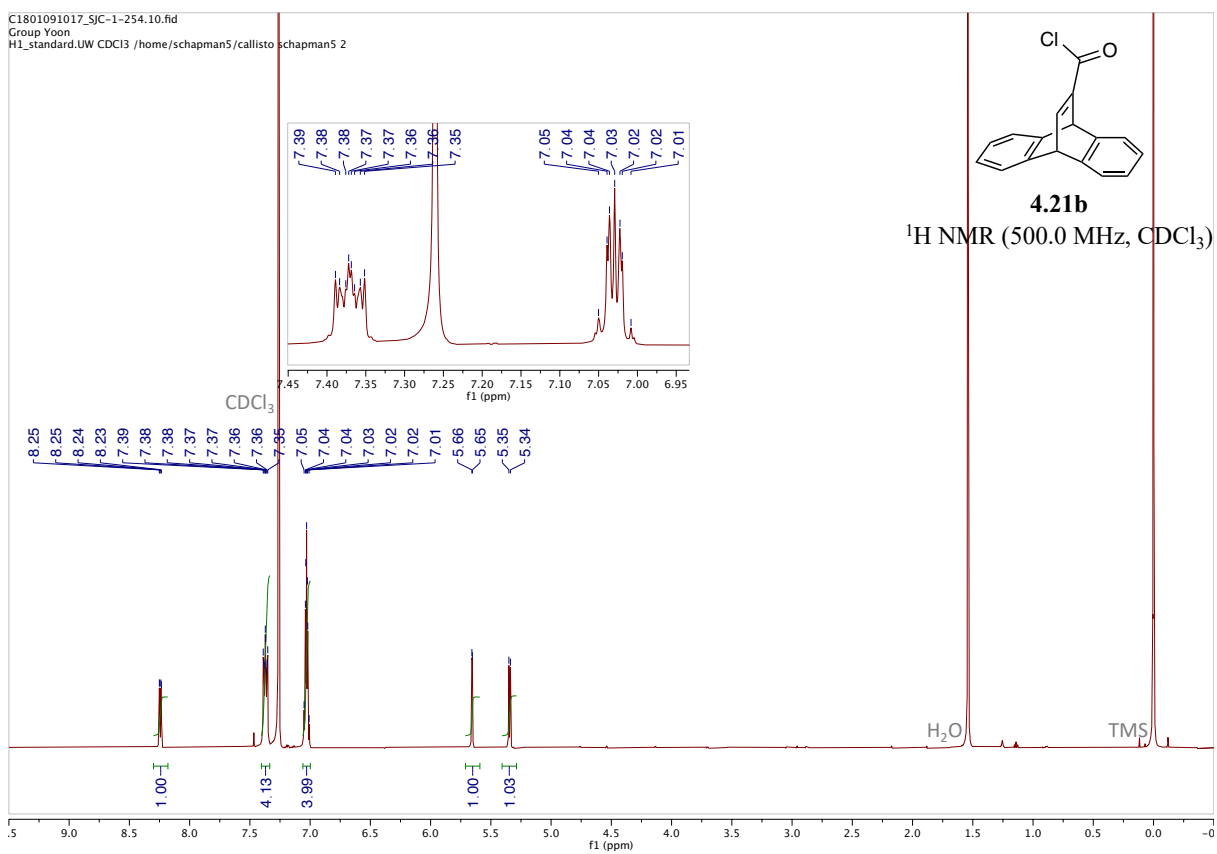
IR (ATR, thin film): 2952.16, 2923.96, 1728.34, 1621.67, 1470.67, 1444.05, 1371.57, 1341.17, 1309.96, 1229.12, 1203.44  $\text{cm}^{-1}$ .

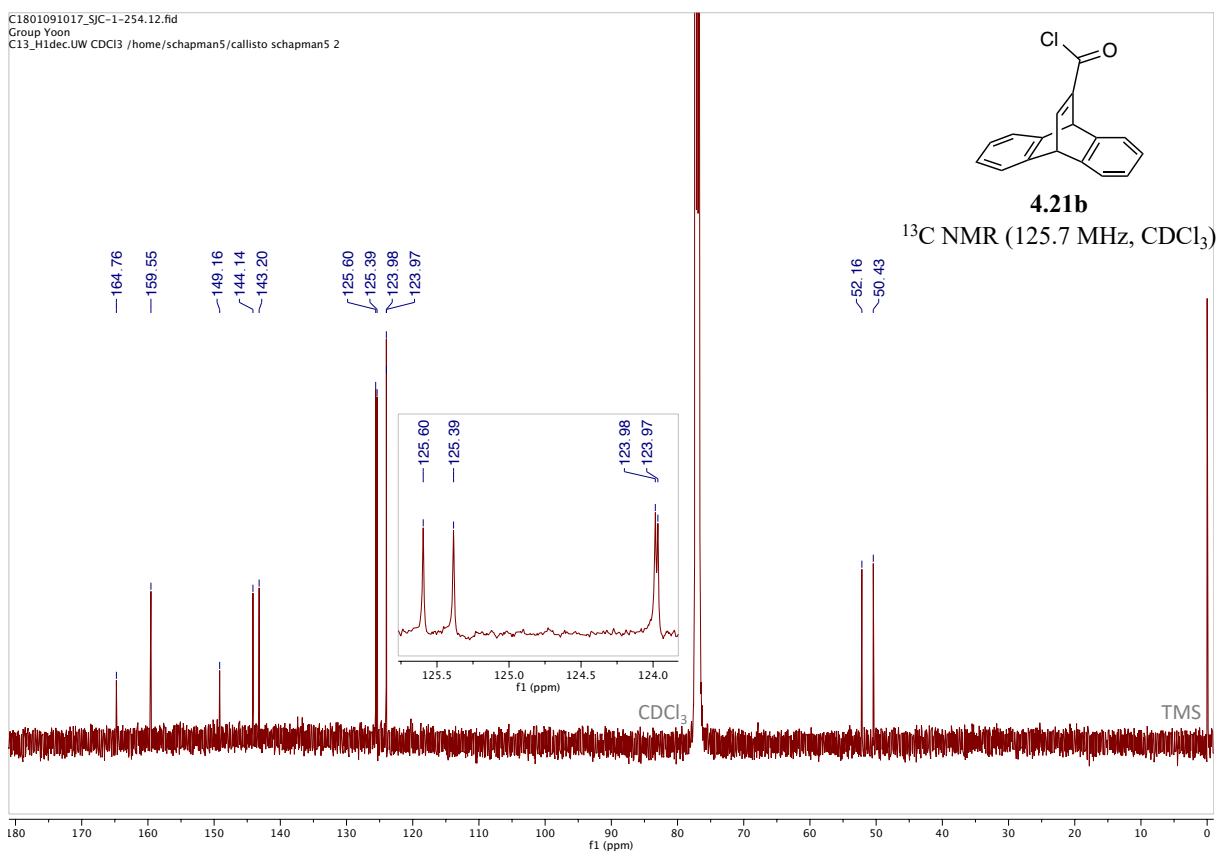
#### 4.9.5. $^1\text{H}$ and $^{13}\text{C}$ NMR Spectra

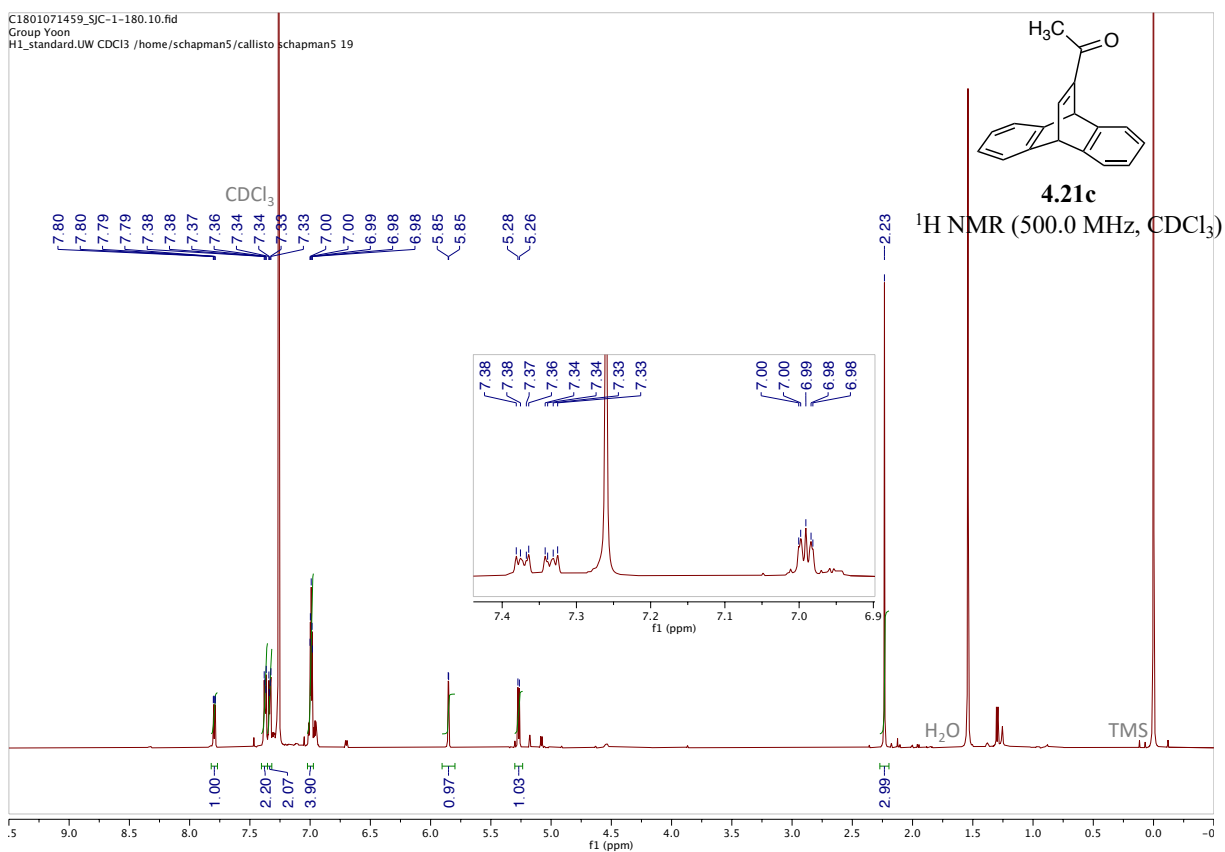


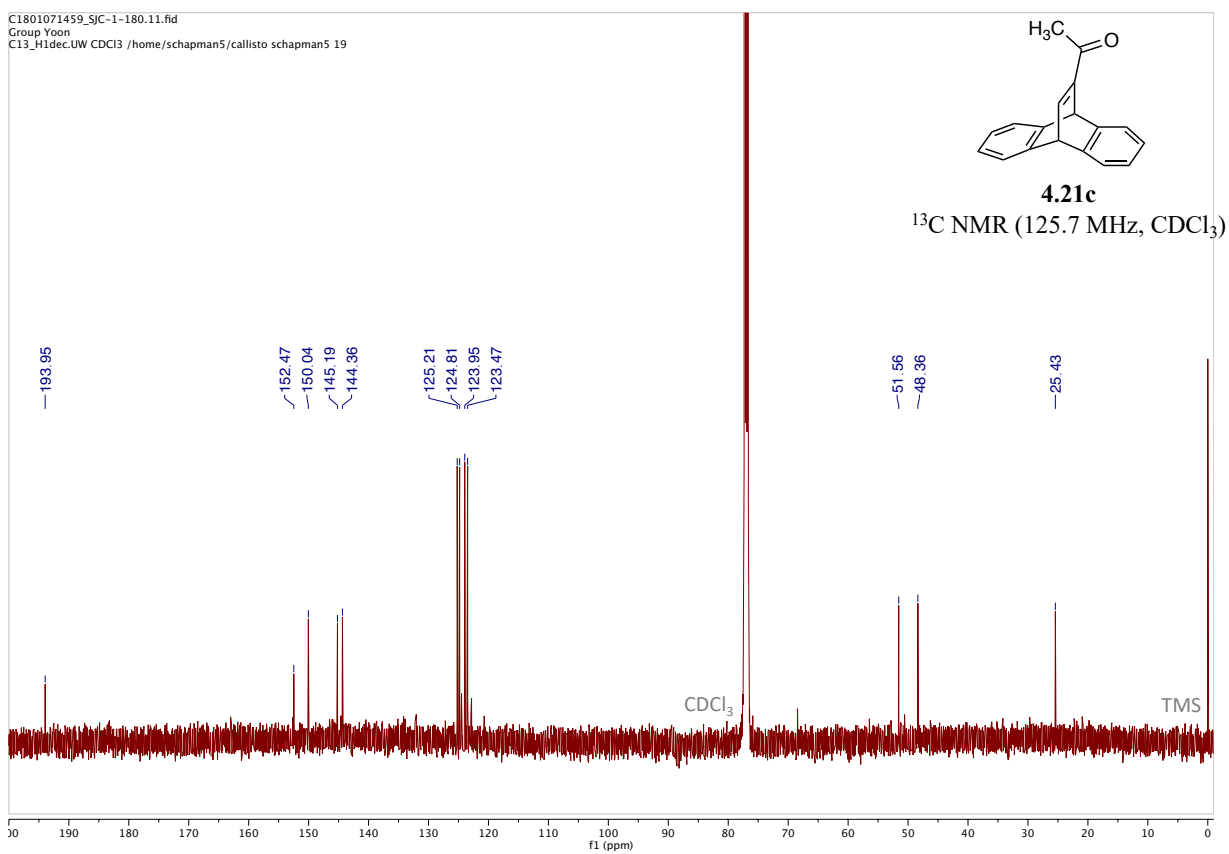


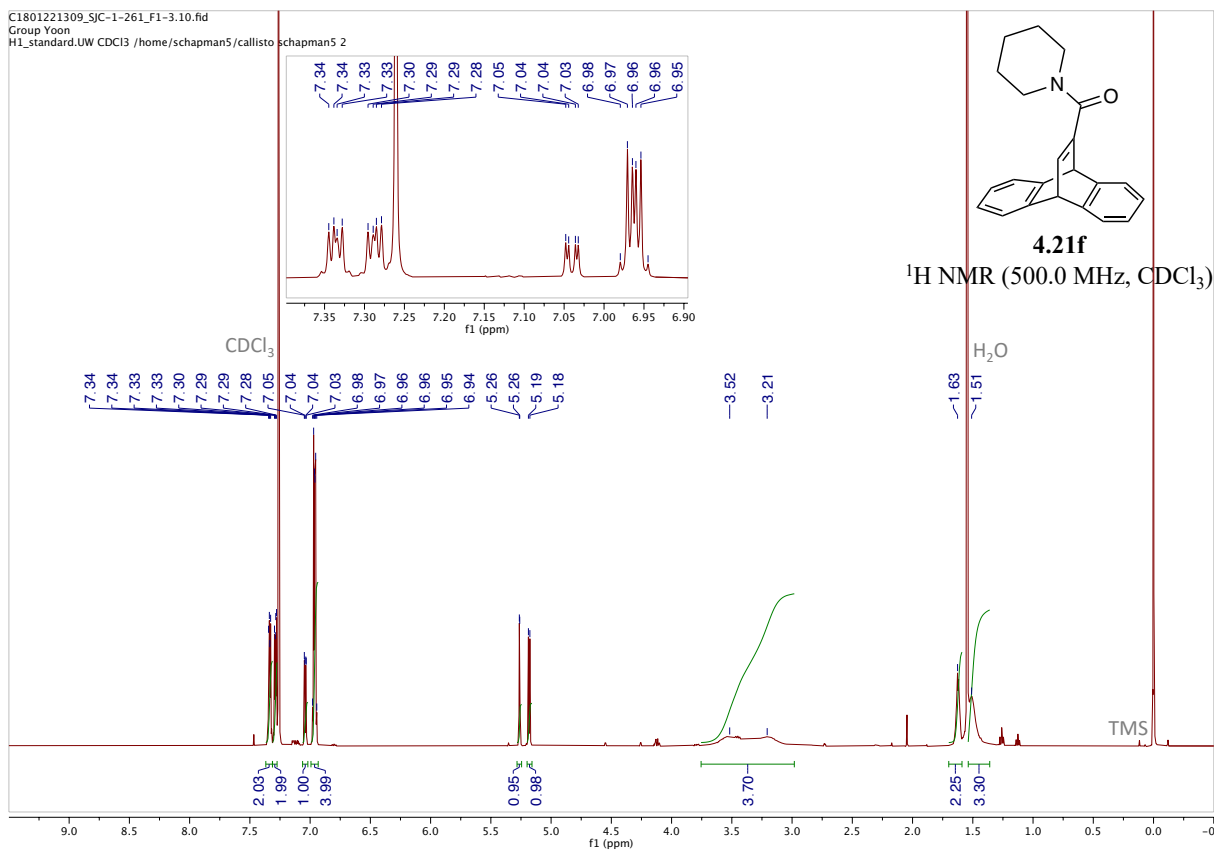


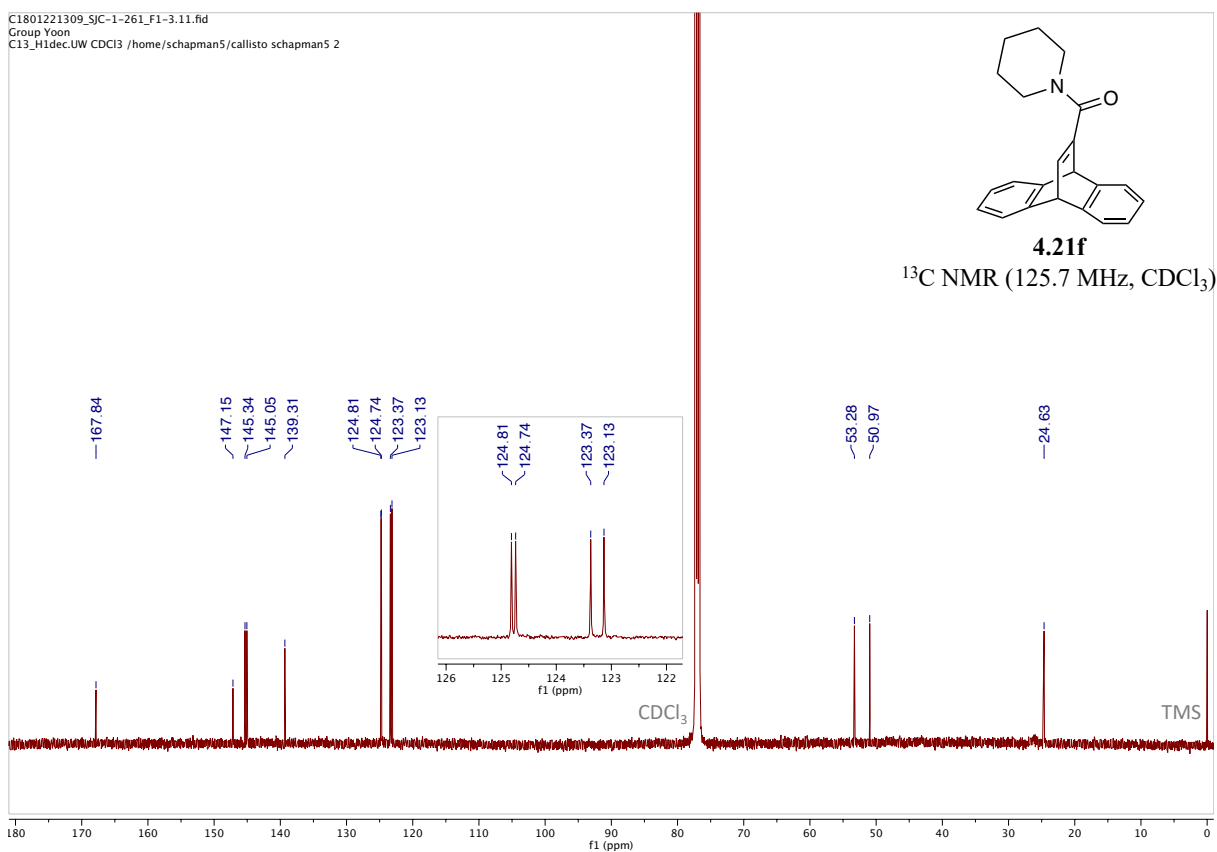


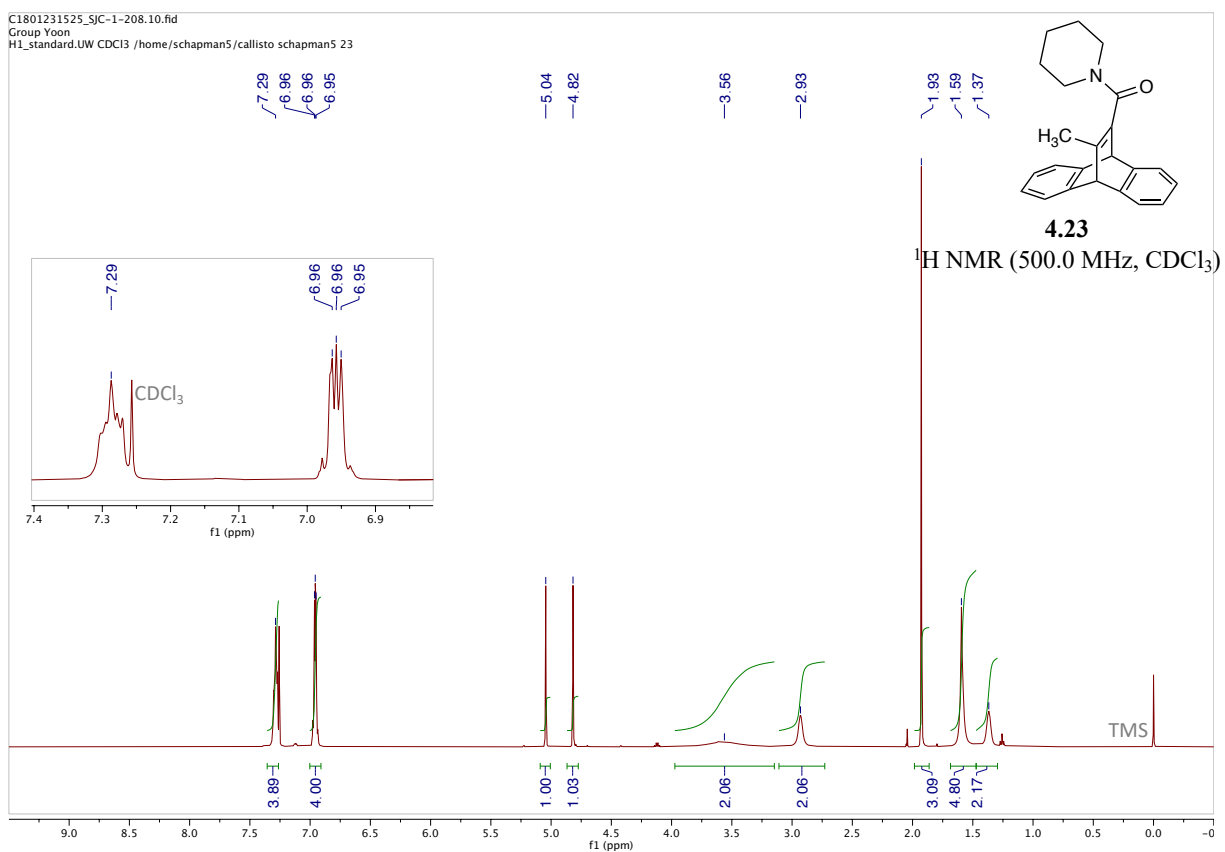




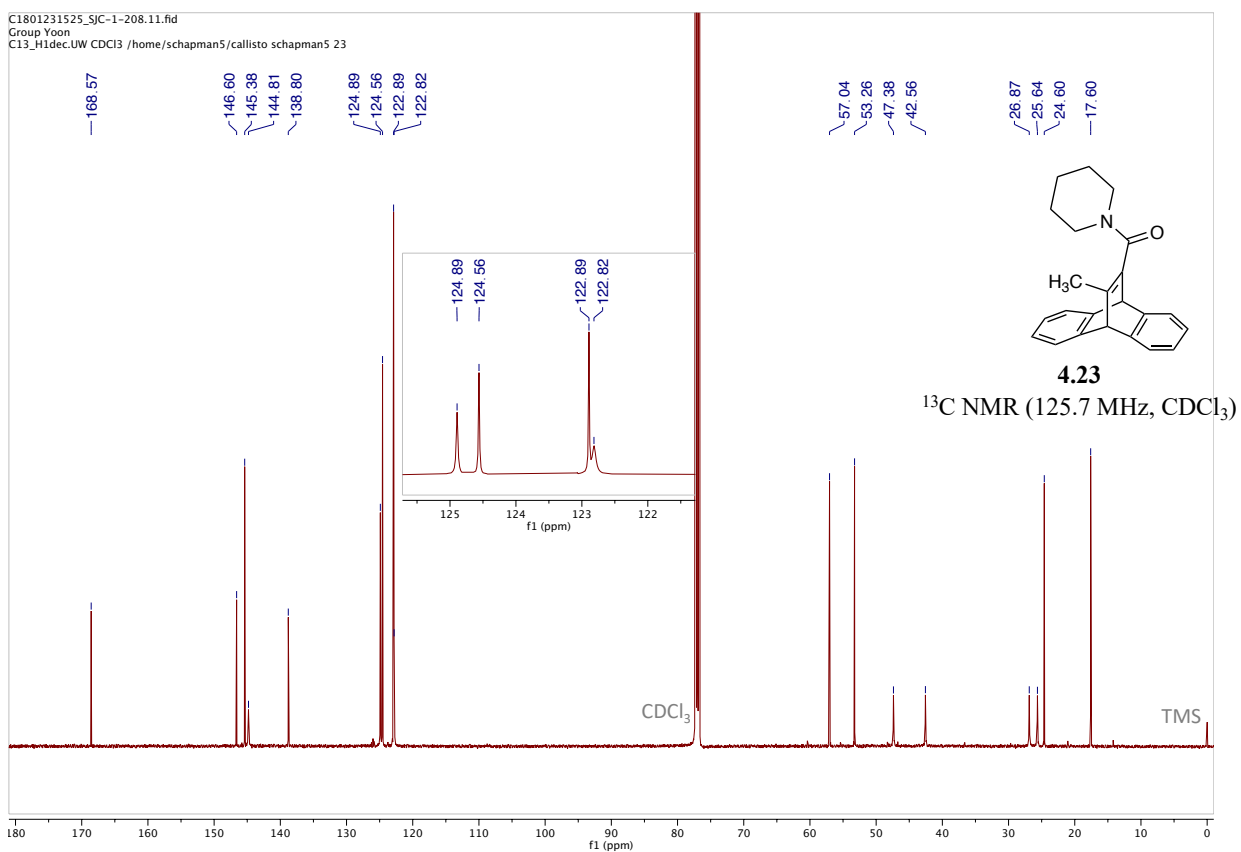


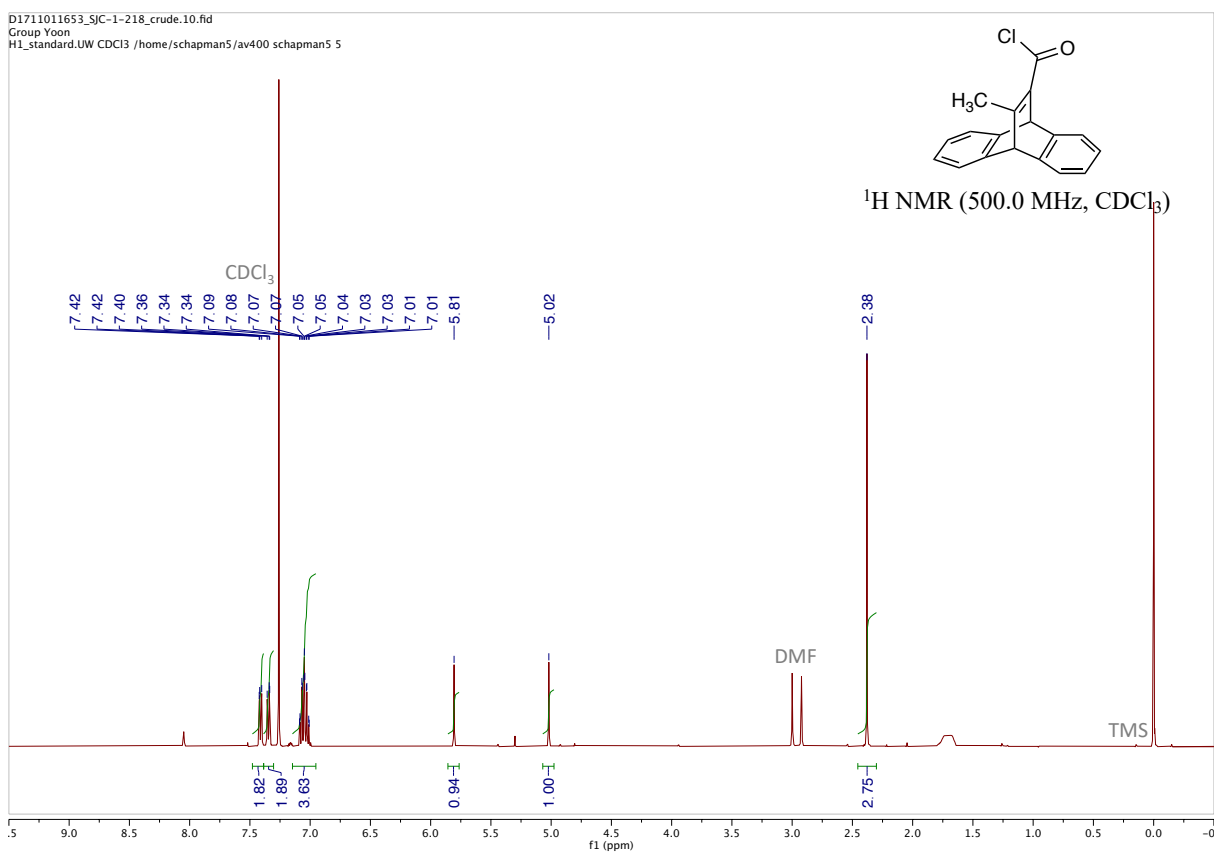


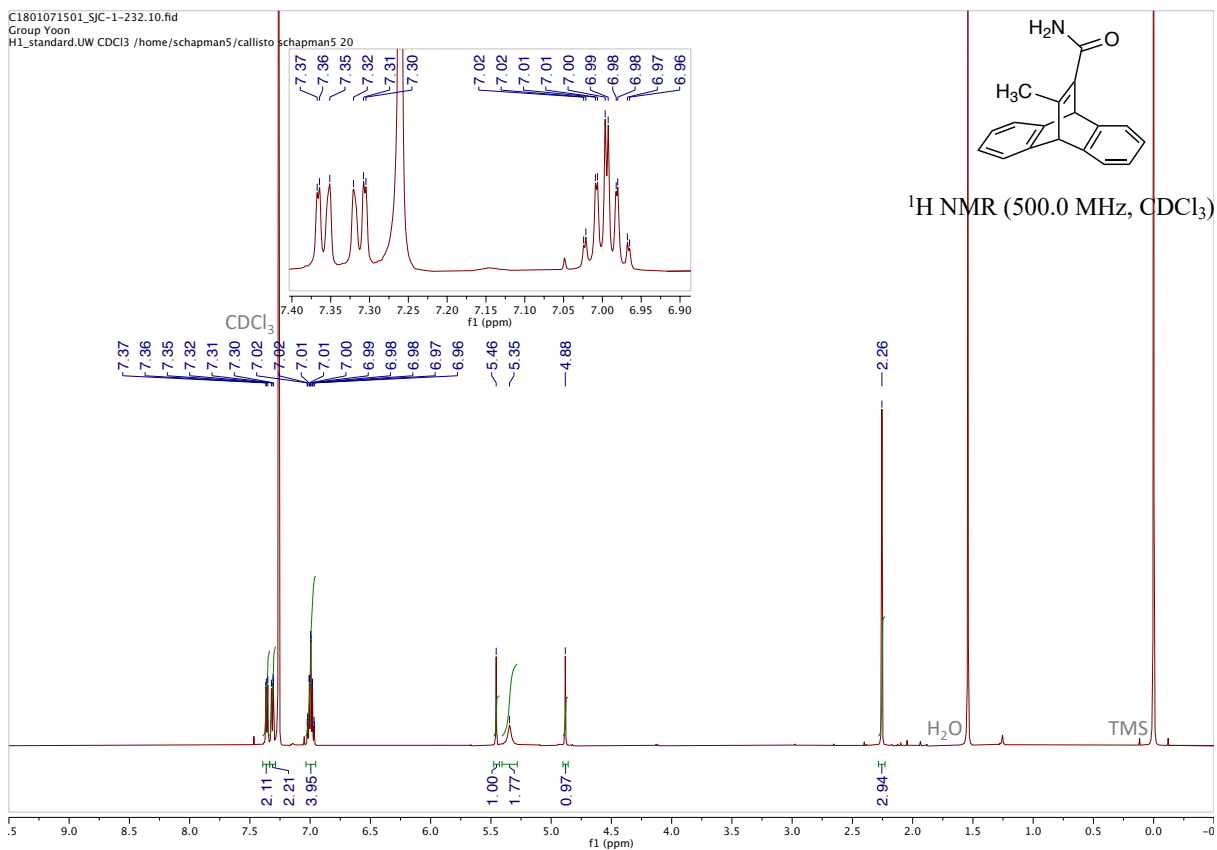


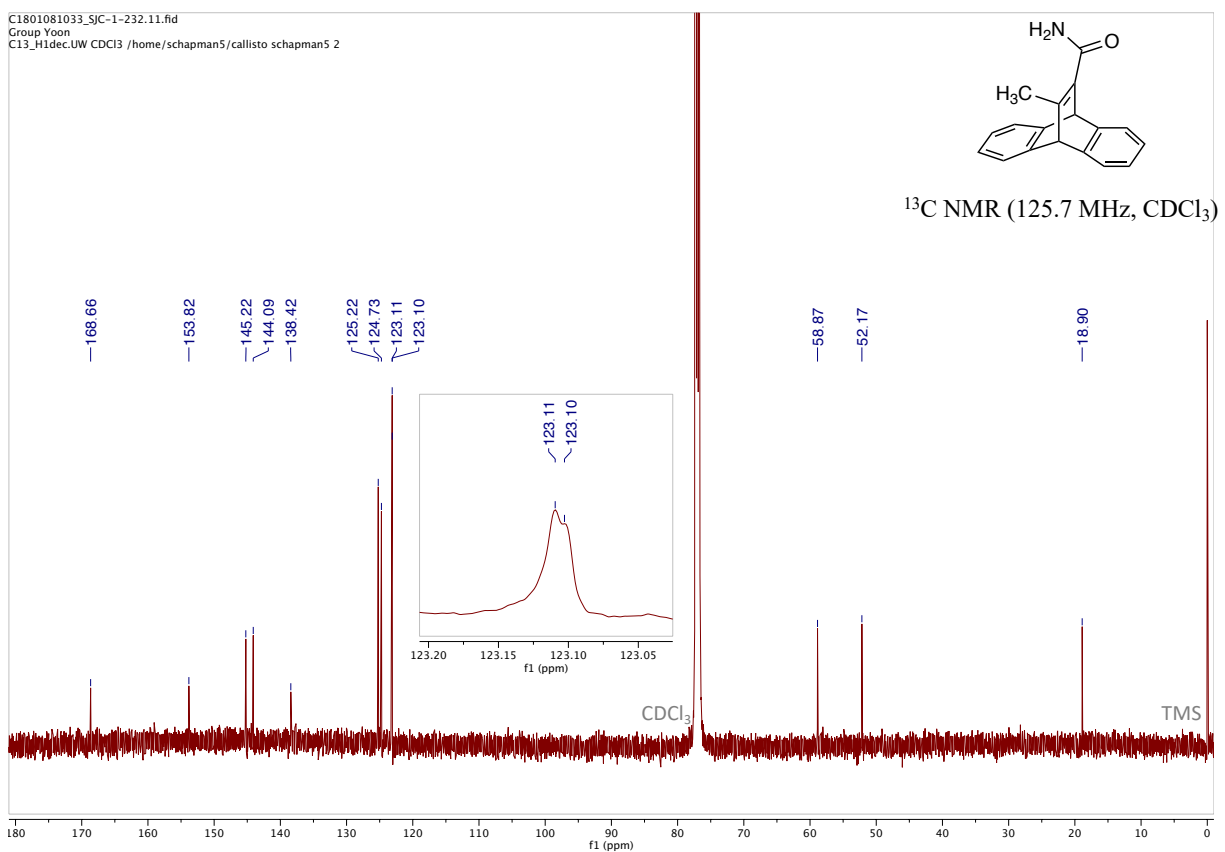


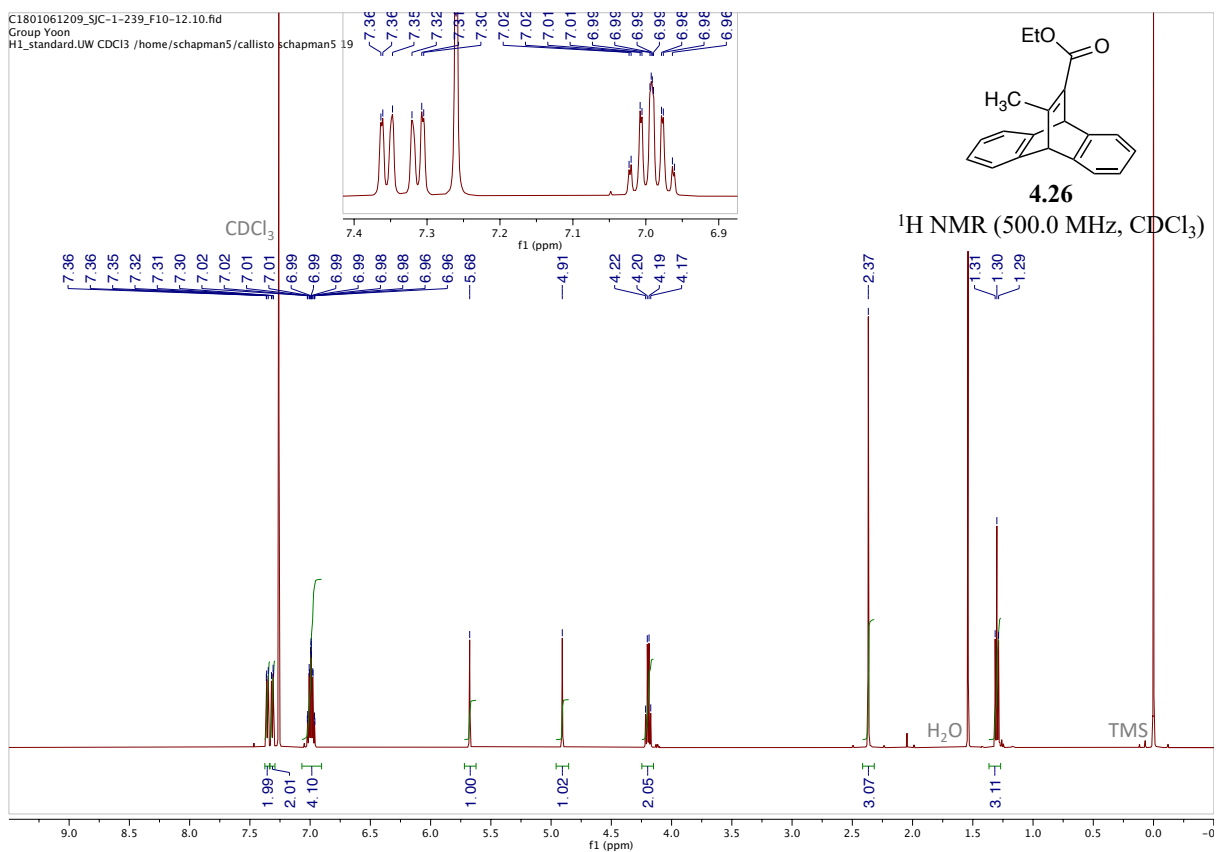


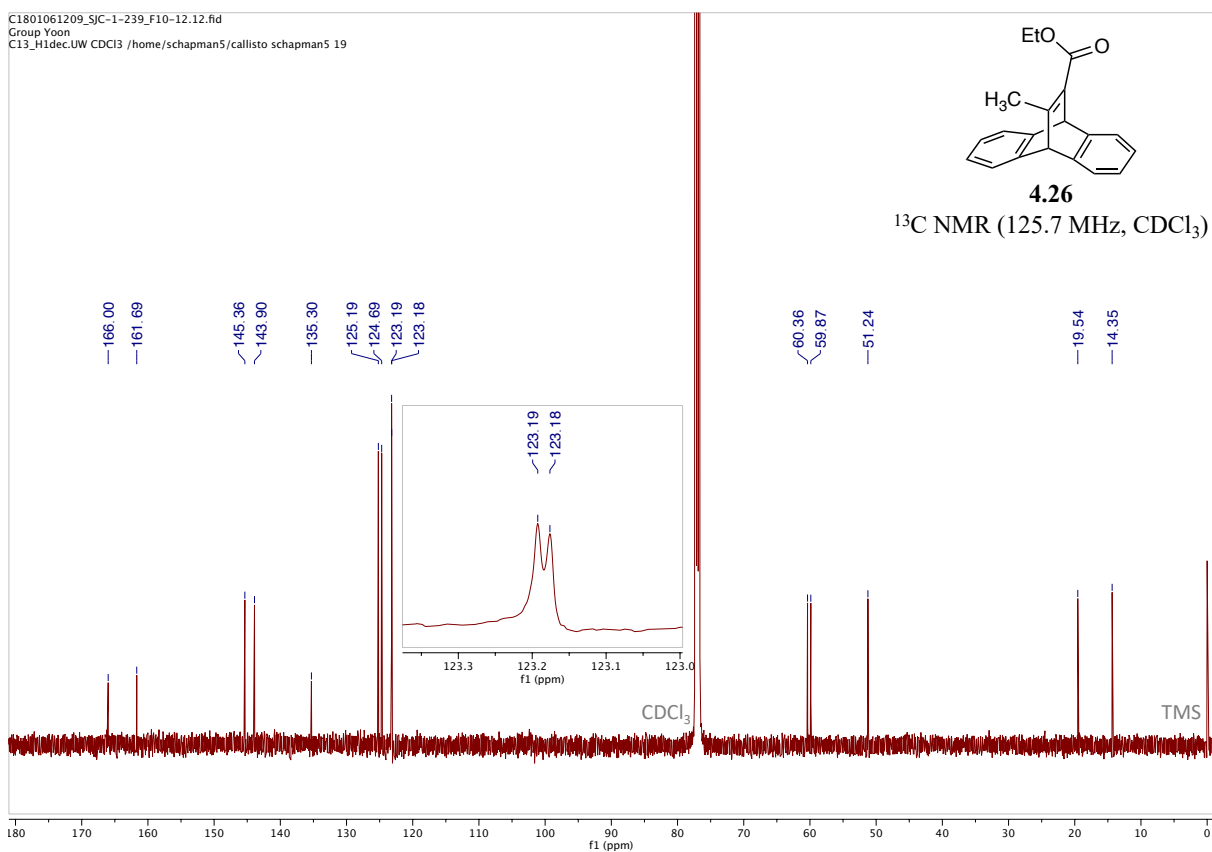


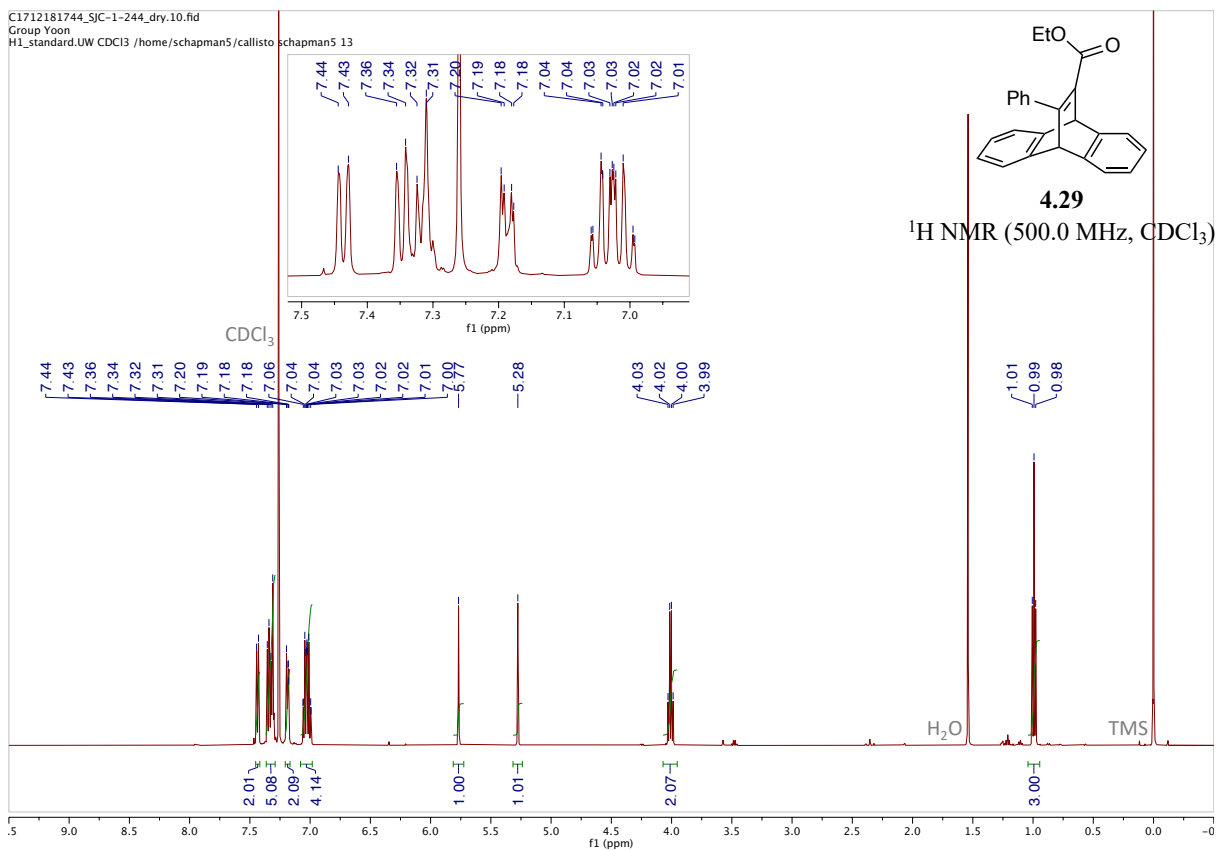


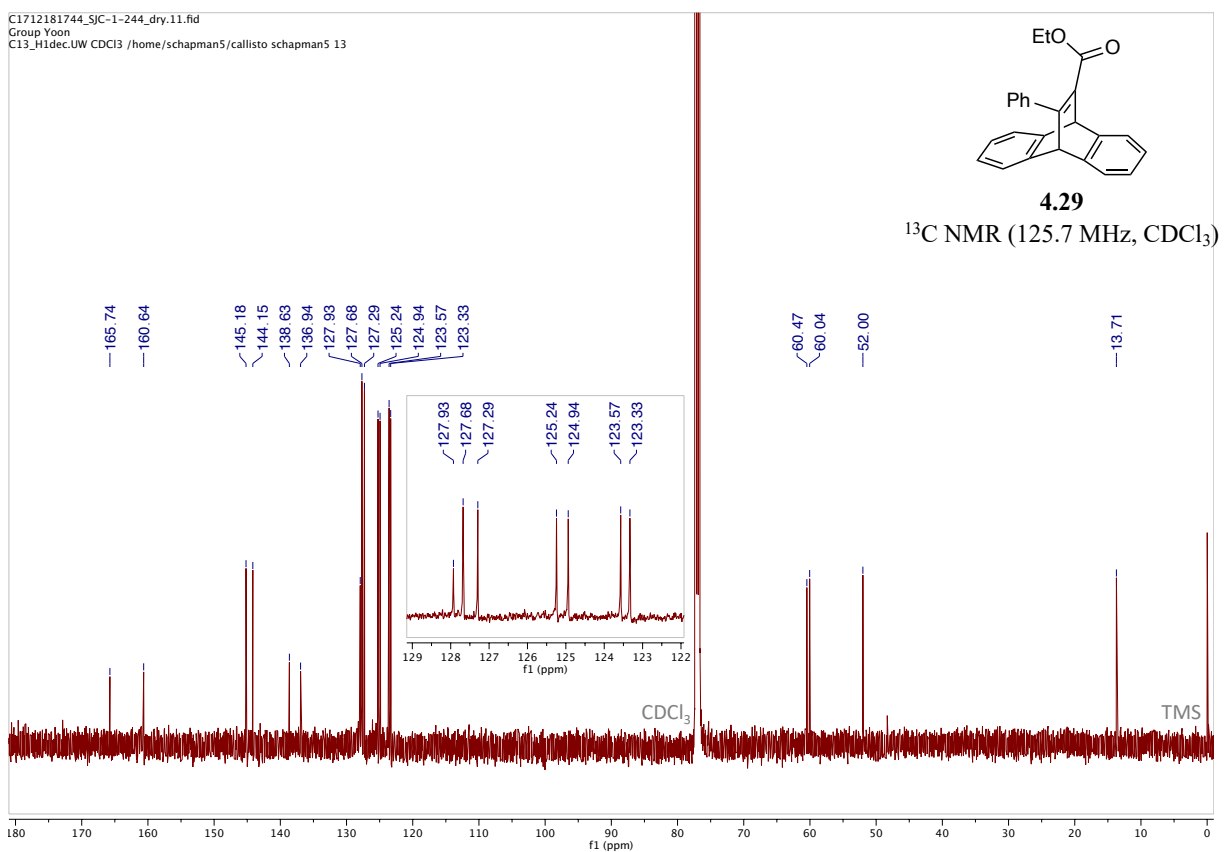




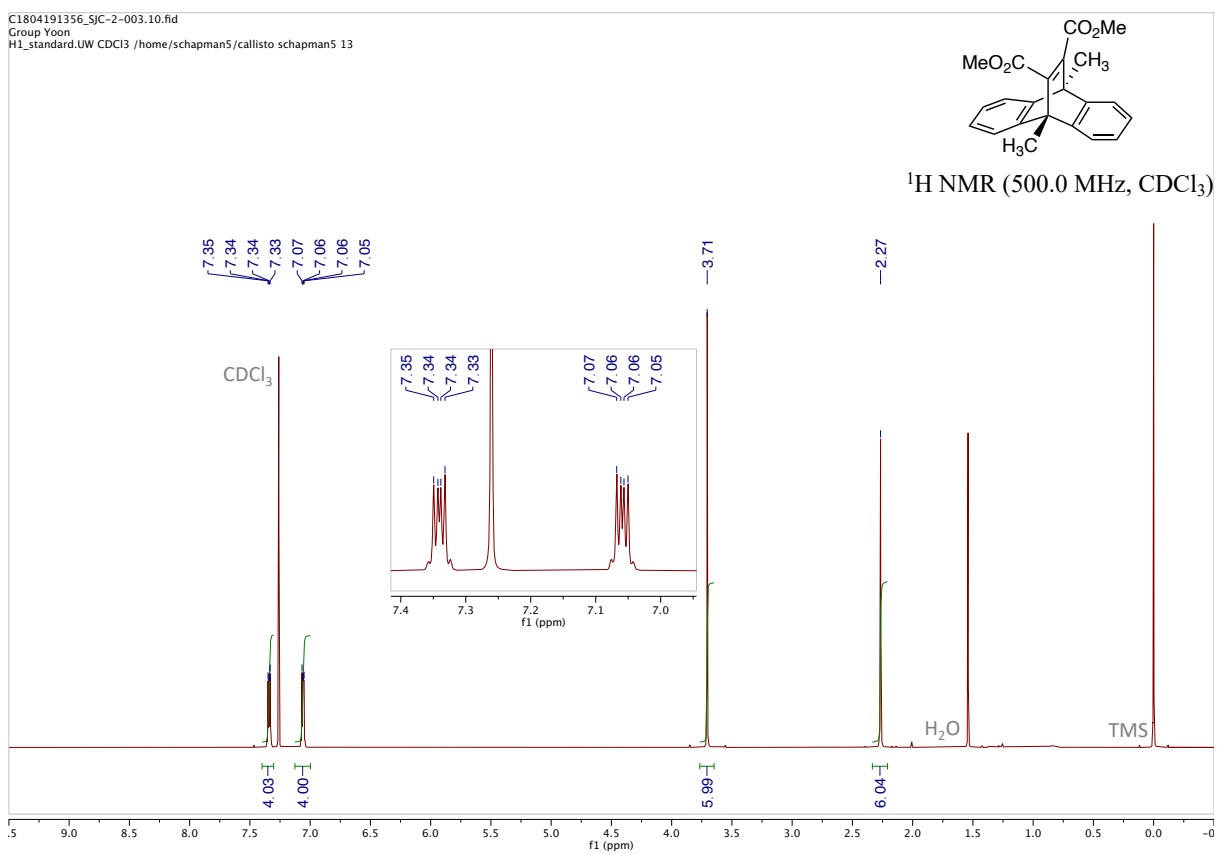


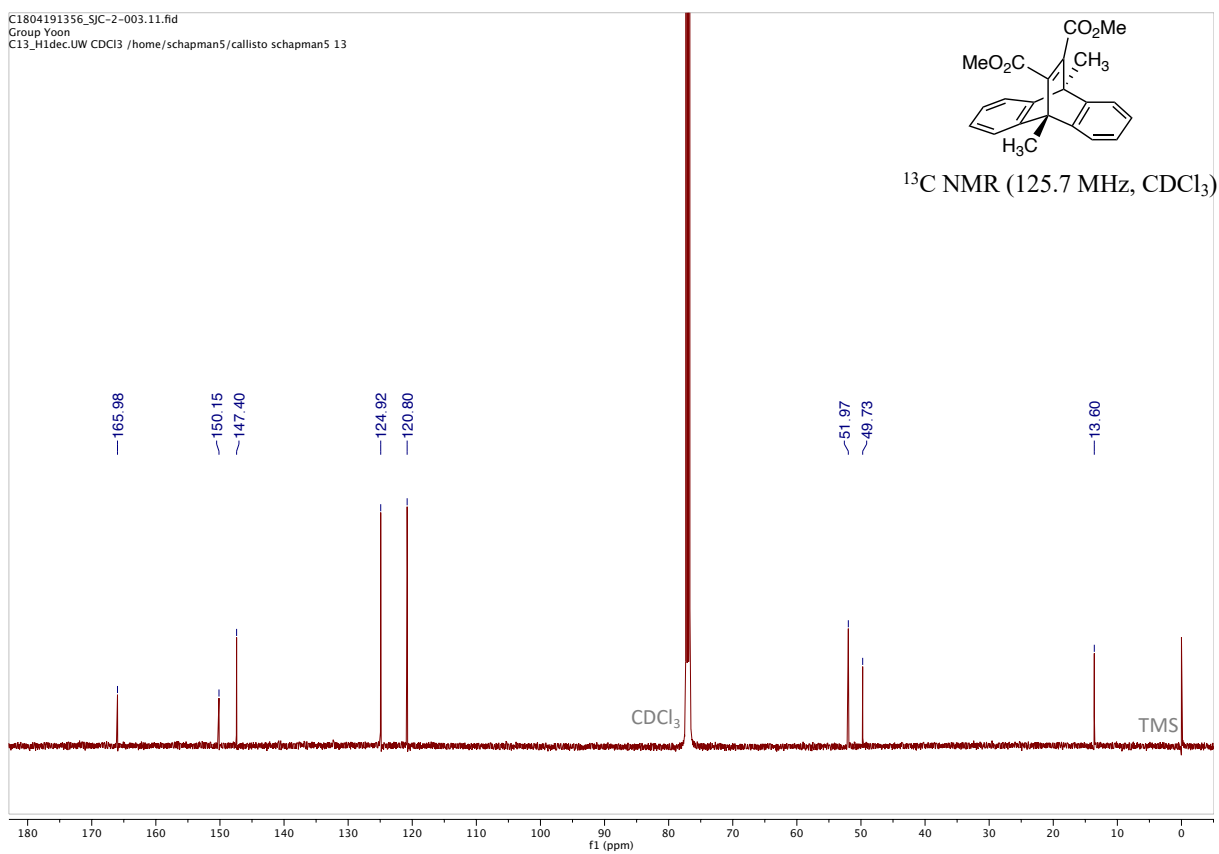


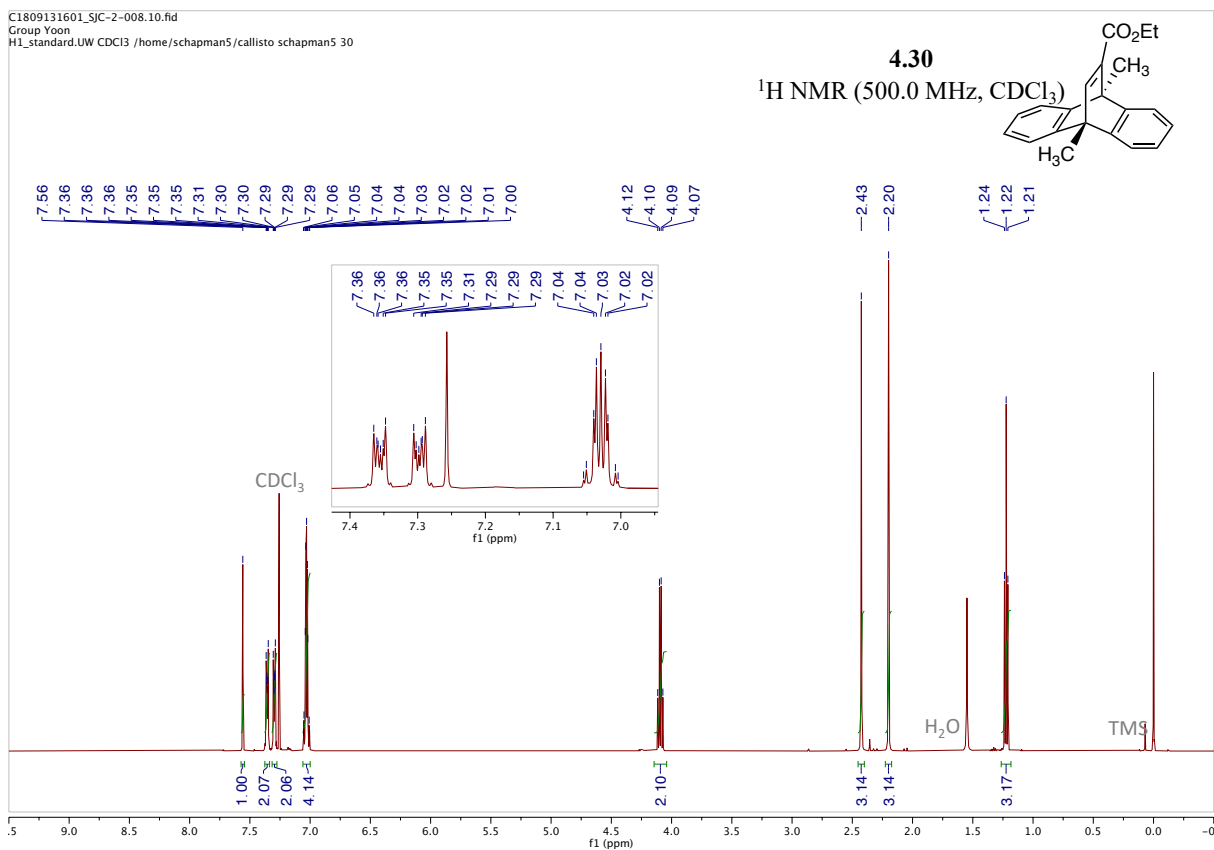


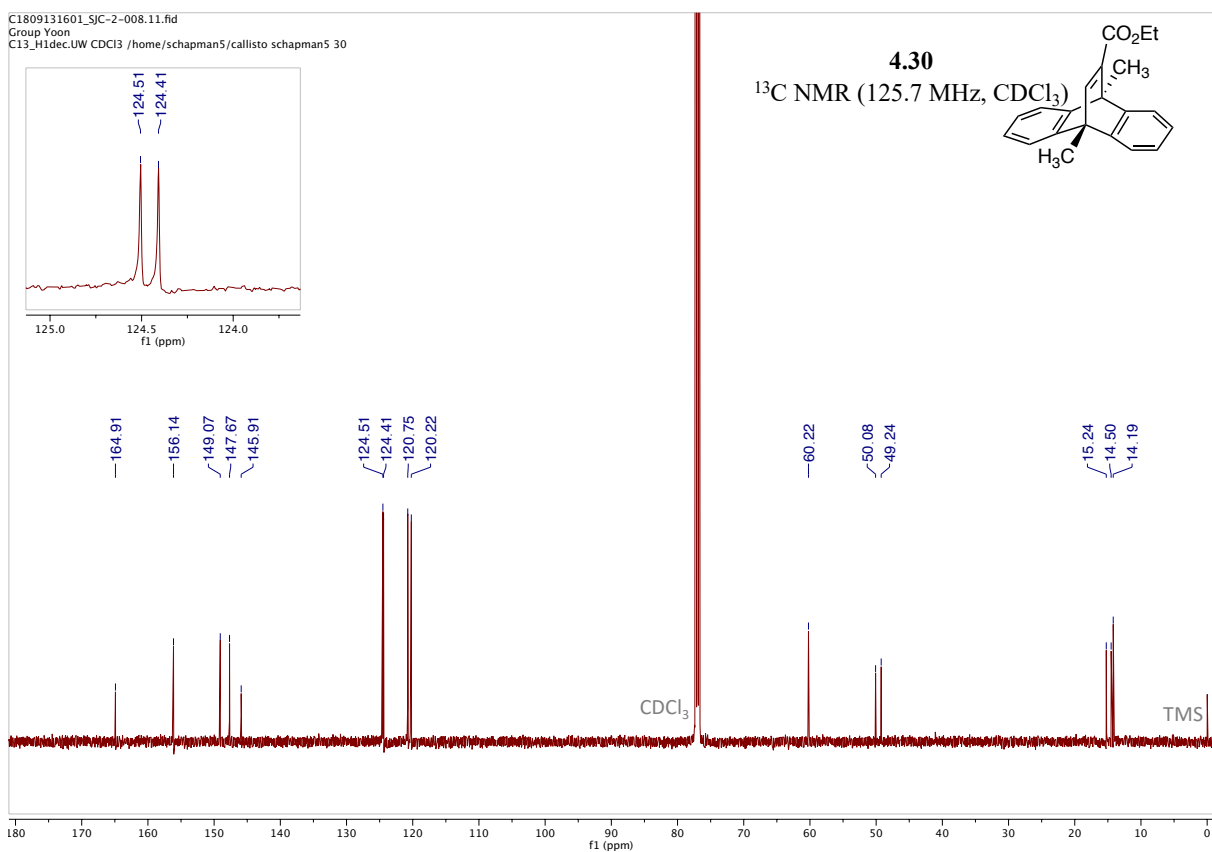


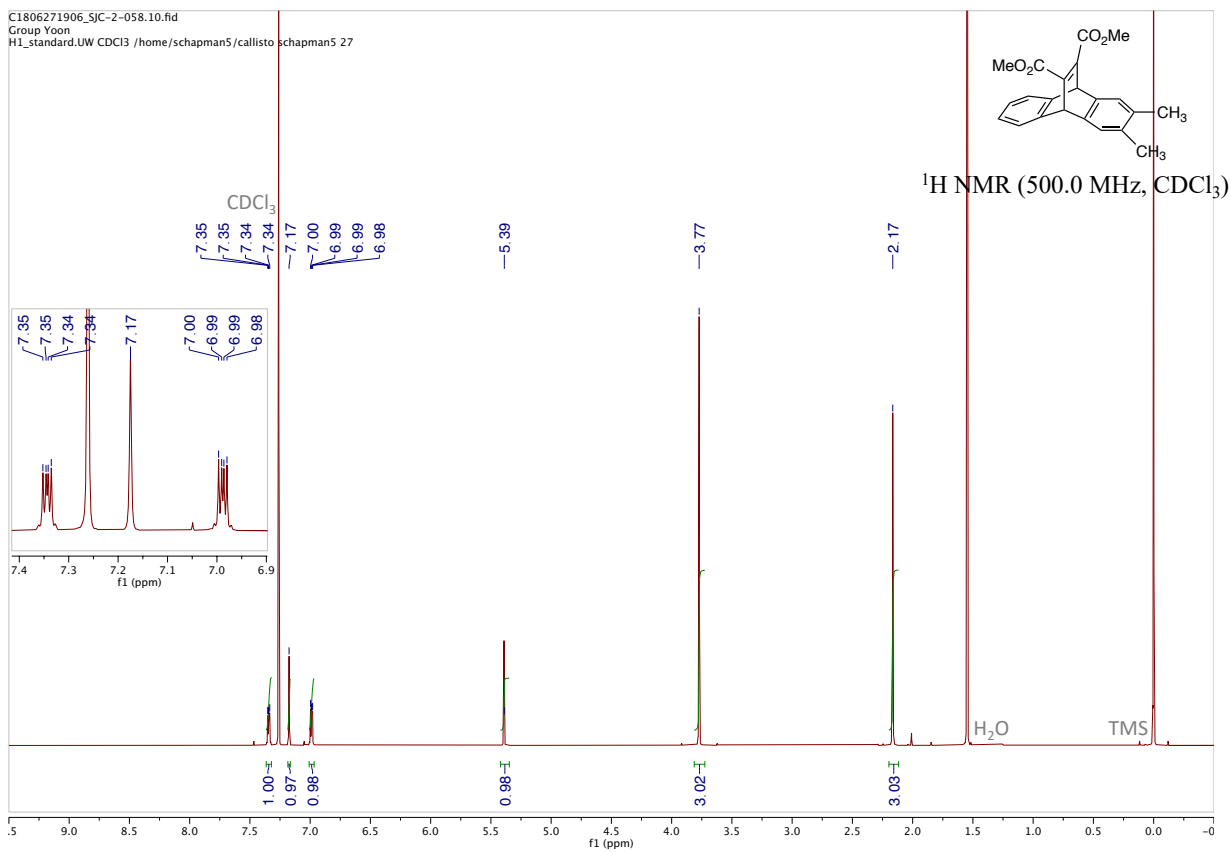


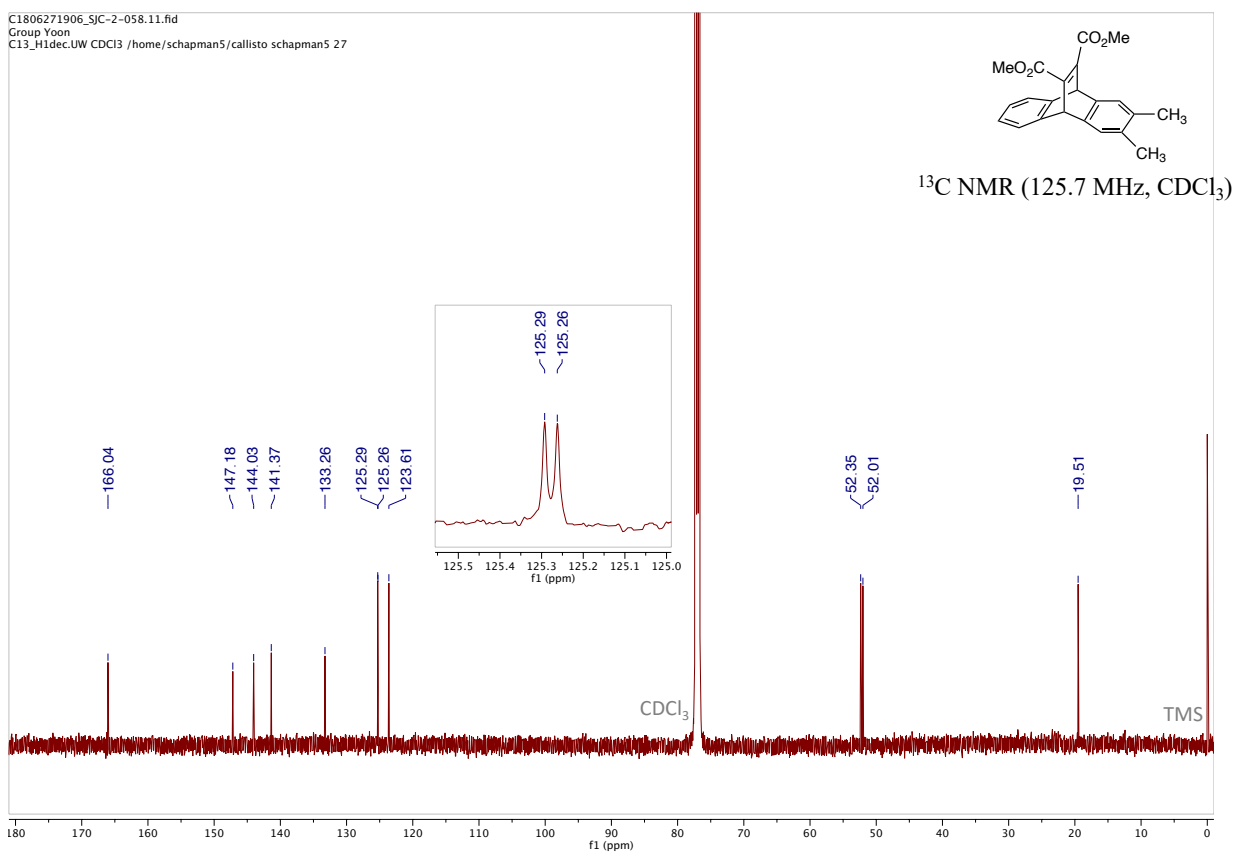


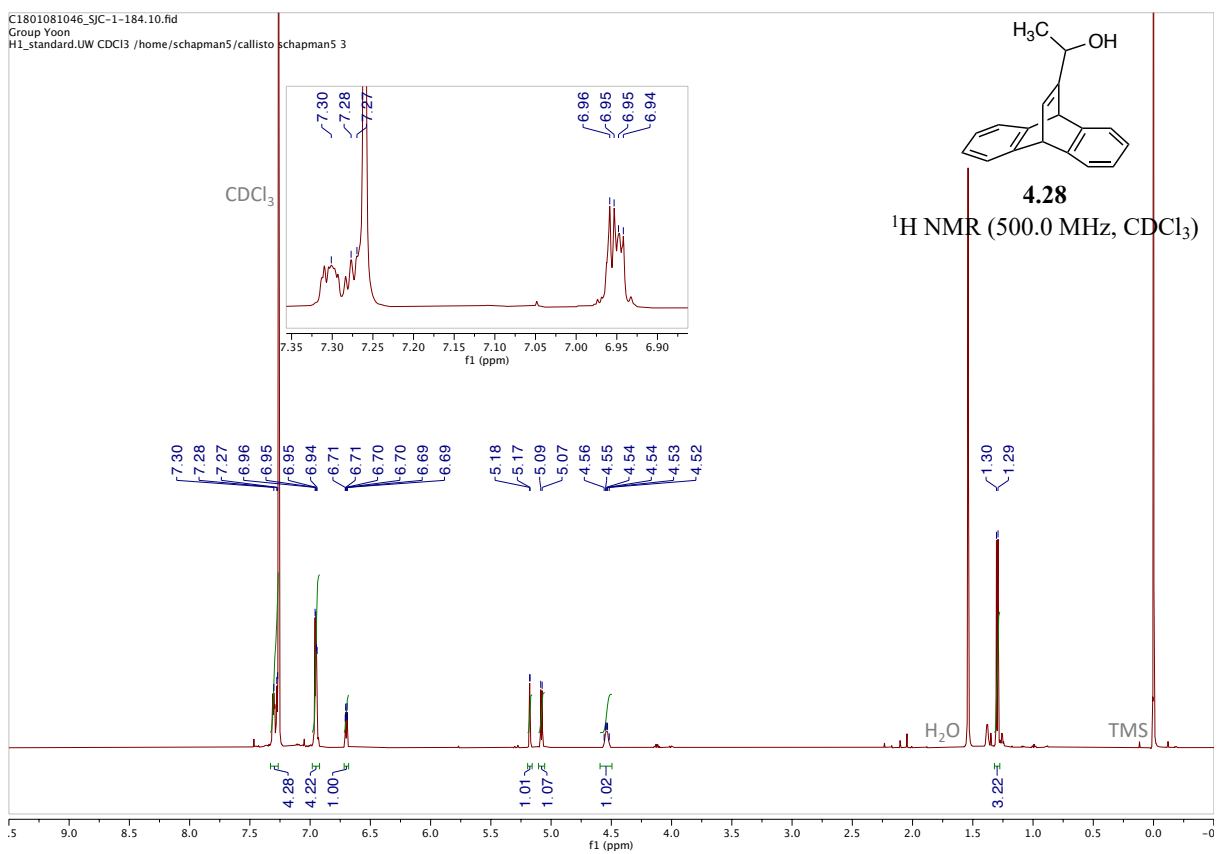


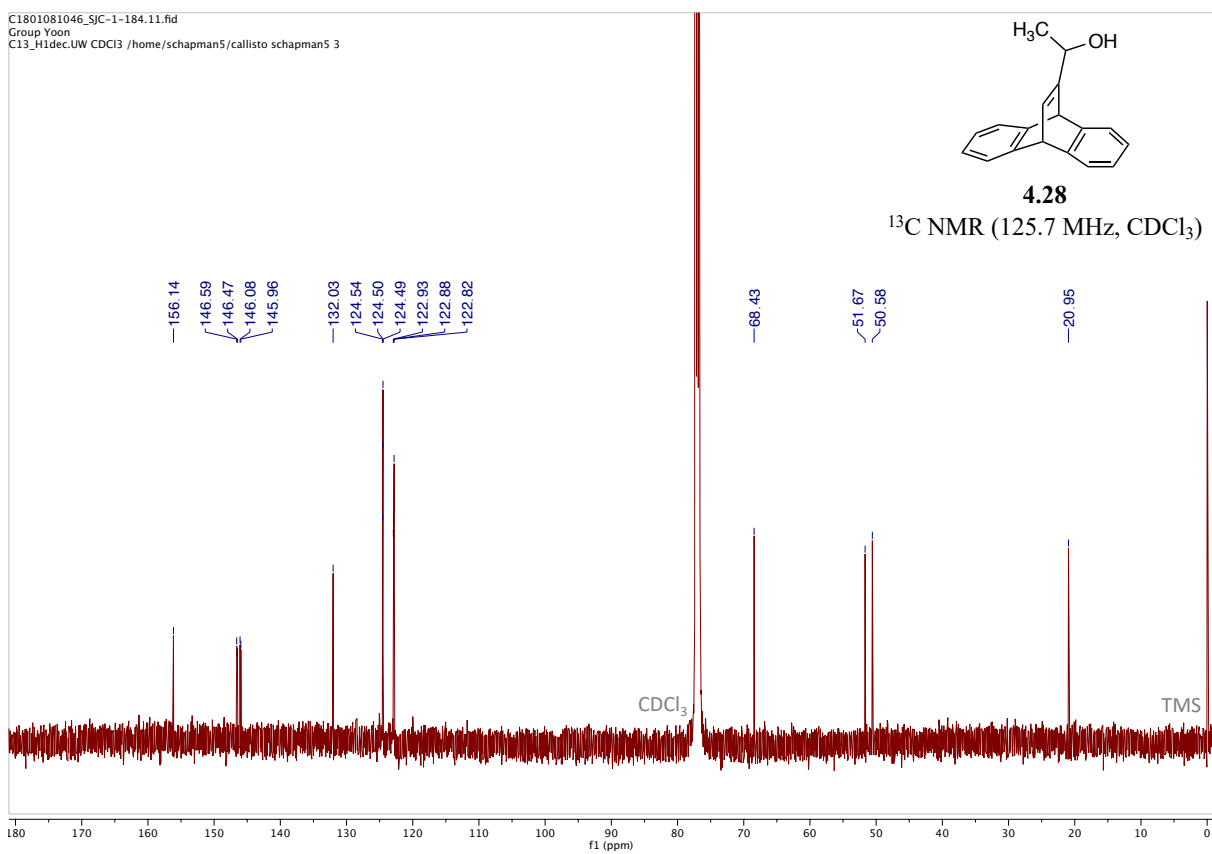




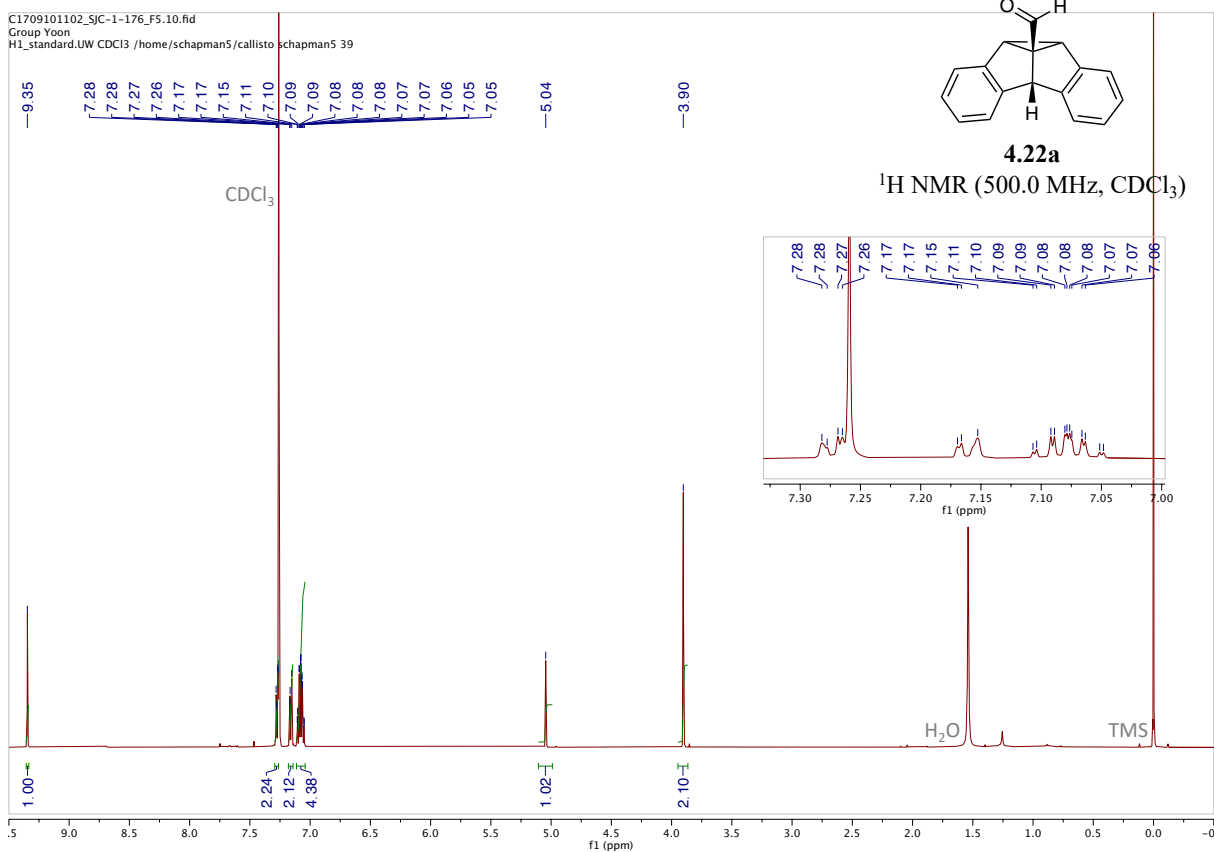


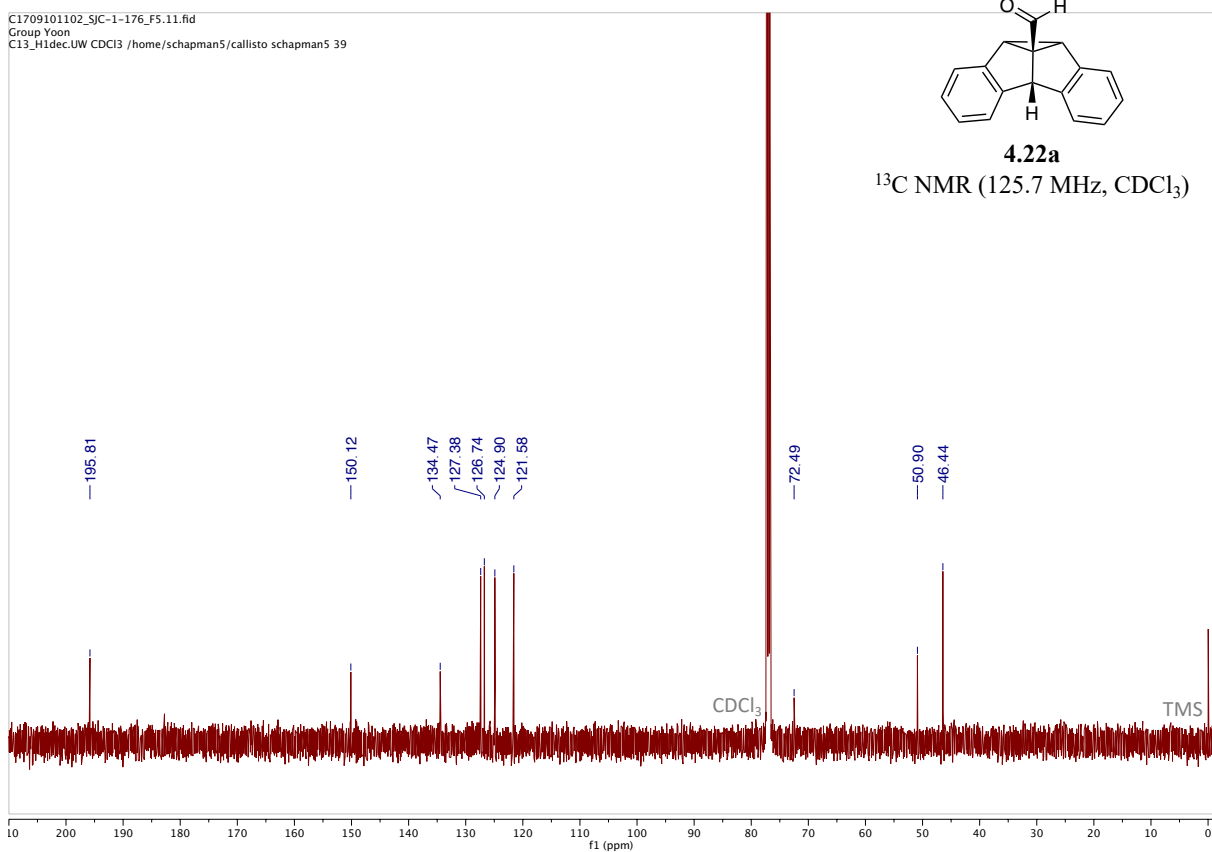


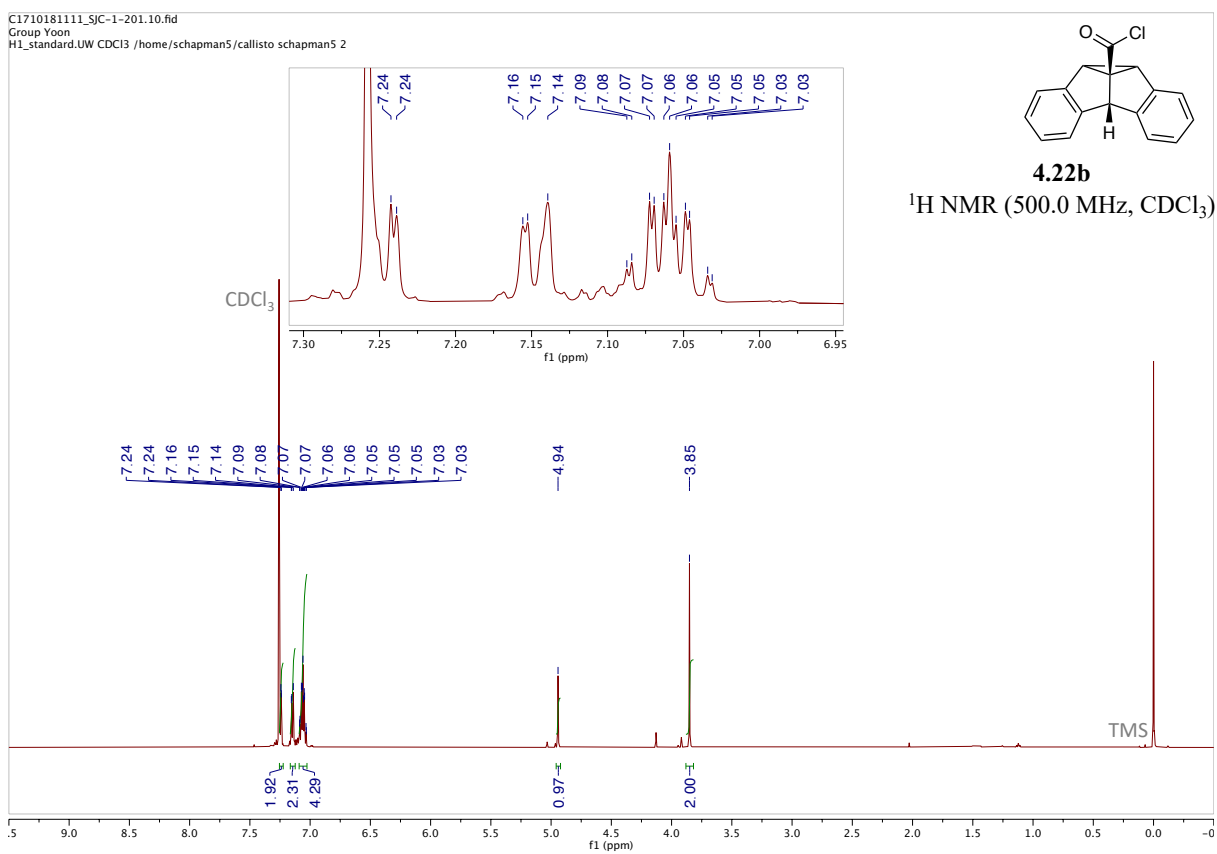


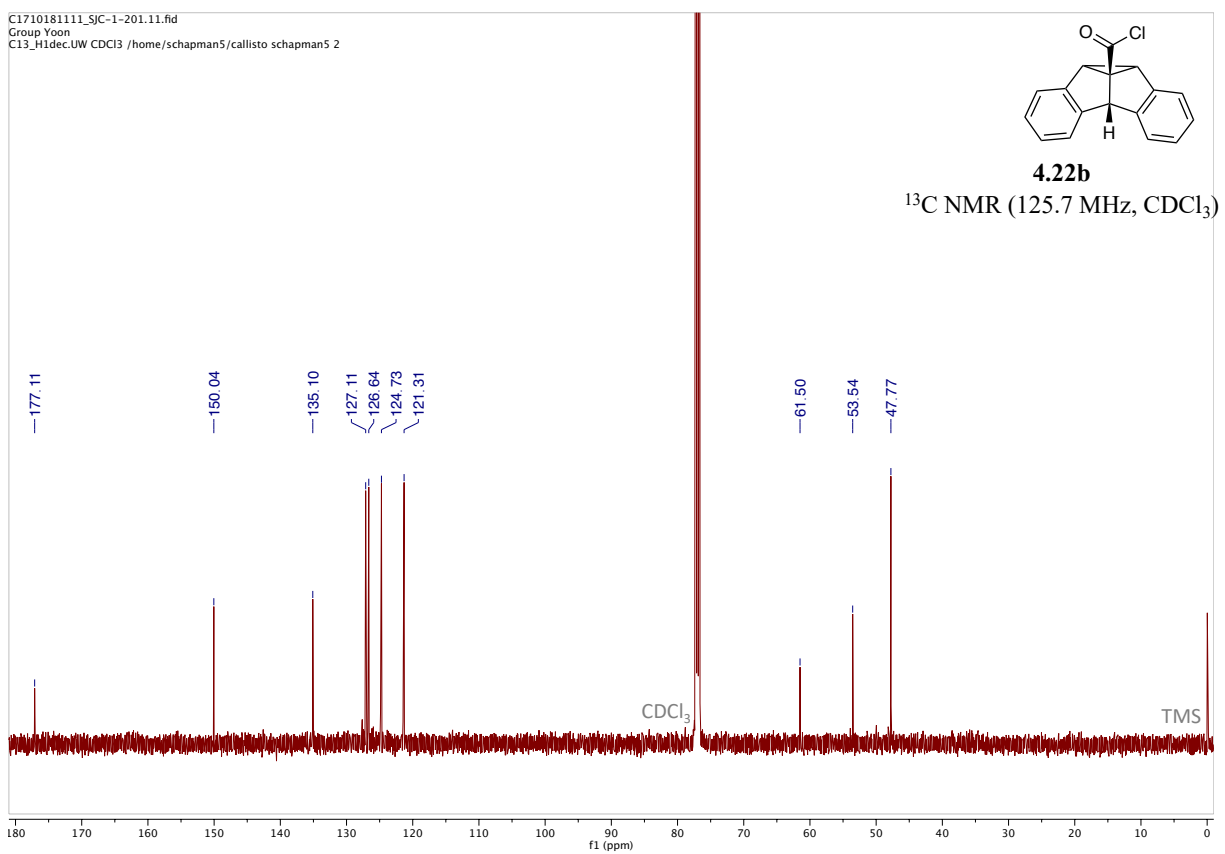


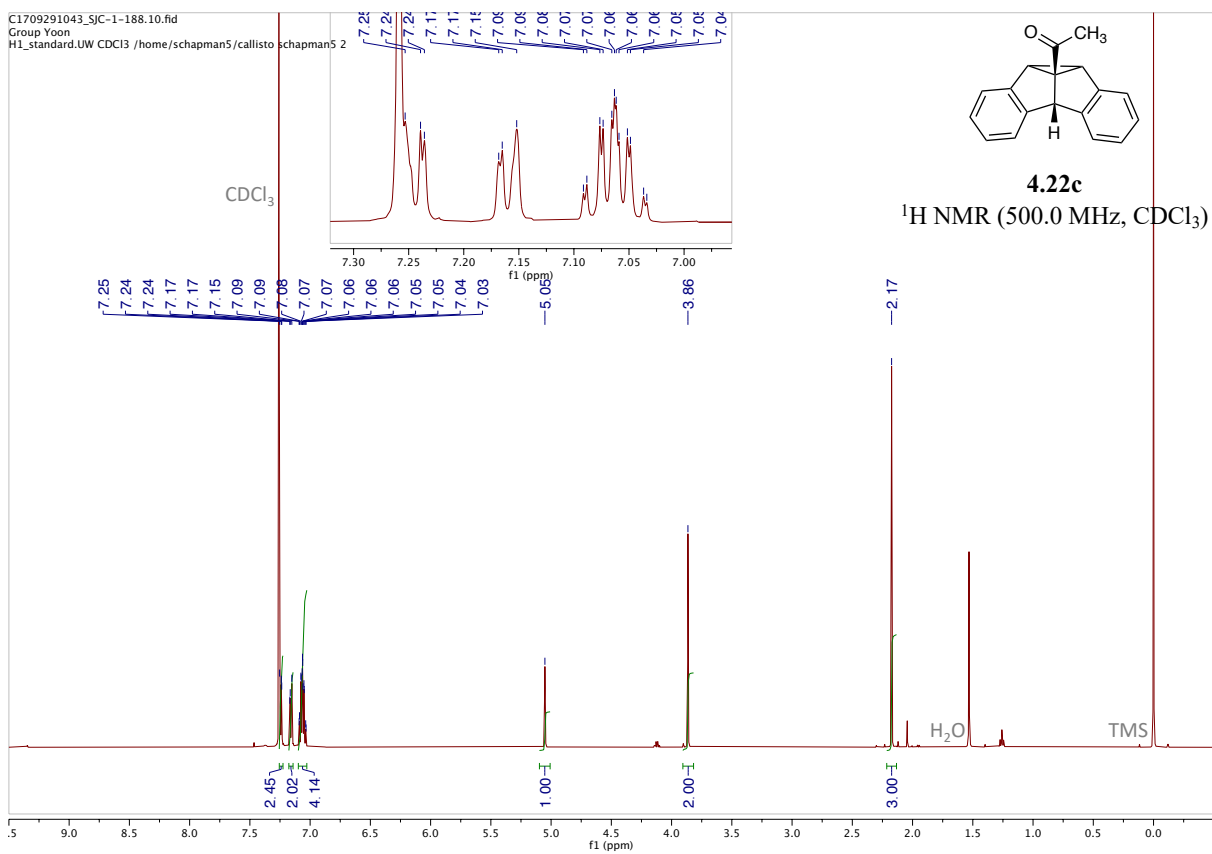


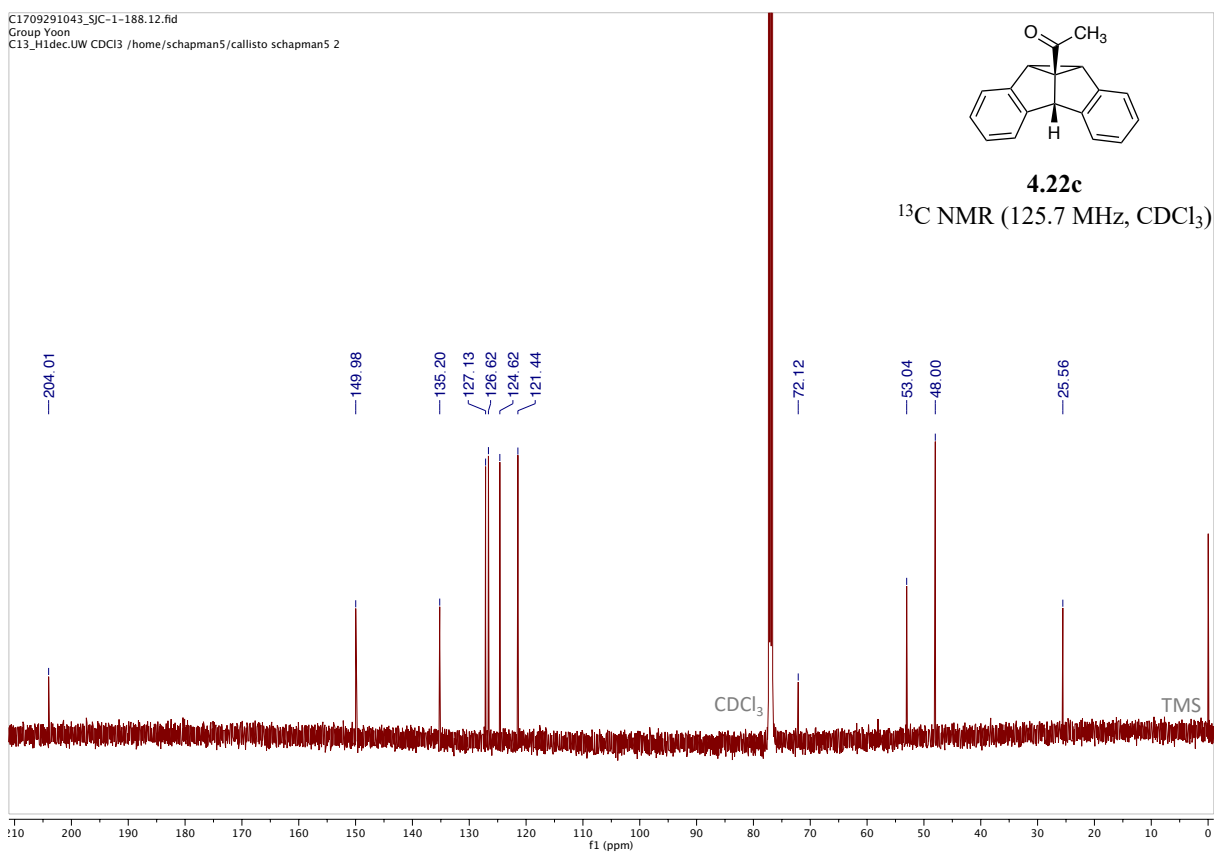


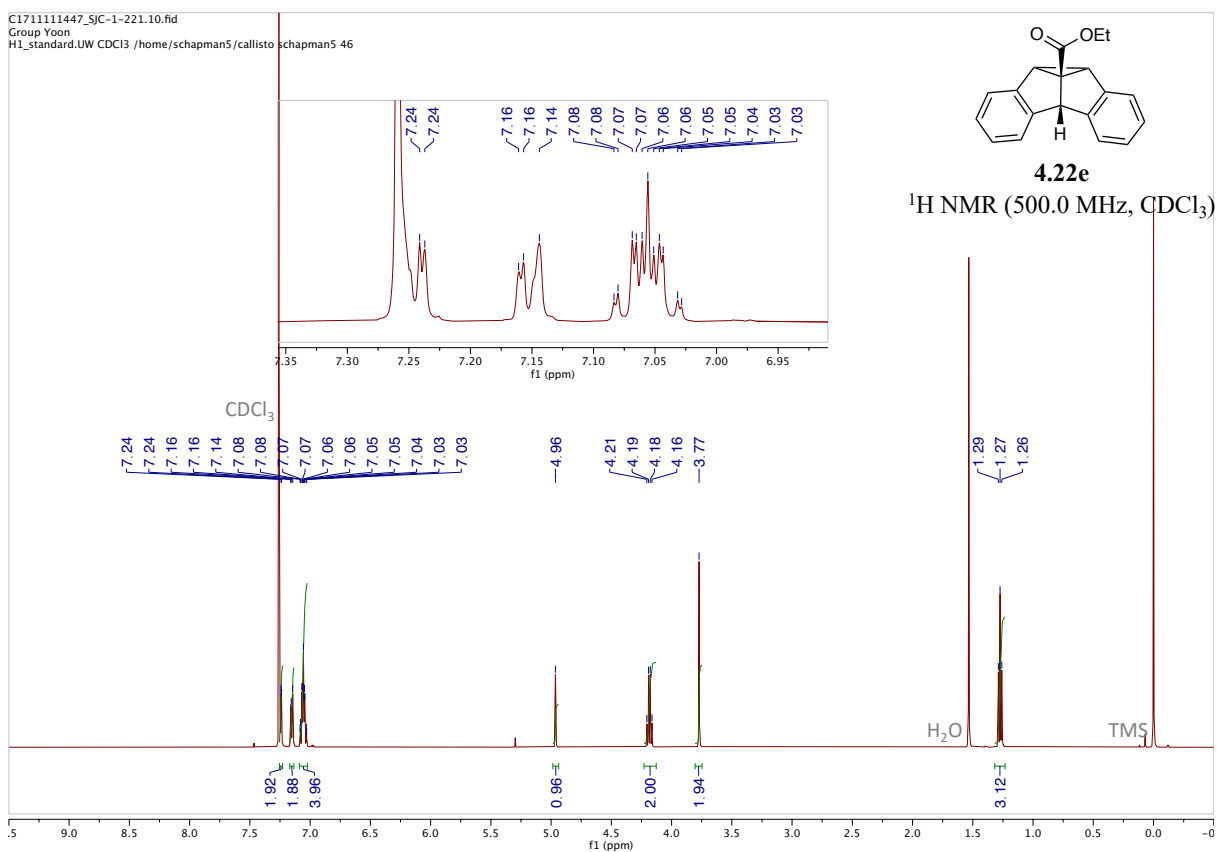


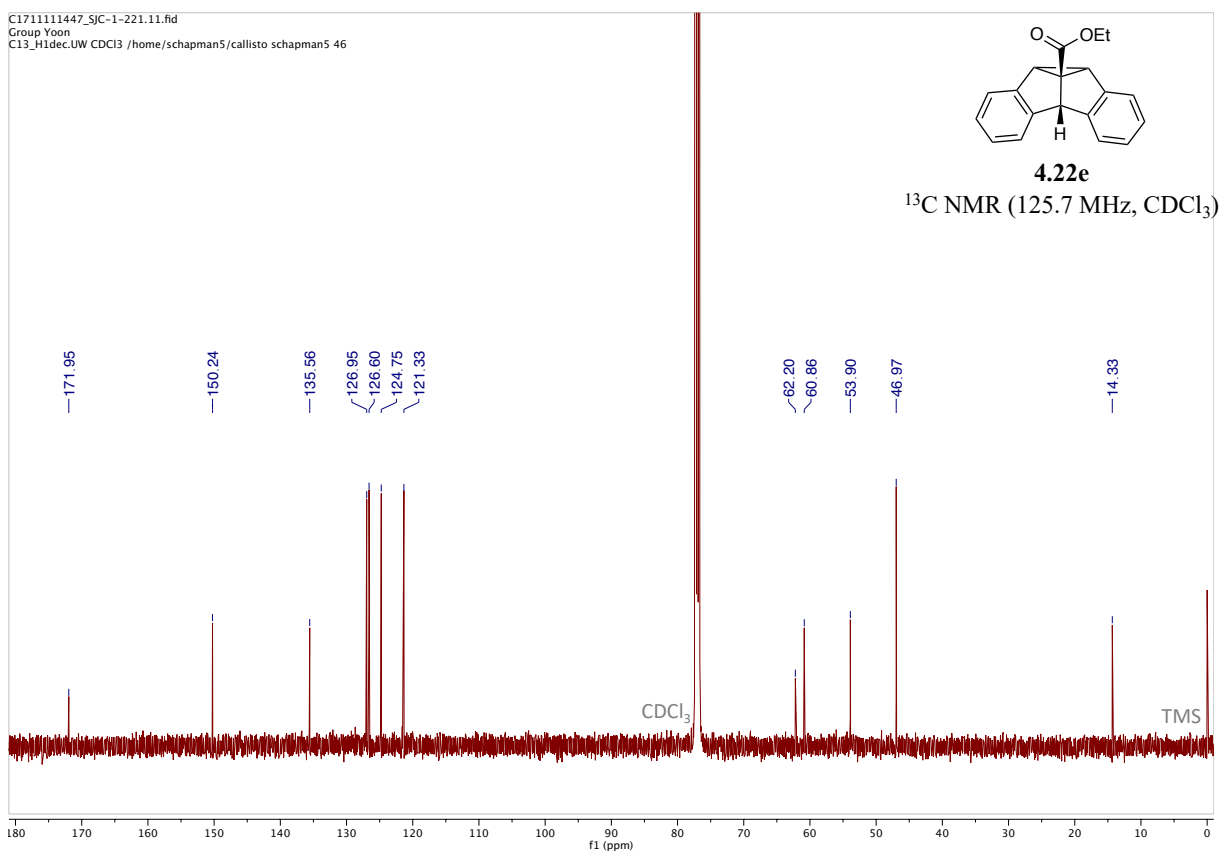




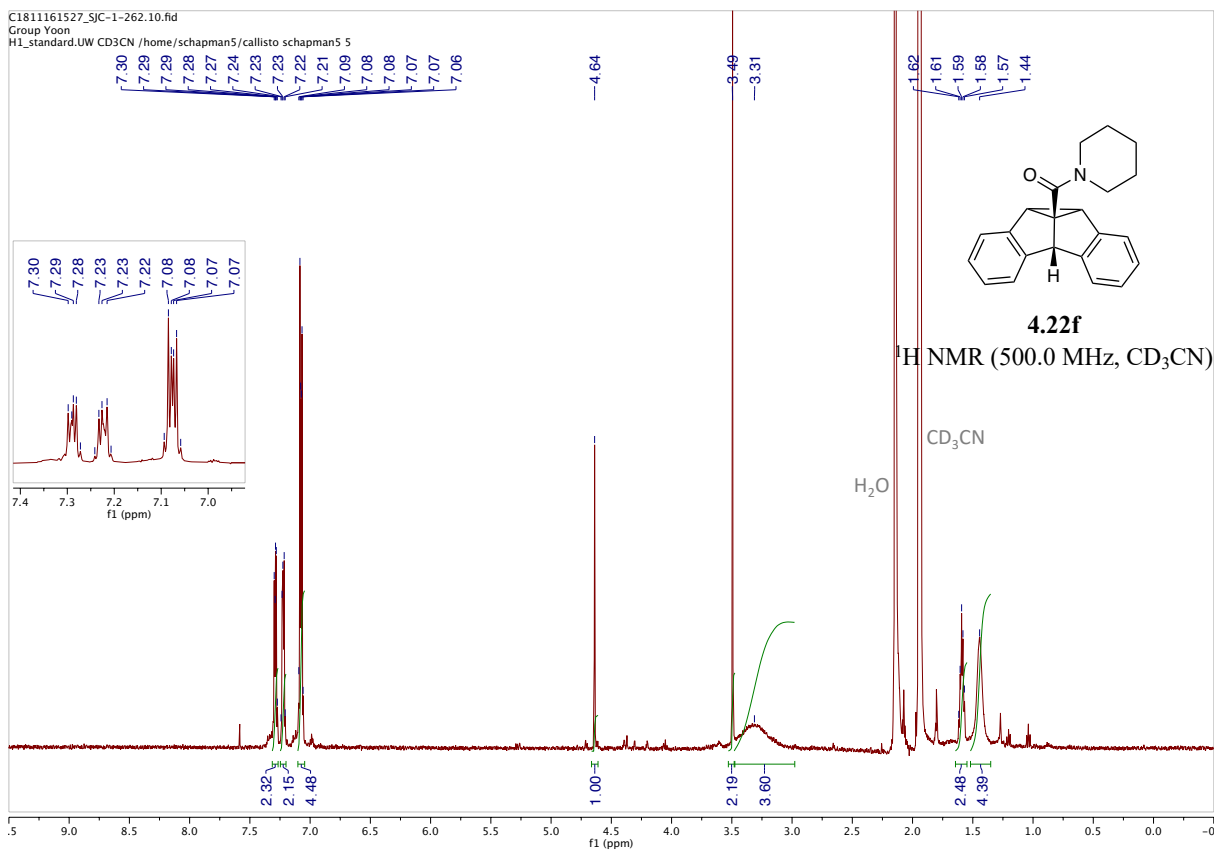


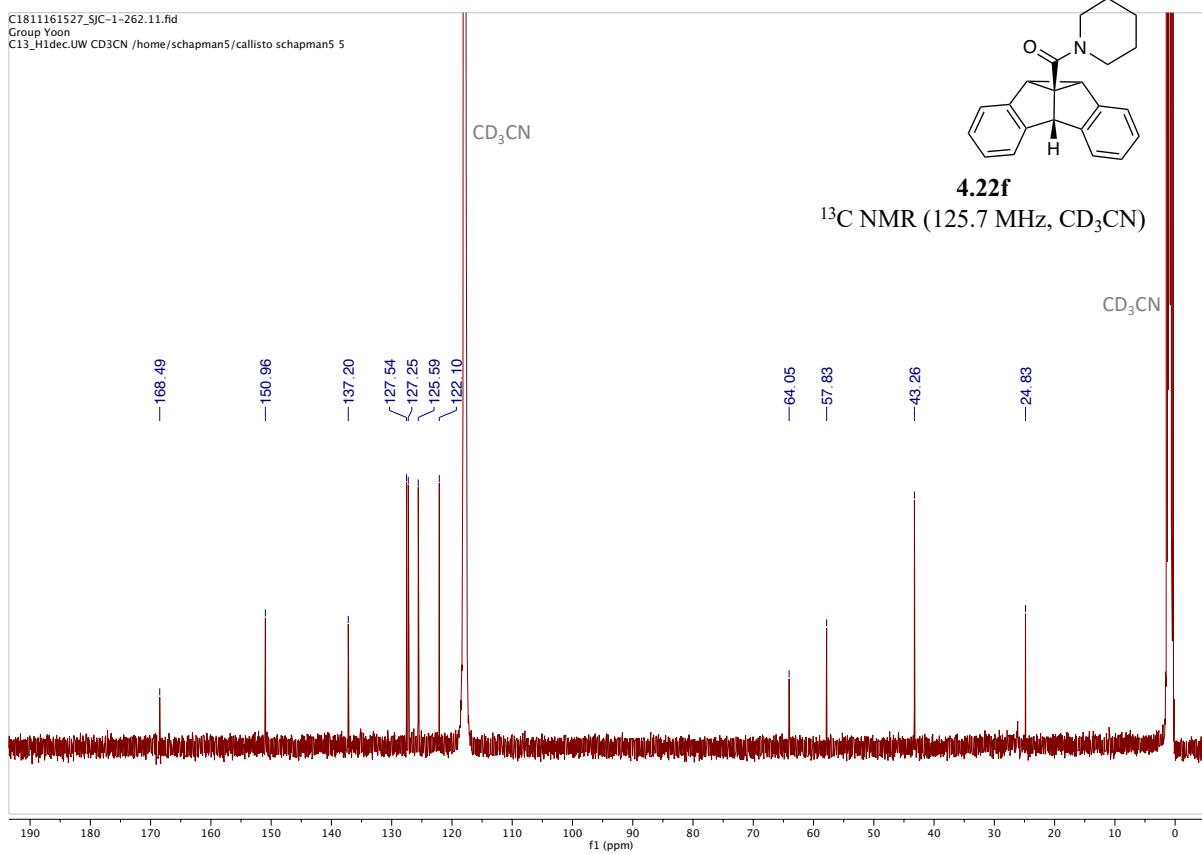


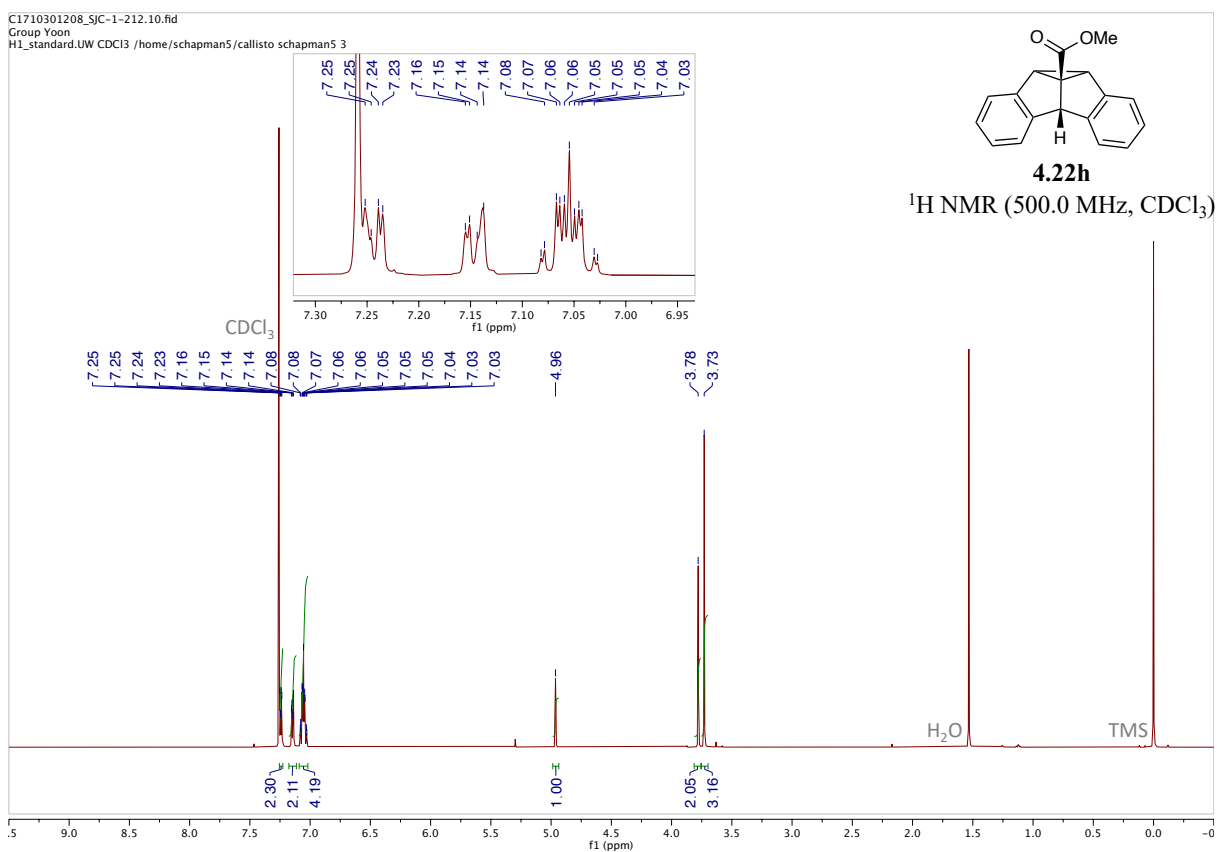


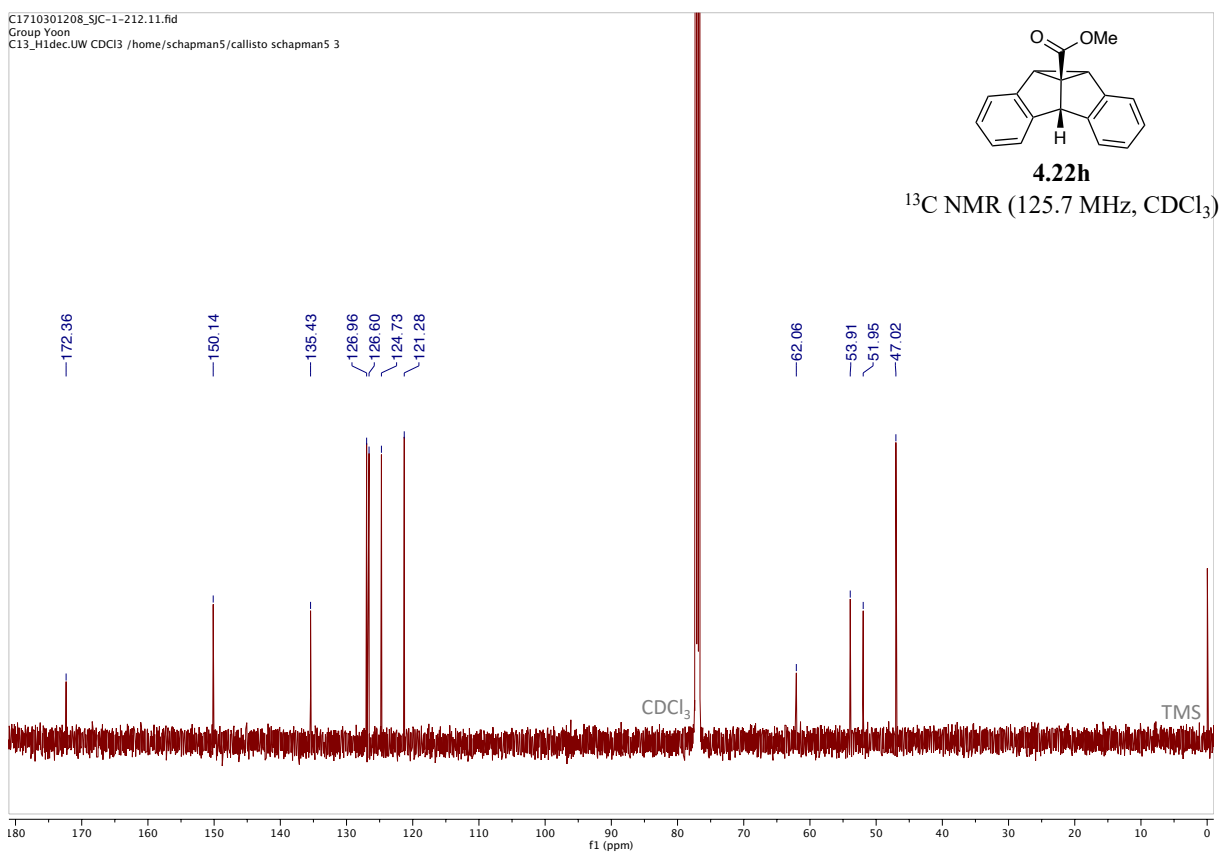


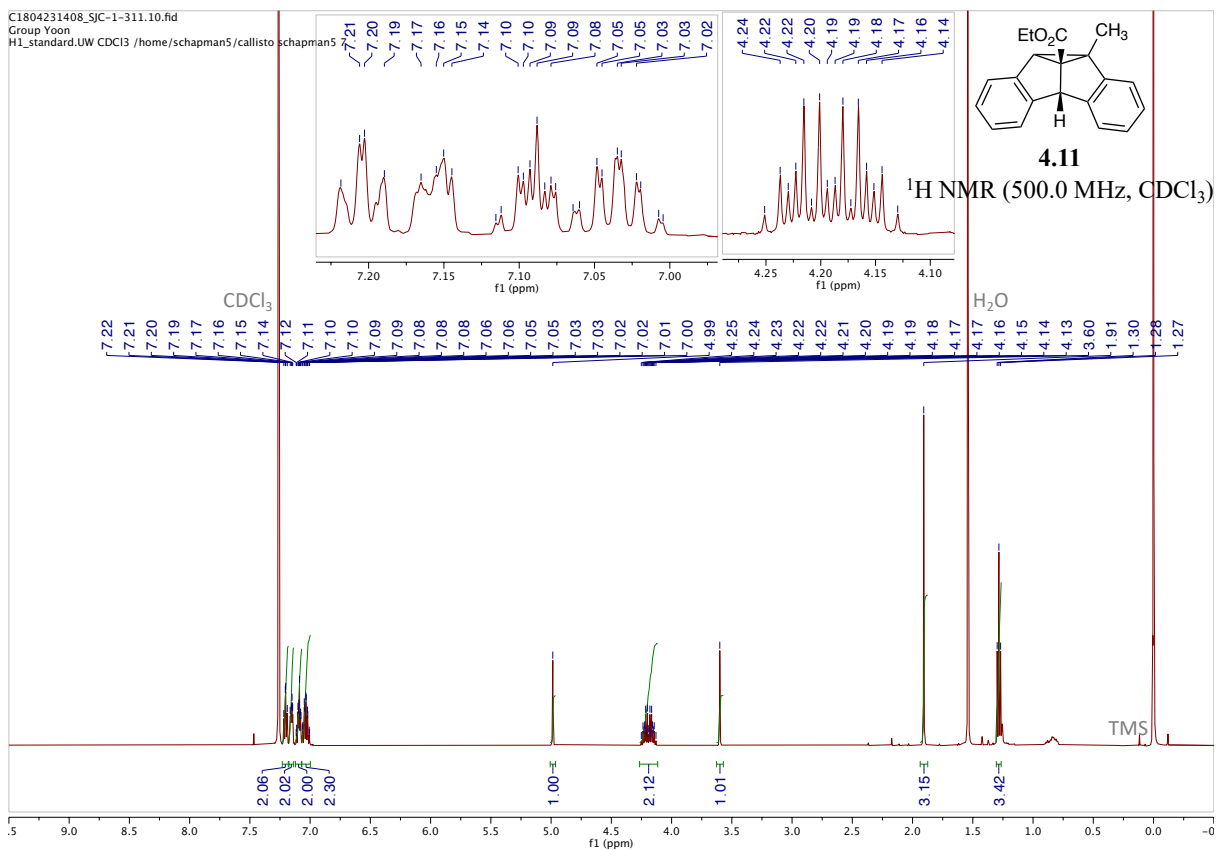


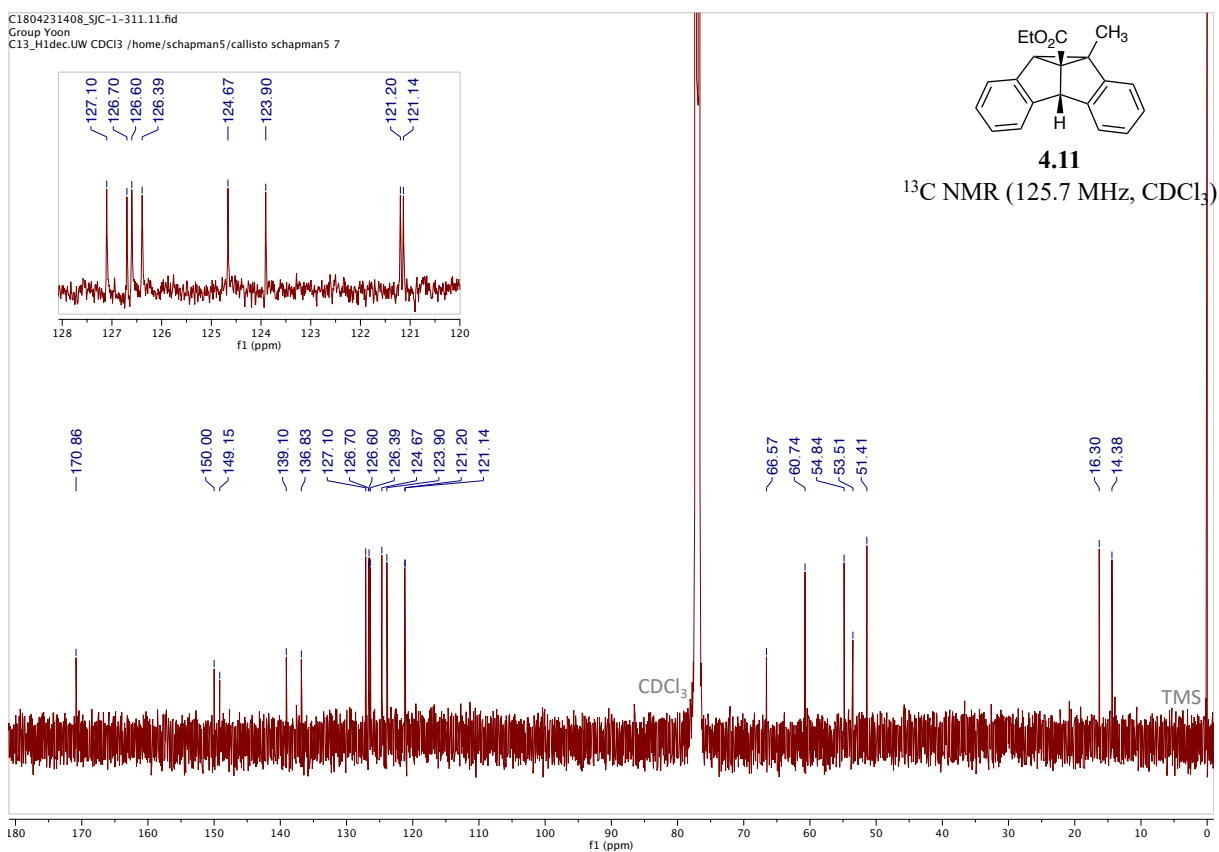


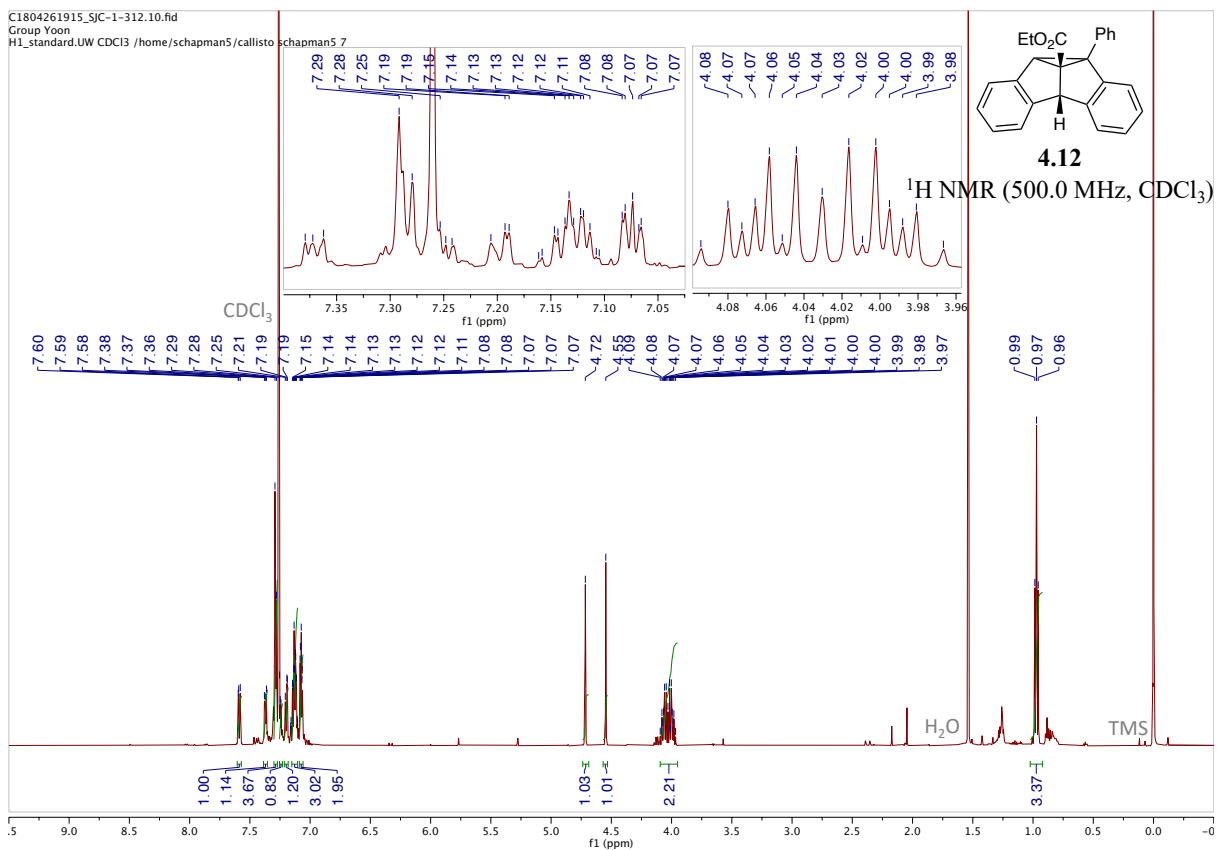


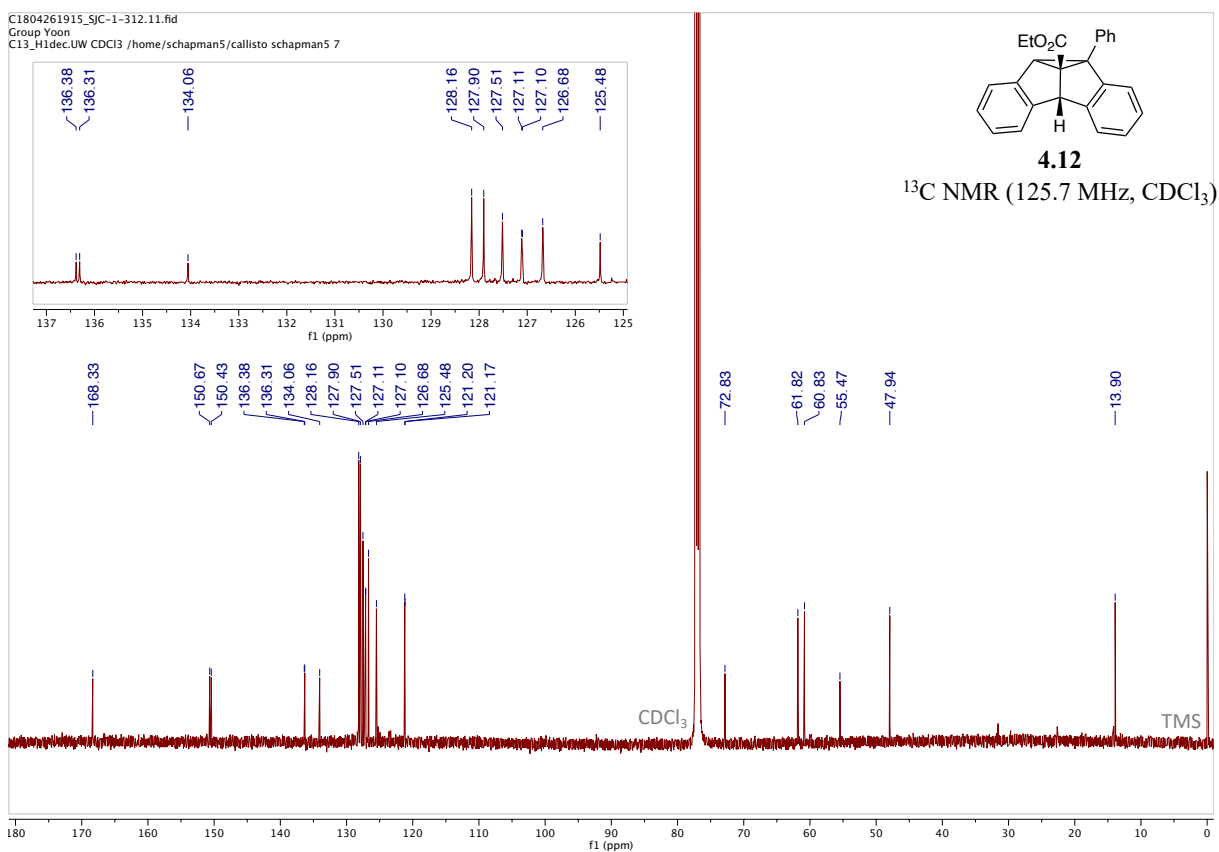




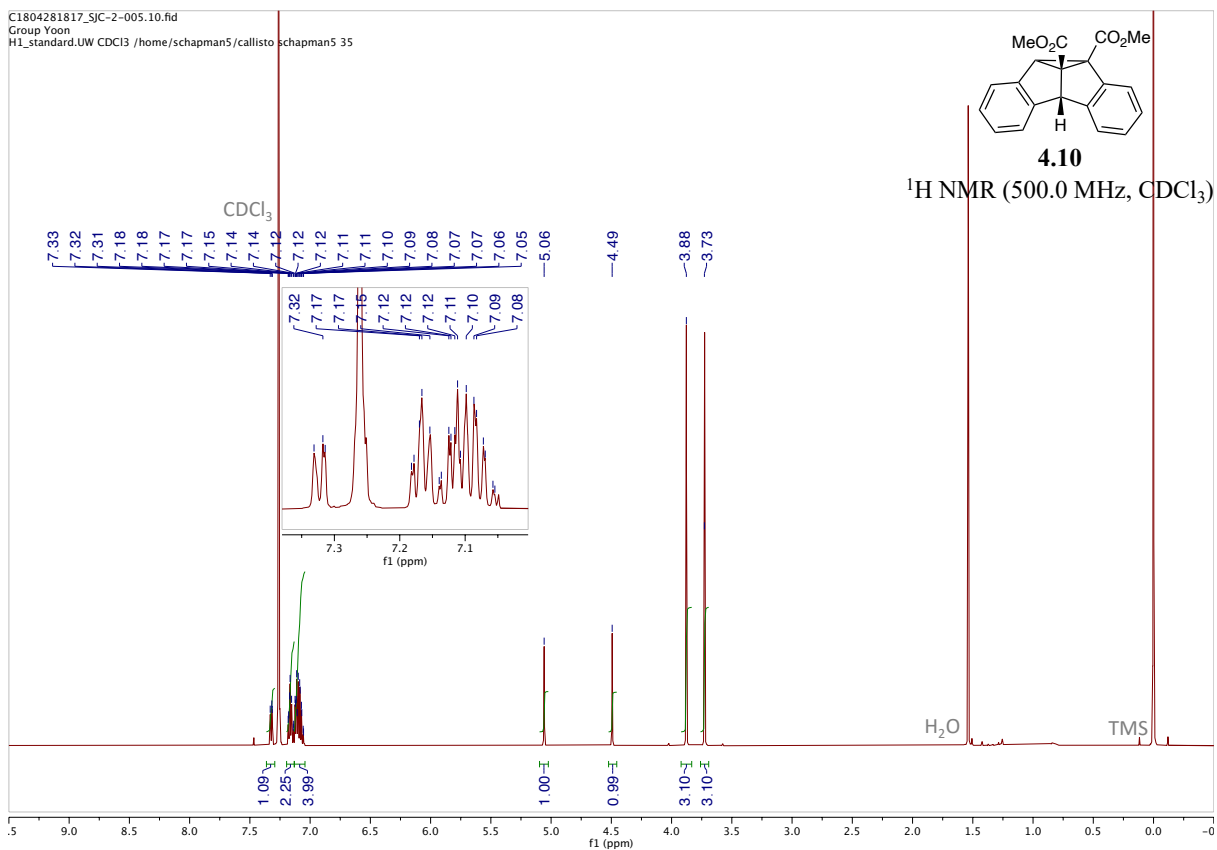


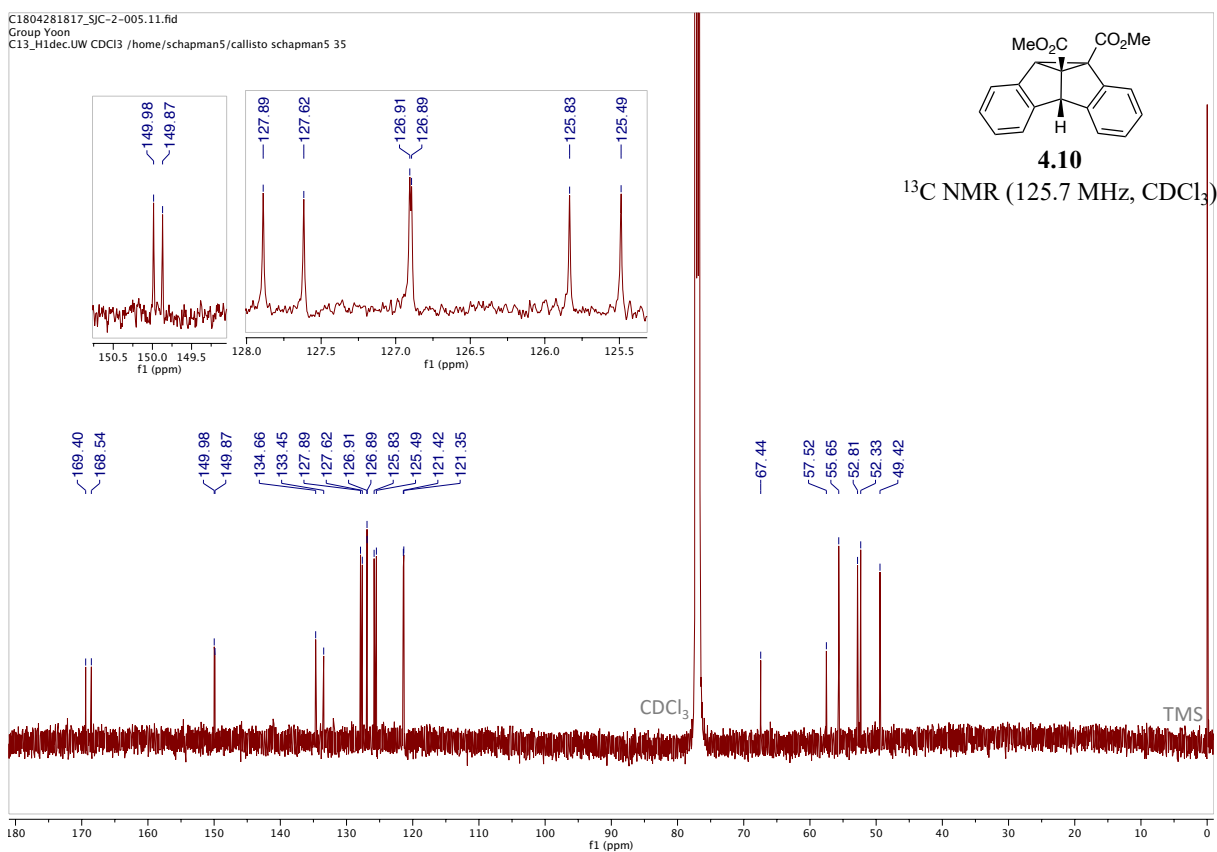


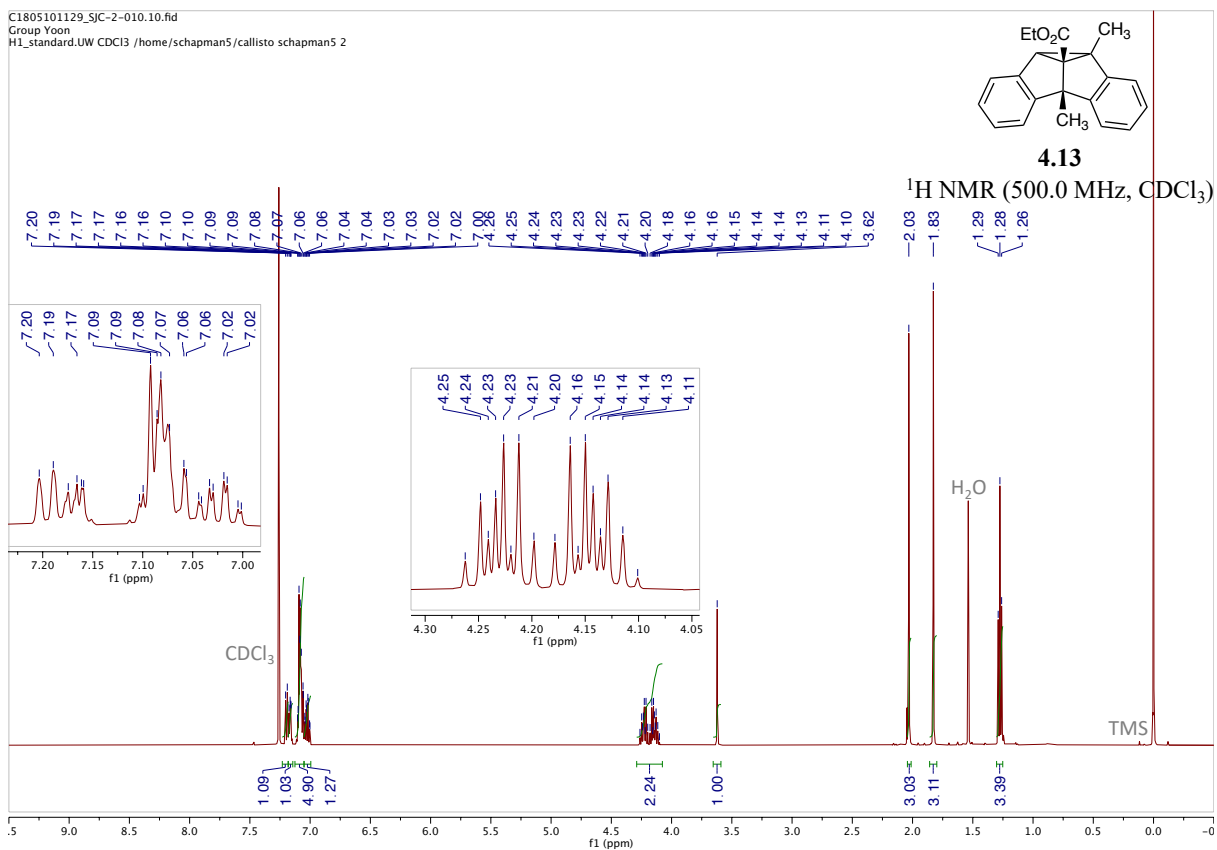


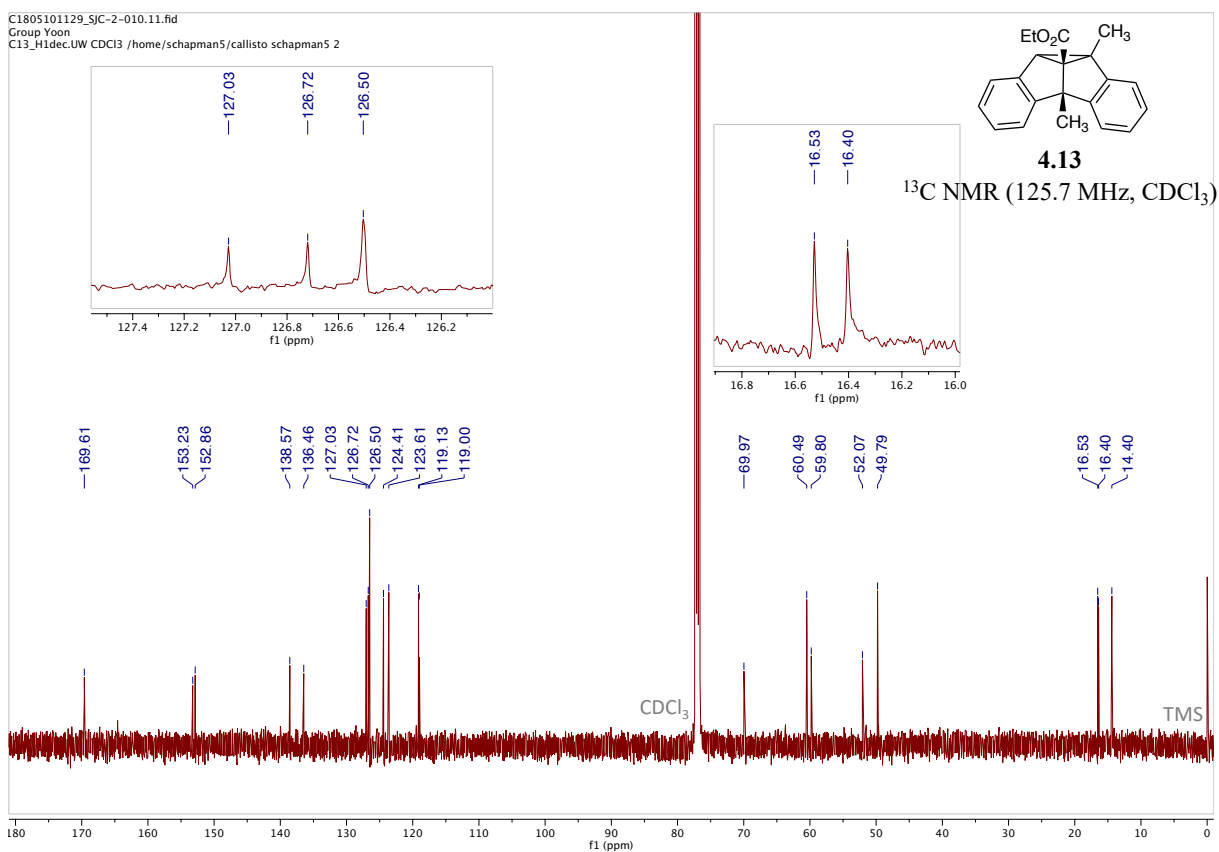


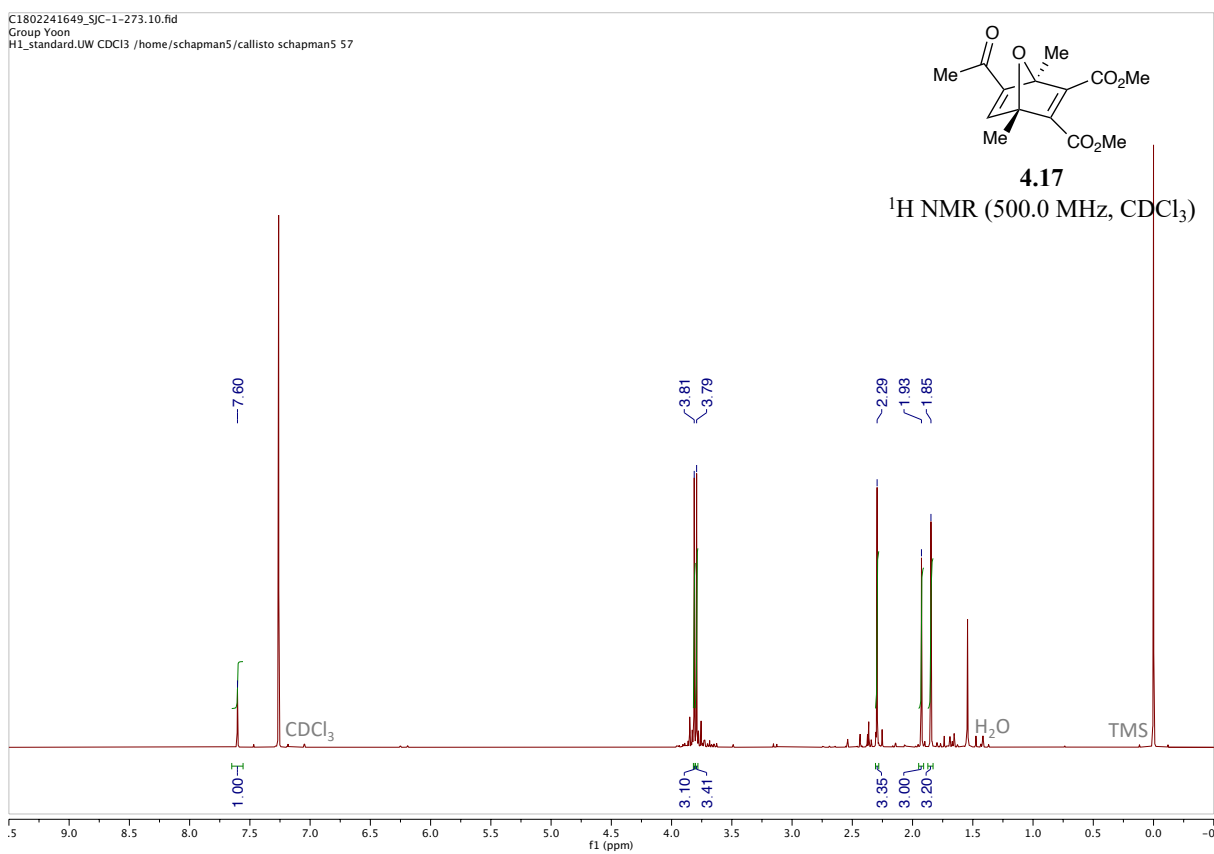


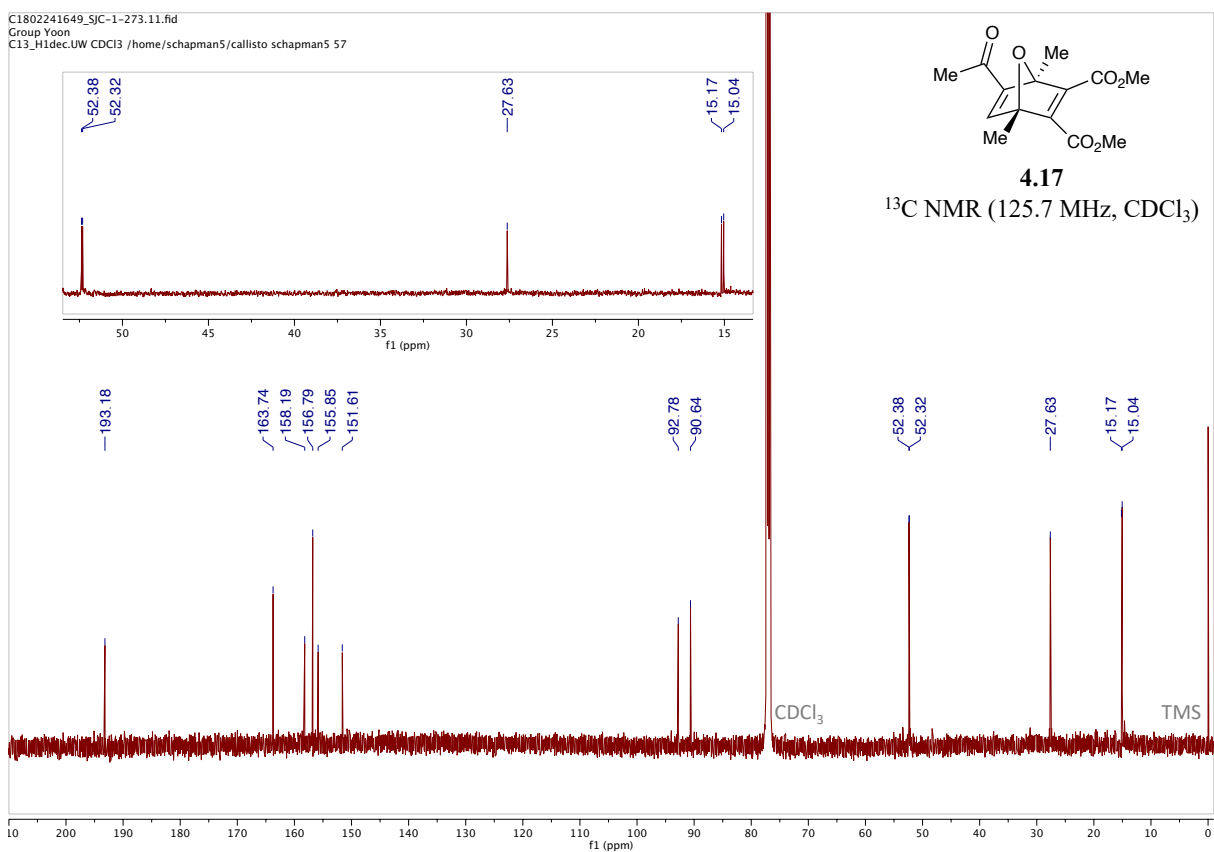


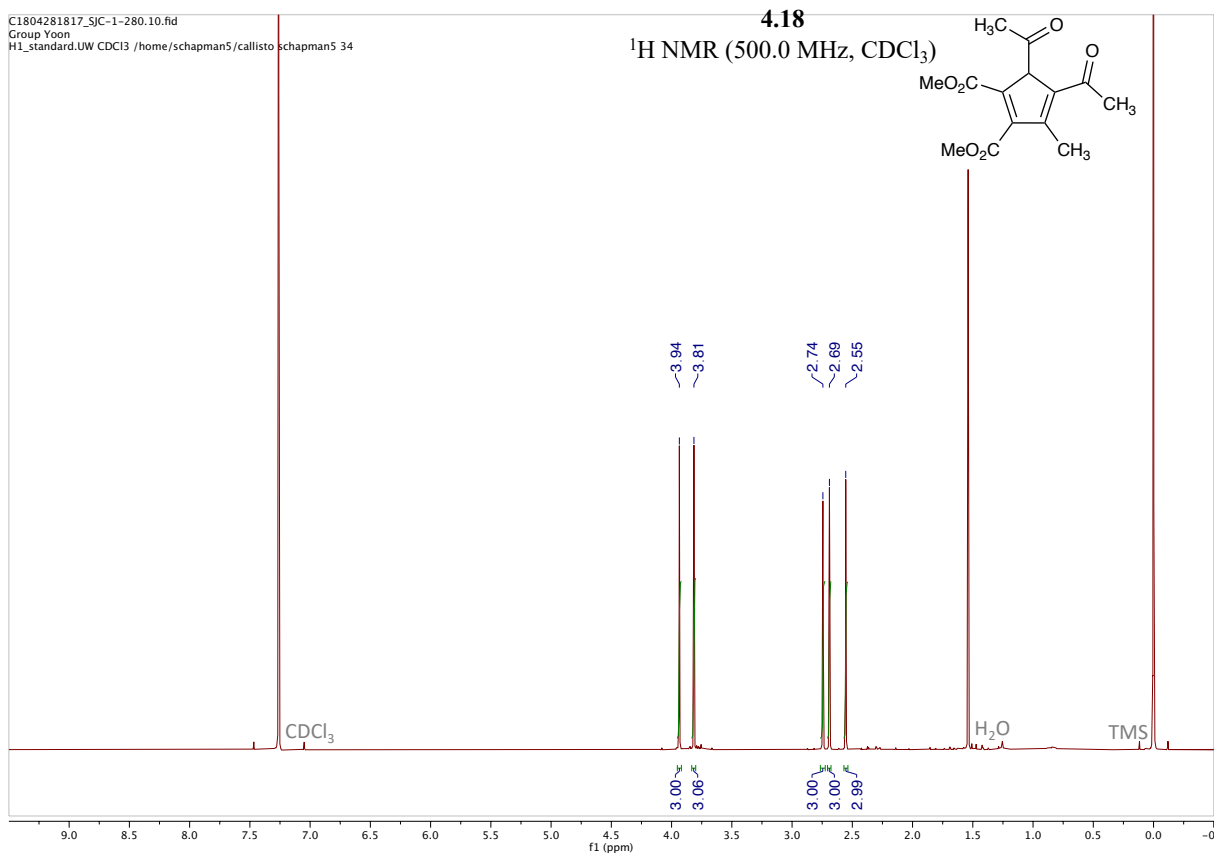


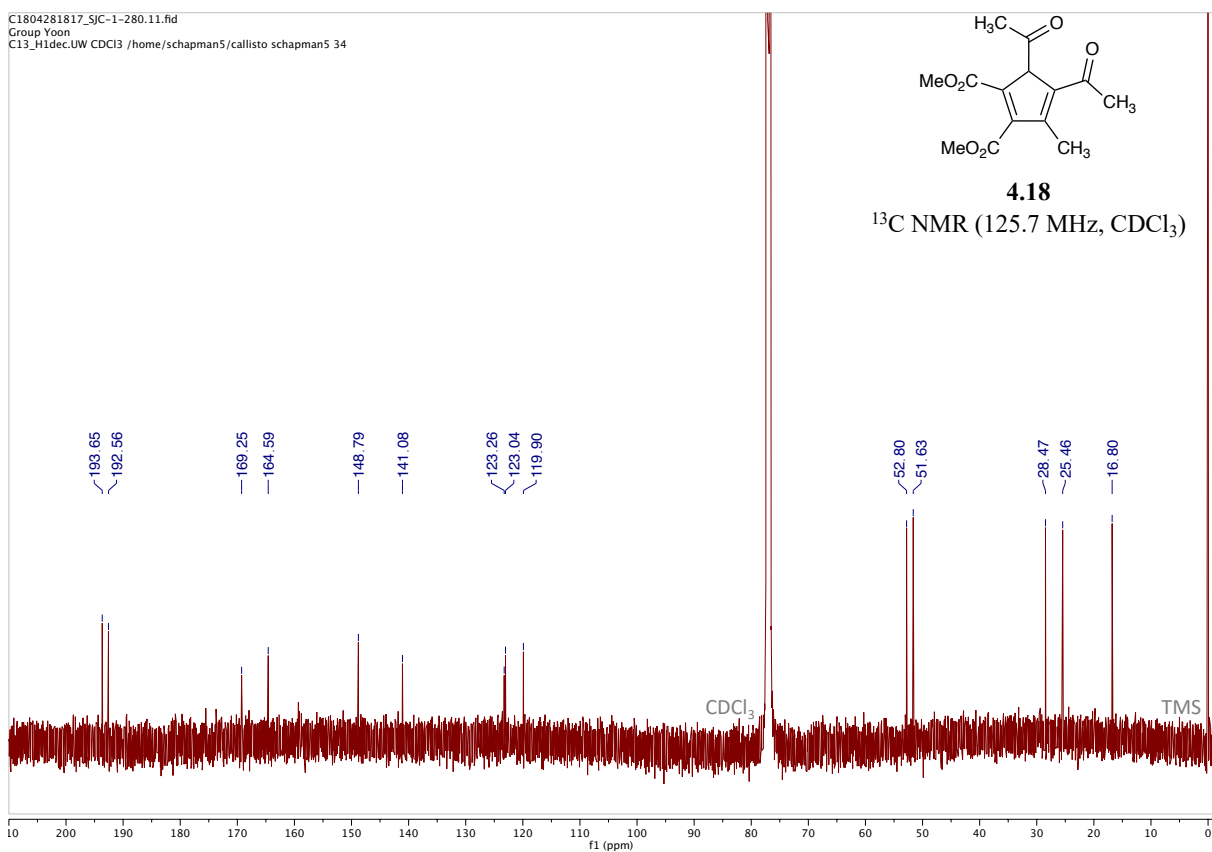




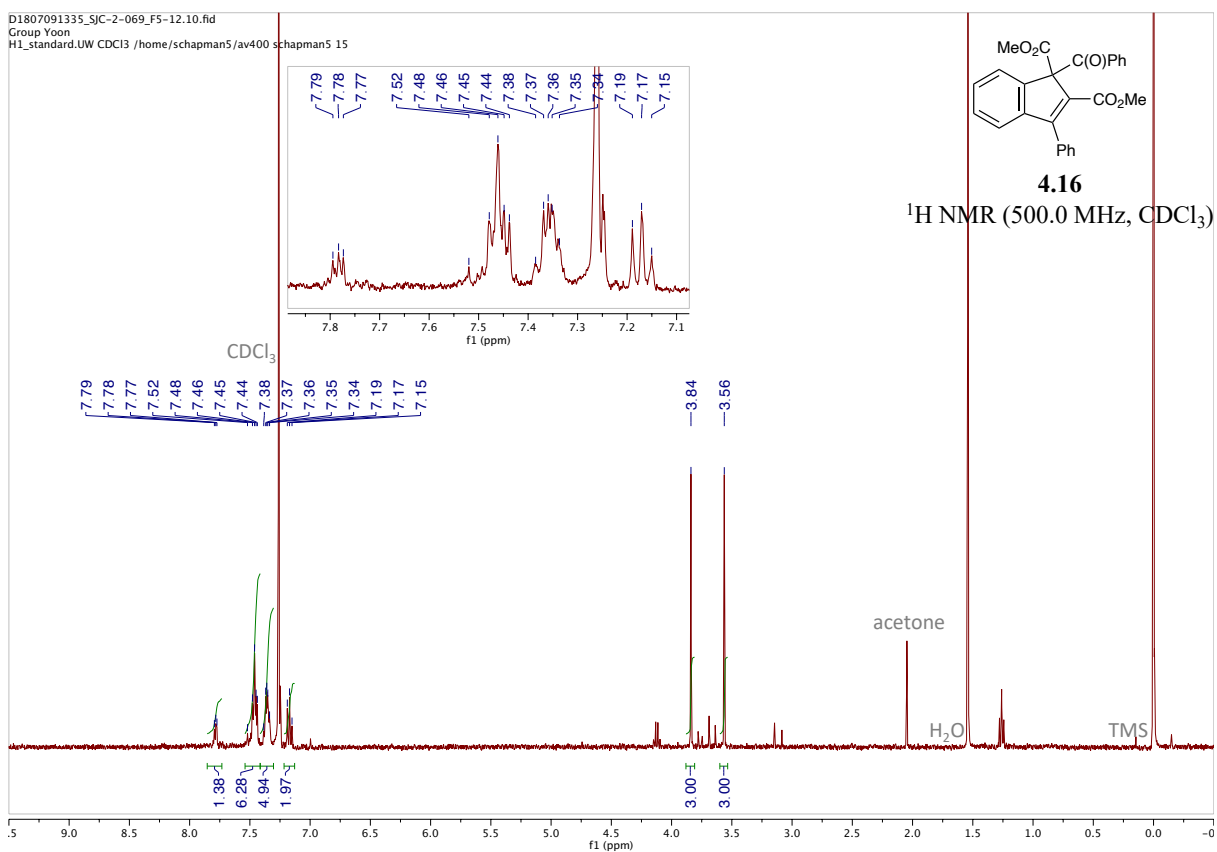


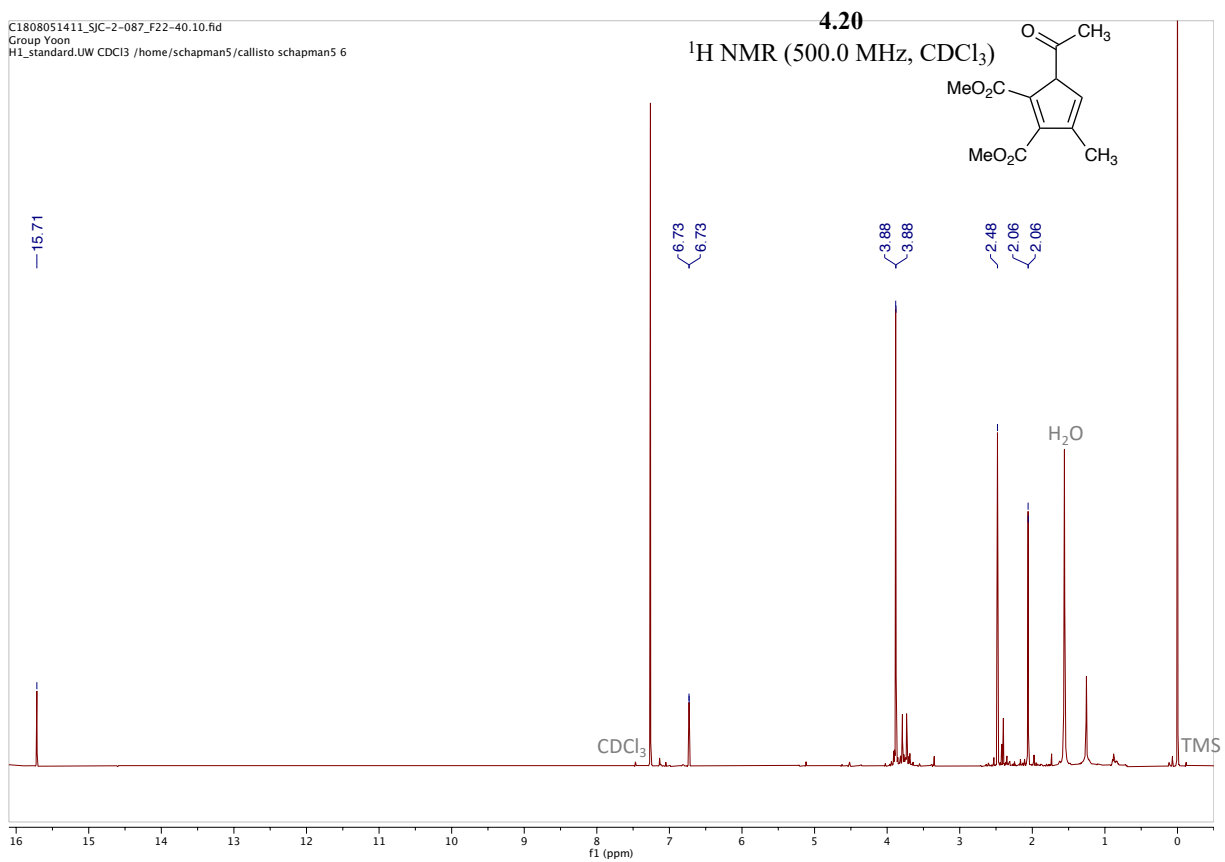


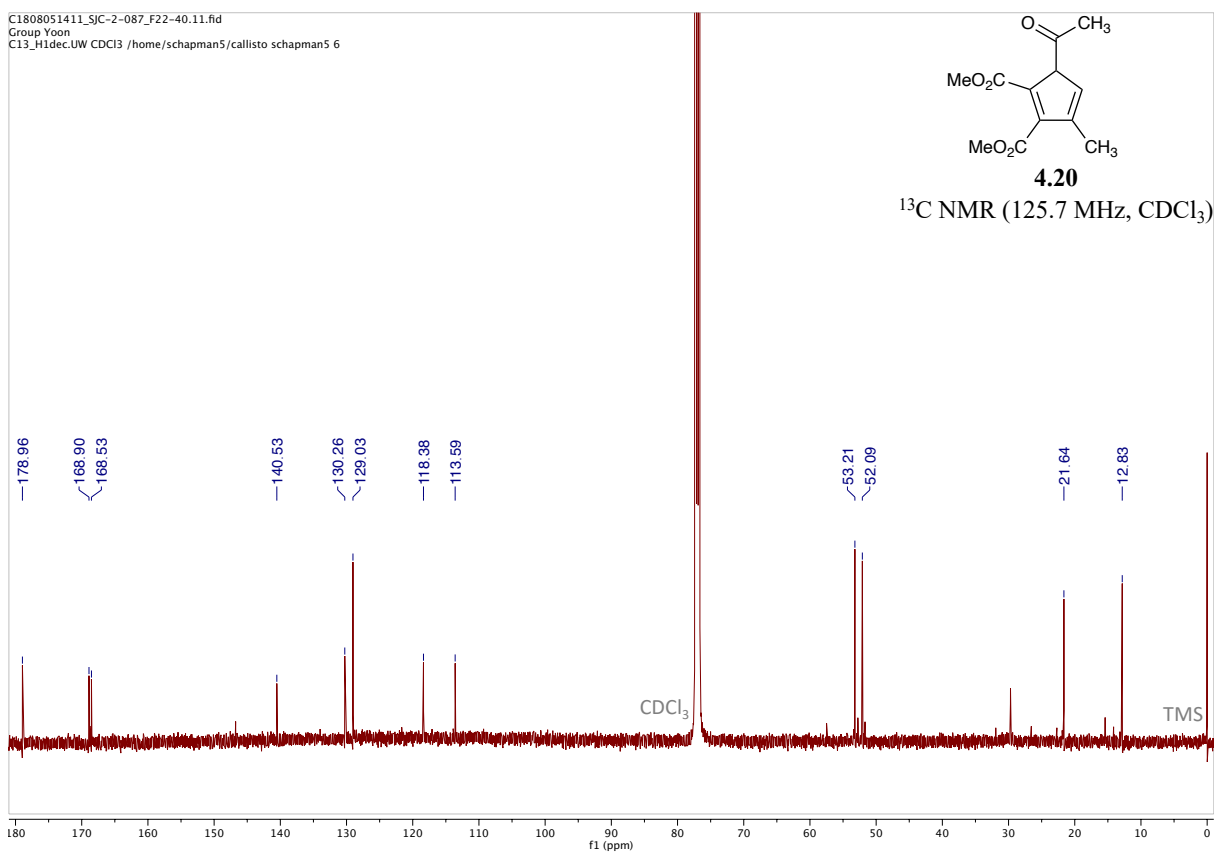




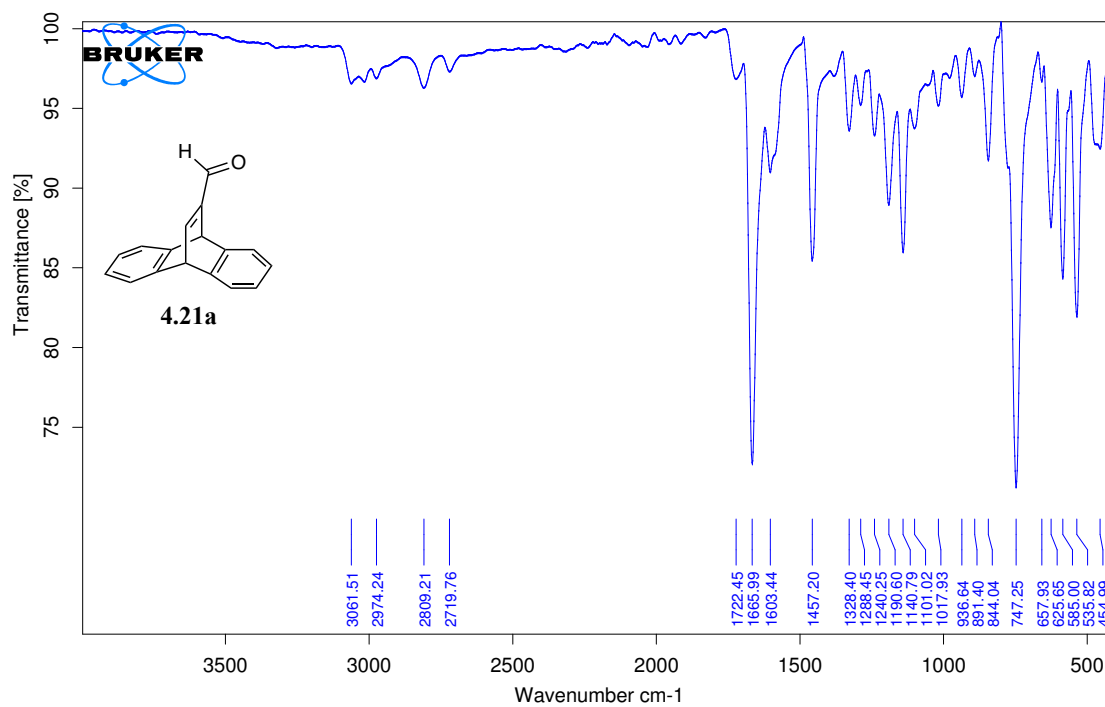








## 4.9.6. IR Spectra

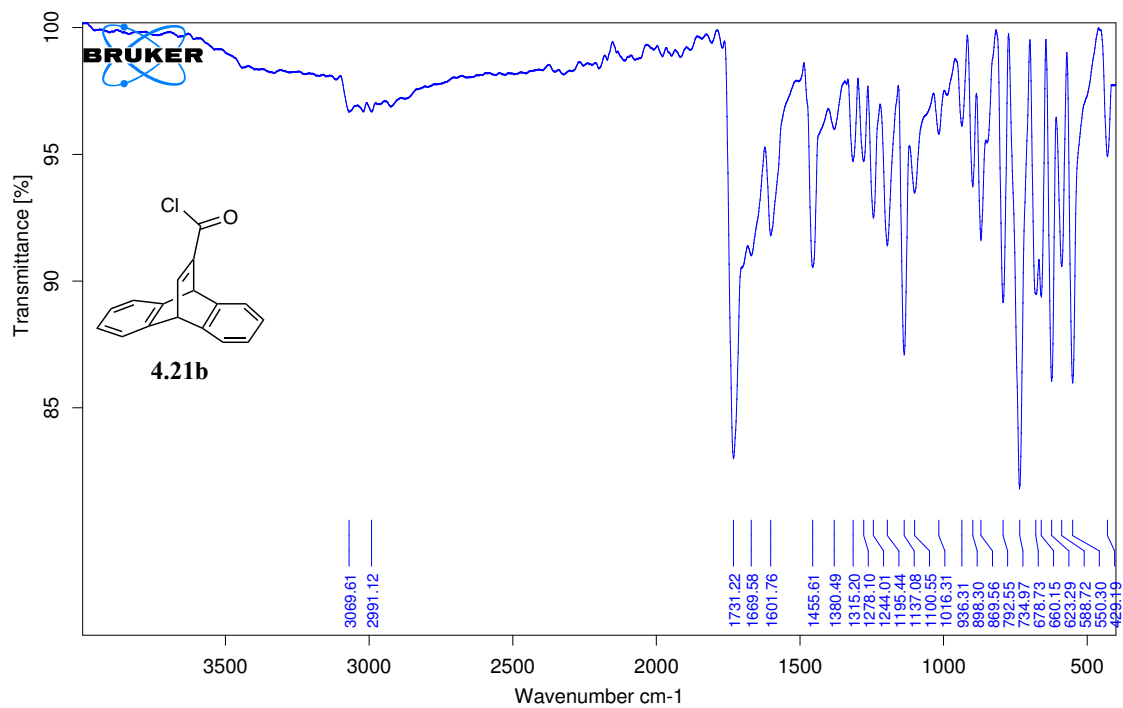


C:\OPUS\_7.0.129\MEAS\3198

SJC-1-178\_IR

Instrument type and / or accessory

1/5/2018

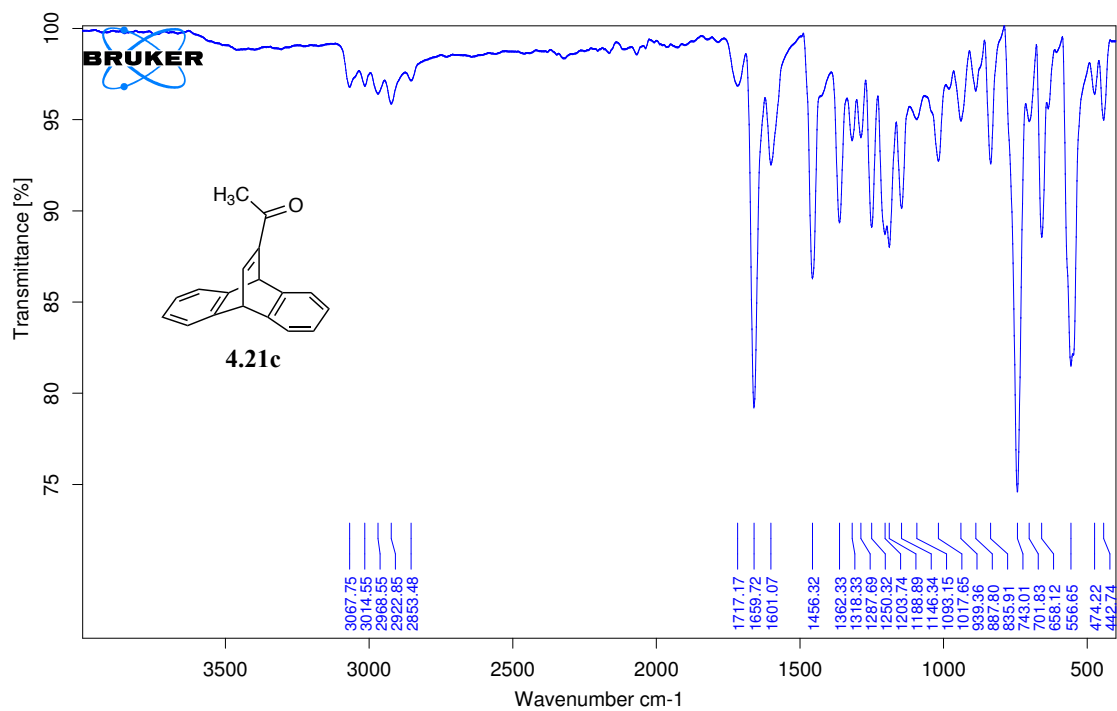


C:\OPUS\_7.0.129\MEAS\3209

SJC-1-254\_IR

Instrument type and / or accessory

1/10/2018

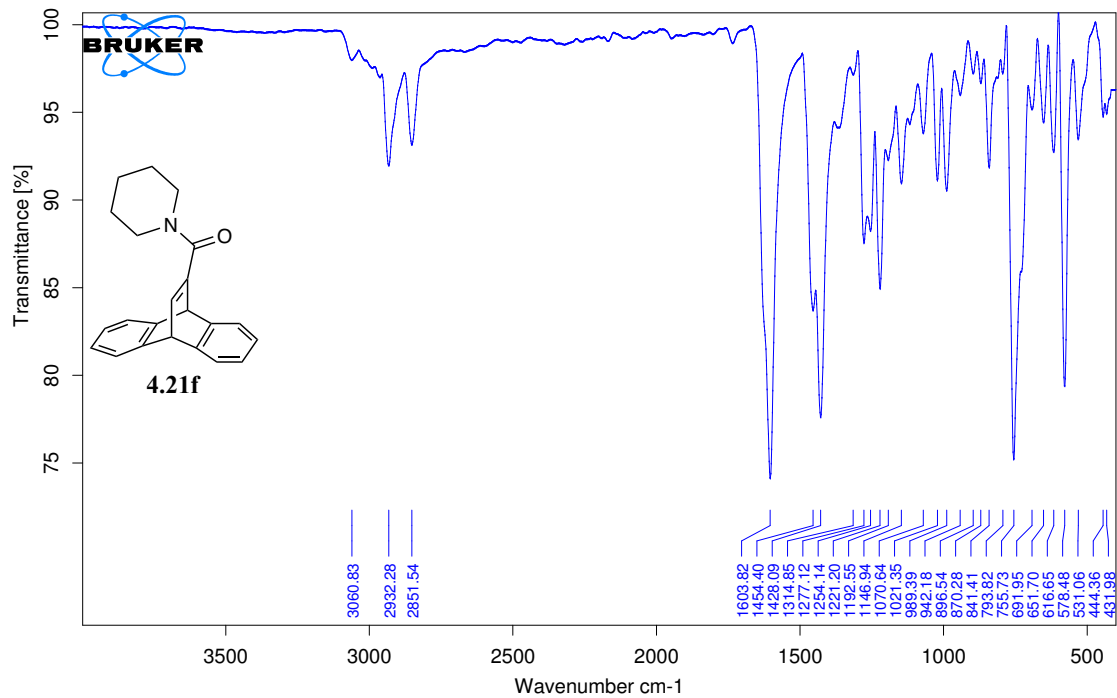


C:\OPUS\_7.0.129\MEAS\3205

SJC-1-180\_IR

Instrument type and / or accessory

1/5/2018

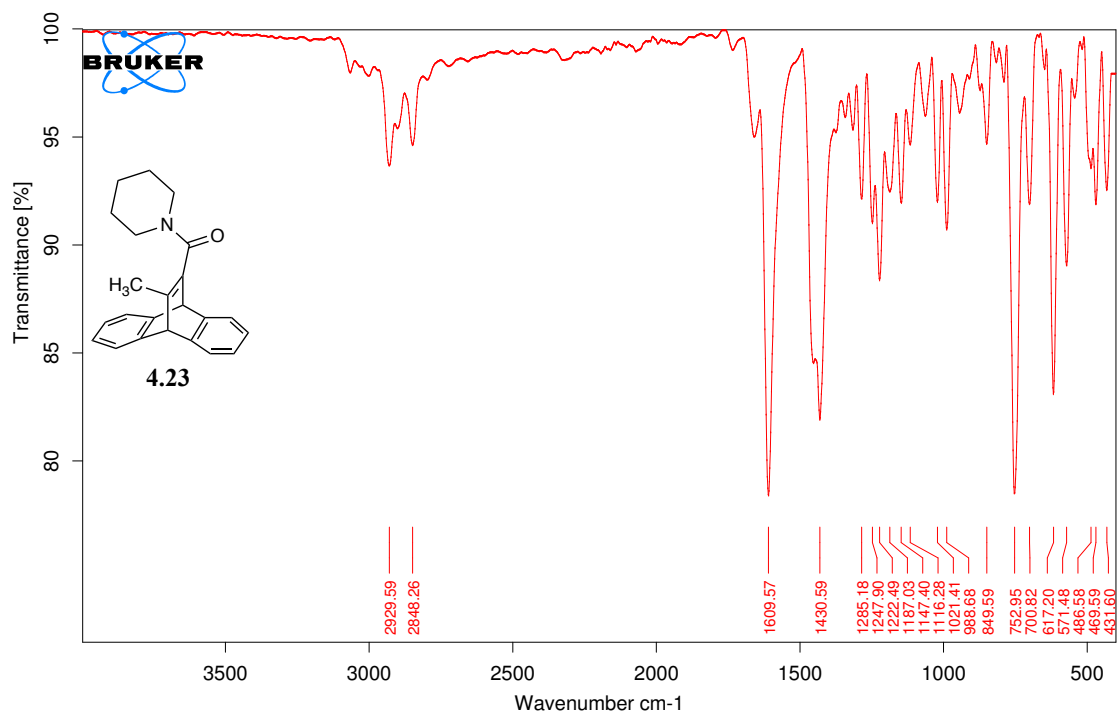


C:\OPUS\_7.0.129\MEAS\3080

SJC-1-261

Instrument type and / or accessory

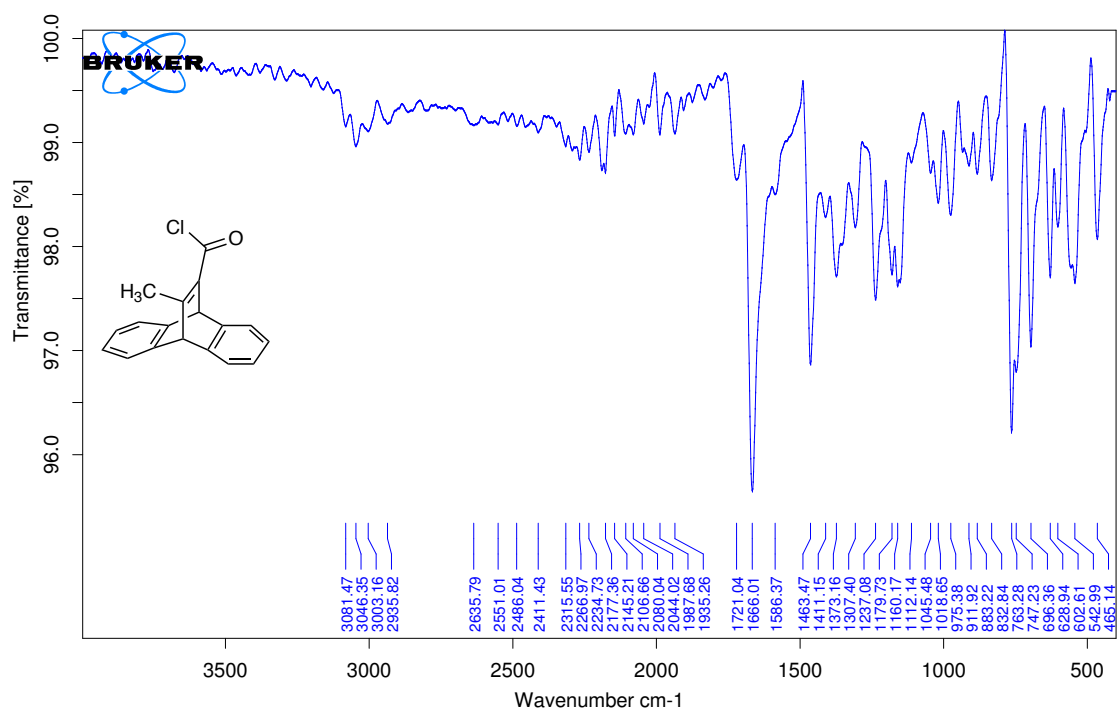
1/23/2018



C:\OPUS\_7.0.129\MEAS\3199 SJC-1-208\_IR Instrument type and / or accessory

1/5/2018



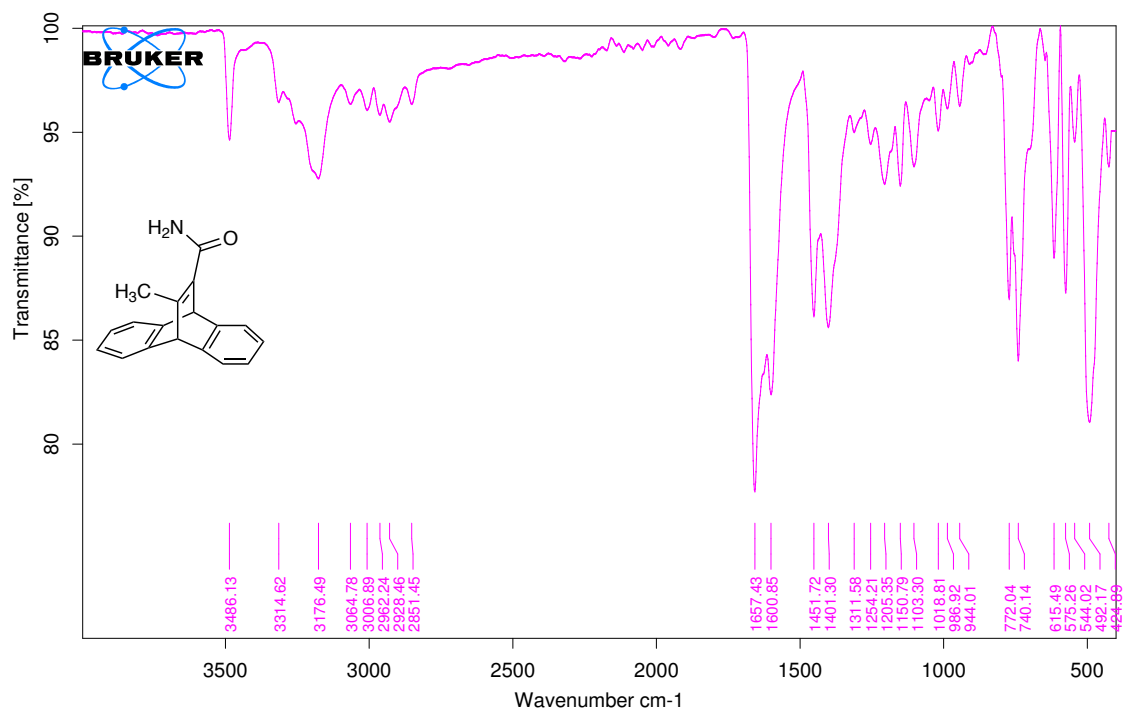


C:\OPUS\_7.0.129\MEAS\3204

SJC-1-218\_IR

Instrument type and / or accessory

1/5/2018

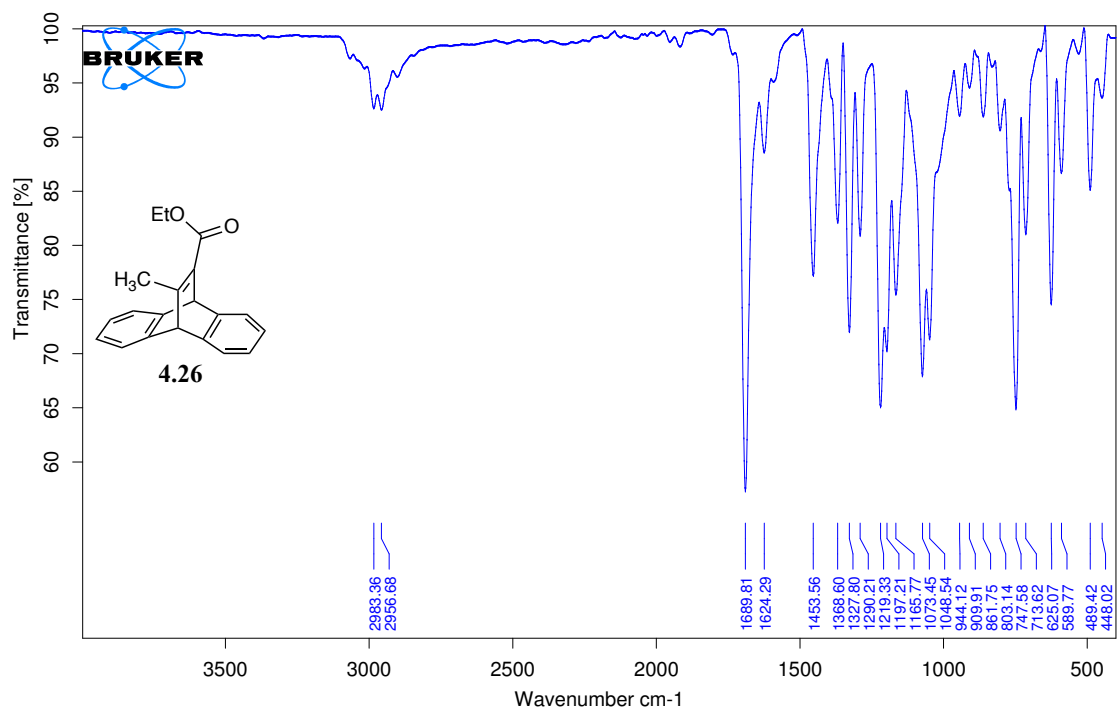


C:\OPUS\_7.0.129\MEAS\3200

SJC-1-232\_IR

Instrument type and / or accessory

1/5/2018

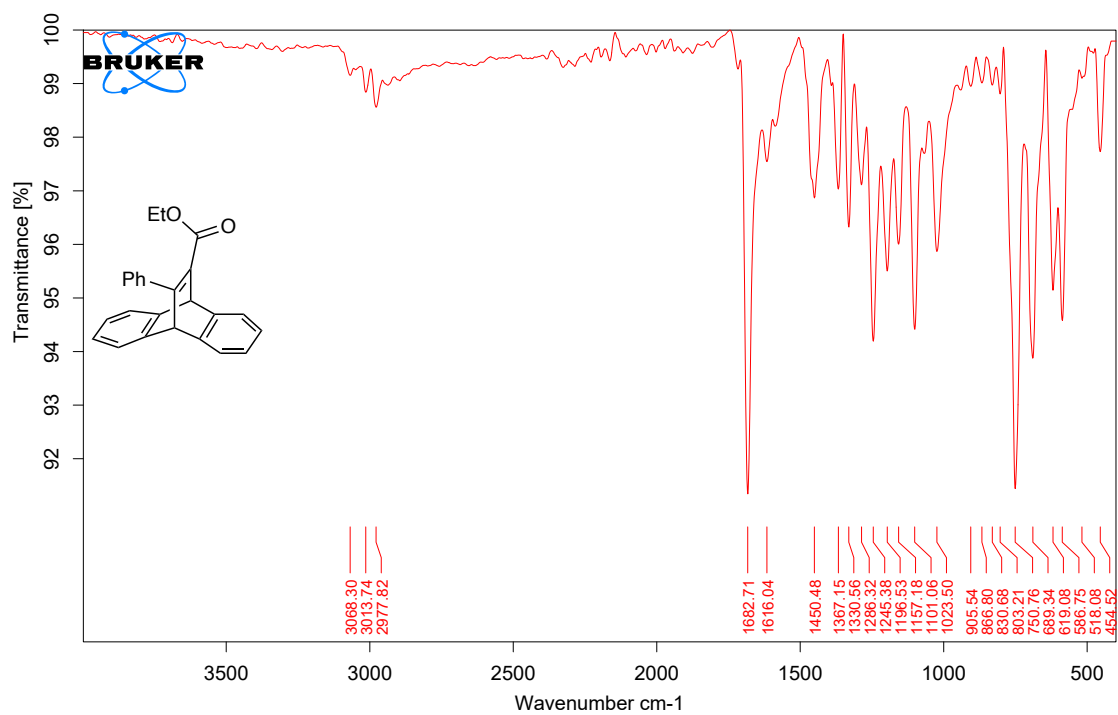


C:\OPUS\_7.0.129\MEAS\3207

SJC-1-239\_IR

Instrument type and / or accessory

1/6/2018

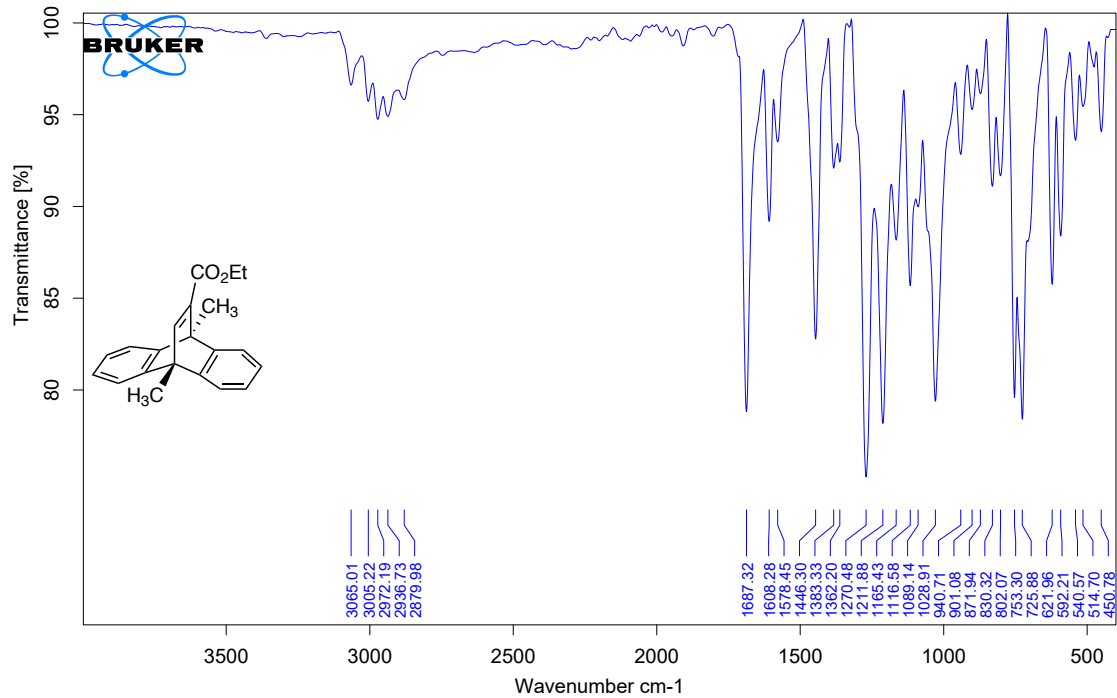


C:\IOPUS\_7.0.129\MEAS\3966

SJC-1-244

Instrument type and / or accessory

9/14/2018

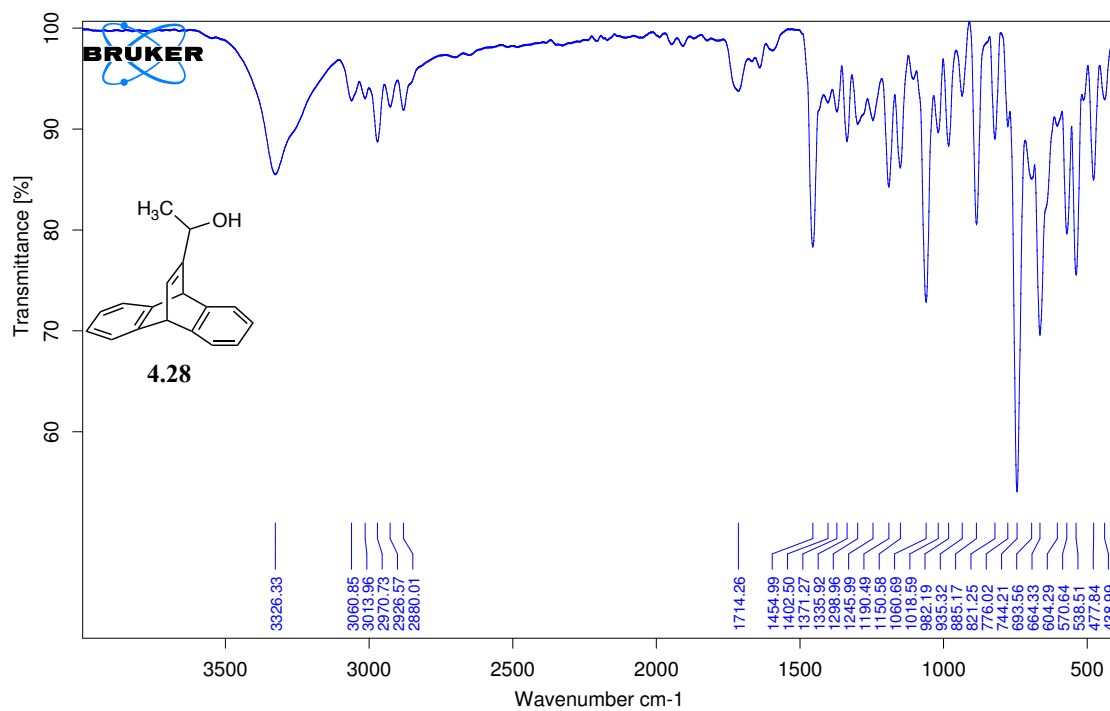


C:\IOPUS\_7.0.129\MEAS\3965

SJC-2-008

Instrument type and / or accessory

9/14/2018

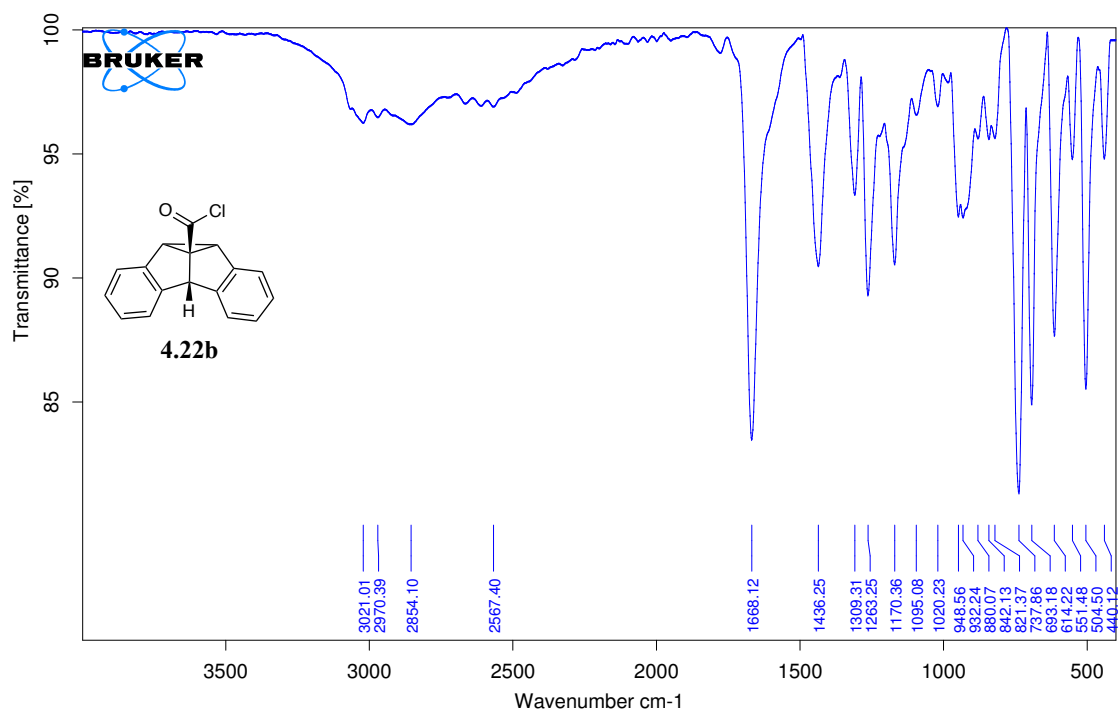


C:\OPUS\_7.0.129\MEAS\3206

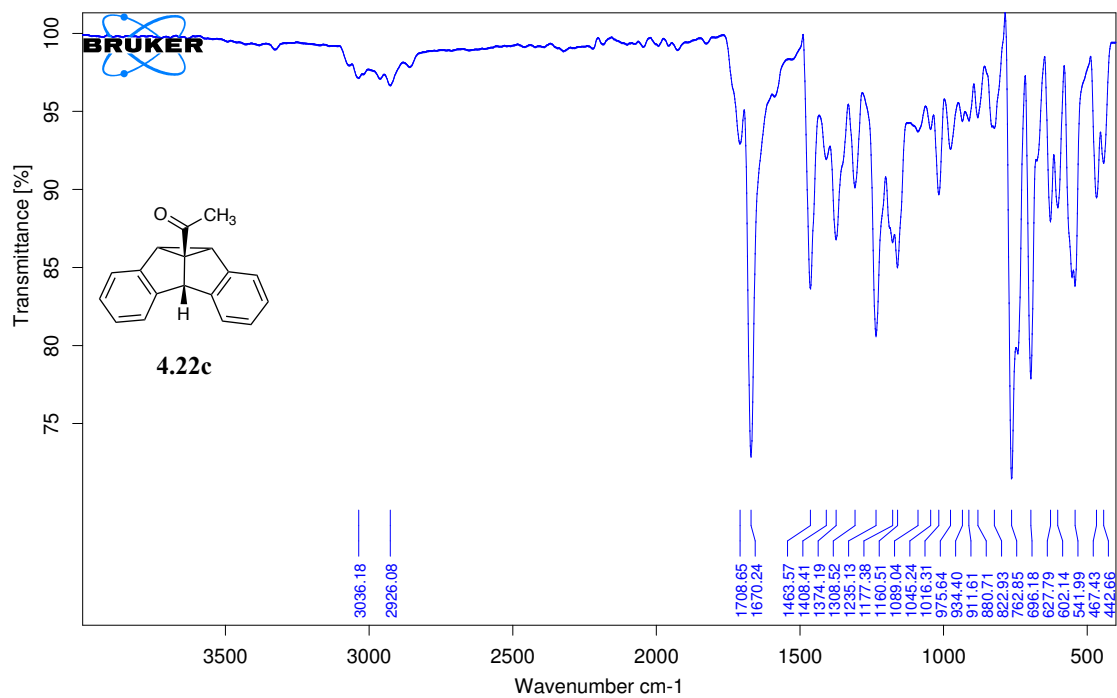
SJC-1-184\_IR

Instrument type and / or accessory

1/5/2018



C:\OPUS_7.0.129\MEAS\3081	SJC-1-201	Instrument type and / or accessory	1/23/2018
C:\OPUS_7.0.129\MEAS\3080	SJC-1-261	Instrument type and / or accessory	1/23/2018



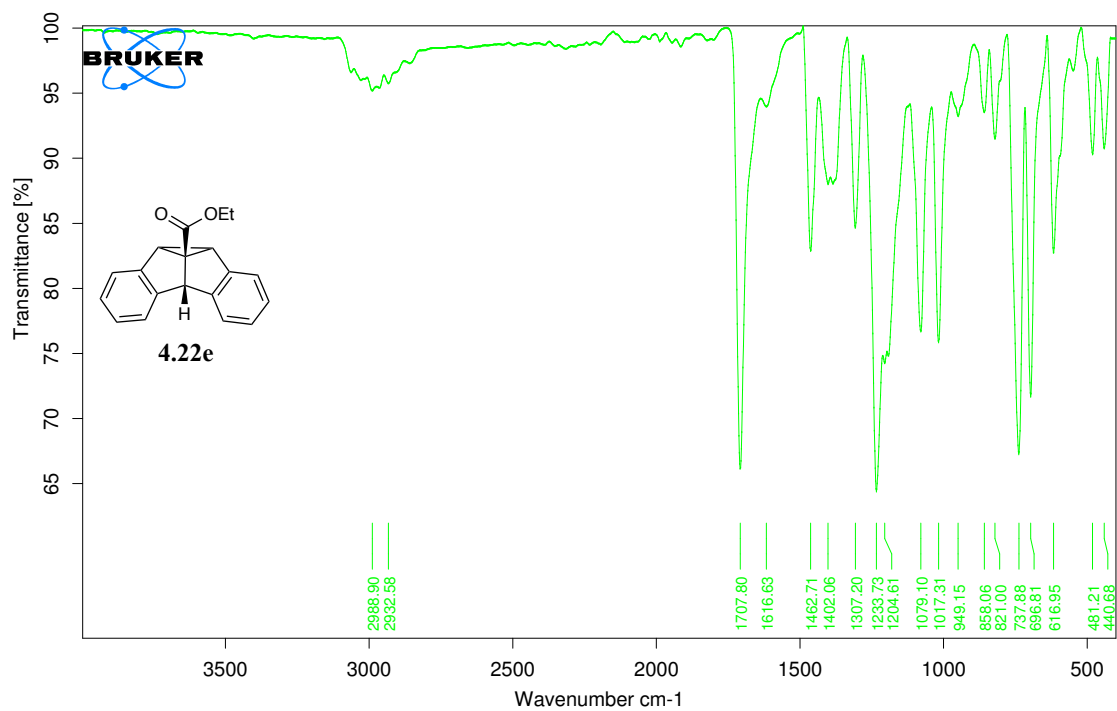
C:\OPUS\_7.0.129\MEAS\3202

SJC-1-188\_IR

Instrument type and / or accessory

1/5/2018



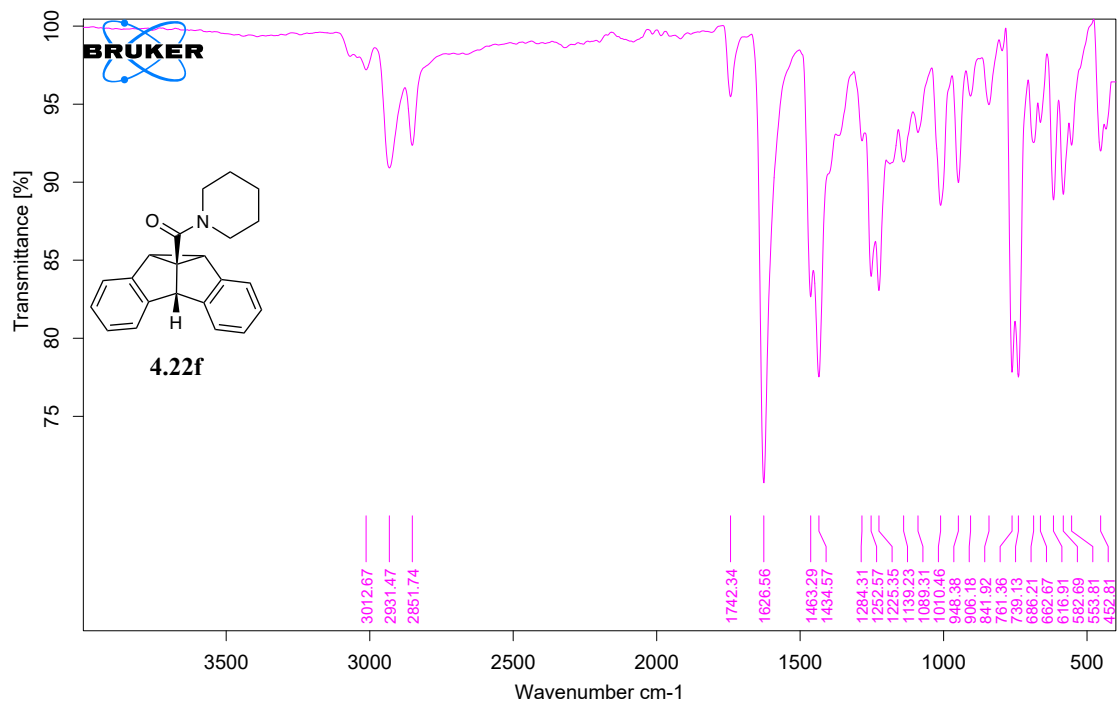


C:\OPUS\_7.0.129\MEAS\3201

SJC-1-221\_IR

Instrument type and / or accessory

1/5/2018

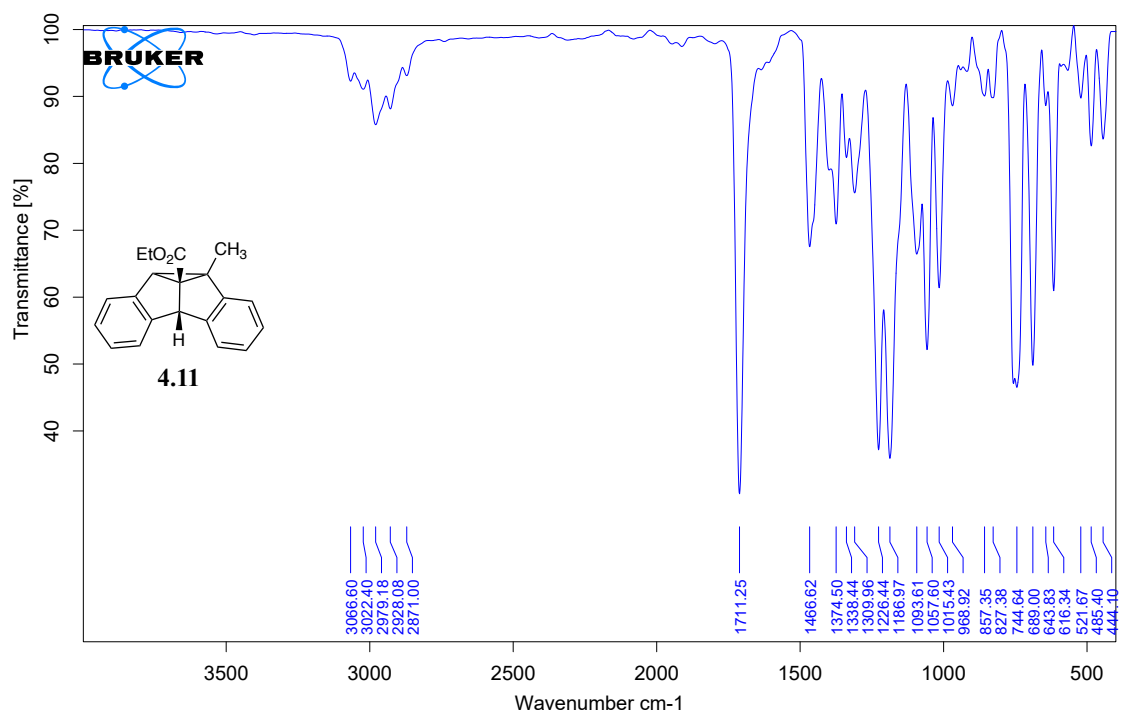


C:\IOPUS\_7.0.129\MEAS\3967

SJC-1-262

Instrument type and / or accessory

9/14/2018

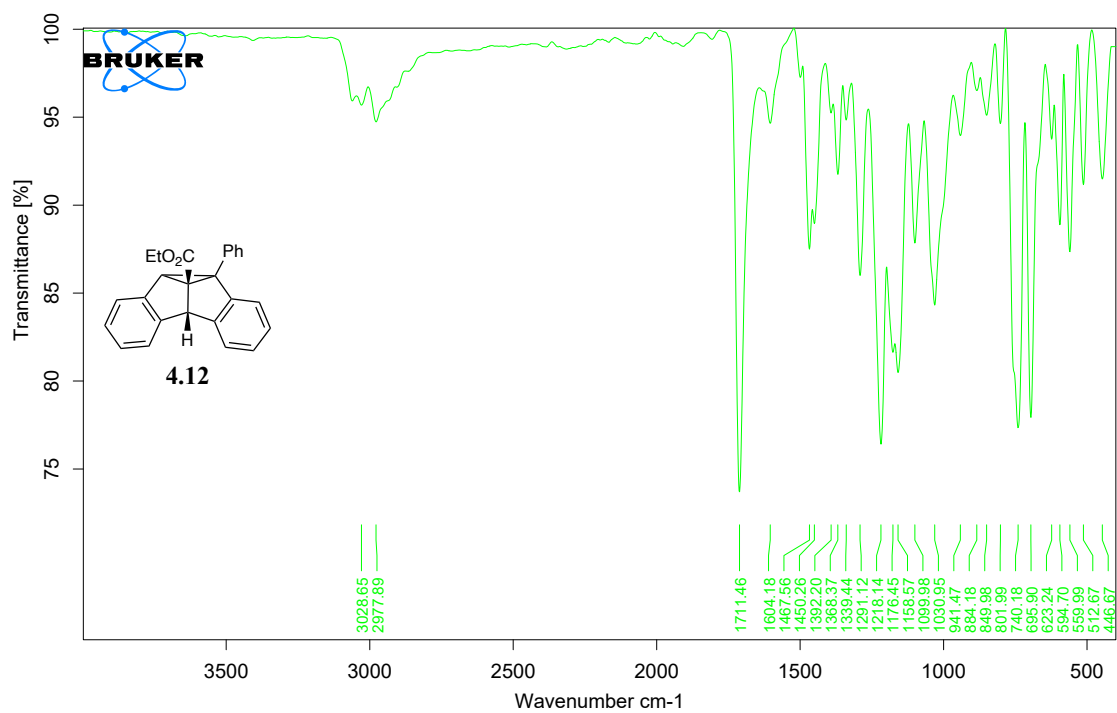


C:\IOPUS\_7.0.129\MEAS\3969

SJC-1-311

Instrument type and / or accessory

9/14/2018

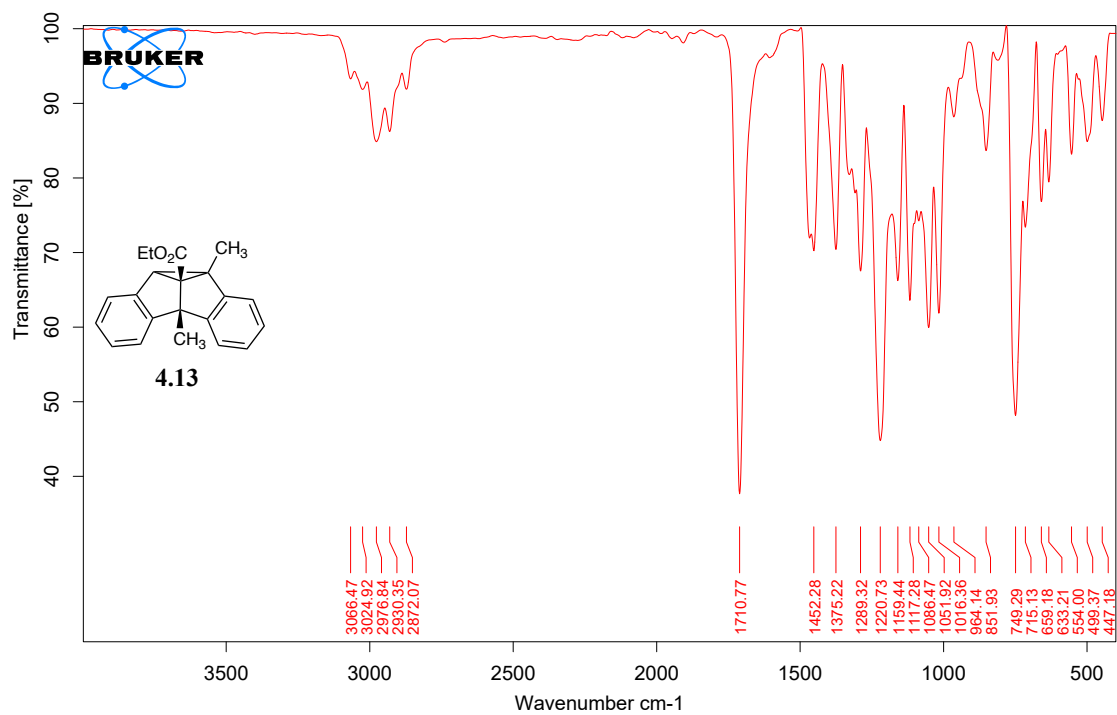


C:\IOPUS\_7.0.129\MEAS\3968

SJC-1-312

Instrument type and / or accessory

9/14/2018

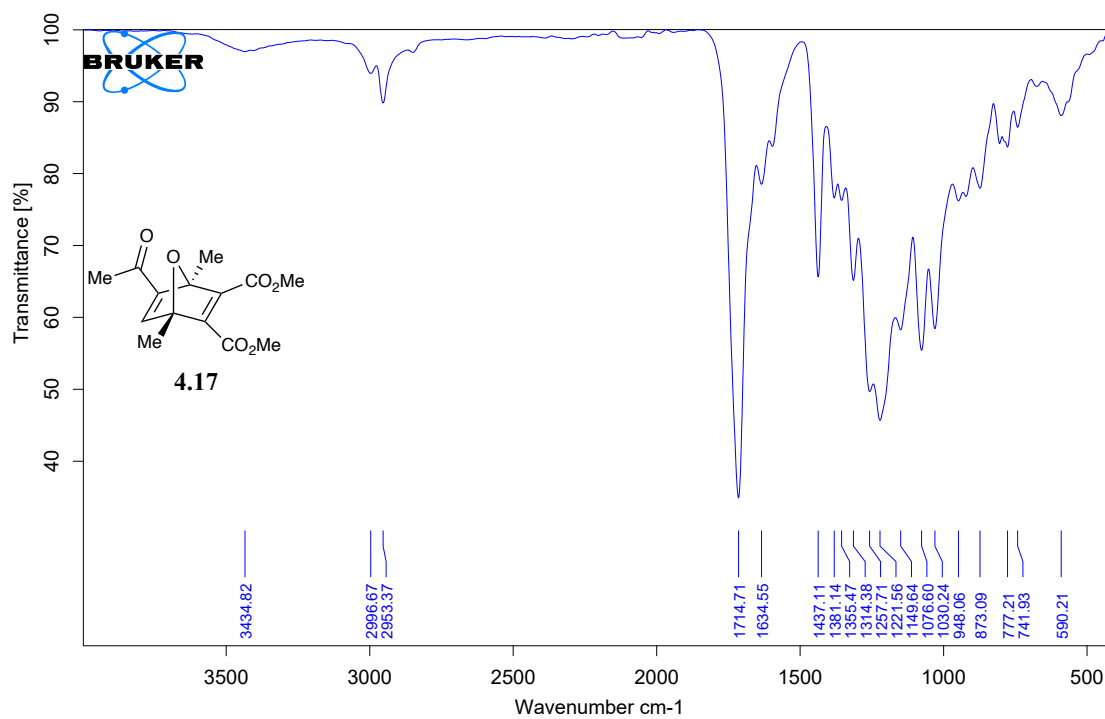


C:\IOPUS\_7.0.129\MEAS\3970

SJC-2-010

Instrument type and / or accessory

9/14/2018

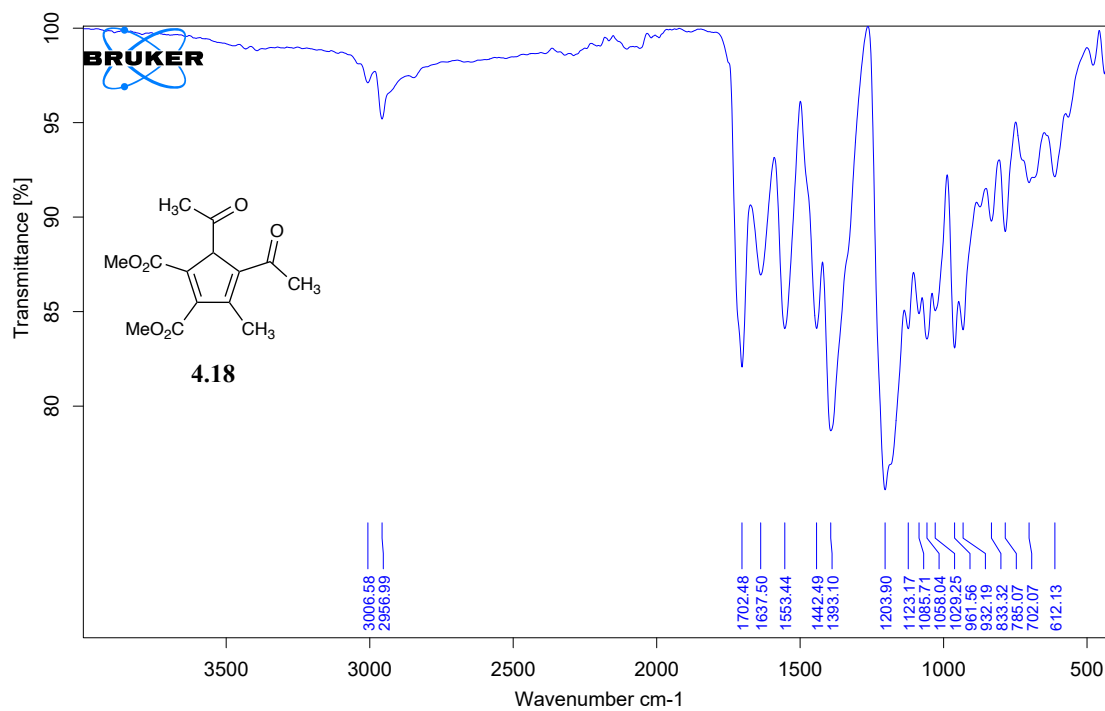


C:\OPUS\_7.0.129\MEAS\4451

SJC-1-273 IR

Instrument type and / or accessory

1/4/2019

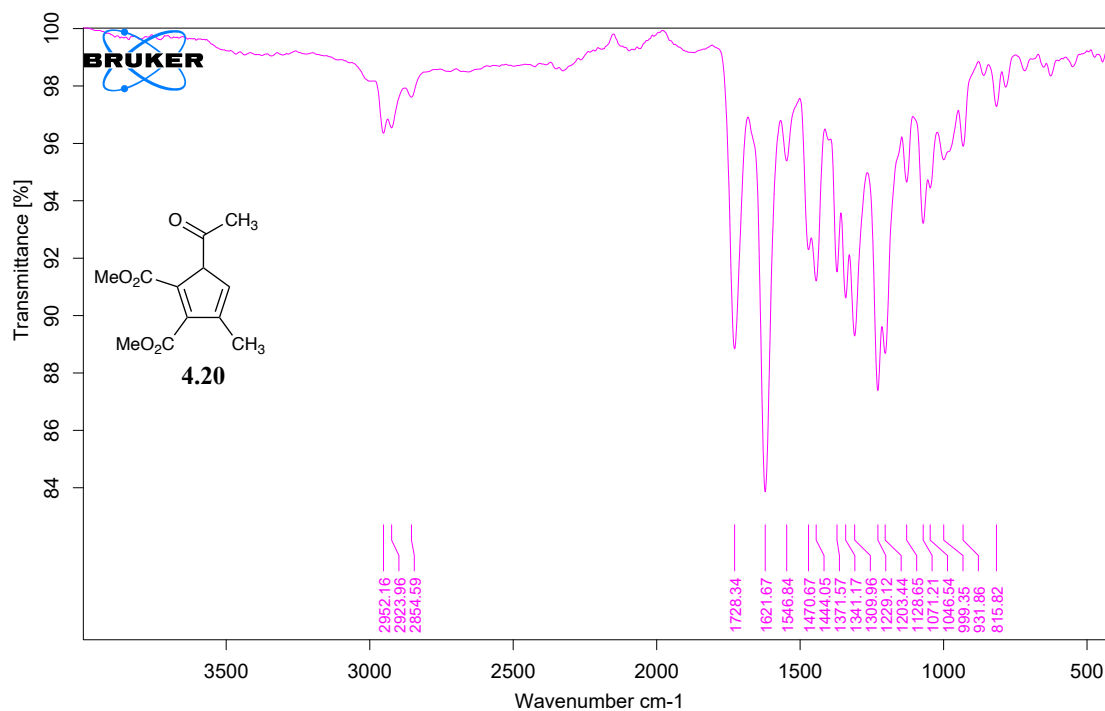


C:\OPUS\_7.0.129\MEAS\4454

SJC-1-280 IR

Instrument type and / or accessory

1/4/2019



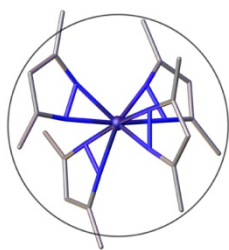
C:\IOPUS\_7\_0.129\MEAS\4453

SJC-2-087 IR

Instrument type and / or accessory

1/4/2019

Page 1/1

4.9.7. X-Ray Structure of **4.18**

## Molecular Structure Laboratory

ILIA A. GUZEI, PH.D.

University of Wisconsin-Madison

☎ 608-263-4694

2124 Chemistry Department

Fax 608-262-0381

1101 University Ave



## Structural report on Yoon55

MARCH 20, 2018

Crystallographic Experimental Section

Data Collection

A colorless crystal with approximate dimensions  $0.205 \times 0.066 \times 0.028 \text{ mm}^3$  was selected under oil under ambient conditions and attached to the tip of a MiTeGen MicroMount©. The crystal was mounted in a stream of cold nitrogen at 100(1) K and centered in the X-ray beam by using a video camera.

The crystal evaluation and data collection were performed on a Bruker Quazar SMART APEXII diffractometer with Mo  $K_\alpha$  ( $\lambda = 0.71073 \text{ \AA}$ ) radiation and the diffractometer to crystal distance of 4.96 cm.<sup>124</sup>

The initial cell constants were obtained from three series of  $\omega$  scans at different starting angles. Each series consisted of 12 frames collected at intervals of  $0.5^\circ$  in a  $6^\circ$  range about  $\omega$  with the exposure time of 10 seconds per frame. The reflections were successfully indexed by an automated indexing routine built in the APEXII program suite. The final cell constants were calculated from a set of 6840 strong reflections from the actual data collection.

The data were collected by using the full sphere data collection routine to survey the reciprocal space to the extent of a full sphere to a resolution of  $0.70 \text{ \AA}$ . A total of 27955 data were harvested by collecting 3 sets of frames with  $0.5^\circ$  scans in  $\omega$  with exposure times of 50 sec per frame. These highly redundant datasets were corrected for Lorentz and polarization effects. The

absorption correction was based on fitting a function to the empirical transmission surface as sampled by multiple equivalent measurements.<sup>125</sup>

## Structure Solution and Refinement

The systematic absences in the diffraction data were uniquely consistent for the space group *Pbca* that yielded chemically reasonable and computationally stable results of refinement.<sup>126,127,128,129,130,131</sup>

A successful solution by the direct methods provided most non-hydrogen atoms from the *E*-map. The remaining non-hydrogen atoms were located in an alternating series of least-squares cycles and difference Fourier maps. All non-hydrogen atoms were refined with anisotropic displacement coefficients. All carbon-bonded hydrogen atoms were included in the structure factor calculation at idealized positions and were allowed to ride on the neighboring atoms with relative isotropic displacement coefficients. Atom H5 participating in the O5...H5...O6 charge-assisted hydrogen-bonding interaction was found in the difference Fourier map and refined without restraints. The D...A distance and D...H...A angle are 2.402(2) Å and 174(3)°.

The final least-squares refinement of 190 parameters against 3008 data resulted in residuals *R* (based on  $F^2$  for  $I \geq 2\sigma$ ) and  $wR$  (based on  $F^2$  for all data) of 0.0399 and 0.1050, respectively. The final difference Fourier map was featureless.

## Summary

**Crystal Data** for C<sub>14</sub>H<sub>16</sub>O<sub>6</sub> ( $M = 280.27$  g/mol): orthorhombic, space group *Pbca* (no. 61),  $a = 10.307(4)$  Å,  $b = 7.965(4)$  Å,  $c = 31.832(11)$  Å,  $V = 2613.0(17)$  Å<sup>3</sup>,  $Z = 8$ ,  $T = 100.0$  K,  $\mu(\text{MoK}\alpha) = 0.112$  mm<sup>-1</sup>,  $D_{\text{calc}} = 1.425$  g/cm<sup>3</sup>, 27955 reflections measured ( $2.558^\circ \leq 2\Theta \leq 55.024^\circ$ ), 3008 unique ( $R_{\text{int}} = 0.0432$ ,  $R_{\text{sigma}} = 0.0235$ ) which were used in all calculations. The final  $R_1$  was 0.0399 ( $I > 2\sigma(I)$ ) and  $wR_2$  was 0.1050 (all data).

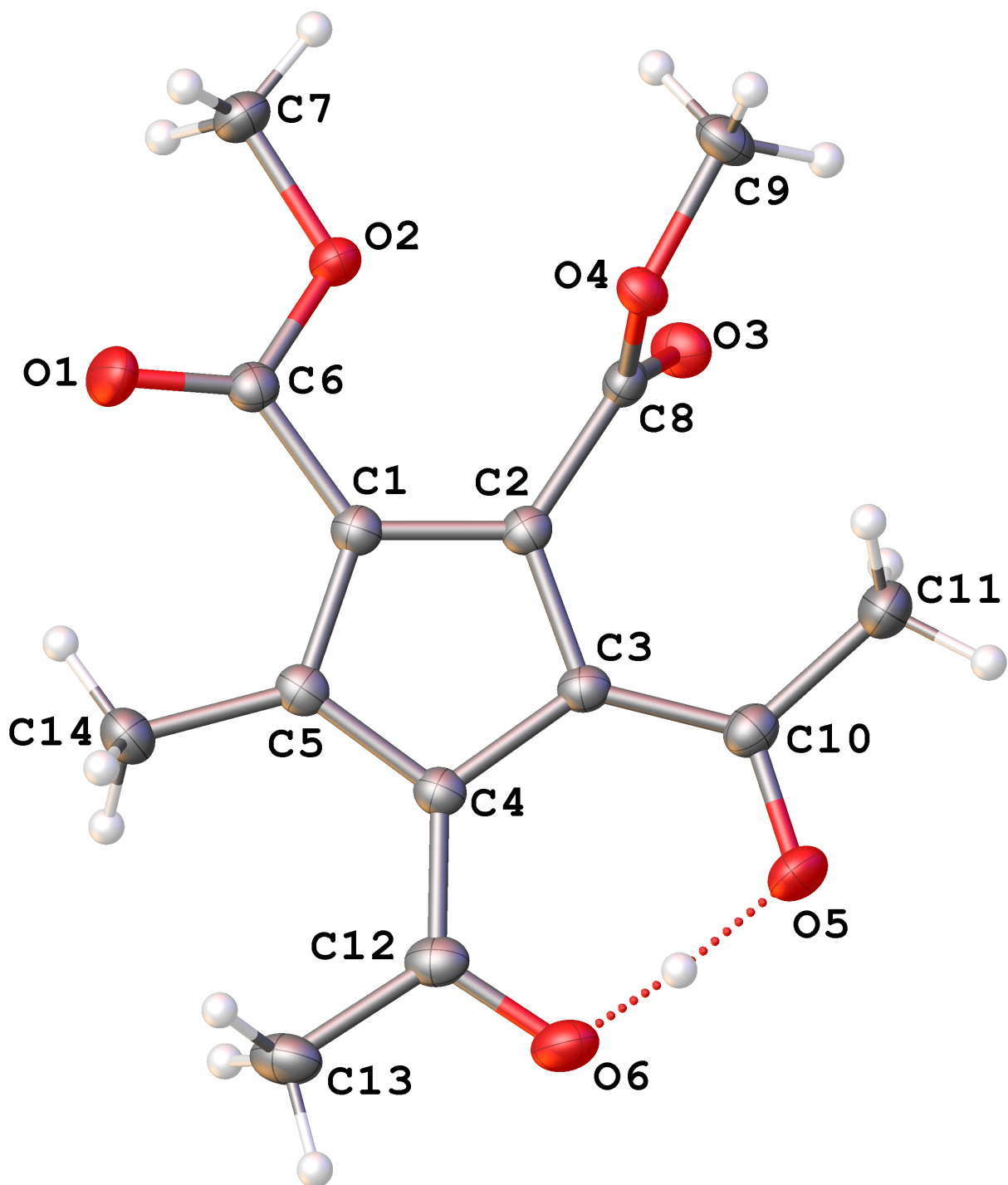


Figure 4.1 A molecular drawing of Yoon55 shown with 50% probability ellipsoids.

**Crystal Table 1 Crystal data and structure refinement for yoon55.**

Identification code	yoon55
Empirical formula	C <sub>14</sub> H <sub>16</sub> O <sub>6</sub>
Formula weight	280.27
Temperature/K	100.0
Crystal system	orthorhombic
Space group	Pbca
a/Å	10.307(4)
b/Å	7.965(4)
c/Å	31.832(11)
$\alpha$ /°	90
$\beta$ /°	90
$\gamma$ /°	90
Volume/Å <sup>3</sup>	2613.0(17)
Z	8
$\rho_{\text{calc}}/\text{cm}^3$	1.425
$\mu/\text{mm}^{-1}$	0.112

F(000)	1184.0
Crystal size/mm <sup>3</sup>	0.205 × 0.066 × 0.028
Radiation	MoK $\alpha$ ( $\lambda$ = 0.71073)
2 $\Theta$ range for data collection/°	2.558 to 55.024
Index ranges	-12 ≤ h ≤ 13, -10 ≤ k ≤ 10, -41 ≤ l ≤ 40
Reflections collected	27955
Independent reflections	3008 [R <sub>int</sub> = 0.0432, R <sub>sigma</sub> = 0.0235]
Data/restraints/parameters	3008/0/190
Goodness-of-fit on F <sup>2</sup>	1.072
Final R indexes [I ≥ 2 $\sigma$ (I)]	R <sub>1</sub> = 0.0399, wR <sub>2</sub> = 0.0986
Final R indexes [all data]	R <sub>1</sub> = 0.0522, wR <sub>2</sub> = 0.1050
Largest diff. peak/hole / e Å <sup>-3</sup>	0.34/-0.26

**Crystal Table 2 Fractional Atomic Coordinates ( $\times 10^4$ ) and Equivalent Isotropic Displacement Parameters ( $\text{\AA}^2 \times 10^3$ ) for yoon55.  $U_{eq}$  is defined as 1/3 of the trace of the orthogonalised  $U_{ij}$  tensor.**

<b>Atom</b>	<b><i>x</i></b>	<b><i>y</i></b>	<b><i>z</i></b>	<b>U(eq)</b>
O1	7549.6(12)	3276.4(18)	7175.5(4)	32.1(3)
O2	5473.9(11)	2722.4(14)	7017.7(3)	22.7(3)
O3	3599.4(11)	3022.0(14)	6282.6(3)	24.3(3)
O4	3842.4(10)	5380.7(13)	6660.8(3)	19.2(2)
O5	5595.3(12)	6518.9(16)	5226.0(4)	29.8(3)
O6	7919.3(13)	6297.9(17)	5212.8(4)	32.9(3)
C1	6707.3(15)	4076.0(18)	6502.8(5)	18.0(3)
C2	5617.5(15)	4498.2(18)	6258.9(5)	16.9(3)
C3	6031.3(15)	5176.8(19)	5872.5(4)	17.8(3)
C4	7464.2(15)	5143.8(18)	5881.2(4)	17.6(3)
C5	7845.0(15)	4458.9(18)	6273.5(5)	17.9(3)
C6	6664.3(15)	3341.0(19)	6927.5(5)	19.6(3)
C7	5348.2(17)	1918(2)	7422.7(5)	25.9(4)
C8	4249.9(15)	4192.0(19)	6396.2(5)	17.6(3)
C9	2561.4(16)	5099(2)	6833.7(5)	24.9(3)
C10	5180.3(16)	5855(2)	5562.2(5)	21.5(3)

C11	3733.5(17)	5880(2)	5609.1(5)	28.8(4)
C12	8324.2(16)	5704(2)	5559.5(5)	22.6(3)
C13	9775.6(17)	5653(2)	5588.7(5)	29.0(4)
C14	9188.3(15)	4126(2)	6432.5(5)	24.5(3)

**Crystal Table 3 Anisotropic Displacement Parameters ( $\text{\AA}^2 \times 10^3$ ) for yoon55. The Anisotropic displacement factor exponent takes the form:  $-2\pi^2[h^2a^{*2}U_{11}+2hka^*b^*U_{12}+\dots]$ .**

Atom	$U_{11}$	$U_{22}$	$U_{33}$	$U_{23}$	$U_{13}$	$U_{12}$
O1	24.0(6)	50.4(8)	21.9(6)	6.4(5)	-6.4(5)	-5.2(6)
O2	20.3(6)	28.8(6)	18.9(5)	5.2(5)	0.4(4)	-1.1(5)
O3	22.6(6)	27.0(6)	23.4(6)	-3.2(5)	0.0(5)	-6.7(5)
O4	16.6(5)	19.5(5)	21.4(5)	0.1(4)	2.0(4)	1.5(4)
O5	31.9(7)	36.1(7)	21.5(6)	9.9(5)	1.1(5)	2.0(5)
O6	31.4(7)	44.3(8)	22.9(6)	6.4(5)	4.0(5)	-5.9(6)
C1	19.2(7)	17.0(7)	17.8(7)	-2.6(6)	-0.1(6)	-1.1(6)
C2	19.9(7)	15.4(7)	15.5(7)	-3.2(5)	-0.1(6)	-0.4(6)
C3	20.2(7)	16.9(7)	16.2(7)	-2.0(6)	1.4(6)	-1.5(6)

C4	18.7(7)	16.2(7)	17.8(7)	-3.5(6)	1.2(6)	-1.0(6)
C5	19.4(7)	14.1(7)	20.1(7)	-4.1(6)	0.6(6)	-1.1(6)
C6	20.0(7)	20.4(7)	18.2(7)	-1.6(6)	0.8(6)	0.6(6)
C7	26.6(9)	32.1(9)	19.0(8)	6.3(6)	0.7(6)	-0.9(7)
C8	18.5(7)	19.6(7)	14.8(7)	1.2(6)	-1.6(6)	1.7(6)
C9	17.0(7)	28.0(8)	29.7(8)	1.1(7)	6.0(7)	2.0(6)
C10	25.6(8)	20.7(7)	18.2(7)	-0.6(6)	-0.2(6)	0.7(6)
C11	26.0(9)	38.5(10)	21.9(8)	4.9(7)	-1.8(7)	2.6(7)
C12	26.7(8)	21.9(8)	19.3(7)	-5.0(6)	3.6(6)	-4.6(6)
C13	26.9(9)	33.5(9)	26.6(9)	-3.8(7)	7.0(7)	-8.7(7)
C14	18.8(8)	27.6(8)	27.0(8)	0.4(7)	0.7(6)	0.5(6)

**Crystal Table 4 Bond Lengths for yoon55.**

Atom Atom Length/Å			Atom Atom Length/Å		
O1	C6	1.2076(19)	C1	C6	1.474(2)
O2	C6	1.3529(19)	C2	C3	1.410(2)
O2	C7	1.4458(19)	C2	C8	1.496(2)



O3	C8	1.2036(19)	C3	C4	1.477(2)
O4	C8	1.3349(18)	C3	C10	1.427(2)
O4	C9	1.4479(19)	C4	C5	1.418(2)
O5	C10	1.2680(19)	C4	C12	1.426(2)
O6	C12	1.271(2)	C5	C14	1.498(2)
C1	C2	1.406(2)	C10	C11	1.499(2)
C1	C5	1.414(2)	C12	C13	1.499(2)

**Crystal Table 5 Bond Angles for yoon55.**

<b>Atom Atom Atom Angle/°</b>				<b>Atom Atom Atom Angle/°</b>			
C6	O2	C7	115.59(12)	C1	C5	C14	123.63(14)
C8	O4	C9	114.64(12)	C4	C5	C14	128.42(14)
C2	C1	C5	109.02(13)	O1	C6	O2	122.07(14)
C2	C1	C6	125.27(14)	O1	C6	C1	126.43(15)
C5	C1	C6	125.72(14)	O2	C6	C1	111.49(13)
C1	C2	C3	109.37(14)	O3	C8	O4	124.29(14)
C1	C2	C8	123.54(13)	O3	C8	C2	124.29(14)

C3	C2	C8	127.06(14)	O4	C8	C2	111.42(13)
C2	C3	C4	106.22(13)	O5	C10	C3	122.32(15)
C2	C3	C10	124.27(14)	O5	C10	C11	114.46(14)
C10	C3	C4	129.35(14)	C3	C10	C11	123.20(14)
C5	C4	C3	107.45(13)	O6	C12	C4	122.40(15)
C5	C4	C12	125.50(14)	O6	C12	C13	113.04(14)
C12	C4	C3	127.05(14)	C4	C12	C13	124.56(15)
C1	C5	C4	107.93(13)				

**Crystal Table 6 Torsion Angles for yoon55.**

A	B	C	D	Angle/°	A	B	C	D	Angle/°
C1	C2	C3	C4	0.72(16)	C5	C1	C2	C3	-0.74(17)
C1	C2	C3	C10	-175.08(14)	C5	C1	C2	C8	177.26(13)
C1	C2	C8	O3	-99.56(19)	C5	C1	C6	O1	16.4(3)
C1	C2	C8	O4	80.42(17)	C5	C1	C6	O2	-163.91(14)
C2	C1	C5	C4	0.46(16)	C5	C4	C12	O6	179.57(15)
C2	C1	C5	C14	-178.18(14)	C5	C4	C12	C13	-0.1(2)

C2C1C6 O1 -164.08(16)	C6 C1C2 C3 179.69(14)
C2C1C6 O2 15.6(2)	C6 C1C2 C8 -2.3(2)
C2C3C4 C5 -0.43(16)	C6 C1C5 C4 -179.98(14)
C2C3C4 C12-179.96(14)	C6 C1C5 C141.4(2)
C2C3C10O5 176.94(15)	C7 O2C6 O1 -2.5(2)
C2C3C10C11-1.6(2)	C7 O2C6 C1 177.81(13)
C3C2C8 O3 78.1(2)	C8 C2C3 C4 -177.20(14)
C3C2C8 O4 -101.94(17)	C8 C2C3 C107.0(2)
C3C4C5 C1 -0.01(16)	C9 O4C8 O3 4.6(2)
C3C4C5 C14178.54(15)	C9 O4C8 C2 -175.34(12)
C3C4C12O6 -1.0(3)	C10C3C4 C5 175.07(15)
C3C4C12C13 179.37(15)	C10C3C4 C12-4.5(3)
C4C3C10O5 2.2(3)	C12C4C5 C1 179.53(14)
C4C3C10C11-176.41(16)	C12C4C5 C14-1.9(2)

**Crystal Table 7 Hydrogen Atom Coordinates ( $\text{\AA}\times 10^4$ ) and Isotropic Displacement Parameters ( $\text{\AA}^2\times 10^3$ ) for yoon55.**

<b>Atom</b>	<b><i>x</i></b>	<b><i>y</i></b>	<b><i>z</i></b>	<b>U(eq)</b>
H5	6820(30)	6420(40)	5201(9)	76(9)
H7A	5855.86	877.21	7424.91	39
H7B	4433.36	1656.83	7475.59	39
H7C	5670.03	2673.03	7642.25	39
H9A	1953.08	4847.37	6605.64	37
H9B	2273.52	6108.62	6983	37
H9C	2590.64	4150.51	7029.6	37
H11A	3347.98	6487.07	5372.1	43
H11B	3502.2	6444.2	5872.24	43
H11C	3404.33	4726.08	5613.51	43
H13A	10068.28	4481.92	5591.07	44
H13B	10055.22	6209.2	5847.89	44
H13C	10152.01	6233.32	5346.16	44
H14A	9624.48	5194.33	6490.1	37
H14B	9678.63	3501.44	6219.86	37
H14C	9140.74	3462.77	6691.38	37

## 4.10. References

- 
- <sup>105</sup> Zimmerman, H. E.; Grunewald, G. L. The Chemistry of Barrelene. III. A Unique Photoisomerization to Semibullvalene. *J. Am. Chem. Soc.* **1966**, *88*, 183.
- <sup>106</sup> During our studies, a manuscript was published describing the visible light sensitization of similar DPM scaffolds. Schlosser, J.; Cibulka, R.; Groß, P.; Ihmels, H.; Mohrschladt, C. J. Visible-Light-Induced Di- $\pi$ -Methane Rearrangement of Dibenzobarrelene Derivatives. *ChemPhotoChem* **2020**, *4*, 132–137.
- <sup>107</sup> Armesto, D.; Ortiz, M. J.; Agarrabeitia, A. R.; Martin-Fontecha, M.; El-Boulifi, N.; Duran-Sampedro, G.; Enma, D. Remarkable Observations on Triplet-Sensitized Reactions. The Di- $\pi$ -methane Rearrangement of Acyclic 1,4-Dienes in the Triplet Excited State. *Org. Lett.* **2009**, *11* (18), 4148.
- <sup>108</sup> Armesto, D.; Ortiz, M. J.; Agarrabeitia, A. R.; El-Boulifi, N. The Effects of Triplet Sensitizers' Energies on the Photoreactivity of  $\beta,\gamma$ -Unsaturated Methyl Ketones. *Angew. Chem.* **2005**, *117*, 7917–7919.
- <sup>109</sup> Zimmerman, H. E.; Armesto, D.; Amezua, M. G.; Gannett, T. P.; Johnson, R. P. Unusual organic photochemistry effected by cyano and methoxy substitution. Exploratory and mechanistic organic photochemistry. *J. Am. Chem. Soc.* **1979**, *101* (21), 6367–6383.
- <sup>110</sup> Zimmerman, H. E.; Armesto, D. Synthetic Aspects of the Di- $\pi$ -methane Rearrangement. *Chem. Rev.* **1996**, *96*, 3065–3112.
- <sup>111</sup> Matheson, R. A. F.; McCulloch, A. W.; McInnes, A. G.; Smith, D. G. Photochemistry of 1,4-diphenyl-1,4-epoxy-1,4-dihydronaphthalene 2-carboxylate and 2,3-dicarboxylate esters. *Canadian Journal of Chemistry* **1977**, *55*(8), 1422–1432.
- <sup>112</sup> Blum, T. R.; Miller, Z. M.; Guzei, I. A.; Yoon, T. P. Enantioselective photochemistry through Lewis acid-catalyzed triplet energy transfer. *Science* **2016**, *354*, 1391–1395.
- <sup>113</sup> Hixson, S. S.; Mariano, P. S.; Zimmerman, H. E. Di- $\pi$ -methane and oxa-di- $\pi$ -methane rearrangements. *Chem. Rev.* **1973**, *73*, 531–551.
- <sup>114</sup> Lowry, M. S.; Goldsmith, J. I.; Slinker, J. D.; Rohl, R.; Pascal, R. A., Jr.; Malliaras, G. G.; Bernhard, S. Single-Layer Electroluminescent Devices and Photoinduced Hydrogen Production from an Ionic Iridium(III) Complex. *Chem. Mater.* **2005**, *17*, 5712–5719.
- <sup>115</sup> Fruziński, A.; Karolak-Wojciechowska, J.; Alibert-Franco, S.; Santelli-Rouvier, C.; Barbe, J. Synthesis and X-ray structure of 11-N-benzylamido-9,10-dihydro-9,10-ethenoanthracene. *Journal of Chemical Crystallography* **1999**, *29* (11), 1201–1204.
- <sup>116</sup> Cristol, S. J.; Schloemer, G. C.; James, D. R.; Paquette, L. A. Rearrangements attending attempts to form the 1-dibenzosemibullvalenylcarbinyll (1-dibenzotricyclo[3.3.0.0<sup>2,8</sup>]octadienylcarbinyll) cation. *J. Org. Chem.* **1972**, *37* (24), 3852–3856.

- <sup>117</sup> Wheeler, S. E.; McNeil, A. J.; Müller, P.; Swager, T. M.; Houk, K. N. Probing Substituent Effects in Aryl-Aryl Interactions Using Stereoselective Diels–Alder Cycloadditions. *J. Am. Chem. Soc.* **2010**, *132*, 3304–3311.
- <sup>118</sup> Karunakaran, J.; Nandakumar, M.; Kumar, N. S.; Mohanakrishnan, A. K. Synthetic transformation of 1,3-diarylisobenzofuran-DMAD adducts: a facile preparation of trip-substituted  $\alpha$ -naphthols. *Org. Biomol. Chem.* **2016**, *14*, 4247–4259.
- <sup>119</sup> Lv, W.; When, S.; Yu, J.; Cheng, G. Palladium-Catalyzed *Ortho*-Silylation of Aryl Iodides with Concomitant Arylsilylation of Oxanorbornadiene: Accessing Functionalized (*Z*)- $\beta$ -Substituted Vinylsilanes and Their Analogues. *Org. Lett.* **2018**, *20* (16), 4984–4987.
- <sup>120</sup> Paquette, L. A.; Meehan, G. V. Mechanistic features of the base-induced decomposition of dibenzosemibullvalene 1-carboxaldehyde tosylhydrazone. *J. Am. Chem. Soc.* **1970**, *92* (10), 3039–3044.
- <sup>121</sup> Cristol, S. J.; Jarvis, B. B. Bridged Polycyclic Compounds. XXXVIII. Stereochemistry of Cyclopropane Ring Formation from  $\gamma$ -Chlorosulfones in the Dibenzobicyclo[3.2.1]octadiene System. *J. Am. Chem. Soc.* **1966**, *88* (13), 3095–3099.
- <sup>122</sup> Bohshar, M.; Heydt, H.; Regitz, M. 5-(diazomethyl)-5h-dibenzo[a,d]cycloheptenes-intermediates on the way to new dibenzosemibullvalene and dibenzocyclooctene syntheses. *Tetrahedron*, **1985**, *42* (6), 1815–1822.
- <sup>123</sup> Ciganek, E. The Photoisomerization of Dibenzobicyclo[2.2.2]octatrienes. *J. Am. Chem. Soc.* **1966**, *88*, 2882–2883.
- <sup>124</sup> Bruker-AXS (2016). *APEX3*. Version 2016.5-0. Madison, Wisconsin, USA.
- <sup>125</sup> Krause, L.; Herbst-Irmer, R.; Sheldrick, G. M.; Stalke, D. J. Comparison of Silver and Molybdenum Microfocus X-ray Sources for Single-Crystal Structure Determination. *Appl. Cryst.* **2015**, *48*, 3–10.
- <sup>126</sup> Sheldrick, G. M. (2013b). *XPREP*. Version 2013/1. Georg-August-Universität Göttingen, Göttingen, Germany.
- <sup>127</sup> Sheldrick, G. M. (2013a). The *SHELX* homepage, <http://shelx.uni-ac.gwdg.de/SHELX/>.
- <sup>128</sup> Sheldrick, G. M. SHELXT–Integrated Space-Group and Crystal-Structure Determination. *Acta Cryst. A* **2015**, *71*, 3–8.
- <sup>129</sup> Sheldrick, G. M. Crystal Structure Refinement with SHELXL. *Acta Cryst. C* **2015**, *71*, 3–8.
- <sup>130</sup> Dolomanov, O. V.; Bourhis, L. J.; Gildea, R. J.; Howard, J. A. K.; Puschmann, H. J. OLEX2: a Complete Structure Solution, Refinement, and Analysis Program. *Appl. Crystallogr.* **2009**, *42*, 339–341.
- <sup>131</sup> Guzei, I. A. (2007-2013). Programs *Gn*. University of Wisconsin-Madison, Madison, Wisconsin, USA.

Chapter 5. Reaction Progress Kinetic Analysis using *in situ* LED-NMR

## 5.1. Background

### 5.1.1. Reaction Progress Kinetic Analysis

Reaction Progress Kinetic Analysis (RPKA) is a general term that encompasses the many methods to help determine the rate law of a reaction and to help with elucidating a reaction mechanism. RPKA methods use timecourse data sets that are obtained from continuous monitoring of a reaction. Pioneered by Blackmond,<sup>132</sup> RPKA allows for the study of chemical reaction kinetics under synthetically relevant conditions.<sup>133</sup> In many cases when the reaction kinetics is dependent on reagent concentrations, traditional pseudo-first-order analyses that require a large excess of various reagents may provide results inconsistent with the kinetics at standard conditions. Therefore, strategies for mechanistic elucidation under synthetically relevant conditions are particularly important, and RPKA can often provide a more accurate mechanistic analysis than pseudo-first-order analysis in these cases. Additionally, RPKA can easily determine mechanistic features including catalyst deactivation and product inhibition, which can be challenging to determine by traditional kinetic approaches.

Photochemistry provides access to unique chemical pathways that are often difficult to access via traditional thermal methods. Enantioselective photochemistry has experienced a renaissance over the past two decades, due in part to the potential pharmacological utility of the accessible stereodefined products. While many efficient and highly stereoselective methods have been developed in recent years to control the enantioselectivity of photochemical reactions, few reports have included a full rate analysis and subsequent mechanistic investigation of these reactions.<sup>134</sup> Because photochemical reactions are often dependent on the photon flux introduced to the reaction vessel, the photon is frequently considered a reagent or catalyst in the proposed



mechanism. As a result, altering the magnitude of the photon flux in the reaction can result in a significant change to the rate law of a reaction. Mechanistic analysis under the optimized synthetic conditions would be ideal, rather than the pseudo-first-order analysis conditions. Additionally, we were intrigued how photocatalyst degradation and product inhibition may affect the enantioselectivity of an excited-state reaction. Therefore, we thought RPKA would be an ideal way to elucidate an enantioselective energy transfer reaction under synthetically relevant conditions.

RPKA has proven to be a powerful tool for mechanistic investigations, as an abundant amount of rate data can be revealed in relatively few experiments. This analysis can be performed with nearly any instrumentation that can detect reaction progress over time, including *in situ* IR, UV-Vis, or NMR. We became interested in using *in situ* LED-NMR to standardize light irradiation while rapidly collecting reaction progress data. Then, analysis of these data with the RPKA methods would enable us to study the rate law and elucidate the mechanism for an enantioselective, intermolecular [2+2] photocycloaddition.<sup>135</sup>

#### 5.1.2. “Same Excess” Protocol for RPKA

RPKA is ideally suited for studying the robustness of the catalyst over the course of a reaction. Two common pathways that could account for a decrease in catalyst performance are catalyst degradation and product inhibition. The “same excess” protocol was developed to differentiate these two pathways.<sup>136</sup> This protocol is comprised of three separate experiments visualizing the data as substrate concentration vs time. The first experiment is a timecourse of the reaction under standard reaction conditions (Table 5.1, entry 1). The second experiment is a timecourse where the initial substrate concentrations are equal to those when the first reaction reaches 50% conversion (Table 5.1, entry 2). Visualizing the data together as substrate

concentration vs time enables the observation of any rate differences between the reactions. There are two significant differences between these two experiments. In experiment 1, the catalyst has undergone a number of catalyst turnovers when the reaction reaches 50% conversion, while in experiment 2, the catalyst is presumably at its initial state. Any degree of catalyst degradation over these turnovers would manifest as a decrease in the rate of experiment 1 compared to experiment 2. Also, in experiment 1, a considerable amount of product has accumulated at 50% conversion, while in experiment 2, no product is present. If the product binds competitively to the catalyst and prevents binding of the substrate, the rate of experiment 1 would again be diminished compared to that of experiment 2. These first two experiments cannot distinguish between the catalyst degradation or product inhibition pathways. Therefore, a third experiment is required in which the reaction product is added to the start of the reaction along with the starting materials at 50% conversion (Table 5.1, entry 3). If this data visualization overlays with experiment 2, then catalyst degradation is implied. If this data visualization overlays with experiment 1, then product inhibition is implied. Thus, the same excess protocol can provide important insights into factors that are deleterious to reaction rate in just three simple experiments.

Table 5.1 Example set of reactions for the “same excess” experiment.

$$\mathbf{A} + \mathbf{B} \xrightarrow{\text{cat C}} \mathbf{D}$$

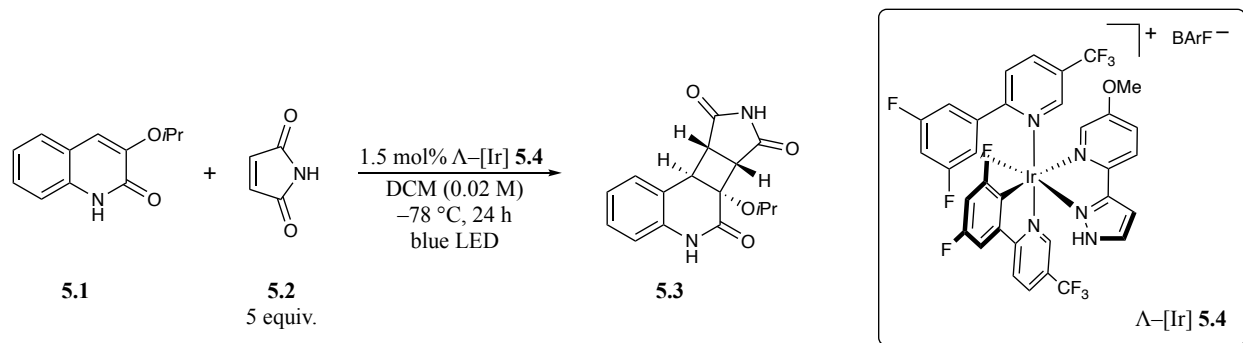
entry	[A] (M)	[B] (M)	[D] (M)
1	0.50	0.70	0.0
2	0.25	0.45	0.0
3	0.25	0.45	0.25

### 5.1.3. Variable Time Normalization Analysis

A recent advance in RPKA includes variable time normalization analysis (VTNA). This technique allows for the rapid investigation into the reaction order with respect to a single reagent. VTNA requires only two data sets to determine the reaction order.<sup>137</sup> The first set is the reaction timecourse at standard reaction conditions, and the second set is the reaction timecourse at either half or double the concentration of the reagent of interest. A mathematical “time-normalization” is applied to the reagent of interest for the timecourse, and a power term in this time-normalization represents the reaction order for the reagent.<sup>138</sup> The reagent order is elucidated by manually changing this power term in the calculation until the two data sets align most accurately. The power term responsible for the best fit alignment between the data sets is the reagent order. Because elucidating the order of each reagent only requires two data sets, a full reaction rate law can often be rapidly determined using this technique. To our knowledge, VTNA has not currently been used in the mechanistic elucidation of an enantioselective photochemical reaction using *in situ* LED-NMR.

## 5.2. Preliminary Results

Our lab previously published a report on an enantioselective, intermolecular [2+2] photocycloaddition between quinolone and maleimide (Scheme 5.1).<sup>135</sup> The proposed mechanism of this reaction involves a ground-state, hydrogen-bonding induced preorganization of the quinolone and the enantiopure [Ir] photocatalyst. Photoexcitation of this complex induces energy transfer to maleimide, which in turn reacts inside the solvent cage with the bound quinolone.



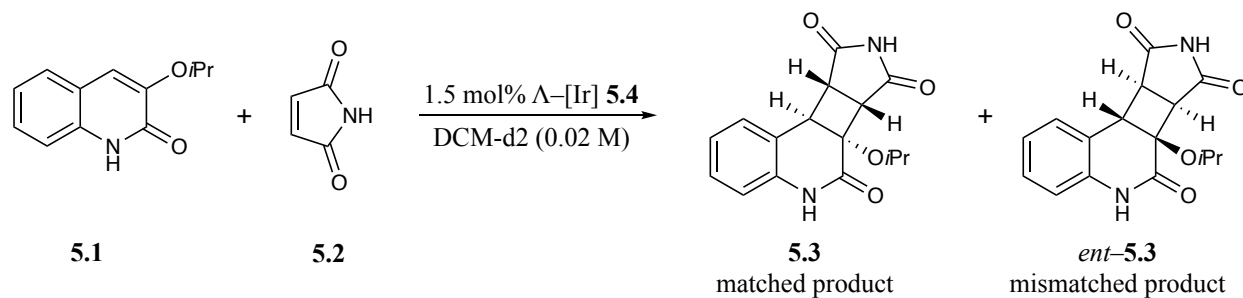
Scheme 5.1 Enantioselective [2+2] photocycloaddition via a chiral- $\Lambda$ -[Ir] photocatalyst.

While this reaction affords cyclobutane products **5.3** in high enantioselectivity highlighting the effectiveness of this energy transfer rebound mechanism, there are multiple deleterious pathways accessible to erode the enantioselectivity of the transformation. Notably, the solvent cage escape of photosensitized maleimide could promote reactivity with unbound quinolone, resulting in a racemic [2+2] pathway. In addition, we wondered if product inhibition could be a significant factor in the performance of the enantiopure photocatalyst **5.4**. In the event of a ground state, hydrogen bonding induced preorganization of the product with the photocatalyst, photoexcitation and sensitization to maleimide is still active, but the desired enantioselective cycloaddition with quinolone cannot occur because it is not bound within the chiral catalyst. Any route accessible that promotes an undesired racemic photocycloaddition must be suppressed to afford the product in high selectivity. Because of the complex nature of this enantioselective transformation, we chose to study this reaction with modern RPKA and VTNA kinetic techniques using *in situ* LED-NMR.

### 5.2.1. “Same Excess” Experiments

We began our studies by performing the “same excess” protocol to determine the effectiveness of the [Ir] photocatalyst over the course of the reaction. Our “same excess” experiments are outlined in Table 5.2.

Table 5.2 “Same excess” experiments for the desired [2+2] cycloaddition using both matched and mismatched products.



entry	[ <b>5.1</b> ] (mM)	[ <b>5.2</b> ] (mM)	[ <b>5.3</b> ] (mM)	conditions
1	20	100	0	standard rxn
2	10	90	0	50% <b>5.1</b>
3	10	90	10	50% <b>5.1</b> + 50% matched <b>5.3</b>
4	10	90	10	50% <b>5.1</b> + 50% mismatched <i>ent</i> - <b>5.3</b>

The consumption of **5.1** was monitored vs time and plotted in Figure 5.1.

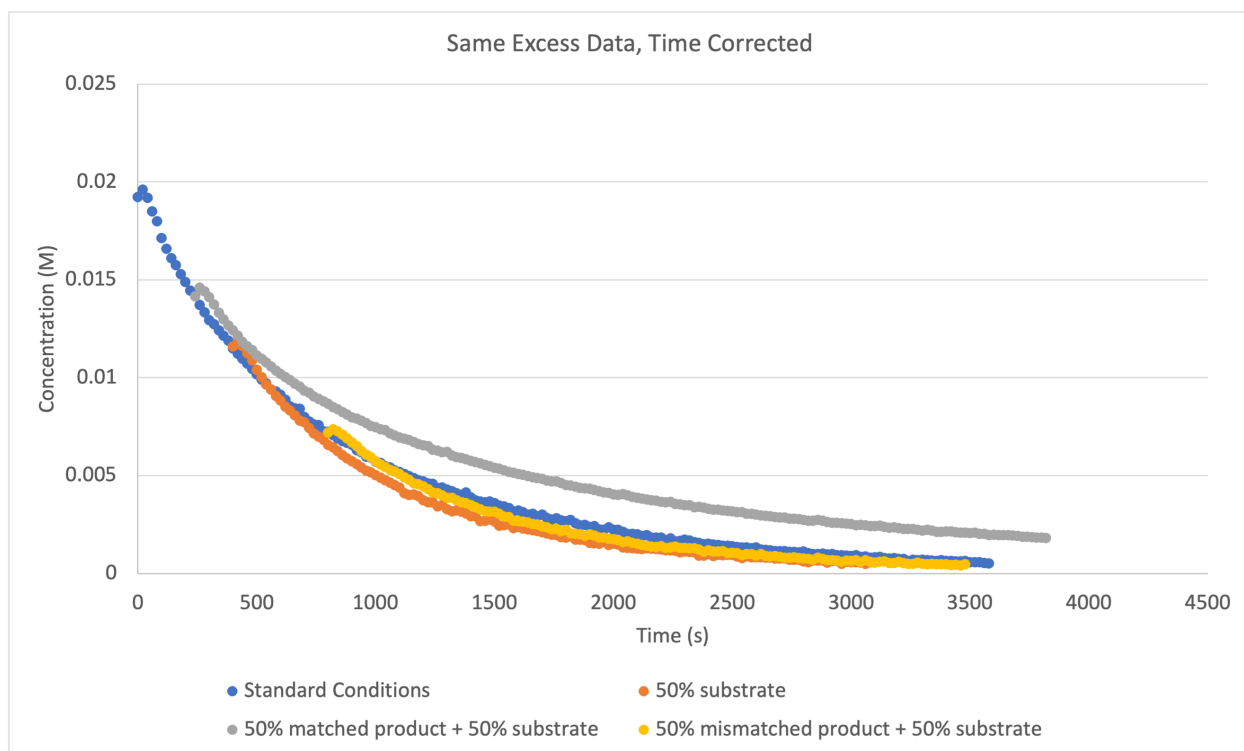


Figure 5.1 “Same excess” timecourses. Time corrected for initial substrate **5.1** concentration overlay.

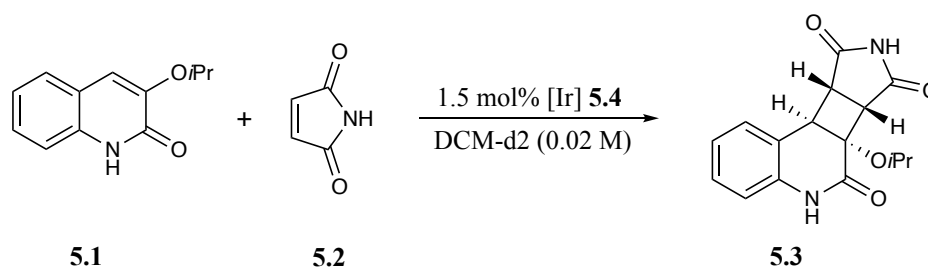
Comparing to the standard reaction conditions (blue trace), the “same excess” experiment (orange trace) proceeds at a faster rate, indicating there is [Ir] catalyst decomposition or product inhibition in the reaction. To differentiate these possibilities, we performed two additional reactions including 50% of both the matched and the mismatched products. The mismatched product inhibition experiment (yellow trace) has a similar rate to the standard reaction and a slightly slower rate compared to the “same excess” experiment. This indicates the mismatched product has a small product inhibition effect on the reaction. However, the matched product inhibition experiment (gray trace) shows a significantly lower reaction rate. This indicates a significant product inhibition from the matched enantiomer of the product. This is consistent with

our hypothesis that a ground state coordination with the photocatalyst **5.4** is instrumental for productive reactivity and selectivity.

### 5.2.2. VTNA Experiments

To determine the order of each component in the reaction, we relied on VTNA analysis. We performed the reaction with half and with double each reaction component to compare the reaction timecourse to the standard reaction conditions. The reactions we prepared to determine the reaction order of **5.1**, **5.2**, **5.4**, and light are shown in Table 5.3.

Table 5.3 Experiments for VTNA analysis.



entry	[ <b>5.1</b> ] (mM)	[ <b>5.2</b> ] (mM)	conditions
1	10	100	half substrate <b>5.1</b>
2	40	100	double substrate <b>5.1</b>
3	20	50	half maleimide <b>5.2</b>
4	20	200	double maleimide <b>5.2</b>
5	20	100	half [Ir] <b>5.4</b> (0.75 mol%)
6	20	100	double [Ir] <b>5.4</b> (3.0 mol%)
7	20	100	half light intensity (150 mW)
8	20	100	double light intensity (540 mW)

Anna L. Dunn (GlaxoSmithKline) overlaid these timecourses and applied a mathematical time-normalization.<sup>138</sup> We can visually observe the order of each reagent by manually changing

the power term associated with this time-normalization. The plots shown in Figure 5.2 are each with the power term optimized for the best overlay of the data.

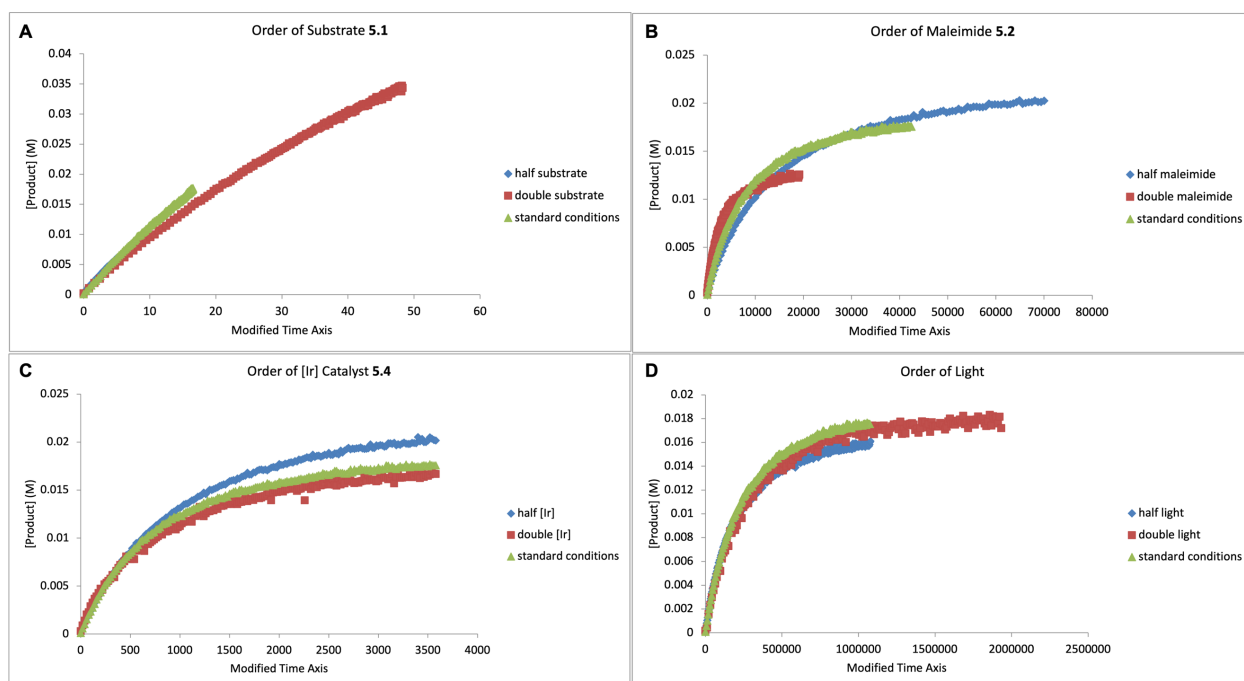


Figure 5.2 VTNA analysis. (A) Overlay showing 1<sup>st</sup> order of the substrate. (B) Overlay showing an apparent -1<sup>st</sup> order of the maleimide. (C) Overlay showing 0 order of the [Ir] photocatalyst. (D) Overlay showing 1<sup>st</sup> order of light.

The reaction is 1<sup>st</sup> order with respect to the substrate **5.1**. The reaction has an apparent -1<sup>st</sup> order with respect to maleimide **5.2**. The reaction is 0 order with respect to the [Ir] photocatalyst **5.4**. The reaction is 1<sup>st</sup> order with respect to light, treated mathematically as a catalyst. However, the VTNA analysis for maleimide suffered from experimental complications and therefore must further be verified. Because we are tracking the formation of desired product vs time, the maleimide analysis does not account for the significant maleimide dimer product being formed during the reaction. We can more accurately determine the order of maleimide by also tracking the formation of the dimer side-product over time. However, the maleimide dimer is insoluble under

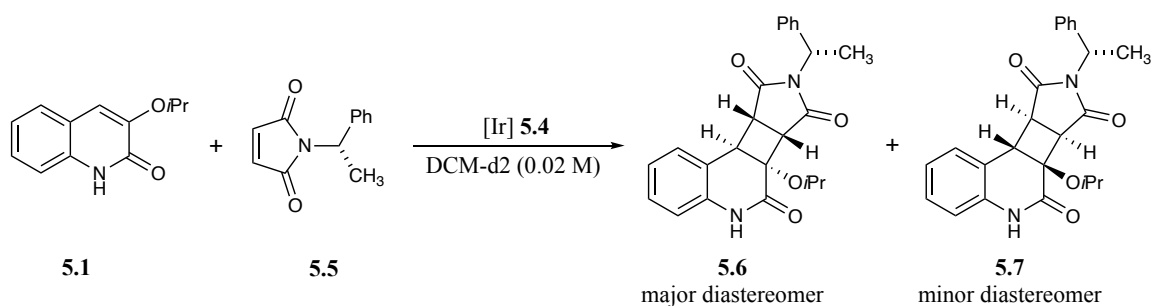


our reaction conditions, preventing its analysis by  $^1\text{H}$  NMR. Future experiments include performing these half maleimide and double maleimide experiments with a maleimide derivative that is more soluble as the dimer.

### 5.2.3. Diastereotopic Reaction using a Chiral Maleimide

We were also intrigued about the enantioselectivity of the reaction over time. However, to observe the enantioselectivity of the reaction during LED-NMR, we needed to form diastereotopic products rather than enantiomeric products. To address this, we used (*S*)-(-)-*N*-(1-phenylethyl)maleimide **5.5** instead of maleimide **5.2** to generate diastereomeric products **5.6** and **5.7**. The experiments we performed are outlined in Table 5.4.

Table 5.4 Experiments to Determine Diastereoselectivity vs Light Intensity.



entry	[ <b>5.1</b> ] (mM)	[ <b>5.5</b> ] (mM)	[ <b>Ir</b> ] <b>5.4</b>	conditions
1	20	100	1.5 mol% $\Lambda$ -[Ir] (300 $\mu\text{M}$ )	300 mW light
2	20	100	1.5 mol% $\Delta$ -[Ir] (300 $\mu\text{M}$ )	300 mW light
3	20	100	0.3 mol% $\Delta$ -[Ir] (60 $\mu\text{M}$ )	150 mW light
4	20	100	0.3 mol% $\Delta$ -[Ir] (60 $\mu\text{M}$ )	300 mW light
5	20	100	0.3 mol% $\Delta$ -[Ir] (60 $\mu\text{M}$ )	540 mW light

We performed entries 1 and 2 to determine which enantiomer of the [Ir] photocatalyst provides the higher d.r. of the product. We identified the  $\Delta$ -[Ir] as the more selective catalyst; therefore, we used  $\Delta$ -[Ir] for entries 3–5. To gauge the reaction selectivity on light intensity, we performed the reaction across a range of light intensities from 150 mW – 540 mW. These data are

plotted in Figure 5.3. As expected, the rate of the reaction increased with increased light intensity. However, the selectivity of the reaction seems independent of the light intensity, although there may be a slight increase in the concentration of the major diastereomer at higher light intensity. This increase is modest, and therefore would need further replication and confirmation. We justify the unusual behavior at the end of the 540 mW timecourse (gray trace) by poor  $^1\text{H}$  NMR shimming that affected the NMR integrations at extended timepoints. We expect that duplication of this timecourse should provide a smoother data set consistent with the shape of the 150 mW and 300 mW data sets.

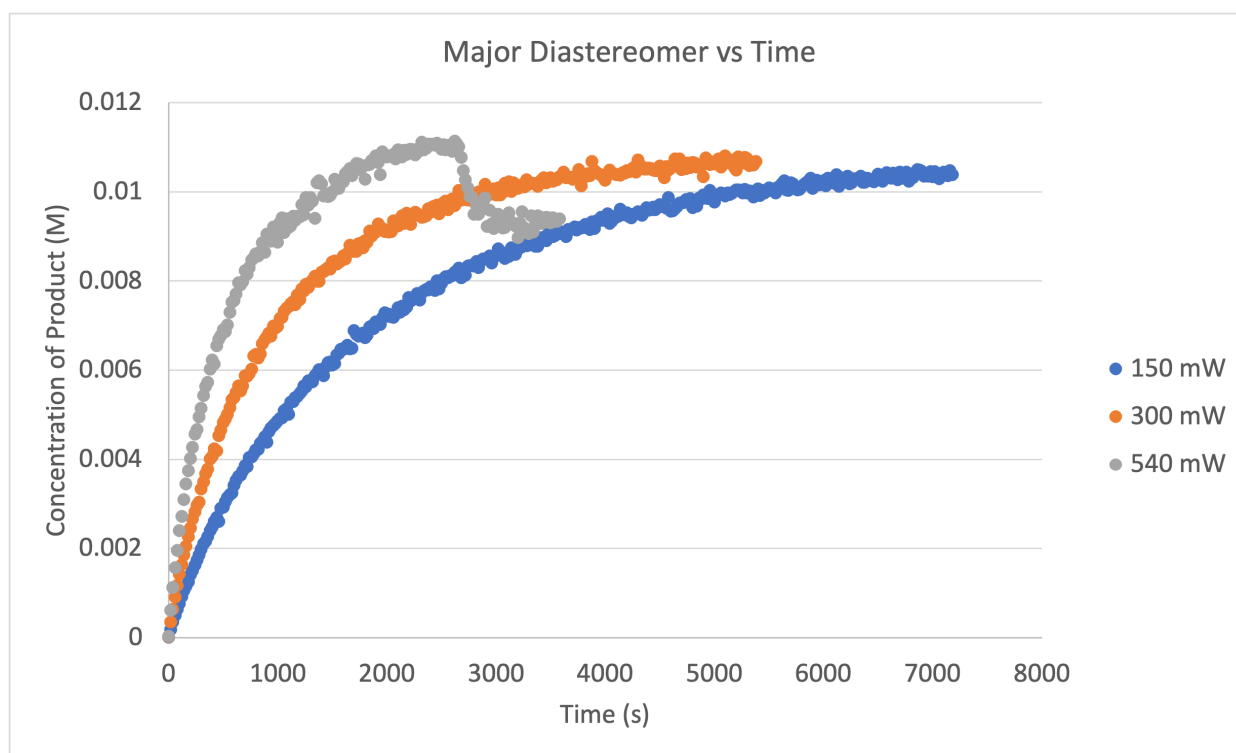


Figure 5.3 Major diastereomer **5.6** concentration vs time over a range of light intensity.

### 5.3. Future Directions

We plan to compare the order of the reaction from VTNA to the order of the reaction from initial rate data. Therefore, Wesley B. Swords is collecting initial rate data of this reaction at room temperature to simulate the LED-NMR conditions and initial rate data at  $-78\text{ }^{\circ}\text{C}$  to simulate the batch scale conditions from Zheng *et. al.*<sup>135</sup>

### 5.4. Contributions

Wesley B. Swords and Steven J. Chapman (University of Wisconsin – Madison) performed the *in situ* LED-NMR experiments. W.B.S. did the initial data workup and preliminary analysis. Anna L. Dunn (GlaxoSmithKline) performed the RPKA and the VTNA and provided guidance and advice on experiments. Heike Hofstetter (University of Wisconsin – Madison) provided helpful conversation, feedback, and training for the LED-NMR instrumentation.

### 5.5. Supporting Information

#### 5.5.1. General Methods and Materials

Dichloromethane ( $\text{CH}_2\text{Cl}_2$ , HPLC grade) was purchased from Fisher Scientific and dried through a solvent purification system (Pure Process Technology). Deuterated dichloromethane ( $\text{CD}_2\text{Cl}_2$ ) was purchased from MilliporeSigma or Cambridge Isotope Laboratories (99.5% D). Hexamethylbenzene ( $\geq 99\%$ ) was used as an internal standard for all NMR experiments and was purchased from MilliporeSigma. 5 mm NMR tubes were purchased from Norell and 4 mm Precision NMR tubes from Wilmad. A 466 nm blue LED array (powerPar 15 W LED bulb, Hydrofarm) was the irradiation source for initial batch ex situ experiments and in reference to the previous report of this reaction.<sup>135</sup> A 450 nm ultra-high-power (UHP) LED was used for in situ

NMR experiments (UHP-Mic-LED-blue, Prizmatix). A 456 nm LED (PR-160L, Kessil) was used to measure initial rates at both room temperature and  $-78$  °C. Maleimide and benzyl-maleimide were purchased from Oakwood and MilliporeSigma respectively and used without purification. The quinolone substrate and iridium photocatalyst were synthesized following previously published procedures and spectral data aligned with the published reports.<sup>135,139</sup>

### 5.5.2. NMR Data Acquisition

Room temperature experiments were conducted at 25 °C on an AVIII-HD 600 MHz spectrometer (Bruker Biospin Corp., Billerica, MA, USA) on a 5 mm TCI-F ( $^1\text{H}$ ,  $^{19}\text{F}/^{13}\text{C}/^{15}\text{N}$ ) cryoprobe with a z-gradient using TopSpin 3.2 software. Transmitter frequency centered on 3703.82 Hz in the  $^1\text{H}$  channel with a SW of 19.9437 ppm. All spectra were referenced to the residual solvent signal (either  $\text{CD}_2\text{Cl}_2$ , 5.33 ppm, or  $\text{CDCl}_3$ , 7.26 ppm). Spectra for in situ experiments were acquired using a single scan and an inter-scan delay (D20) of 20 s. As described more below,  $^1\text{H}$  NMR scans were collected as pseudo-2D experiments, the write time was completed at the end of the entire experiment with the LED turned off, thus the distance between each data point is the D20. The relaxation times ( $T_1$ ) for the quinolone, maleimide, and product were collected in  $\text{CD}_2\text{Cl}_2$  using an inversion recovery sequence. The 20 s D20 was long enough to ensure full proton relaxation for the protons of interest (Figure 5.5).

### 5.5.3. LED Kinetic Data Acquisition

*Setup.* The LED-NMR setup was described in detail previously.<sup>134a</sup> Briefly, the 450 nm UHP-LED was controlled using a Benchtop Current Controller with CW operation mode, TTL input, and analog input (UHPLCC-AIN). A fiber patch cord (POF, core 1500  $\mu\text{m}$ ) was attached to the LED using a fiber coupling adaptor. The other end of the 4 m long POF was shielded with a 4

mm glass sleeve and inserted into the 5 mm NMR tube. Power output was measured at the tip of the POF using an optical power meter equipped with a probe head. This setup is portable and can be easily moved between different spectrometers.

*LED-NMR pulse programs.* The ON-OFF function of the LED can be managed by the NMR spectrometer consol. A BNC connected the LED current controller to the spectrometer console TTL ports. The addition of dedicated TTL pulse sequences to a standard Bruker pseudo-2D kinetics pulse program provided the means to turn the LED ON (TTL\_LOW) at the start and Off (TTL\_HIGH) at the end of the experiment. Unlike the previous study, the pseudo-2D experiment allowed the TTL pulses to be placed outside of the 1D-single scan loop such that there was no interruption of the LED during the experiment, providing constant illumination over the entity of data collection. Two single scan ‘dark’ spectra were collected prior to the illumination using a standard Bruker zg30 pulse sequence. Both the dark and pseudo-2D light pulse programs are provided below.

*Dark Pulse Program.*

```
;zg30
```

```
;
```

```
;$CLASS=HighRes
```

```
;$DIM=1D
```

```
;$TYPE=
```

```
;$SUBTYPE=
```

```
;$COMMENT=
```

;\$RECOMMEND=y

#include <Avance.incl>

#include <Delay.incl>

"DELTA=d20-((d1+aq)\*(ns+ds))-30m"

"acqt0=-p1\*0.66/3.1416"

1 ze

2 d1

p1\*0.33 ph1

go=2 ph31

30m mc #0 to 2 F0(zd)

DELTA

Exit

ph1=0 2 2 0 1 3 3 1

ph31=0 2 2 0 1 3 3 1

;p11 : f1 channel - power level for pulse (default)

;p1 : f1 channel - 90 degree high power pulse

;d1 : relaxation delay;  $1-5 * T1$

;d20 : delay between start of different 1D spectra

;NS:  $1 * n$ , total number of scans:  $NS * TD0$

;\$Id: zg30,v 1.12 2012/01/31 17:49:31 ber Exp \$

*Light Pulse Program.*

;zg2d

;

;\$CLASS=HighRes

;\$DIM=2D

;\$TYPE=

;\$SUBTYPE=

;\$COMMENT=

;\$RECOMMEND=y

```
#include <Avance.incl>
```

```
#include <Delay.incl>
```

```
"DELTA=d20-((d1+aq)*(ns+ds))-30m"
```

```
"acqt0=-p1*0.66/3.1416"
```

```
1 ze
```

```
1u TTL3_LOW
```

```
2 30m
```

```
3 d1
```

```
p1*0.33 ph1
```

```
go=3 ph31
```

```
30m wr #0 if #0 ze
```

```
DELTA
```

```
lo to 2 times td1
```

```
1u TTL3_HIGH
```

```
Exit
```



ph1=0 2 2 0 1 3 3 1

ph31=0 2 2 0 1 3 3 1

;p11 : f1 channel - power level for pulse (default)

;p1 : f1 channel - 90 degree high power pulse

;d1 : relaxation delay;  $1-5 * T1$

;d20 : delay between start of different 1D spectra

;NS:  $1 * n$ , total number of scans:  $NS * TD0$

;td1: number of experiments

;\$Id: zg2d,v 1.6 2009/07/02 16:40:47 ber Exp \$

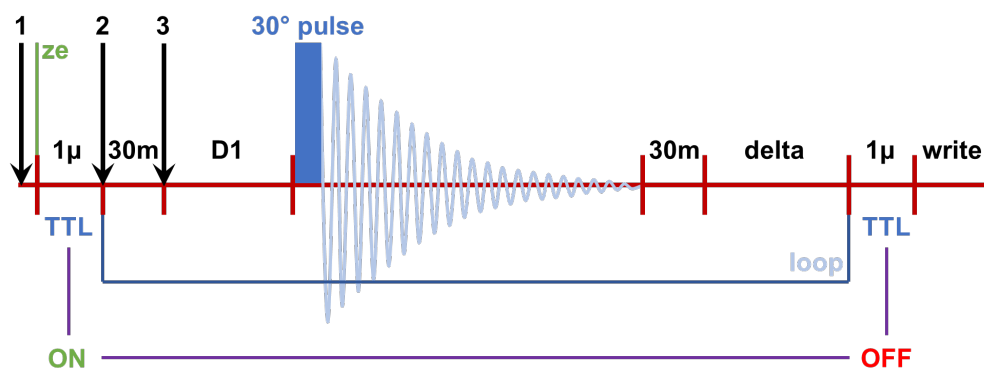


Figure 5.4 Graphical representation of the pseudo-2D pulse program used to collect kinetic data in LED-NMR experiments.

**Data Analysis.** NMR spectra were processed in MestreNova V.12.0. The spectra were autophased, and the baseline was corrected through application of the Whitaker Smoother functionality. Special interest was paid to the baseline region between 0 and 5 ppm, as that range includes the proton resonances of interest for the substrate, product, and internal standard (see Figure 5.5). Substrate and product concentrations were calculated based on the internal standard, hexamethyl benzene. Data were analyzed in Microsoft Excel and Origin 2020. Figures were prepared in the Microsoft Office Suite, Origin 2020, and ChemDraw 17.

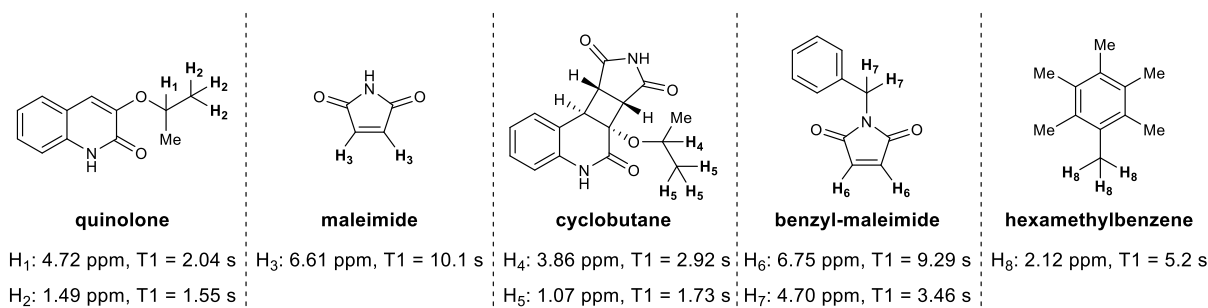


Figure 5.5 T<sub>1</sub> relaxation times for selected protons on quinolone, maleimide, and product cyclobutane. Both quinolone and cyclobutane protons were monitored for kinetic analysis.

#### 5.5.4. In Situ Experiments

In general, for all in situ LED-NMR experiments, a stock solution of the  $\Delta$ -[Ir] photocatalyst was prepared in CD<sub>2</sub>Cl<sub>2</sub>. To this stock solution was added hexamethylbenzene for use as an internal standard. In some experiments (see below) quinolone might also be added to make a  $\Delta$ -[Ir] + quinolone stock solution. These stock solutions were then used to dissolve the other reagents required, maleimide and quinolone when not included in the stock solution. Typically, 1 mL of the stock was used to dissolve all reagents and for all in situ experiments 0.5 mL was transferred to a 5 mm NMR tube. This provides ~2.8–3 mm of solution within the NMR tube and appropriately places the liquid-air interface only slightly above the detection region. The

glass shrouded optical fiber is then placed within the solution such that tip of the optical fiber is submerged in solution. The tip is positioned such that it is close to, but not within the detection region. Care is taken to eliminate bubbles between the tip and solution. The optical fiber-NMR tube setup is inserted into a spinner and lowered into the magnet through the bore. All data acquisition and LED control is performed on the NMR console. Unless otherwise stated, the LED power was set to 300 ( $\pm 5\%$ ) mW as measured by a power meter at the tip of the optical fiber.

### 5.5.5. Light Intensity Initial Rates; room temperature

A stock solution containing 12.2 mg quinolone substrate (0.06 mmol, 20 mM), 29.4 mg maleimide (0.30 mmol, 0.10 M), and 1.7 mg  $\Delta$ -[Ir] photocatalyst (1.0  $\mu$ mol, 0.3 mM) were dissolved in 3 mL  $\text{CD}_2\text{Cl}_2$ . No internal standard was used, and relative integration was used instead of concentration to measure relative initial rates. The solution was divided between four NMR tubes (0.5 mL each). The tubes were irradiated at different powers with the LED-NMR system (150, 300, 450, and 570 mW). Initial rates were measured by monitoring the integration of the isopropyl CH over the first 15% of quinolone substrate conversion.

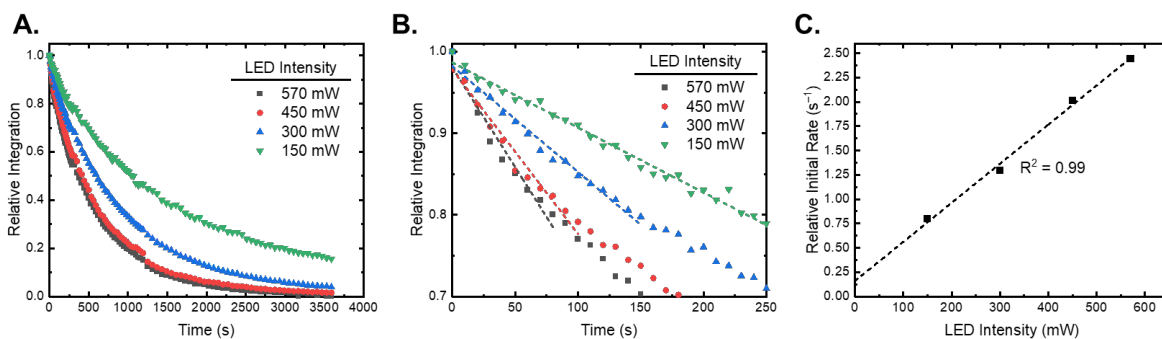


Figure 5.6 Initial rates measured at various light intensities at room temperature. A) Time-courses recorded for initial rate measurements. B) Initial rates at different light intensities. The dotted lines

correspond to linear regressions of the data. C) A linear trend between light intensity and initial reaction rate.

#### 5.5.6. Same Excess Experiments

Sample preparation for the same excess experiments<sup>132,136,140</sup>: The  $\Delta$ -[Ir] photocatalyst stock solution was prepared with 2.7 mg of the photocatalyst (1.54  $\mu\text{mol}$ , 5 mL  $\text{CD}_2\text{Cl}_2$ , 0.3 mM). To 4 mL of this stock solution was added 2.2 mg hexamethylbenzene as internal standard (0.014 mmol, 3.3 mM). Maleimide, quinolone, and the enantioenriched cyclobutane product were weighed directly into vials for the four different conditions, see Table 5.5. The four conditions were: standard,  $\frac{1}{2}$  quinolone concentration,  $\frac{1}{2}$  quinolone +  $\frac{1}{2}$  matched enantiomeric product, and  $\frac{1}{2}$  quinolone +  $\frac{1}{2}$  mismatched enantiomeric product. The enantioenriched product was prepared using the  $\Delta$ -[Ir] photocatalyst according to the ex situ  $-78\text{ }^\circ\text{C}$  conditions and isolated in 96% ee. The matched and mismatched cyclobutane products were based on the photocatalyst used ( $\Delta$ - or  $\Lambda$ -[Ir], respectively). The hypothesis being that given the product was formed from the  $\Delta$ -[Ir] photocatalyst, a shape matching may favor product inhibition over the opposite diastereomeric pairing. Note, for the standard and  $\frac{1}{2}$  quinolone without added product conditions the enantiomer of the photocatalyst does not matter. For the nonstandard conditions the concentration of maleimide was correct assuming a stoichiometric (1:1) loss through reaction with quinolone. While dimerization is known to occur, the low association constant between maleimide and the photocatalyst alone with the results of these experiments make it clear that product inhibition is the major pathway of photocatalyst deactivation.

Table 5.5 Conditions for preparation of the same excess experiments. Concentration of  $\Delta$ - or  $\Lambda$ -[Ir] was constant for all conditions (0.3 mM).

Conditions (photocatalyst enantiomer)	Quinolone Mass (mg)	Quinolone Conc (mM)	Maleimide Mass (mg)	Maleimide Conc (mM)	Product Mass (mg)	Product Conc (mM)
Standard ( $\Lambda$ -[Ir])	4.0	20	9.7	100	0	0
$\sim 1/2$ quinolone ( $\Lambda$ - [Ir])	2.1	10	8.7	90	0	0
$\sim 1/2$ quinolone + $1/2$ matched product ( $\Delta$ -[Ir])	2.0	10	8.7	90	3.0	10
$\sim 1/2$ quinolone + $1/2$ matched product ( $\Lambda$ -[Ir])	2.0	10	8.9	90	2.7	10

#### 5.5.7. VTNA Methods

*Photocatalyst stock solution #1:* A stock solution of the  $\Delta$ -[Ir] photocatalyst (5.1 mg, 2.9  $\mu$ mol, 0.6 mM) was prepared in  $\text{CD}_2\text{Cl}_2$  (5 mL). To this solution was added hexamethylbenzene as an internal standard (4.8 mg, 0.03 mmol).

*Photocatalyst stock solution #2:* A stock solution of the  $\Delta$ -[Ir] photocatalyst (2.1 mg, 1.2  $\mu$ mol, 0.3 mM) was prepared in  $\text{CD}_2\text{Cl}_2$  (4 mL). To this solution was added hexamethylbenzene as an internal standard (3.1 mg, 0.02 mmol).

*Standard reaction:* To a scintillation vial was added 4.0 mg quinolone substrate (0.01 mmol), 9.7 mg maleimide (0.10 mmol), and 1 mL of the  $\Delta$ -[Ir] photocatalyst stock solution described in the *same excess section*. To a 5 mm NMR tube was transferred 0.5 mL of this solution.

*$\frac{1}{2} \times$  quinolone concentration:* To a scintillation vial was added 1.9 mg quinolone substrate (0.005 mmol), 10.0 mg maleimide (0.10 mmol), 0.5 mL of  $\Delta$ -[Ir] photocatalyst stock solution #1, and 0.5 mL of  $\text{CD}_2\text{Cl}_2$ . To a 5 mm NMR tube was transferred 0.5 mL of this solution.

*$2 \times$  quinolone concentration:* To a scintillation vial was added 8.2 mg quinolone substrate (0.04 mmol), 9.6 mg maleimide (0.10 mmol), 0.5 mL of the  $\Delta$ -[Ir] photocatalyst stock solution #1, and 0.5 mL of  $\text{CD}_2\text{Cl}_2$ . To a 5 mm NMR tube was transferred 0.5 mL of this solution.

*$\frac{1}{2} \times$  maleimide concentration:* To a scintillation vial was added 4.1 mg quinolone substrate (0.02 mmol), 4.9 mg maleimide (0.05 mmol), 0.5 mL of the  $\Delta$ -[Ir] photocatalyst stock solution #1, and 0.5 mL of  $\text{CD}_2\text{Cl}_2$ . To a 5 mm NMR tube was transferred 0.5 mL of this solution.

*$2 \times$  maleimide concentration:* To a scintillation vial was added 3.9 mg quinolone substrate (0.019 mmol), 19.4 mg maleimide (0.2 mmol), 0.5 mL of the  $\Delta$ -[Ir] photocatalyst stock solution #1, and 0.5 mL of  $\text{CD}_2\text{Cl}_2$ . To a 5 mm NMR tube was transferred 0.5 mL of this solution.

*$\frac{1}{2} \times \Delta$ -[Ir] concentration:* To a scintillation vial was added 4.2 mg quinolone substrate (0.02 mmol), 9.6 mg maleimide (0.1 mmol), 0.25 mL of the  $\Delta$ -[Ir] photocatalyst stock solution #1,

and 0.75 mL of CD<sub>2</sub>Cl<sub>2</sub>. To a 5 mm NMR tube was transferred 0.5 mL of this solution. The Δ-[Ir] photocatalyst concentration was 0.15 mM.

*2 × Δ-[Ir] concentration:* To a scintillation vial was added 4.2 mg quinolone substrate (0.02 mmol), 9.8 mg maleimide (0.1 mmol), 1.0 mL of the Δ-[Ir] photocatalyst stock solution #1. To a 5 mm NMR tube was transferred 0.5 mL of this solution. The Δ-[Ir] photocatalyst concentration was 0.60 mM.

*½ × LED Intensity:* To a scintillation vial was added 4.0 mg quinolone substrate (0.02 mmol), 9.7 mg maleimide (0.1 mmol), 1.0 mL of the Δ-[Ir] photocatalyst stock solution #2. To a 5 mm NMR tube was transferred 0.5 mL of this solution. The LED power was set to 150 mW at the tip of the optical fiber.

*2 × LED Intensity:* To a scintillation vial was added 4.2 mg quinolone substrate (0.02 mmol), 9.5 mg maleimide (0.1 mmol), 1.0 mL of the Δ-[Ir] photocatalyst stock solution #2. To a 5 mm NMR tube was transferred 0.5 mL of this solution. The LED power was set to 560 mW at the tip of the optical fiber.

## 5.6. References

---

<sup>132</sup> Blackmond, D. G. Reaction Progress Kinetic Analysis: A Powerful Methodology for Mechanistic Studies of Complex Catalytic Reactions. *Angew. Chem., Int. Ed.* **2005**, *44*, 4302–4320.

<sup>133</sup> Mathew, J. S.; Klussmann, M.; Iwamura, H.; Valera, F.; Futran, A.; Emanuelsson, E. A. C.; Blackmond, D. G. Investigations of Pd-Catalyzed ArX Coupling Reactions Informed by Reaction Progress Kinetic Analysis. *J. Org. Chem.* **2006**, *71*, 4711–4722.

<sup>134</sup> (a) Skubi, K. L.; Swords, W. B.; Hofstetter, H.; Yoon, T. P. LED-NMR Monitoring of an Enantioselective Catalytic [2+2] Photocycloaddition. *ChemPhotoChem.* **2020**, *4*, 685–690. (b) Lehnerr, D.; Ji, Y.; Neel, A. J.; Cohen, R. D.; Brunskill, A. P. J.; Yang, J.; Reibarkh, M. Discovery of a Photoinduced Dark Catalytic Cycle Using *in Situ* LED-NMR Spectroscopy. *J. Am. Chem. Soc.* **2018**, *140*, 13843–13853. (c) Ji, Y.; Bottecchia, C.; Lévesque, F.; Narsimhan, K.; Lehnerr,

---

D.; McMullen, J. P.; Dalby, S. M.; Xiao, K.-J.; Reibarkh, M. Benzylic Photobromination for the Synthesis of Belzutifan: Elucidation of Reaction Mechanisms Using In Situ LED-NMR. *J. Org. Chem.* **2021**, Article ASAP. DOI: 10.1021/acs.joc.1c01465 (accessed 2021-11-16).

<sup>135</sup> Zheng, J.; Swords, W. B.; Jung, H.; Skubi, K. L.; Kidd, J. B.; Meyer, G. J.; Baik, M.-H.; Yoon, T. P. Enantioselective Intermolecular Excited-State Photoreactions Using a Chiral Ir Triplet Sensitizer: Separating Association from Energy Transfer in Asymmetric Photocatalysis. *J. Am. Chem. Soc.* **2019**, *141*, 13625–13634.

<sup>136</sup> Blackmond, D. G. Kinetic Profiling of Catalytic Organic Reactions as a Mechanistic Tool. *J. Am. Chem. Soc.* **2015**, *137*, 10852–10866.

<sup>137</sup> Nielsen, C. D.-T.; Burés, J. Visual Kinetic Analysis. *Chem. Sci.* **2019**, *10*, 348–353.

<sup>138</sup> (a) Burés, J. A Simple Graphical Method to Determine the Order in Catalyst. *Angew. Chem. Int. Ed.* **2016**, *55*, 2028–2031. (b) Burés, J. Variable Time Normalization Analysis: General Graphical Elucidation of Reaction Orders from Concentration Profiles. *Angew. Chem. Int. Ed.* **2016**, *55*, 16084–16087.

<sup>139</sup> Skubi, K. L.; Kidd, J. B.; Jung, H.; Guzei, I. A.; Baik, M.-H.; Yoon, T. P. Enantioselective Excited-State Photoreactions Controlled by a Chiral Hydrogen-Bonding Iridium Sensitizer. *J. Am. Chem. Soc.* **2017**, *139*, 17186–17192.

<sup>140</sup> Meek, S. J.; Pitman, C. L.; Miller, A. J. M. Deducing Reaction Mechanism: A Guide for Students, Researchers, and Instructors. *J. Chem. Educ.* **2016**, *93* (2), 275–286.



Appendix A. Tri-Catalytic, Chiral Hydrogen Bonding Catalysis for the Brønsted  
Acid Activation of Enantioselective [2+2] Photocycloadditions

## A.1 Background

Chapter 2 detailed a chiral phosphoric acid (CPA) catalyzed enantioselective [2+2] photocycloaddition. The optimization of CPA scaffolds for enantioselective transformations is a formidable synthetic challenge.<sup>141</sup> A plethora of chiral backbones are available to host the phosphoric acid binding site; some common examples are shown in Figure A.1. Each backbone provides a different chiral sphere of influence for the reaction of interest and causes slight differences in the pKa of the phosphoric acid.<sup>142</sup> Therefore, with CPA catalysts, the chiral environment and the acidity of the acid are intimately linked.

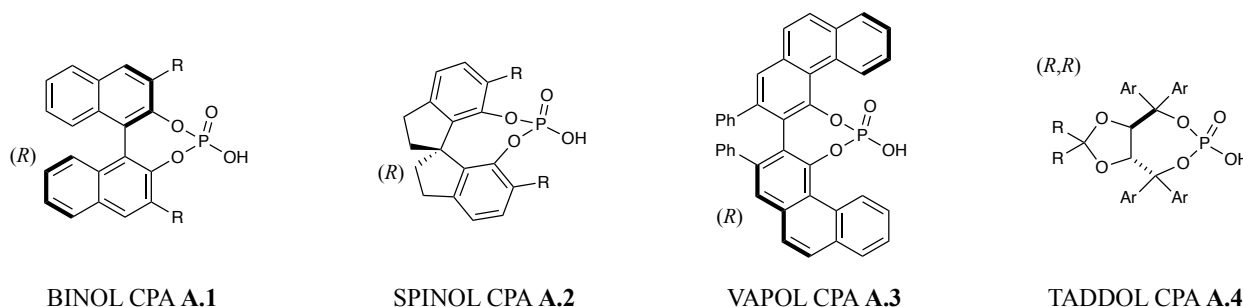
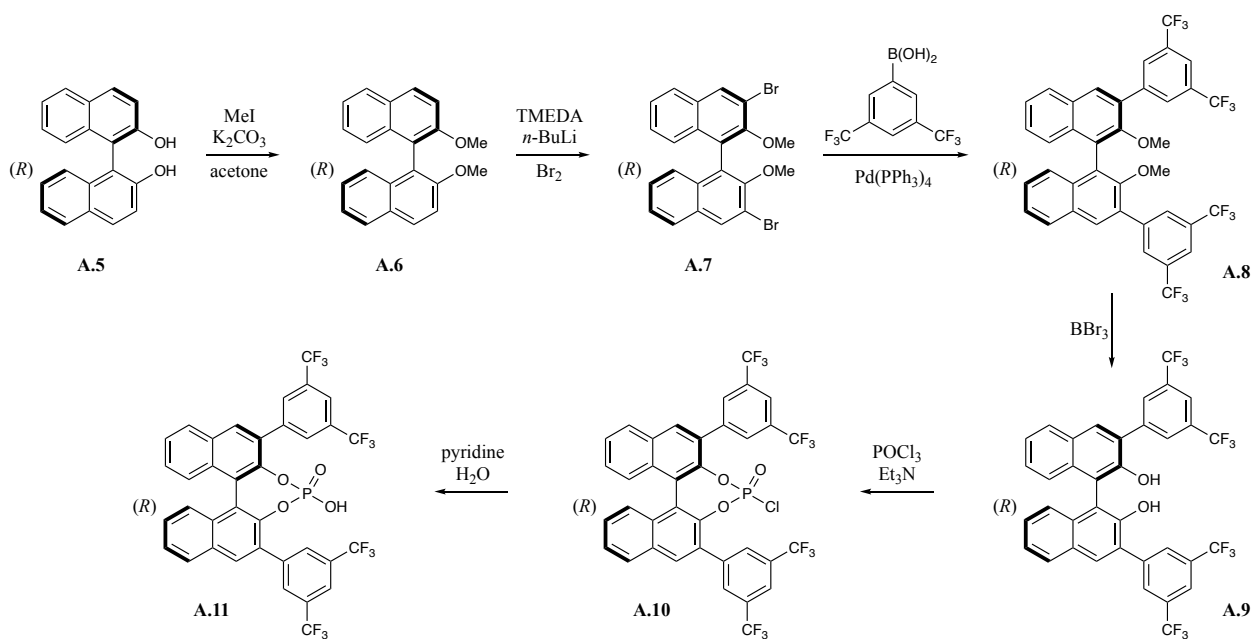


Figure A.1 Select Examples of Common Chiral Phosphoric Acid Backbones.

Frequently, BINOL CPAs (**A.1**) are used because they are often most synthetically accessible and most affordable. Most often, 3,3'-substitution of the BINOL scaffold is required for a desired reaction outcome and stereoselectivity. These 3,3' substitutions often require lengthy synthetic procedures (~6 steps) involving harsh reaction conditions (Scheme A.1).<sup>143</sup> Traditionally, the BINOL scaffold **A.5** requires protection of the diol with a strong alkylating agent (e.g. MeI, MOMCl) before bromination of the desired 3,3' positions to afford **A.7**. Then the scaffold is amendable to transition metal catalyzed cross-coupling conditions. However, the cross-coupling reactions on these bulky scaffolds are often demanding and untranslatable to different nucleophilic

coupling partners. Fortunately, the frequent use of BINOL CPAs in the literature has provided published routes for a small variety of successful cross-coupling conditions for the synthesis of 3,3'-substituted CPAs. However, most of these reactions are optimized for standard  $C(sp^2)-C(sp^2)$  bond formation with an aryl boronic acid coupling partner. These cross-coupling conditions do not always translate to different chiral scaffolds, and this approach is also subject to the same limitations as standard cross-coupling methodology (e.g. including a necessary electronic match between the nucleophile and electrophile and prohibiting a general  $C(sp^2)-C(sp^3)$  cross-coupling).<sup>144</sup> Therefore, after an often arduous synthesis of a desired 3,3'-substituted chiral scaffold **A.8**, the protected diol must be cleaved to recover the free alcohols **A.9**. This is followed by the conversion of the diol to the phosphorus chloride **A.10**. Finally, conversion to either the phosphoric acid or the phosphoric-based triflimide affords the final CPA structure of interest **A.11**.



Scheme A.1 Representative Route to a Common BINOL CPA.

This synthesis is required for each CPA scaffold to test during an optimization of a reaction, which is an inefficient and time-consuming expense for the researchers involved. Unfortunately, there is no current way to predict well performing CPA structures for a particular application. Empirical screening and synthesis are required, individually optimizing the chiral backbone structure, the 3,3'-substitution substituents, and the identity of the acidic proton (phosphoric acid, triflimide, etc.) within the chiral environment. If screening begins with a phosphoric acid but a stronger acid is required for the activation of a target reaction, a chiral triflimide scaffold changes the interactions with the substrate, often resulting in a re-optimization of the chiral ligands for high enantioselectivity.

The challenges associated with the synthesis of CPA scaffolds and their difficult optimization for an enantioselective transformation inspires alternative approaches to chiral Brønsted acid catalyzed chemistry. Preferably, new chiral Brønsted acid catalyzed methods would introduce a modular system that allows for independent tuning of the chiral environment from the pKa of the acid. As a result, optimization of a single variable at a time would allow for easier screening and easier identification of reaction trends, as compared to a CPA system where these variables are intimately linked.

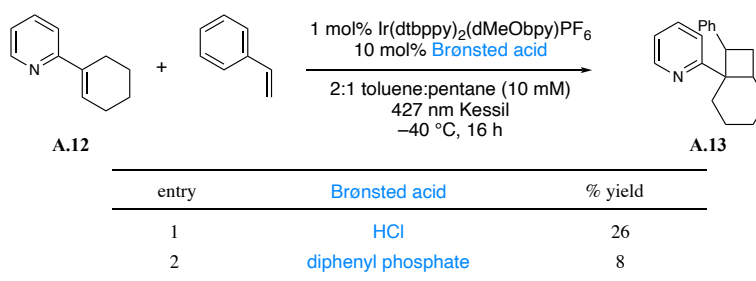
Herein, we discuss preliminary results highlighting a modular system involving an achiral Brønsted acid and a chiral hydrogen bond donor catalyst for an enantioselective photochemical [2+2] photocycloaddition. This synthetic result is inspired by the transformation in Chapter 2, yet the chiral environment is defined by a new catalytic system. Motivated by the privileged class of chiral hydrogen bond donor scaffolds pioneered by Jacobsen,<sup>145</sup> we hypothesized these same chiral catalysts would be efficient for excited state photochemical transformations. As a result, we hoped

to optimize a tri-catalytic system for enantioselective [2+2] photocycloaddition reactions involving a photocatalyst, an achiral Brønsted acid, and a chiral hydrogen bond donor.

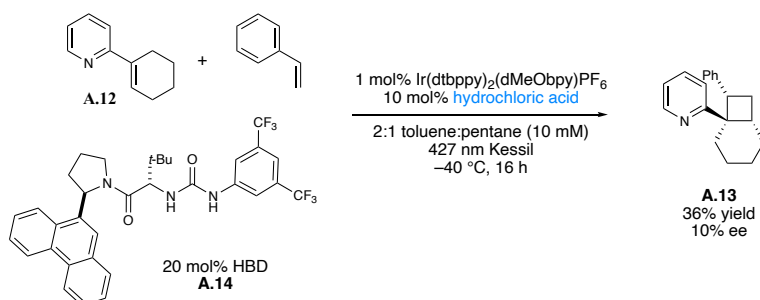
## A.2 Preliminary Results

From the data in Chapter 2, we knew productive [2+2] reactivity was observed with catalytic quantities of trifluoroacetic acid (TFA) instead of a CPA in the titular transformation. Several racemic reactions were performed with TFA in Chapter 2. In addition, a small screen of achiral Brønsted acids indicates that productive reactivity to **A.13** is observed for two additional acids (Table A.1).

Table A.1 Desired [2+2] Reactivity with Different Achiral Brønsted Acids



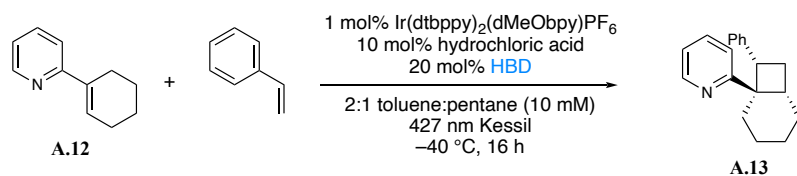
This observation was promising. We thought this would enable independent optimization of the pKa of the achiral acid based on its identity while using the same chiral hydrogen bond donor scaffold. We tested our key hypothesis by adding both an achiral Brønsted acid and a chiral hydrogen bond donor **A.14** to our previously identified standard reaction conditions in place of a CPA. To our delight, using 10 mol% hydrochloric acid, we afforded the desired cycloadduct **A.13** in a modest enantiomeric excess (ee) and yield (Scheme A.2).



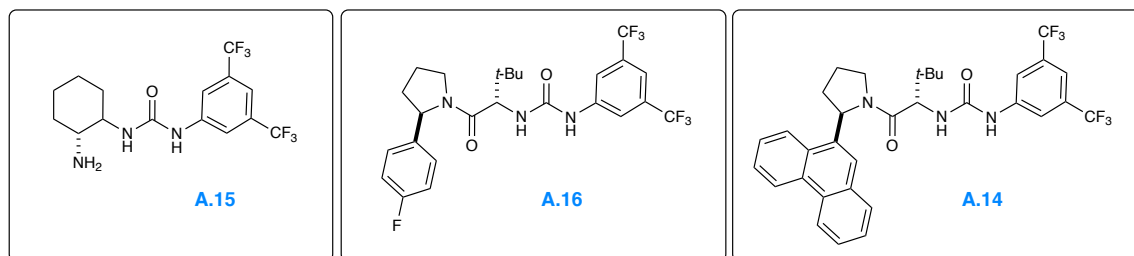
Scheme A.2 Initial Result Showing Proof-of-Concept Enantioselective Cycloaddition.

Using HCl as a representative achiral Brønsted acid, we examined three common chiral hydrogen bond donor scaffolds (**A.14** – **A.16**) for an effect on the outcome of the reaction (Table A.2). Each chiral scaffold afforded the desired cycloadduct. Entries 2–3 show catalytic Brønsted acid turnover indicated by the modest yields in the mid 30%. However, while using HCl as the acid, the enantioselectivity of the product **A.13** remained low, only achieving 10% ee.

Table A.2 Preliminary HBD Screen using HCl as the Achiral Brønsted Acid.

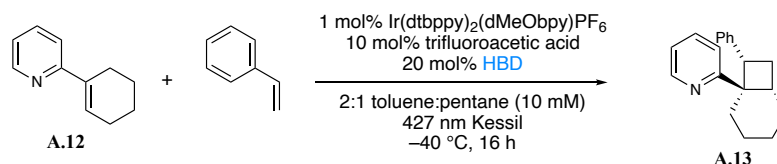


entry	HBD	% yield	% ee
1	<b>A.15</b>	5	6
2	<b>A.16</b>	34	7
3	<b>A.14</b>	36	10

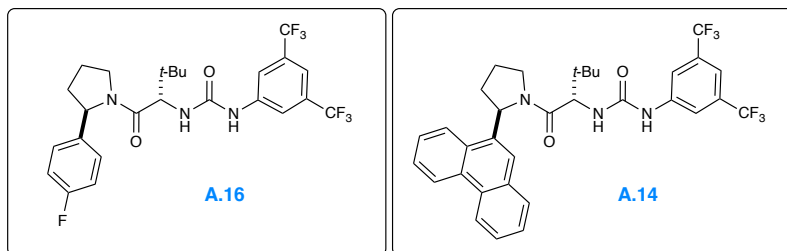


As expected, changing the identity of the achiral Brønsted acid influences the selectivity of the reaction. Use of TFA with the same chiral hydrogen bond donors increases the product enantioselectivity up to 28% ee in our preliminary results (Table A.3).

Table A.3 Preliminary HBD Screen using TFA as the Achiral Brønsted Acid.



entry	HBD	% yield	% ee
1	<b>A.16</b>	33	17
2	<b>A.14</b>	35	28



These data show turnover for all three catalysts in the reaction based on the yields in the mid 30% and the ee up to 28%. These preliminary results show great promise for the optimization of a highly selective, tri-catalytic, chiral hydrogen bonding activation of vinyl pyridines for enantioselective [2+2] photocycloaddition reactions.

### A.3 Future Directions

A full reaction optimization will be required to afford the desired cycloadduct in synthetically useful yields and enantioselectivity. Additionally, we are interested if this tri-catalytic system has the same cooperative stereinduction effect with the chiral [Ir] photocatalyst. This importance mechanistic distinction will be simple to discern by subjecting the optimized reaction

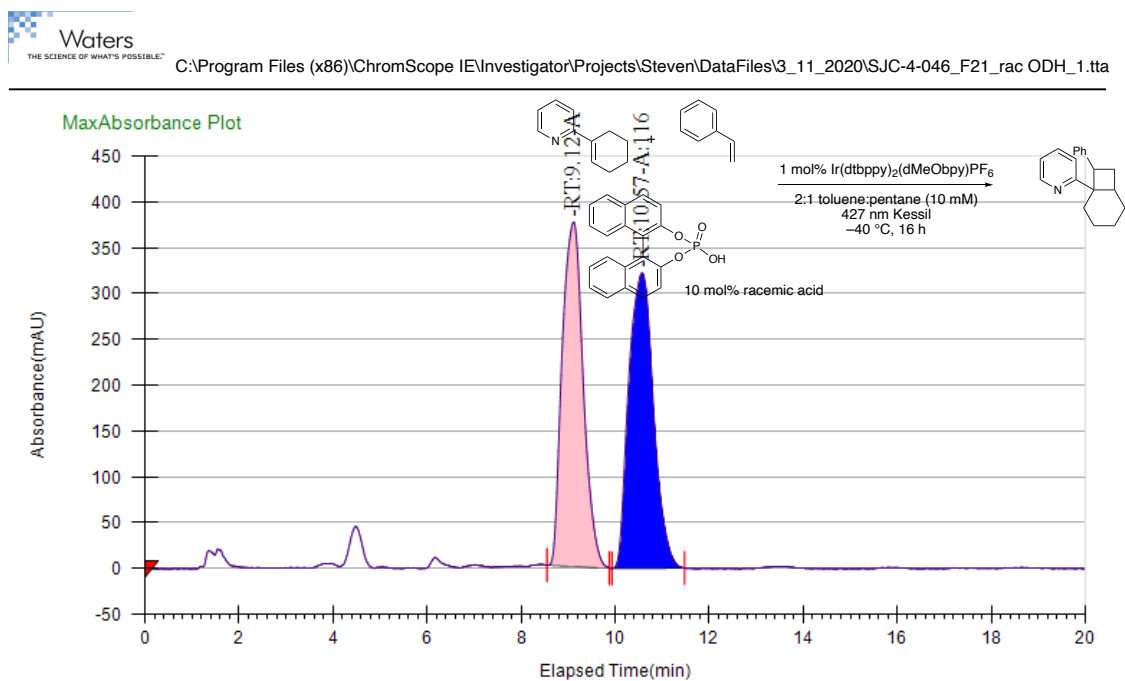
to both enantiopure [Ir] photocatalysts to observe any differences in the rate or the selectivity of the photocycloaddition.

We hypothesize this tri-catalytic system is more modular than the previously optimized CPA reaction in Chapter 2. Therefore, we hope to extend the reaction scope beyond vinyl pyridine substrates. We hope to target Brønsted basic substrates including vinyl imidazoles, vinyl pyrazoles, vinyl pyrazines, and vinyl quinolines. Because these chiral hydrogen bond donor catalysts are a privileged scaffold for ground state transformations, we hypothesize these catalysts may be equally effective for a variety of excited state transformations. This platform may be promising beyond cycloadditions, including rearrangements and other acid catalyzed photochemical reactions.



## A.4 Supporting Information

## A.4.1 SFC traces



## General Information

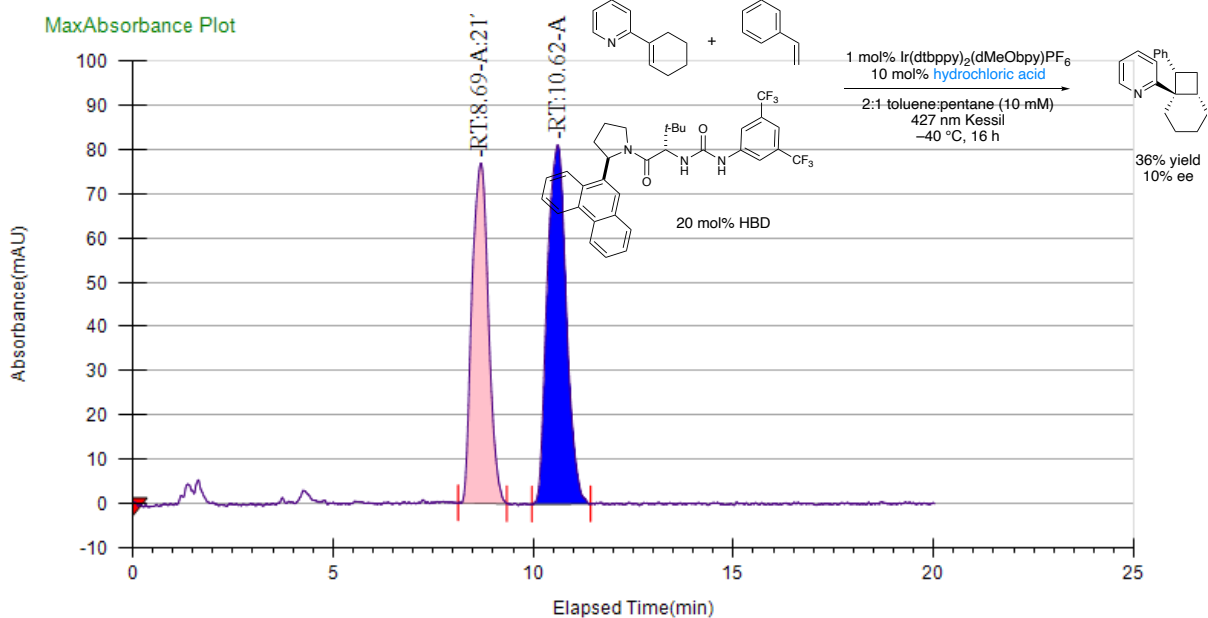
Log Author	Log Date	Report By	Report Date	Notes
Administrator	3/11/2020 2:05:12 PM	Administrator	3/11/2020	

## Run Information

Instrument Method	Inj. Vol.	Solvent	Column	Sample	Well Location	Temp. (C)	Flow (g/min)	% Modifier	Pressure (Bar)
5%IPA-20min	20 uL	IPA	Column 1	SJC-4-046_F21_rac	12F	35	3	5	100

## Peak Information

Peak No	% Area	Area	Ret. Time	Height	Cap. Factor
1	49.7424	11563.1224	9.12 min	375.897	0
2	50.2576	11682.8778	10.57 min	322.1577	0



### General Information

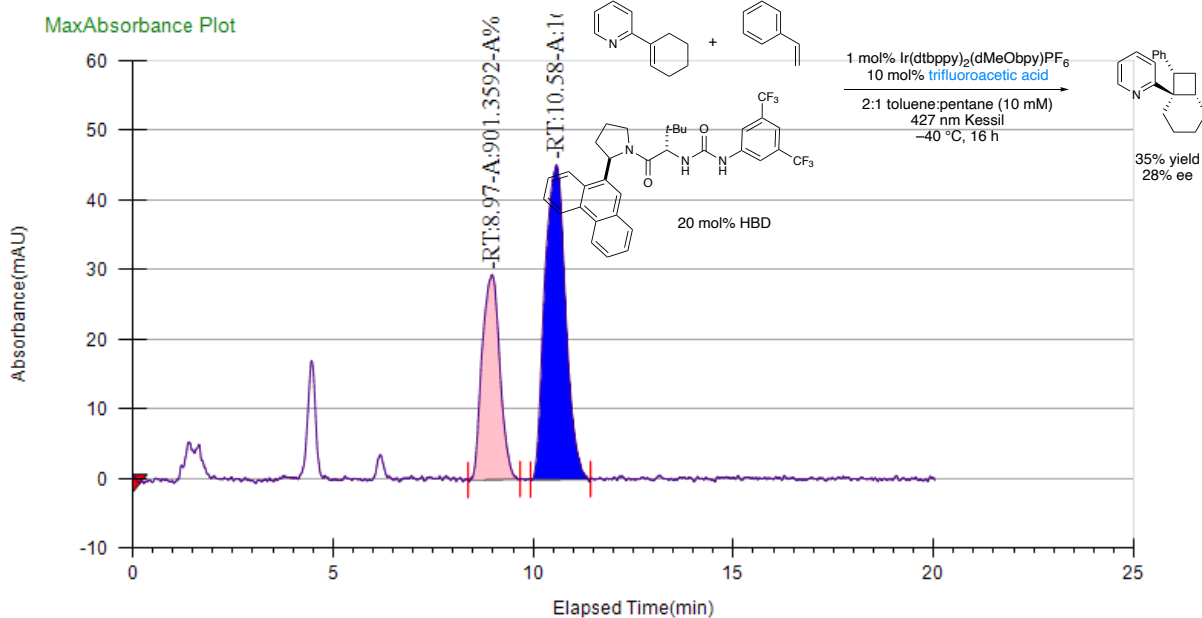
Log Author	Log Date	Report By	Report Date	Notes
Administrator	9/3/2019 1:38:13 PM	Administrator	9/3/2019	

### Run Information

Instrument Method	Inj. Vol.	Solvent	Column	Sample	Well Location	Temp. (C)	Flow (g/min)	% Modifier	Pressure (Bar)
5%IPA-20min	20 uL	IPA	Column 1	SJC-3-071_F16	18F	35	3	5	100

### Peak Information

Peak No	% Area	Area	Ret. Time	Height	Cap. Factor
1	44.8731	2176.1922	8.69 min	76.7439	0
2	55.1269	2673.47	10.62 min	81.1459	0



### General Information

Log Author	Log Date	Report By	Report Date	Notes
Administrator	9/14/2019 5:15:35 PM	Administrator	9/16/2019	

### Run Information

Instrument Method	Inj. Vol.	Solvent	Column	Sample	Well Location	Temp. (C)	Flow (g/min)	% Modifier	Pressure (Bar)
5%IPA-20min	20 uL	IPA	Column 1	SJC-3-089_F15	12F	35	3	5	100

### Peak Information

Peak No	% Area	Area	Ret. Time	Height	Cap. Factor
1	35.8011	901.3592	8.97 min	29.4497	0
2	64.1989	1616.3237	10.58 min	45.2313	0

## A.5 References

- 
- <sup>141</sup> Select reviews include: (a) Rueping, M.; Kuenkel, A.; Atodiresei, I. Chiral Brønsted acids in enantioselective carbonyl activations – activation modes and applications. *Chem. Soc. Rev.* **2011**, *40*, 4539–4549. (b) Rahman, A.; Lin, X. Development and application of chiral spirocyclic phosphoric acids in asymmetric catalysis. *Org. Biomol. Chem.* **2018**, *16*, 4753–4777. (c) Maji, R.; Mallojjala, S. C.; Wheeler, S. E. Chiral phosphoric acid catalysis: from numbers to insights. *Chem. Soc. Rev.* **2018**, *47*, 1142–1158.
- <sup>142</sup> Parmar, D.; Sugiono, E.; Raja, S.; Rueping, M. Complete Field Guide to Asymmetric BINOL-Phosphate Derived Brønsted Acid and Metal Catalysis: History and Classification by Mode of Activation; Brønsted Acidity, Hydrogen Bonding, Ion Pairing, and Metal Phosphates. *Chem. Rev.* **2014**, *114*, 9047–9153.
- <sup>143</sup> Fu, Z.; Cao, X.; Hao, G.; Shi, Q.; Cai, H. Synthesis of (±)-3,3'-diphenyl-2,2'-binaphthol via different routes using Pd and Ni as catalyst respectively. *Chemical Papers* **2021**, *75*, 831–836.
- <sup>144</sup> (a) Miyaura, N.; Suzuki, A. Palladium-Catalyzed Cross-Coupling Reactions of Organoboron Compounds. *Chem. Rev.* **1995**, *95*, 2457–2483. (b) Cox, P. A.; Reid, M.; Leach, A. G.; Campbell, A. D.; King, E. J.; Lloyd-Jones, G. C. Base-Catalyzed Aryl-B(OH)<sub>2</sub> Protodeboronation Revisited: From Concerted Proton Transfer to Liberation of a Transient Aryl Anion. *J. Am. Chem. Soc.* **2017**, *139*, 13156–13165.
- <sup>145</sup> For select examples, see: (a) Xu, H.; Zuend, S. J.; Woll, M. G.; Tao, Y.; Jacobsen, E. N. Asymmetric Cooperative Catalysis of Strong Brønsted Acid-Promoted Reactions Using Chiral Ureas. *Science* **2010**, *327*, 986–990. (b) Wendlandt, A. E.; Vangal, P.; Jacobsen, E. N. Quaternary Stereocenters via an enantioconvergent catalytic S<sub>N</sub>1 reaction. *Nature* **2018**, *556*, 447–451. (c) Klausen, R. S.; Kennedy, C. R.; Hyde, A. M.; Jacobsen, E. N. Chiral Thioureas Promote Enantioselective Pictet–Spengler Cyclization by Stabilizing Every Intermediate and Transition State in the Carboxylic Acid-Catalyzed Reaction. *J. Am. Chem. Soc.* **2017**, *139*, 12299–12309. (d) Ford, D. D.; Lehnerr, D.; Kennedy, C. R.; Jacobsen, E. N. On- and Off-Cycle Catalyst Cooperativity in Anion-Binding Catalysis. *J. Am. Chem. Soc.* **2016**, *138*, 7860–7863. (e) Banik, S. M.; Levina, A.; Hyde, A. M.; Jacobsen, E. N. Lewis acid enhancement by hydrogen-bond donors for asymmetric catalysis. *Science* **2017**, *358*, 761–764.